UNIVERSITÉ DE STRASBOURG

ÉCOLE DOCTORALE 182

[UMR 7504]

THÈSE présentée par :

Mathieu LAMBLIN

soutenue le : **28 Novembre 2024**

pour obtenir le grade de : **Docteur de l'université de Strasbourg**

Discipline / Spécialité : Sciences Physiques

Quantum Spintronic Energy Harvesters

THÈSE dirigée par :

Mr. BOWEN Martin	Dr, IPCMS, Université de Strasbourg

RAPPORTEURS :

Mme. HAACK Géraldine	Dr, Université de Genève
Mr. DROUHIN Henri-Jean	Dr, Ecole polytechnique, Institut Polytechnique de Paris

---

AUTRES MEMBRES DU JURY :

Mr. JAFFRES Henri	Dr, Laboratoire Albert Fert, CNRS, Thales
Mr. HUARD Benjamin	Pr, Ecole Normale Supérieure de Lyon
Mr. COUET Sébastien	Dr, Interuniversity Microelectonics Center
Mr. ANSERMET Jean-Philippe	Pr, Ecole Polytechnique Fédérale de de Lausanne

Aperçu

Titre : Récolte d'énergie par les moteurs quantiques spintroniques

Mots Clés : Spintronique, Thermodynamique Quantique, Jonctions Magnétiques Tunnel, Démon de Maxwell, Boites Quantiques, Fluctuations Quantiques, Mesure Quantique, Intrication, Cohérence Quantique, Électronique Stochastique, Blocage de Coulomb, Magnétorésistance, Memristance.

Résumé : Cette thèse a pour but d'apporter des éléments de compréhension sur le fonctionnement des moteurs quantiques spintroniques. Le moteur quantique spintronique est un dispositif novateur qui a récemment présenté la génération spontanée d'un courant électrique associé à une tension à vide et semble donc générer une puissance électrique sans apport externe d'énergie. Ce comportement contre intuitif qui semble aller à l'encontre de la seconde loi de la thermodynamique reste encore inexpliqué sur le plan théorique et mérite que les expériences soient reproduites et développées afin de confirmer cette génération d'énergie et d'identifier les mécanismes à l'oeuvre qui permettent l'émergence de ce phénomène. L'objectif de cette thèse est donc double. D'abord, pour le volet expérimental, l'enjeu était de répéter des expériences de magnéto-transport sur de nouvelles jonctions tunnel MgO présentant des impuretés de carbone dans le but d'identifier les signatures électroniques déterminantes pour le fonctionnement du moteur. Puis, pour le volet théorique, le but était de proposer des modèles permettant de rendre compte de la génération d'énergie, en identifiant notamment les ressources hors-équilibre utilisées par le dispositif afin d'assurer la production constante d'énergie dans le cadre des limites thermodynamiques.

Le manuscrit est divisé en trois parties. La première partie consiste en une revue de l'état de l'art relatif à la fois à la spintronique et aux moteurs quantiques en vue d'introduire le moteur spintronique et son fonctionnement. Le Chapitre 1 rend compte des fondations de la physique décrivant le transport spintronique au travers des jonctions magnétiques tunnel. Le Chapitre 2 décrit les bases de la thermodynamique quantique, qui apparaît comme le cadre adéquat à la description fine des ressources consommées par le moteur. Le Chapitre 3 fait état des principales pistes de recherche en cours concernant le développement à la fois théorique et expérimental des moteurs quantiques. Enfin, en s'appuyant sur les concepts décrits dans ces trois mises en bouche, le Chapitre 4 expose l'architecture du moteur spintronique, les résultats expérimentaux obtenus précédemment sur ces dispositifs et les idées générales qui aspirent à expliquer la génération d'énergie permise par ce moteur.

La seconde partie est consacrée aux expériences réalisées pour ce travail de thèse. Le Chapitre 5 présente brièvement les méthodes expérimentales utilisées pour la fabrication et l'analyse des échantillons étudiés. Le Chapitre 6 dévoile les résultats des expériences et montre comment les jonctions magnétiques tunnel étudiées peuvent servir de système de stockage d'information. Le Chapitre 7 discute de l'interprétation de ces résultats et identifie les mécanismes atomiques à l'origine des signaux électroniques observés lors des expériences.

La troisième partie est dédiée aux travaux théoriques effectués en vue de comprendre le fonctionnement des moteurs spintronique. Le Chapitre 8 propose un modèle quantique du

transport au travers d'impuretés atomiques localisées dans la barrière isolante de jonctions ferromagnétiques qui prédit correctement la puissance délivrée par le moteur spintronique alimenté naturellement par une différence de potentiel de spin. Le Chapitre 9 établit ensuite un modèle diffusif mésoscopique dans lequel une diode de spin permet de rectifier les fluctuations thermiques du courant pour produire de la puissance et de récolter l'énergie du champ magnétique d'interface maintenu par la non-colinéarité de l'aimantation des deux électrodes ferromagnétiques. Puis le Chapitre 10 présente un modèle électronique macroscopique qui rend compte de la génération d'énergie permise par deux diodes de spin connectées à des réservoirs d'aimantation différentes. Enfin le Chapitre 11 discutent des perspectives qu'ouvrent le présent travail de recherche et esquisse les pistes à suivre pour répondre aux questions qui restent en suspens.

L'Appendice A1 recueille des résultats d'expérience additionnels utilisés pour supporter l'interprétation des signatures électroniques avancées au Chapitre 7. L'Appendice A2 contient le détail des calculs nécessaires à l'établissement de la théorie du moteur spintronique quantique présentée au Chapitre 8. L'Appendice A3 est rempli de données de simulation supplémentaires servant de support à la preuve numérique du fonctionnement du moteur quantique développé au Chapitre 8.

Outline

Title: Quantum Spintronic Energy Harvesters

Keywords: Spintronics, Quantum Thermodynamics, Magnetic Tunnel Junctions, Maxwell's Demon, Quantum Dots, Quantum Fluctuations, Quantum Measurement, Quantum Entanglement, Quantum Coherence, Stochastic Electronics, Coulomb Blockade, Magnetoresistance, Memristance.

Outline : This thesis aims at bringing new elements towards the understanding of the inner workings of quantum spintronic engines. The quantum spintronic engine is a cutting edge device which recently behaved as an electrical current generator featuring a built-in voltage such that it delivers a constant power output without requiring any external energy input. This counter-intuitive result which seems to go against the second law of thermodynamics remains unexplained on the theoretical footing and deserves additional experiments to reproduce and improve this result so that the mechanisms responsible for this energy generation be identified. The objective of this thesis is thus double. First, for the experimental part, the stake is to repeat the magneto-transport experiments on new MgO magnetic tunnel junctions containing carbon impurities in order to identify the electronic signatures that are required for the engine to work. Then, for the theoretical part, the goal is to propose different models able to explain this active behavior and in particular identify the non-equilibrium resources used by the device to produce a constant energy output within the limits of thermodynamics.

The manuscript is divided into three parts. The first part gives an overview of the state-of-the-art related to both spintronics and quantum thermodynamics in order to introduce the spintronic engine and its inner mechanisms. Chapter 1 introduces the underlying physics that govern spintronic transport across magnetic tunnel junctions. Chapter 2 describes the basis of quantum thermodynamics, which appears as the adequate framework to study the resources consumed by the engine. Chapter 3 presents the main ongoing research leads regarding both the theoretical and experimental development of quantum engines. Chapter 4 showcases the architecture of the spintronic engine, the previous experimental results obtained on those devices and the general ideas that explains the energy generation observed in this engine.

The second part focuses on the experiments performed during this laboratory thesis. Chapter 5 briefly presents the experimental methods used to fabricate and analyze the samples studied in this work. Chapter 6 reveals the results of the experiments and shows how the magnetic tunnel junctions can be used as an information storage device. Chapter 7 discusses the interpretation of these results and identifies the atomic mechanisms that generate the observed electronic signals.

The third part is dedicated to the theoretical work performed in order to understand the electrical power generation of spintronic engines. Chapter 8 studies a quantum model of transport across atomic impurities localized inside the insulating barrier of ferromagnetic tunnel junctions and correctly predicts the output delivered by the spintronic engine, structurally powered by a spin potential. Chapter 9 proposes a diffusive mesoscopic model in which a spin diode is rectifying current fluctuations to pro-

duce electronic power and harvests the magnetic energy stored in the vicinity of an interface, self-sustained by the magnetization difference between the two electrodes. Then, Chapter 10 presents a macroscopic electronic model that shows the generating ability of a device consisting of two spin diodes connected to two spin reservoirs with different magnetizations. Finally, Chapter 11 discusses the perspectives opened by this research work and addresses the leads to answer the questions that remain after this work.

Appendix A1 gathers additional experimental results used to support the interpretation of the electronic signatures presented in Chapter 7. Appendix A2 contains the calculation details necessary to establish the atomic theory of the quantum spintronic engine presented in Chapter 8. Appendix A3 is filled with simulation data supporting the numerical proof of energy generation of the model presented in Chapter 8.

Résumé

Les moteurs quantiques génèrent beaucoup d'entrain car ils promettent de réaliser des sources d'énergie abondantes, denses, microscopiques, non-intermittentes, économes en matériaux et respectueuses de l'environnement. Cette thèse tente d'abord de reproduire les expériences ayant démontré la récolte d'énergie par un moteur spintronique reposant sur des jonctions ferromagnétiques tunnel contenant des impuretés magnétiques sujettes à des fluctuations électroniques. Cette étude n'a pas permis de mettre en évidence des dispositifs actifs, néanmoins les jonctions considérées ont présenté des caractéristiques physiques remarquables pour le stockage de l'information.

Dans une seconde partie, ce travail propose trois modèles théoriques qui permettent d'expliquer l'origine de la génération d'énergie observée dans ces dispositifs. Le premier est un modèle quantique microscopique dans lequel une chaîne de spin connectée à deux réservoirs électroniques polarisés et prédit correctement l'ordre de grandeur de la puissance mesurée dans ces moteurs. Le second est un modèle phénoménologique mésoscopique qui repose sur une diode de spin rectifiant les phénomènes magnétiques localisés à l'interface entre deux électrodes ferromagnétiques désalignées. Et le troisième est un modèle électronique macroscopique qui étudie la caractéristique de deux diodes de spin orientées dans le sens inverse et connectées à deux réservoirs d'aimantations opposées.

Les conclusions similaires de ces trois approches montrent donc la possibilité de récolter l'énergie magnétique provenant de l'alignement progressif de deux électrodes ferromagnétiques grâce aux propriétés d'une interface microscopique rectifiant le transport spintronique. Cette recherche ouvre la voie à de nouvelles expériences en vue d'étudier le micromagnétisme de ces interfaces et posent de nouvelles questions théoriques quant à l'exploitation de phénomènes quantiques non-linéaires hors équilibre pour développer de nouvelles sources d'énergie potentiellement illimitée.

Abstract

Quantum engines have attracted extensive research as they provide a glimpse of abundant, continuous, dense, microscopic, material-efficient, and environmentally friendly power sources. The first intent of this thesis is to reproduce the experiments that proved the concept of energy harvesting using a spintronic engine based on ferromagnetic tunnel junctions containing magnetic impurities undergoing electronic fluctuations. Although the present study does not report any active device, the considered junctions presented remarkable physical characteristics for information storage.

In a second part, this work proposes three theoretical models that explain the energy generation observed in these spintronic devices. The first is a microscopic quantum model in which a spin chain is connected to two spin-polarized electronic reservoirs and correctly predicts the magnitude of the output power measured in the experiments. The second one is a phenomenological mesoscopic model based on a spin diode rectifying the magnetic phenomena at the interface between two misaligned ferromagnetic electrodes. And the third one is an electronic macroscopic model which studies the characteristic of two spin diodes in the antiparallel configuration connected to two reservoirs with different magnetizations.

The concomitant conclusions of those three approaches thus show the possibility of harvesting the magnetic energy that originates from the slow alignment of two ferromagnetic electrodes due to the quantum properties of a microscopic interface able to rectify the spin current. This research paves the way to new experiments that aim at probing the micromagnetism of those interfaces and opens up to new theoretical questions regarding non-linear, out-of-equilibrium quantum phenomena which could be leveraged to develop new potentially unlimited energy sources.

« La nature, même dans le chaos, ne peut procéder autrement que régulièrement et selon l'ordre. »

Emmanuel Kant

Remerciements

J'aimerais commencer par remercier mon tuteur Martin Bowen pour son encadrement très bienveillant, libre, responsabilisant et toujours stimulant. J'ai beaucoup apprécié travailler avec toi sur ce sujet passionnant et je me sens ainsi très chanceux d'avoir pu bénéficier d'une si bonne relation constructive durant ces trois ans de thèse. Je m'estime heureux de toutes nos longues discussions où nos sensibilités souvent très proches ont pu s'enrichir de nos points de vue différents pour créer une alchimie très stimulante. J'espère que notre collaboration fructueuse pourra s'étendre au-delà de ce cadre.

Je dois ensuite remercier mes collègues doctorants pour avoir entretenu une ambiance studieuse et amicale tout au long de nos travaux. Merci à Quentin, Louis, Mohamed, Satakishi, Ankita, Valerius, Raj, José, Ashfaque et Talha pour votre compagnie et bien sûr pour tous les petits déjeuner de la cantine que vous avez pu me fournir !

J'adresse des remerciements tout particuliers à Véronique Werner en charge des missions pour sa gentillesse à toute épreuve, sa disponibilité et son efficacité dans la préparation des trajets.

Je remercie aussi tout le personnel de la plateforme STNano et les ingénieurs du DMONS pour l'aide précieuse qu'ils m'ont apportée durant mon travail en laboratoire. Merci à Benoit Gobaut, Sabine Siegwald, Romain Bernard, Hicham Majjad, Wolfgang Weber, Victor Da Costa, Loic Joly pour tout le support que vous m'avez fournis pour ces expériences et les formations que vous m'avez délivrées afin que je puisse manipuler en autonomie ces différents outils de pointe.

Puis, je tiens tout particulièrement à remercier Cyril Elouard pour ses nombreux conseils sur le plan théorique, ses commentaires toujours très avisés sur mon travail ainsi que pour ses lectures attentives de mon article et du présent manuscrit.

Je puis également remercier Eric Lutz et Franklin Rodrigues pour de stimulantes discussions qui m'ont permis de d'améliorer grandement la pertinence, la précision et l'impact de mon papier de recherche, ainsi que mon ancien professeur Jean-Eric Wegrowe qui m'a orienté vers la formulation d'un modèle spintronique phénoménologique.

Évidemment, cette thèse n'aurait pu voir le jour sans le soutien régulier de ma famille et de mes proches à qui je dédie toute mon affection, avec une attention toute particulière à ma voisine et partenaire de tout chemin Perrine Kretz.

Enfin, je remercie gracieusement l'Ecole Polytechnique pour son financement au travers de la bourse AMX sans quoi ce travail n'aurait pu être possible.

Contents

List of Figures

List of Tables

Liste des abréviations

AC Alternative Current. 14

ADC Analog-to-Digital Converters. 10

a.e. almost everywhere. 177

AES Auger Electron Spectroscopy. 89

AFM Anti-ferromagnetic. 25, 27, 86, 97

AI Artificial Intelligence. 3

ANE Anomalous Nernst Effect. 53

AP Anti-parallel. 21, 78, 97, 103, 104, 114–117, 163, 164, 197–199

bcc body-centered cubic. 86

CMOS Complementary Metal Oxide Semi-conductor. 7

CPP Current-perpendicular-to-plane. 11

CPTP Completely Positive and Trace preserving. 31

DC Direct Current. 14

DFT Density Functional Theory. 12, 27, 33, 81

DMONS Département Magnétisme des Objets NanoStructurés. ix

DOS density of states. 79

e.g. *exempli gratia.* 10, 50, 52, 62, 63, 129

EQD Environmental Quantum Dot. 110–112

FM Ferromagnetic. 21, 26–28, 74, 76, 79–81, 86

FP Fokker-Planck. 174, 181

GKSL Gorini–Kossakowski–Sudarshan–Lindblad. 33

GMR Giant Magnetoresistance. 7, 11

HOMO highest occupied molecular orbital. 24

ICFP International Center for Fundamental Physics. 1

i.e. *id est*. 29, 60, 75, 77, 79, 80, 99, 109, 112, 115, 123, 131, 134, 136, 168, 173, 199

IETS Inelastic Electron Tunneling Spectroscopy. 25

iff *if and only if*. 152, 159, 161

IJL Institut Jean Lamour. 85

IoT Internet of Things. 3

IPCMS Institut de Physique et de Chimie des Matériaux de Strasbourg. 1, 87, 92, 97

ISHE Inverse Spin Hall Effect. 52

L Left. 123, 125

LUMO lowest unoccupied molecular orbital. 24

ML *monolayer*. 85, 86

MR Magnetoresistance. 97

MRAM Magnetic Random Access Memory. 10

MTJ Magnetic Tunnel Junction. 7–14, 17, 20–23, 52, 73, 74, 85, 87–89, 91–93, 107, 114–117, 197–199

NBE Neutral Beam Etching. 88–90

NDR Negative Differential Resistance. 13, 14, 20, 141

NGEF Non-Equilibrium Green Function. 33

NRG Numerical Renormalization Group. 15

OSC Organic semiconductors. 23–25

P Parallel. 21, 23, 78, 97, 103, 104, 114–117, 163, 164, 166, 197–199

Pc Phthalocyanines. 24, 25

PE Particle Exchange. 50

PM Paramagnetic. 74–76, 79, 80

PMA Perpendicular Magnetic Anisotropy. 22

PSB Pauli Spin Blockade. 19, 20

QD Quantum Dot. 14, 16, 17, 20, 51, 59, 111, 122–129, 131, 132, 134–137, 207, 223, 228–230

R Right. 123, 125

ReRAM Resistive Random Access Memory. 12

RNG Random Number Generator. 10

RS Resistive Switching. 12, 13

SDSE Spin-dependent Seebeck Effect. 52

SET Single-Electron Transistor. 15–18

SOC Spin-Orbit Coupling. 22

SOT Spin-Orbit Torque. 10

SSE Spin Seebeck Effect. 52, 53

STM Scanning Tunneling Microscopy. 15, 25

STS Scanning Tunneling Spectroscopy. 15, 25

STT Spin-Transfer Torque. 10, 12, 13

TEG Thermoelectric Generator. 50–52

TMR Tunnel Magnetoresistance. 7–12, 16, 17, 21–25, 72, 74, 86, 98, 99, 104, 115, 116, 199

TQD Transport Quantum Dot. 110–112

UHV Ultra High Vacuum. 88, 89, 92

w.r.t. With respect to. 126

WS Working Substance. 35, 61, 62, 77–80, 121, 122, 127, 128

ZBA Zero Bias Anomaly. 16, 104

Avant-propos

Cette thèse est le prolongement naturel du stage de fin d'étude que j'ai effectué à l'IPCMS dans le cadre de la quatrième année de formation d'ingénieur de l'Ecole Polytechnique, passée au sein du master ICFP de l'Institut Polytechnique de Paris, hébergé par l'Ecole Normale Supérieure.

Étant très concerné par les perspectives de déclin civilisationnel dans cette période post-moderne caractérisée par une société en crise permanente, j'ai un intérêt très fort pour tout ce qui concerne les problématiques environnementales. Convaincu que le plus grand défi de l'humanité sera de faire face à la raréfaction des ressources et à la destruction des écosystèmes dans un monde au climat instable et soulevé par des conflits géopolitiques d'intensités grandissantes, le sujet de l'adaptation à des conditions matérielles de vie dégradées est pour moi central si nous voulons ensemble maintenir notre confort et garantir la stabilité de notre organisation collective. Face à ces enjeux colossaux, je me suis fixé comme objectif de vie la quête de nouvelles façons innovantes et résilientes de produire et de manipuler l'énergie. Cette aspiration, en conjonction avec mon profond désir d'explorer les mystères du monde quantique m'ont de suite mené vers ce projet, dès le début de mon master. Parmi tous les sujets de physique fondamentale ou appliquée qui se proposaient à moi lors de mes études, aucun autre ne me paraissait s'aligner aussi bien avec à la fois ma quête de sens et mon attrait pour la plus contre intuitive des physiques. C'est donc tout naturellement que je me suis orienté très tôt vers ce projet qui s'accorde parfaitement avec mes valeurs morales en ce qu'il promet de réaliser à terme des dispositifs qui pourraient être au cœur d'une prochaine révolution industrielle.

Ayant beaucoup apprécié le travail de recherche effectué lors du stage, j'ai alors cherché un financement pour continuer sur ce même sujet, et j'ai eu la chance de voir mon dossier retenu pour l'obtention d'une bourse au travers du programme AMX de l'Ecole Polytechnique. C'est ainsi que j'ai été recruté initialement afin d'effectuer un travail expérimental sur une implémentation des moteurs quantiques spintroniques. Mon désir initial était effectivement de mener des expériences en laboratoire car j'avais le désir de me détacher des écrans, des équations et du monde des idées après ces longues années d'études afin de pouvoir enfin décoller de ma chaise et travailler avec mes mains pour avoir un impact matériel dans le monde réel. L'objectif initial était donc de fabriquer des jonctions ferromagnétiques tunnel oxide présentant des impuretés magnétiques et des interfaces polarisées puis d'analyser leur réponse électronique et magnétique en vue de reproduire pour valider les résultats d'expériences de mes prédécesseurs et de gagner plus d'intuitions sur leurs structures et leur fonctionnement afin d'améliorer la reproductibilité et d'orienter la recherche

vers l'établissement de dispositifs plus performants.

Après plus d'un an à travailler sur ce volet expérimental, je me suis alors trouvé face à plusieurs difficultés. D'une part, bien que les dispositifs étudiés présentaient des caractéristiques intéressantes à la fois en termes fondamentaux et applicatifs, encore peu répertoriés dans la littérature, je ne parvenais pas à observer l'effet de génération d'énergie recherché et je commençais alors à me décourager face aux centaines d'heures de travail que je mettais dans la fabrication et l'analyse de ces échantillons et qui se traduisaient souvent par des échecs : lithographies défaillantes, gravures incertaines, connexions au circuit électrique hasardeuses et fastidieuses pour finir avec l'essentiel des jonctions sans intérêt : soit ohmiques, soit en circuit ouvert. Au début de ma deuxième année de thèse, alors que je commençais à me questionner sur ce projet de laboratoire, le compresseur utilisé pour les expériences de transport a cessé de fonctionner, ce qui a interrompu mon travail expérimental, pour une durée indéterminée estimée à au moins quelques mois. J'avais alors déjà commencé à réfléchir à un modèle afin d'expliquer le fonctionnement du moteur, en lien avec tous les articles de recherche sur les machines thermiques quantiques que j'avais parcourus jusqu'à lors. L'impossibilité pour moi de continuer les expériences m'a donc amené à me concentrer sur l'identification théoriques des ressources nécessaires au moteur et à la mise en équation de ces dispositifs. Il s'est ensuite rapidement avéré que je tenais un modèle quantique intéressant, novateur et prometteur qui pourrait permettre d'expliquer les résultats et, avec mon tuteur, nous avons donc naturellement convenu que mon sujet de thèse se réorienta entièrement sur la théorie relative à ces moteurs quantiques spintroniques.

Je me suis dès lors attelé à développer en premier le modèle quantique microscopique que je présente dans ce manuscrit et qui montre comment récupérer l'énergie de la cohérence quantique induite par thermalisation au moyen de la mesure quantique. Étant le seul théoricien dans une équipe principalement formée d'expérimentalistes, je me suis alors trouvé face à un manque d'interlocuteurs aptes à évaluer, critiquer et valider ou corriger mon travail. Je me suis alors tourné vers Cyril Elouard de l'Université de Nancy, qui m'a alors beaucoup aidé pour affiner mon modèle microscopique jusqu'à la publication de mon article sur le sujet.

Après ce premier travail, je me suis alors rendu compte de la difficulté et de l'importance de lier les différentes communautés de spintronique et de thermodynamique quantique entre elles afin de pouvoir fédérer autour de ce sujet que je juge crucial et j'ai donc entrepris de formuler un modèle plus simple qui pourrait permettre de simplifier mon discours afin de le rendre plus abordable auprès de chacune de ces deux branches. J'ai alors eu l'idée du modèle électronique macroscopique reposant sur deux spin diodes branchées en parallèles et étudié grâce au formalisme de thermodynamique stochastique. Suite à cette première ébauche, j'ai alors pris conseil auprès de Jean-Eric Wegrowe de l'Ecole Polytechnique qui m'a orienté vers le troisième modèle que je présente basé sur une approche phénoménologique essentiellement spintronique.

Finalement, je m'estime fier du travail que j'ai pu réaliser tout au long de cette thèse transdisciplinaire thèse très riche qui m'a permis de gagner une expertise certaine dans des branches très variées de la physique tout en m'initiant à un premier travail expérimental d'envergure.

Introduction

The rapid advancement in fields like communication, computing, transportation, clean energy, among others, is largely driven by the transformative impact of semiconductors. These materials, often dubbed as the nerve center of modern electronics, enable the creation of progressively complex products at reduced costs. Examples of these advancements include neuromorphic computing, Internet of Things (IoT), energy harvesting devices, automation, energy-efficient sensors, robotics, and artificial intelligence (AI). These technologies have the potential to drastically change society. Among these emerging fields, spintronics, an area focusing on electron spin-based electronics, offers significant support.

In particular, recent progress has showcased the ability to leverage spintronics as a powerful platform to develop new kinds of energy devices, either behaving as engines that harvest the surrounding thermal [1, 2, 3, 4] or electromagnetic radiations [4, 5, 6], or as batteries that store energy as a form of magnetic structures embedded within the devices [7, 8, 9].

In parallel, the emerging field of quantum thermodynamics has risen from the possibility to design quantum thermal machines [10], able to produce work at the nanoscale by harnessing additional resources that are specific to the quantum world such as quantum coherence [11, 12, 13] or quantum measurements [14, 15, 16].

From this perspective, A. Auffèves, one of the leaders in the field, recently argues [17] that quantum technologies must urgently plan for the creation and structuration of a transverse quantum energy initiative, connecting quantum thermodynamics, quantum information science, quantum physics, and engineering. Such an initiative is the only path towards energy-efficient, sustainable quantum technologies, and to possibly bring out an energetic quantum advantage.

In this context, my team at IPCMS is currently working on bridging the field of spintronics with quantum thermodynamics in the hope of designing groundbreaking technologies that challenges this issue of energy and our impact on the environment. Initially focused on building new spintronic information devices, the story behind my team's project began in 2019 [18] when the group found a surprising electrical behavior in a fairly standard magnetic tunnel junction, a device made with two ferromagnetic electrodes separated by a tunnel barrier. This junction behaved as an engine, generating a continuous electrical current and voltage at ambient temperature with no direct energy input.

Since then, the team has tried to reproduce those results in different setups and give thermodynamical explanations of this so-called *spintronic engine*. In particular, they achieved

to engineer a much more powerful device generating up to 100 nW of power (representing a 1000x increase compared to the original implementation) by using molecular instead of oxide magnetic tunnel junctions [19]. Although these experiments are exciting, much progress remains to be made in order to make these proof-of-principles a real technology and understand completely the physics behind these results.

The origin of such an active behavior remains largely unexplained yet, but several crucial ingredients have been highlighted. The architecture of the spintronic engine must be composed of three main elements: a pair of ferromagnetic electrodes, a barrier containing atomic centers magnetically oriented, and a spintronic selector at the interface between the ferromagnets and the barrier which acts as a spintronic filter mediating the interaction between the atomic centers and the electrodes.

To gain significant traction in the scientific community, the research first needs to be directed towards the development of systematic and reliable protocols that would facilitate the routine production of these spintronic engines. An accumulation of proofs and working devices would indeed be a convincing argument that such an abundant and dense energy source can be practically realized and is not a mirage originating from a faulty experimental setup. Secondly, a convincing description of the device operation is still lacking; importantly, according to the laws of thermodynamics, the resource, the fuel which the engine needs to consume in order to produce this electrical power has not been clearly identified yet. A comprehensive, consistent, economic framework able to explain the inner-working of the spintronic engine is therefore missing to demystify the results of the experiments and give predictive insights on the efficiencies of these machines so as to guide their conception.

The work presented in this thesis aims to address these two challenges. The original main objective was experimental, with a preliminary goal of first reproducing the experiments on oxide junctions and improving their reliability and fabrication process. Then, as new conceptual ideas were being investigated and integrated on the theory side, the interest shifted towards building minimalist models, with as few out-of-equilibrium assumptions as possible, able to quantitatively predict an active device delivering a sizable output power using ingredients of spintronics and quantum thermodynamics.

This manuscript is organized in three parts. In Part I, we present the concepts needed to understand the technical details of this work and review the science that led to the spintronic engine. In Part II, we report on the experimental results obtained on oxide junctions and in Part III, we develop three complementary approaches that describe the engine at different scales and reveal the essential features of the device which allow for its generative behavior.

Part I

State of the art

Chapter 1

Spintronic transport across Magnetic Tunnel Junctions

The electron spin, a quantum mechanical property, is a crucial aspect of quantum devices' functionality and underlines permanent magnetism. This has led to the development of a new branch of electronics known as spintronics, which operates based on the connection between spin degrees of freedom and electron charge, unlike conventional electronics which operate based on the motion and charge properties of electrons. Spintronics is also closely linked to magnetism. Recent advancements in the field of spintronics have the potential to impact key areas of information technology and microelectronics, including non-volatile memories, magnetic sensors, microwave devices, beyond-CMOS logic, and more. Spintronic devices promise to enhance the speed and storage capacity of devices and have the potential to bring quantum physics to application.

The discovery of "giant magnetoresistance" (GMR) by Albert Fert [20] and Peter Grünberg [21] in 1988 is the origin of the development of spin-based electronics. This technology involves a mechanism called a spin valve, which controls current flow based on the magnetization direction of layers within a thin film stack. The GMR effect has been widely used in magnetic recording for computer hard drives, revolutionizing the data storage industry. The first commercial use of GMR-based sensor technology was by IBM in 1997, which released a hard disk drive with a storage capacity of 16.8 Gb. In 2007, Fert and Grünberg were awarded the Nobel Prize in Physics for their contributions [22].

Spintronics has evolved over time, and now hard disk read heads primarily employ tunneling magneto-resistance (TMR) instead of GMR. TMR devices are based on extremely thin insulating barriers, mere nanometers thick, placed between ferromagnetic electrodes. This thin insulator results in a spin-conserved tunneling of the electrons from one ferromagnetic element to another that is very sensitive to interface changes. These TMR devices are typically referred to as magnetic tunnel junctions (MTJs).

This Chapter first reviews the physics ofMTJs to see the typical behaviors one can obtain in magneto-transport experiments on those devices. This work focuses on two kinds of devices: MgO oxide junctions containing atomic impurities and molecular junctions based

on phthalocyanine molecules, which are considered as promising candidates to build spintronic engines. A particular emphasis will also be given on the properties of interfaces with a ferromagnetic metal as their fine tuning seems to be a crucial ingredient towards engineering powerful engines.

1.1 Tunneling Magnetoresistance in Magnetic Tunnel Junctions

1.1.1 Tunneling Magnetoresistance

Tunneling magnetoresistance (TMR) is a quantum mechanical phenomenon that describes the dependence of the resistance of the MTJ on the relative orientation of the magnetizations in the two ferromagnetic layers. When the magnetizations are parallel, the resistance is generally low, and when they are antiparallel, the resistance is generally high [23] (see Figure 1.1). This allows the MTJ to be switched between high and low resistance states. The magnitude of the TMR effect is measured by the ratio between the resistance in the parallel and the anti-parallel states. It is related to the spin polarization of the ferromagnetic electrodes, such that higher spin polarization leads to larger TMR ratios.

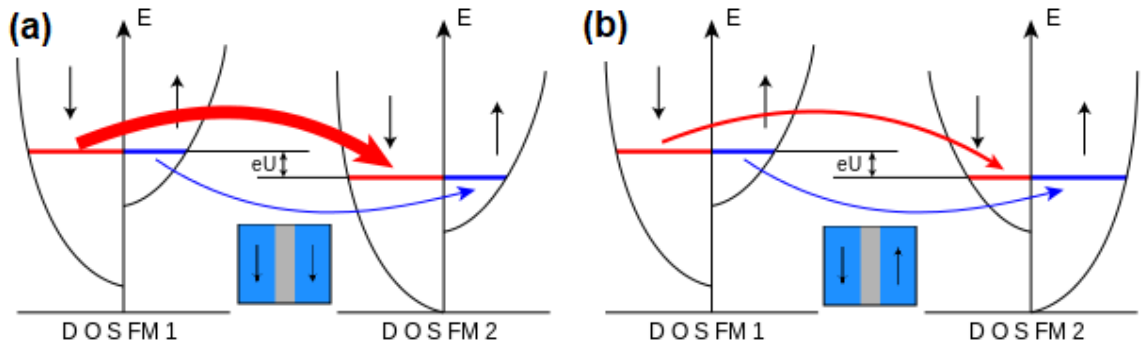

Figure 1.1: **Tunnel Magnetoresistance.** Sketch of the density of states of the left and right ferromagnetic electrodes in the parallel case in (a) and in the anti-parallel case in (b).

The Julliere model is a simple model used to estimate the magnitude of the TMR in MTJs. It is based on two main assumptions:

- The spin of electrons is conserved during the tunneling process. Tunneling of up-spin and down-spin electrons are independent processes, so the conductance occurs through two independent spin channels.

- The conductance for a particular spin orientation is proportional to the product of the effective density of states of the two ferromagnetic electrodes, which corresponds to the Fermi golden rule.

According to these assumptions, the TMR ratio can be expressed as:

$$TMR := \frac{R_{AP} - R_P}{R_P} = \frac{2P_1P_2}{1 - P_1P_2} \tag{1.1}$$

where R_P and R_{AP} are the resistances of the parallel and anti-parallel states, and P_1 and P_2 are the spin polarizations of the two ferromagnetic electrodes. The spin polarization is defined as $P = (N_\uparrow - N_\downarrow)/(N_\uparrow + N_\downarrow)$, where $N_\uparrow$ and $N_\downarrow$ are the densities of states at the Fermi level for majority and minority spins, respectively. The Julliere model provides a simple way to estimate TMR from the known values of spin polarization of the ferromagnetic electrodes obtained in experiments on superconductors. However, it does not take into account the details of the tunneling process and the properties of the insulating barrier, it does not accurately describe the magnetoconductance of free electrons tunneling through a barrier and the band electrons shows features not well described by any free electron picture [24, 25]. Henceforth, more sophisticated descriptions of spin-dependent tunneling like the Slonczewski model are generally needed [26, 25]. In the limit of thick barriers, this model gives an expression for TMR similar to Julliere's, but with a different definition of the spin polarization [27].

1.1.2 Experimental advances in Magnetic Tunnel Junctions

The first MTJ devices were introduced in 1995 by Moodera [28] and Miyazaki and Tezuka [29], who independently used amorphous alumina Al_3O_3 as barrier material. This produced a TMR amplitude of about 10% at room temperature. Efforts to improve the TMR magnitude involved enhancing the device interfaces with Al_3O_3 films to improve homogeneity and roughness and decrease defects. The major advancement in MTJs was the switch from an amorphous tunnel barrier (AlO_x) to a crystalline Magnesium Oxide (MgO) barrier layer which helped preserve the electron's orbital character, leading to higher TMR values [30, 31], with a present record of 600% TMR at 295 K [32].

Since then, MTJs have seen significant experimental advances in recent years:

- Ion beam etch processes have been used for forming MTJ structures, resulting in improved performance and reliability.
- Nanoscale skyrmions have been directly observed in CoFeB/MgO-based MTJ devices at room temperature [33].
- MTJs with amorphous AlO_x tunnel barriers have exhibited significant TMR ratios of nearly 100% at room temperature [34, 35].
- Synthetic antiferromagnet structures with the reference layer have been used to cancel stray magnetic fields in MTJs, mitigating their effect on device performance [36].

These advances in materials, fabrication techniques, and device architectures have led to improved performance, reliability, and energy efficiency of MTJs, enabling their use in a wide range of applications. Latest developments include:

- Magnetic Random Access Memory (MRAM): MTJs are the core storage elements in MRAM, a non-volatile memory technology that combines the speed of SRAM, density of DRAM, and non-volatility of flash memory [37, 38]. MRAM offers high-speed read/write, low power consumption, and unlimited endurance.

- Spin-Transfer Torque MRAM (STT-MRAM): MTJs can be switched on/off using a spin-polarized current flowing across the junction, enabling STT-MRAM which has higher density and lower power consumption compared to conventional MRAM [37, 38].

- Spin-Orbit Torque MRAM (SOT-MRAM): By utilizing spin-orbit torques generated by a current flowing across one of the MTJ electrodes, SOT-MRAM achieves ultrafast switching (sub-ns) of MTJs with narrow statistical distributions, which is promising for high-performance embedded memories [39, 40, 41, 42].

- Magnetic Sensors: The tunneling magnetoresistance effect in MTJs allows them to be used as highly sensitive magnetic field sensors, *e.g.* in hard disk read heads [38].

- Random Number Generators (RNGs): The stochastic switching behavior of superparamagnetic MTJs can be harnessed for true random number generation, useful in cryptography and probabilistic computing [37].

- Analog-to-Digital Converters (ADCs): MTJs exhibit a linear resistance response to applied voltage, enabling their use in high-resolution ADCs with low power consumption [37].

- Neuromorphic Computing: The tunable resistance states of MTJs can emulate the weighted connections in artificial neural networks for energy-efficient cognitive computing [37].

While MTJs have shown promise in various applications, overcoming limitations through advancements in materials, fabrication techniques, and device architectures is crucial for their widespread adoption in next-generation spintronic devices. Challenges involve:

- Achieving low dimensions and scalability: Maintaining bit stability while downscaling the magnetic volumes of MTJs is a challenge due to spontaneous switching of magnetization at smaller dimensions [43]. The present record holds for 2 nm lateral size junctions [44].

- Fabricating high-quality MTJs at extremely small scales is difficult. Long-term reliability and endurance: MTJs can suffer from reliability issues over time, such as degradation of the tunnel barrier, leading to a decrease in TMR ratio and device performance [45, 46, 47].

- Energy efficiency: While MTJs offer lower power consumption compared to some technologies, further improvements in energy efficiency are needed, especially for high-density memory and computing applications [48].

- Fabrication challenges: Achieving good quality MTJ structures with high TMR ratios requires precise control over the fabrication process, including the deposition of ultrathin tunnel barriers and control of interfacial properties [45, 48].

- Integration challenges: Integrating a large number of highly coherent MTJs with control and readout electronics is a fundamental challenge, especially for scaling up to practical applications [48].

- Addressing and switching challenges: Proper addressing of MTJs without disturbing neighboring cells and achieving reliable, low-power switching are ongoing challenges, particularly for high-density memory arrays [43].

1.1.3 Phenomenological theory of Magnetic Tunnel Junctions

The canonical theory explaining GMR and TMR was initially proposed by Thierry Valet and Albert Fert in the early 1990s [49]. The model is a theoretical framework used to describe spin-dependent transport and magnetoresistance effects in magnetic multilayers and spin-valve structures. The key aspects of the Valet-Fert model are:

- Diffusive transport regime: the model assumes that the electron transport in the ferromagnetic and non-magnetic layers occurs in the diffusive regime, where the mean free path of electrons is much shorter than the layer thicknesses.

- Spin accumulation: The model considers the spin accumulation that occurs at the interfaces between ferromagnetic and non-magnetic layers due to the difference in conductivities for majority and minority spin electrons.

- Spin-dependent scattering: It incorporates spin-dependent scattering parameters, such as the spin asymmetry coefficients and spin diffusion lengths, to account for the different scattering rates of majority and minority spin electrons in the ferromagnetic layers.

- Current-perpendicular-to-plane (CPP) geometry: The Valet-Fert model is particularly useful for describing the GMR effect in the CPP geometry, where the current flows perpendicular to the plane of the multilayer structure.

- Magnetoresistance calculation: By solving the diffusion equations for spin-up and spin-down electrons, the model allows for the calculation of the magnetoresistance ratio in magnetic multilayers and spin-valves, providing insights into the dependence on layer thicknesses, interface properties, and spin-dependent scattering parameters.

While originally developed for GMR in metallic multilayers, the Valet-Fert model has been extended and adapted to describe spin-dependent transport in other spintronic devices, such as MTJs [50, 51]. Some key modern extensions include:

- Spin-Dependent Interfacial Effects: Extensions have been made to incorporate the influence of the insulating barrier material and the quality of the ferromagnetic electrode-barrier interfaces on the TMR effect. The spin polarization and density of states at the interfaces play a crucial role in determining the TMR [52].
- Spin-Transfer Torque (STT): The Valet-Fert model has been combined with the Slonczewski equation of motion to describe spin-transfer torque effects in MTJs. This is essential for understanding and optimizing STT-MRAM devices [53].
- Half-Metallic Electrodes: The model has been adapted to account for the use of half-metallic ferromagnetic electrodes in MTJs, which can exhibit 100% spin polarization and enable true "on-off" switching behavior [54, 55].
- First-Principles Calculations: Modern extensions involve integrating first-principles calculations based on density functional theory (DFT) to accurately model the electronic structure, spin polarization, and interfacial properties of MTJs with different materials and configurations [52, 56, 57, 55].

The theoretical descriptions of MTJs are divided into phenomenological models akin to the Valet-Fert model, and *ab-initio* numerical approaches. Challenges in these approaches aim at accounting for disorder, randomness [58], interfacial effects [59], complex material system [59], 2D materials [48], spin-transfer torque [60], scaling and size effects [59].

1.2 Transport through nano-objects trapped in tunnel junctions

1.2.1 Resistive switching

The resistive switching (RS) effect is observed in capacitor-like devices such as tunnel junctions where a dielectric barrier material, typically a transition metal oxide, exhibits a sudden and non-volatile change in its electrical resistance when subjected to an external electrical bias (voltage or current pulse). The resistance change is reversible and can be switched between a high resistance state (HRS) and a low resistance state (LRS) by applying appropriate voltage or current pulses [61, 62, 63]. the controlled switching behavior can be used to write, read, and erase bits by simple voltage pulses and hence employ these devices as memory element [64, 62, 65]. This effect thus allows the fabrication of novel non-volatile resistive random-access memories (ReRAMs) that can be engineered in both MTJs or molecular junctions [61, 62, 65, 66].

Several physical mechanisms that can lead to resistive switching behavior:

- **Redox Reactions**: Oxygen ion migration and redox reactions at the electrode interface, forming conductive filaments or modifying the interfacial barrier height can induce local changes in the electronic structure and modify the transport properties

through those defects [67, 68, 62, 69, 70, 71, 72, 73, 74, 66]. In particular, oxygen vacancies migration have been attributed to bistable states in oxide MTJs [75].

- **Phase Transitions**: Structural phase changes in the barrier material, such as crystalline to amorphous transitions or metal-insulator transitions, induced by Joule heating or electric field can change the properties of the material and lead to RS [62, 76].
- **Spin-Polarized Tunneling**: In MTJs, spin-dependent tunneling leads to resistance states that depend on the relative magnetization orientation of the electrodes. The switch can therefore be triggered directly by an external magnetic field or indirectly via spin-transfer torque (STT) [77], spin blockade effects [78] or other kinds of spintronic interactions [79].
- **Ferroelectric Polarization**: Resistance modulation in ferroelectric materials due to the polarization state and associated changes in the Schottky barrier height at the electrode interface can result in sudden current jumps [80].
- **Conformal Transformations**: The piezoelectric effect or strain-related phenomena can change the structure of the tunneling material in molecular junctions, leading to different resistance states [64, 63, 81, 82].
- **Charge deposition**: Voltage-induced charge deposition on an impurity trapped within the tunnel barrier can thus directly change the conductivity of a transport channel or indirectly via a capacitive coupling [63, 83, 84, 85, 86]. This charging effect is reminiscent of the Coulomb blockade effect (see Section 1.2.4).
- **Polaron formation**: electron-boson interactions can give rise to resistive switching akin to the Franck-Condon blockade mechanism in electronic quantum systems interacting with vibrational modes (see Section 1.2.4). Polaron formation can lead to hysteretic switching and NDR [87, 88].

1.2.2 Resonant Tunneling

Resonant tunneling is a quantum mechanical phenomenon where electrons can tunnel through a potential barrier with near-perfect transmission probability at certain specific energy levels. This occurs in tunnel junctions with multiple potential barriers, such as a double-barrier structure [89, 90, 91, 92]. This effect is therefore characteristic of electron transport through quantum dots, quantum wells [93], and more generally through the localized states of defects or impurities trapped within tunnel junctions [94, 89, 95].

Due to their quantum wave-like nature, electrons can tunnel through a potential barrier even when their energy is less than the barrier height. Resonant tunneling thus occurs commonly in a double-barrier structure, forming a quantum well between the barriers and results in inelastic electron transport, which translates into non-linearities in the conductance spectrum of the junction. A characteristic of this process is that, as temperature or voltage increases, the dominant contribution to the conduction comes from channels with larger and larger numbers of localized states leading, to a resistance with an increasing slope [94, 95], and a decrease in in conductance and magnetoresistance [89, 96, 95].

In a double-barrier structure, the transmission probability of electrons exhibits sharp peaks at certain "resonant" energies, where the electron wave function constructively interferes inside the potential well between the barriers. At these resonant energies, the transmission probability can approach 100%, allowing the electrons to pass through the double-barrier structure with minimal reflection [93]. The resonant energies are determined by the geometry and material properties of the double-barrier structure, which create the quantized energy levels in the potential well [92]. Resonant tunneling can lead to negative differential resistance (NDR) in the current-voltage characteristics of devices like resonant tunneling diodes, enabling high-speed electronic applications. NDR has been experimentally observed in many nanoscale structures such as QDs [97] or MTJs [95, 92], although this effect is not always due to resonant tunneling. For example, in molecular junctions, it can be linked to oxidation/reduction reactions of the molecule, resulting in a closure of transport channels with increasing bias, and thus a drop in conductance [98].

Of particular interest to us in the quest for energy harvesting devices, rectennas are a special type of receiving antenna that can directly convert electromagnetic energy into direct current (DC) electricity thanks to a diode that rectifies the AC current induced in the antenna into DC power [93]. Rectennas were invented in 1964 by American engineer William C. Brown, who demonstrated powering a model helicopter using microwaves received by a rectenna and proposed to power small wireless devices by beaming microwaves to them [99]. Optical rectennas, which use nanoantennas to capture light and heat and convert it to electricity [100], have recently been demonstrated with record-breaking efficiencies of up to 90.6% at 2.45 GHz [101]. This is a major advance towards practical energy harvesting applications. Challenges in creating efficient optical rectennas include fabricating antennas small enough to couple with optical wavelengths, and developing ultrafast diodes capable of rectifying the high frequency oscillations [102].

1.2.3 Kondo Effect

The Kondo effect is a phenomenon observed in materials containing magnetic impurities, where the electrical resistance shows a characteristic minimum at low temperatures. It arises due to the scattering of conduction electrons by localized magnetic moments (spins) of the impurities. At high temperature, the scattering of electrons by the impurity spins is incoherent, leading to an increase in resistance with decreasing temperature (see Figure 1.2(a)). However, at sufficiently low temperatures, the conduction electrons start to screen the impurity spins through an antiferromagnetic exchange interaction, forming a spin-singlet state known as the Kondo cloud or Kondo resonance (see Figure 1.2(b)). This screening process enhances the scattering of electrons, causing the resistance to increase again as the temperature is lowered further, resulting in a resistance minimum at a characteristic Kondo temperature T_K (see Figure 1.2(a)).

The canonical model that predicts the Kondo resistance peaks is the Anderson impurity model [105] (see Figure 1.2(c)). The corresponding Hamiltonian can be split into three terms:

$$H_A = \left(\epsilon_\uparrow d_\uparrow^\dagger d_\uparrow + \epsilon_\downarrow d_\downarrow^\dagger d_\downarrow + U d_\uparrow^\dagger d_\uparrow d_\downarrow^\dagger d_\downarrow\right) + \sum_{\alpha k\sigma} \epsilon_{\alpha k\sigma} c_{\alpha k\sigma}^\dagger c_{\alpha k\sigma} + \sum_{\alpha k\sigma} (\gamma_{\alpha k\sigma} c_{\alpha k\sigma}^\dagger d_\sigma + h.c.), \quad (1.2)$$

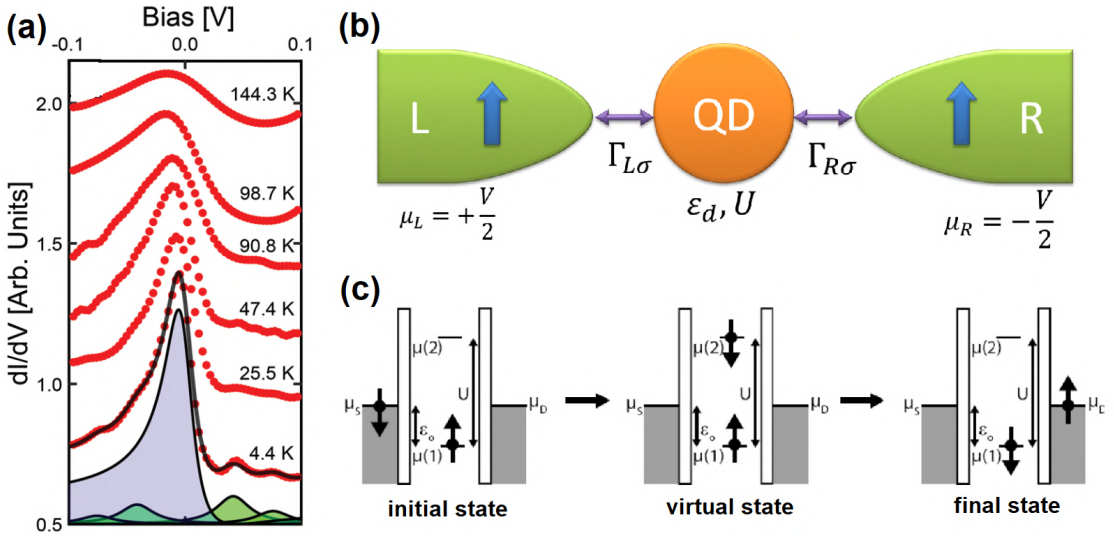

Figure 1.2: **Kondo effect.** (a) Temperature-dependent near-Fermi conductance spectra showing the the Kondo effect taken at various temperatures (in red) and the corresponding Fano lineshape fit (in black). Adapted from Reference [103]. (b) Schematic of an impurity model. Taken from Reference [104] . (c) Energy-level diagram showing the tunneling of a spin through a virtual state of the impurity.

where the first term represents the Hamiltonian of the impurity (with $d^\dagger_\sigma$ the creation operator of a spin σ on the impurity), the second term represents the Hamiltonian of the two left and right leads $\alpha \in \{L, R\}$ (with $c^\dagger_{\alpha k\sigma}$ the creation operator of an electron of momentum k and spin σ in the lead α), and the third term represents the hybridization operator that allows for the tunneling of the fermions. The parameters of the model are fully contained within the bare energy levels of the impurity ϵ_σ and the Coulomb repulsion term U, the energy levels of the leads $\epsilon_{\alpha k\sigma}$ encompassed in the Fermi distribution function $f_\alpha(\epsilon) = \sum_{k\sigma} \delta(\epsilon - \epsilon_{\alpha k\sigma}) = [e^{\beta_\alpha(\epsilon-\mu_\alpha)} - 1]^{-1}$, and the tunneling coefficients $\gamma_{\alpha k\sigma}$ gathered in the coupling function $\Gamma_{\alpha\sigma}(\epsilon) = \pi \sum_k |\gamma_{\alpha k\sigma}|^2 \delta(\epsilon - \epsilon_{\alpha k\sigma})$.

The Kondo effect was first explained theoretically by Jun Kondo in 1964 using perturbation theory, predicting the logarithmic increase in resistivity as T approaches 0 K [106]. Later, the description of the phenomenon was completed by Fano [107], Frota [108] and subsequent works [109], who predicted the shape of the Kondo resonance in more details. Nowdays, numerical *ab-initio* methods modeling extensions of the Anderson model aim at refining these analytical results to more complex cases, taking into account tunneling from interferences [110, 111] and exotic couplings [112, 113, 114] such as interactions with vibrations [115, 116, 117], notably through numerical renormalization group (NRG) methods [118, 119, 120, 121, 104] which reveal a particular importance in regards to spin polarization within MTJs [121, 104, 122].

The Kondo effect was first observed in metals doped with magnetic impurities, then in a variety of systems such as single-electron transistors (SET) [123, 120], superconductors [111], molecular junctions or single atoms probed by scanning tunneling microscopy (STM) and scanning tunneling spectroscopy (STS) techniques [112, 124, 113, 115, 125, 110, 119, 126], The Kondo effect is also observed in quantum dot systems, where the localized spin

is provided by an unpaired electron on the quantum dot [127, 128, 122]. It has played a crucial role in understanding strongly correlated electron systems, such as heavy fermion materials and Kondo insulators, which involve lattices of magnetic impurities.

Kondo screening can also give rise to the zero-bias anomaly (ZBA) which refers to a situation where there is an anomalous increase or decrease in conductance around zero bias voltage in certain nanostructures. Although the ZBA may not always be due to Kondo physics, the zero-bias anomaly is found to be strongly related to electron correlation effects and the spatial distribution of the density of states, usually localized by interfaces [129] or nano-objects within a junction [130, 131, 132, 133, 134]. For example, in Co atoms deposited on noble metals, the anomaly may be caused by spin-excitations and the formation of many-body bound states called "spinarons", rather than Kondo screening [135]. The zero-bias anomaly has been observed in STM setups [135], disordered two-dimensional films [136], quantum point contacts [137] and tunnel junctions [129, 131, 132, 91, 133]. This zero-bias anomaly usually results in a conductance peak around zero bias in magnetic tunnel junctions whose intensity depends on the magnetic alignment of the electrodes, which produces a TMR signal that decreases when one increases the bias voltage [129, 131, 91, 133].

1.2.4 Blockade effects

Coulomb Blockade

In a single-electron transistor (SET), a small conductive island (QD) is sandwiched between two tunnel junctions connected to the source and drain electrodes. The electrical potential of the island can be tuned by a gate electrode that is capacitively coupled to it (see Figures 1.3(a) and (b)). The Coulomb blockade is a phenomenon observed in such small electronic devices where the flow of electrons is suppressed at low bias voltages due to the electrostatic charging energy required to add or remove an electron from the device. It arises from the quantization of charge and the strong Coulomb repulsion between electrons in small, low-capacitance devices. When the device is small enough, the Coulomb repulsion prevents additional electrons from flowing, leading to a suppression of electrical conductance at low bias voltages (see Figure 1.3(d)). The current-voltage characteristic exhibits a staircase-like behavior, with regions of zero conductance (Coulomb blockade) separated by sharp increases in conductance when the bias voltage overcomes the charging energy (see Figure 1.3(d)). This phenomenon gives rise to Coulomb blockade oscillations with the gate voltage, which describe the periodic oscillations of the conductance of the device produced as higher and higher discrete energy levels of the island are filled because of the gate potential [138]. The condition for Coulomb blockade is that the bias voltage must be lower than the energy required to add one electron from the source to the drain. This charging energy is given by $E_C = e^2/2C$, where e is the electron charge and C is the self-capacitance of the device.

When plotting the conductance of a SET as a function of the gate voltage V_G and the source-drain voltage V_{SD}, the characteristic structures of Coulomb blockade, also known as Coulomb diamonds, emerge (see Figure 1.3(c) and (e)). The regions with Coulomb blockade are located around $V_{SD} = 0$. At zero temperature, there is no current and one state with

n electrons is stable. The stability changes with the gate voltage and at high enough bias voltage, the stability is lost at the degeneracy edges, when one energy level of the QD enters in resonance with the Fermi energy of one lead. The degeneracy points, forming the vertices of the diamonds, correspond to configurations where two energy levels of the dot are in resonance with the chemical potential of both electrodes. The slopes of the edges defining the Coulomb diamond can directly depend on the capacitances of the source, the drain and the gate (see Figure 1.3(c)).

First principles studies of the Coulomb blockade effect usually deal with extensions of the previous Anderson model to a larger set of impurities, leading to more capacitively-coupled energy levels. The corresponding model, named the Anderson-Hubbard model [139], has been substantially studied within the literature for single [140], double [141, 142, 134, 143, 144] or triple quantum dots [145, 146], and revealed interesting spintronic results such as TMR oscillations [147, 141, 148, 140, 146, 144], non-linear response regimes [147, 141, 139], spin accumulation [147, 139, 140, 146] or inverse currents [149].

Experiments on QDs [148], SETs [150] and MTJs [151, 152, 131, 153, 154] have confirmed the qualitative features of the theory, in particular the null intensity plateau close to zero source-drain voltage, intensity steps associated with conductance peaks and the peculiar shape of the Coulomb diamonds [150] (see Figure 1.3(e)).

Franck-Condon Blockade

The Franck-Condon blockade is a phenomenon that occurs in molecular electronics and nanoelectromechanical systems, where strong coupling between electronic and vibrational degrees of freedom leads to a suppression of current flow at low bias voltages [150, 156]. During an electronic transition in a molecule, the most likely vibrational transitions are those where the vibrational wavefunctions of the initial and final states have a significant overlap (see Figure 1.4(a-c)) [157, 158]. This implies that electronic transitions are much faster than the timescale of nuclear motion.

In molecular junctions or suspended nanostructures like carbon nanotubes, the electronic states can be strongly coupled to quantized vibrational modes (vibrons) of the nanostructure [150]. When this electron-vibron coupling is strong, it leads to the formation of polaronic quasi-particles consisting of an electron dressed by a cloud of vibrons. The theoretical description of this phenomenon usually involves the study of an Anderson-like impurity model (Equation 1.2) with a bosonic mode, leading to the Anderson-Holstein model [159, 166, 158, 157, 167, 168, 169, 170, 171, 160, 161, 159, 162, 163, 164, 165, 87] which is usually studied via the polaron or Lang-Frisov transformation [171, 163, 164, 87].

The Franck-Condon blockade occurs when the energy required to add an electron to the system is much larger than the thermal energy, due to the large polaronic distortion caused by the strong electron-vibron coupling. This effectively blocks electron tunneling at low bias voltages, leading to a suppression of current [150, 158] (see Figure 1.4(g)).

Franck-Condon blockade induces a low-bias current suppression due to the large polaronic distortion energy [150, 173, 174, 175] (see Figure 1.4(d)). Transport proceeds via

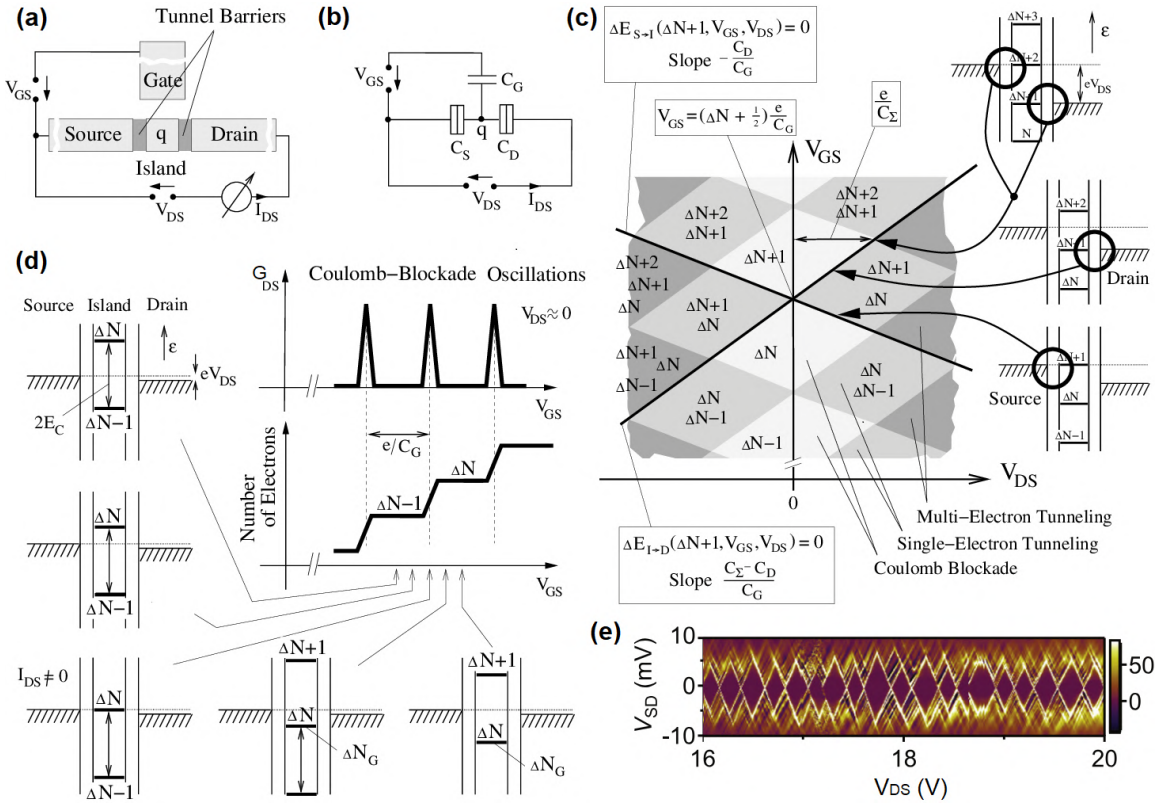

Figure 1.3: **Coulomb blockade.** (a) Schematic and (b) corresponding electrical circuit of a single-electron transistor. (c) Representation of the Coulomb oscillation of the intensity and the corresponding Coulomb steps of the conductance accompanied with energy diagrams illustrating the tunneling mechanisms at each step. (d) Representation of the Coulomb diamonds and the corresponding energy diagrams illustrating the tunneling at the borders of the diamonds. (e) Differential conductance, $\mathrm{d}I/\mathrm{d}V_{SD}$, as a function of the bias V_{SD} and the back gate voltage V_{BG} in InAs/InP nanowire heterostructure quantum dots. Adapted from Reference [155]

avalanches of multiple electrons interrupted by long waiting times, leading to enhanced shot noise and power-law noise spectra [173, 172, 158, 176, 177, 160, 175, 162] (see Figure 1.4(h)). These avalanches may thus lead to an oscillation of the resistance of the junction between multiple discrete resistance states, which translates into a telegraphic noise in the electronic response [178, 172, 167, 177, 170, 171, 179, 162, 87] (see Figure 1.4(e)). This multi-stability induces a hysteretic behavior that can be controlled by electrical modulation [167, 170, 179, 87]. Coupling to the vibrational degrees of freedom can also lead to negative differential conductance [178, 168, 169, 179, 87] and vibrational sidebands in the Coulomb blockade regime, which translates into additional conductance maxima within a Coulomb diamond in a SET [173, 172, 158, 176, 181, 174, 160, 161, 159, 165, 180] (see Figure 1.4(g)).

Franck-Condon blockade has been experimentally observed in suspended carbon nanotube quantum dots [166, 181] and many organic [150, 172, 173, 178, 174, 177, 182, 175, 183, 180] or inorganic [184] molecular junctions and transistors, providing a quantitative

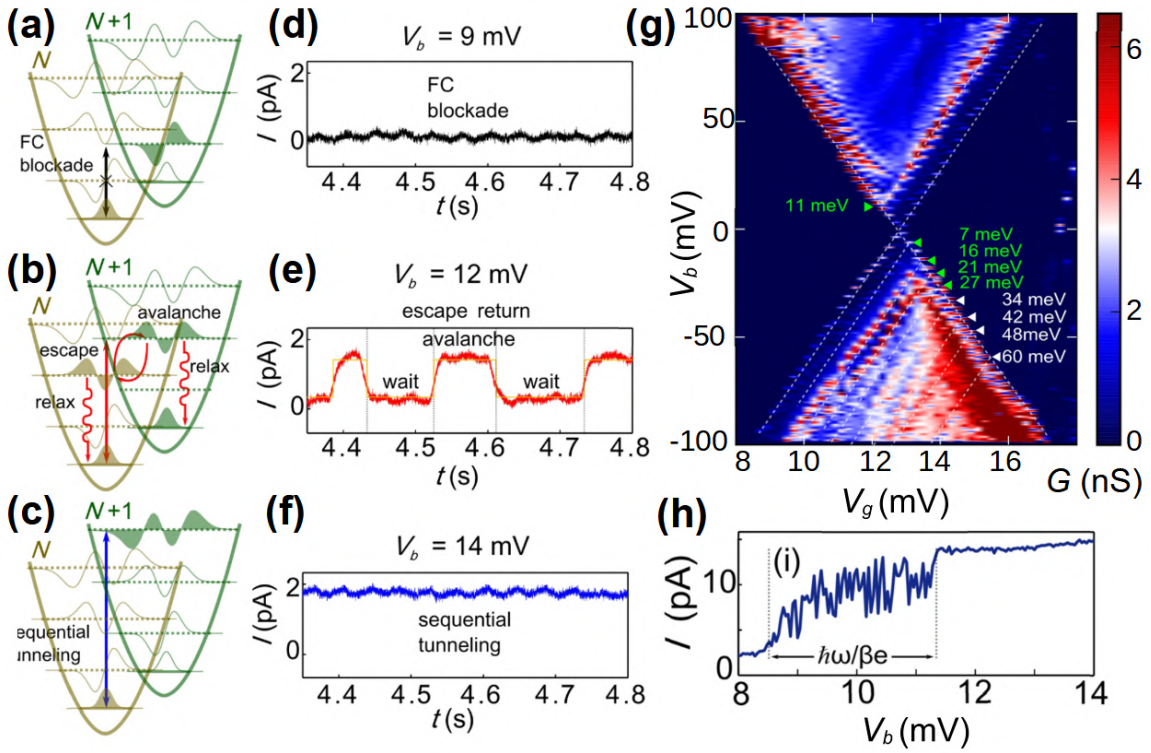

Figure 1.4: **Franck-Condon Blockade in graphene-fullerene single-molecule transistors.** (a-c) Energy diagram illustrating avalanche transport. (d-f) Current-time traces at $V_b = 9$, 12, and 14 mV and $V_g = 10.15$ V. (g) Differential conductance stability diagram of the $N + 1$ to $N + 2$ transition. Excited states are indicated by the white and green arrows. (h) IV traces at $V_g = 10.1$ V. The current noise extends over an applied bias corresponding to $\hbar\omega/\beta e$. Adapted from Reference [172].

.

understanding of vibron-assisted transport in the strong electron-vibron coupling regime. It highlights the remarkable potential of nanoelectromechanical systems for studying and exploiting electron-vibration interactions at the single-molecule level.

Spin Blockade

Pauli spin blockade (PSB) and other kinds of spin blockades are phenomena observed in quantum dot systems, where the transport of electrons through the nano-object is blocked due to spin selection rules and the Pauli exclusion principle, which states that two identical fermions cannot occupy the same quantum state. It occurs when two electrons with opposite spins occupy different quantum dots, forming a spin-triplet state. In this configuration, the transition to a spin-singlet state, required for further electron transport, is forbidden by spin conservation rules [185, 186, 187, 78]. This blockade of current can be lifted by either spin relaxation or spin flip processes, allowing the transition to the spin-singlet state. PSB provides a way to initialize and read out spin states in quantum dots, making it a crucial phenomenon for spin-based quantum computing [188, 189, 190].

The canonical theoretical description of this effect involves an Anderson-like impurity model with at least two spin-split QDs and aim at identifying different regimes of conduction depending on the spin-states of the dots and the external constraints such as a potential bias, a gate voltage or an external field [191, 192, 189, 193].

PSB is extensively used to investigate the coherence of single-spin and two-spin states in quantum dots [194, 187, 191]. It can give rise to NDR [194, 193], current rectification [187, 191, 193], enhanced current fluctuation and shot noise [193], reversible switching associated with dramatic changes in conductance depending on the spin state of the QDs [81, 187, 195, 193, 78], and spin-to-charge conversion, allowing the readout of spin states by monitoring the current through the double quantum dot [196]. PSB is a key mechanism for manipulating and reading out spin qubits in various quantum dot systems, including GaAs, silicon, and graphene [186, 188, 197].

1.3 Magneto-transport in MgO oxide junctions

The different phenomenon presented in the next section will be of use in Part II for the experimental study of the junctions tested during this thesis. In this next part, we investigate on MgO MTJs which are considered as promising candidates to build a spintronic engine for their wide use in the field of spintronics, their industrializable fabricating procedure, along with their recently discovered energy generation capabilities [18].

1.3.1 Structure and properties the MgO/Fe interface

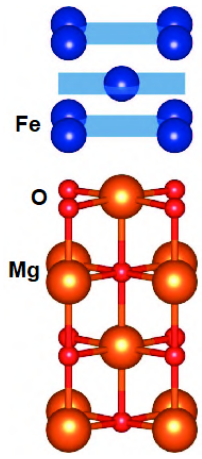

Figure 1.5: **MgO/Fe crystal structure.**

Magnesium oxide (MgO) is an ionic oxide that consists of magnesium and oxygen ions with +2 and -2 charges respectively. The crystal structure of MgO is face-centered cubic (*fcc*), with each atom having six connections. The lattice constant is 4.207 Åat absolute zero [198].The electron system comprises a filled valence band, mostly composed of oxygen states, and an empty conduction band, primarily made of magnesium states. The creation of the crystal triggers an electron transfer from the Mg $3s^2$ orbital to the $2p^4$ orbital of Oxygen, resulting in MgO's insulating properties [199]. Reflectance spectroscopy measurements reveal that the band gap of MgO is 7.8 eV [200].

Crystalline barrier materials, such as the MgO crystal, inevitably have defects. These can be dislocations or vacancies in the crystal's atomic structure. One key defect is known as a point vacancy. Recent research into MgO vacancies has revealed intriguing optical, catalytic, and transport properties [201]. Types of lattice vacancies that may occur in MgO include cationic or anionic vacancies, which can be neutral or charged. Oxygen vacancies, with the lowest formation energy, are the most likely to occur [199].

Iron (Fe) is a ferromagnetic transition metal which typically crystallizes in a body-centered cubic (bcc) structure with a lattice constant of 2.867 Å[202]. To achieve structurally ordered magnetic hetero-junctions, the lattice constants of both materials need to be similar. This can be observed in bcc(001) Fe electrodes and fcc(001) MgO barriers through a 45° in-plane rotation, resulting in only a small 3.8% lattice mismatch [203]. Experimental evidence shows that oxygen atoms are placed on top of iron atoms during the Fe/MgO growth process [204].

The Julliere and free-electron models accurately represent the magneto-resistive characteristics of inorganic junctions with amorphous tunnel barriers (see Section 1.1.1), but crystal tunnel junctions are more complex due to the influence of crystal structures on electron wave functions. The wave functions can be categorized by symmetry and each reacts differently to states in a crystalline barrier. The symmetry of the wave function, along with electron spin, is preserved during transport. Butler *et al.* [30] and Mathon *et al.* [31] provided a theoretical model for the Fe/MgO/Fe system, predicting high TMR for crystalline MTJs. This is based on the match between the Bloch states for the majority and minority spins of ferromagnetic (FM) electrodes and the tunnel barrier's evanescent wave functions. The TMR value is also heavily influenced by the electron's direction, the coupling of Bloch states during tunneling, and the decay rate of the channels. Iron Fe in the bcc(001) direction has four bands crossing the Fermi energy: Δ_1, Δ_2 and Δ_5 (see Figure 1.6(a)). In the P state, the fully spin-polarized Δ_1 band is the dominant transport channel for majority spins, while for the minority spins Δ_1 has no matching electrons in the receiving electrode so Δ_5 becomes the dominant transport channel, justifying the spin-polarization of the current [205] (see Figures 1.6(b) and (c)). By comparing Figures 1.6(b) and (c) to their AP counterparts from Reference [205], the TMR can also be qualitatively explained.

1.3.2 Properties of MgO Magnetic Tunnel Junctions

The development of TMR technology has been accelerated by advances in manufacturing and materials. In 2001, Bowen *et al.* [207] first reported MgO MTJs with a 60% TMR, and breakthroughs have led to the achievement of a 600% TMR signal in CoFeB/MgO/CoFeB MTJs at room temperature [32] (see Figure 1.6(d)). This has allowed for significant improvements in storage technology, particularly in hard disk read heads [208, 206, 25]. Efforts to improve TMR ratios and reduce the size of MTJs have met with challenges related to interfacial anisotropy, but solutions have been found by using shape anisotropy materials and magnetization switching [44]. Despite these advances, the theoretical TMR amplitude of over 1000% at room temperature [31] has not been achieved, likely due to defects and structural issues in tunnel junctions [32].

When Magnesium Oxide (MgO) is deposited onto an Iron surface, a layer of Iron (II) Oxide (FeO) forms [212], significantly altering the spin-dependent tunneling [213]. It is challenging to create a nearly defect-free interface that prevents Fe oxidation such as to favor coherent tunneling. Studies suggest that Mg or Au layers could maintain the primary symmetry state during tunneling [214, 215].

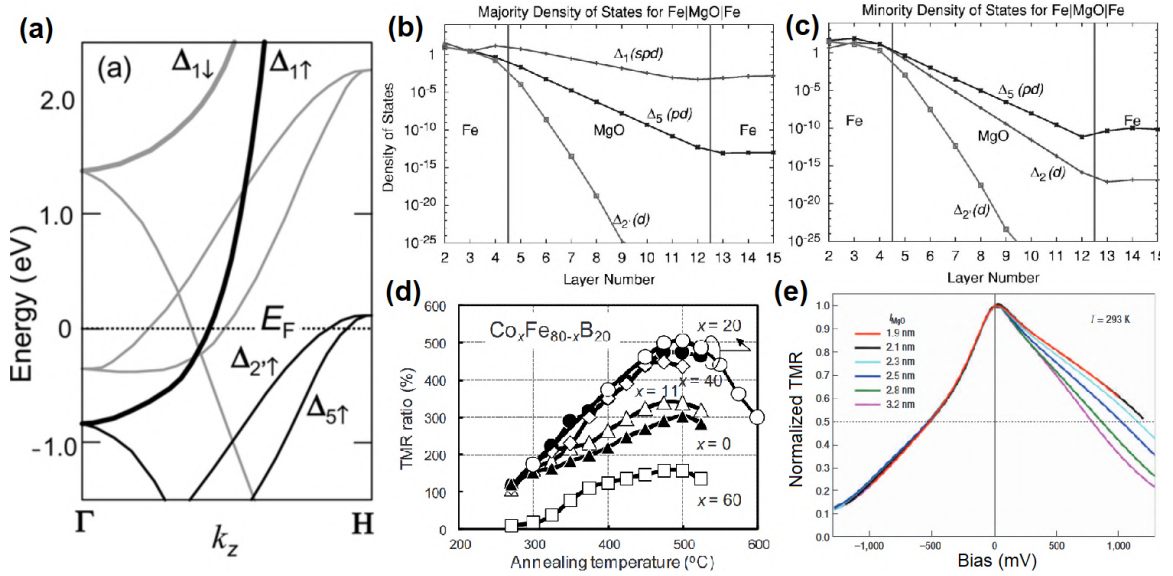

Figure 1.6: **MgO Magnetic Tunnel Junctions Properties.** (a) Band dispersion of bcc Fe in the (001) (Γ–H) direction. Adapted from Reference [205]. (b) and (c) Tunnelling DOS of majority and minority spin states for $k_{||} = 0$ in Fe(001)/MgO(001)(8 ML)/Fe(001) with parallel magnetic state. Adapted from Reference [30]. (d) TMR ratio as a function of annealing temperature for MTJs having $Co_xFe_{80-x}B_{20}$ electrodes with $x = 0\% - 60\%$ and $t_{CoFeB} = 4.3$ nm. The MgO thickness of the MTJs is 1.5 nm except for the open circles (2.1 nm). Adapted from Reference [32]. (e) Relation between bias voltage V and the normalized TMR ratio at room temperature of Fe(001)/MgO(001)/ Fe(001) tunnel junctions with various MgO thicknesses t_{MgO}. Adapted from [206].

Tunneling is also influenced by perpendicular magnetic anisotropy (PMA) in Fe/MgO interfaces. Theory suggests PMA at these interfaces results from spin-orbit coupling (SOC), with varying levels dependent on factors such as Fe and MgO thickness and iron-oxygen orbital hybridization [216]. Experiments have also found Fe-O bonding and anisotropic orbital magnetic moments to be contributors [217]. The presence of both PMA and Bloch state symmetry filtering has been found in FM/MgO interface which contribute to robust electrical spin injection in certain materials [218]. From these works, optimum anisotropy and reduced damping in MTJs seems to be reached with a balanced CoFeB composition along with an interfacial layer [203, 219, 220]. CoFeB/MgO films have been found to exhibit high spin polarization, making them suitable for industrial use in spintronic selectors [220, 18] but controlling defect species, such as oxygen vacancies, is necessary for managing the transport path across and deliver useful spintronic devices [221, 222].

Oxygen vacancies in MgO tunnel barrier MTJs can lead to structural changes, electronic modifications, and increased reactivity, leading to incoherent tunneling [223]. Annealing has been found to be a crucial step in the fabrication of the junctions in order to mitigate the formation of those defects and increase the TMR signal [208, 221, 222, 32]. These defects can be manipulated by adding oxygen to the Argon plasma when growing the samples, which impacts the spectral peaks related to various oxygen defects in the MgO and can increase barrier heights by up to 10% [224]. This increased O_2 concentration could re-

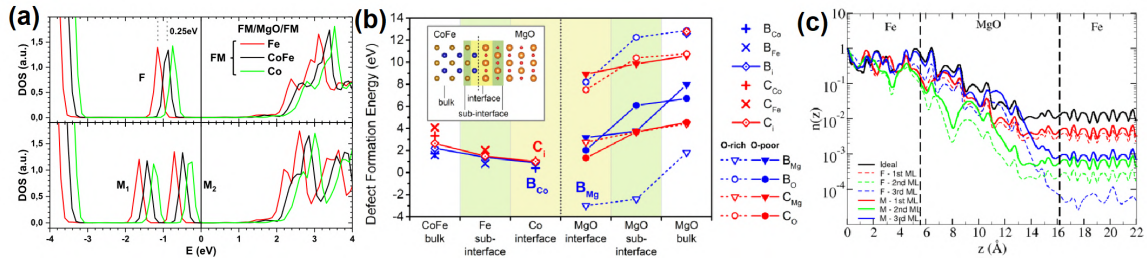

Figure 1.7: **Impact of defects in MgO Magnetic Tunnel Junctions.** (a) Ab initio densities of states of MgO (001) comprising (top) F and (bottom) M centers, calculated for a MTJ stack as the interface is switched from bcc Fe (001) (black) to FeCo (001) (red) to Co (001) (green). Adapted from Reference [209]. (b) Formation energies of defects created at different regions in the CoFe/MgO/CoFe MTJ (model of CoFe/MgO interface shown in inset). Adapted from Reference [210]. (c) Spin up Δ_1 scattering state distribution along the transport direction z for various vacancy configurations of Fe/F-MgO(5ML)/Fe and Fe/M-MgO(5ML)/Fe in the MTJ's P magnetic state. Adapted from Reference [211].

move defects created by hotspots. It was found experimentally that these oxygen defects can significantly affect magneto-transport in CoFeB/MgO MTJs [225]. On the theory side, multiple studies have examined the band structure of MgO barriers with FeCo as ferromagnetic electrodes for MTJs [226, 227]. The studies found that double oxygen vacancies lower the barrier height, which can enhance spintronic performance relative to the case with single oxygen vacancies. Following experiments then showed that CoFeB/MgO-based MTJs made through a process involving sputtering and oxidation with annealing favored those defects and increased TMR despite a lower barrier height [226]. Additionally, it was found that Boron atoms from the CoFeB electrode migrated into the adjacent layers, inducing crystallization of FeO and interstitial defects in Ta or MgO [228, 229, 210] such as it was theoretically suggested that Carbon impurities could be a better dopant that Boron and increase the TMR [210]. These works determined a strong correlation between layer quality, interface nature, defect roles, and MTJs' magnetoresistance. These findings indicate the need for comprehensive experimental analysis to fully comprehend the properties of defects in MgO MTJs, and their effects on tunneling transport. Unfortunately, studying these nanoscale impurities has remained marginal given the trajectory of the industry which is focused on technologies that can accommodate those defects, such as the field of MgO MTJs lacks connections with quantum technologies.

1.4 Magneto-transport in Phthalocyanine molecular junctions

1.4.1 Tunneling in molecular junctions

Research in molecular spintronics includes using single-molecule organic semiconductors (OSC) as an efficient functional circuit component, essentially miniaturizing devices. Or-

ganic semiconductors are molecular materials composed of carbon-based compounds, typically containing conjugated π-electron systems. Initial studies have shown the possibility of using single-molecule junctions to make rectifiers [230], then experiments demonstrated the successful incorporation of organic semiconductors into spintronic devices, leading to spin injection and transport [231]. Further studies reported varying levels of magnetoresistance at different temperatures using different materials initiating deeper investigation of effects at the metal/molecule interface [232, 233, 234] and revealing exceptionally high TMR ratios exceeding $10^3\%$ in theory [235] and magnetoresistance of 770% in experiments [19].

Organic molecules, due to their numerous and variable sizes, offer unlimited potential for designing organic semiconductors, an advantage over inorganic semiconductors. While inorganic materials are made up of a continuum of energy states with delocalized electrons, organic materials have discrete energy levels. In organic semiconductors, electrons participate in a p-bond, increasing their delocalization, which results in molecular energy levels. These levels give rise to the highest occupied molecular orbital (HOMO) level and lowest unoccupied molecular orbital (LUMO) level, similar to the valence and conduction bands of inorganic solids [236, 237]. The conductivity of these semiconductors results from the overlapping of delocalized p-electrons when a p-conjugated molecular system is bound to a solid. The cohesion of molecular layers is due to weak van der Waals interactions, giving electrons a free path nearly equivalent to the semiconductor's inter-molecular distance [236, 237].

OSCs present unique advantages for spintronics, including weak electron-spin and orbital momentum coupling [238], a low coupling strength between electron spin and nuclear magnetic moments [238] leading to the capability to preserve and transport spin information over microscopic length scales [239]. Additionally, OSCs potentially facilitate the exploration of molecular scale limit device dimensions and offer the ability to adjust the molecules' chemical and physical properties thanks to multiple deposition techniques [240]. Despite drawbacks, such as a low charge mobility [241], OSCs are being actively researched, with potential applications including use as tunnel barriers in organic magnetic tunnel junctions [242, 243].

1.4.2 Properties of phthalocyanine molecules

Metal phthalocyanine (MPc) is a family of planar aromatic molecules composed of four isoindole units with a metal ion or two hydrogen atoms in the center (see Figure 1.8(a)). They are chemically and thermally stable, with low vapor pressure, making them suitable for use in heterostructures and ultra-high vacuum environments. The spatial geometry of MPc molecules is determined by the van der Waals forces and π-π interactions between them. They occur in polymorphic phases and the most common metastable forms are the α- and β-phases [244] (see Figure 1.8(b)). The difference between these two phases is the stacking angle of the molecule within the columns and their arrangements in the crystalline structure. The MPc's central metal atom's electronic states and the properties of metal phthalocyanines are defined by its molecular stacking geometry and the electronic ground states at the metal site which impact its conductivity. Various substrates and deposition

techniques can be used to achieve unique polymorphic phases of MPcs [245, 246].

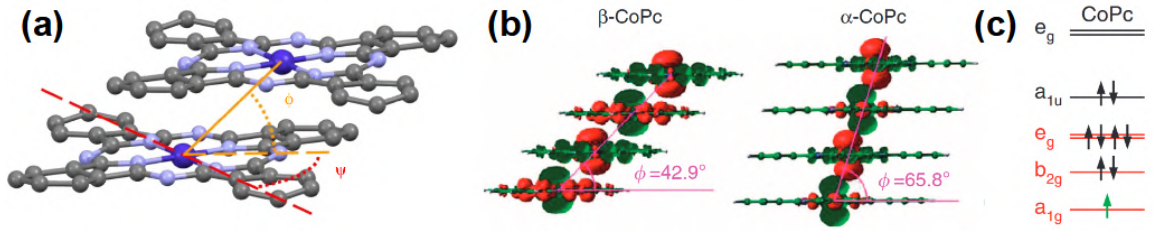

Figure 1.8: **Cobalt Phthalocyanine molecular structure.** (a) Schematic of the molecular stacking geometry in CoPc crystals. Co atoms are in blue, N in light blue, C in black and H atoms are not shown. The orange line corresponds to the Co–Co distance and forms an angle ϕ (stacking angle) with the molecular plane. Its projection on the plane (orange dashes) and the Co–N axis (red dashes) define the sliding angle ψ. (b) Spin densities of CoPc in the α- and β-configurations. (c) Energy levels for CoPc; the levels with mainly d-orbital contribution are in red, the single spin is symbolized in green, and the dotted arrow represents the HOMO-LUMO gap. Adapted from Reference [246].

The CoPc molecule is a paramagnetic atom with a 4-fold rotational symmetry and complex multiplet structure (see Figure 1.8(c)). Its magnetic state is determined by the higher d state (d_{z^2}), which points out of the molecular plane. Antiferromagnetic ordering of the CoPc molecular layers occurs due to the superexchange mechanism [247]. This process magnetically links two adjacent Co^{2+} metal ions of stacked CoPc molecules, thereby forming a spin chain (see Figure 1.9(a)). The standard STM and STS and inelastic electron tunneling spectroscopy (IETS) allowed for temperature-dependent studies which suggested strong antiferromagnetic exchange coupling interaction between 80 K to 100 K [248]. X-ray diffraction on CoPc thin films shows strong anti-ferromagnetic coupling in the α-phase and weak coupling in the β-phase [249]. A magnetic phase transition is observed at 100 K for CoPc molecules [246]. Imperfections in the spin chains can weaken exchange interactions.

Additionally, magneto-transport experiments allowed to probe the differential conductance of this spin chain and demonstrated that the conductance showed three distinct steps under an external magnetic field [248, 250] (see Figure 1.9(b)). The steps indicate transitions from the singlet ground state to the excited triplet state due to the magnetic field's effect. Subsequent work showed that these states could also be addressed electronically such as to encode information within the magnetic state of the spin-chain within the junction [251]. The electrically driven TMR can be used to switch the sign of MR using low-voltage addressing (see Figures 1.9(c-d)), and to transmit spin-wave encoded information across an OSC using AFM pulsed voltage approach. These studies of cobalt phthalocyanines' structural and electronic properties has provided essential data on electron spin distribution and spin chain coupling. This research is crucial in understanding how these molecules can stimulate unique phenomena when used as spacers in a spintronic device.

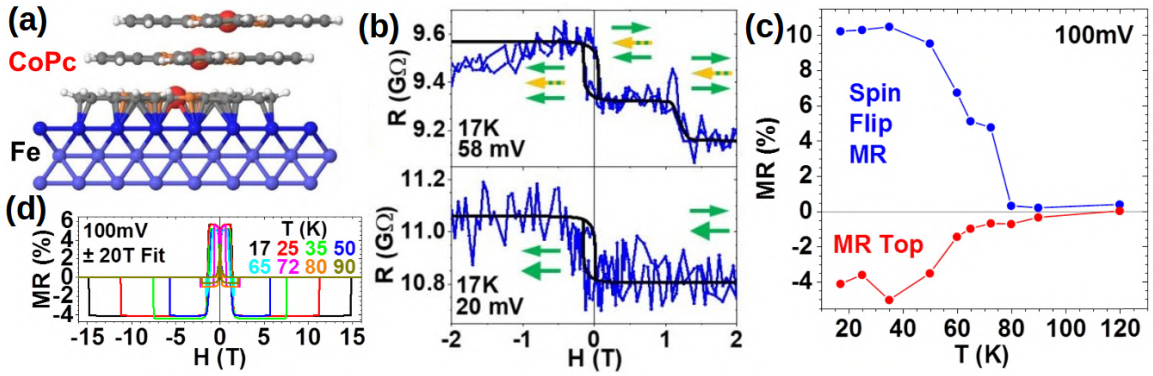

Figure 1.9: **Encoding information in the spin state of a molecular spin chain in a CoPc molecular junction.** (a) CoPc molecular spin chain on top of a Fe electrode. (b) $R(H)$ loops at 17 K for 20 < V (mV) < 80 and associated fits also represented in panel (d) for $\pm$20 T. (c) Temperature dependencies of the two spin-states of the molecular junction. Adapted from Reference [251]

.

1.4.3 Spinterfaces

When a single molecule is brought near a metal, the molecular orbitals hybridize with the metal's electronic energy levels, leading to spin injection at the interface. This hybridization results in two phenomena: the lifetime of the molecular level becomes finite as the charge can escape to the metal, resulting in energy broadening [252]; and a shift in the energy of the molecular level due to the interaction with the metal [253]. This leads to spin polarization and spin splitting [254]. The coupling between the metal and first molecular layer is called a "spinterface" [255, 256]. The spinterface induces two typical effects: a high spin polarization and an inversion relative to the surface layer depending on the intensity of the coupling between the ferromagnet and the molecule [257] (see Figure 1.10(a)). This spin-dependent hybridization can alter the magnetic and electronic properties of the surface such as to act as spin filters [254]. Experimental evidence of such phenomena has been observed in several types of molecules, making them potential candidates for spintronic applications [258, 259, 260, 261, 262, 263].

In particular, evidence for inverse spin polarization was discovered in phthalocyanines deposited on a ferromagnetic surface, with high spin polarization of about 80% observed for MnPc deposited on a cobalt surface [264] (see Figures 1.10(c-d)). Additional studies suggests that high spin polarization at the interface is a common phenomenon, regardless of the molecule involved [262, 257] .

Then, in a follow-up study, my group showed spin-dependent hybridization at the interface of Fe/C_{60} molecules, with a 89.1% spin polarization at Fermi energy [257]. This high level of spin polarization could be beneficial in energy harvesting applications. Changes in electronic properties due to spin-dependent hybridization can affect the magnetic properties of ferromagnetic surfaces, changing the easy axis of the FM layer from in-plane to out-of-plane [265]. Furthermore, it has been discovered that C_{60} molecules can induce permanent ferromagnetism in diamagnetic metals such as copper [266].

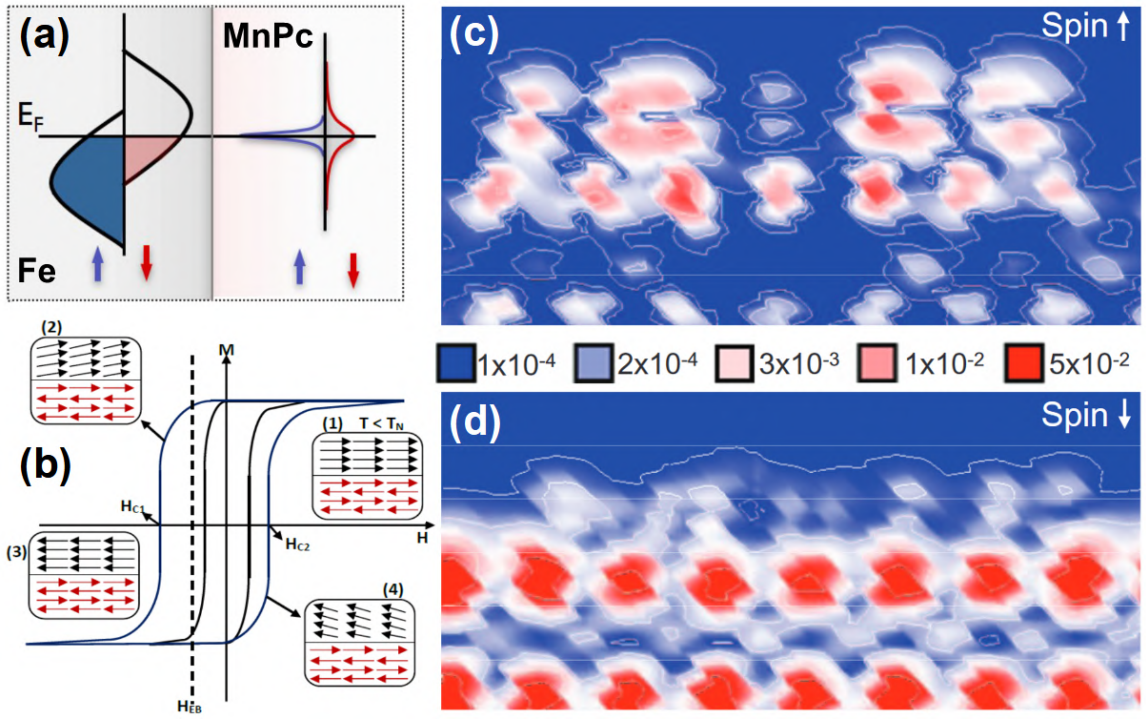

Figure 1.10: **Properties of spinterfaces.** (a) Typical density of states of the Fe/MnPc interface showing an inversion of spin polarization. (b) Graphical representation of the hysteresis loop along with the spin configurations of a coupled FM/AFM system at different stages of field cooling. H_{C1} and H_{C2} are the coercivities while H_{EB} represents the exchange bias field. (c–d) Spatial charge density maps show how the numerous C and N sites of MnPc exhibit a highly spin-polarized density of states at E_F hybridized with Co states and thus contribute to conduction. The maps are in units of $e\text{Å}^{-3}$. Adapted from Reference [264].

Spinterfaces are essential to exchange bias, a magnetic coupling phenomenon that occurs due to interface exchange coupling between ferromagnetic (FM) and anti-ferromagnetic (AFM) layers [267, 268, 269]. Exchange bias, which is key in spintronics, allows the AFM layer to remain unchanged by small magnetic fields while shifting the hysteresis loop of the FM layer in one field direction [270]. This leads to a unidirectional anisotropy, essential in pinning the magnetization direction of one of the FM layers. The exchange bias effect can be established using a field cooling procedure on the FM/AFM system, leading to shifts in the hysteresis loop along the magnetic field axis. The exchange bias field $\vec{H}_{EB} := \frac{1}{2}(\vec{H}_{C1}+\vec{H}_{C2})$ and coercivity $\vec{H}_C := \frac{1}{2}(\vec{H}_{C2} - \vec{H}_{C1})$ are calculated from the coercive fields $\vec{H}_{C1}$ and $\vec{H}_{C2}$ obtained from the hysteresis loop (see Figure 1.10(b)). Factors like interface roughness, defects, and domain structures in the AFM play crucial roles that are not fully captured by simple theories such as understanding this phenomenon remains a challenge [271]. For AFM structures made of molecular spin chains, *ab-initio* density functional theory (DFT) simulations have been particularly used to predict the magnetism of these structures [272, 262, 266] suggesting a mechanism based on magnetic hardening of the metal atoms, owing to electron transfer [266].

Magneto-transport measurements on Co/CoPc/Co MTJs showed inverse tunneling mag-

netoresistance and exhibit a lower coercive field amplitude for higher bias values [273]. Experiments also showed that exchange bias could be achieved on cobalt layers by depositing MnPc molecules [272]. Other molecules such as CoPc, FePc, and ZnPc when deposited on a Co film also exhibit exchange bias effects [274, 275, 276, 277, 278]. Understanding and controlling the magnetic exchange interaction at the FM metal/molecule interface is crucial to achieving multi-functional spintronic devices [251].

1.5 Framing summary

This Chapter introduced the basic concepts necessary to study the transport properties of magnetic tunnel junctions, with a particular emphasis on effects that can be used for memory applications such as resistive switching and tunnel magnetoresistance, along with phenomena that can be leveraged for energy harvesting applications such as rectification or negative differential resistance.

This introduction shed light on quantum mechanisms that may be at the center of an upcoming quantum revolution in technology that aims at drastically reducing the power consumption and the size of electrical components, and lead to efficient nanoscale energy converters. To this end, many efforts must be channeled in order to improve the reproducibility, the reliability and the fabrication process of these new devices so as to push forward the commercial industrialization.

In line with this objective, the experimental work at the center of this thesis, detailed in Part II, aimed at understanding in more depth the transport mechanisms occurring inside standard MgO MTJs, enriched with spinterfaces and controlled impurities in the hope of finding active devices or memories presenting the benefit of being routinely fabricated.

The mechanisms presented in this Chapter will therefore be necessary to analyze the results of the experiments presented in Part II. In the next Chapter, we present the necessary notions of thermodynamics which will be of use in Part III of this thesis devoted to the theoretical modeling of the spintronic engine.

Chapter 2

Quantum Thermodynamics

Quantum thermodynamics is an emerging field that aims to understand how the principles of thermodynamics emerge from quantum mechanics and how they apply to quantum systems. Quantum thermodynamics studies the thermodynamic behavior of small quantum systems, even down to the single particle level, that are coupled to a reservoir or environment [279]. It investigates how thermodynamic quantities such as energy, entropy, and temperature arise from the underlying quantum dynamics and quantum statistical properties of open quantum systems far from equilibrium [280]. Rather than being defined phenomenologically as in classical thermodynamics, in some cases, thermodynamic quantities can emerge from the underlying quantum mechanical laws [279].

Quantum thermodynamics differs from classical thermodynamics in several key ways. Quantum thermodynamics accounts for intrinsically quantum phenomena like superposition, entanglement, and quantum coherence, which do not have classical analogs. These quantum effects can lead to new thermodynamic phenomena and possibilities beyond classical bounds such that quantum systems, enabled by the use of engineered quantum reservoirs or coherent control over the system dynamics. Harnessing quantum resources such as coherence and entanglement may thus allow quantum thermal machines like engines and refrigerators to outperform their classical counterparts in efficiency or work extraction under certain conditions. Moreover, while classical thermodynamics deals primarily with systems near equilibrium, quantum thermodynamics can describe the full non-equilibrium dynamics of open quantum systems that are strongly coupled to environments and can potentially describe the thermodynamics of individual quantum trajectories *i.e.* not be limited to statistical ensembles.

Quantum thermodynamics promises to deliver new technologies in the fields of quantum computing, electronics, sensing, and energy devices. One of the most promising areas is the development of quantum heat engines, refrigerators, and other thermal machines that can outperform classical counterparts by harnessing quantum resources like coherence, entanglement, and quantum correlations, eventually extend limits like the Carnot efficiency. Quantum thermodynamics could also enable development of quantum batteries and power cells with enhanced energy storage and transfer capabilities.

This Chapter aims at presenting the basic notions of quantum thermodynamics that

will be of use in Part III of this thesis, devoted to the description of the quantum spintronic engine. The following presentation will be centered on tools that are of particular use in the study of quantum engines, which are the main focus of this work. These concepts will be utilized in the next Chapter to review the current prospects of quantum heat engines.

2.1 Dynamics of open quantum systems

Open quantum system techniques are crucial for quantum mechanics studies because closed quantum systems are an idealization; everything in nature interacts with some environment. Open Quantum Theory addresses this problem by dividing the whole system into the 'system of interest' and 'an environment', providing a means to effectively remove the environment from the equations of motion [281]. The objective is to make the reduced equations of motion easier to solve than the comprehensive dynamics of the system. In this aspect, open quantum systems serve as a basis for quantum thermodynamics, which deals with quantum systems in interaction with macroscopic heat baths.

2.1.1 Dynamics of closed quantum systems

Before presenting the tools of open quantum systems, let us refresh the main concepts of quantum mechanics. Quantum theory is based on a Hilbert space $\mathcal{H}$ whose elements $|\psi\rangle \in \mathcal{H}$ of unit norm are called *state vectors* or *pure states*. The Hilbert space is built as the minimal set containing all physical states of the system. In this regard, a composite system of N subsystems can be constructed by taking the tensor product of each subspace $\mathcal{H} = \mathcal{H}_1 \otimes \cdots \otimes \mathcal{H}_N$, in which case states of the form $|\psi\rangle = |\psi_1\rangle \otimes \cdots \otimes |\psi_N\rangle$ are called *separable* while other states are called *entangled*.

A possible measurement is described by a Hermitian operator O which we call an *observable*. Due to the spectral theorem, each observable O can be decomposed in an eigenbasis such that $O = \sum_i o_i P_i$ where the (o_i) are the eigenvalues, corresponding to the measurement outcomes and the $(P_i = |o_i\rangle\langle o_i|)$ are orthonormal projectors that map any state onto the post-measurement state $|o_i\rangle$.

The dynamics of a closed system are contained within the Hamiltonian H, which is a Hermitian operator representing the total energy of a system. The time evolution $|\psi(t)\rangle$ of any initial unit state $|\psi(0)\rangle \in \mathcal{H}$ is then determined by two processes. First, the state is driven by the deterministic, Markovian, continuous-time, linear, causal Schrödinger equation $i\hbar\frac{\mathrm{d}|\psi\rangle}{\mathrm{d}t} = H|\psi\rangle$, called "Process 2" by Von Neumann [282]. Then, at some moment in time, the operator measures the system via an observable O, triggering a second discrete-time, stochastic, non-linear, non-causal process called "Process 1" [283], which returns a particular measurement outcome o_i and a measurement state $|o_i\rangle$. This process is determined by the Born rule which states that the probability of measuring the state $|o_i\rangle$ is simply given by $P(o_i) = \langle\psi|P_i|\psi\rangle = |\langle o_i|\psi\rangle|^2$, such that the output state $|\psi_i\rangle$ after the measurement is $|\psi_i\rangle = \frac{P_i|\psi\rangle}{\sqrt{\langle\psi|P_i|\psi\rangle}}$. Summing up the probabilities, we also obtain the average value of the observable as $\langle O\rangle = \langle\psi|O|\psi\rangle$.

However, in most cases, we have only imperfect information about the state so that we may only know that a quantum system can be in one state of an ensemble of pure states $\{|\psi_i\rangle\}$ with probabilities p_i. If more than one p_i is different from zero, we have a *mixed state* that is described by the *density matrix* $\rho = \sum_i p_i |\psi_i\rangle\langle\psi_i|$. The density matrix is hermitian, positive and has a unit trace. The *purity* $\mathrm{Tr}(\rho^2)$ is 1 iff ρ represents a pure state. In an arbitrary basis, the diagonal elements of ρ are called the *populations* and the off-diagonal elements are the *coherences*.

The dynamics for the pure states can be easily generalized for mixed states. Schrodinger's equation for pure states thus transforms into the Von Neumann equation for mixed states and others correspondences are written in Table 2.1. For density matrices, the formalism allows for a third process called *unselective* measurements. Unlike *selective* measurements which are stochastic and non-linear, one can consider not to look at the result of a measurement so that the post-measurement density matrix will be transformed into the weighted average of the post-measurement states for all possible measurement outcomes. The resulting linear map $\rho \to \sum_i P_i \rho P_i$ is called a *quantum channel* and corresponds to some projection of the density matrix onto the measurement basis relative to the observable O. Such a map is completely positive and trace-preserving (CPTP) such as it conserves the properties of the density matrix, which is a requirement for consistent operations on quantum states.

To eliminate some degrees of freedom, the total density matrix may be studied on a subspace $\mathcal{H}_a$ of the total bipartite Hilbert space $\mathcal{H} = \mathcal{H}_a \otimes \mathcal{H}_b$. The resulting reduced density matrix of the subsystem a is defined by the partial trace $\rho_a = \mathrm{Tr}_b(\rho)$.

	pure states	mixed states
tensor product	$\lvert\psi_1\rangle \otimes \cdots \otimes \lvert\psi_N\rangle$	$\rho_1 \otimes \cdots \otimes \rho_N$
time evolution	$i\hbar \frac{\mathrm{d}\lvert\psi\rangle}{\mathrm{d}t} = H\lvert\psi\rangle$	$i\hbar \frac{\mathrm{d}\rho}{\mathrm{d}t} = [H, \rho]$
Born rule	$P(o_i) = \langle\psi\rvert P_i \lvert\psi\rangle$	$P(o_i) = \mathrm{Tr}(P_i \rho)$
observable average	$\langle O\rangle = \langle\psi\rvert O \lvert\psi\rangle$	$\langle O\rangle = \mathrm{Tr}(O\rho)$
projection	$\lvert\psi_i\rangle = \frac{P_i\lvert\psi\rangle}{\sqrt{\langle\psi\rvert P_i \lvert\psi\rangle}}$	$\rho_i = \frac{P_i \rho P_i}{\mathrm{Tr}(P_i\rho)}$
unitary operation	$\lvert\psi'\rangle = U\lvert\psi\rangle$	$\rho' = U\rho U^\dagger$

Table 2.1: Table of correspondence between pure states and mixed states.

From now on, we adopt a system of natural units such that $\hbar = k_B = 1$.

2.1.2 Master equations

The time evolution of closed quantum systems is governed by unitary operators. However, this approach is inaccurate for open systems due to the interaction between the system and its environment. To determine the time evolution of open quantum systems, effective equations of motion or so-called master equations are used [281]. Exact solutions of these equations are challenging due to the size and complexity of the environment so the theory

of open quantum systems attempts to simplify the dynamics of the system and its observables, like energy and the robustness of quantum coherence. To overcome the difficulty in solving the master equations, various techniques have been developed, often aiming to derive a reduced description of the system's dynamics [284]. The basic assumption is that the whole system-environment combination is a large closed system with its time evolution governed by a unitary transformation under a global Hamiltonian. The usual assumption consists in decomposing the total Hamiltonian as $H = H_S + H_B + H_{SB}$, where H_S is the Hamiltonian of the system alone, H_B is the Hamiltonian of the bath and H_{SB} is the Hamiltonian of the system-bath interaction.

Non-Markovian equations

By tracing out the Von-Neumann equation for the density matrix ρ of the whole system $\frac{\mathrm{d}\rho}{\mathrm{d}t} = -i[H, \rho] \equiv L(\rho)$, one obtain the Nakajima-Zwanzig equation for the reduced density matrix of the system ρ_S [285, 286, 287]:

$$\partial_t \rho_S = \mathcal{P} L \rho_S + \int_0^t \mathrm{d}t' \mathcal{K}(t') \rho_S(t - t'), \tag{2.1}$$

where $\mathcal{P} = 1 - \mathcal{Q}$ is a projection operator that projects the total density operator ρ onto the subspace of the system of interest, and $\mathcal{K}(t')$ is a complicated memory kernel that captures the effects of the bath on the system over the time interval from $(0, t)$, reflecting non-Markovian dynamics where the system's history influences its future evolution.

While the Nakajima-Zwanzig equation is an exact equation, it can be very difficult to solve due to its non-Markovianity [287]. This means that approximations generally need to be introduced to reduce the complexity of the problem into something more manageable. For example, a bath with a fast relaxation time-scale leads to a time local equation.

Markovian equations

To simplify the previous master equation, assumptions need to be considered so as to recover a Markovian equation. Various approaches can be considered depending on the approximate dynamics of the bath and the system-bath coupling, which lead to different equations [288, 289]. The main issue with most of those approaches is that they often lead to equations that do not conserve the trace of the density matrix or its positivity, such that their results must be taken with care. For example, the Redfield equation does not preserve positivity [288, 289].

In this Thesis, we will mainly focus on the approach of the Lindbladian, which is a general type of master equation that has the advantage of preserving all properties of the density matrix. The derivation of this master equation usually relies on three hypotheses [287], although newer approaches allow some generalizations [289, 290]. First, it assumes that the system and the bath are initially uncorrelated: $\rho(0) = \rho_S(0) \otimes \rho_B(0)$. Then, the weak-coupling or Born approximation is used, stating that correlations between the system and the environment develop slowly, which corresponds to a perturbation to $\mathcal{H}_{SB}$. Next,

the Markov approximation is considered, such that excitations caused by the system on the environment decay quickly, which usually results in considering the invariance of the reduced density matrix of the bath $\rho(t) = \rho_S(t) \otimes \rho_B(0)$. And finally, the secular or rotating wave approximation is often used so as to discard the fast-oscillating contributions that do not interfere with the timescale of the system.

These assumptions lead to the Gorini–Kossakowski–Sudarshan–Lindblad (GKSL) or Lindblad equation [287] (see Appendix E for complete details of the derivation on a special case):

$$\dot{\rho_S} = -i[H_S + H_{LS}, \rho_S] + \mathcal{D}(\rho_S) \equiv \mathcal{L}(\rho_S), \tag{2.2}$$

where the first term describes the unitary evolution of the system and the second term corresponds to the dissipative part. The *dissipator* $\mathcal{D}$ is a superoperator that can usually be cast under the form:

$$\mathcal{D}(\rho_S) = \sum_{i,\omega} \left(L_i(\omega) \rho_S L_i^\dagger(\omega) - \frac{1}{2} \left\{ L_i(\omega) L_i^\dagger(\omega), \rho_S \right\} \right), \tag{2.3}$$

where $L_i(\omega)$ are called Lindblad or jump operators. The additional unitary contribution H_{LS} is called the *Lambd shift* and its role is to renormalize the system energy levels due to the interaction with the environment.

For a time-independent Hamiltonian, the kernel ρ_{ss} of the Lindbladian solving $\mathcal{L}(\rho_{ss}) = 0$ is called the *steady-state* and corresponds to a fixed point of the evolution to which the system may converge at infinite time. Solving this time-independent equation to find the steady-state is essential in quantum thermodynamics as it corresponds to the *thermalized state* of the system, in contact with thermal baths. For time-dependent Hamiltonians, under the assumption of *quantum adiabaticity*, solving the equations $\mathcal{L}(t)(\rho) = 0$ yields the instantaneous steady-state $\rho_{ss}(t)$ of the evolution, which approximates the trajectory of the system when the dynamics of the Hamiltonian are slow enough compared to the transient time-scale of the evolution of the system. The existence, unicity and attractivity of the steady-state is not guaranteed in the general case, so that the system may reach an asymptotic time-dependent final state [291], but some conditions may be checked to ensure the wanted properties [292]. In general, the reached steady-state will depend on the initial condition [291, 293], revealing the need for a careful preparation of the system and a fundamental link with the ergodic theorem [293].

Even if the Lindblad equation is Markovian, it can be very challenging to solve for very large systems. Thus, other techniques are being developed to approximate and reduce the amount of computations, such as Non-Equilibrium Green Functions (NGEF) plus Density Functional Theory (DFT) [294, 295], keeping in mind that large systems will see a fast emergence of partial equilibrium towards Boltzmann subspaces [296].

2.2 Quantum thermodynamic principles and quantities

Quantum thermodynamics aims to establish a consistent framework for describing thermodynamic quantities and principles at the quantum scale. It investigates the role of quantum

coherence and fluctuations in thermodynamic processes, which can lead to extensions of classical thermodynamic relations. Different laws of thermodynamics thus emerge from quantum phenomena and require the use of new quantities with no classical analogs, with the hope of using them to build more efficient thermal machines.

2.2.1 Thermodynamic quantities

Entropy is at the center of the theory of thermodynamics. It quantifies the amount of disorder of a system and is therefore crucial to quantify irreversibility, which is ruled by the second law. Let us then start by defining this concept.

Entropy

Quantum information theory is deeply linked with quantum thermodynamics through their extensive use of entropy as a measure of heat flow, extractable work and quantum information [297, 298]. The famous thought experiment of Maxwell's demon, able to separate cold from hot using information, is a direct example of this connection in classical physics (see Section 3.2).

There are many ways to define the entropy of a quantum system [299], but the canonical definition consists in adapting the Shannon entropy to the quantum state. The probability of getting the outcome o_i after measuring an observable $O = \sum_i o_i P_i$ is $p_i = \mathrm{Tr}(P_i \rho)$, so we can define the entropy S_O of the observable O as:

$$S_O(\rho) = -\sum_i p_i \ln p_i, \tag{2.4}$$

By minimizing this entropy for all observable, Von Neumann showed that the entropy that bears its name S is the most informative quantity that does not depend on a particular representation of the density matrix and is equal to the entropy of the Hamiltonian for thermal states:

$$S(\rho) = -\mathrm{Tr}\big(\rho \ln \rho\big). \tag{2.5}$$

It has all the necessary properties one can expect from an entropy. The Von Neumann entropy is invariant under unitary transformations, concave, null for pure states, maximal for maximally mixed states, sub-additive, additive for independent systems, and strongly sub-additive [300, 301].

From this definition, one can define a handful of additional quantities which may be of use in different contexts. Let us list the most important ones.

The relative entropy $S(\rho|\delta)$ allows to compare the information between two states ρ and δ:

$$S(\rho|\delta) = \mathrm{Tr}\big(\rho(\ln \rho - \ln \delta)\big). \tag{2.6}$$

The entropy of coherence $C(\rho)$ quantifies the amount of information stored within the off-diagonal components of the density-matrix:

$$C(\rho) = \min_{\delta \in I_H} S(\rho|\delta) = S(\delta_\rho) - S(\rho), \tag{2.7}$$

where I_H is the set diagonal states in the energy basis called the *incoherent states* and $\delta_\rho = \sum_j \langle\epsilon_j|\rho|\epsilon_j\rangle|\epsilon_j\rangle\langle\epsilon_j|$ is the diagonal part of the density matrix in the energy basis.

Ergotropy

When operating an engine, one usually wants to apply a cycle of several strokes, during which the system of interest, called the working substance (WS), will be connected to heat baths and exchange energy with an operator that will use it to perform work. Thanks to coherence, quantum states can be depleted of additional energy stored within the internal correlations of the system. We therefore need a metric to quantify the amount of energy that can be extracted from a system by applying a unitary cyclic process in a closed environment.

This leads to the concept of *ergotropy* $\mathcal{E}(\rho)$ theorized by Allahverdyan *et al.* [302], which replaces the free energy for finite systems and reads:

$$\mathcal{E}(\rho) = \max_{U \in \mathcal{U}_c} W(\rho, U), \tag{2.8}$$

where $\mathcal{U}_c$ is the set of unitary cyclic processes, meaning unitaries generated in a given interval $(0, \tau)$ by a time-dependent Hamiltonian such that $H(0) = H(\tau)$. In this context, $W(\rho, U) = \mathrm{Tr}\big(H\rho - HU\rho U^\dagger\big)$ is the work associated with this operation.

From this definition, one can discriminate from *passive state* with zero ergotropy, from *active states* which can produce work by a unitary cyclic process.

By diagonalizing $\rho = \sum_k r_k|r_k\rangle\langle r_k|$ with $r_{k+1} \leqslant r_k$ and $H = \sum_k \epsilon_k|\epsilon_k\rangle\langle\epsilon_k|$ with $\epsilon_k \leqslant \epsilon_{k+1}$, we can calculate the ergotropy:

$$\mathcal{E}(\rho) = \sum_k \epsilon_k(\rho_{kk} - r_k), \tag{2.9}$$

where $\rho_{kk} = \sum_{k'} r_{k'}|\langle r_{k'}|\epsilon_k\rangle|^2$ is the population in the energy basis. The passive state $P_\rho = \sum_k r_k|\epsilon_k\rangle\langle\epsilon_k|$ then results from the optimal cyclic process $U = \sum_k |\epsilon_k\rangle\langle r_k|$. The passive state is therefore the diagonal state in the energy basis with the same populations as ρ but in decreasing order: the highest population fills the lowest energy state.

Francica *et al.* [13] then separate the contributions coming from coherent and incoherent transformations:

$$\mathcal{E}(\rho) = \mathrm{Tr}\big(H\delta_\rho - HP_\rho\big) + \mathrm{Tr}\big(H\sigma_\rho - HP_\rho\big) = \mathcal{E}_i(\rho) + \mathcal{E}_c(\rho). \tag{2.10}$$

Here, σ_ρ possesses the same coherence as ρ but less average energy. $\mathcal{E}_i$ is the *incoherent ergotropy* when using only incoherent operations that reshuffle the energy basis up to a phase or erase all coherence by dephasing maps, and $\mathcal{E}_c$ is the *coherent ergotropy*, which is the maximum extractable work while keeping coherence unchanged.

Ergotropy has been used to prove that it is possible to extract work from coherences. As a first example, one can separate a bipartite quantum correlated system through suitably chosen partial measurements [303]. As another example, a system of collectively coupled qubits coupled to a thermal bath at a finite temperature can generate a steady state that has coherences in the energy eigenbasis, such that we may extract ergotropic work from this "thermal charging" [304]. The concept is therefore central in the study of quantum batteries [305].

Temperature

Temperature is a fundamental concept in thermodynamics, but its definition and interpretation in quantum systems have been the subject of ongoing research and debate. Temperature in an out-of-equilibrium small quantum system is generally not defined, given the intrinsically macroscopic nature of this quantity [306], although a local instantaneous temperature may be identified in some contexts for different purposes. In quantum thermodynamics, temperature T and its inverse β usually refer to a property of a macroscopic reservoir in a thermal state, represented by a Gibbs density matrix $\gamma = e^{-\beta H}/Z$ where $Z = \mathrm{Tr}(e^{-\beta H})$.

When coupled to such a heat bath, a small-sized system can inherit temperature-like behaviors such as it may be useful to generalize this concept [307]. The ability of a quantum system to heat up or cool down a thermal reservoir can be quantified by defining effective temperatures for the system [307]. For example, the local temperature measurement of an interacting quantum electron system arbitrarily far from equilibrium via a floating thermoelectric probe can be developed such that the local temperature and chemical potential of the probe are completely determined by the zeroth and first moments of the local energy distribution in the system, just as it is in an equilibrium system [308, 309].

Recent research has explored the concept of negative absolute temperatures, which can be realized synthetically by coupling positive temperature baths [310], for example by tailoring an attractive interaction in an ensemble of ultracold bosons [311]. Surprisingly, a bath with a negative temperature is found to be "hotter" than any positive temperature bath, requiring an amendment to the Kelvin-Planck statement of the second law [310]. However, the overall entropy production remains positive, obeying the Clausius statement [310].

2.2.2 Separating work and heat, the challenge of the first law

The first law of quantum thermodynamics is a statement about the conservation of energy in quantum systems and establishes the equivalence between work and heat [312].

Energy conservation during Process 2

Conservation of energy is trivial in closed quantum systems during the deterministic evolution of the system given the unitarity of the Schrödinger and Von Neumann equations. From the evolution of closed systems, energy and particle currents from/to the environment can be defined for non-unitary open systems driven by master equations in order to verify global energy conservation. In the case of open quantum systems weakly coupled to multiple reservoirs, a statement of energy conservation can be written. In the Lindbladian framework, the dissipator $\mathcal{D}$ can be separated in different contributions coming from different reservoirs α such as $\mathcal{D} = \sum_\alpha \mathcal{D}^\alpha$ [313]. This separation makes it possible to define the energy transfer rate from the system to the reservoir α as $\dot{E}_\alpha = \mathrm{Tr}\big(H_S \mathcal{D}^\alpha(\rho_S)\big)$, such that the conservation of energy reads:

$$\frac{\mathrm{d}E}{\mathrm{d}t} = \sum_\alpha \dot{E}_\alpha, \tag{2.11}$$

where $E = \mathrm{Tr}\big(H_S \rho_S\big)$ is the internal energy of the system.

In a more general approach, for a time-dependent, out-of-equilibrium system consisting of interacting electronic and phononic degrees of freedom that are strongly coupled to an environment of non-interacting electrons and phonons, Kumar and Stafford [314] are able to derive a first law of thermodynamics reading:

$$\frac{\mathrm{d}}{\mathrm{d}t}\langle U\rangle \equiv \frac{\mathrm{d}}{\mathrm{d}t}\mathrm{Tr}\big(\rho_S(t)(H_S(t) + H_{SE})\big) = \dot{W}_{ext}(t) - \sum_\alpha \mu_\alpha I^N_\alpha(t) - \sum_\alpha I^Q_\alpha(t), \tag{2.12}$$

where $\dot{W}_{ext}(t) = \mathrm{Tr}\big(\rho_S(t)\dot{H}_S(t)\big)$ is the external power applied to the system by the time-dependent Hamiltonian, μ_α are the electrochemical potentials of the reservoirs and I^N_α and I^Q_α refer to average particle and heat currents to the reservoir α respectively. This formula is intriguing compared to the classical case because this partitioning requires that the internal energy operator U be identified as the sum of the System Hamiltonian $H_S(t)$ and the full coupling Hamiltonian H_{SR} describing the interface.

It is important to point out that this conservation of energy is only valid at a statistical average level, such as it may not hold for single trajectories, which may only be observed using a measurement involving Process 1. This observation is deeply linked with the curious nature of the time-energy Heisenberg uncertainty relation $\Delta E \Delta t \geqslant \frac{\hbar}{2}$ (which still lacks a solid systematic mathematical justification, because time is not an operator in standard quantum mechanics [315, 316, 317]).

Energy conservation during Process 1

Owing to the fact that the measurement process is considered as a black box in standard quantum mechanics in the Copenhagen interpretation, energy conservation during Process 1 is a matter of ongoing fundamental research and debate in the field. It is generally believed that energy is conserved at least on average during this process through a transfer between the measurement apparatus and the system, although no definitive framework

is widely accepted within the community. We review briefly some attempts to model the measurement process and its thermodynamics.

Kurt Jacobs [318] showed that it is only when a measuring device has access to a zero-temperature reservoir (that is, never) that measurement requires no energy. To obtain a given amount of information, all measuring devices must pay a cost equal to that which a heat engine would pay to obtain the equivalent work value of that information.

Rogers *et al.* [319]. proposed two possible measurement implementations: one is a quantum clock model with a completely time-independent Hamiltonian, while the other is a Jaynes-Cummings model that is time-dependent but conserves the total excitation number. They show that when a measurement is performed on the system, energy and heat are transferred between the system and the measurement apparatus.

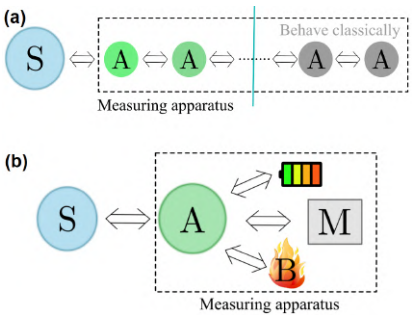

Figure 2.1: **Modeling the measuring apparatus.** (a) Von Neumann chain model of the objectification process. (b) The model of measuring apparatus considered in the article of Latune and Elouard [320]. Adapted from Reference [320]

Alternatively, Latune and Elouard [320] showed that it is possible to perform thermodynamically reversible measurements, thus reaching the minimal work expenditure using a special process modeling the measurement apparatus (see Figure 2.1). For finite-time measurement protocols, they illustrate the increasing work cost induced by rising entropy production that is inherent to finite-time thermodynamic processes. This highlights an emerging trade-off between the velocity of the measurement and the work cost, on top of a trade-off between efficiency of the measurement and work cost.

The measurement problem may be the most critical ontological issue in all of physics as it is deeply rooted in the way reality is being constructed, so I guess that a definite model of the thermodynamics of measurements will only be settled once a final answer is given to the interpretation problem of quantum mechanics through an observer theory. This issue is profoundly linked with the non-causal nature of measurements in quantum field theories [321] and quantum gravity [322].

Defining work and heat

In classical thermodynamics, the first law states that the variation of the conservative internal energy of the system $\mathrm{d}U$ is linked to an infinitesimal change in work δW and heat δQ such as $\mathrm{d}U = \delta W + \delta Q$. This definition is therefore intrinsically contextual as it depends on the specific trajectory of the system within a specific experimental setup.

In quantum thermodynamics, this work-heat separation is even less clear and depends on the approach of the experiment. In the case of the spintronic engine, we are interested in electrochemical work, so our main interest will be the particle current flowing from one reservoir to the next, through the quantum system. Let us present briefly a couple of

frameworks.

The first, trivial and widely used approach consists in differentiating the internal energy of the system U and identifying the two terms as work and heat:

$$\mathrm{d}U = \mathrm{d}\mathrm{Tr}\big(H_S\rho_S\big) = \mathrm{Tr}\big(\mathrm{d}H_S\rho_S\big) + \mathrm{Tr}\big(H_S\mathrm{d}\rho_S\big) = \mathrm{d}W + \mathrm{d}Q, \tag{2.13}$$

so that work is identified as the variation of the energy while heat corresponds to the variation of populations and coherences. This naive approach may have some relevance in some contexts but needs to be used with precautions as work may be extracted from coherences in particular setups. Indeed, Shi *et al.* [12] showed in the particular example of an XY model that additional work from coherences may be extracted in this setup such as the differential work and heat read:

$$\mathrm{d}W = \mathrm{Tr}\big(\mathrm{d}H_S\rho_S\big) + T\mathrm{d}C \;\text{ and }\; \mathrm{d}Q = \mathrm{Tr}\big(H_S\mathrm{d}\rho_S\big) - T\mathrm{d}C, \tag{2.14}$$

where C is the entropy of coherence (Equation 2.7).

In many contexts such as the widely-used "two-measurement" approach [323, 324] and other studies [323, 325], work is defined only like above, as the energy change of the system due to an external driving force W_{ext} (see Equations 2.12 and 2.13) incorporated through a time-dependent Hamiltonian $H(\lambda(t))$, where $\lambda(t)$ is the externally controlled work parameter. This definition is consistent with the classical definition of work as the energy required to change a parameter of the Hamiltonian against a generalized force. However, this approach requires an explicit time-dependence in the system Hamiltonian to extract work.

An alternative view is that work can be extracted from a system by using another quantum system as a "work storage" device, even with a time-independent Hamiltonian. The key idea is that the interactions between the two systems can facilitate work extraction such that non-equilibrium thermodynamic processes affecting the system S involve work exchange with its environment B, without needing an external time-dependent driving, but merely due to the $S - B$ interactions [326].

Any operational definition of work must therefore allow for two facts: first, that work characterizes a process rather than an instantaneous state of a system and, second, that quantum systems are sensitive to the interactions with a measurement apparatus, leading to inevitable fluctuations around mean values [323]. Because of the intrinsic stochastic nature of quantum physics, the first law of thermodynamics is shown to lead to an inequality, not an equality, such that it corresponds to a maximum change in the local entropy as the nonequilibrium state of the system is changed [309]. Some of these works also claim to derive the second law of thermodynamics in a quantum context [313, 309, 325] from first principles and minimal assumptions, which is the subject of the next section.

2.2.3 Deriving the second law from open system dynamics

The second law of thermodynamics in the context of quantum thermodynamics takes on a more nuanced and generalized form compared to its classical thermodynamic definition.

The traditional statement of the second law, which forbids heat flow from a cold to a hot body without the application of an external force, is still mostly valid in the quantum regime on the largest scale. However, quantum mechanics imposes additional constraints on allowed state transformations, often leading to a family of "second laws" rather than a single one [327].

To highlight the difficulty in establishing a clear second law in quantum thermodynamics, let us start by observing that the usual statement that entropy tends to a maximum for closed isolated (that is, never) quantum system is questionable in the context of quantum mechanics. Indeed, Process 2 is unitary so entropy is constant during the time-evolution of a system, and Process 1 reduces the wave packet with a projection operator, so that entropy is supposed to decrease from this localization. Let us then dissipate this apparent contradiction.

Information transfer during Process 2

Let us proceed just as in the previous section and start by deriving the second law for the continuous evolution ruled by Process 2 for open quantum systems weakly coupled to reservoirs. In the context of the Lindbladian, if we assume that the grand canonical ensembles are stationary states of the dissipators of each reservoirs α, meaning that $\mathcal{D}^\alpha(\rho_{eq}^\alpha) = 0$ with

$$\rho_{eq}^\alpha = e^{\beta_\alpha(H_S - \mu_\alpha N)}/Z_\alpha, \qquad Z_\alpha = \mathrm{Tr}\big(e^{\beta_\alpha(H_S-\mu_\alpha N)}\big) \tag{2.15}$$

then Spohn's inequality [328]:

$$-\mathrm{Tr}\Big(\mathcal{D}^\alpha(\rho_S)\big(\ln\rho_S - \ln\rho_{eq}^\alpha\big)\Big) \geqslant 0 \tag{2.16}$$

lead to the following *partial Clausius inequalities* for entropy production associated with each dissipator [313]:

$$\dot\sigma_\alpha = \dot S_\alpha - \beta_\alpha \dot Q_\alpha = -\mathrm{Tr}\Big(\mathcal{D}^\alpha(\rho_S)\ln\rho_S\Big) - \beta_\alpha \mathrm{Tr}\Big(\mathcal{D}^\alpha(\rho_S)(H_S - \mu_\alpha N)\Big) \geqslant 0, \tag{2.17}$$

where $\dot S_\alpha$ is the rate of change of the entropy due to the dissipator α and $\dot Q_\alpha$ is the heat current from reservoir α. Using the particle current $W_\alpha = \mu_\alpha \mathrm{Tr}\big(\mathcal{D}^\alpha(\rho_S)N\big)$ and the partial free energy rate $\dot F_\alpha = E_\alpha - T_\alpha S_\alpha$, this inequality also reads $T_\alpha\sigma_\alpha = W_\alpha - F_\alpha \geqslant 0$. Summing these all up we get the standard Clausius inequality:

$$\dot\sigma = \sum_\alpha \dot S_\alpha - \sum_\alpha \beta_\alpha \dot Q_\alpha \geqslant 0. \tag{2.18}$$

Although the above assumptions are fairly general, many systems with properties like non-Markovianity may fall outside of these prerequisites such that they could falsify the above derivation. Although some attempts could prove it with larger assumptions [325, 309], it appears more as an experimental phenomenological law than a consequence of first principles. For example, microscopy experiments of an evolving quantum system indicate that the full quantum state remains pure, whereas thermalization due to entanglement occurs on a local scale, thereby creating entropy and justifying the use of statistical physics for local observables [329].

The second law appears as a symmetry-breaking selection principle, limiting the observables and density functions to the class that tends to thermodynamic equilibrium in the future. By studying a large class of non-unitary transformations, Prigogine *et al.* [330] deduced that the microscopic content of the second law appears as expressing a limit to observations and manipulations, exactly as does the second law on the macroscopic level. Correlations cannot be controlled to an extent that they undo the effect of collisions. The probabilistic interpretation of entropy, which presupposes a direction of time, becomes only possible as a consequence of this negative statement.

Information transfer during Process 1

Process 1 seems incompatible with the second law of thermodynamics since selective measurements reduce the entropy of a system [331]. But the reduction of the wavepacket naturally transfers information from the system to the measurement apparatus [331, 332, 333], so that a measurement is never an operation on a closed system and entropy must increase in the apparatus [331].

On the contrary, non-selective quantum measurements represented by quantum channels usually increase the entropy of a system since they introduce additional mixing due to the consideration of all measurement outcomes [334], but they can also reduce it like in the case of spontaneous emission such as it is difficult to characterize the information exchange between the system and the measurement apparatus in the most general case.

These two measurement processes are deeply linked with the concepts of Maxwell's demon and Landauer erasure, which will be studied in Chapter 3. They reveal the crucial importance of the thermodynamic work cost of acquiring, using and removing the memory of a measurement stored within the apparatus. We will study the arguments that predict the minimal work needed to perform a measurement and remove the memory in line with the second law, along with their limitations.

Contemporary controversies with the second law

It seems that the second law is deeply rooted in the initial conditions, markovianity, ergodicity and linearity of a system, both in classical and quantum thermodynamics. In particular, living systems are known to be non-ergodic, meaning that their phase space is changing as they evolve, in direct violation of the second law if one does not account for the dissipated energy they need to behave as feedback loops [335, 336].

In the context of this Thesis, Giorgio Parisi obtained the 2021 Nobel Prize in Physics for his work [337] showing that spin glass systems below the freezing temperature present instances trapped in a non-ergodic set of states: the system may fluctuate between several states, but cannot transition to other states of equivalent energy. Intuitively, one can say that the system cannot escape from deep minima of the hierarchically disordered energy landscape [338]. Ergodicity breaking implies that the system cannot access all microstates, which seems to contradict the idea of maximizing entropy [339]. However, recent studies have shown that ergodicity breaking in spin glasses and other complex systems does not

violate the second law [340, 341, 342]. The key point is that the entropy being maximized is the total entropy, including both configurational and vibrational contributions, maximizing entropy within a subset of microstates rather than over all possible phase-space [340].

Initial conditions can not only break the time-reversal symmetry of the otherwise reversible dynamics, but can also determine the direction of a process, so that the arrow of time is not an absolute but a relative concept. Micadei *et al.* [343] emphasized the limitations of the standard local formulation of the second law for initially correlated systems and offer at the same time a mechanism to control heat on the microscale as they have observed the reversal of the energy current for the case of two spins which never fully thermalize due to their finite size, although they still obey a generalized second law.

This experiment shows that, given the atomic nature of matter, whose behavior is well described by statistical physics, the second law could not hold unconditionally, but only statistically. It is not an absolute law. There is yet no known fundamental physical law to exclude its possible macroscopic violation but it has never been violated. And although many proposals claimed to break this principle [344], all attempts were disproved when including all processes in the equation [336], revealing the profound fact that at the statistical level, an energy cost must always be consumed to decrease entropy in a finite temperature equilibrium system.

In essence, the second law originates from the coarse-graining of reality, inherent to the fact that observers, whether classical or quantum, are computationally bounded and causally connected. This inaccessibility of the full counting of all degrees of freedom entails that information is intrinsically inaccessible and hidden in the thermal and entanglement degrees of freedom. As time evolves, chaos and causality imply that non-interacting observers are progressively losing track of the computations occurring during each collision, thereby forcing a dilution of information into the inaccessible degrees of freedom. Computational simulations of billiard tables indeed show that, no matter the phase-space precision of the recorded data, there exists a time after which the billiard becomes "quantum" such that a statistical description becomes inevitable [345, 346]. Controversies around the second law also reveal that entropy is observer-dependent [347, 348] since one can arbitrarily choose the degrees of freedom relevant to this observer such that apparent violations of the second law may be found: when one chooses to ignore an outside input of energy required to fuel a non-linear or non-Markovian interaction building a feedback loop, a system can be perceived as self-organizing, giving rise to permanent oscillations like in the Van der Pol oscillator [349].

In the end, at the microscopic level, it would seem that information is conserved, but is becoming less and less accessible to macroscopic inert observers, that are forced to make approximations which accumulate over time, thereby progressively reducing the knowledge one has on a system and creating entropy. In my opinion, physics would need a fundamental informational and computational theory of the Universe containing a clear axiomatic description of an observer in order to firmly ground the second law on generalized principles. I believe that such a framework would create big connections between the measurement problem, entanglement, quantum gravity and thermodynamics. The Wolfram model is an interesting first attempt towards this goal [350].

2.3 Non-thermal baths and conserved charges

This section presents the quantum features of reservoirs with no classical analogues that an operator can exploit to extract energy. These additional properties challenge the classical laws of thermodynamics and can be used to extract work from a single heat bath or overcome the Carnot efficiency limit, mainly by harvesting energy from quantum coherence.

2.3.1 Phaseonium

As a premise, let us first present *phaseonium*, which represents the simplest system that exhibits quantum coherence effects on thermodynamic processes. This concept, first theorized by Scully *et al.* [351], was the first demonstration of the use of coherence as a fuel to power an engine. They study a quantum Carnot engine in which the atoms in the heat bath are given a small bit of quantum coherence. The induced quantum coherence becomes vanishingly small in the high-temperature limit at which we operate and the heat bath is essentially thermal. However, the phase, associated with the atomic coherence, provides a new control parameter that can be varied to increase the temperature of the radiation field and to extract work from a single heat bath.

This engine works thanks to a mirror cavity with a piston that hosts a three-level photon bath that exhibits some small coherence between two nearly degenerate energy levels. This bath is non-thermal as it does not appear in a Gibbs state but can be assigned a "hot" temperature T_h through the average number of photons in the cavity. Through a four-stroke cycle, they are able to extract energy from this bath by depleting the bath of its coherence and dumping the resulting entropy in a cold bath of temperature T_c. They demonstrate an efficiency η of

$$\eta = 1 - \frac{T_c}{T_h}(1 + 3\epsilon\overline{n}\cos\phi) \tag{2.19}$$

where $\overline{n}$ is the average number of photons in the cavity, ϵ is the magnitude and ϕ is the phase of the coherence between the two nearly-degenerate ground states. We thus see that for $\phi = \pi$, work exceeds the Carnot limit and can be extracted even when $T_h = T_c$.

Theoretical studies have then extended the phaseonium concept to multi-level systems and explored engineering optimal quantum fuel states for thermodynamic tasks [352, 353].

2.3.2 Squeezing

The idea of the phaseonium has been generalized through the concept of squeezed thermal baths. They correspond to stationary, nonequilibrium reservoirs that are characterized by a temperature as well as further parameters. The nonequilibrium quantum nature of the reservoir induces an entropy transfer with a coherent contribution while modifying its thermal part, allowing work extraction from a single reservoir, as well as great improvements in power and efficiency for quantum heat engines [354].

Usually, a squeezed bath represents a thermal reservoir of bosons with Hamiltonian $H_R = \sum_k \omega_k b_k^\dagger b_k$, with b_k the bosonic ladder operator, that has been applied the squeezing operator $\mathcal{S}(\xi) = \exp\left(\frac{1}{2}(b_k^2 \xi^* - b_k^{\dagger 2}\xi)\right)$ such that its state π_R reads:

$$\pi_R = \mathcal{S}(\xi)\frac{e^{-\beta H_R}}{Z}\mathcal{S}^\dagger(\xi), \tag{2.20}$$

where β is the inverse temperature of the bath and $Z = \mathrm{Tr}(e^{-\beta H_R})$ [354, 355]. Essentially, squeezing thus changes the quadrature of two canonically conjugated variables.

By unsqueezing the bath, several processes have therefore shown how to extract mechanical work from a single squeezed thermal reservoir efficient, highly miniaturized engines [356, 354], charge a quantum battery [357] and to surpass the classical efficiency Carnot limit while still limited by an extended second law, bounding the maximum extractable work by the ergotropy [358, 355].

Other implications of this quantum property include quantum synchronization enhanced by squeezing [359] or optimized control and reversed heat flow in optomechanical systems [360].

2.3.3 Conserved charges

Finally, the concept of squeezing has recently been generalized further into the framework of thermodynamics with conserved quantities. The concept was first proposed by Vaccaro [361] in the specific case of systems of spins used to erase a memory at low cost (see Section 3.2.1) and later generalized by Guryanova *et al.* [362].

Let us first introduce the topic through an excursion in classical statistical physics by observing that imposing symmetry restrictions diminishes the entropy of a system and decreases its temperature [363]. In the case of elementary magnets made of N non-interacting spins, for example, imposing a symmetry axis reduces the number of possible configurations, such that the Boltzmann entropy decreases by $\frac{N}{2}\ln 2$ when N is large [363]. Moreover, classical thermodynamics can accommodate the treatment of particle exchange and chemical equilibrium through the concept of chemical potential, which appears as a Lagrange multiplier of the particle number in the definition of the internal energy differential $\mathrm{d}U = T\mathrm{d}S - P\mathrm{d}V + \mu N$.

In the context of quantum thermodynamics, these additional constraints one can impose on a system by reducing its symmetry or by fixing a chemical filling are generalized to the concept of *charges*, which translate into any conserved quantity a system may have [362] and formally relate to dynamical symmetries of the system [364]. To each conserved quantity is assigned both an operator A_i (like the Hamiltonian H) and a *charge* β_i (like the temperature β for H), which acts as a Lagrange multiplier that statistically quantifies the associated operator. The generalized thermal state τ thus reads:

$$\tau = \frac{e^{\beta_1 A_1 + \cdots + \beta_N A_N}}{Z}, \qquad Z = \mathrm{Tr}\left(e^{\beta_1 A_1 + \cdots + \beta_N A_N}\right). \tag{2.21}$$

Two things are important to note: first, the definition of the operators A_i is very nonrestrictive, allowing them especially to not commute and not be functionally dependent on one

another. Most importantly, energy need not be one of the conserved charges. In fact there is no reason to single out energy, or any other quantity for that matter as it is possible to conceive of situations in which everything is degenerate in energy, and thus where energy plays absolutely no role.

The generalized thermal state may then be associated with a *free entropy* $\mathcal{F}$ reading:

$$\mathcal{F}(\rho) = \sum_i \beta_i \mathrm{Tr}(A_i \rho) - S(\rho), \tag{2.22}$$

such that τ minimizes $\mathcal{F}$. The free entropy thereby generalizes the usual free energy of systems that conserve energy and other quantities in the framework of the grand canonical ensemble.

The essential result involving generalized heat baths comes from the possibility to trade one conserved charge with another at vanishing entropic cost, allowing a work-free conversion of two quantities [362]. Taking a bath with two conserved charges A_1 and A_2 with charge temperatures, a quantum system connected to the bath with initial state $\rho = \rho_s \otimes \tau$ can exchange A_1-type and A_2-type work after a global unitary transformation U defined as

$$\Delta W_{A_1} = -\Delta A_1^s - \Delta A_1^b \text{ and } \Delta W_{A_2} = -\Delta A_2^s - \Delta A_2^b, \tag{2.23}$$

where $\Delta A_i^s = \mathrm{Tr}\big(\mathrm{Tr}_b(A_i)(\mathrm{Tr}_b(U\rho U^\dagger) - \rho_s)\big)$ and $\Delta A_i^b = \mathrm{Tr}\big(\mathrm{Tr}_s(A_i)(\mathrm{Tr}_s(U\rho U^\dagger) - \tau)\big)$. A generalized principle stating the minimization of the global state with respect to the free entropy leads to a second law reading:

$$\beta_1 \Delta W_{A_1} + \beta_2 \Delta W_{A_2} \leqslant -\Delta \mathcal{F}_s = \mathcal{F}(\rho_s) - \mathcal{F}(\mathrm{Tr}_b(U\rho U^\dagger)). \tag{2.24}$$

Subsequently, by looking at the effects of small perturbations in the population of the states, it is possible to prove that a reversible process exists in which one can trade one conserved quantity with another, at zero free entropic cost [362]. This shows that we can extract as much of any individual conserved quantity as desired, as long as the other conserved quantities are appropriately consumed in the process, with the second law dictating how much of the others are necessarily consumed.

The formalism of conserved charges also generalizes the squeezing effect since a squeezed thermal reservoir can be cast under a generalized thermal state:

$$\pi_R = \frac{e^{-\beta_R(H_R - \mu_R A_R)}}{Z_R}, \qquad Z_R = \mathrm{Tr}\big(e^{-\beta_R(H_R - \mu_R A_R)}\big), \tag{2.25}$$

with $\beta_R = \beta \cosh 2\xi$, $\mu_R = \tanh 2\xi$ and $A_R = -\frac{1}{2}\sum_k \omega_k(\beta_k^2 + \beta_k^{\dagger 2})$ [355].

This framework opened a new area of research studying thermodynamics in the presence of non-commuting charges. Conserved charges introduce degeneracies, which can affect thermodynamic ensembles and non-commutation can prevent the charges from sharing an eigenspace, generating non-classical behaviors that can be used to challenge the usual thermodynamic limits [365]. Among others, the charges' noncommutation has been found to invalidate derivations of the thermal state's form, decrease entropy production [366, 367], increase the efficiency of engines [355] and put constraints on charge-conserving

dynamics, [367]. Evidence suggests that noncommuting charges may hinder thermalization in some ways while enhancing thermalization in others [367]. Knowing whether noncommutation will be beneficial or detrimental to the considered experiments remains an open and active question.

Non-commutativity also comes with challenging mathematical difficulties, and many efforts are devoted to understanding the extent to which classical concepts can apply to these kinds of reservoirs. For example, microcanonicals subspace can extend to non-commuting charges [368] but no degenerate microcanonical subspace necessarily exists [365] and non-commutativity has been shown to asymptotically reduce to the commutative case in the limit of large degrees of freedom [367].

And on the experimental side, challenges remain to confirm and find systems that will naturally thermalize towards a generalized thermal state with non-commuting charges [369], although spin chains seem to be a preferred platform to engineer this state naturally [365, 369].

2.4 Framing summary

This chapter presented the basic notions of quantum thermodynamics in relation with quantum thermal machines and showed how quantum coherence can give rise to additional resources that can be used to perform work. In close relations to open quantum systems for which the Markovian approximation allows a consistent treatment that contains natural extensions of the first and second laws of thermodynamics, we highlighted the specificities of quantum systems that require additional care so as to account for the effects of entanglement and measurements on their dynamics. Considering these difficulties, we challenged the second law of thermodynamics and showed the frontiers of fundamental quantum information theory, which shall intrinsically incorporate a limit on the amount of work that can be extracted on a given statistical system. However, this bound may be counter-intuitive, allowing to exceed the Carnot limit or extract energy from single heat baths with singular properties.

Of particular importance are the notions of *ergotropy* and *conserved charges*. Ergotropy quantifies the maximum amount of work from an open quantum system that can be extracted through unitary cyclic processes, and conserved charges enable a generalized framework to treat quantum systems in interactions with thermal baths that have special kinds of macroscopic symmetries. We shed light on the equivalent concept of squeezed baths, which can be used as a source of ergotropic work, and showed how infinite work can be extracted from a bath with conserved quantities, since energy can be traded with other conserved charges such as particles or angular momentum.

This framework should be able to describe the role of the three main ingredients of the machine: the ferromagnetic electrodes, the interface and the atomic centers. And in order to understand the quantum spintronic engine, these concepts must be utilized so as to clearly identify the origin of the autonomous electrical power generation, and correctly model the flow of energy, momentum, and particle currents. Energy must come from a non-

equilibrium phenomenon so as to avoid paradoxes originating from violations of a limit rooted in a generalized formulation of the second law. From this conceptual introduction, we can already point out key ingredients that may be part of the explanation. First, there is a crucial need for a detailed description of the ferromagnetic electrode baths, and that the ferromagnetic state, essentially behaving as a magnetically oriented reservoir, could be used both as an entropy and an angular momentum sink such that two conserved charges may be traded by the device to perform work at vanishingly low entropic cost. The work thus appears as an exchange of electronic charge for spins between the two electrodes. And then, the atomic centers in the barrier and the interfaces must be correctly modeled, accounting for the effects of quantum coherence, so as to explain how their interactions with the electrodes allow for such conversion of spin to charge. This requires a precise understanding of the dynamics of quantum information flows in the global system, which we will begin in Chapter 8.

Chapter 3

From thermoelectric generators to Quantum Engines

Heat can be transformed into electricity through the phenomenon of thermoelectricity, which includes the Seebeck and Peltier effects. The former directly converts heat into electricity and is used in power generators, while the latter is its inverse mechanism, used in thermoelectric cooling devices like refrigerators.

Although thermoelectricity has been known since the 1820s, this effect did not generate much interest until recently as it suffered from very low efficiencies which greatly limited its technological use cases. However, driven by the newest experimental techniques, allowing the precise fabrication of nanoscale devices, the field was resurrected in the XXIst century, allowing their potential use notably as reliable cooling systems for electronics [370] and generators able to harvest the waste heat generated by power sources [371, 370], eventually leading to self-powered wearable electronics [372].

Facing the difficulties of scaling up the efficiencies of thermoelectric devices so as to produce commercial applications [371], research on quantum engines has emerged in parallel, promising new eco-friendly, efficient and dense alternatives to produce energy by harvesting additional sources of work from quantum properties.

This Chapter starts by presenting the phenomenon of thermoelectricity and its applications in spintronic devices. Then, building upon the principles of quantum thermodynamics presented in the previous Chapter, we will focus on the fundamental controversy of Maxwell's demon and see how its modern understanding can give rise to energy applications. This study will then give us the necessary tools to review the latest developments in the field of quantum engines and batteries so as to gain insights into the possible mechanisms at work within the spintronic engine in the next parts of this thesis.

3.1 Thermoelectricity in spintronic nanogenerators

3.1.1 Classical thermoelectric devices

Conventional thermal devices work on classical effects like Seebeck and Peltier (see Figure 3.1) and are called particle exchange (PE) heat engines. This includes thermoelectric and thermionic devices [373]. They involve a thermal difference that drives a heat flow between two electrode reservoirs, which is converted into a charge current.

Most classical thermoelectric devices consist of two dissimilar semiconductor legs (one n-type and one p-type) that are connected electrically in series and thermally in parallel (see Figure 3.1). The semiconducting legs are typically made of bismuth telluride (Bi_2Te_3) or lead telluride (PbTe) based alloys. The p-type leg usually has a larger cross-section than the n-type leg due to lower hole mobility. Devices can be further stacked in multiple stages to utilize larger temperature differences more efficiently [370].

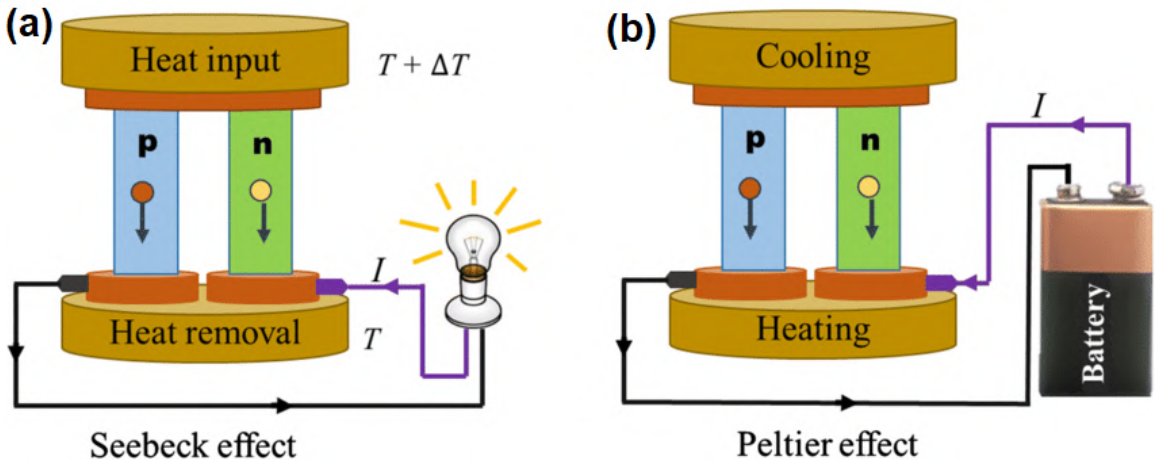

Figure 3.1: **Seebeck and Peltier effects.** Schematic principle of: (a) Seebeck effect and (b) Peltier effect. Adapted from Reference [374].

When a temperature gradient is applied across the two semiconductor legs, charge carriers (electrons or holes) diffuse from the hot side to the cold side, creating a voltage difference. This voltage difference, which is proportional to the thermal gradient, can drive an electric current through an external load, thereby generating power. The discovery of this phenomenon, known as the Seebeck effect, is attributed to Thomas Seebeck in 1821 [375].

Classical thermoelectric generators (TEGs) have been used for low-power applications like remote sensing, space probes (*e.g.*, Voyager, Pioneer) [370]. They are suitable for waste heat recovery and converting heat from combustion sources (*e.g.*, natural gas, propane) into electricity [370]. But they suffer from low conversion efficiency, which are typically below 10% for bismuth telluride devices. Material limitations and trade-offs between electrical and thermal properties restrict further efficiency improvements [371, 370].

3.1.2 Nanoscale thermoelectric devices

Nanoscale TEGs are an emerging technology that aims to overcome the limitations of classical thermoelectric devices by leveraging nanoscale materials and phenomena [372]. Classical thermal devices have a long length-scale, which allows all electrons in the device to achieve thermal equilibrium. This is explained via Boltzmann transport theory. Nanoscale thermal devices, however, have smaller length scales such that they display a strong non-equilibrium electron distribution that is explained by quantum transport theory. These nano devices, due to a size that is comparable to the electron wavelength, are considered to act as artificial atoms. They serve as a platform for exploring quantum physical phenomena. Practical applications for these nanoscale devices could include on-chip refrigeration and waste heat recovery systems for use in nano-electronics.

The study of thermoelectricity at the nanoscale therefore extensively uses quantum dot (QD) systems. Quantum point contact defects, intentionally placed within a semiconductor device, have shown promising abilities to harvest heat at the nanoscale. Theoretical works have focused on studying systems of QDs connected to different kinds of baths [376] so as to calculate the electronic and heat flows that are necessary to optimize their efficiencies [377, 378, 379, 376]. Compatibility with the laws of thermodynamics has been a major issue so as to correctly predict the limits of their power output [379, 378] and study the roles of fluctuations [379, 377]. In particular, these studies revealed that non-linearities and asymmetries in the system are necessary to achieve high rectification and boost performance [377, 379].

In parallel, experiments on QDs embedded into a semiconductor nanowire illustrated the theory and showed that that thermoelectric power conversion can, in principle, be achieved close to the thermodynamic limits, achieving 70% of the Carnot efficiency while maintaining a finite power output [378].

Other approaches have focused on the thermopower from defect-induced Seebeck domains in nanoscale pn junction TEGs that can potentially achieve higher efficiencies compared to conventional thermoelectrics. In this regard, single material like molybdenum disulfide (MoS_2) has been shown to overcome the efficiency-limiting electron-hole recombination issue present in conventional pn junction TEGs by engineering its grain boundaries [380], which ultimately enables high integration densities. Another study explored using graphene nanoribbons as the thermoelectric material, which exhibit high flexibility, stability at room temperature, and potential for efficient energy conversion [381]. The nanoribbon geometry allows the tuning of electronic and thermal transport properties.

3.1.3 Spin thermoelectric devices

The science of thermoelectricity evolved to incorporate electron spin properties, leading to a new field of physics known as spin caloritronics (or thermal spintronics). This combines spintronics (spin-dependent transport) and thermoelectricity (heat transport) to examine the interaction between spin and heat currents in magnetic tunnel junction devices. Spin caloritronics, which investigates effects in bulk materials and at their interfaces, has gar-

nered significant research interest.

The spin-dependent Seebeck effect (SDSE) occurs in ferromagnets due to spin-split states in their electronic band structure. A spin current is generated due to a temperature gradient applied across the spin-polarized ferromagnet, creating unequal spin up and down charge currents. In 2008, a different type of thermo-magnetic effect, the spin Seebeck effect (SSE), was discovered [382] (see Figure 3.2). The SSE takes place at the interface between a highly spin-polarized ferromagnet and a normal metal. It involves two steps: first a pure spin current is generated, which drives the spin carriers out of equilibrium, and then it's injected into the normal metal, which converts it into a transverse charge current via the inverse spin Hall effect (ISHE). Unlike the SSE, the SDSE does not require an interface and can occur without thermal spin injection. The basic structure of a spintronic TEG consists of a bilayer of a magnetic insulator (*e.g.*, Bi-YIG) and a non-magnetic metal with strong spin-orbit coupling (*e.g.*, Pt) [383].

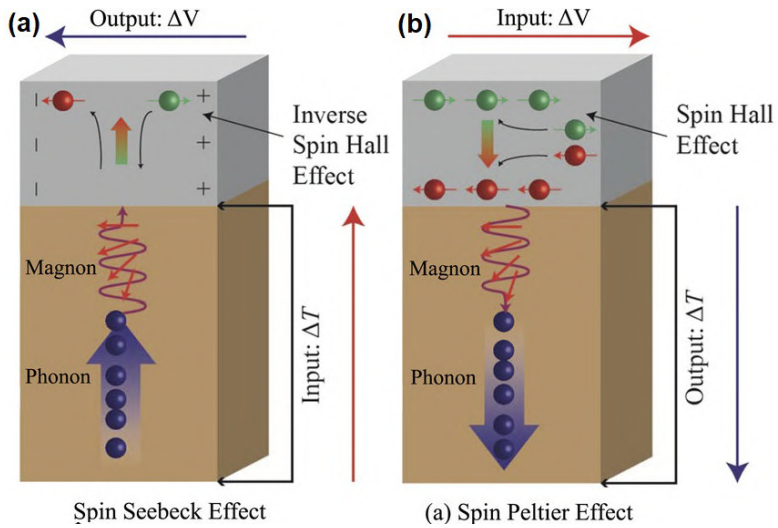

Figure 3.2: **Spin Seebeck and Spin Peltier effects.** Schematic principle of: (a) Spin Seebeck effect and (b) Spin Peltier effect. Adapted from Reference [384].

Anti-ferromagnets display promising thermoelectric performance due to their localized magnetic behavior below the Néel temperature. Materials like metallic Cr [385] and the iron superconductor $EuFe_2As_2$ [386] displayed increased thermopower around their critical temperature. Recent data suggests that the phase transition of the IrMn antiferromagnet enhances thermopower as a high Seebeck coefficient was recorded for IrMn/CoFeB MTJs, proving that the FM/AFM interface is crucial in the spin Seebeck effect [3]. The transition from charge-based Seebeck devices to spin Seebeck devices is seen as a significant step to explore thermal effects in spintronics and address heating issues in modern solid-state devices.

Advantages of using the SSE for designing TEGs is that it separates the thermal and electrical transport properties into different materials, allowing independent optimization. It benefits from direct power conversion that is proportional to device area, enabling scalability for large generators. It does not require continuous external magnetic fields once magnetized and potentially allows for higher efficiencies than conventional thermoelectrics

by suppressing recombination losses [4].

The anomalous Nernst effect (ANE) is another spin-based thermoelectric mechanism in which the output current is perpendicular to the temperature gradient. The ANE may have advantages over the SSE in terms of thermal instabilities and conversion efficiency limits [387, 388, 389, 390, 391].

3.2 Energy harvesting through Maxwell's demon

3.2.1 The controversy of Maxwell's demon

Maxwell's demon

Maxwell's demon is a thought experiment proposed by the physicist James Clerk Maxwell in 1867 to challenge the second law of thermodynamics [392]. The thought experiment involves an imaginary being (the "demon") that controls a small door between two chambers filled with gas molecules (see Figure 3.3). The demon's task is to observe the molecules and sort them based on their velocities. It allows only the faster-moving molecules to pass through the door into one chamber, while the slower-moving molecules are directed into the other chamber. As a result, one chamber becomes hotter (containing faster molecules) while the other becomes cooler (containing slower molecules), decreasing the overall entropy of the system without expending any energy. This seems to violate the second law of thermodynamics, which states that the total entropy of an isolated system cannot decrease over time.

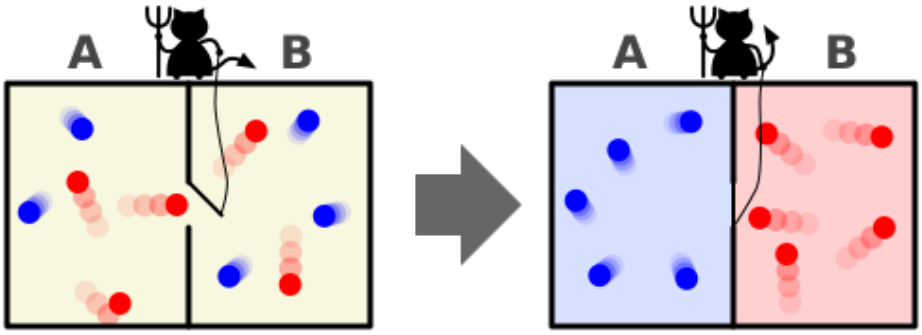

Figure 3.3: **Maxwell's demon.** Illustration of the thought experiment of Maxwell's demon. The demon has control over the trap door separating reservoir A from reservoir B and blocks the low-energy particle from reservoir A to go to reservoir B such as A is cooling down while B is heating up.

However, most scientists argue that Maxwell's demon cannot actually violate the second law because the demon itself must expend energy to measure the velocities of the molecules

and operate the door. The act of acquiring information about the molecules' velocities and processing that information to sort them increases the overall entropy of the system, compensating for the entropy decrease caused by separating the molecules [393].

The thought experiment has stimulated extensive discussions and research in physics, particularly in the fields of thermodynamics, information theory, and quantum mechanics [394]. It highlights the deep connections between information, entropy, and the second law of thermodynamics. While no practical device has been shown to violate the second law in the way envisioned by Maxwell, the concept has inspired various experimental realizations and theoretical explorations in modern physics [394, 392].

Szilard's engine

The Szilard engine is a thought experiment that demonstrates the interplay between information and thermodynamics. It is a hypothetical device that can extract useful work from a single heat bath by utilizing information about the microscopic state of the system. The Szilard engine is composed of a single particle confined in a box or container connected to a heat bath, a barrier that can divide the container into two equal parts and a mechanism (traditionally a "Maxwell's demon") that can measure the position of the particle and insert/remove the barrier accordingly.

The operating cycle of the Szilard engine involves four strokes (see Figure 3.4). First, the barrier is inserted into the container, dividing it into two equal parts. This step does not require work since the particle is equally likely to be on either side. Secondly, the position of the particle is measured to determine which side it is on. This acquires one bit of information. This information is then used to extract work by allowing the particle to push against the partition and expand into the full container volume, performing work on the surroundings. And finally, the barrier is removed in an isothermal, reversible process to reset the engine for the next cycle.

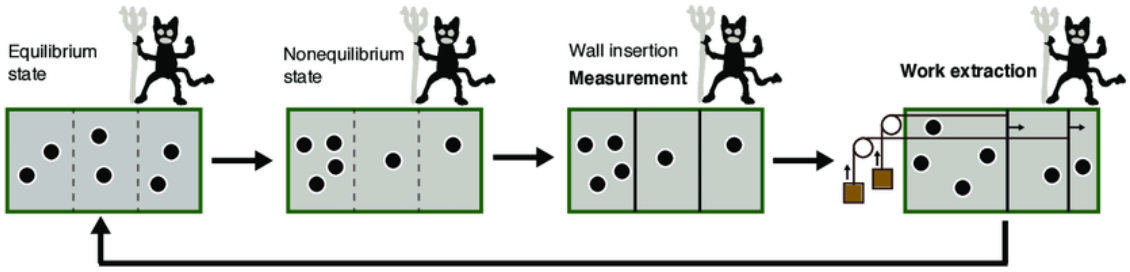

Figure 3.4: **Szilard's engine.** Illustration of a Szilard engine's cycle with $N = 6$ particles and $q = 3$ partitions. Adapted from Reference [395].

The key insight is that the information about the particle's position allows the extraction of work from a single heat bath, which seems to violate the second law of thermodynamics. However, the resolution lies in accounting for the entropy cost of erasing the one bit of information stored by the "demon" during the measurement step, as described below by Landauer's principle [396]. This entropy cost exactly balances the extracted work, preserving the second law.

Landauer erasure

Landauer's principle, also known as the Landauer erasure principle, states that erasing or resetting one bit of classical information by placing it in contact with a thermal reservoir is a logically irreversible operation that must dissipate a minimum amount of heat energy equal to $\beta^{-1}\ln 2$ [396]. In direct relation to the second law, it establishes a fundamental physical limit on how little heat must be generated when erasing a bit of classical information. This heat dissipation is required to remove the entropy associated with the unknown state of the bit before erasure.

The demonstration is straightforward. Let us consider a qubit with two energy states $|0\rangle$ and $|1\rangle$ with energy E. The two states are initially degenerate, with energy 0. We can erase the qubit state by placing it in contact with a reservoir at inverse temperature β and then inducing an energy splitting between the qubit states so that $|0\rangle$ has energy 0, but the state $|1\rangle$ has energy E. The splitting is induced adiabatically, that is, sufficiently slowly so that the qubit remains in thermal equilibrium with the thermal reservoir. The state of the qubit when the energy splitting is E has a Gibbs density matrix:

$$\rho = \frac{|0\rangle\langle 0| + e^{-\beta E}|1\rangle\langle 1|}{1 + e^{-\beta E}}. \tag{3.1}$$

The work required to increase the splitting from E to $E + \mathrm{d}E$ while in contact with the reservoir is given the probability of occupation of the state $|1\rangle$ multiplied by $\mathrm{d}E$ such as the total work in increasing the splitting from zero to infinity to recover the state $|0\rangle$ is:

$$W = \int \mathrm{d}W = \int_0^{+\infty} \frac{e^{-\beta E}}{1 + e^{-\beta E}}\,\mathrm{d}E = \beta^{-1}\ln 2. \tag{3.2}$$

Landauer's principle connects the concepts of information and thermodynamic entropy at a fundamental level and has profound implications for the ultimate physical limits of computing, as computations inherently involve logically irreversible operations like erasure.

The principle has been experimentally verified for classical systems as well as quantum for individual atoms coupled to a thermal reservoir. In the quantum regime, the von Neumann entropy replaces the Shannon entropy, but the minimum erasure heat remains $\beta^{-1}\ln 2$ per qubit erased. For example, Bozkurt *et al.* [397] verified this principle in a quantum spin Hall device in the presence of a spin bath by quantifying the amount of energy required to properly initialize a nuclear spin subsystem that can be used as a memory, then showed how a to use this resource for a Maxwell's Demon to harvest available heat energy from the reservoirs and induce charge current that can power an external electrical load.

Breaking the Landauer bound

Landauer argued that the process of erasing the information stored in a memory device incurs an energy cost in the form of a minimum amount of mechanical work. It is important to keep in mind the assumptions of the Landauer bound, which supposes adiabaticity of the

information erasure protocol and thermal equilibrium of the reservoir used as an entropy sink. Relaxing these hypotheses thus allows to erase a bit of information at vanishing energetic cost.

Indeed, non-equilibrium systems can break the Landauer bound, allowing for an erase of memory with greater efficiency. Ciampini *et al.* [398] showed experimentally that the nonequilibrium character of a an optomechanical double-well memory state enables full erasure with reduced energy consumption of as low as $0.07kT$ as well as negative heat production.

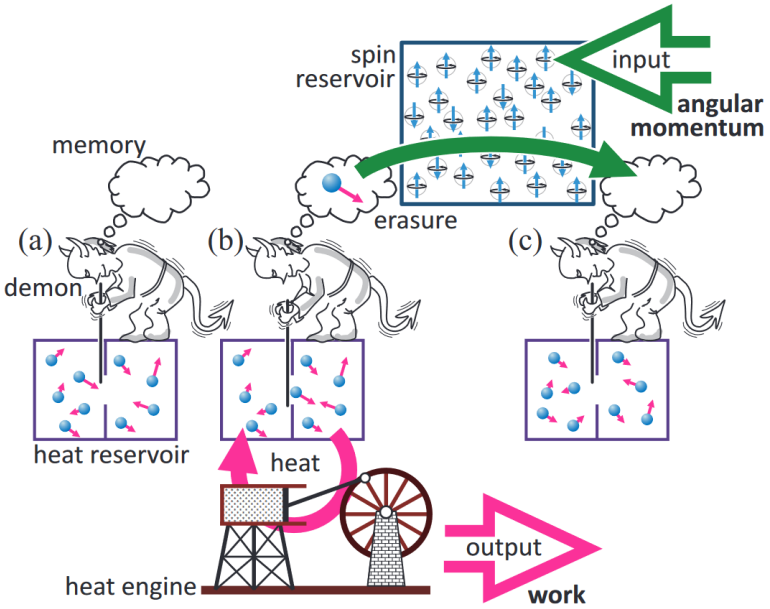

Figure 3.5: **Information erasure without an energy cost.** In step (a) the demon has no memory and the gas in the heat reservoir is in thermal equilibrium. Next, in step (b), the demon performs measurements of the speeds of the molecules and partitions the reservoir in two, trapping the fastest moving molecules in the partition on the right side and uses a heat engine operating between the two partitions to extract work. Finally in step (c) the demon's memory is erased using a spin reservoir and the two partitions are allowed to return to equilibrium. Adapted from Reference [361].

In parallel, Vaccaro *et al.* [361] theoretically showed that the energy cost can be reduced to zero by paying a cost in angular momentum or any other conserved quantity of a non-thermal reservoir with conserved charge (see Figure 3.5). Erasing the memory of Maxwell's demon in this way thus implies that work can be extracted from a single thermal reservoir at a cost of angular momentum and an increase in total entropy (see Section 2.3.3 on the thermodynamics of systems with conserved charges). Indeed, when building a Szilard's engine, the measurement of the velocity of a particle in a box can be stored in a system of spins, which can be reset at no energetic cost via a spin reservoir (see Figure 3.5).

Building upon this initial work, the team subsequently proposed an optical heat engine that operates under a single thermal reservoir and a spin angular momentum reservoir coupled to a three-level system with two energy degenerate ground states and showed that the

heat engine operates without producing waste heat and goes beyond the traditional Carnot engine where the working fluid is subjected to two thermal baths at different temperatures [399].

And in their latest work, Vaccaro's group [400] derived fluctuation theorems associated with spin reservoirs, and applied them to analyze the costs of information erasure for the generalized protocols such as to derive a number of bounds on the *spinlabor* and *spintherm* costs, which represent the equivalents of work and heat for a system exchanging angular momentum with a spin bath. The team proved a generalized bound on the spinlabor erasure cost $\langle \mathcal{L}_s \rangle \geqslant \gamma^{-1} \ln 2 - \hbar/2$, where γ represents a measure of an inverse *spin-temperature* that is related to the spin-polarization of the spin bath.

Alternatively, Klaers [401] theoretically analyzed a minimalist mechanical model of a one-bit memory operating with squeezed thermal states and showed that the Landauer energy bound is exponentially lowered with increasing squeezing factor. Squeezed thermal states, which may naturally arise in digital electronic circuits operating in a pulse-driven fashion, thus can be exploited to reduce the fundamental energy costs of an erasure operation. In that case, the additional resource used to reset the memory is paid by unsqueezing, so by converting one quadrature into its conjugate.

These works are important for the design and implementation of new kinds of heat engines and batteries that use multiple conserved quantities, particularly if the quantities are discrete. They show how the generalized framework of quantum thermodynamics can be used to study the interaction of non-equilibrium systems exchanging different kinds of quasi-particles with non-thermal reservoirs existing in meta-stable states, while respecting an arbitrary number of symmetries. This allows the thermodynamic description of systems where a quantity such as energy is irrelevant.

3.2.2 Classical implementations

Over the years, there have been many attempts to implement a microscopic demon able to filter the particles exchanged by two reservoirs in order to reverse the flow of heat. In this context, a Maxwell demon consists of an asymmetric filtering barrier that allows the flow of high-energy particles from the cold to the hot reservoir while blocking the inverse flow. In this last decade, breakthroughs in the downscaling of experimental setups have opened the possibility of measuring individual quasi-particles and, depending on the outcome, applying a particular feedback so as to realize a classical Maxwell demon.

Chida *et al.* [403] have demonstrated feedback cooling of thermal fluctuations in the number of electrons in a Si single-electron device, based mainly on single-electron detection with a high-charge-sensitivity detector and control of electron transition rates (see Figure 3.6). Thanks to these elements, the single-electron device is cooled down effectively from 300 K to 110 K. A further reduction in temperature would be possible by finely controlling the transition rate and reducing the time interval between measurements. In a subsequent work [402], the team demonstrated that their Maxwell demon can generate and output electric current and power of 0.5 zW with individual randomly moving electrons in small transistors. Real-time monitoring of electron motion shows that two transistors functioning

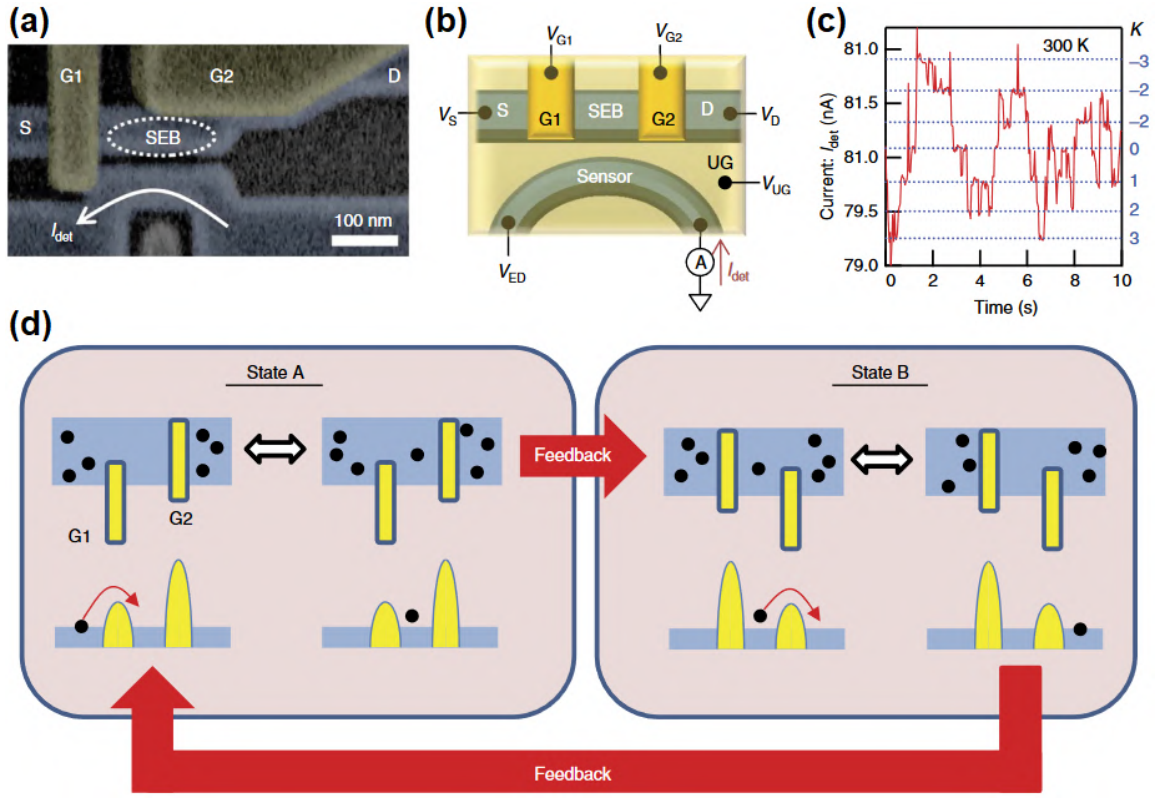

Figure 3.6: **Classical Maxwell demon.** (a) False-color scanning electron microscope image and (b) schematics of the fabricated device. Two gate terminals are formed to make field-effect transistors Gate (G) G1 and G2. The single-electron box (SEB) is electrically formed between the source (S) and drain (D). Above the whole area, there is an upper gate (UG), to which a positive voltage is applied. (c) Single-electron detection at room temperature. (d) Schematics of current generation by rectifying randomly moving electrons. The four upper and lower illustrations are schematics and energy-band diagrams along the S, SEB and D, respectively. State A(B) is when G1 opens (closes) and G2 closes (opens). When G1 opens (closes), its energy barrier lowers (rises) and an electron shuttles between the S and SEB faster (slower). Adapted from Reference [402].

as gates control an electron's trajectory so that an electron moves directionally. Power generation is increased by miniaturizing the room in which the electrons are partitioned by decreasing the charging energy of the box which depends inversely on the capacitance. This suggests that evolving transistor-miniaturization technology can increase the demon's power output.

In a quite similar implementation, Koski *et al.* [404] experimentally realized an autonomous Maxwell demon that extracts microscopic information from a system and reduces its entropy by applying feedback. It is based on two capacitively coupled single electron devices that are both integrated on the same electronic circuit cooled down at 40 mK. The operation of the demon is directly observed as a temperature drop in the system and a simultaneous temperature rise in the demon arising from the thermodynamic cost of generating the mutual information.

Bergfield *et al.* [405] showed that the temperatures of individual atomic orbitals or bonds in a conjugated molecule with a temperature gradient across it exhibit quantum oscillations, whose origin can be traced to a realization of Maxwell's demon at the single-molecule level. These oscillations may be understood in terms of the rules of covalence describing bonding in π-electron systems, in that they selectively permit electrons from the hot or cold reservoir to tunnel onto the probe when it is at specific locations near the molecule, and block electrons from the other reservoir. This study thus suggests that the non-linear and discrete laws governing the formation of complex bounds in molecular systems could be used to engineer a Maxwell demon that respects the laws of thermodynamics at the macroscopic level which emerge as a consequence of coarse graining. However, there is no violation of the second law, because electrons within the molecule "remember" which electrode they came from. There is no "mixing" of the hot and cold electrons in the absence of inelastic scattering such as it is insufficient to perturb this particular embodiment of Maxwell's demon without dissociating the molecule itself.

These studies show that interfacial quantum dots systems treated in mesoscopic classical setups are promising platforms to implement Maxwell's demon. The fine-tuning of their couplings with the reservoirs along with their discrete filling rules can be used to reverse the heat flow through appropriate feedback and eventually in an autonomous manner.

3.2.3 Quantum implementations

Propelled by the newest experimental techniques allowing the manipulation of single atoms, recent studies have showcased the possibility to engineer Maxwell's demon in fully quantum devices, thereby harnessing the special features of quantum superposition and quantum measurements to implement new kinds of quantum information devices. Indeed, the perturbing nature of quantum measurements, which destroys interferences by projecting the system, is an operation that can be used to reverse a heat or particle current without requiring any feedback. Two kinds of approaches are envisaged: either the device works continuously and applies constant feedback based on the mutual information shared between the demon and the system, or the demon works in a discrete fashion through quantum measurements.

For the first approach, Ptaszynski [406] proposed a device displaying an autonomous feedback mechanism via a quantum iSWAP gate acting on two coupled QDs, which allow one of the dots to act as a feedback controller that reads out the spin state of the second dot and blocks transport with the bias while enabling tunneling in the reverse direction (see Figure 3.7(a)). This leads to electron pumping against the bias, which generates the locally negative entropy production. Interestingly, one finds that in the considered system, a sum of the entropy production in one dot and the information flow from this dot to another one is always non-negative, which acts as a local version of the second law of thermodynamics. In a follow-up study, Ptaszynski then showed that the excess entropy then flows into the baths where a displacement from its equilibrium generates mutual information between initially uncorrelated degrees of freedom [408].

Another study by Najera Santos *et al.* [409] implemented experimentally a Maxwell's

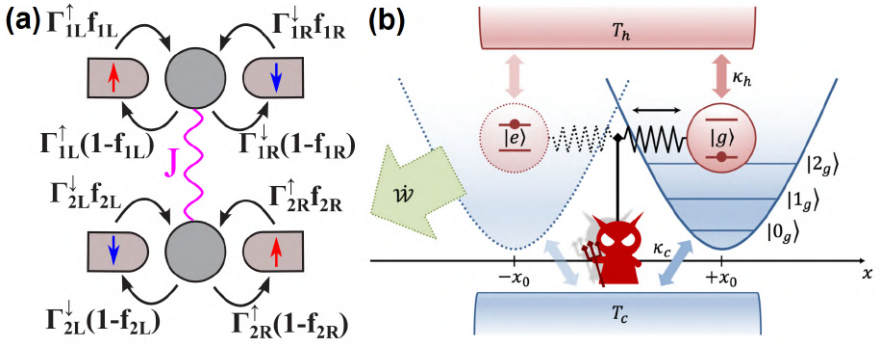

Figure 3.7: **Quantum implementations of Maxwell's demon**. Autonomous quantum Maxwell's demon based on two exchange-coupled quantum dots. Adapted from Reference [406]. Quantum Engine Driven by Pointer Measurements. Adapted from Reference [407].

demon with a single Rydberg atom and a high-quality microwave resonator. The atom simulates both a qubit interacting with the cavity and a demon carrying information on the qubit state. While the cold qubit crosses the hot cavity, the demon prevents energy absorption from the cavity mode. Taking into account the change of the mutual information between the demon and the qubit-cavity system gives rise to a generalized expression of the second law that can be recast into an entropy conservation law, as expected for a unitary evolution.

For the second approach, Seah *et al.* [407] proposed a spin-boson model for a measurement-driven engine, in which a demon generates work from thermal excitations of a quantum spin via measurement and feedback control. The demon's action is restricted to pointer measurements, *i.e.*, random or continuous interrogations of a damped mechanical oscillator that assumes macroscopically distinct positions depending on the spin state. The spin can be thermally excited by a hot bath and it displaces the equilibrium position of the pointer to x_0 depending on its state (see Figure 3.7(b)). Then a cold bath of temperature thermalizes the pointer around its equilibrium point.

Alternatively, Fu *et al.* [410] proposed a finite-time cycle model of a measurement-based quantum cooler, where projective measurements provide the power to drive the cooling cycle. The measurement-feedback information is capable of moving heat from the cold to hot bath without any work input and even making the maximum coefficient of performance larger than the Carnot limit. The causes that this seemingly paradoxical result does not violate the laws of thermodynamics can be clearly explained through the derivation of a generalized Clausius inequality including the mutual information.

Finally, Campisi *et al.* [411] proposed a theory of feedback-controlled heat transport in quantum systems based on modeling heat engines as driven multipartite systems subject to projective quantum measurements and measurement-conditioned unitary evolutions, thereby unifying various results presented previously in the literature. Feedback control breaks time reversal invariance. This in turn results in the fluctuation relation not being obeyed. Its restoration occurs through appropriate accounting of the gain and use of information via measurements and feedback. The theory is then illustrated by an experimental proposal.

3.3 Quantum engines and batteries

The previous discussion on Maxwell's demon and the Landauer bound illustrated the deep link between quantum information and the quantum resources needed to perform an operation on a quantum system, so as to extract work, reverse heat flow or erase a memory. In Chapter 2 and in the previous section, we started to show how one can take advantage of the laws of quantum thermodynamics to build quantum thermal machines that can potentially be more efficient than their classical counterparts and obey generalized forms of the Carnot or Clausius inequalities by using additional resources originating from quantum coherence. In the following, we review the literature on quantum energy devices so as to gain insights into the techniques used to study these new kinds of engines.

3.3.1 Quantum heat engines

Quantum heat engines refer to thermal machines that are able to extract work from heat baths. These machines involve an open quantum system, called the working substance (WS), which may be connected and disconnected from different baths, and is allowed to evolve unitarily by evolving freely with time or by the action of an external operator. In order to simplify the mathematical treatment of such machines, their operation is separated into different strokes that define the engine's operating cycle, allowing a clear differentiation between heat strokes and work strokes. In reality though, in most setups where the system is constantly connected to the heat baths, such a separation may not be justified and one needs to describe the engine as a continuous thermal machine [10]. We will start by presenting the most widely studied four-stroke quantum engine, namely the quantum Otto engine and its variations, before looking briefly at two-strokes and continuous quantum engines.

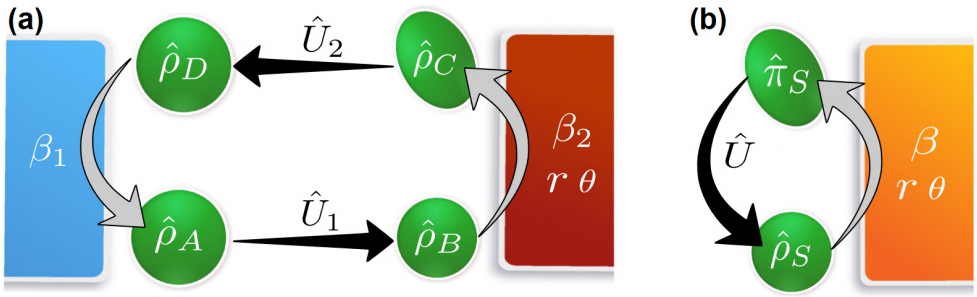

Figure 3.8: **Quantum heat engines cycles.** Schematic diagrams of (a) the four-stroke Otto-like cycle operating between reservoirs at different temperatures and (b) the two-stroke protocol introduced to extract work from a single squeezed reservoir. The unitary U_1 represents the adiabatic compression, while U_2 represents the adiabatic expansion and unsqueezing. Adapted from Reference [354].

Four-stroke quantum engines

Four-stroke quantum engines usually rely on a quantum version of the classical Otto cycle [412]. The WS is sequentially connected and disconnected to a hot and a cold bath, leading to a cycle with four steps (see Figure 3.8(a)):

1. **Quantum isochoric heating**: The WS is brought into thermal contact with a hot reservoir and allowed to equilibrate, increasing its energy.
2. **Quantum adiabatic expansion**: The WS is isolated from the hot reservoir, and its energy levels are modified adiabatically (*e.g.* by changing an external parameter like a magnetic field), causing its state to expand.
3. **Quantum isochoric cooling**: The WS is connected to a cold reservoir and thermalized, which decreases its energy and releases heat.
4. **Quantum adiabatic compression**: The working substance is isolated again, and its energy levels are modified adiabatically in the opposite way as the expansion stroke, causing its state to compress.

The quantum Otto engine is usually studied with the tools of the Lindblad equation, under the weak-coupling approximation [413]. Spin chains or sets of qubits have been extensively considered as the working substance to build the engine since external electric or magnetic fields can be easily implemented to build the isochoric strokes [413, 414, 415, 416, 417]. Depending on the parameters of the model, it is usually shown that the Otto cycle can result in different behaviors, acting either as a quantum heat engine, a refrigerator, a heater or a thermal accelerator [413, 418, 414, 417]. The search for optimal parameters that maximize the output power and efficiency is essential in the study of these engines. In this regard, exceptional points of Liouvillians where the eigenvalues and their associated eigenvectors coalesce are linked with better performance [419, 420].

In the case of a spin-based WS connected to spin reservoirs, one can use spin-reservoirs with different spin-temperatures as the non-thermal baths. The spin-temperature corresponds to the value (Lagrange multiplier) assigned to the conserved charge corresponding to the magnetization operator (see Section 2.3.3). Using this magnetic resource, different kinds of Otto efficiency limits can be obtained, leading to counter-intuitive results originating from negative spin-temperatures [421]. Quantum Otto engines can potentially exceed the efficiency of classical engines by operating between non-thermal baths like squeezed thermal baths, allowing the use of additional resources from conserved quantities [422, 356, 354]. Adding an indefinite causal order to the isochoric cooling stroke of an Otto engine through reservoir engineering can lead to an efficiency that may reach one and increase power output [416].

Using a WSs with special quantum properties can result in increased efficiencies of quantum machines. For example, many-body-localized (MBL) systems that do not thermalize under their intrinsic dynamics have been shown to lead to a quantum advantage [368]. Using quantum systems with unequally spaced energy levels, allowing inhomogeneous level shifts during the adiabatic strokes can also surpass the Carnot limit, just like in the

phaseonium example presented in Chapter 2 [422]. The unique properties of Bose-Einstein condensates also showed enhanced engine performance, including increased power output and higher efficiency at maximum power [423, 424].

Engineering the coupling between the system and the bath can also be beneficial for the engine. For Otto engines operating close to the Carnot efficiency, collective coupling always enhances the output power [425]. In the strong coupling regime, non-Markovianity of the interaction with the bath can also generate more work-per-cycle and reduce the work fluctuations [415, 426]. It has also been shown that partial thermalization due to a finite-time interaction with the bath can enhance the efficiency of the engine, due to the residual coherence [427, 428]. However, coherence can also be detrimental as faster expansion and compression strokes can increase the inner friction and therefore reduce the efficiency [427, 428]: the field of quantum control indeed teaches us that complex driving schemes can be engineered to speed up the preparation of a target state, such as speeding up may not allow the system to react optimally to the applied constraint [429, 430].

However, some quantum effects have been shown to be detrimental to the engine, *e.g.* friction by non-adiabatic effects can induce a sort of quantum friction that diminishes the efficiency [418].

Quantum Otto engines have been realized experimentally in various setups: trapped ions [414], single-atoms [431] or spin systems [432] and reveal the crucial impact of thermal and quantum fluctuations on the device, which can ultimately kill the average output power [432, 431]. For example, Peterson *et al.* [432] reported a proof-of-concept quantum heat engine which is able to reach an efficiency for work extraction ($\eta \approx 42\%$) very close to its thermodynamic limit ($\eta \approx 44\%$). [432].

Two-stroke quantum engines

In an attempt to simplify the cycle to make it more realistic for systems that are always connected to the baths, two-strokes engines are also considered. The two stages allow to separate heat from work easily and may be easier to justify in the case where a fast interaction occurs in congruence with a slower equilibration process.

In this context, Molitor *et al.* [433] developed a general framework to describe stroboscopic two-stroke engines in generic quantum chains, which may thus be an ingredient to model the spintronic engine in this Thesis. The framework describes a cycle that alternates between pure heat and pure work strokes and predicts a transient evolution towards a limit cycle. Once the limit cycle has been reached, the energy of the internal sites of the chain no longer changes, and the heat currents are exclusively associated with the boundary sites. This work shows the importance of periodic steady-states along with the boundary conditions which act as some kind of holographic artifacts containing the essential properties of the limit dynamics of the steady-state inner system.

The possibility of harvesting the non-equilibrium features of a reservoir such as squeezing described in Chapter 2 also opens the path to quantum heat engines that can extract work from a single bath in two strokes, with a first step consisting in a charging of the sys-

tem by contact with the bath, and a second step to generate work from a unitary evolution of the system alone [355, 354] (see Figure 3.8(b)).

Klatzow *et al.* were able to demonstrate experimentally such a two-stroke engine by using nitrogen vacancy centers in diamond forming a three-level system connected to a source of microwave radiation. Thanks to the quasi-degenerate property of the two lowest energy levels akin to the phaseonium presented in Section 2.3.1, internal coherence is preserved in this system over long timescales, such that work can be extracted from the coherent motion of the system excited by an incoherent light source, which experimentally shows a quantum advantage [434]. This engine can also be described in a continuous manner and we shall briefly present the tools that are used to study such engines.

Continuous engines

The difficulty in the study of continuous engines lies in the resolution of the time-dependence of the non-Hermitian equation governing the evolution of the open quantum system in contact with the heat bath. Contrary to an engine driven by a time-dependent Hamiltonian, continuous engines aim to describe the time evolution of a system in a static environment over long timescales. No external control or cyclic variation of parameters is required. The engine autonomously reaches a steady state and continuously extracts work from the heat flow.

In the Lindbladian approach, the system often converges towards a steady-state ρ_{ss} that does not depend on time. Although this final state is usually passive, since it generates no work coming from a cyclic evolution of the system, it is associated to particle and heat flows coming in/out of the baths, which can produce electrical work from the non-equilibrium thermodynamic forces that the reservoirs apply to the system. The solution of the Lindbladian can also lead to periodic steady-states or rich time-dependent evolution that decay over very large timescales, allowing the engineering of systems evolving under a cycle which can act as heat engines. This especially happen in systems with purely imaginary eigenvalues. Exceptional points have also shown interest in the literature as they lead to trajectories akin to critically damped oscillators [420].

3.3.2 Quantum batteries

Quantum batteries are systems that can absorb energy from a charging mechanism, store it during an appropriate time-scale and then deliver the energy back during a discharge process. Compared to classical ones, quantum batteries can exploit quantum phenomena like quantum coherence to enhance their performance by delivering additional ergotropic forms of energy (see Section 1.2.1). Potential advantages include faster charging rates [435], higher energy densities [436] and improved efficiency through non-dissipative charging mechanisms [437, 438].

Systems of qubits or spins are the most studied platform to implement quantum batteries [439, 440, 441, 442, 443, 438]. Compared to classical batteries, the main advantage of these

systems is that they can be charged in contact with generalized reservoirs, like coherence reservoirs, so as to gain extractable energy not just from particle or heat exchange but from information exchange through quantum correlations that build up inside the system [439]. Usually, the amount of extractable work is bounded by the ergotropy of the system, which is controlled by the amount of coherence injected in the system during the charging process [440, 442, 443].

Different processes have been envisaged to charge a quantum battery. Using a coherent drive source [439, 440, 441, 442] or a hot heat bath [444, 440, 443] are the most studied methods. More exotic processes have also been considered and showed improvements. For example, charging the quantum system via a non-equilibrium steady state can be used as a resource to improve the efficiency [437]. Adding a feedback mechanism to the drive has been shown to counteract the randomizing influence of environmental noise and allow for stable and effective battery charging. [438]. And a protocol featuring indefinite causal order can increase the amount of energy charged and the thermal efficiency can be boosted simultaneously [445].

3.3.3 Quantum drive

A third kind of quantum energy device relies on quantum drives. A quantum drive is a time-dependent Hamiltonian that originates from an external power source. Using Equation 2.12 we can see that this time dependence of the Hamiltonian is associated with an input external work $W_{ext}(t)$ that can be converted into a heat or particle flow, such that the system can behave as a heat pump or a refrigerator [314, 446].

In particular, periodically-driven quantum thermal machines are widely considered as potential energy harvesters [447, 448]. Most studies focus on the limit-cycle stage of operation characterized by a periodic state of the system [10]. This regime is not immediately accessible for experimental verification, so additional frameworks are being developed to analyze work and heat through a complete description of the first law of thermodynamics that requires a new contribution, which vanishes only in the limit-cycle phase [447]. In this context, coupling modulation can be suitably engineered to perform thermodynamic tasks such that asymmetric couplings to two heat baths can be used to extract heat from the cold reservoir and achieve an ideal heat rectifier, where the heat current can be blocked either in the forward or in the reverse configuration by simply tuning the frequency of the couplings' modulation [448].

Specifically, coherent drives have been extensively studied to model the interaction of quantum thermodynamical systems with lasers in the context of quantum optics. Indeed, the application of a coherent drive associated with a waveguide has been used to measure thermodynamic work and heat/ This suggests that waveguide spectroscopy is a useful means to study quantum heat engines and refrigerators [449].

Alternatively, quantum measurements can be considered as a drive pulse that can act as an energy pump. From a thermodynamic point of view, this measurement backaction on the energy is at the core of the class of quantum thermodynamic engines that are powered by measurements instead of heat baths [450].

3.3.4 Quantum information engines

Quantum information engines are devices that extract work from quantum states and thermal reservoirs using principles of quantum mechanics and information theory. In particular, these quantum machines rely on quantum measurements to generate power using quantum resources based on quantum coherence and correlations stored within the system. We will focus on two approaches: quantum Zeno engines and quantum measurement engines.

Quantum Zeno engines

The quantum Zeno effect is a phenomenon in quantum mechanics where frequent measurements of a system can inhibit its evolution [451]. This effect is named after the Greek philosopher Zeno and his paradoxes about motion. In the context of quantum heat engines, the quantum Zeno effect can be used to control and manipulate the dynamics of the working fluid (typically a quantum system like a two-level atom or a harmonic oscillator) [452].

Quantum Zeno engines operate in the regime where the driving or control of the system is faster than the correlation time of the thermal bath it's coupled to. This puts the engine in a non-Markovian regime. The key advantage of quantum Zeno engines is that they can potentially achieve a significant boost in output power compared to conventional quantum heat engines. This power enhancement is achieved through a phenomenon called anti-Zeno dynamics [452, 453]. In the anti-Zeno dynamics regime, the energy exchange between the system and the bath is enhanced or sped up, rather than suppressed as in the standard Zeno effect. This allows for faster thermalization and thus higher power output [452, 453].

Importantly, the quantum advantage observed in these engines stems directly from quantum mechanical principles, specifically the time-energy uncertainty relation allowing effective cooling and challenging the second law of thermodynamics by keeping the system out-of-equilibrium. This suggests that non-Markovian implementations of quantum heat engines could reverse heat flow and allow cooling or state purification in a more efficient manner [334]. The operation of a quantum Zeno engine typically involves a rapid modulation of the energy levels of the working fluid, combined with frequent coupling and decoupling from thermal baths [334]. The entropy and temperature of both the system and the bath can be found to either decrease or increase depending only on the rate of observation, contrary to the standard thermodynamical rules that hold for memory-less baths. From a practical viewpoint, these anomalies may offer the possibility of very fast control of heat and entropy in quantum systems, allowing cooling and state purification over an interval that is much shorter than the time needed for thermal equilibration or for a feedback control loop [453].

At extremely high modulation frequencies, the system can enter the quantum Zeno dynamics regime, where heat currents and power output vanish, making this regime unsuitable for heat engine operation. Optimizing the time interval between the projective measurements is thus crucial to design efficient quantum engines and batteries [454].

The quantum Zeno effect can be linked to quantum Maxwell's demon engine where work is directly extracted from the measurement channel, such that no heat bath is required. In the Zeno regime of frequent measurements, memory erasure costs may eventually vanish [15].

Quantum measurement engines

A quantum measurement engine is a device that can harvest energy from the quantum measurement of a system. When the observable does not commute with the Hamiltonian of the system, the projective nature of the measurement can indeed destroy coherence in the energy basis, thus resulting in a projected system with a different average energy than the initial system [455]. The measurement has a direct *back-action* on a system which exchanges energy with the measurement apparatus as a form of *quantum heat* which can be converted into useful work [456]. Quantum measurement can therefore be used as a fuel in a quantum cycle [455].

The interest in quantum measurement engines has recently generated substantial interest through a rising number of theoretical studies describing processes and machine cycles that strongly rely on quantum measurements to perform work. Initial studies have focused on the realization of a quantum Maxwell demon (see Section 3.2.3) performing quantum measurement then feedback control on a system in order to build some kind of quantum Szilard engine. Such implementations have notably been studied by Erez *et al.* who showed that single-temperature measurement engines could be built using either selective or non-selective measurements, and linked the maximum extractable work bound to the energy required to reset the memory of the demon in the heat bath [453]. This should be related to the work of Jacobs *et al.* who argued that all measuring devices must pay a cost equal to that which a heat engine would pay to obtain the equivalent work value of that information [318]. In a parallel approach Mohammady *et al.* studied an engine based on a system, a weight and a quantum Maxwell demon that can function without heat from a thermal reservoir only if repeatability of measurements, invariant of weight entropy or positive work extraction for all measurement outcomes, are abandoned [457]. Additionally, Ji *et al.* showed that a quantum advantage can be obtained if the demon can truly *steer* the working medium's quantum state, thereby generating non-classical correlations. [458].

Later, Yi *et al.* showed a cyclically working quantum mechanical engine that operates at a single temperature and where the energy input is delivered by a quantum measurement but without feedback control like one would expect in a classical Maxwell demon engine: the measurement back-action is sufficient to extract work [459]. The work of Bresque *et al.* then shed new light on the measurement-based fueling process in entangled quantum dots and provided a unified view on quantum measurements that act *akin* to heat reservoirs delivering *quantum heat* [456] (see Figure 3.9(a)). These ideas were subsequently adapted to different systems and cycles: Elouard *et al.* constructed an engine from the process of observation to move a particle against a force, showing that feedback is only required for optimal performance and obtained unit efficiency under specific conditions [14]. Then Elouard *et al.* designed a modified version of the Elitzur-Vaidman bomb tester to show how energy could be exchanged at distance despite local interactions [460] and Anka *et al.*

proposed to replicate a quantum Otto engine where the role of the heat source is played by a quantum measurement in a system of quantum spins [16].

The latest studies on the topic which are of particular interest to us (see Chapter 5) are the work of Jussiau *et al.* [461] and Ferreira *et al.* [462]. Both suggest that a quantum measurement process may be at the center of the operation of the quantum spintronic engine. The first paper showed how quantum measurements can reveal the quantum vacuum fluctuations of the global ground state in the local basis and provide the energy required to energize a system: quantum measurements are used to produce an excited state that then relaxes towards its entangled steady-state in contact with the cold bath such as work can be extracted from this cycle [461] (see Figure 3.9(b)). And the second team analytically studied how noninteracting fermionic systems undergoing continuous monitoring and driven by biased reservoirs can generate competing elastic and inelastic current, such that monitoring-induced inelastic processes lead to nonreciprocal currents, allowing one to extract work from measurements without active feedback control [462].

Alternatively, quantum measurements have also been at the center of thermal machines using this fuel to do different kinds of operation on a system such as cooling [463] or purifying [455] by acting as a kind of quantum lubricant, suppressing the effect of coherence, which can be detrimental in some cases. Indeed, coherence is basis-dependent, such as it can scramble information in the orthogonal space of the useful reference frame; its effect thus depends on the specific design and operating conditions of the device [464].

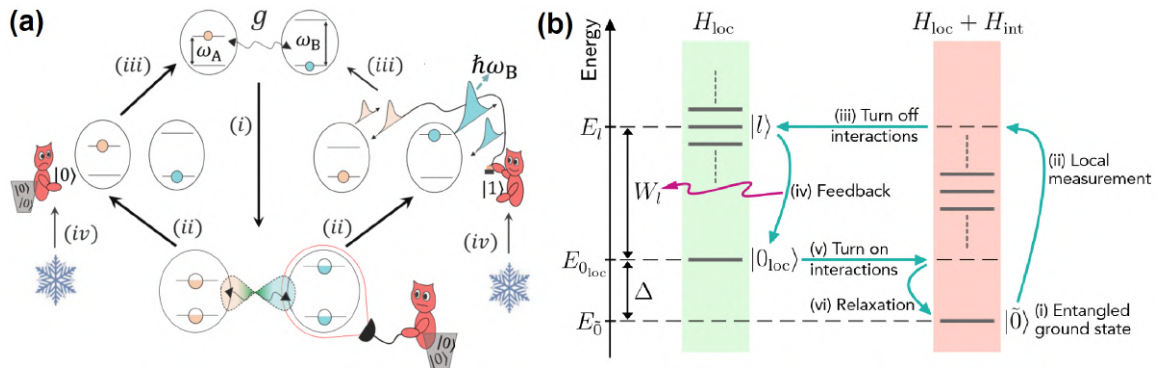

Figure 3.9: **Quantum Measurement Engines.** (a) Scheme of the cycle of a two-qubit engine fueled by local measurements. (i) The qubits get entangled. (ii) A demon performs an energy measurement on qubit B (iii) If B is found in the excited state, a π pulse is applied to each qubit. The energy of B is extracted and A is reexcited. If not, nothing is done. (iv) Reset of the demon's memory. Adapted from Reference [456]. (b) Schematic depiction of the energy levels for the local (left) and interacting (right) Hamiltonians of a many-body quantum vacuum fluctuation engine. The cyan arrows represent the energy changes throughout one possible realization of a cycle for the many-body vacuum fluctuation engine. Adapted from Reference [461].

3.4 Framing summary

This chapter started with a brief reminder on thermoelectricity, which has been the main approach towards building nanoscale generators within the spintronic community so far. Nevertheless, thermoelectricity continues to suffer from severe efficiency drawbacks that limit their practical applications and commercial use-cases. The spintronic engine, which seemingly does not require a temperature gradient and delivers sizable output power at ambient temperature, thus most likely does not belong to these kinds of devices.

This new kind of behavior indicates that a quantum thermodynamical phenomenon must be at the center of the engine so, building upon the notions developed in the previous chapter, we dived into the concepts of Maxwell's demon and Landauer erasure, which are needed to understand how information (and therefore heat) can be used and erased at the microscale so as to build a quantum engine.

Subsequently, we challenged these fundamental thought experiments in light of the newest studies on the topic and showed how classical limitations could be partially lifted by quantum systems, suggesting that these original ideas be included in a larger framework in which quantum information plays a central role by bounding the efficiency of quantum machines. In particular, we showed how quantum systems can be used to practically engineer a Maxwell demon, and how quantum thermodynamical concepts like squeezed baths could be used to reset a quantum memory at vanishingly low energetic cost.

These preliminary notions then allowed us to review the literature on quantum energy devices, focusing on quantum heat engines, quantum batteries, quantum drives and quantum information engines. All these complementary approaches give us the necessary modern tools to build a model of the quantum spintronic engine and, from all the systems, processes and cycles studied in detail in these works, many parallels can be drawn with our subject. In particular, we will make extensive use of these concepts in Chapter 5 where we will present our quantum model of the spintronic engine.

This chapter concludes the introductory part of this thesis which aims at presenting the necessary fundamental background needed to understand the results. Before moving to the main part of the thesis, the next chapter finishes the contextualization of this PhD work by giving an overview of the present understanding and past results on the spintronic engine.

Chapter 4

The Spintronic Engine

Attempts to increase the magnetoresistance device performance metric have led to modifications to the spacer layer and magnetic electrode materials. In the process of studying these materials modifications, three groups published results within 2009-2019 on what appears, retrospectively, to be implementations of a quantum spintronic engine, generating electrical power at room temperature with no external energy input.

These surprising results raise a lot of questions and prospects. Given the output power, these devices could lead to a revolution in energy technologies as it promises nanoscale engines with incredible power densities up to 1000x more efficient than a solar panel without suffering from intermittency (see Figure 4.1(b)). The experimental milestone would then consist in achieving routine and then industrial fabrication of those devices, while the essential theoretical issue remains in finding a thermodynamical model, consistent with the laws of thermodynamics, that describes where the output energy comes from and whether/how quantum information circulates in the system.

The spintronic engine is based on magnetic tunnel junctions that host magnetic atomic complexes within their barriers, along with carefully tuned interfaces between the electrode material and the spacer layer called *spinterfaces* (see Figure 4.1(a)).

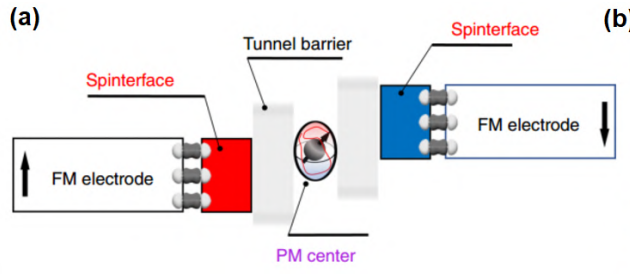

(b)

	Source	Typ. Pd (mW/cm²)	Constraint
Natural	Paramagnetic fluctuators in a MTJ	30000	R&D / Engineering...
Artificial	Solar	50	Not 24/7
	Thermoelectric	30	T gradient
	RF power	1	Distance/ Harmonics
	Vibration/PZT	0.2	Vibration frequency
	Vibration/EM	10	AC/DC conversion

Figure 4.1: **The spintronic engine.** (a) Architecture of the spintronic engine. (b) Table representing the power density of the different energy technologies. The power density of the spintronic engine was extrapolated using the device of Katcko *et al.* [18] (0.1 nW) with the density of devices that can be achieved in today's industrial platforms (1.2^{12} cm^{-2}) with a load resistance of $R = 20$ kΩ. Adapted from Reference [18].

This chapter reviews the latest studies on the spintronic engine and summarizes the experimental results obtained on both oxides and molecular junctions obtained by my group at the IPCMS. Then, from these elements, I present the qualitative description of the mechanisms underlying the engine which we put together at the beginning of my thesis.

4.1 The oxide spintronic engine

4.1.1 Context

Strategies to increase the spin polarization of the transport electronic state in MTJs have been one of the main issues in spintronics. To this end, one may tune the properties of the barrier, the electrodes and the interface between the two. The barrier most widely used barriers are oxides like AlOx and epitaxial/polycrystalline MgO which have achieved high TMR values up to 600% at room temperature due to the synergy between the band structures of the (001)-oriented MgO tunnel and the bcc-alloy Fe electrodes (see Section 1.3.1) [32]. MgO-based magnetic memories have achieved industrial penetration and are considered a prime example of the commercial potential of spintronic technologies. As for the electrodes, ferromagnetic metals or "half-metallic" materials, which have only one spin subband present at the Fermi surface have been considered[54]. And for the interface, a technique discovered in the 2010s involves decorating the surface of $3d$ transition metals with molecules. The resulting "spinterface" state [256], formed by $p-d$ bonds[465], was found to exhibit high spin polarization of electronic states at the Fermi level [18, 19, 272], with effective magnetoresistance values up to 770%, corresponding to a spin-polarization of 89% [19] (see Section 1.4.3).

With the nominal aim of improving spintronic performance, using barrier and electrode materials described in the previous section, research has discovered some MTJ devices that generated long-lasting electrical power of unknown origin. This unusual behavior thus raised both skeptical and exciting interest towards both finding a coherent theoretical description of these active devices and reproducing the experiments so as to find systematic routes to fabricate them.

4.1.2 Experiments

Three teams have reported active devices and started the quest towards building a spintronic engine.

In 2009, the Barnes and Maekawa groups reported on magnetotransport experiments at 10 K across MnAs nanoparticles within a GaAs matrix [466]. Although one MnAs ferromagnetic (FM) electrode was used (see Figure 4.2(a)), large values of MR were observed, and attributed to spin-polarized carriers on the MnAs nanoparticles acting as the analyzer of spin-polarized transport originating from the MnAs electrode. Interestingly, when at low temperature, applying an external magnetic field H past a certain critical value causes the IV to shift into the ($V > 0$, $I < 0$) power generating quadrant (see Figure 4.2(b)).

Removing H caused a return to the passive device state. This switchover from a passive to an active device state is confirmed using $I(H)$ curves (see Figure 4.2(c)). An enduring bias voltage was observed over minutes, even when a passive resistance load was connected.

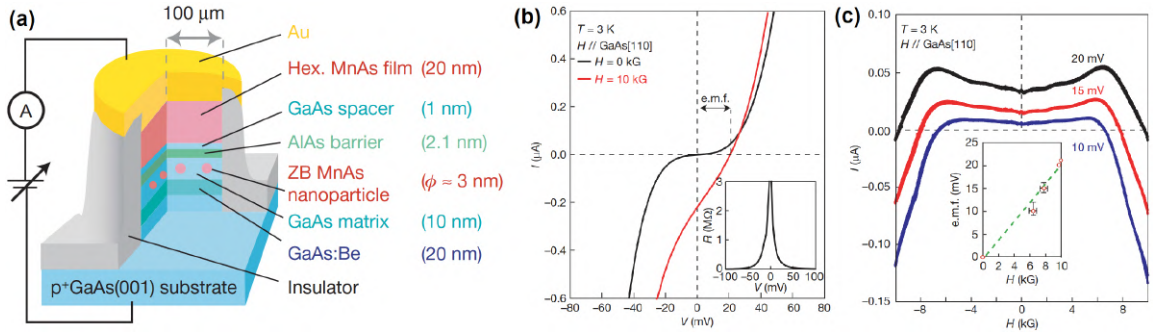

Figure 4.2: **Experiments on MnAs nanoparticles MTJs.** (a) Schematic of the device considered in the Barnes and Maekawa groups' report, showing the single MnAs ferromagnetic electrode and MnAs nanoparticles. (b) $I(V)$ data for $H = 0$ and $H = 10$ kOe. (c) I(H) data confirming that the magnetic field induces current and bias offset. This indicates a spintronic origin of the effect. Adapted from Reference [467].

In 2014, the Moodera group reported on magnetotransport experiments at 1 K across Al nanoparticles sandwiched between EuS spin filter tunnel barriers [466] (see Figure 4.3(a-b)). The authors observed a spontaneous bias voltage across the device whose amplitude and sign depend on the relative orientation of the two ferromagnetic tunnel barriers' magnetizations (see Figure 4.3(c)). This spintronic manipulation also leads to a change in the spontaneous current (see Figure 4.3(d)) upon connecting the device to a load resistance, which stays constant up to 10 MΩ load. This implies an output power of 27 fW at 1 K.

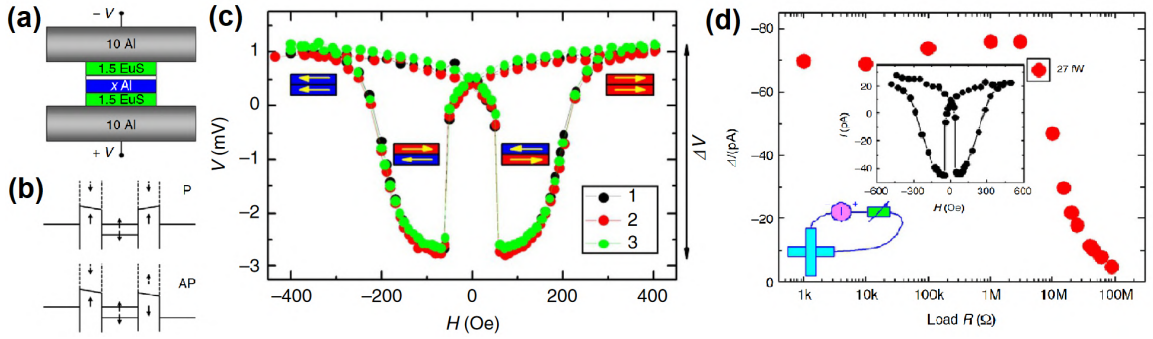

Figure 4.3: **Experiments on Al nanoparticles MTJs.** (a) Schematic of the device considered in the Barnes and Maekawa groups' report, showing the single MnAs ferromagnetic electrode and MnAs nanoparticles. (b) $I(V)$ data for $H = 0$ and $H = 10$ kOe. (c) I(H) data confirming that the magnetic field induces current and bias offset. This indicates a spintronic origin of the effect. Adapted from Reference [466].

In Katcko *et al.* from 2019 [18], my group reported on magnetotransport experiments at 295 K across C atoms within a MgO MTJ with Co/C spinterfaces. The authors observed up to 0.1 nW of output power (see Figure 4.4(a)) with a current of around $I = -100$ nA for

a voltage of $V = 1$ mV along with peculiar features such as spectroscopic data with sub-spectral resolution in the conductance and TMR plots (see Figure 4.4(a)) pointing towards a quantum signal linked to the inserted carbon. Interestingly, the measured TMR presented two sharp peaks with a width of about 1 mV, one of which has a negative value reaching down to -200%. This shows a strong dependence of the nanotransport path on the magnetic orientation of the ferromagnetic layers, which suggests a significant magnetic coupling between the inserted C atoms and the electrodes. The main weakness of the work was that the effect was observed on only one device out of 216. This underscores the difficulty to control the insertion and position of individual impurities within an ultrathin oxide layer.

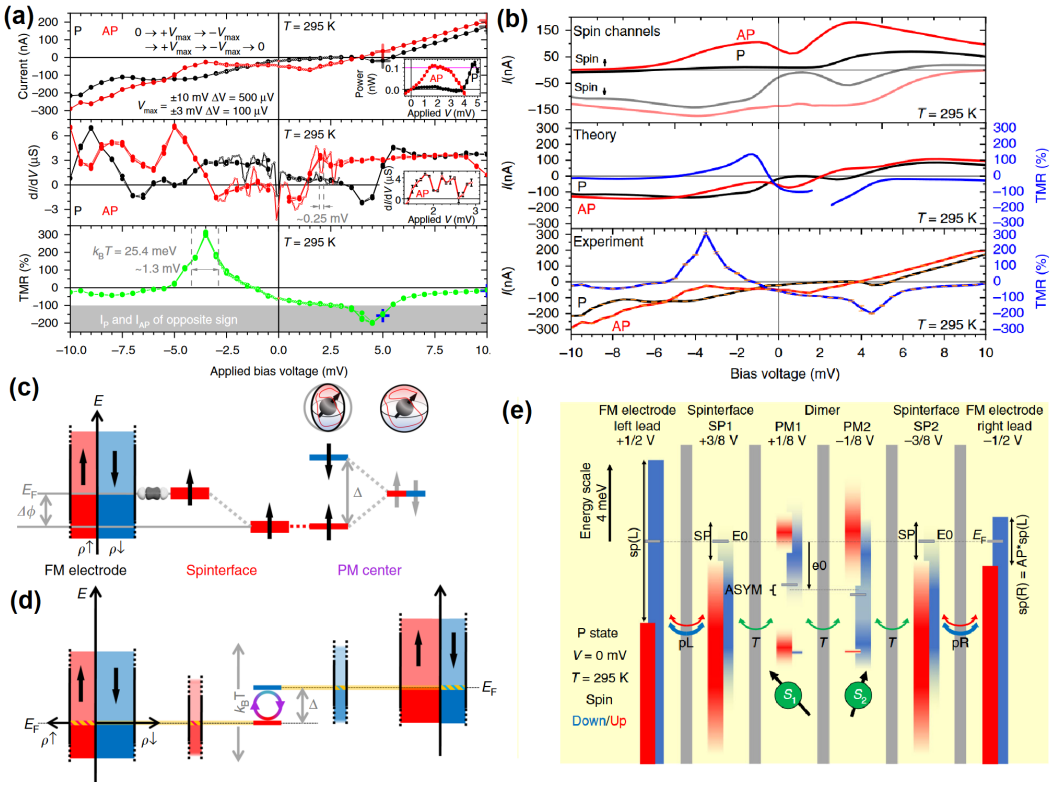

Figure 4.4: **Experiments on C-MgO MTJs.** (a) Bias dependence of current I, numerically derived conductance $\mathrm{d}I/\mathrm{d}V$ in the MTJ's parallel (black) and antiparallel (red) states, and the inferred TMR bias dependence. (b) Theoretical bias dependence of spin ↑ (solid) and spin ↓ (semitransparent) current, with the theoretical and averaged experimental bias dependencies of current, along with the calculated TMR (green) in the magnetic tunnel junction's parallel (black) and antiparallel (red) magnetic states. (c) Spin-conserved quantum tunneling between a spinterface and a PM center deforms the PM center's Bloch sphere, thereby splitting [468, 469] its spin states by Δ, and shifts the spinterface's Fermi level E_F by $\Delta\phi$. (d) The spintronic landscape across a magnetic tunnel junction, comprising spinterfaces and a PM center, in its antiparallel (AP) magnetic state exhibits a spontaneous bias voltage $\Delta V \leqslant \Delta$ (e) Schematic of the analytical model of spin-conserved transport across a paramagnetic dimer (PM1 & PM2 centers) separated from each FM lead by a spinterface. Adapted from Reference [18].

4.1.3 Theory

We now discuss how the effects observed were at the time explained. The Barnes and Maekawa groups' report attributed the observed bias voltage to the magnetic energy of paramagnetic clusters [467], which was criticized at the time [470]. The theoretical justification involves nonconservative spin derived forces reflecting the conversion of stored magnetic into electrical energy which modifies Faraday's Law which should involve the derivative of the spin average Berry phase and not just the magnetic flux [471]. This term adds a contribution to the motive force occurs, with static external fields, in circumstances where there is no usual electromagnetic induction.

The Moodera [466] and Bowen [18] groups' articles attributed the effect to harvesting spin fluctuations on paramagnetic centers using spin-polarized currents that generate spin-splitting on the PM centers and pin the electrode Fermi level to the corresponding spin state (see Figure 4.4(c-d)). It was in turn proposed, without thermodynamical proof, that the ensuing potential profile drop leads to an effective potential bias between the electrodes.

With this hypothesis, in Katcko *et al.* [18], the authors reproduced the experimental IV data (see Figure 4.4(b)) using an analytical model involving a C dimer sandwiched between fully spin-polarized quantum dots (the spinterfaces). The model supposes the presence of a spin-split chemical potential on the leads, evidences the role of spintronic anisotropy, *i.e.* the change in magnetic anisotropy of a junction's components due to a spin-polarized current, and describes the net current flow as the result of an imbalance in oppositely flowing spin channels of charge current.

Assuming this potential drop, the Bowen group also proposed a phenomenological model of transport (see Figure 4.4(d-e)), which relies on the basic electronic interactions that result from the interplay between the spinterface and the paramagnetic center, allowing for spin-polarized transport through a spin-split impurity. In this description, the energy is thought to come from quantum fluctuations of the spin state of the PM centers, which are rectified by the spinterface thanks to their asymmetric spin-dependent coupling to the centers. When describing the needed intersection between spintronics and quantum thermodynamics to explain the effect, the Bowen group report alluded to quantum heat engines [404, 472, 406], but the link with quantum information engines remained tenuous [473].

4.2 The molecular spintronic engine

We begin this Section by presenting an overview of the experiments performed on molecular spintronic junctions that the Bowen group obtained in the Chowrira *et al.* 2022 report [19]. This report strongly bridges, for the first time, the spintronics and quantum thermodynamics communities and details the current theoretical understanding of the spintronic engine. We then describe the main features that allow power generation which I participated in laying down at the start of my thesis.

4.2.1 Context

The report of Chowrira *et al.* [19] describes the ingredients of engine much as did Katcko *et al.* [18] in 2019, but more explicitly associates concepts of quantum thermodynamics with the spintronic interactions that are present. Furthermore, the paper contains a description of purely quantum mechanical effects that can procure a quantum advantage (color-coded in green in Figure 4.8) relative to a classical nanoscale heat engine. The device's electronic potential landscape is crafted to take into account the electron's quantum spin property, and contains two carefully interlocking ingredients (see Figure 4.8(a)): an ensemble of PM centers as thermal spin fluctuators; and spinterfaces on either side of these PM centers that select electrons of one spin for transport. As we will describe hereafter, these two ingredients are believed to deploy so-called quantum resources and combine to enable thermal fluctuations to rectify quantum fluctuations of transport across the device, thereby generating a bias voltage, and an electrical current if the circuit is closed.

Chowrira *et al.* studied vertical molecular junctions, in which transport is proceeding between Fe thin film FM electrodes across 3 monolayers of Co phthalocyanine (CoPc) molecules with a Co PM center. The Fe and CoPc layers are separated by ultrathin C_{60} layers, and Fe/C_{60} spinterfaces [257] are the spintronic selector. The fluctuating $S = 1/2$ spin is borne by the Co out-of-plane d_{z^2} orbital, such that spins can couple antiferromagnetically through superexchange, forming a spin chain [246]. Despite the mesoscopic (diameter 300 nm) size of the device's vertical pillar, transport is also expected to proceed across a reduced number of nanotransport paths involving CoPc spin chains. Indeed, the intra-chain superexchange promotes the main transport path, while there is very little crosstalk between chains due to very low wavefunction overlap between neighboring (but not stacked) CoPc molecules [246, 248, 250, 273, 251].

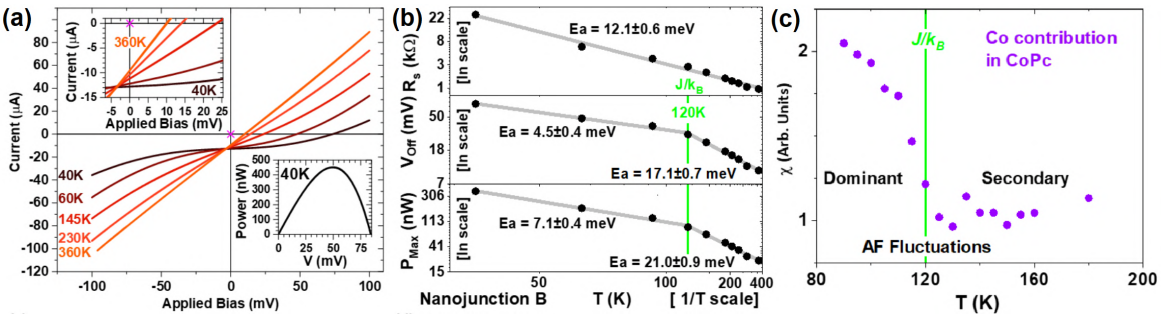

Figure 4.5: **Thermal activation in CoPc spintronic engine MTJs.** (a) $I(V)$ data at $H = 0$ within 40 < T (K) < 360. Top inset: zoom at low bias. Lower inset: power-voltage $P(V)$ data showing a maximum $P_{Max} = 450$ nW at 40 K. The magenta crosspoint is the experimental error. (b) temperature plot of (top) resistance $R_s(1/T)$ around $V = 0$, (middle) the offset voltage $V_{Off}(1/T)$ and (bottom) maximum power $P_{Max}(1/T)$. P_{Max} decreases from 370 nW at 40 K to 24 nW at 360 K per two thermal activation regimes, with a 120 K crossover temperature. The activation energy E_a is given for each regime. (c) Temperature dependence of the Co contribution in CoPc to the Electron Spin Resonance Intensity. A signal increase is observed for $T < 120$ K. Adapted from Reference [19].

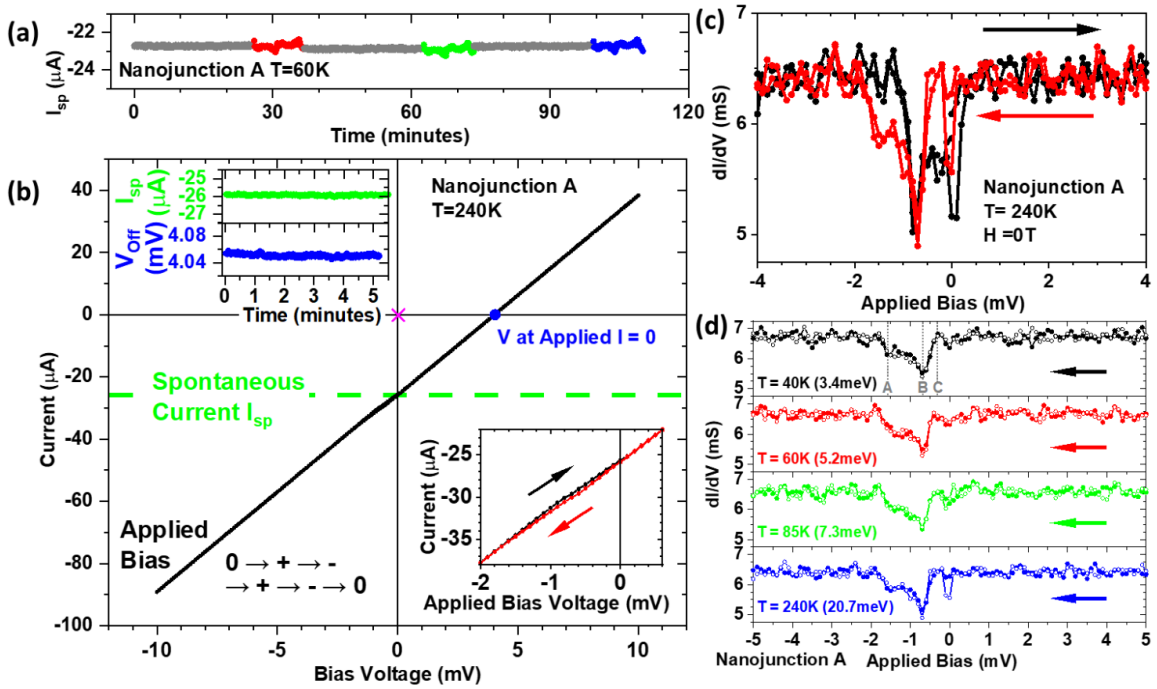

Figure 4.6: **Electrical signals in CoPc MTJs.** (a) time dependence of the spontaneous current I_{sp} at external applied field $H = 0$ (grey) and upon applying a H field (red, green, blue) orthogonal to the electrode magnetizations. (b) $I(V)$ data at 240 K. The magenta cross-point represents the experimental (V, I) error. The top insets show the time dependence of I_{sp} and the offset voltage V_{Off}, while the zoom around $V = 0$ (lower inset) reveals an $I(V)$ hysteresis that contains non-thermal spectral features for which the current derivative $\mathrm{d}I/\mathrm{d}V$ is represented in (c). Forward (black) and return (red) traces are shown. (d) Return $\mathrm{d}I/\mathrm{d}V$ traces for 40 K, 60 K, 85 K and 240 K reveal essentially identical features with a sub-k_BT spectral resolution, *i.e.* the thermodynamical signature of a quantum phenomenon. (c) Temperature dependence of the Co contribution in CoPc to the electron spin resonance intensity. A signal increase is observed for T < 120 K caracteristic of the phase transition of the CoPc WS. Adapted from Reference [19].

4.2.2 Experiments

Using this molecular implementation, Chowrira *et al.* report energy harvesting on 9 devices, with power reaching 24 nW at 360 K, 27 nW at 295 K, and 450 nW at 40 K (see Figure 4.5(a)), *i.e.* a 270x increase over the previous record set by Katcko *et al.* [18]. Referring to Figure 4.5, a spectral resolution 100x better than k_BT is observed (*i.e.* similar to the 2019 report [18]), despite the usual 2-3 k_BT broadening expected during electronic transport. This is a feature of feedback-driven transport [474, 403, 475] that would appear due to a non-thermal bath, and that can generate electrical power [402]. Furthermore, the temperature dependence of the device offset voltage and output power reveals that the thermal activation energy changes at 120 K (see Figure 4.5(b)). This suggests that the magnetic exchange energy of Co sites in CoPc [246, 248] can constitute an experimental signature of the WS's magnetic phase transition from antiferromagnetically correlated to uncorrelated fluctuations. The

increased thermal activation energy for $T > 120$ K could be due to hopping transport [145] across the spin chain's uncoupled fluctuating sites. This interpretation is confirmed from the temperature dependence of magnetic susceptibility acquired using electron spin resonance on a similar stack (see Figure 4.5(c)), with a change in trend attributed to the phase transition of the molecular spin chain.

To support the claim of device electrodes with a high spin polarization, Chowrira *et al.* performed magnetotransport measurements (see Figure 4.5). In panel (a), the raw $I(H)$ data show that, depending on the value of applied bias, the device can block current in either the P or AP magnetic state, leading to magnetocurrent values of 1500%. The current direction can even be reserved by switching the magnetic state. $I(V)$ data shown in panel (b) reveal the presence of different bias offsets for each junction magnetic state. Finally, in panel (c), the slope resistance is plotted as a function of external applied magnetic field, and reveals a magnetoresistance $MR = 770\%$ that corresponds to a record spin polarization $P = 89\%$ at 40 K in of the Fe/C_{60} spinterface.

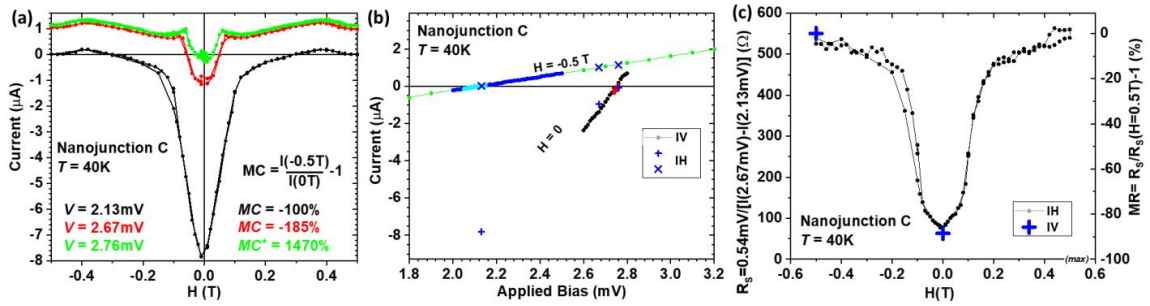

Figure 4.7: **Spintronic features of the molecular engine.** (a) $I(H)$ data acquired at 40 K. (b) $I(V)$ data at $H = 0$ T and $H = -0.5$ T, revealing a linear behavior with $R_S = 63\ \Omega$ and $R_S = 550\ \Omega$ around $V_{Off} = 2.13$ mV and $V_{Off} = 2.76$ mV, respectively. The blue crosses reflect the $I(H)$ data from panel (a). (c) $R_S(H)$ calculated from two $I(V_0, H)$ datasets from panel (a). The blue crosses indicate R_S inferred from panel (b). Adapted from Reference [19].

4.2.3 Theory

According to Chowrira *et al.* [19], the crucial point is to implement so-called quantum resources that place the engine's WS and thermal reservoirs out of thermodynamical equilibrium [476]. This applies if the WS exhibits a coherent superposition of quantum states with population inversion [434] or a phase transition [477]. The engine's reservoirs can be *non-thermal* if the thermal stroke (*i.e.* the transport fluctuation between spinterface and PM center) has an action that is faster than the thermalization or decoherence processes ('Zeno effect' from Section 3.3.4), or exhibits some asymmetry between the two quadratures of conjugated quantities ('squeezed bath' from Section 2.3.2) or if it injects quantum coherence into the WS. Chowrira *et al.* argue that the experimental data can be interpreted as bearing the signature of two quantum resources: squeezed baths and a WS at a phase transition [477].

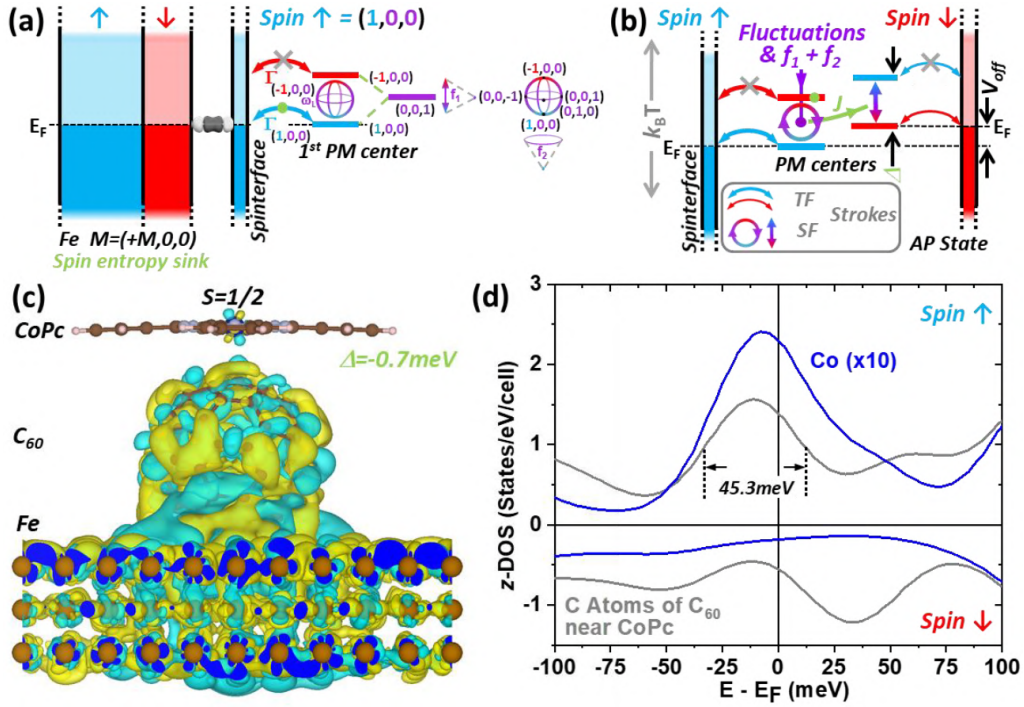

Figure 4.8: **Theory of the molecular spintronic engine.** (a) Energy diagram schematic: spintronic implementation of the transport fluctuation stroke between the device electrode in its FM ground state and the spin states of the WS's nearest PM center, mediated by a spinterface with full transport spin polarization. Quantum coherence and decoherence processes on the WS are shown. (b) Engine schematic that also shows the transport fluctuation and the spin flip strokes on a PM center's spin states, and between the PM centers forming the WS, against thermal fluctuations for $k_BT > \Delta$. (c) Ab-initio calculated spatial charge transfer maps across Fe/C_{60}/CoPc reveal sizeable hybridization on C_{60} (*i.e.* the spinterface) and electron tunneling between C_{60} and CoPc across an antibonding state. (d) The antibonding state's calculated density of states (DOS) around the Fermi energy E_F reveals how the Co d_{z^2} and C p_z orbitals share a spectral feature that appears only in the spin ↑ band. This illustrates the high spin polarization and bandwidth of the transport fluctuation stroke (see panel (a)). Adapted from Reference [19].

Based on these experimental observations, Chowrira *et al.* proposed the following spintronic implementation of quantum resources in an engine at the intersection between atomic/mesoscopic thermodyndamics and spintronics. The engine is schematized in Figure 4.8(a-b), which features quantum resources that are color-coded in green, and an electronic interaction stroke that is evaluated in the 100-1400 GHz range (see Figure 4.8(c-d)). The engine requires at a minimum *spintronic selectors*, *i.e.* electrodes that select a spin channel for transport. As one spintronic selector, the FM metal/molecule interface, also called the spinterface [256], is believed to spintronically implement a non-thermal bath [478, 358] that constantly energizes the WS made out of the magnetic spin chain formed by the Co atoms. Indeed, at the Fe/C_{60} interface (see Figure 4.8(c-d), the spinterface exhibits a low density of spectrally confined, highly spin-polarized states [257], with a fixed spin referential along $(x, y, z) = (-1, 0, 0)$ of the Bloch sphere that originates from the FM state of the metal.

The subsequent electronic interactions between the FM electrode and PM centers across the spinterface lift the spin degeneracy of their energy levels (see Figure 4.8(a)). Indeed, according to density functional theory calculations (see Figure 4.8(c-d)), the electronic interaction between the spinterface and the neighboring PM center causes a lifting $\Delta = -0.7$ meV of energy degeneracy between the spin states of a PM center, which fits within the 1.4 meV experimental energy window (see Figure 4.2(c) and Reference [18]) that was observed. While spin fluctuations introduce both $(\pm 1, 0, 0)$ spin relaxation and orthogonal $(0, \pm 1, \pm 1)$ phase decoherence (coded in purple in Figure 1b). With $k_B T > |\Delta| = 0.7$ meV, spin fluctuations are operative up to 169.5 GHz. Since the 1 MHz phase decoherence frequency of CoPc [479] is much slower than the 140 THz spinterface stroke and the 169.5 GHz on-site spin mixing stroke, the engine is resilient against phase decoherence. Note how the mesoscopic (diameter 300 nm) device's effective nanotransport path [480] should comprise several PM centers forming a spin chain, across which small energy asymmetries can be present [18].

According to Chowrira *et al.*, the non-thermal properties of the spinterface associated with the quantum nature of spintronic transport across these atomic centers result in this active behavior. By lifting the spin degeneracy on the WS (*i.e.* spintronic anisotropy [251, 480]), the spinterface-based stroke promotes a superposition of quantum states of the WS upon which spin mixing can promote population inversion. This population inversion is driven by two concurrent asymmetric mechanisms: the electronic transport across the spinterface [18, 469, 481] and the quantum iSWAP [406] process moderated by the magnetic exchange coupling J.

From these considerations, the mechanism of the engine can be decomposed in two strokes that correspond to the two different processes that affect the WS.

First, the transport fluctuation stroke corresponds to the exchange of electrons between the electrodes and the centers. Because this interaction is spectrally narrow and mediated by the spinterface's full spin polarization along the $(1, 0, 0)$ direction, it imposes the injection of coherent spins into the WS [351] (coded in blue in Figure 4.8(b)) in a repeated interaction that causes the sub-$k_B T$ resolution (see Figure 4.6(c-d)) as a consequence of spectral squeezing. This orientation reduces the possible channels of spin decoherence and describes an autonomous measurement of the WS state. The spinterface thus acts as an autonomous Maxwell demon that gains information on the WS and uses it as feedback to control the electron transfer rate across the barrier. The transport fluctuations stroke therefore quantum correlates the spinterfaces with the endmembers of the WS's spin quantum dots, thereby imposing boundary conditions on the WS.

Second, the WS has an antiferromagnetic ground state that is promoted by the magnetic exchange coupling between the spin chain members, and is reinforced when the two FM electrodes are antiparallel-oriented. From this one can propose a spin flip stroke that supplies magnetic energy to the WS (charging), which will be extracted during the transport fluctuation stroke via an ergotropic return from an excited state to the ground state.

Separating the engine operation into two strokes is justified by asymmetric regimes of operation, enabled by the structural/electronic asymmetries of the device, which generate different electronic frequencies and spin-splitting values on each PM centers.

4.3 Framing summary

In this Chapter, we reviewed the pioneering work around the spintronic engine with a special focus on the latest work of my team at IPCMS. They report active nanoscale devices that generate up to 100 nW of power without any external energy input to maintain *dc* current and voltages. We saw the importance of key ingredients that are the FM electrodes, the spinterfaces and the magnetic centers whose interactions need to be finely tuned in order to produce the power-generating effect. Then we gave qualitative elements of explanation of the underlying mechanism which suggests potential routes that may be followed by further theoretical analysis which are needed to fully understand these engines.

On the experimental side, the junctions made with oxides suffer from reproducibility issues which question their validity such as one needs to discard any possible unaccounted artifact, while molecular junctions present fabrication challenges due to the physical properties of molecules which necessitates the development of non-standard processing routes [19]. Both implementations have their advantages: the oxide platform is easily industrializable with current technologies but reproducibility is very low due to a positioning of C impurities within the MgO barrier that is difficult to control, and their output power is 1000x lower than the molecular implementation. Efforts must therefore be made in the field in order to produce more working devices whose magnetic and electronic responses must be carefully investigated. In this regard, the first objective of my thesis was to pursue the work on the MgO architecture, with the hope of finding more active devices and propose architectures or protocols that would facilitate the production of these engines and maximize their output power.

On the theory side, these previous reports have shed light upon features and mechanisms that suggest that unconventional quantum phenomena are taking place within the device and give rise to the power output along with the singular spectral signals. Although argumented qualitative explanations of the spontaneous current and voltages have been proposed based on *ab-initio* simulations such as DFT, a convincing, minimalist and fully thermodynamical approach of this machine is still missing. Indeed, the analytical model developed in Katcko *et al.* [18] assumes a chemical potential difference between the two electrodes which is not a satisfying hypothesis unless one describes the physical effect that continuously gives rise to the permanent voltage. These studies thus call for further fundamental investigations that should build upon elements of both spintronics and quantum thermodynamics to design a model of the device in which the energy and information fluxes are carefully studied using a minimal number of assumptions relative to the out-of-equilibrium properties of the environment. To this end, the second objective of my thesis was to build a theoretical model able to clearly identify the resources consumed by the engine and justify its persistence for the duration of the experiment and beyond, with the hope of finding the essential parameters of the engine so as to ultimately guide the experimentalists in the engineering of devices with optimal performances.

In the next parts, I present the results I obtained pursuing those goals.

Part II

Experimental Part

Chapter 5

Experimental Methods

In this chapter, we report on the experimental methods used to fabricate and characterize the devices studied in this thesis. The objective of this laboratory work was to build upon the previous achievements presented in the previous Chapter on oxide junctions in order to find more energy harvesters, improve the reproducibility and identify the conditions and mechanisms under which a device can become active and generate a continuous long-lasting power output. To this end, we start by presenting the sputtering procedure used to grow the MgO stacks, then we detail the lithography and etching protocol we followed to process these stacks into functional MTJ, and finally we explore the experimental setup we used to perform *operando* magneto-transport measurements.

5.1 Growth procedure of MgO stacks

The oxide MTJs with MgO spacer studied in this thesis were fabricated by sputtering by Dr. Michel Hehn and his collaborators from IJL in Nancy. In this section, only a general growth procedure for MgO stacks is described ; more details can be found in J. Bernos and M. Hehn et al. [482].

Name	Sample Composition
7181	Ta(5)/Pt(5)/IrMn(8)/Co(4)/C(1ML)/MgO(0.9)/C(0.1ML)/MgO(1.7)/C(1ML)/Co(10)/Ta(2)/Pt(1)
7182	Ta(5)/Pt(5)/IrMn(8)/Co(4)/C(1ML)/MgO(0,6)/C(0.1ML)/MgO(2)/C(1ML)/Co(10)/Ta(2)/Pt(1)
7183	Ta(5)/Pt(5)/IrMn(8)/Co(4)/C(1ML)/MgO(0.9)/C(0.01ML)/MgO(1.7)/C(1ML)/Co(10)/Ta(2)/Pt(1)
7184	Ta(5)/Pt(5)/IrMn(8)/Co(4)/C(1ML)/MgO(0.6)/C(0.01ML)/MgO(2)/C(1ML)/Co(10)/Ta(2)/Pt(1)
7185	Ta(5)/Pt(5)/IrMn(8)/Co(4)/C(1ML)/MgO(0.9)/C(0.1ML)/MgO(1,7)/CoFeB(3.5)/Ta(2)/Pt(1)
7186	Ta(5)/Pt(5)/IrMn(8)/CoFeB(3.5)/MgO(0.9)/C(0.1ML)/MgO(1.7)/CoFeB(3.5)/Ta(2)/Pt(1)
7187	Ta(5)/Pt(5)/IrMn(8)/Co(4)/C(1ML)/MgO(0,9)/C(0.01ML)/MgO(1.7)/CoFeB(3.5)/Ta(2)/Pt(1)
7188	Ta(5)/Pt(5)/IrMn(8)/CoFeB(3.5)/MgO(0.9)/C(0.01ML)/MgO(1.7)/CoFeB(3.5)/Ta(2)/Pt(1)

Table 5.1: **MgO stacks.** Table of MgO stacks grown by sputtering. Unless specified all numbers specify the thicknesses of each layer in nm. ML stands for monolayer.

The stacks we ordered from Nancy are referenced in Table 5.1. Tantalum is used as a buffer followed by a Platinum layer to improve further texturization. The next layer is IrMn, an antiferromagnet which acts as a pining layer for the adposed ferromagnetic electrode, made either of Cobalt or CoFeB. A single monolayer (ML) of Carbon was then deposited on the Cobalt electrodes and stands for the bottom spinterface. The following structure corresponds to the MgO tunneling barrier in which different concentrations of Carbon impurities have been inserted within the barrier. Their position has been carefully chosen so that a crucial asymmetry between top and bottom is respected, and their placement was varied within the barrier. The next layer corresponds to the top electrode, either made from uncoated CoFeB or Cobalt with a 1 ML Carbon spinterface. Finally, the stack was protected with a capping of Ta/Pt bi-layer.

The stacks were chosen so as to study the influence of three parameters on the response of the junctions. The electrode material was varied from plain CoFeB to a Carbon coated Cobalt electrode acting as a spinterface. Keeping the total thickness of the oxide barrier constant (2.6 nm), the position of the Carbon impurities was varied within the barrier, either they were placed 0.6 mn away from the bottom electrode or 0.9 nm away. Finally the concentration of impurities within the barrier was chosen between two values 0.1 ML or 0.01 ML. These variations were carefully selected in the hope of discriminating the relevant parameters for maximizing the efficiency of the device.

CoFeB, being an amorphous material, allows for the initial mono-layers of MgO to similarly form in an amorphous structure. As MgO layers increase, a transition to a crystalline structure occurs. This resulting MgO is not purely epitaxial but a textured (001) crystal with varied grain boundaries and amorphous regions [483]. The additional CoFeB electrode also forms amorphously on the MgO layer. To fully achieve crystallinity in both the barrier and interfaces, the whole stack is annealed, prompting a distribution of the crystalline structure from the MgO spacer's textured areas. The crystallization transforms the insulator/FM interface into a body-centered cubic (bcc) crystal structure that aligns with the MgO cubic configuration [483, 484]. Despite the polycrystalline nature of the MgO barrier, its impact on electron transport is minimal. Non-annealed MgO samples exhibit lower TMR values due to their incoherent transport-promoting, amorphous system [484, 485]. Further to crystallinity, annealing also assists in securing the magnetization of the electrodes thanks to the alignment of the FM domains with the AFM IrMn domains via exchange bias. In our experiment, the fully grown MgO stacks were post-annealed for an hour, in vacuum, at various temperatures between 200-300°C. This process, amplified by an external magnetic field of 200 Oe, allows alignment of antiferromagnetic IrMn and ferromagnetic CoFeB electrode domains, achieving desired exchange bias. However, this method isn't without flaws, particularly during annealing where Mn diffusion from the IrMn can weaken the pinning strength due to Mn deficiency, most noticeable when the annealing temperature or duration is increased [215].

5.2 Junction processing

The grown MgO stacks from Nancy were processed at the IPCMS by the author, following a protocol described in the present section. After a brief overview of the laser lithography and etching techniques, we describe the four steps we followed to build the MTJs devices from the thin film stacks.

5.2.1 Laser Lithography

Photolithography is a popular technique in semiconductor patterning, utilizing radiation to create patterns on a substrate surface. In classical lithography, a photomask, a transparent plate with patterned chromium areas, is used with a UV-sensitive resist/polymer. On the other hand, laser lithography, uses lasers to create patterns on a substrate, without the need for a mask, by directly firing a focused laser beam on the substrate to imprint a chosen motif programmed numerically, thus offering the flexibility of easily printing a tailored motif that does not need a material support but suffering from a longer processing time given the need for the laser to draw the motif for each sample. Lithography uses a polymer that undergoes chemical changes when exposed to specific wavelengths, becoming more soluble in the developer. There are two types of photoresists: positive and negative.

Positive photoresists weaken and become more soluble during exposure, creating an exact copy of the photomask design on the substrate, which serves as a stencil for subsequent processing steps. These are widely used in the semiconductor industry due to their good resolution and thermal stability.

On the other hand, negative photoresists undergo polymerization upon exposure, remaining on the exposed substrate surface, and removed from the unexposed areas. This results in a pattern opposite of the original photomask. Despite creating reverse patterns, negative resists are favored for their good adhesion to silicon, affordability, and shorter processing time.

The laser lithography protocol involves three steps. First, the appropriate photoresist is deposited on the sample using the spin-coating technique in order to form a thin and uniform polymer film on the substrate. Then, the sample is placed under the laser beam which imprints the desired motif, and finally the sample is placed in the developer solution which will remove the soluble parts of the polymer, revealing the motif.

In this thesis, we used the AZ5214 negative resist at every step of the protocol to imprint patterns onto the sample. The laser power was set to 5 mW. The mask used for the process was initially designed at UMPhy CNRS/Thales in 2002, after several iterations of refinement by Dr. Filip Schleicher and Dr. Martin Bowen within the group, and the present design can be seen in Figure 5.1

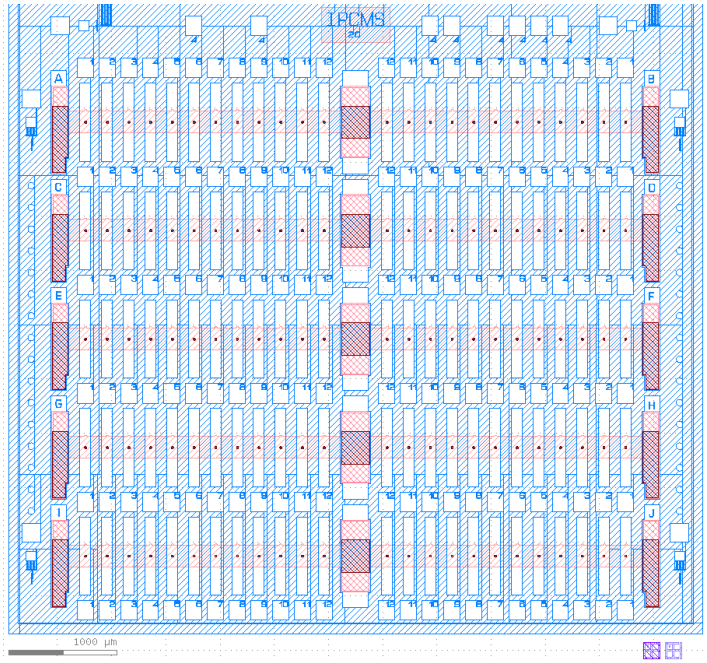

Figure 5.1: **Lithography Mask.** Laser lithography mask used for MgO patterning containing the four steps needed to process the devices. Only the bottom half of the mask is show for clarity, the top half being identical. Each mask allows to create 2x12 junctions connected to the same electrodes, for a total of 120 junctions in total for this half mask.

5.2.2 Neutral Beam Etching

The first two steps of the protocol involve etching in order to access the bottom electrode and to create the nano-pillars which define the junctions. Making micro-pillars is needed in order to isolate just a few Carbon impurities within a microscopic device which will form the spin-chain that is at the origin of the energy harvesting capabilities of the device.

Nano-pillars are etched by a neutral beam that removes uncovered materials. The Neutral Beam Etching (NBE) technique is advantageous as it can etch large areas without causing electrical or physical damage, which is essential for preserving the MTJ. The damage-free instrument includes an ion source to extract and accelerate an ion beam of a specific polarity. It has a grid with multiple apertures for the ion beam to pass, and a reflector with an equal number of holes connected closely to the grid. In our system, we introduce argon gas into the chamber, which splits into ions to create a plasma. The argon ions are neutralized by an electron-emitting filament and then accelerated towards the sample. We evacuate the charge from the sample by covering its side pads with aluminum foil strips using high-temperature Kapton tape suitable for ultra-high vacuum (UHV) conditions. This helps read the sample current and detect Auger signals. We maintain uniform etching by positioning the sample at a 45-degree angle to the beam and rotating it throughout the process. We carefully monitor and control the sample current during etching. To precisely control etching depth, in situ the technique of Auger electron spectroscopy described hereafter is used to analyze the thin film layers before and after etching. The etching dose is calculated by measuring the sample current per unit time (mA.min). The objective of the

etch step is to create a junction pillar with all top layers up to the middle of the tunnel barrier. Over-etching can result in the underlying ferromagnetic layer becoming too thin, affecting its electrical conductivity and magnetic coercive field. Excessively etched material could redeposit on the tunnel barrier leading to short circuits.

Auger Electron Spectroscopy (AES) is a technique based on the Auger Effect that uses a high-energy electron beam to excite atoms. The emitted Auger electrons, produced when excited atoms release excess energy, are collected and their kinetic energies are measured. These energy measurements correspond to specific elements on a sample's surface, enabling the chemical analysis of thin film samples. Typically, AES can sample depths of 2-5 nm, making it an effective tool for surface-sensitive analysis. An AES system includes an electron gun for sample examination and an energy analyzer to detect Auger electron peaks in the overall secondary electron energy distribution. In the setup used in this thesis, the AES is housed in the etching chamber and uses a 3 keV energy electron beam. The recorded Auger peaks often overlap with a continuous background, so we differentiate the energy distribution function $N(E)$ to identify them more easily. The differentiated Auger spectrum is expressed as the function $\frac{\mathrm{d}N}{\mathrm{d}E}$. The magnitude of an Auger peak in a differentiated spectrum corresponds to the surface concentration of the element that produced the Auger electrons. In our study, we examined the kinetic energies of Auger electrons emitted from the top few nanometers of the thin film surface, up to 1000 eV. The Auger gun and the detector are positioned differently from the etching gun in the experimental setup so we conduct AES measurements by transferring the sample to the Auger position under UHV conditions. We record an initial spectrum and then analyze the spectra after each etching to determine the etching dose. Moving back and forth between AES and NBE, a few layers of material are removed at each step until we are satisfied with the Auger spectrum analysis, giving us the targeted elements in the aimed proportion.

5.2.3 Processing Protocol

The MgO based thin film stacks are processed in four steps using laser lithography, etching and deposition. The first step is to define the junction's nano-pillars, followed by electrode patterning, passivation and metallization. The following subsections details all the steps involved to make MgO MTJs.

Step 1: Micro-pillars

The cleaned sample is spin coated with a negative resist AZ5214 which provides a uniform surface (Figure 5.2(a)). One crucial point to remember is to determine the micro-pillars along the direction of the exchange bias, which is defined during the annealing of the MgO growth process. The motif printed by laser lithography shall thus be aligned with this orientation given. After heating the sample at 105°C to fix the resin the the substrate, the mask is applied, then the sample is heated again at 120°C for 1.5min and flooded under UV light for 35s in order to invert the polarity of the resist (Figure 5.2(b)). Finally, the sample was placed in the developer solution AZ726MIF for 45s. On development the resist

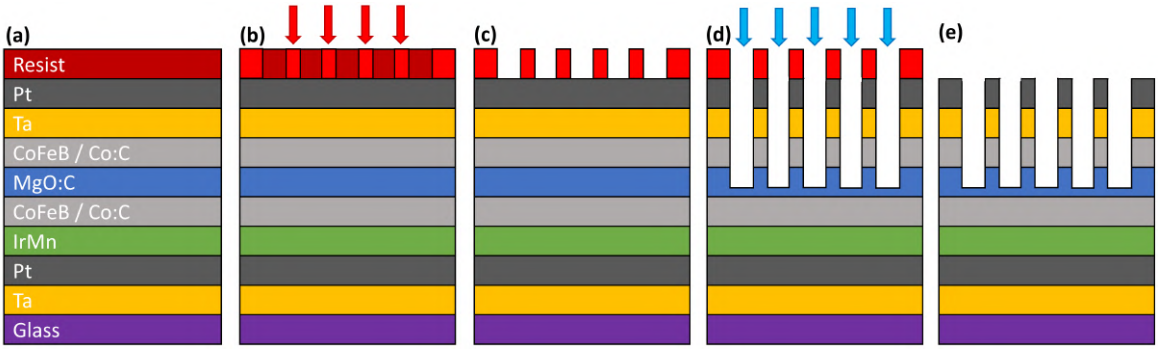

Figure 5.2: **Schematics of the different protocol phases in step 1.** (a) The resist is uniformly deposited on the surface using by spin-coating. (b) The mask is printed by laser lithography, changing the activity of the resist where the laser is applied. (c) After developing, the soluble parts of the resist disappear. (d) The sample is etched up to the mid of the MgO layer. (e) The solvent wash removes the remaining resist.

is removed from all areas except on the pads and the micro pillars circular region, see Figure 5.2(c).

After this lithography procedure, the sample is brought to the NBE and etched up to the middle of the MgO tunnel barrier. In Figure 5.3(a), we report the Auger spectra obtained after a few steps of the etching process showing the increase and decrease of the Oxygen signal, certifying that we correctly etched up to the oxide layer, leaving only a few layers of MgO (see Figure 5.2(d)). Microscopy pictures after the lithography and the etching are provided in Figure 5.3(b) and (c).

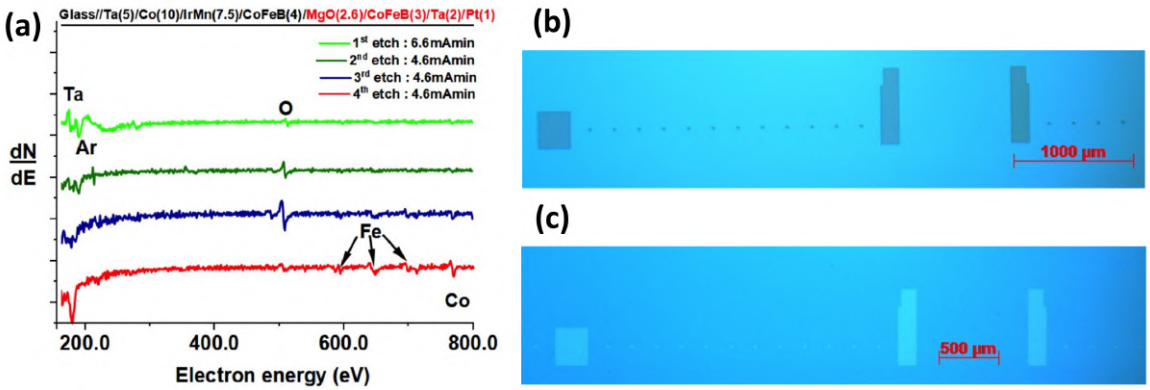

Figure 5.3: **Auger spectra and pictures of the MgO stack at step 1 of the protocol.** (a) Auger spectra after four consecutive etching steps. The etching dose of each step is indicated in mA.min. Several peaks can be correctly identified using reference spectra: Ta: 165 eV, 170 eV ; Ar: 180 eV ; O: 503 eV ; Fe: 598 eV, 648 eV, 701 eV, 715 eV, and Co: 771 eV. (b) Microscopy image of the nano-pillars and the electrodes after the lithography procedure. (c) Microscopy image of the nano-pillars and the electrodes after the etching procedure.

Step 2: Bottom electrode

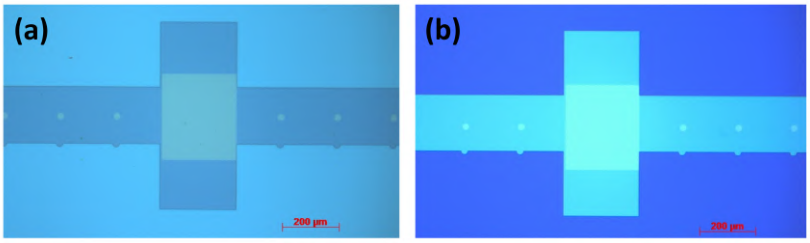

Figure 5.4: **Pictures of the MgO stack at step 2 of the protocol.** (a) Microscopy image of the nano-pillars and the central pad after the lithography procedure. (b) Microscopy image of the nano-pillars and the central pad after the etching procedure.

Once the pillars are defined, the photoresist from step 1 is removed by ultrasonication process using acetone and ethanol solvents for ten minutes each. The bottom electrode is defined following the same laser lithography procedure as step 1, the pattern used is represented in Figure 5.4(a).

Post development, the sample is etched down to the substrate, making sure to not over-etch it so as to avoid short-circuit issues. The present motif defines the contact pads that allow the current to flow towards the bottom electrode. Once etching is completed the sample is solvent-cleaned revealing the bottom electrode and nano-pillars (Figure 5.4(b)).

Step 3: Passivation

A third lithography is performed using the same protocol in order to cover the nano-pillars and the contact pads (Figure 5.5(a)). This protection is followed by a deposition of 135 nm thick SiO_2 which is used to passivate the whole surface of the sample apart from the MTJs and the contacts in order to isolate electrically every device (Figure 5.5(b)). After passivation, a lift-off is needed in order to remove the resist coating of the contacts and the MTJs. Due to the limited adhesion of the SiO_2 layer to various materials, it is not possible to selectively remove the resist and SiO_2 from the pillar using ultrasounds. As a result, the sample is soaked in an acetone bath for at least two hours. The acetone is able to strike the exposed sides (without SiO_2) of the negative resist layer, dissolving it, and leaves an electrical opening in the passivation layer for direct access to the MTJ (see Figure 5.5(c)).

This lift-off procedure turned out to be somewhat hazardous. Due to the microscopic size of the nano-pillars and the poor stickiness of the SiO_2 to the surface, removing the resist on the nano-pillars cleanly came with a varying success rate. Since SiO_2 is transparent, we came up with a polarized microscopy technique which allowed us to verify whether a junction was open or closed (still covered by an SiO_2 layer), see Figure 5.5. We proceeded onto the next step only when a sufficient number of junctions was accessible, else, we required more flooding in acetone using a mechanical flow of solvent.

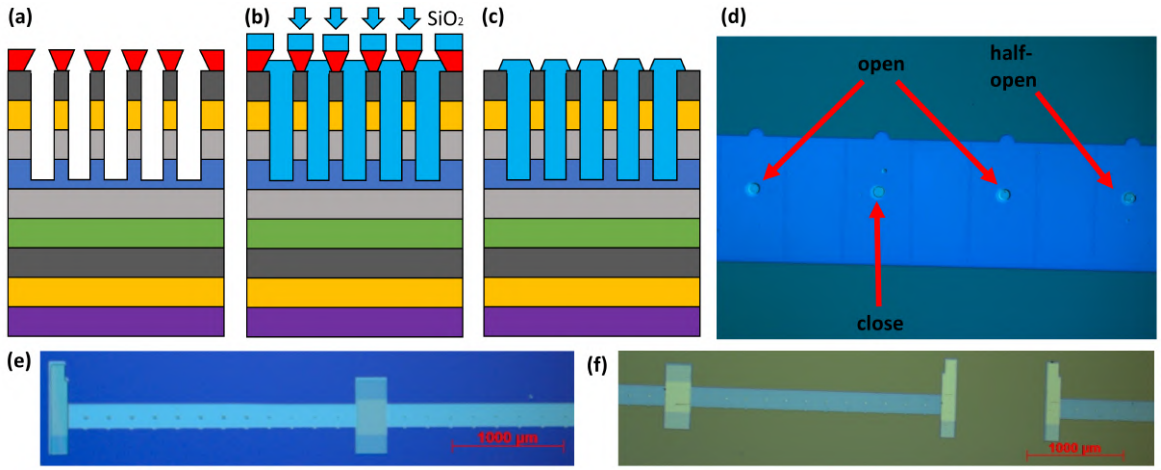

Figure 5.5: **Schematics and pictures of the different protocol phases in step 3.** (a) After the third lithography, the resist covers the nano-pillars and the electrodes, forming overhangs over them. (b) SiO_2 is deposited and passivates the surroundings of the devices. (c) After the lift-off process, the remaining resist is removed, exposing the nano-pillars and the electrodes. (d) Microscopy picture under the C-DIC polarizing lens showing four junctions, two open, one close and one half-open. (e) Microscopy picture after the lithography procedure. (f) Microscopy picture after the SiO_2 deposition procedure.

Step 4: Top contacts

Now that the SiO_2 insulating layer covers the sample, excluding the junction pillar and bottom electrodes, a final lithography procedure is performed similarly, preserving all areas except where the conductive contact pads will be placed, as shown in Figure 5.6(a). A bilayer of Al(110 nm)/Au(35 nm) is then deposited on the sample in a UHV environment, creating a metallization layer (Figure 5.6(b)). This step allows for an easy lift-off due to the large surface area covered by the resist. Brief ultrasonic pulses in acetone dissolve the resist, leaving only the metallic contacts with a 12 µm optical opening for the 20 µm MgO MTJs (Figure 5.6(c)). This concludes the MgO MTJs processing and the samples are now ready for probing, bonding, and further measurements.

5.3 Characterization techniques

This section presents the setup used in order to analyze the devices processed along the protocol detailed in the previous section. The experiments presented in the next chapter were performed on the magneto-transport Fert bench at IPCMS which allows to probe the electronic responses of the junctions in response to varying temperatures, magnetic fields and voltage. Prior to studying the measurement process, we start by describing the post-processing steps required to put the devices into the Fert experimental setup.

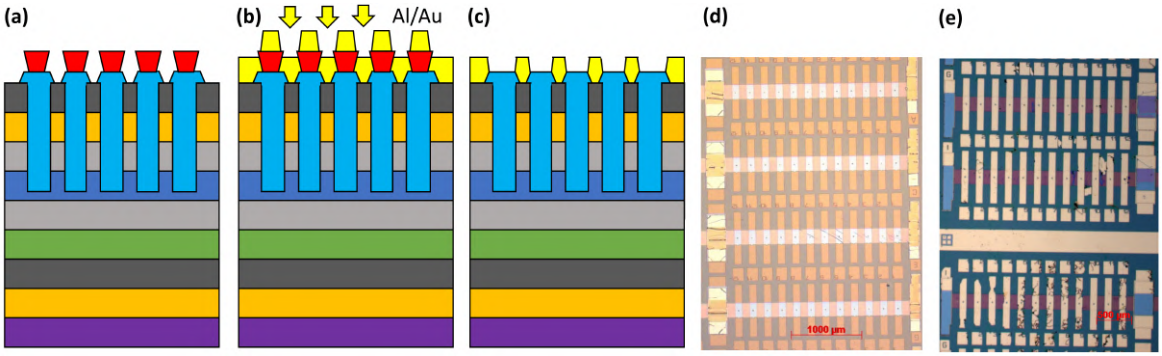

Figure 5.6: **Schematics and pictures of the different protocol phases in step 4.** (a) After the fourth lithography, the resist covers the surroundings of the nano-pillars and the electrodes, forming overhangs over them. (b) Al/Au is deposited and creates the top contacts over the electrodes and the MTJs. (c) After the lift-off process, the remaining resist is removed, leaving the nano-pillars and the electrodes covered with Al/Au and the surroundings exposed to insulating air. (d) Microscopy image after the fourth lithography procedure. (e) Microscopy image after the Al/Au deposition.

5.3.1 Post-processing

Probing

After the final step of the processing protocol, a rapid probing of the junctions is performed in order to check for defective junctions using a Keithley Instrument multimeter. Indeed, as we detailed above, the processing protocol often results in failures that originate from metallic shortcuts leading to Ohmic junctions, or failed lift-off resulting in open-circuit junctions. The objective of the probing is therefore to identify devices which might present some interesting behaviors by measuring their resistances and plot a coarse IV characteristic. Although a four-point measurement is preferred to separate the probe from the input and obtain more precise electrical information on the devices, in this work we limited ourselves to two-point measurements, which was sufficient to give the coarse indications we needed to discriminate between potentially interesting and useless junctions. The junctions were measured using a very low bias voltage in order to minimize the risk of breaking them as a result of a strong electrical input and the IVs were recorded on the smallest possible range of the multimeter.

A working bottom electrode yields a resistance of 100 Ω to 500 Ω. Short-circuit junctions present resistances below 1 kΩ while open-circuit junctions have resistances of around 1 GΩ. Interesting junctions that were potentially kept for further analysis on the BMF bench had resistances ranging between 1 kΩ and 100 MΩ.

Cutting and wire bonding

After probing the junctions, the MgO devices are once again coated with resist, then cut into 16 chips using a wire saw cutter or Accretech SS10 dicing machine, leading to 5x7 mm^2 sized samples which we clean with solvent.

The MgO samples are then fixed onto Fert sample holders' chips and wire bonded using the Hybond 527A machine in the STNano platform. This process includes grounding the sample electrically to prevent potential electrostatic currents from damaging the device. We then probe the bonded samples on the chip to ensure that the device state remains undisturbed from wire bonding and after all this, the devices are finally set to be introduced into the magnetotransport measurement bench.

5.3.2 Magneto-transport setup

The BMF magneto-transport setup comprises a cryostat, two magnets, a Keithley sourcemeter, and a proportional-integral-derivative temperature controller. The team's work has added unique enhancements including four precision motors for cryostat and magnet movement in the XY plane, and an electrical multiplexer.

The bench provides multiple automated options for device measurement. Once the wire-bonded sample is mounted in vacuum inside the cryostat, situated between a potent 2 T electromagnet, the system allows for low-temperature measurements, achieved by filling the cryostat with helium gas. Depending on the sample's position in the cryostat, both in-plane and out-of-plane magnetic field measurements can be acquired. With a LabView and Python software interface, the system can perform automatic, temperature-dependent studies. This feature uses a multiplexer to switch between samples, control applied bias, and manage magnetic fields. The setup also permits magnetotransport measurements for multiple sample-to-field angles. Additionally, the system can execute precise temperature-dependent current-voltage characteristics and resistance-field plots. These functions enable researchers to examine the response of the devices to a handful of carefully controlled parameters such as the magnetic orientation of the ferromagnetic electrodes and study the electrical impact of the nanoscopic impurities within the material [480].

The cryostat operates on the Grifford-McMahon (GM) cycle [486], which includes components such as a cold head, chamber, regenerator, displacer, valves, rotating valve, and motor. Our group's cryostat operates using a pneumatically driven two-stage refrigerator. The main component is the expander where cooling occurs. In a first stage, the expander holds a radiation shield which safeguards the "cold finger" from room-temperature thermal radiations, cooling it to 77 K. Then, it directly cools down this cold finger, reaching temperatures as low as 4.2 K. A vacuum shroud secures everything in place, designed to provide optical access to the sample. Approximately 34 delicate copper wires electrically connect the sample holders, including two temperature sensors and a heater. These elements are essential for performing precise magnetotransport measurements by allowing for accurate temperature control near the expander's second stage. The temperature readings are facilitated by two sensors: one on the heating station at the top of the cold finger and the other

at the end of the cold finger next to the sample holders. The latter provides the best indication of the sample temperature. The electrical setup allows the connection of 10 devices in two-point mode or 5 devices in four-point mode. The wire connector plugs into an electrical multiplexer, acting as a relay between the Keithley instrument and the sample, enabling regular switching between devices. This automatic switching facilitates measurements on multiple samples. Through advanced LabView programming, the system can conveniently plot $I(V)$, $R(H)$, and $R(T)$ measurements. For more details on setup calibration, refer to U. Halisdemir's thesis [487]. The results discussed in the next Chapter were obtained using this setup.

Chapter 6

Encoding information into oxide tunnel junctions

The following Chapter presents the experimental results obtained on the oxide MTJs which were fabricated for this thesis under the process described in the previous Chapter. As detailed in Chapter 4, my team at IPCMS recently published a study in which they demonstrated positive electrical power output generated by magnetic tunnel junctions (MTJs) at room temperature [18]. The device aims to bridge the fields of spintronic and quantum thermodynamics by utilizing the magnetic energy stored inside ferromagnetic electrodes in order to generate an electrical current. This is achieved by stabilizing the thermal fluctuations of the carbon paramagnetic center trapped inside the junction's MgO barrier. These promising first results have thus pushed my team to work towards better understanding how this so-called spintronic engine operates, and to develop new techniques in order to improve the stability and the reproducibility of the device.

Following the initial milestone of the team, the goal of my experimental internship was to investigate the magneto-transport properties of MTJs used as spintronic engines in order to better understand key design features. Although no active device was observed, some junctions revealed an interesting behavior, which appears to be linked to the charging of the Carbon localized states, and which may be of use for information and computation technologies.

Traditionally, spintronic solid-state devices store information as '0' and '1' by converting the magnetic states of two neighboring electrodes, parallel (P) and anti-parallel (AP), into two unique resistances. This process, known as magnetoresistance (MR) which we introduced in Chapter 1, enables the detection and processing of this data in an electrical circuit and forms the basis for electron spin-based information encoding and transmission. For new memory data storage, only one electrode, the free layer, needs to switch its magnetization, while the second electrode remains unaltered and serves as a reference layer. This reference layer is fixed by coupling it with an antiferromagnetic (AFM) layer corresponding to the IrMn layer in our devices. The transport across a device's metallic or semiconducting AFM layer can induce significant effects like tunneling anisotropic magnetoresistance and interface charging effects which were presented in Chapter 1. Moreover, experiments

indicate that the magnetoresistance data of a solid-state device can be used to investigate the quantum states of magnetic impurities or spin chains trapped within the barrier [251]. The study of spintronic devices that leverage these distinct spin states reveals a particular importance, as it could greatly enhance current quantum information technologies.

6.1 Changing the junction's state with an applied bias

Among the junctions which presented potential during the probing (562/4156 = 13% of the junctions considered), we performed precise magnetotransport experiments on 149/562 = 27% of them and found 32/149 = 21% of them with an interesting behavior that do not correspond to simple ohmic or open-circuit junctions, which corresponds to a proportion of 0.77% of unusual junctions among the total number of junctions which were successfully fabricated. In particular, we found 10 junctions featuring distinct junction states characterized by different resistance values that could be addressed by varying the bias voltage. The transition between states is discontinuous and translates into a current branch jump in the intensity-voltage characteristic. The transition between states is reversible but the writing process is somewhat unreliable.

6.1.1 Reading

In Figure 6.1.(a) and (b), we show the IV characteristic and the corresponding $\mathrm{d}I/\mathrm{d}V$ signal for a switching junction. Two distinct current branches can be identified: the ON branch in green features a conductance peak CP at -120 mV while for the OFF branch in blue, no conductance peak is seen at -120 mV but a smaller peak is present at -20 mV. The state of

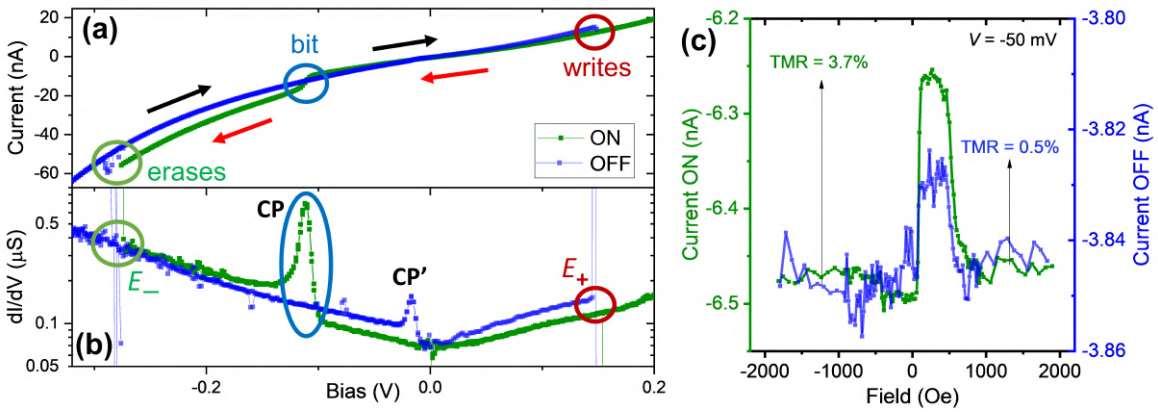

Figure 6.1: **Reading the state of the junction.** (a) IV characteristic of junction A showing the ON state in green and the OFF state in blue. (b) Corresponding differential conductance showing the bit of information read as a conductance peak at -120 mV. (c) Current-Field $I(H)$ plot showing the two signals obtained for the ON and OFF branches at -50 mV. The state can be read by measuring the tunnel magnetoresistance (TMR) which differs in the two states.

the junction can thus be read by measuring its resistance or its conductance, preferentially at the targeted bias voltage of -120 mV such that a bit of information can be encoded in the state of the junction corresponding to the presence or the absence of the conductance peak CP. Additionally, Figure 6.1.(c) shows us that each of the two branches have a different TMR such that the information encoded within the state of the junction can also be read by probing the magnetic response of the junction.

6.1.2 Writing

In Figure 6.1.(a) and (b), we see two discrete events around E_+ at 150 mV and E_- at -240 mV during which the current is discontinuous and switches between the two intensity branches. Thus, we observe that the branch jump at E_+ corresponds to the switch from the OFF branch to the ON branch such as it writes the bit of information encoded by the peak CP, while the branch jump at E_- corresponds to a switch back to the OFF and therefore erases the peak. The junction's change of state is therefore reversible: to write the conductance peak, a positive bias voltage exceeding 150 mV is applied, and to revert back to the initial state a negative bias voltage larger than -240 mV is applied.

To confirm that these branch jumps do indeed code for the writing/erasing events, we performed additional experiments on another similar junction where we inverted the direction of the voltage sweep right before the jump and right after the jump. In Figure 6.2(a), starting in the ON branch, characterized by the conductance peak, we see that when inverting the sweeping before the event E_+, the junction stays on the ON branch. Then in Figure 6.2(b), we check that when changing the voltage direction right after the branch jump of the event E_+, the junction does change to the OFF state, leading to no conductance peak. In Figures 6.2.(c) and (d), we equally show, using the same method, that, starting in the ON

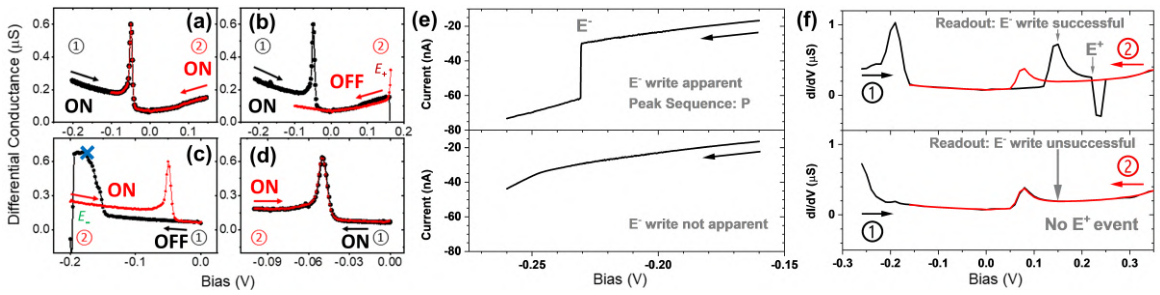

Figure 6.2: **Writing the state of the junction.** (a-d) $\mathrm{d}I/\mathrm{d}V$ data upon sweeping bias to test the interplay between the presence of the conductance peak and the writing events E_- and E_+. The black data labeled 1 code for the initial branch state of the junction, then the sweep direction is inverted and the return branch is represented in red and labeled 2. The blue cross in panel (c) pinpoints the bias and junction state in which the data of Figure 6.1 was acquired. (e) Examples of IV traces showing E_- write events that are (top) apparent, with 1 write peak observed, and (bottom) not apparent, *i.e.* with no write peak observed. (f) Corresponding readouts, with (top) confirmation and (bottom) information that the E_- event-driven junction state was written.

branch, the event E_{-} does trigger the switch back to the OFF branch.

We also studied the reproducibility of these writing events. In Figure 6.2(e), we show an example of two IV traces, one where the event E_{-} does happen and trigger a branch jump, and one where the writing fails and the junction stays in the same state while the voltage exceeds the bias threshold for switching. Then, in Figure 6.2(f) we confirm that the line shape of $\mathrm{d}I/\mathrm{d}V$ changes with the event E_{-}, featuring shifted conductance peaks after the branch jump, and we witness that, without the event E_{-}, the $\mathrm{d}I/\mathrm{d}V$ remains unchanged.

Then, we studied in more detail the writing events statistics in order to evaluate the robustness of the encoding. In Figure 6.3(a) and (b), we plotted the distribution of the number of current jumps during the writing sweep for a junction at 10 K, in both cases when the writing succeeds or fails. We witness that cases with an odd number of current jumps dominate even cases in the case where the writing succeeds. For this set of data, we obtain an encoding success rate of 573/679 = 84%.

Finally, in Figure 6.3(c) and (d), we plot the bias dependence of the frequency of a current jump when the erasing event E_{-} fails or succeeds. We note that the switching events appear after a bias threshold of -0.2 V and increase for larger absolute voltages. The data also seems to indicate that there is an optimal bias range between -0.22 V and -0.24 V where the encoding chances of success are the highest as a limited number of failed events are measured above -0.24 V.

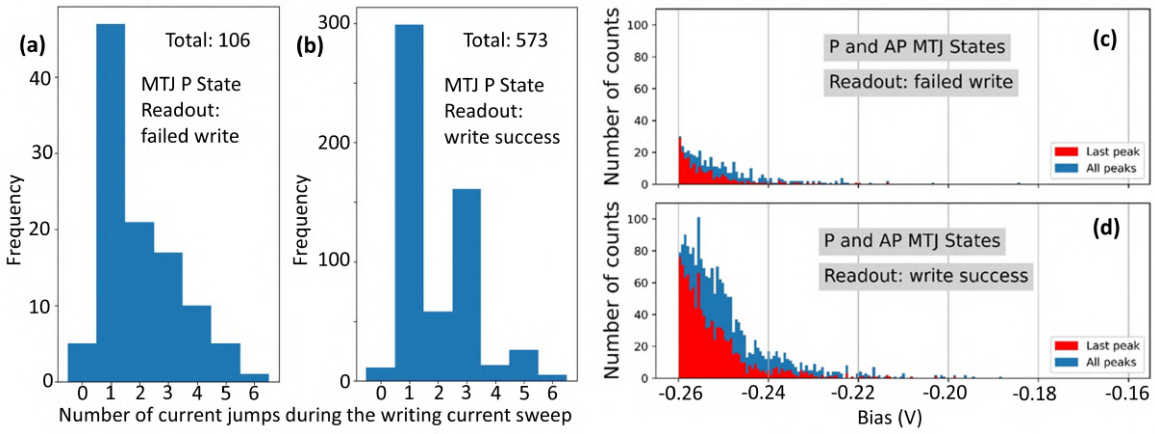

Figure 6.3: **Writing event statistics.** (a-b) Statistics of the number of current jumps during the writing current sweep. (c-d) Bias dependence of the frequency of a current jump when the writing event fails or succeeds.

6.2 Changing the junction's state with temperature

Following these initial experiments performed at 10 K, we investigated the state changes of the junctions with temperature. The numerous temperature sweeps we performed allowed us to witness behavioral changes of the junctions upon warming and cooling cycles. The measurement of the junctions' resistances at increasing or decreasing temperature points

also showed some rich features, revealing a zoology of junctions' states and phase transitions.

6.2.1 Changing behaviors upon warming and cooling cycles

During the magnetotransport experiments, we performed several cool-downs to 10 K and warm-ups to room temperature. After each cycle we noticed that the behavior of the junctions changed, most likely due to some structural rearrangement within the device. In Figure 6.4, we show six IV characteristics at different stages of the temperature cycles. Starting at room temperature in Figure 6.4(a), the junction is noisy such that the current varies stochastically between an upper branch and a lower branch. Upon the first cooldown in (b), the junction now features a single branch with a conductance peak at -0.1 V. After returning to room temperature in (c), the junction has changed and now features a single branch with a noisy part at voltages above 0.1 V. After the second cooldown in (d), the junction displays two branches with mergers and reversible current jumps at positive and negative biases. Then, warming again and the junction in (f) has no noise but two branches at negative biases. Finally, in a last cooldown, the behavior of the junction changes once again, but with features staying qualitatively similar to the previous cooldown in (d).

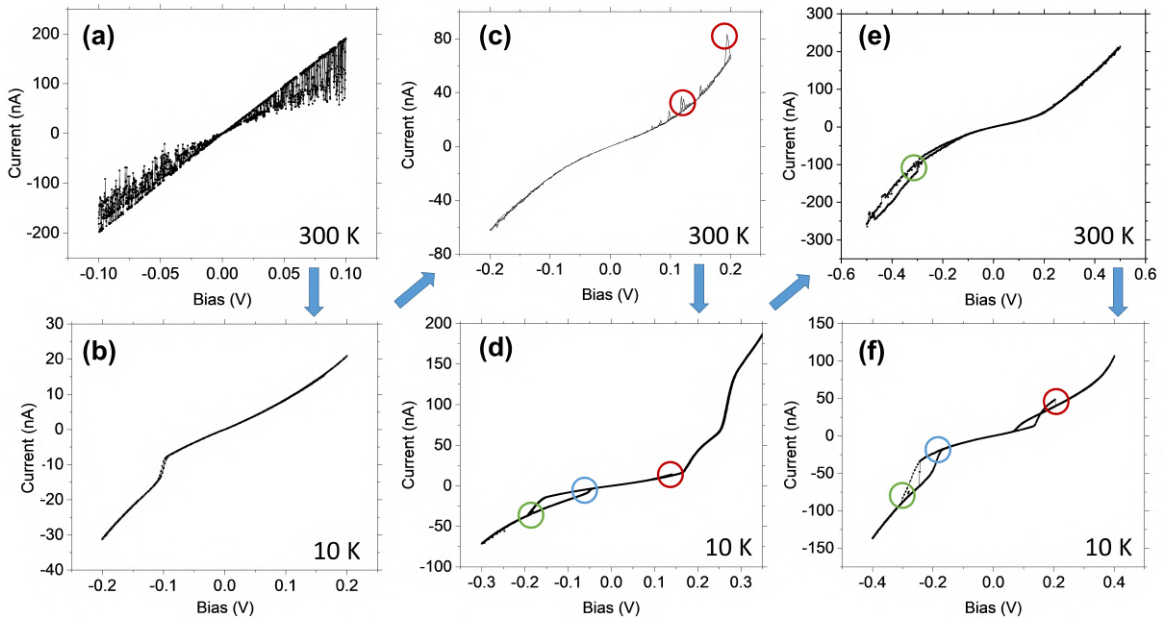

Figure 6.4: **Temperature cycles changing the properties of the junction.** (a-f) IV characteristics of the same junction at the different stages of the warming and cooling cycle, the top figures were obtained at 300 K upon warming up, and the bottom figures at 10 K after cooling down. The blue arrows indicate the chronological steps of the three warm-up and cool-down cycles which matches the alphabetical order of the figures. Red circles indicate events E_+ corresponding to branch jumps at positive bias. Green circles identify events E_- so branch jumps at negative bias. Blue circles identify intensity branch merger.

These results show that, although the general features of the junctions remain somewhat stable with temperature changes, the precise positions and magnitudes of the peculiar signatures of the junction such as current branch jumps and conductance peaks are quite sensitive to temperature changes. This instability may be detrimental to the use of such junctions for practical applications as information storage devices.

6.2.2 Temperature dependence of the intensity

A finer sweep in temperature revealed further properties of the junctions and led to the observation of peculiar phase transitions. In Figure 6.5(a), IV characteristics are plotted with color on a graph showing their variation with temperature. Three different regimes can be identified and confirmed with the help of Figure 6.5(b). Below 50 K the device stays in a noiseless OFF branch over the whole considered bias range, from 0 V to -0.22 V. Then, between 50 K and 70 K, a second ON branch becomes available and the junction shows a telegraphic noise. From 70 K to 100 K, the telegraphic noise disappears, leaving the junction in a so-called MID branch, close to the ON branch, but with strong diffusive current noise around it. And finally, above 100 K, the device is definitely in a noiseless OFF state.

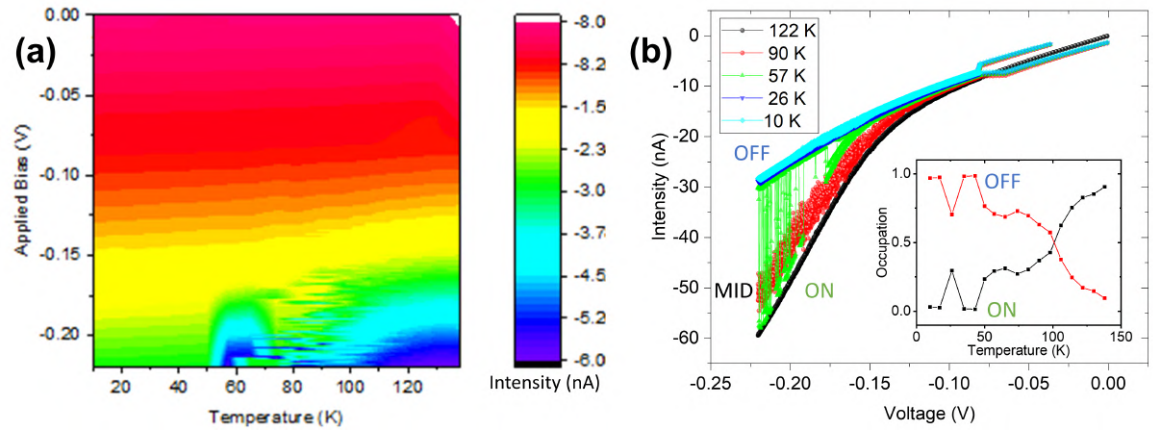

Figure 6.5: **Temperature dependence of the current.** (a) Color plot of IV characteristics at different temperatures. (b) Plot of five IV characteristics at different temperatures showing the transition of the junction from the OFF branch to the ON branch.

6.3 Characterizing the phase transition

The interesting property of this transition with temperature is that behavior of the junction does not change smoothly with temperature such as it transitions through a MID branch and reveals intermediary regimes with different types of noise: telegraphic and diffusive.

6.3.1 Telegraphic noise

The inset of Figure 6.5(b) shows the occupation frequency of the ON and OFF branches as a function of temperatures such that we clearly see the gradual transition from the OFF to the ON branch as the temperature increases. In this Figure, we can see the complex evolution of the junction: around 60 K, a chaotic phenomenon occurs where the junction rapidly switches between the OFF state and the ON state below -0.17 V. The alternating switching between these two branches is characterized by seemingly random and fast branch jumps, featuring rarely an intermediary current point between the two branches. At low temperature, the MID branch seems inaccessible such that only two distinct branches can be identified. Then, at higher temperatures, around 80 K, the noisy MID branch appears such that it becomes difficult to distinguish between the two types of noises, telegraphic or diffusive. In the next chapter, we will propose a physical mechanism that shines light onto the microscopic phenomena responsible for these branch jumps.

6.3.2 Diffusive noise

The diffusive low-amplitude noise around the MID branch in Figure 6.5(b) was also observed in other junctions. In Figure 6.6, we study these fluctuations in more details, in another state of the same junction. We plotted the $\mathrm{d}I/\mathrm{d}V$ curve of the junction in the P and AP cases and witnessed a localized zone ranging from -0.2 V to -0.15 V where the noise was particularly strong. Figures 6.6(b) and (c) then show a zoom of the IV and the $\mathrm{d}I/\mathrm{d}V$ on this specific voltage range. For this example, we can see that in the P state, this noise is

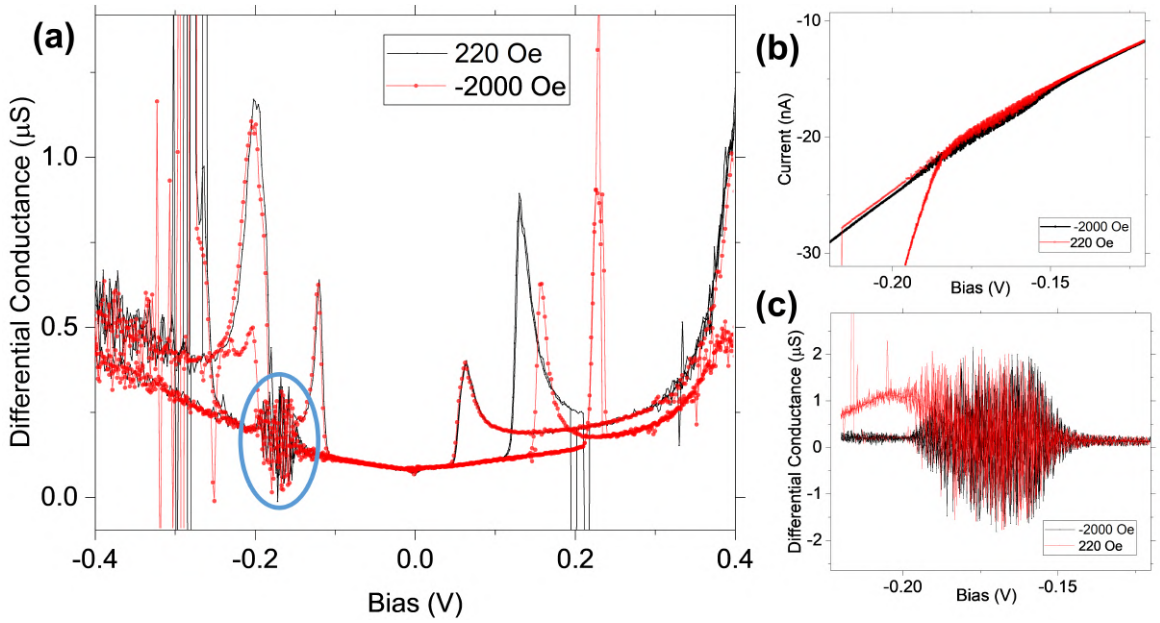

Figure 6.6: **Localized diffusive noise.** (a) $\mathrm{d}I/\mathrm{d}V$ plot of junction X in the P and AP states at 10 K showing a localized diffusive noise centered around -180 mV circled in blue. (b) Zoom of the corresponding IV characteristics around -180 mV. (c) Zoom on the $\mathrm{d}I/\mathrm{d}V$ spectrum in the same range.

correlated with a current branch merger, while in the AP case, only a single branch can be identified. It indicates that this noise may originate from interferences between at least two nanotransport paths such as around -0.17 V, the potential bias is such as the two paths enter in resonance, and generate these large localized fluctuations.

6.4 Other junctions

Apart from the rich junctions A and B presented above, we tested 147 more junctions, some of which displayed similar behaviors, with branch jumps and conductance peaks. In Figure 6.7, we present the IVs, $\mathrm{d}I/\mathrm{d}V$s along with the TMR of three different junctions to show the other types of behaviors one can expect from those junctions. In Figure 6.7(a), we see that junction F10 features a V-shaped conductance profile that leads to TMR that is maximal around 0 V, reaching up to 55%. This behavior is characteristic of transport through an impurity near the Fermi level [466] and corresponds to the Zero Bias Anomaly (ZBA) [129, 488, 489]. Then, the noise visible in the linear part of the conductance, above 50 mV and below 50 mV should indicate the presence of two or more states close in energy which would result in several interfering nanotransport paths. An asymmetry is also observed in this figure: at negative bias the conductance is higher than at positive bias, in particular in the AP state which suggests that a structural asymmetry renders the electrodes nonequivalent. The drop in the junction resistance with increasing bias voltage is greater for antiparallel alignment of the magnetic electrodes than for parallel alignment which has been accounted for by spin excitations localized at the interfaces between the electrodes and the tunnel barrier [129].

In Figure 6.7(b) junction B11 presents a $\mathrm{d}I/\mathrm{d}V$ curve with two very distinct and sharp conductance peaks at positive and negative voltages, which are completed by a smaller wide peak around 0.1 V. This line-shape is more similar to the results one should expect when probing a regular MgO tunnel junctions without impurities inside the barrier [225, 480, 209]. Finally, in Figure 6.7(c), junction B5 features a richer conductance spectrum with two very distinct sharp peaks that are present in two intensity branches. Just like for junction A, the branch switches correspond to discrete branch jumps that randomly occur within a specific bias voltage window. The writing of a state can be achieved by imposing a voltage

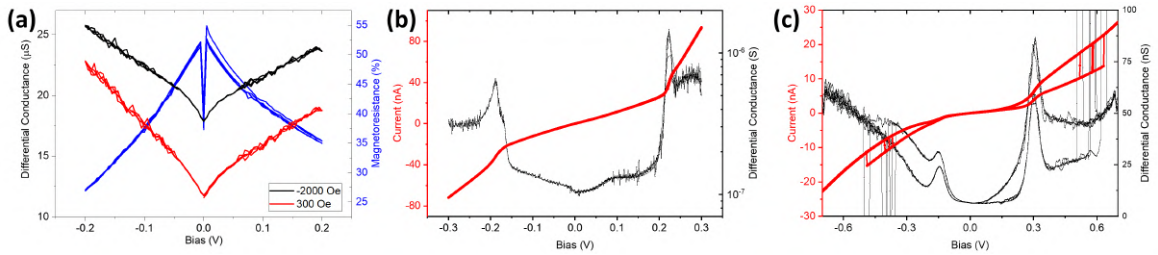

Figure 6.7: **Magnetotransport experiments on other junctions.** (a) Differential Conductance for the P (black) and AP (red) states and TMR (blue) plots at 10 K for junction F10. (b) and (c) Intensity-potential (black) and differential conductance (red) plots at 10 K and -2000 Oe for junctions B11 and B5 respectively.

exceeding the bias threshold for switching, and it can be reversed by applying a sufficient voltage with the opposite sign. Of the 149 devices which have been tested, four other junctions displayed memristive behaviors, similar to G10 and C5, containing branch jumps and conductance peaks which suggests the potential reproducibility of this phenomenon. Five other junctions also presented non-linear intensity-potential characteristics (see Figure 6.7(b)) translating into sharp conductance peaks, but without branch jumps, looking more like standard MgO junctions without Carbon inside, but with a lower magnetoresistance.

Chapter 7

Coulomb Blockade, Interferences and Magnetomemristance in oxide junctions

Research on model atomic and molecular junctions has strongly progressed in the last two decades thanks to atomic tip and lateral junction building techniques. These technological advancements have helped reveal intriguing transport mechanisms, such as Coulomb blockade inside single-atom transistors [490], Coulomb drag and co-tunneling effects in capacitively coupled quantum dots [491], Franck-Condon blockade within carbon nanotubes [492], spin-phonon coupling in single-molecule magnets [493], Kondo effect with spin-oriented molecules [494], memristance and hysteresis linked to resistive switching [81, 495] and strong current fluctuations caused by vibrational coupling and structural changes [173]. More recently, quantum phenomena involving internal coherence and superposition have been reported, such as phonon interference [496], quantum interference and decoherence [497].

If ferromagnetic electrodes are used to establish a fixed spin referential, then the resulting spintronic device can better exploit the electron spin to encode quantum information [251] or harvest thermal energy using discrete spin states [18, 19]. While molecules offer elegant means of inserting discrete electronic states within a device, molecular spintronic strategies are still far from industrial deployment [250, 251].

Finally, much research has focused on transposing robust state changes to a junction's spintronic response from more exotic barriers such as $SrTiO_3$ [75] to the most widely developed industrial spintronic platform: the FeCoB/MgO/FeCoB magnetic tunnel junction (MTJ), with applications ranging from next-generation memories [498] and neuromorphic computing [499] to agile microwave emitters and artificial energy harvesting [500].

In the previous Chapter, we described the experimental results obtained on MgO MTJs containing Carbon impurities and showed that some samples could be used as information storage devices. The study revealed a zoology of junction states depending on the temperature and the voltage bias and in particular, we observed two distinct types of localized noise

which suggest interferences between nanotransport paths.

In this Chapter, we investigate these results further in order to identify the underlying physical mechanisms and thus demonstrate several of the aforementioned quantum effects.

7.1 Memristance and Coulomb Blockade

In the previous Chapter, we observed that microscale MTJs with C atoms in the MgO barrier can exhibit noise and two/multi-level states of electrical transport (see Figures 6.1, 6.2 and 6.6) and presented evidence that the C-borne spin states can be electrically manipulated to encode information through a memristive effect. In this section, we present additional results on these states and propose physical explanations to the conductance peaks and current jumps.

7.1.1 Origin of the conductance peaks

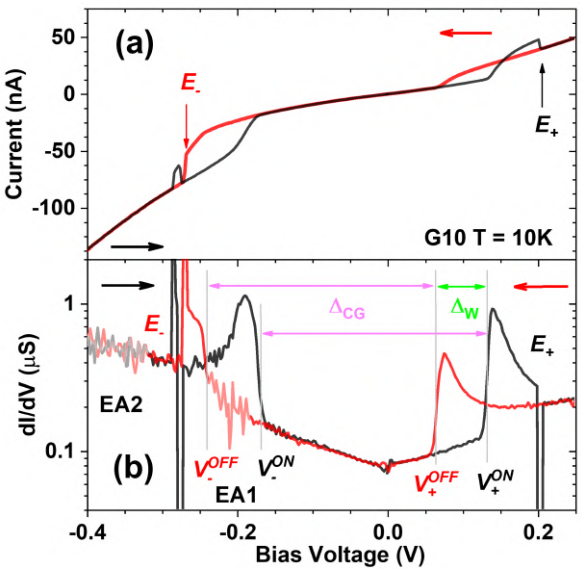

Figure 7.1: **Memristive Coulomb blockade at the atomic level.** (a) IV and (b) differential conductance $\mathrm{d}I/\mathrm{d}V$ data at $T = 10$ K on junction G10. The E_+ and E_- writing events cause a shift $\Delta_W = 73$ mV in the otherwise constant energy gap $\Delta_{CG} = 310$ mV between conductance peaks. Transport noise due to interference with an environmental atom are shown using semi-transparent data points.

Much like in Figure 6.1, the cyclical IV traces of junction G10 in Figure 7.1(a) show two current branches that are linked through events E_- and E_+. Between these two events, the ON branch is represented in black while the OFF branch is in red. In Figure 7.1(b) the corresponding set of differential conductance ($\mathrm{d}I/\mathrm{d}V$) is represented. We witness the presence of two conductance peaks at bias positions that depend on the direction of the voltage sweep. In the ON branch, they manifest around $V = V_+^{ON}$ and $V = V_-^{ON}$, and they are shifted by $\Delta_W \approx 70$ mV compared with the OFF branch. As discussed in Appendix C, the constant voltage gap $\Delta_{CG} = 300$ mV between the pair of conductance peaks can be tracked across several other states of the junction G10. Within this voltage gap, we observe an exponential increase in junction current. We therefore propose that these conductance peaks correspond to the edges of the Coulomb blockade regime across the MgO MTJ thanks to electronic states of C atoms in the

MgO barrier. We also propose that the shift in the energy position of the Coulomb gap be the result of charging on 'environmental' C atoms that do not participate in transport. This is supported in Figure 7.1(a) by the presence of noisy regions EA1 and EA2 (semi-transparent data points). Indeed, the spectral position and width of these regions do not correspond to Coulomb blockade peaks in the present dataset, but rather in other datasets acquired on the same junction but with different 'transport' and 'environmental' attributions of the C atoms. See Appendix C for details.

To obtain atomic insight into the nanojunction's nanotransport path, we use $\Delta_{CG} = 300$ mV as a lower bound for the Coulomb gap of the 'transport' quantum dot generated by the carbon atoms. Using an appropriate capacitance model, this allows us to estimate a 0.2 nm radius for the transport quantum dot (see Appendix D), *i.e.* approximately one monolayer of MgO. This large Coulomb gap thus indicates that transport is proceeding across the electronic states of an individual carbon atom. Furthermore, if the voltage shift $\Delta_W \approx 70$ mV between junction states corresponds to changing the environmental atom's charge by 1 electron, then we infer that it is positioned at twice the radius away from the 'transport' C atom (see Appendix D).

The nanotransport path thus consists of at least one C atom, which is capacitively coupled to a nearby 'environmental' C atom. Our survey of Coulomb blockade peaks (see Appendix C) suggests that several C atoms can be in the transport path, and that a given atom may switch between 'transport' and 'environmental' roles depending on the atomic-level configuration of the nanotransport at each junction cool-down.

Given the low electric field amplitude and the ionic nature of MgO, an explanation of events E_- and E_+ in terms of electromigration of oxygen vacancies is very unlikely [70]. Indeed, the ionic bonding of the MgO lattice makes it difficult for oxygen vacancies and other on-site defects to move within the crystal structure at room temperature and below [72]. Therefore, the observed resistive switching cannot be attributed to the migration of O^{2-} ions as this is frequently the case in other oxides such as NiO [69]. It is possible, however, that an electromigration scenario be more favorable if the oxygen vacancies are filled [72] as is the case here.

Nevertheless, analogous hysteretic behavior induced by conductance jumps have been reported in molecular junctions [175, 64, 74] and scanning tunneling microscopy experiments [86, 501, 502, 143] but we now have showed that this phenomenon can also be observed in standard oxide-based junctions. The abrupt switching between two conductance branches results from a charging mechanism similar to the effect reported by Wu *et al.* [86]. Their results corroborate very well with our description featuring at least one control 'environmental' atom, whose charge can be directly tuned by the voltage, which in return capacitively influences the energy landscape of the 'transport' atom, as a gate voltage would control the current flow in single-electron transistors. In chemical words, the oxidation or reduction of the trapped C atom acting as the control quantum dot changes the nanotransport path taken by the electrons, which translates into different intensity branches.

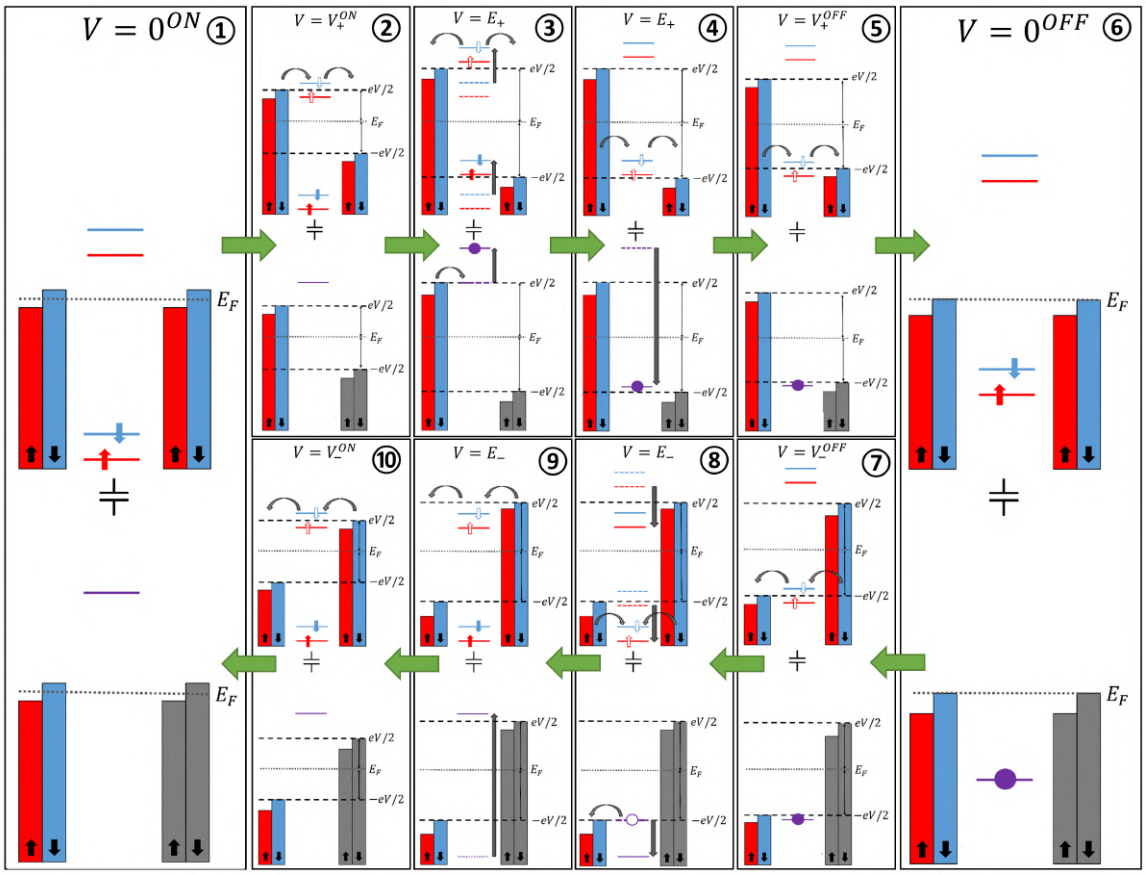

Figure 7.2: **Model of the memristive Coulomb blockade effect.** Model of a memristive Coulomb blockade involving at least one atom in the transport path, and at least one 'environmental' atom that is capacitively linked to the transport atom but does not participate directly in electronic transport across the junction. The various operations of the memristive cycle, showing how charging/discharging the environmental atom controls the energy levels of the transport atom, are shown.

7.1.2 Origin of the current jumps

We present in Figure 7.2 the schematic of a two-atom model that can explain this memristive Coulomb blockage behavior. We consider two quantum dots: the upper one is the 'transport' quantum dot (TQD) and is connected to both leads, while the lower one is 'environmental' or 'control' quantum dot (EQD) and is connected only to the left lead. Both quantum dots are capacitively coupled together.

Starting at $V = 0$ in the OFF branch, the lower lying levels of the TQD are filled, the upper lying are empty, and the single level of the EQD is empty (see Figure 7.2.①). By increasing the voltage, a first conductance peak is seen on the $\mathrm{d}I/\mathrm{d}V$ plot around $V = V_+^{ON}$ which corresponds to the upper edge of the Coulomb blockade region. The potential of the left lead is approaching the upper level of the TQD, allowing for the start of sequential tunneling (see Figure 7.2.②). By increasing the voltage to $V = E_+$, the potential of the left electrode aligns with the level of the EQD. A single electron can thus jump from the

electrode to this level, which has the effect of lifting up the levels of both QDs in a first round. The upper lying levels of the TQD are now above the potential, while the lower levels rise between the potential window offered by the electrodes (see Figure 7.2.③). During a second round, after equilibration, the electrons tunnel out of the TQD higher levels and sequential tunneling starts through the lower levels. The new dynamic filling of the energy levels of the TQD act capacitively in return on the EQD, which has the effect of lowering its level (see Figure 7.2.④). Therefore, this capacitive back action traps the electron that filled the EQD level, preventing it from jumping back into the electrode. A conductance jump from the ON branch to the OFF branch is thus observed in this case and we can see that the potential will have to decrease to negative values in order to remove this trapped electron and revert back to the ON state.

From this unstable state in Figure 7.2.③, the system can either go back to configuration ② if the reverse jump process happens, or it can switch to the next transport regime if the filling of the transport atom changes because of this capacitive interaction. Hence, there is a small bias window in which the system can eventually fluctuate between two states before it stabilizes when the electron/dot on the environmental atom gets trapped as a result of a favorable capacitive coupling. The intensity of the fluctuation is driven by the ratio between the hopping frequencies of the environmental dot by the transport dot. If the jump frequency of the tunneling processes on the TQD is much higher than that on the EQD, then the equilibration of the TQD will happen before any reverse jump can occur on the EQD, resulting in a single branch jump.

If the voltage is now decreased, another conductance peak is observed around $V = V_{+}^{OFF}$ which corresponds this time to the end of sequential tunneling through the lower lying level of the TQD (see Figure 7.2.⑤). Going back to $V = 0$, the Coulomb blockade region is recovered but the levels of the TQD are now arranged differently because of the presence of the electron in the EQD level (see Figure 7.2.⑥). When the bias is decreased to negative values, sequential tunneling can start again through the lower levels of the TQD around $V = V_{-}^{OFF}$ (see Figure 7.2.⑦). Approaching $V = E_{-}$, the potential of the left electrode now aligns again with the EQD level, allowing for the trapped electron to jump back into the lead. This change of charge borne by the EQD lowers the levels of QDs. Similarly, the upper levels are now located inside the potential window, while the lower levels are shifted below the potential of both electrodes, so they must be filled to reach equilibrium (see Figure 7.2.⑧). This triggers a second round of effects where sequential tunneling now goes through the upper lying levels, while the lower lying levels stay filled. This change of electronic environment of the TQD acts again capacitively on the EQD, lifting up the energy level (see Figure 7.2.⑨). The removal of the trapped electron thus triggers a branch jump from the OFF branch back to the ON branch. By increasing the potential, a final conductance peak is observed around $V = V_{-}^{ON}$ which corresponds to the end of sequential tunneling through the upper lying level of the TQD (see Figure 7.2.⑩). The cycle is completed at $V = 0$ where the junction has indeed returned to the ON branch (see Figure 7.2.①).

Close to $V = E_{-}$, we notice that several branch jumps between the ON and OFF branches can occur. This behavior is qualitatively expected by our schematics which can describe several jumps at this potential, resulting from multiple electron processes but the

precise mechanisms that trigger these transitions remain to be detailed. We infer that at this special bias, the position of the energy levels is such that cotunneling phenomena mediated by phonons can trigger an avalanche of electrons which will momentarily fill the energy levels of the TQD, thereby lowering the level of the EQD, which would allow for an electron to fill it by tunneling from the left lead. This would make a jump back to the OFF branch momentarily possible, leading back to the situation in Figure 7.2.⑨. The hysteretic nature of this phonon catalysis would allow for these multiple jumps only in the forward path but not during the reverse path. Indeed, according to polaron dynamics [88, 87], a population inversion between two phononic minima occurring around $V = E_-$ would change the interaction between the electrons and the phonons such that the phonons would favorably be in a higher potential well allowing for the reverse jump during the forward sweep, but they would be in the lower well during the reverse sweep, thus stabilizing the device in the OFF state. We point out that this hysteretic population change of the phonons could be linked to a structural rearrangement of the surroundings of the C atoms, notably in the angles of its bondings with the leads and the other species involved in transport [82, 143]. We also note that, depending on the position of the energy levels of the transport quantum dots relative to the environmental quantum dot, the events E_- or E_- may or may not occur around a conductance peak. A situation where the jump at E_+ occurs inside the Coulomb blockade region is presented in Figure 6.2(b). We described the situation of Figure 7.1(b), but we can easily convince ourselves that if we place the upper levels of the TQD below the empty level of the EQD in the ON state, the potential of the left electrodes would address the level of the EQD around $V = E_-$ before reaching the edge of the Coulomb blockade region.

7.2 Interference and noise

In the previous Chapter, we presented current and differential conductance data which presented strong localized noise around restricted temperature and voltage bias windows (see Figures 6.5 and 6.6). Two types of noises were identified: telegraphic and diffusive. In the previous section, we already detailed a transport mechanism that takes place during the branch jumps and thus relates to the telegraphic noise. In the present section, we give further details about the different kinds of noise we can observe in those junctions and give a more solid explanations of these fluctuations.

7.2.1 Experimental characterization of the noise

We present in Figure 7.3(a) the temperature dependence of the resistance R measured on junction G10 at $V = -170$ mV. As seen in Figure 7.1(c), the junction is bistable at 10 K at this bias. Upon cooling down from 140 K, the current broadens into two branches ON and OFF, with intermediate spectral weight of low intensity (MID branch). Further evidence of these regimes appears in Figure 6.5. Since temperature alone can promote a dominant transport branch, we conclude that electron-phonon interactions, *i.e.* vibrons, also be involved in the quantum interference transport here, in line with prior literature [158, 503, 88, 243].

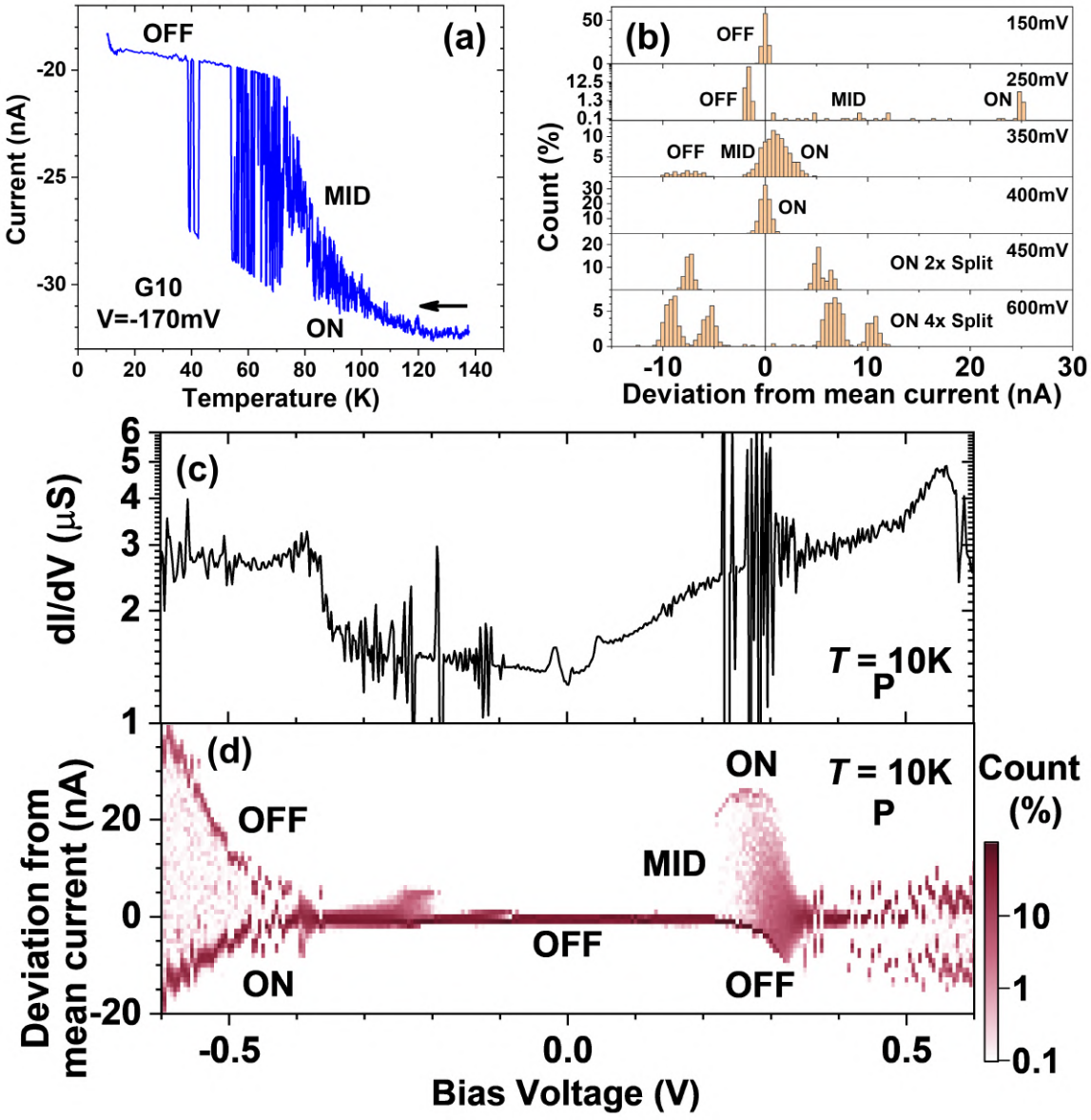

Figure 7.3: **Quantum transport interference between individual carbon atoms.** (a) Intensity as function of temperature at -2000 Oe and -170 mV. (c) Differential conductance of junction C5 at 10 K for the P magnetic state. (d) Color map of the statistic weight of the current deviation from the mean current as a function of applied bias of junction C5. The junction P magnetic state was used. At each bias value, 1000 current measurements were acquired. Datasets at select voltage values are shown in panel (b).

We use bias-dependent current statistics to observe transport branches due to quantum interference. We begin by plotting in Figure 7.3(b) differential conductance data in the P magnetic state of junction C5 at $T = 10$ K. On the log scale, we observe sizeable increases in conductance, and the clear appearance of noise for $V < -0.4$ V and for $V > 0.3$ V. Within $-0.6 < V$ (V) $< +0.6$, after setting the dc applied bias, we measured the current 1000 times. The statistics of a given current deviation from the mean current as a function of applied bias are plotted in panel (c). Within $|V| < 0.2$ V, the current remains essentially stable along the OFF branch. For $|V| > 0.2$ V, the transition to the MID state can appear. This is especially visible within $0.2 < V$ (V) < 0.4. While the OFF branch shifts to values below the mean, the MID branch collapses into the dominant branch around $V = 0.4$ V. A higher resolution map of this region is shown in Appendix A. For $V > 0.4$ V, this branch splits into two branches labeled ON and OFF. A similar branching is seen for $V < -0.4$ V. Erratically, each of these two branches can split into two subbranches, for a total of four branches (see Figure 7.3(d)). The noise in conductance thus arises from transport interference between these branches which are visualized by our current statistics.

7.2.2 Origin of the interferences

Overall, these experimental findings support a picture of vibron-mediated co-tunnelling and/or Coulomb drag between nanotransport paths [491] due to blockade effects such as Franck-Condon blockade [158]. According to the theory of out-of-equilibrium polaron dynamics [88, 87], transport through an impurity with discrete energy levels such as a quantum dot or a molecular orbital which is strongly coupled to a vibrational degree of freedom and tunnel coupled to two leads explains the observed multi-stability of different states and the telegraphic switching between the different intensity branches. The voltage acts as an effective temperature and a force modulating the potential of the oscillator. Around specific voltage biases, the effective vibron energy potential landscape develops several minima, and thus promotes metastability between different occupation states. Two scenario are possible: either thermally activated switching between different intensity branches related to each of the well separated potential minima can occur [495], or large fluctuations around a single intensity branch occur when at least two minima are close enough so that the quasi-degenerate states they encode trigger an interference effect [504, 174]. In this latter case, intermediate states outside the well minima are measured.

7.3 Magnetoresistance and Spintronic signatures

The memristive behavior of the Coulomb blockade peak due to environmental charging represents one level of information encoding. Repeated testing indicates a write success rate of at least 84% (see Section 6.1.2). The MTJ's two ferromagnetic leads enable us to examine how the spin polarization of the charge current impacts the atom-level memristive Coulomb blockade effect and quantum interference effects. To experimentally obtain spintronic contrast in our data, we examine the impact on transport of switching the orientation of electrode magnetization from parallel (P) to antiparallel (AP).

7.3.1 Results on magnetoresistance

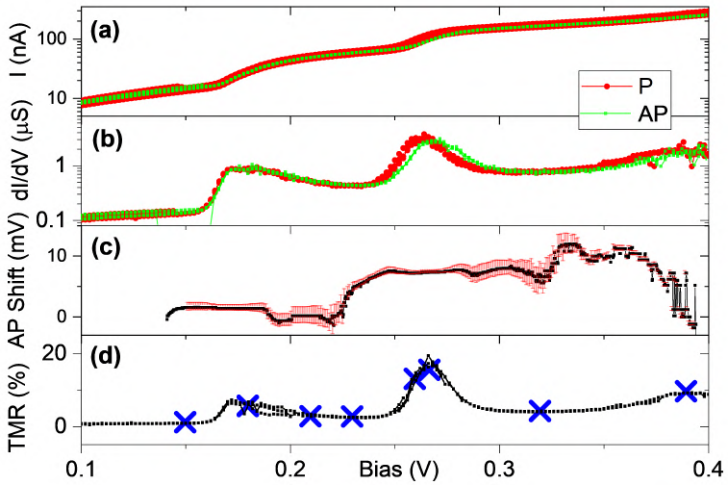

Figure 7.4: **Spintronic impact of Coulomb blockade along transport branches**. (a) Current-voltage characteristic for the P (red) and AP (green) junction states, and (b) the resulting $\mathrm{d}I/\mathrm{d}V$ differential conductance. (c) Voltage shift between the P and AP conductance data. (d) Bias dependence of the TMR calculated from (a). Blue crosses indicate TMR amplitudes obtained from $I(H)$ experiments as in Figure 6.1(c).

We plot in Figure 7.4(a) the IV in the MTJ's P and AP states at $T = 10$ K. Both exhibit a series of plateaus and increases that are absent in junctions without C atoms [225, 480, 209]. The corresponding differential conductance ($\mathrm{d}I/\mathrm{d}V$) data (see panel (b)) reveals a series of peaks. While the P and AP datasets share similar traits, the AP plot appears to shift to higher bias as the onset of each conductance increase is reached. This is confirmed through an analysis of the correlated shift between the two datasets in Figure 7.4(c). The voltage shift is calculated by doing a curve fitting of AP data over P data using a rolling window of 40 mV width. The fit and estimation of uncertainties are realized with the help of python module LMFIT [1] (Non-Linear Least-Squares Minimization and Curve-Fitting). The calculated voltage shift is then defined as the voltage shift of the mean bias value of the rolling window.

In our MgO MTJs without C [225], we observe TMR ≈ 200 % at 10 K around $V = 0$, and a mostly monotonous TMR decreasing with increasing $|V|$. When C atoms are introduced into MgO, we observe only a few % TMR around $V = 0$. Instead, due to the shift in AP conductance to higher bias with each succeeding conductance peak, the TMR bias dependence closely mimics the junction conductance (compare panels (c) and (d) of Figure 7.4). This highly structured TMR bias dependence is confirmed through discrete $I(H)$ datasets at fixed V (crosses in Figure 7.4(d)). We observe local TMR maxima precisely on the conductance peaks, with an absolute maximum of 15%.

To discuss the impact on spintronics of the memristive Coulomb blockade effect, we presented $I(H)$ data in Figure 6.1(c) in both the ON and off state of the junction, taken at $V = -50$ mV; *i.e.* precisely at the bias value corresponding to the memristive Coulomb blockade peak shown in panels (a-c) of Figure 6.2. We observe that I_P increases and that I_P-I_{AP} is multiplied by 7, so that the TMR increases from 0.5% in the OFF state to 3.7% in the

[1] https://lmfit.github.io/lmfit-py/

ON state due to the Coulomb blockade peak. Within the paradigm of MgO tunneling spintronics[505], this suggests that the Coulomb blockade peak effectively opens an additional transport channel with dominant majority spin carriers.

7.3.2 Origin of the voltage shift and the tunnel magnetoresistance

According to the theoretical work of Płomińska and Weymann [144], the similar set of bias-dependent conductance peaks in the MTJ's P and AP states, leading to a similar TMR trace, is the signature of a special kind of Coulomb blockade effect named Pauli Spin blockade [191, 506, 193]. As the electronic level of the carbon transport atom is reached with applied bias, sequential tunneling is suppressed while co-tunnelling mechanisms become dominant and modify the spin state (and eventually the charge [18]) of the paramagnetic C atom, as a form of spintronic anisotropy [507, 468, 187]. With increasing voltage, the FeCoB/MgO tunnelling-induced accumulation of mostly spin up carriers lifts degeneracy of the spin states. This effectively lowers the spin up state relative to the spin down state. This spin splitting differs between the MTJ's P and AP states due to different energy alignments of the C electronic levels [144, 18]. This effect is also modeled by our schematic in Figure 7.2 which features this spin splitting. Indeed, we witness that in the P state of the the electrodes presented in this Figure, the potential of the electrodes will align with the split spin energy levels of the transport quantum dot at lower absolute bias than in the AP state, which would result in a voltage shift between the onsets of the conductance peaks leading to a positive TMR. Appendice B provides additional evidence of this effect.

The conductance shift of Figure 7.4(c) is thus an experimental manifestation of spin accumulation. Spin accumulation also explains the shift in quantum interference data and the spin polarization of the transport branch therein (see Appendix B). It also explains why the TMR bias dependence tracks that of junction conductance (see Figure 7.4(d)), as well as the huge increase in I_P-I_{AP} due to the memristive Coulomb peak (see Figure 7.1(g)) leading to the seven-fold TMR enhancement. The best agreement between the results of Płomińska and Weymann [144] and our experimental datasets is that of 'parallel' or 'T-shaped' electronic transport across spin states, rather than the other series scenario proposed. This supports the atomic description of the effective nanotransport path across our microscale MTJs.

7.4 Discussion

To conclude, inserting C atoms into ultrathin MgO layers generates localized paramagnetic [18] states. Experiments on micronic FeCoB/MgO/FeCoB magnetic tunnel junctions, which are crafted using straightforward technological processes, show that the effective nanotransport path [480] involves individual C atoms. Their discrete energy levels promote Coulomb blockade effects that can be reproducibly shifted in energy by charging events on neighboring C atoms. The tunnel coupling between these transport and environmental carbon atoms promotes quantum interference effects. Spin-polarized transport induces spin accumulation that lifts the spin degeneracy of the unpaired C electron in MgO.

This leads to a voltage shift in Coulomb peaks and quantum interference effects between the datasets in the MTJ's P and AP magnetic states. Spin accumulation also accounts for the huge enhancement of the spintronic performance when a Coulomb peak is memristive controlled. We thus demonstrate how to use both the electron charge and spin to encode information on an individual paramagnetic atom in a solid-state, industrializable device. These results showcase MgO tunneling spintronics as a promising industrial platform for quantum technologies at potentially practical temperatures, to deploy quantum transport effects that are normally only seen in model junctions. One track to achieve these effects at room temperature will be to engineer the impedances that electronically link the transport and environmental atoms to the magnetic tunnel junction electrodes. Final applications of quantum spintronics not only encompass information encoding [251], but also energy harvesting [18, 19] vectors.

Part III

Theoretical Part

Chapter 8

The Quantum Model

In Chapter 2, we presented the emerging field of quantum thermodynamics [508], specifically of quantum energetics [319], with a focus on quantum thermal machines [10] in the hope of finding new ways of producing energy. Among the various kinds of quantum engines based on on Maxwell's demon [406, 407], a cycle between different baths [413, 354, 433] or an external drive [509, 440, 441], we put a particular emphasis on systems that specifically rely on quantum features such as coherence [13, 12, 439, 442] and coherence [463, 456, 461] in order to extract energy from the environment using the singular properties of quantum superposition and quantum measurements. These new kinds of quantum engines which have been demonstrated experimentally [18, 19, 434, 458, 343] redefine the notion of temperature when examining engine efficiencies against the Carnot limit [358, 510, 354, 356], notably when harvesting energy from a single heat bath [351, 459].

Quantum measurements constitute a critical process that could lead to active devices that use coherence as a fuel [14, 303]. Indeed, the resulting projection that such a measurement performs on a quantum state involves an irreversible energy exchange between the state and the environment [319] that can be viewed as a form of quantum heat [15]. The information obtained from the measurement can either be used by a Maxwell demon [15, 456] that can extract energy by applying some unitary transformation to the working substance (WS), or the measurement back-action itself can result in an energy increase that can be harvested into useful work [459].

In these engine models, the proposed cycle is not autonomous and can be difficult to implement experimentally [461, 12, 439, 358], while the practical cost of turning on/off interactions within the system [461] or between the WS and the baths [511, 413, 356, 433, 358, 354] is ignored. In this Chapter, we model a quantum electronic engine that mostly lifts these limitations. The engine is powered by quantum measurements that release the correlation energy stored within the WS, and identifies the influence of the vacuum as it favors the emergence of a current in a system featuring no direct tunneling link between the two leads and connected to an environment with no out-of-equilibrium properties. Strikingly, we also show that it gives a coherent quantum description of the spintronic engine presented in Chapter 4 as it yields a power output comparable to the experimental results if a bosonic bath is included along with an out-of-equilibrium hypothesis.

8.1 The Quantum Measurement Spintronic Engine

We build upon the initial formalism [191, 141, 469] used to phenomenologically model magnetotransport across the spintronic device under the assumption of effective work [18]. This Chapter is a first step towards removing this assumption and describing this class of spintronic devices within a broader quantum thermodynamical framework. We pedagogically describe the several concepts and interactions for our solid-state spintronic engine hereafter, while calculations are shown in the Appendices.

The quantum spintronic engine's WS is composed of two spin-split atomic quantum dots (QDs) that exhibit a tunnel coupling γ, a magnetic exchange interaction J, and coulombic repulsion U to prevent excessive charging. This open system is connected in series with two ferromagnetic, fully spin-polarized leads. Since the engine is a solid-state device, electronic interactions are inherently always-on and time-independent, such that the engine cycle is only driven by periodic quantum measurements through two strokes: an instantaneous measurement stroke that partially projects the QD system (i.e. WS), followed by a thermalizing stroke of duration τ during which the WS relaxes towards the steady-state.

8.1.1 Hamiltonian

General Hamiltonian

In this Chapter, we consider two QDs. Each QD, or atomic dot, consists in two non-degenerate electronic energy levels that code for two opposite spins on the Bloch sphere. The two QDs are coupled with one another by a tunneling interaction of magnitude γ and a magnetic exchange interaction of magnitude J. A Coulombic repulsion term U is also considered so as to prevent excessive charging on each dot. The environment is composed of two ferromagnetic leads, the left one L and the right one R, each of them respectively coupled to the left and right QDs. From these elements, the total Hamiltonian H can be separated as:

$$\boxed{H = H_S + H_E + H_{SE}.} \tag{8.1}$$

The first term H_S, called the Hamiltonian of the system, represents the two spin qubits and can be written as:

$$\begin{aligned} H_S = \epsilon_{L\uparrow} n_{L\uparrow} + \epsilon_{L\downarrow} n_{L\downarrow} + \epsilon_{R\uparrow} n_{R\uparrow} + \epsilon_{R\downarrow} n_{R\downarrow} + (\gamma c^\dagger_{L\uparrow} c_{R\uparrow} + \gamma^* c_{L\uparrow} c^\dagger_{R\uparrow} + \gamma c^\dagger_{L\downarrow} c_{R\downarrow} + \gamma^* c_{L\downarrow} c^\dagger_{R\downarrow}) \\ -U((1-n_{L\uparrow})n_{L\downarrow}+n_{L\uparrow}(1-n_{L\downarrow}))-U((1-n_{R\uparrow})n_{R\downarrow}+n_{R\uparrow}(1-n_{R\downarrow}))-J(n_{L\uparrow}n_{R\uparrow}+n_{L\downarrow}n_{R\downarrow}). \end{aligned} \tag{8.2}$$

Where we have defined $c^\dagger$ and c the raising and lowering operators with the left index identifying the left or right quantum dot and the right index identifying the spin. The n correspond to the number operators defined as $n = c^\dagger c$. Let us explain the physical meaning of those terms. The first terms in ϵ correspond to the bare energy of each of the four electrons that can occupy the two quantum dots. We assume that the energies ϵ are different for each level and we will see below that their relative values can be tuned through

the couplings.
The terms in γ code for the hopping electron transmission between the QDs. The spin is preserved during this transfer as no spin flip is possible during the hopping to leading order. The electron hopping argument γ is taken as independent of the tunneling spin for simplicity. Although this tunneling argument should strongly depend on the considered spin channel given the spin-splitting of the energy level, this assumption is not critical here given the approximations we make later.
The terms in J represent the magnetic coupling between the two quantum dots. Since prior literature indicates antiferromagnetic coupling and spontaneous current flow at $V = 0$ [18, 19], we therefore assume that $J < 0$. As we can see, this contribution adds an energy penalty of $-J$ when an electron of the same spin is present on both QDs. This repulsion term J is considered independent of the spin orientation for simplicity, and we will see in the following that this approximation holds given the weak relevance of J in the next results.
Finally, the terms in U correspond to the Coulombic repulsion which lowers the energy when a quantum dot is singly occupied. The term has been included to avoid excessive charge being retained on the system. We assume that this Coulomb repulsion energy is identical on the two sites.

This Hamiltonian can be simplified by rescaling the energies. Redefining $\epsilon \equiv \epsilon - U$ and $U \equiv U/2$, we get:

$$H_S = \epsilon_{L\uparrow} n_{L\uparrow} + \epsilon_{L\downarrow} n_{L\downarrow} + \epsilon_{R\uparrow} n_{R\uparrow} + \epsilon_{R\downarrow} n_{R\downarrow} + (\gamma c^\dagger_{L\uparrow} c_{R\uparrow} + \gamma^* c_{L\uparrow} c^\dagger_{R\uparrow} + \gamma c^\dagger_{L\downarrow} c_{R\downarrow} + \gamma^* c_{L\downarrow} c^\dagger_{R\downarrow}) - J(n_{L\uparrow} n_{R\uparrow} + n_{L\downarrow} n_{R\downarrow}) + U(n_{L\uparrow} n_{L\downarrow} + n_{R\uparrow} n_{R\downarrow}) \quad (8.3)$$

The second contribution to the Hamiltonian describes the energy of the ferromagnetic reservoirs, *i.e.* the environment of the QDs. It can be split into two terms $H_E = H_L + H_R$ describing each electrode:

$$H_L = \sum_{k\sigma} \epsilon_{k\sigma}\, c^\dagger_{k\sigma} c_{k\sigma},\ H_R = \sum_{p\sigma} \epsilon_{p\sigma}\, c^\dagger_{p\sigma} c_{p\sigma}\ , \quad (8.4)$$

where the index σ accounts for the spin degrees of freedom while the indexes k and p are used for the left (L) and right (R) leads respectively, such that $\epsilon_{k,\sigma}$ and $\epsilon_{p,\sigma}$ are the energies of each fermionic mode of the field while $c^\dagger_{k,\sigma}$, $c^\dagger_{p,\sigma}$, $c_{k,\sigma}$ and $c_{p,\sigma}$ are the creation and annihilation operators. Only a single band is considered on each lead. This hypothesis is in line with a description of dominant transmission from a specific wavefunction in most tunneling spintronic devices [512]. It is especially valid given prior experiments [18, 19] on the quantum spintronic engine that utilize the ferromagnetic metal/molecule interface (*i.e.* the spinterface [257, 256]) to generate electrodes with a spectrally narrow band of conduction states with full spin-polarization.

The final term H_{SE} describes the tunneling interaction between the system (*i.e.* the QDs) and the environment (*i.e.* the leads). This term can also be split into two parts $H_{SE} = H_{SL} + H_{SR}$. For each lead, we consider two contributions. The first contribution describes the exchange of electrons between the lead and the system, more precisely the adjacent QD

since we initially considered a series geometry. This allows for a current to emerge in the model. The second contribution describes the magnetic pinning exerted by the lead on the nearby site to model the effective magnetic field generated by spintronic anisotropy [18, 19, 466]. Following these assumptions, we get:

$$\begin{aligned} H_{SL} &= \sum_{k\sigma}(\gamma_{k\sigma}\, c^{\dagger}_{L\sigma}c_{k\sigma} + \gamma^{*}_{k\sigma}\, c_{L\sigma}c^{\dagger}_{k\sigma}) + \sum_{k\sigma} J_{k\sigma}\, n_{L\sigma}n_{k\sigma}, \\ H_{SR} &= \sum_{p\sigma}(\gamma_{p\sigma}\, c^{\dagger}_{R\sigma}c_{p\sigma} + \gamma^{*}_{p\sigma}\, c_{R\sigma}c^{\dagger}_{p\sigma}) + \sum_{p\sigma} J_{p\sigma}\, n_{R\sigma}n_{p\sigma}\ . \end{aligned} \tag{8.5}$$

The coefficients γ represent the hopping coefficients between the QDs and the electrodes, while the J represent the magnetic coupling. Note that our Hamiltonian does not describe an external bias voltage applied across the device: we are considering the case of spontaneous current flow.

Primary approximations

The Hamiltonian we are considering is too complex to be tackled as such analytically. We therefore physically justify the three following approximations.

First, the spinterface present in experimental devices generates conduction electrons of only one spin that, furthermore, are fixed on the Bloch sphere due to the remanent magnetization of the ferromagnetic electrode underscoring this interfacial effect [19]. Furthermore, experiments indicate better current output when the device's electrode magnetizations are oriented anti-parallel. As a result, assuming identical L & R interfaces, we will consider only spin $\uparrow$ electrons in the left lead and spin $\downarrow$ electrons in the right lead. This consideration leads to an approximation of the electrodes and the tunnel Hamiltonians such that:

$$\boxed{H_L = \sum_k \epsilon_k\, c^{\dagger}_k c_k,\ H_R = \sum_p \epsilon_p\, c^{\dagger}_p c_p,} \tag{8.6}$$

and

$$\begin{aligned} H_{SL} &= \sum_k(\gamma_k\, c^{\dagger}_{L\uparrow}c_k + \gamma^{*}_k\, c_{L\uparrow}c^{\dagger}_k) + \sum_k J_k\, n_{L\uparrow}n_k, \\ H_{SR} &= \sum_p(\gamma_p\, c^{\dagger}_{R\downarrow}c_p + \gamma^{*}_p\, c_{R\downarrow}c^{\dagger}_p) + \sum_p J_p\, n_{R\downarrow}n_p. \end{aligned} \tag{8.7}$$

It should be pointed out that $c^{\dagger}_k$ creates an excitation with spin $\uparrow$ and momentum k in the left lead, while $c^{\dagger}_p$ creates an excitation of spin $\downarrow$ and momentum p in the right lead.

Our second assumption is that the effective magnetic field generated through spintronic anisotropy by the fully spin-polarized transport from a lead onto the adjacent QD is constant. This holds at constant bias voltage [18], consistently with the absence of an applied bias in our model. This is also reasonable to first order during engine operation given the much lower formation energy of the ferromagnetic state relative to the engine energies, owing in part to a much larger size compared to that of the atomic dots. We therefore rely on a mean field approach which allows to approximate the magnetic couplings as:

$$\begin{aligned} \sum_k J_k n_k &= \left\langle \sum_k J_k n_k \right\rangle \equiv J_L, \\ \sum_p J_p n_p &= \left\langle \sum_p J_p n_p \right\rangle \equiv J_R. \end{aligned} \tag{8.8}$$

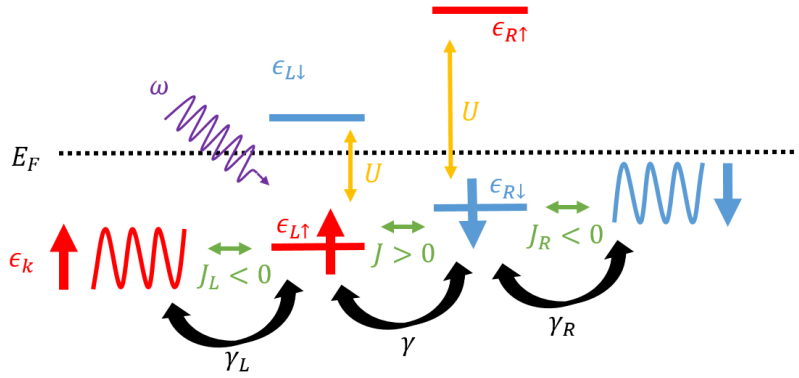

Figure 8.1: **Energy levels and Interactions in the Quantum Model.** Illustration of the model quantum spintronic engine, featuring two quantum dots trapped in series between two ferromagnetic leads in an antiparallel configuration with fully spin-polarized interactions. Blue/red levels represent spin ↓/↑ energy levels. Green double arrows represent the magnetic couplings; yellow double arrows, capacitive couplings and black arrows, tunnel couplings.

This approximation allows us to omit the magnetic coupling term in the system-lead interaction and add it to the system Hamiltonian without changing its structure by rescaling the QDs' energy level. Redefining $\epsilon_{L\uparrow} \equiv \epsilon_{L\uparrow} + J_L$ and $\epsilon_{R\downarrow} \equiv \epsilon_{R\downarrow} + J_R$, the system Hamiltonian remains unchanged and the tunnel Hamiltonian now reads:

$$\boxed{\begin{aligned} H_{SL} &= \textstyle\sum_k (\gamma_k\, c^\dagger_{L\uparrow} c_k + \gamma^*_k\, c_{L\uparrow} c^\dagger_k), \\ H_{SR} &= \textstyle\sum_p (\gamma_p\, c^\dagger_{R\downarrow} c_p + \gamma^*_p\, c_{R\downarrow} c^\dagger_p). \end{aligned}} \tag{8.9}$$

Finally, the quantum spintronic engine concept as proposed [18, 19] includes an asymmetry in the tunneling coefficients γ_L and γ_R. This not only helps to further break detailed balance of transport, but also enables one electrode to set a dominant spin referential on the QDs. As a result, the QD that is adjacent to that electrode will experience a larger spin splitting than the other QD. Therefore, we assume that the right QD is positioned such as $\epsilon_{R\uparrow} \gg \epsilon_{R\downarrow}, \epsilon_{L\uparrow}, \epsilon_{L\downarrow}$. Placing this energy level farther above the other ones allows us to discard all the states where a spin ↑ occupies the right QD, thereby reducing the dimensionality of the system Hamiltonian from 16 down to 8:

$$\boxed{H_S = \epsilon_\uparrow n_\uparrow + \epsilon_\downarrow n_\downarrow + \epsilon_R n_R + \gamma\, c^\dagger_\downarrow c_R + \gamma^*\, c_\downarrow c^\dagger_R + J\, n_\downarrow n_R + U\, n_\uparrow n_\downarrow\,,} \tag{8.10}$$

where we have redefined $\epsilon_\uparrow \equiv \epsilon_{L\uparrow}$, $\epsilon_\downarrow \equiv \epsilon_{L\downarrow}$ and $\epsilon_R \equiv \epsilon_{R\downarrow}$ for simplicity, now that the ambiguity between the spin and the L/R QD has been lifted. This approximation is therefore leaving only one transport channel, which justifies the previously stated independence of γ on the spin.

Bosonic bath

The previous Hamiltonian does not feature a direct tunnel interaction between the two leads such as a current can only result from multiple electron processes through the vac-

uum. This connection is absent because the model does not take into account any spin-flip mechanism that would allow the jump of electrons between the lower spin ↑ level and the higher spin ↓ level on the left QD. The idea is now to consider an interaction which would facilitate this spin flip, thereby allowing current to flow more easily through the dots. The intuition tells us that some bosons may therefore be good candidates which could allow for such catalysis. Indeed, photons, phonons, vibrons or magnons may bring sufficient energy to flip a spin. This could be possible at room temperature with phonons since the energy difference between the two spin energy levels may be of the order of $\delta \equiv \epsilon_\downarrow - \epsilon_\uparrow \approx 1 - 10$ meV $\approx 10^2$ K [18, 19].

Let us then add two terms to the Hamiltonian. The Hamiltonian of the bosonic bath

$$\boxed{H_B = \sum_q \omega_q a_q^\dagger a_q \,,} \tag{8.11}$$

where ω_q is the energy of the mode q and $a_q^\dagger$ and a_q are the bosonic laddering operators. And the Hamiltonian of coupling of the system to this bosonic bath

$$\boxed{H_{SB} = \sum_q \lambda_q c_\uparrow^\dagger c_\downarrow (a_q + a_q^\dagger) + h.c. \,,} \tag{8.12}$$

where λ_q, represent the spin-boson couplings. We expect the distribution λ to be sharply peaked as only specific modes of the boson field will have the required energy to flip a spin. In the analytical part of this chapter, we will first discard the effect of this bath, which we will turn on in the simulations.

8.1.2 Master Equation

In Appendix E, we use the Born approximation in the weak coupling regime to establish the master equation describing the evolution of this open quantum system:

$$\boxed{\begin{aligned}\frac{\mathrm{d}\rho}{\mathrm{d}t} = -i[H_S, \rho] + \mathcal{T}_L^- \mathcal{D}[c_\uparrow^\dagger](\rho) + \mathcal{T}_L^+ \mathcal{D}[c_\uparrow](\rho) + \mathcal{T}_R^- \mathcal{D}[c_R^\dagger](\rho) + \mathcal{T}_R^+ \mathcal{D}[c_R](\rho) \\ + \Lambda^- \mathcal{D}[c_\downarrow^\dagger c_\uparrow](\rho) + \Lambda^+ \mathcal{D}[c_\uparrow^\dagger c_\downarrow](\rho),\end{aligned}} \tag{8.13}$$

where $\rho = \mathrm{Tr}_E\, \rho_{SE}$ is the QD system's reduced part of the full density matrix ρ_{SE} w.r.t. the environment degrees of freedom, $\mathcal{T}_L^-$ and $\mathcal{T}_R^-$ represent the electron hopping intensity between the QD and the left/right lead respectively, while $\mathcal{T}_L^+$ and $\mathcal{T}_R^+$ are the hole counterparts; and with the superoperator $\mathcal{D}[c](\rho) \equiv c\rho c^\dagger - \frac{1}{2}\{c^\dagger c, \rho\}$. We emphasize that the temperature of the baths is implicitly accounted in these coefficients and that we do not separately introduce any thermal bias between the reservoirs. The last two terms represent the coupling to the bosonic bath that will be turned on later in Section 8.2.5: Λ^+ and Λ^- code for the pump and relaxation of the bosons, respectively. In what immediately follows, no explicit spin-flip mechanism is present. In Appendix E, we give expressions for these coupling constants to the baths as a function of filling of the energy levels of the baths and the couplings γ_k, γ_p and λ_q. The magnitude of these coefficients thus depends on the thermodynamical parameters of the baths: temperature, chemical potential... In the following,

we will study the influence of these couplings on the engine and show that energy can be generated even when the baths are at thermodynamical equilibrium and that the power output can be greatly enhanced when a minimal non-equilibrium resource is considered.

8.1.3 Engine's Cycle

Phenomenological description and motivation

The theory of quantum mechanics involves two very distinct processes. A system first evolves through a continuous, linear, reversible, deterministic process described by the Schrödinger equation, and then is projected onto a definite state through the discrete, non-linear, irreversible and stochastic process of quantum measurements. Considering that our QD system is subject to probing of its quantum state by the environment such as its evolution first follows the master equation described above, and then a projection due to the measurement is very natural. This assumption is backed by several physical arguments.

Thermal, quantum and shot noise in these magnetic junctions under quasi-equilibrium conditions has been a matter of study [513, 514, 515] and suggests that the quantum measurements could be linked to discrete charge fluctuations in the vicinity of the QD system. Further evidences showing nonlinear chaotic oscillations [516, 517] in these devices along with rectification and feedback properties [518, 519, 520] are also supporting the possibility of self-sustained oscillations in similar resonant tunneling quantum well structures which could trigger these measurements. And finally, a key element of our quantum spintronic engine is the ferromagnetic metal/molecule interface. This so-called spinterface exhibits a low density of spatiospectrally confined states with high spin polarization (89% [19]) at the Fermi level [257, 256, 18, 19]. The proposal that a Maxwell demon can operate electronically at the molecular level [405], along with recent thermodynamic theory on quantum measurements [521, 453, 334], indicate that the spinterface could [19] act as an autonomous quantum measurement apparatus by performing frequent projective measurements on the nearby QD's spin state, thereby collapsing the WS's quantum state [331, 318, 332]. The ability of the ferromagnetic electrode to maintain a constant spin polarization, allowing it to behave as an entropy sink [19] also support the possibility of these measurements. Indeed, information erasure would require a much lower entropy cost than the Landauer bound by involving the transfer of spin angular momentum into a large spin reservoir, rather than energy [399, 363, 361].

Following related studies that all postulate an external non-thermal quantum resource [351, 456, 461, 15, 459], and in line with the current conception of quantum mechanics that treat the measurement as a black box, we thus assume that the spinterface can perform these quantum measurements with an energy cost which we assume come from an external source that is part of the device. Hence, we suppose that our device is endowed with a built-in quantum clock that interacts periodically with the system.

Using our Hamiltonian, we consider a two-phased engine cycle (see Figure 8.2). The first 'thermalizing' stroke places the QDs into equilibrium with the electrode baths. The relaxation of the QD systems during this time-dependent evolution transfers energy from the

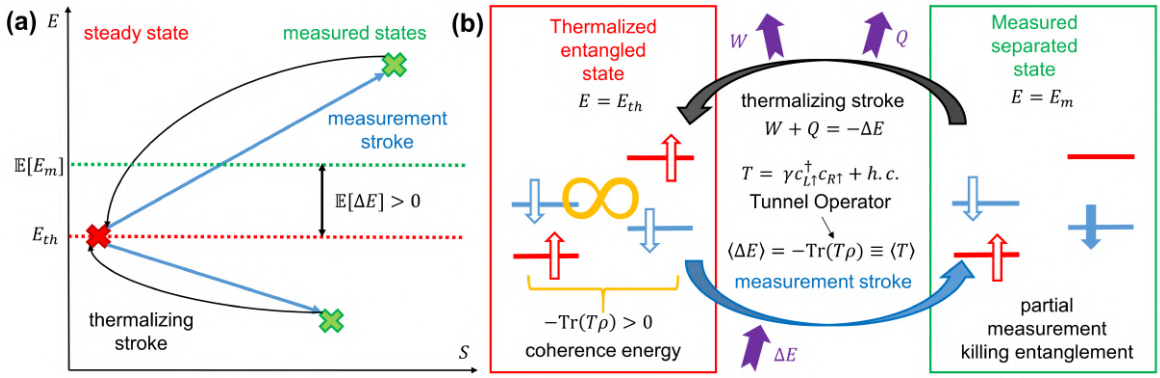

Figure 8.2: **Illustration of the Engine's Cycle.** (a) Energy-entropy illustration of the engine cycle. The unselective measurement stroke (straight blue arrows) instantly projects the thermalized steady-state (red) onto several possible separated states (green) with higher entropy and potentially higher energy. The thermalizing strokes (curved black arrows) reset the system to the steady-state while allowing for work extraction on average. (b) Illustration of the population of the energy levels during the two phases of the cycle. In the thermalized state, coherence energy is stored in the system; then the measurement stroke projects the right QD, destroying the superposition. The excessive energy of this localized ground state is then dissipated into the baths during the thermalizing stroke which restores coherence. In a solid-state implementation [18, 19], these strokes reflect the inherent electronic interactions between a pair of exchange-coupled paramagnetic atoms, and with fully-spin polarized leads such as the ferromagnet/molecule interface [257].

system to the baths, some of which is harvested to produce useful electrical work. Then, once the system reaches its steady-state, in which the two spin QDs are quantum correlated, the 'measurement' stroke on a single QD splits the WS into two separated subsystems, thereby destroying coherence. As we shall show, this projective partial unselective measurement acting on a superposed mixed state with indefinite energy is mathematically described by a quantum channel that leads to a projected system with a higher average energy than the previous steady-state. The measurement is thus projecting the system from a global low-energy ground state to a local high-energy ground state. The energy difference that results from this back-action [456, 407, 459] of the measurement is then dissipated into the baths during the next 'thermalizing' stroke. We shall show that it can be used to produce electrical work.

Analysis of the cycle

Let us initialize our engine at $t_0 = 0$ in a state $\rho(0)$. After completing the first thermalization process, the electrode performs a partial projective measurement of the entangled QDs at time $t_1 \equiv \tau$, which represents the duration of one cycle. This measurement projects the system from the steady state $\rho(\tau^-) \equiv \overline{\rho}$, which may only partially thermalized, to a projected state $\rho(\tau^+)$ that depends on the measurement outcome. Assuming that the right electrode operates frequent unselective measurements of the occupation of the right QD at

times $t = t_n \equiv n\tau$, the associated observable is simply n_R. The measurement yields either the presence (n_R = 1) or the absence (n_R = 0) of one electron on the right QD. The two possible projectors on the respective eigenspaces are $\Pi_0 = 1 - n_R$ and $\Pi_1 = n_R$, leading to the projected state:

$$\rho(\tau^+) = \Pi_0\overline{\rho}\Pi_0 + \Pi_1\overline{\rho}\Pi_1 = \overline{\rho} + 2\mathcal{D}[n_R](\overline{\rho}). \tag{8.14}$$

Upon choosing the basis:

$$\begin{array}{c} |0\rangle \equiv |00\rangle,\ |1\rangle \equiv |0\downarrow\rangle,\ |2\rangle \equiv |\uparrow 0\rangle,\ |3\rangle \equiv |\uparrow\downarrow\rangle, \\ |4\rangle \equiv |\downarrow 0\rangle,\ |5\rangle \equiv |\downarrow\downarrow\rangle,\ |6\rangle \equiv |20\rangle,\ |7\rangle \equiv |2\downarrow\rangle \end{array}, \tag{8.15}$$

The density matrix at all times can be written as (see Appendix G):

$$\rho = \sum_{i=0}^{7} \rho_{ii}|i\rangle\langle i| + \rho_{14}|1\rangle\langle 4| + \rho_{41}|4\rangle\langle 1| + \rho_{36}|3\rangle\langle 6| + \rho_{63}|6\rangle\langle 3| \ . \tag{8.16}$$

Note that the off-diagonal terms do not contribute to the projected state because they encode the tunneling of one electron from one site to the next, leaving either the initial state or the final state with no electron on the right side. Hence we calculate $\rho(\tau^+) = \sum_{i=0}^{7} \overline{\rho_{ii}}|i\rangle\langle i|$ so that $\rho(\tau^+)$ is the diagonal part of $\overline{\rho}$, while $-2\mathcal{D}[n_R](\overline{\rho})$ is the off-diagonal part.

The average energy of the system changes by an amount $\Delta E_1 \equiv \Delta E$:

$$\Delta E = \mathrm{Tr}[H_S\rho(\tau^+)] - \mathrm{Tr}[H_S\rho(\tau^-)] = 2\mathrm{Tr}\Big[H_S\mathcal{D}[n_R](\overline{\rho})\Big] \ , \tag{8.17}$$

which in turn represents the energy of the off-diagonal part:

$$\boxed{\Delta E = -2\Re[\gamma(\overline{\rho}_{14} + \overline{\rho}_{36})] = -\langle C(\tau^-)\rangle = -\mathrm{Tr}[C\overline{\rho}] \ .} \tag{8.18}$$

Here $C \equiv \gamma c_\downarrow^\dagger c_R + \gamma^* c_R^\dagger c_\downarrow$ is the inter-dot tunnel operator, which contains the coherence of the system. Thus, the measurement induces a back-action on the system by destroying the correlations, leading to an energy change ΔE compared to the thermalized state.

The energy increment gained after the n-th cycle is $\Delta E_n \equiv -\mathrm{Tr}[C\rho(n\tau^-)]$. This shows that at time $t = n\tau^+$, if the system thermalizes completely to a unique steady-state $\overline{\rho}$, then the system has received a total average energy $\sum_{k=1}^{n} \Delta E_k = n\Delta E = -n\mathrm{Tr}[C\overline{\rho}]$ from quantum measurements. Therefore, if $\Delta E > 0$, then the measurement on average energizes the system, and a fraction of that energy upon deexciting to the thermalized state can be harvested in the form of electron transport.

We tested other measurement scenarios. We find that the engine operation/output is unchanged when measuring an observable that acts on only one QD (*e.g.* when the occupation of the left QD, or the charge (or spin) of the right QD, is measured). Measuring an observable that operates on both QDs, such as the total charge, does not yield this energy increment: the thermalized and measured states have the same average energy. Work extraction from these cycles is possible only when the measurement separates the two QDs. If the quantum measurements are selective, then the energy increment relation holds by linearity while entropic considerations differ. See Appendix G.

8.1.4 Thermodynamic Quantities

The previous analysis of the cycle describes an engine which harvests the 'quantum heat' ΔE provided by the measurement. The measurement acts like a hot heat bath that energizes the system, which then relaxes and dissipates its energy into the electrode baths, a fraction of which can be collected as a form of an electrical current to produce work. Let us then briefly study the thermodynamics of the cycle by applying the laws of thermodynamics during the thermalization stroke to evaluate the finality of the energy input ΔE provided by the measurement.

Free Energy

The previous derivations allow us to define the maximum extractable work during the thermalization process. This quantity W_{th} is defined by the difference between the average free energy of the initial state at the beginning of a cycle at time $n\tau^+$ and the free energy of the final state at the end of the thermalizing stroke at time $(n+1)\tau^-$. So we obtain directly:

$$W_{th} = -\Delta E + T\Delta S \,, \tag{8.19}$$

where ΔS is the difference in Von Neumann entropy between the states at times $n\tau^+$ and $(n+1)\tau^-$ (see Appendix G for precise estimations of this quantity for different measurement protocols). We can thus expect to extract energy at finite temperature whenever $W_{th} < 0$. It leads to a critical temperature $T_c \equiv \Delta E/\Delta S$ above which this engine cannot possibly work.

Efficiency

We may define the engine efficiency η as the ratio of the electronic work W_{el} obtained during the thermalization process to the total average energy provided by the quantum measurement:

$$\eta \equiv \frac{W_{el}}{\Delta E} \,. \tag{8.20}$$

By definition, this quantity is less than unity. Indeed, according to the first law of thermodynamics which should hold during the time-dependent evolution of the thermalizing stroke according to Kumar and Stafford [314], we may write

$$\Delta E = W_{el} + Q \tag{8.21}$$

with $\Delta E \leqslant W_{th} \leqslant W_{el} \leqslant 0$ as we expect $Q \leqslant 0$. This means that heat should be dissipated to the reservoir as the system thermalizes with the environment (a negative Q, with the same sign as W_{el} means that the heat has been transferred from the system to the environment). Using this inequality, we should therefore have

$$\eta \leqslant \frac{W_{th}}{\Delta E} \leqslant 1 - \frac{T}{T_c} \,, \tag{8.22}$$

so, as expected, the engine efficiency is still bounded by a form of the Carnot efficiency. As a final remark on this quantity, we should state that it does not have a very practical importance in the design of the engine as it can have in classical or other semi-classical quantum engines. Indeed, as our engine relies on the energy provided by quantum measurements performed by the environment, the fuel we are harvesting is present in infinite quantities in the self-sustained bath we are exploiting. Therefore, even a poor efficiency can be of interest given the limitless, constantly refueling amount of energy we are trying to harvest. This energy might come from the local breaking of the second law of thermodynamics during the measurement processes [522, 523, 344], from a minuscule temperature gradient between the measurement bath considered as hot and the opposite electrode bath considered as cold, or from other non-thermal resource such as squeezing [354, 356, 511]. We note that our formalism does not take into account the thermodynamic cost of information erasure as the spinterface electronically interacts with the ferromagnetic electrode acting as an entropy sink [19]. We suppose here that the overall energy balance will be favorable, and will address the thermodynamic cost of interfacial spin accumulation in a future paper.

Power Output

The power P follows instantly from the previous section. It is defined as

$$P \equiv \frac{W_{el}}{\tau} \leqslant \frac{W_{th}}{\tau} \equiv P_{th}. \tag{8.23}$$

It is inversely proportional to the duration of a cycle. This means that devices with fast measurement frequencies can maximize this quantity. In the end, since only a fraction of the energy provided by the measurement stroke is recoverable as an electrical current, $P_{max} = \frac{\Delta E}{\tau}$ provides at this point an upper bound of the electrical power generated by the device and thus represents a good estimation. In this article we shall not try and study the time-dependent dynamics of the thermalizing stroke to give a quantitative estimation of this fraction and focus on ΔE, keeping in mind that the real engine might only deliver a portion of this energy at each cycle.

8.1.5 Perturbative Solution

Density Matrix in the Perturbative Regime

To gain numerical insights, we first derive the density matrix $\rho \equiv \rho_{ss}$ such as $\frac{\mathrm{d}\rho}{\mathrm{d}t} = 0$ so that ρ nullify the right hand side of Eq.8.13. To obtain an approximate analytical solution, we use a perturbation approach on γ (see Appendix F), *i.e.* assume that other interaction energies dominate [19] the hybridization between the QDs. The solution is given by an affine space, parameterized by the initial population $\mu = \langle n_{\downarrow}(0) \rangle$ of the spin $\downarrow$ energy level

on the left QD. We obtain the full density matrix ρ^{μ} after thermalization:

$$\begin{cases} \rho_{00} = \frac{1-\mu}{\mu}\rho_{44} = \alpha(1-\mu)\mathcal{T}_L^+\mathcal{T}_R^+ \\ \rho_{11} = \frac{1-\mu}{\mu}\rho_{55} = \alpha(1-\mu)\mathcal{T}_L^+\mathcal{T}_R^- \\ \rho_{22} = \frac{1-\mu}{\mu}\rho_{66} = \alpha(1-\mu)\mathcal{T}_L^-\mathcal{T}_R^+ \\ \rho_{33} = \frac{1-\mu}{\mu}\rho_{77} = \alpha(1-\mu)\mathcal{T}_L^-\mathcal{T}_R^- \\ \rho_{41} = \rho_{14}^* = \frac{\mathrm{i}\gamma\alpha\beta^{\mu}\mathcal{T}_L^+}{\det B^*}\left(\frac{2\mathcal{T}_L^+ + 2\mathcal{T}_L^- + \mathcal{T}_R^- + \mathcal{T}_R^+}{2} + \mathrm{i}(\Delta + U)\right) \\ \rho_{63} = \rho_{36}^* = \frac{\mathrm{i}\gamma\alpha\beta^{\mu}\mathcal{T}_L^-}{\det B^*}\left(\frac{2\mathcal{T}_L^+ + 2\mathcal{T}_L^- + \mathcal{T}_R^- + \mathcal{T}_R^+}{2} + \mathrm{i}\Delta\right) \end{cases} \tag{8.24}$$

where $\beta^{\mu} \equiv \mu\mathcal{T}_R^+ - (1-\mu)\mathcal{T}_R^-$, $1/\alpha \equiv (\mathcal{T}_L^+ + \mathcal{T}_L^-)(\mathcal{T}_R^+ + \mathcal{T}_R^-)$, $\Delta \equiv \epsilon_{\downarrow} - \epsilon_R$ and B are referenced in Appendix F and the other terms are null.

To study the thermalized state of the next cycle, we consider the particle number with spin $\downarrow$ in the left QD. Since the projected state is diagonal, we directly obtain:

$$\mathrm{Tr}[n_{\downarrow}\rho(\tau^+)] = \rho_{44} + \rho_{55} + \rho_{66} + \rho_{77} = \mu \tag{8.25}$$

So, for both measurement outcomes, the spin $\downarrow$ occupation number remains unchanged after both the thermalizing and measurement strokes. Therefore, the second cycle starts again with $\langle n_{\downarrow}(\tau^+)\rangle = \mu$, and so it yields the same thermalized state just before the second measurement as in the previous cycle, such that $\rho(2\tau^-) = \rho(\tau^-) = \rho$ and thus an instant recursion yields the system state after each cycle n:

$$\rho(n\tau^+) = \rho(n\tau^-) + 2D[n_R](\rho) = \rho + 2D[n_R](\rho). \tag{8.26}$$

In this approximation, the total energy produced after the n-th cycle will be $n\Delta E$ and the power output shall thus be $\frac{\Delta E}{\tau}$ where τ is the duration of a unit cycle.

Energy in the Perturbative Regime

We can express the energy $\Delta E = -2\Re[\gamma(\rho_{14} + \rho_{36})]$ associated with the measurement back-action as:

$$\Delta E = \frac{\beta^{\mu}|\gamma|^2}{|\det B|^2}\frac{(s+r)^2}{sr}(s\Delta + mU)\ , \tag{8.27}$$

with $s \equiv \mathcal{T}_L^+ + \mathcal{T}_L^-$, $m \equiv \mathcal{T}_L^-$, $r \equiv \frac{\mathcal{T}_R^+ + \mathcal{T}_R^-}{2}$. and

$$|\det B|^2 = r^2(r+s)^2 + [(s+2r)\Delta + (m+r)U]^2\ . \tag{8.28}$$

To study ΔE, we first assume (see Appendices E and H) that all the energies involved in the system $\mathcal{T}_L^+$, $\mathcal{T}_L^-$, $\mathcal{T}_R^+$, $\mathcal{T}_R^-$, Δ and U are strictly positive. This immediately leads to $s, m, r > 0$ and then to ΔE having the same sign as β^{μ}. Therefore, the measurement energizes the two QDs whenever $\mu < \frac{\mathcal{T}_R^-}{\mathcal{T}_R^+ + \mathcal{T}_R^-} \equiv \mu^c$. Thus, at the critical value μ^c, the off-diagonal terms describing the first-order perturbation vanish, and the model cannot describe if energy harvesting occurs.

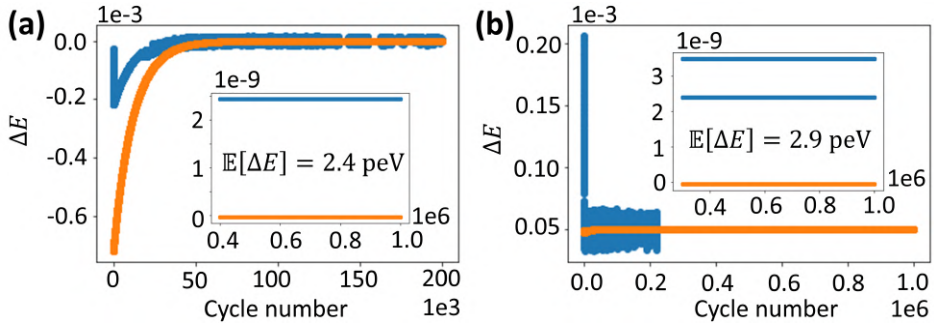

Figure 8.3: **Simulation of the Engine's Cycle.** Simulation results of ΔE for (a) $\rho_0 = |\downarrow\downarrow\rangle\langle\downarrow\downarrow|$ and (b) $\rho_0 = \frac{1}{2}|\uparrow\downarrow\rangle\langle\uparrow\downarrow| + \frac{1}{2}|\downarrow\downarrow\rangle\langle\downarrow\downarrow|$.. The corrected perturbative results (orange) derived from SI. Note 3. and the numerically calculated solution at 4 ps (blue) are shown. Here $\epsilon_\downarrow = 8$, $\epsilon_\uparrow = -3$, $\epsilon_R = 1$, $J = 8$, $U = 1000$, $\gamma = 0.1$, $\mathcal{T}_L^+ = \mathcal{T}_L^- = 0.1$, $\mathcal{T}_R^- = \mathcal{T}_R^+ = 0.01$, i.e. the two leads are both at infinite temperature (all units may be taken in meV and justification for their values may be found in SI. Note 6).

8.2 Simulations

8.2.1 Simulating the Engine's Cycle

To evaluate these analytical results and confirm that the measurement reliably provides energy over many cycles, we simulated the engine operation. We show in Figure 8.3 the results of measuring n_R across 10^6 cycles (see also Appendix H). Starting from the pure state $\rho_0 = |\downarrow\downarrow\rangle\langle\downarrow\downarrow|$, we first see in Figure 8.3(a) that ΔE presents three trends: the first 10^5 cycles see a increase of ΔE towards 0, then a stochastic regime ensues where ΔE oscillates randomly around 0 until cycle number 4.10^5, before reaching a stable non-equilibrium steady-state, where $\mathbb{E}[\Delta E] = 2.4$ peV. The drift originates from the partial thermalization, which gradually dilutes the information contained in the initial state ρ_0, resulting in a power output driven towards a steady-state attractor. Indeed, each new cycle introduces an additional mixing that can be understood as a statistical superposition of passive and active pure initial states which reduces the average energy increment of the next cycle.

To support this claim, in Figure 8.3(b) we show that, starting from a mixed state $\rho_0 = \frac{1}{2}|\uparrow\downarrow\rangle\langle\uparrow\downarrow| + \frac{1}{2}|\downarrow\downarrow\rangle\langle\downarrow\downarrow|$, we find that ΔE converges more quickly towards a different power-generating limit cycle featuring two stable energy branches that result in $\mathbb{E}[\Delta E] = 2.9$ peV.

These experiments show that, during the transitional and stochastic regimes, the information on the initial condition is progressively lost through the non-unitary system evolution caused by thermalization, but it can never be entirely wiped out! Indeed, the engine acts as a chaotic non-ergodic machine as we have shown that the system can get trapped in an active steady-state when a certain priming is feeding favorable initial conditions.

In Appendix H, we present additional data exploring different parameters, measurement protocols, as well as the case of selective measurements. These results show similar behav-

iors, *i.e.* all exhibit the ability to extract energy. The essential difference lies in the reading of the measurement. When using selective measurements, the situation changes qualitatively as the randomness of the measurement will frequently fail to energize the system and place it in a lower energy state (see Figure 8.2). This means that we cannot extract work during the thermalizing stroke for a large proportion of the cycles in which the measurement is taking energy from the system. It leads inevitably to a strongly chaotic behavior originating from the non-linearity of the intrinsically stochastic measurement readout, which could then kill the efficiency of the device because of strong power fluctuations.

8.2.2 Partial Thermalization

In Appendix I, we test the speed of the thermalization process by comparing the calculated steady-state of the master equation ρ with the density matrix σ calculated at time $t = 1$ meV$^{-1} \approx 4$ ps. We consider ΔE, starting from different pure states and with different parameters taken randomly within an experimentally reasonable range [18, 19]. The results presented show that the error made on the trace distance verifies $T(\rho, \sigma) < 0.9$ and leads to an error on the energy increment ΔE lower than 1% only for 1% of the test runs. This shows that, for a wide range of parameters, it is unreasonable to approximate the state at the end of the thermalizing stroke as the steady-state solution. Thus, in this general case, we can only hope to reach a partial thermalization, though it is beneficial to the power output of the device, as it forces the system to stay out of equilibrium and to remain active even when it is connected to passive thermal baths. Indeed, statistics (not shown) on the steady-state coherence energy reveal that, at infinite time $|\langle C \rangle| \approx 10^{-9} - 10^{-16}$ meV for standard parameter ranges and passive thermal couplings, while after $t = 1$ meV$^{-1} \approx 4$ ps, we can reach up to $|\langle C \rangle| \approx 10^3$ meV and obtain an energy-generating limit cycle while in the same equilibrium parameter configuration for special initial conditions. This suggests a higher energy increment. Indeed, the average energy increment per cycle is still given by $\Delta E = -\langle C \rangle$ in this general case, so that the previous energetic description of the cycle remains valid here. A proof of this assertion is given in Appendix G along with a numerical justification based on measurement statistics.

8.2.3 Maximizing the Coherence Energy

To study how the parameters that impact the partially thermalized state ρ affect the coherence energy $-\langle C \rangle$, we show in Figure 8.4 several color plots of $-\langle C \rangle$ calculated after the thermalizing stroke starting from the pure state $\rho_0 = |\uparrow\downarrow\rangle\langle\uparrow\downarrow|$ as a function of the most relevant different pairs of parameters (see Appendix J for other plots), keeping other parameters fixed, and with $\gamma \sim U \gg \epsilon \gg \mathcal{T}$. In Fig 8.4(a), we notice that $-\langle C \rangle$ is maximized when $U \approx 10^3 - 10^4$ and $\mathcal{T}_L^+ = \mathcal{T}_L^- < 1$. Indeed, a higher U could lead to a bigger coherence energy that is related to the charging energy of a QD, while a lower $\mathcal{T}_L$ favors the tunneling between the QDs over the tunneling from/to the electrodes. In Fig 8.4(b), we observe that the asymmetry between $\mathcal{T}_L$ and $\mathcal{T}_R$ is quite irrelevant for this set of parameters for low $\mathcal{T}_R$: the engine generates power and energy harvesting may be possible. Above a phase transition around $\mathcal{T}_R \approx 10$ (see also Fig 8.4(d)), a chaotic phase ensues,

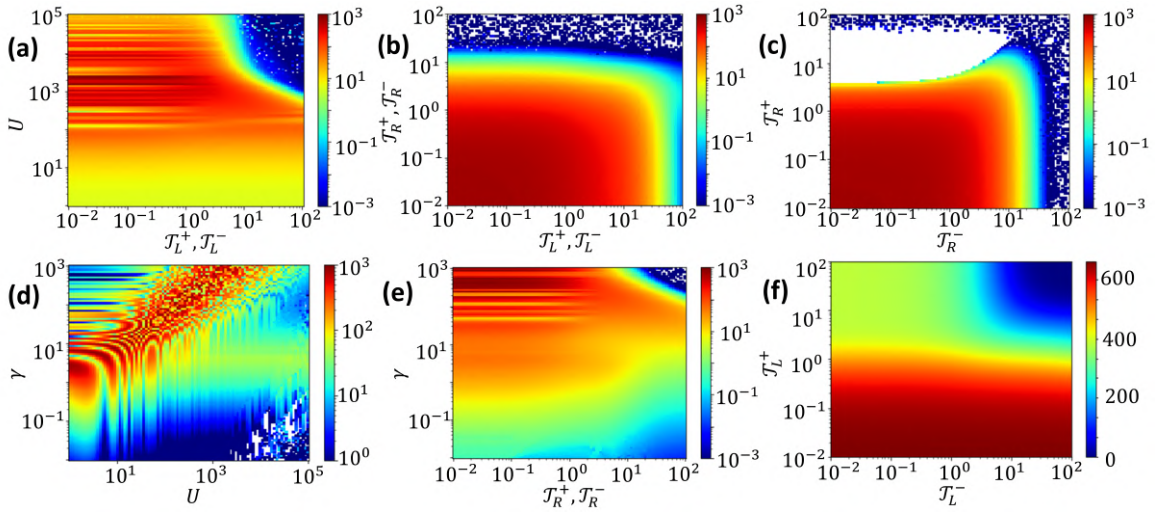

Figure 8.4: **Coherence Energy Color Plots.** Parameter pair dependence of the coherence energy $-\langle C \rangle$, calculated at 4 ps starting from the pure state $\rho_0 = |\uparrow\downarrow\rangle\langle\uparrow\downarrow|$, with $\epsilon_\downarrow = 8,\ \epsilon_\uparrow = -3,\ \epsilon_R = 1,\ J = 8,\ U = 1000,\ \gamma = 1000,\ \mathcal{T}_L^+ = \mathcal{T}_L^- = \mathcal{T}_R^+ = \mathcal{T}_R^- = 0.1$. (a) $\mathcal{T}_L^+ = \mathcal{T}_L^-$ versus U, (b) $\mathcal{T}_L^+ = \mathcal{T}_L^-$ versus $\mathcal{T}_R^+ = \mathcal{T}_R^-$, (c) $\mathcal{T}_R^-$ versus $\mathcal{T}_R^+$, (d) U versus γ, (e) $\mathcal{T}_R^+ = \mathcal{T}_R^-$ versus γ, (f) $\mathcal{T}_L^-$ versus $\mathcal{T}_L^+$.

coherence energy almost vanishes and its sign strongly depends on small parameter fluctuations: we cannot extract energy in this configuration. Note that We may also be outside of the weak coupling regime that is needed for the Lindblad master equation to hold. Intuitively, this chaotic phase results from a dominating interaction with the right electrode that completely overcomes the tunneling interaction between the QDs, thereby nullifying the potential coherence energy between the two sites. In Fig 8.4(c), we examine the electron/hole asymmetry on the right electrode. The data reveal a third, dissipative phase with no energy extraction with $-\langle C \rangle < 0$ (in white). Finally, in Fig 8.4(d), the U / γ dependence reveals two branches that maximize coherence energy: one for $\gamma \approx 1$ that weakly depends on U, and a second for $\gamma \approx U$. This may help tune experimental device parameters to maximize energy harvesting as this data shows an advantage in strong Coulombic repulsion U along with a strong inter-dot coupling g, indicating that the two sites should be close and have a large electronic affinity.

Although maximizing ΔE starting from a particular initial state is a first step towards finding the maximum power output, it is not straightforwardly linked to the power output since it corresponds to an average over many cycles with different initial states.

8.2.4 Power fluctuations

Using the data of Figure 8.4 along with Appendix J, we infer a regime wherein the coherence energy is highest with $\mathcal{T} \ll \epsilon \ll \gamma \approx U \approx 1000\epsilon$. To confirm the high power output $P = \frac{\mathbb{E}[\Delta E]}{\tau}$ within this parameter space, we simulated 10^6 engine cycles (see plots in Fig 8.5). Strikingly, we observe strong fluctuations of ΔE that ultimately kill the temporal average of the energy increment. This shows that maximizing $-\langle C \rangle$ also yields a strong depen-

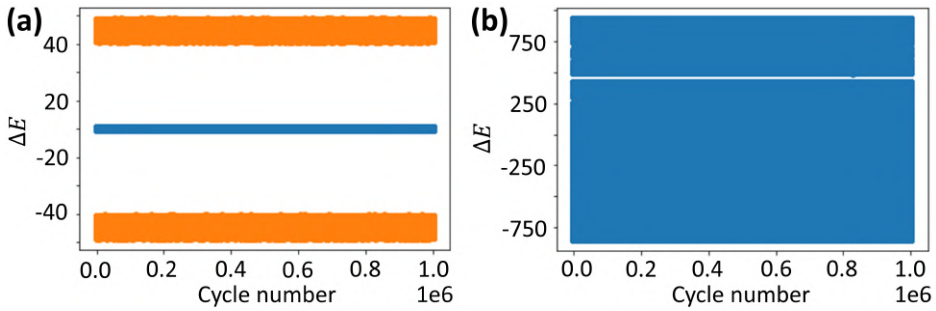

Figure 8.5: **Simulation results with strong power fluctuations.** Simulation results of ΔE for 10^6 cycles when measuring the charge Q of the left QD using (a) unselective and (b) selective measurements. The numerical calculation (orange) and the perturbative solution (blue) are shown. $\epsilon_\downarrow = 8$, $\epsilon_\uparrow = -3$, $\epsilon_R = 1$, $J = 8$, $U = 1000$, $\gamma = 1000$, $\mathcal{T}_L^+ = \mathcal{T}_R^+ = \mathcal{T}_L^- = \mathcal{T}_R^- = 0.1$ (all units may be taken in meV), and with the initial condition $\rho_0 = |\uparrow\downarrow\rangle\langle\uparrow\downarrow|$.

dence of the tunneling energy after partial thermalization on the initial conditions. This increases the fluctuations and negatively impacts P: maximizing P requires balancing energy and fluctuations. Indeed, from the Heisenberg uncertainty relations, when selectively measuring n_R, we may write:

$$\Delta C \Delta n_R \geqslant \frac{1}{2}|\langle[C, n_R]\rangle| = \frac{1}{2}|\langle[H_S, n_R]\rangle| \approx \frac{1}{2}\left|\frac{\mathrm{d}\langle n_R\rangle}{\mathrm{d}t}\right|. \tag{8.29}$$

Here, at the end of each cycle, $\Delta n_R \lesssim 1$ is known and fixed by the statistical outcomes of the measurements and should be of order unity since the measurement alternatively projects the system into a $n_R = 0$ or 1 state. Moreover, the right-hand side describes the n_R oscillation rate, which is strongly driven by the energy scale of the coherence energy $|\langle C\rangle|$. Thus, Eq. 8.29 justifies that $\Delta C \gtrsim |\langle C\rangle|$.

A second Heisenberg inequality can be written regarding the initial condition decisive observable $n_\downarrow$, and which shows that the fluctuations of T are also related to the momentum dispersion of the initial conditions $\dot{\mu}$, which is mainly impacted by the partial thermalization. For some parameters, the characteristic time of the system is such that it keeps the information about its initial state longer in memory, thus resulting in stronger fluctuations that can also be observed for the unselective case (see Fig 8.5(a)).

8.2.5 Bosonic Catalysis

Powering the Engine with a Bosonic Pump

Our work thus showcases how to harvest energy as an electrical current between two leads across quantum dots despite no direct electronic connection, *i.e.* how to generate continuous power from the measurement back-action through the vacuum. The predicted output power is much lower than that measured [18, 19], which suggests the experimental presence of an additional quantum resource. Since our QDs are embedded in an atomic matrix,

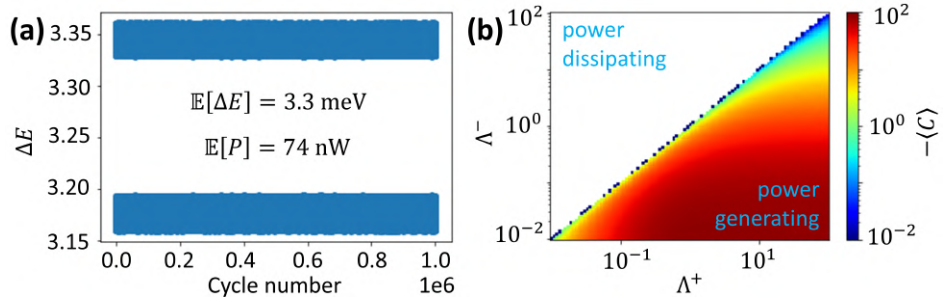

Figure 8.6: **Simulation with Bosonic Catalysis powered by a Bosonic Pump.** (a) Simulation results of ΔE for 10^6 cycles powered by a non-thermal bosonic bath when measuring the population n_R in the case of two identical electrodes at thermal equilibrium with infinite temperature. Parameters are $\epsilon_\downarrow = 8$, $\epsilon_\uparrow = -3$, $\epsilon_R = 1$, $J = 8$, $U = 1000$, $\gamma = 1000$, $\mathcal{T}_L^+ = \mathcal{T}_R^+ = \mathcal{T}_L^- = \mathcal{T}_R^- = 0.1$ and $\Lambda^+ = 2\Lambda^- = 0.01$. (b) Color plot of $-\langle C \rangle$ calculated at 4 fs as a function of the bosonic coupling parameters Λ^+ and Λ^-, starting from the pure state $\rho_0 = |\uparrow\downarrow\rangle\langle\uparrow\downarrow|$. All other parameters are the same as (a).

we examine the impact of bosons, such as spintronic magnons, lattice phonons or vibrons on the QD complex, through an additional interaction with a bosonic bath that can flip the spin of the left dot (see Eq. 8.13). We then repeated the experiments presented in Figure 8.3-8.4.

As expected, Figure 8.6.(b) shows that the device remains passive whenever the system interacts with a thermal bath in which $\Lambda^- > \Lambda^+$ for the same equilibrium parameters as above. Nonetheless, the simulation presented in Figure 8.6.(a) shows that the energy increment ΔE can reach up to $\Delta E \approx 10$ meV for a weak asymmetric coupling $\Lambda^+ = 2\Lambda^- = 0.01$ (negative temperature), leading to a power output $P \approx 100$ nW when choosing a cycle duration triggered by the electronic frequency of $\tau^{-1} = 140$ THz in line with experiments [19]. This bosonic pump greatly decreases the thermalization time: the information on the initialization of each cycle is almost completely removed, and relative power fluctuations are much lower compared to having only vacuum fluctuations.

It is possible to engineer this autonomous non-thermal bosonic interaction using a finite bath (the complex vibrons) coupled to a larger infinite thermal bath (the lattice phonons). This would generate the non-unitary coupling Hamiltonian necessary to build such asymmetric coefficients through squeezing [358, 354, 356, 511], broken symmetries [524], non-Hermitian skin effect [525, 526] or nonlinear processes [527]. We leave details of this non-thermal bosonic bath to future studies.

Powering the Engine with a Spin-bias

Although a non-thermal bosonic bath might be present in our spintronic engine, without further evidence, supposing the influence of such a drive is not satisfactory. Let us then look for another non-thermal resource that can power the device, and suppose that the bosonic bath is thermal, meaning that $\Lambda^- > \Lambda^+$.

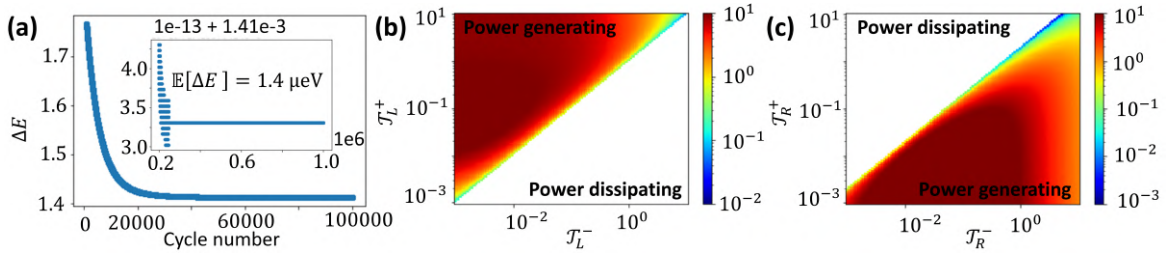

Figure 8.7: **Simulation with Bosonic Catalysis powered by Spin Bias.** (a) Simulation results of ΔE for 10^6 cycles powered by a spin bias bath when measuring the population n_R. Parameters are $\epsilon_\downarrow = 8,\ \epsilon_\uparrow = -3,\ \epsilon_R = 1,\ J = 8,\ U = 1000,\ \gamma = 1000,\ \mathcal{T}_L^+ = 0.2, \mathcal{T}_R^+ = \mathcal{T}_L^- = \mathcal{T}_R^- = 0.1, \Lambda^+ = 0.01$ and $\Lambda^- = 0.0101$. (b) Color plot of $-\langle C\rangle$ calculated at for the steady state as a function of the bosonic coupling parameters $\mathcal{T}_L^-$ and $\mathcal{T}_L^+$, starting from the pure state $\rho_0 = |\uparrow\downarrow\rangle\langle\uparrow\downarrow|$. All other parameters are the same as (a). (c) Color plot of $-\langle C\rangle$ as a function of $\mathcal{T}_R^-$ and $\mathcal{T}_R^+$ with the same set of parameters.

Following the formalism of thermodynamics with conserved quantities developed in Chapter 3, thanks to the fixed magnetization of the electrodes, we can consider the spinterfaces as mesoscopic spin reservoirs for which spin polarization is a conserved charge. Let us then focus on the left electrode, considered as the reference. Its free energy then reads:

$$F_L = \langle H_L\rangle - \mu_L\langle N_L\rangle - m_L\langle P_L\rangle - T_L S_L, \tag{8.30}$$

where H_L has been defined in Eq 8.6, $N_L = \sum_{k,\sigma} n_{k,\sigma}$ is the total number operator on the left, $P_L = \sum_k n_{k,\uparrow} - n_{k,\downarrow}$ is the spin polarization operator, $S_R = \mathrm{Tr}(\rho_L \ln \rho_L)$ is the Von-Neumann entropy ; and μ_L, m_L, and T_L are the conjugated generalized charges such as μ_L is the usual electrochemical potential, T_L is the temperature, and m_L is a spin potential.

The Generalized Gibbs state τ_L corresponding to this spin reservoir thus reads:

$$\tau_L = \mathcal{Z}_L^{-1} e^{-\beta_L(H_L - \mu_L N_L - m_L P_L)} \text{ where } \mathcal{Z}_L = \mathrm{Tr}(e^{-\beta_L(H_L - \mu_L N_L - m_L P_L)}). \tag{8.31}$$

Using the commutation relations of the individual number operators, we obtain

$$\mathcal{Z}\tau_L = \prod_{k,\sigma} e^{-\beta_L(\epsilon_{k,\sigma} - \mu_L - \sigma m_L) n_{k,\sigma}} = \prod_k \left[e^{-\beta_L(\epsilon_{k,\sigma} - \mu_L - \sigma m_L)} n_{k,\sigma} + (1 - n_{k,\sigma})\right] \tag{8.32}$$

such as

$$\mathcal{Z} = \prod_{k,\sigma} \left[1 + e^{-\beta_L(\epsilon_{k,\sigma} - \mu_L - \sigma m_L)}\right] \tag{8.33}$$

and therefore,

$$N_{k,\sigma} \equiv \langle n_{k,\sigma}\rangle = \mathrm{Tr}\, n_{k,\sigma}\tau = \frac{1}{1 + e^{\beta_L(\epsilon_{k,\sigma} - \mu_L - \sigma m_L)}}. \tag{8.34}$$

The same expression can be obtained for the right electrode with its respective parameters β_R, μ_R and m_R. In the case where the electrodes' filling are well described by a strong magnetization, we can discard the energy term and feed

$$\langle n_{k,\sigma}\rangle = \frac{1}{1 + e^{-\beta_L(\mu_L + m_L)}} \text{ and } \langle n_{p,\sigma}\rangle = \frac{1}{1 + e^{-\beta_R(\mu_R - m_R)}} \tag{8.35}$$

into the expressions for $\mathcal{T}_L^+$, $\mathcal{T}_L^-$, $\mathcal{T}_R^+$ and $\mathcal{T}_R^-$ reported in Sec. 1 of the Supplemental Material such as we can engineer $\mathcal{T}_L^- < \mathcal{T}_L^+$ and $\mathcal{T}_R^+ < \mathcal{T}_R^-$ for well chosen m_L and m_R by acting on their magnetization even if the two electrodes have the same temperature $\beta_L = \beta_R$ and chemical potential $\mu_L = \mu_R$. This calculation thus shows that the coupling coefficients to the bath can be tuned either by acting on electronic potential, or on its magnetization, such that a 'spin bias' can yield the necessary asymmetry required for the device to run as an engine. The spin bias, corresponding to a difference in the magnetic potential of the two electrodes, can be engineered by choosing electrodes featuring different intrinsic spin polarizations, or by imposing a magnetization difference between the two ferromagnets. This thermodynamical resource should therefore persist naturally in our device for an indefinite time without requiring an external energy supply.

In Figure 8.7(a) we show a test run for the engine, using a thermal bosonic bath with $\Lambda^- > \Lambda^+$, and with a regular asymmetry $\mathcal{T}_L^- < \mathcal{T}_L^+$ and $\mathcal{T}_R^+ = \mathcal{T}_R^-$. After about 10^5 cycles, the engine stabilizes in a generative steady-state delivering an average of 1.4 μeV per cycle which shows that a non-thermal bosonic pump is not necessary to run the engine: a favorable asymmetry of the coupling coefficients to the baths finely tuned by a built-in spin bias originating from the magnetization of the electrodes is sufficient to power the engine. In Figure 8.7(b) and (c), we study the dependence of the coherence energy $-\langle C \rangle$ obtained in the steady-state of the master equation with respect to the pairs of parameters $\mathcal{T}_L^-, \mathcal{T}_L^+$ and $\mathcal{T}_R^+, \mathcal{T}_R^-$ for the same set of parameters as the test run and show that the device behaves as an engine whenever $\mathcal{T}_L^- < \mathcal{T}_L^+$ and $\mathcal{T}_R^+ < \mathcal{T}_R^-$, meaning that the left electrode should favor down spin filling with $m_L > -\mu_L$ and the right electrode should favor up spins with $m_R < \mu_R$.

In Appendix K, we provide more data about this bosonic catalysis, study the influence of the different parameters, and show that this power level can also be recovered if we replace the assumption of a negative temperature bosonic bath or a spin bias by another, standard non-equilibrium resource such as a potential or a temperature difference.

8.3 Discussion

We studied a quantum information engine built around solid-state spintronic interactions that can harvest the energy of quantum coherence and can explain recent experiments involving atomic spin qubits [18, 19]. Our model considered a pair of correlated spin quantum dots that electronically interact with spin-selecting electrodes. We derived a master equation that describes a two-step engine: a thermalizing stroke that creates coherence between the two quantum dots and generates electron transport, then a quantum measurement stroke that extracts energy from their correlation. This changes their entropy by separating and projecting the system into a higher energy state on average. When the pump induced by the measurement - understood as the difference between the ground energy states of a thermal system and a system with the measurement interactions turned on - constitutes the only energy source, and without a direct tunneling link between the two electrodes, numerical simulations predict an appreciable finite power output in some cases. We reproduce experimentally measured power levels [19] by including a bosonic bath along

with a non-thermal resource, among which the most natural and sufficient one should be a spin bias, that is automatically present in our system due to the ferromagnetic electrodes. Our work thus explains recent [18, 19], and perhaps also older [528, 466] experiments, and showcases the ferromagnet/molecule interface (the spinterface [257, 256]) with high spin polarization [19] as a quantum measurement apparatus.

Our study sheds light on a quantum engine that relies on quantum measurements in order to extract energy from a system of coupled quantum dots, through the breaking of coherence energy. Using a perturbative approach, we found a regime of parameters for such a system that could lead to energy generation during a large number of cycles, and we confirmed this finding using numerical simulation. Then, we proceeded to find a good set of parameters that would maximize the power output by maximizing the coherence energy generated after each thermalization process, but we found that this gain in energy increment was compensated by increasing fluctuations due to partial thermalization, which ultimately negatively impacts the expected power output. A compromise between fluctuations and the maximum energy output should thus be found in order to maximize the power output but the present study was so far unable to find this optimum. Future work should be able to gain more insights on this point and prove rigorously the definite harvesting capabilities of the device after a long time using ergodic theory.

The present study only focused on the energetics of the device brought by the measurement process. Hence, we could only set a higher bound for the power output, corresponding to the energy we can hope to extract at zero temperature when no energy is lost through irreversible heat exchanges. In order to obtain a more realistic depiction of the thermodynamics of the system at finite temperature and electrochemical potentials, more efforts need to be dedicated towards the study of the thermalization process. This issue will also be the subject of a future work, which will aim at applying the first law of thermodynamics during the time-dependent evolution of the system in order to separate clearly the electrical work we are interested in from the heat that is dissipated during the thermalizing stroke.

Finally, this Chapter opens fruitful research into spintronic interaction dynamics between ferromagnets and paramagnetic centers [529], *e.g.* using scanning tunneling and ferromagnetic resonance techniques [530], to elucidate the thermodynamic role [361, 399] of the spintronic quantum measurement apparatus [18, 19].

Chapter 9

The Mesoscopic Model

It is known that transport through a quantum dot or a quantum well system can give rise to current-rectifying effect and therefore act as a diode. A resonant tunneling diode (RTD) [531] is a device that exhibits quantum tunneling phenomena through discrete energy levels confined in a small region of space. These devices can display nonlinear phenomena such as Negative Differential Resistance (NDR) [532] illustrated by a negative derivative region in their current-voltage characteristic curve. This means that as the voltage across the diode increases, the current through it decreases, which is opposite to the behavior of traditional resistors (see Figure 9.1). Therefore, a resonant tunneling diode can act as a form of filter of the electrons, such that transport is maximum only over a restricted bandwidth when the energy of the electrons in the bath enters into resonance with the discrete energy levels of the wells.

A number of clues are pointing towards the presence of a diode effect in our device. First, structurally, the impurities inserted in the barrier, creating the spin chain indeed act as atomic quantum dots, or trapping quantum wells, with discrete energy levels, that should trigger the resonant tunneling diode effect [480, 251]. Second, the experimental data presented in Chapter 4 does indeed present *IV* characteristics featuring both non-linear responses and current asymmetries suggesting that a strong current rectifying effect is indeed taking place (see Figures 6.1, 6.2, 7.1, 7.4). Third, referring to Chapter 3 on Maxwell's demon and more precisely on Brillouin's paradox [534, 535, 536, 537], it would seem necessary to have a ratchet-like rectifying effect originating from some structural asymmetry in order to filter current fluctuations into a preferred direction and thus generate power. And finally, given the microscopic quantum model we developed in the previous Chapter, which features spin-dependent transport through a pair of atomic orbitals with spin-split, discrete energy levels, it seems reasonable to postulate that this system of quantum dots would phenomenologically act in a similar way as a resonant tunneling diode.

Building upon the classical formalism of spintronics such as the Valet-Fert theory [49] developed in Chapter 1, the objective of this Chapter is two-fold. First, we will introduce a diode effect in the Valet-Fert model to see if it can be used to rectify an uncompensated white noise present in our system so as to continuously extract energy from the fluctuations. Then, we will carefully examine the hypotheses of these models in order to identify those

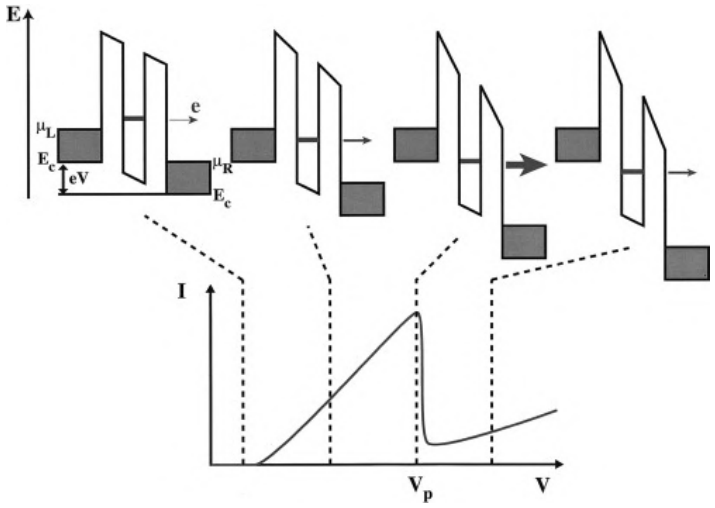

Figure 9.1: **Resonant Tunneling Diode.** Schematic diagram of the operation of a resonant tunneling diode. μ_L (μ_R) is the chemical potential for the left (right) electrode. The grey areas are filled electrons states that provide reservoirs of electrons for tunneling. Only when the subband in the central quantum well has the same energy as an electron in one of the electrodes can electrons tunnel through the system to the other electrode. Extracted from [533]

that could be violated in our system and give rise to a self-sustained non-equilibrium effect, which could feed the continuous power output generated by the device. In the discussion, we will finish by commenting on the magnitudes of the different parameters used in the models that should be reached in order to fit the experimental results, and we will assess the physicality of the model.

All along this Chapter, we will use the parameters referenced in Table 9.1 and we will highlight the hypotheses in bold and reference them in Table 9.2 at the end of this Chapter.

9.1 Rectifying spin-current fluctuations

In this section, we consider an electric wire defined along the x axis, with section a defined as unity, such that we consider the problem to be one-dimensional. This electric wire has a length $2l$ and extends from $x = -l$ to $x = +l$. The wire is connected on both sides to spin-polarized electrodes such that the left electrode has a strong magnetization $\vec{M}_L = M_L\vec{e}_z$ ($M_L > 0$), that is defining the **quantization axis** of the spin along the z direction (hypothesis (HQ) in Table 9.2). The right electrode is then supposed to have a weaker magnetization or a weaker tunnel coupling to the central material, such that it does not interfere with the spin referential fixed by the left electrode. The left electrode is thus considered as the **reference electrode** (hypothesis (HM) in Table 9.2). The magnetization of the right electrode will thus be regarded in the direction of the quantization axis such as $\vec{M}_R = M_R\vec{e}_z + o(\vec{M}_L^2)$ (see Figure 9.2). In this section, we will see how a non-linear conductance profile of the wire can trigger a rectifying effect that can harvest energy from

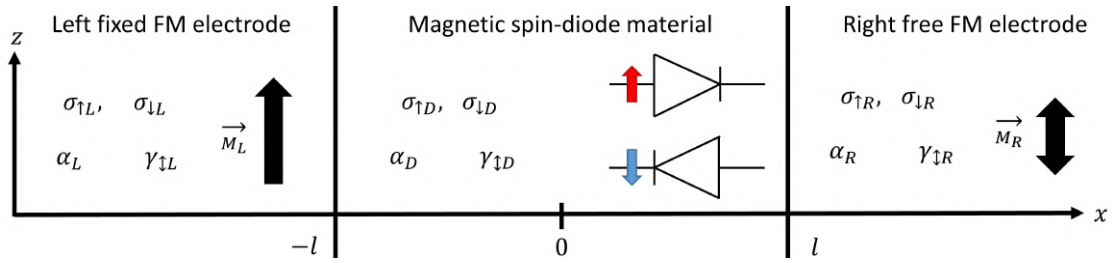

Figure 9.2: **Mesoscopic Diode Model.** Schematic of the three regions defining the spin-diode nanowire between the two ferromagnetic electrodes.

the spin-current fluctuations driven by the projection onto the quantization axis of the magnetization difference between the two electrodes.

9.1.1 The two spin-channels model

We start by postulating that each element of volume $\mathrm{d}x$ can be described by two static variables, $\mathrm{d}N_\uparrow$ and $\mathrm{d}N_\downarrow$, which represent the number of each spin carrier, such that we can define the spin-resolved number densities $n_\uparrow \mathrm{d}x = \mathrm{d}N_\uparrow$ and $n_\downarrow \mathrm{d}x = \mathrm{d}N_\downarrow$. Away from equilibrium, we need to define the associated spin-resolved current densities $j_\uparrow$, $j_\downarrow$ that describe the flow of spin carriers and that relates to the electronic current density $j = -e(j_\uparrow + j_\downarrow)$, where $e > 0$ is the absolute charge of the electron.

Classical spintronics as built in most phenomenological theories is based on three fundamental equations. First, within each material, the chemical conservation laws read:

$$\boxed{\begin{cases} \partial_t n_\uparrow + \partial_x j_\uparrow = -\nu \\ \partial_t n_\downarrow + \partial_x j_\downarrow = \nu \end{cases},} \tag{9.1}$$

where ν is the rate at which down-spins flip to up-spins.

Then, we consider the free energy $F = U - TS$ of one material, with U the internal energy, T the temperature and S the entropy. Let us consider a small perturbation away from equilibrium. The first law of thermodynamics states that $dU = \delta Q + \delta W$. For a **reversible process** (hypothesis (HR)), $\delta Q = TdS$ such that $dF = dU - TdS - SdT = -SdT + \delta W$. Then the work δW is composed of every change in energy driven by conservative forces. In a first approximation, we can identify different forces deriving from potentials that are driving the system. Chemical forces may lead to changes $\mathrm{d}N_\uparrow$ and $\mathrm{d}N_\downarrow$, electric forces may change the total number of electrons $\mathrm{d}N = \mathrm{d}N_\uparrow + \mathrm{d}N_\downarrow$, and magnetic forces may act on the magnetic moment $\mathrm{d}\vec{m}$, defined as the magnetization density. We can thus write:

$$\boxed{dF = -SdT - \mu_\uparrow \mathrm{d}N_\uparrow - \mu_\downarrow \mathrm{d}N_\downarrow + eV\mathrm{d}N - \vec{H}^* \cdot \mathrm{d}\vec{m}.} \tag{9.2}$$

In this equation, we have identified the usual thermodynamic potentials: the chemical potentials $\mu_\uparrow$ and $\mu_\downarrow$, the electrostatic potential Φ and some *magnetization potential* H^* that has the unit of a magnetic field and still needs to be determined. The gyromagnetic ratio of the electron is negative, the magnetization referential chosen above points toward

the $+\vec{e_z}$ direction, and we assume that the spin angular momentum is the main driver of the magnetic moment, considering only the main component along the z direction (HQ). In general, we should also have a component in the yz plane due to magnetic anisotropy and spin precession, but these contributions can be neglected for well-chosen electrode and diode materials, carefully fabricated so as to engineer a strong in-plane magnetization. In this assumption (HQ), we can write:

$$\vec{m} = \gamma\vec{L} = -\frac{g\mu_B}{\hbar}\vec{S} = -\frac{g\mu_B}{2}(N_\uparrow - N_\downarrow)\vec{e_z} \equiv -\mu_e(N_\uparrow - N_\downarrow)\vec{e_z} \tag{9.3}$$

where $g \approx 2$ is the electron spin g-factor (Landé factor) and $\mu_B = e\hbar/2m_e$ is the Bohr magneton with m_e the bare mass of the electron, and we have defined $\mu_e \equiv \frac{g\mu_B}{2} \approx \mu_B$ the absolute magnetic moment of the free electron. Setting $\vec{H^*} \equiv H^*\vec{e_z}$, dividing by the volume element, we obtain the following expression for the free energy density f:

$$\mathrm{d}f = -s\,\mathrm{d}T - (\mu_\uparrow - eV + \mu H^*)\mathrm{d}n_\uparrow - (\mu_\downarrow - eV - \mu H^*)\mathrm{d}n_\downarrow, \tag{9.4}$$

where s is the entropy density. We can thus set a spin-resolved *magneto-electrochemical potential* [538, 539, 540], which gathers the chemical, electrical and magnetic forces that are exerted on each spin carrier:

$$\begin{cases} \overline{\mu_\uparrow} = \mu_\uparrow - e\Phi + \mu H^* \\ \overline{\mu_\downarrow} = \mu_\downarrow - e\Phi - \mu H^* \end{cases}. \tag{9.5}$$

In References [538, 539, 540], H^* is considered to be a thermodynamic force such that $H^* = 0$ at equilibrium. It may contain complicated contributions such as the external applied magnetic field, the magnetic exchange field, the dipolar field, the crystalline anisotropy field and some other contributions coming from quantum effects. It is assumed to vanish unless a clear driving source of external or non-thermal internal field is justified. This assumption of **global equilibrium** (HF) ensures that no external edge force is applied to the system.

Having defined the thermodynamic potential we need, the theory is then based on phenomenological linear relations that link the generalized current densities to the generalized forces called the Onsager relations [541]:

$$\boxed{\begin{cases} -ej_\uparrow = \sigma_\uparrow \partial_x \overline{\mu_\uparrow} \\ -ej_\downarrow = \sigma_\downarrow \partial_x \overline{\mu_\downarrow} \\ \nu = \alpha(\mu_\uparrow - \mu_\downarrow) \end{cases}}, \tag{9.6}$$

where we have introduced the spin-resolved conductivities $\sigma_\uparrow$ and $\sigma_\downarrow$, and α is a constant that depends on the material and is related to a characteristic spin-flip time. The sign of α is not fixed at this point.

The second law of thermodynamics leads us to look for an equilibrium condition that is a fixed point of the energy that ensures that entropy cannot decrease. Considering that the whole system is at **thermal equilibrium** (HT) such that the temperature T is constant and uniform in the device, imposed by the surrounding heat bath, the first law along with the equation of the free energy 9.4 thus leads to the following inequality:

$$T\frac{\partial s}{\partial t} = -\overline{\mu_\uparrow}\partial_t n_\uparrow - \overline{\mu_\downarrow}\partial_t n_\downarrow \geqslant 0. \tag{9.7}$$

Inserting the continuity equation thus leads to

$$T\frac{\partial s}{\partial t} = \overline{\mu_\uparrow}\partial_x j_\uparrow + \overline{\mu_\downarrow}\partial_x j_\uparrow + \nu(\overline{\mu_\uparrow} - \overline{\mu_\downarrow}) \geqslant 0. \tag{9.8}$$

Plugging the Onsager relations then give

$$T\frac{\partial s}{\partial t} = -\overline{\mu_\uparrow}\partial_x\left(\frac{\sigma_\uparrow}{e}\partial_x\overline{\mu_\uparrow}\right) - \overline{\mu_\downarrow}\partial_x\left(\frac{\sigma_\downarrow}{e}\partial_x\overline{\mu_\downarrow}\right) + \alpha(\overline{\mu_\uparrow} - \overline{\mu_\downarrow})^2 \geqslant 0. \tag{9.9}$$

Finally, integrating over a specific material, following the global equilibrium hypothesis (HF) such that the thermodynamical forces vanish at the edges under no external constraint, we integrate by parts and obtain

$$T\frac{\partial S}{\partial t} = \int \mathrm{d}x \left\{\frac{\sigma_\uparrow}{e}(\partial_x\overline{\mu_\uparrow})^2 + \frac{\sigma_\downarrow}{e}(\partial_x\overline{\mu_\downarrow})^2 + \alpha(\overline{\mu_\uparrow} - \overline{\mu_\downarrow})^2\right\} \geqslant 0. \tag{9.10}$$

With these assumptions, the positivity of this functional under every applied potential leads to $\alpha > 0$.

9.1.2 The spin diode characteristic

We postulate that the spintronic engine features a non-linear feedback mechanism that allows it to adapt its behavior to the forces that are acting on it, such that it can generate power by converting some electromagnetic or thermal input into electricity. This consideration is strongly backed by the experimental results of Part II that showcase devices with strongly non-linear behavior (see Figures 6.1, 6.2, 6.6, 7.1). Just as in the Brillouin paradox [534, 535, 536, 537] one phenomenological proposal would be that the engine is acting as a spin diode that rectifies the spin current in order to generate a charge current. Going back to the microscopic view developed in the previous Chapter, it seems reasonable to think that the energy levels of the conducting quantum dots depend on the forces exerted on them, in line with the previous models describing transport in these spintronic devices [18]. In particular, it would mean that the spin-splitting of each energy level would depend on the nearby potentials. And, as we saw in the resonant tunneling diode model presented in the introduction of this chapter (see Figure 9.1), the position of the energy levels relative to the potential directly impacts the conductivity of the material, eventually leading to the phenomenon of negative differential resistance.

The spinterface may play a crucial role in the emergence of this non-linear behavior. Previous studies have indeed highlighted the potential of individual molecules to act as Maxwell demons by selectively permitting the transport of specific electrons with the adequate energy to tunnel across the molecular interface, while blocking the reverse transport [405], thanks to the rules of covalence. These theoretical insights may therefore be completed by several experimental studies on the spinterface that revealed key ingredients corroborating these findings, most notably a strong spin-filtering effect and a narrow energetic bandwidth [264, 480, 465].

These general phenomenological considerations therefore lead us to consider a spin diode characteristic, by proposing the following non-linear dependence of the conductivity

of the spin-diode material that is effectively inside the junction's nanotransport path:

$$\begin{cases} \sigma_\uparrow = \sigma_\uparrow^- + (\sigma_\uparrow^+ - \sigma_\uparrow^-)\theta(\Delta\overline{\mu}) \\ \sigma_\downarrow = \sigma_\downarrow^- + (\sigma_\downarrow^+ - \sigma_\downarrow^-)\theta(\Delta\overline{\mu}) \end{cases}, \tag{9.11}$$

where θ is the Heaviside step function. These relations allow the conductivity of each spin channel to be modulated by the *spin-potential* $\Delta\overline{\mu} \equiv \overline{\mu_\uparrow} - \overline{\mu_\downarrow}$, such as it can take two values depending on the sign of the spin-potential: σ_s^+ when the spin potential is positive and σ_s^- otherwise. Two limit cases have a critical importance: when $\sigma_s^- \ll \sigma_s^+$, then the conduction is favored when the spin-potential is positive, and when $\sigma_s^- \gg -\sigma_s^+$ then the conduction is favored when the spin-potential is negative. Note that, in these limits and at this stage, while each spin channel acts as a spin diode, no correlations between the channels, to determine the relative direction of each spin-sub channel diode, has so far been set.

We define the total conductivity $\sigma \equiv \sigma_\uparrow + \sigma_\downarrow$ and the conductivity asymmetry $\beta \equiv \frac{\sigma_\uparrow - \sigma_\downarrow}{\sigma} \in [-1, 1]$, such that the diode relations read:

$$\boxed{\begin{cases} \sigma = \sigma_- + (\sigma_+ - \sigma_-)\theta(\Delta\overline{\mu}) \\ \beta = \beta_- + (\beta_+ - \beta_-)\theta(\Delta\overline{\mu}) \end{cases}}. \tag{9.12}$$

9.1.3 Solving the equations with a charge current

In this section, we solve the continuity equation with the non-linear Onsager relations we posited under the **stationary current** hypothesis (HJ) stating that the device is connected to a source delivering a constant and uniform charge current. In the next section, we will then use these results to relax this condition and study the response of the device to a **stochastic current** (HS) in order to observe how this device could be used to harvest the noise power provided by some thermal or magnetic fluctuations directly impacting the spin channel-resolved transport in an asymmetrical way.

The spin-potential equation

Having defined the conductivity of the diode material, we can now try to solve the system of equations formed by the continuity equation 9.1 and the Onsager relations 9.6. We want to find a stationary solution such that $\partial_t n_\uparrow = \partial_t n_\downarrow = 0$. The continuity equation thus imposes the uniformity of the charge current $\partial_x j = 0$ and the variation $\partial_x \Delta j = -2\nu$ of the spin-current $\Delta j \equiv j_\uparrow - j_\downarrow$. Setting the electron potential $\overline{\mu} \equiv \overline{\mu_\uparrow} + \overline{\mu_\downarrow}$, we rewrite the Onsager relations as

$$\begin{cases} -ej = \beta\sigma\partial_x\Delta\overline{\mu} + \sigma\partial_x\overline{\mu} \\ -e\Delta j = \sigma\partial_x\Delta\overline{\mu} + \sigma\beta\partial_x\overline{\mu} \\ \nu = \alpha\Delta\overline{\mu} \end{cases}. \tag{9.13}$$

To avoid any complications due to the differentiation of the step functions θ, we place ourselves in the domains where $\Delta\overline{\mu} \neq 0$, in which case differentiating the previous system and injecting it into the stationary conditions leads to the well-known equation [49, 539, 542, 543]:

$$\boxed{\partial_x^2\Delta\overline{\mu} - \lambda^{-2}\Delta\overline{\mu} = 0,} \tag{9.14}$$

where we have defined the spin-diffusion characteristic length $\lambda^{-2} = \frac{e\alpha}{\sigma(1-\beta^2)}$. In the same manner as the conductivity changes with respect to the sign of $\Delta\overline{\mu}$, the above equation has two behaviors that are dictated by two different spin-diffusion lengths which are respectively in the regions where $\Delta\overline{\mu} > 0$ and $\Delta\overline{\mu} < 0$, such that we can also write $\lambda = \lambda_- + (\lambda_+ - \lambda_-)\theta(\Delta\overline{\mu})$, where λ_+ and λ_- are the spin-diffusion lengths in the diode for the two signs of the spin-potential.

The boundary conditions

Now that the equation governing $\Delta\overline{\mu}$ is established, we can solve it with the appropriate boundary conditions. The conditions are set in the far edges of the electrodes $x = \pm x_\infty$ and at the two interfaces between the electrodes and the diode material at $x = \pm l$. Standard approaches [49, 538] give the following conditions at the edges:

- **Global equilibrium** (HF): all potential differences are null between the two edges at equilibrium ($j = 0$): $\overline{\mu_s}(+x_\infty) - \overline{\mu_s}(-x_\infty) = \mu_s(+x_\infty) - \mu_s(-x_\infty) = \Phi(+x_\infty) - \Phi(-x_\infty) = H^*(+x_\infty) - H^*(-x_\infty)$. This condition is set to ensure that the device is not powered by any external thermodynamic force other than the injected current j.

- **Ground fixing** (HG): an arbitrary constant voltage V_0 may be set somewhere in the system, defining a reference point for all potentials.

Then, at each interface, the following conditions are typically considered:

1. **Spin conservation** (H1): the spin currents are continuous across the interface, such as we assume no surface spin relaxation: $j_s(x = \pm l^+) = j_s(x = \pm l^-) = j_s(x = \pm l)$.
2. **Interface resistance** (H2): some kind of spin-scattering effect that occurs at the interface results in a discontinuity of the spin magneto-electrochemical potential and is directly proportional to the spin current, such that there may be a spin-dependent interface resistance r_s that verifies $\overline{\mu}_s(x = \pm l^+) - \overline{\mu}_s(x = \pm l^-) = r_{s\pm} j_s(x = \pm l)/e$. In the following the interface resistances will be set to $r_s = 0$.
3. **Charge conservation** (H3): the electric current $-e(j_\uparrow + j_\downarrow)$ is continuous across the interface. This is in accordance with the assumption of stationarity and uniformity of the current detailed above, which fixes a constant charge current $-ej$ everywhere in the material that, at this point, is provided by an external source. This condition is redundant given the conservation of both spin currents but it holds as stronger if the former assumption were to be relaxed.

The conditions at the edges give two equations for $\Delta\overline{\mu}$, and each interface gives two conditions for the spin potential and its derivative, leading to a total of six conditions. These conditions will be discussed further in the next section. Indeed, these assumptions are usual in the case of passive spintronics, although here, we aim at describing an engine which must be powered by some external thermodynamic force, most likely of magnetic

origin. We will therefore challenge them in what follows in order to account for some kind of magnetic driving which we believe to be permanent or with a negligible decay and self-sustained in our system.

Solutions with a charge current

Let us now solve the equation in the three domains and then link them with the boundary conditions.

- In the left electrode, given the global equilibrium condition, the solution reads for all $x < -l$:

$$\Delta\overline{\mu}(x) = Ae^{x/\lambda_L}, \tag{9.15}$$

  where λ_L is the spin-diffusion length of the left electrode.

- In the diode, the solution depends on the sign of $\Delta\overline{\mu}$. For all $x \in]-l, l[$, we have

$$\begin{cases} \Delta\overline{\mu}(x) = Be^{x/\lambda^-} + Ce^{-x/\lambda^-} & \text{if } \Delta\overline{\mu}(x) < 0 \\ \Delta\overline{\mu}(x) = De^{x/\lambda^+} + Ee^{-x/\lambda^+} & \text{if } \Delta\overline{\mu}(x) > 0 \end{cases} \tag{9.16}$$

  We immediately see that we are faced with a difficulty here. Supposing that the boundary conditions lead to $\Delta\overline{\mu}(-l) < 0$, for any integration constants $B,\ C$, the function $x \to Be^{x/\lambda^-} + Ce^{-x/\lambda^-}$ either has zero or one root in the range $x \in]-l, l[$. In case it has none, then the solution will remain in the negative branch in the diode material. And in case it has one, then we will need to connect the positive and the negative branches at the point where the function vanishes. Applying the same reasoning to the negative branch, we thus conclude that the spin-potential in the diode can only have at most one root. The objective of the study will thus be to characterize those two cases.

- In the right electrode, the solution is for all $x > l$:

$$\Delta\overline{\mu}(x) = Fe^{-x/\lambda_R}, \tag{9.17}$$

  where λ_R is the spin-diffusion length of the right electrode.

The integration constants will be fixed by the interface conditions and the geometry and will determine the number of roots of the spin potential in the diode material.

The thin barrier limit $\Delta\overline{\mu} \neq 0$

Let us first consider that the two interfaces have a **null interface resistance** (H2b) for each spin channel: $r_{s\pm} = 0$. And let us start by assuming the **negative diode hypothesis** (H-), which corresponds to the case where the spin potential in the diode maintains a constant negative sign $\Delta\overline{\mu}(x) < 0$. Using Equation 9.13, we have the derivative:

$$2e\alpha\lambda^2\partial_x\Delta\overline{\mu} = \sigma(1-\beta^2)\partial_x\Delta\overline{\mu} = e\beta j - e\Delta j. \tag{9.18}$$

Therefore, using the continuity of the spin and charge currents at the two interfaces (H1) and (H3), we get:

$$\begin{cases} \alpha_L \lambda_L^2 \partial_x \Delta\overline{\mu}(-l^-) - \alpha_D \lambda_-^2 \partial_x \Delta\overline{\mu}(-l^+) = j(\beta_L - \beta_-)/2 \\ \alpha_R \lambda_R^2 \partial_x \Delta\overline{\mu}(l^+) - \alpha_D \lambda_-^2 \partial_x \Delta\overline{\mu}(l^-) = j(\beta_R - \beta_-)/2 \end{cases} \tag{9.19}$$

Then the continuity of the potential at the interface (H2b) leads to a linear system of 4 equations that we can solve to find the integration constants:

$$\begin{pmatrix} e^{-l/\lambda_L} & -e^{-l/\lambda_-} & -e^{l/\lambda_-} & 0 \\ \alpha_L \lambda_L e^{-l/\lambda_L} & -\alpha_- \lambda_- e^{-l/\lambda_-} & \alpha_- \lambda_- e^{l/\lambda_-} & 0 \\ 0 & -\alpha_- \lambda_- e^{l/\lambda_-} & \alpha_- \lambda_- e^{-l/\lambda_-} & \alpha_R \lambda_R e^{-l/\lambda_R} \\ 0 & e^{l/\lambda_-} & e^{-l/\lambda_-} & -e^{-l/\lambda_R} \end{pmatrix} \begin{pmatrix} A \\ B \\ C \\ F \end{pmatrix} = \frac{j}{2} \begin{pmatrix} 0 \\ \beta_L - \beta_- \\ \beta_R - \beta_- \\ 0 \end{pmatrix} \tag{9.20}$$

To simplify, let us then consider the **uniform spin flip** hypothesis (Hα) such as the spin flip probability is identical in the three materials, namely $\alpha_L = \alpha_R = \alpha_- = \alpha_+ \equiv \alpha > 0$. Inverting the matrix, with discriminant $d_- \equiv (\lambda_L - \lambda_-)(\lambda_- + \lambda_R)e^{-4l/\lambda_-} + (\lambda_L + \lambda_-)(\lambda_- - \lambda_R)$, we obtain the solution:

$$\begin{cases} A = \frac{je^{l/\lambda_L}}{2d\alpha} \Big\{ \big[(\lambda_- + \lambda_R)e^{-4l/\lambda_-} + (\lambda_- - \lambda_R)\big](\beta_L - \beta_-) - 2\lambda_- e^{-2l/\lambda_-}(\beta_R - \beta_-) \Big\} \\ B = \frac{je^{-l/\lambda_-}}{2d\alpha} \Big\{ e^{-2l/\lambda_-}(\lambda_- + \lambda_R)(\beta_L - \beta_-) - (\lambda_- + \lambda_L)(\beta_R - \beta_-) \Big\} \\ C = \frac{je^{-l/\lambda_-}}{2d\alpha} \Big\{ (\lambda_- - \lambda_R)(\beta_L - \beta_-) - e^{-2l/\lambda_-}(\lambda_- - \lambda_L)(\beta_R - \beta_-) \Big\} \\ F = \frac{je^{l/\lambda_R}}{2d\alpha} \Big\{ 2\lambda_- e^{-2l/\lambda_-}(\beta_L - \beta_-) - \big[e^{-4l/\lambda_-}(\lambda_- - \lambda_L) + (\lambda_- + \lambda_L)\big](\beta_R - \beta_-) \Big\} \end{cases} \tag{9.21}$$

These expressions are quite complicated so we need further approximations in order to get insights into the distribution of the spin potential within the junction.

The previous analysis is only valid when $\Delta\overline{\mu}$ stays negative in the diode (H-). To confirm this, we just need to check that $\Delta\overline{\mu}(-l) < 0$ and $\Delta\overline{\mu}(l) < 0$. Indeed, a simple application of the intermediate value theorem shows that, since $\Delta\overline{\mu}$ vanishes at most once in $[-l, l]$, the function $\Delta\overline{\mu}$ has a single root in the diode iff $\Delta\overline{\mu}(-l)$ and $\Delta\overline{\mu}(l)$ have a different sign, otherwise its sign remains constant.

To ensure that $\Delta\overline{\mu}$ does not change sign, physical intuition leads us to consider a **thin barrier** (Hb) which corresponds to case where $l \ll \lambda_-, \lambda_+$. In this approximation, we have:

$$d_- = 2\lambda_-(\lambda_L - \lambda_R)\left(1 + \frac{2l}{\lambda_-}\frac{(\lambda_- + \lambda_R)(\lambda_- - \lambda_L)}{\lambda_-(\lambda_L - \lambda_R)}\right) + o\left(\frac{l}{\lambda_-}\right), \tag{9.22}$$

$$\Delta\overline{\mu}(-l) = \frac{j}{2\alpha}\frac{\beta_L - \beta_R}{\lambda_L - \lambda_R}\left\{1 + \frac{2l}{\lambda_-}\left[1 - \frac{\lambda_R}{\lambda_-}\frac{\beta_L - \beta_-}{\beta_L - \beta_R} - \frac{(\lambda_- + \lambda_R)(\lambda_- - \lambda_L)}{\lambda_-(\lambda_L - \lambda_R)}\right]\right\} + o\left(\frac{l}{\lambda_-}\right), \tag{9.23}$$

and

$$\Delta\overline{\mu}(l) = \frac{j}{2\alpha}\frac{\beta_L - \beta_R}{\lambda_L - \lambda_R}\left\{1 + \frac{2l}{\lambda_-}\left[1 - \frac{\lambda_L}{\lambda_-}\frac{\beta_R - \beta_-}{\beta_L - \beta_R} - \frac{(\lambda_- + \lambda_R)(\lambda_- - \lambda_L)}{\lambda_-(\lambda_L - \lambda_R)}\right]\right\} + o\left(\frac{l}{\lambda_-}\right). \tag{9.24}$$

From these expressions, we see that $\Delta\overline{\mu}(-l) \sim \Delta\overline{\mu}(l) \sim \frac{j}{2\alpha}\frac{\beta_L-\beta_R}{\lambda_L-\lambda_R}$. To comment on this result, we see that $\Delta\overline{\mu}$ is fully determined by the sign of j along with the ratio $\frac{\beta_L-\beta_R}{\lambda_L-\lambda_R}$ intrinsic to the electrodes. Assuming that this quantity is positive, the above expressions are thus valid only if $j < 0$.

The previous calculation yielded a solution for $\Delta\overline{\mu} < 0$ within the negative diode hypothesis (H-), which required $j < 0$. Similarly, the solution for the **positive diode** case (H+) $\Delta\overline{\mu} > 0$ requires $j > 0$ and is obtained by replacing λ_- by λ_+ and β_- by β_+ in the expressions above. We thus now have two different behaviors depending on the sign of j, which reflect the asymmetric behavior of the device, leading to two different distributions of the potential within the diode. In Figure 9.3, we plot the distribution of $\Delta\overline{\mu}$ for $\lambda_+ < \lambda_-$ in the two cases of $j > 0$, and $j < 0$, keeping the same magnitude of the current for both cases. This figure shows the strong asymmetry of the integral under $\Delta\overline{\mu}$ with the direction of the current. This asymmetry will be used in the next section to show how the device can rectify the current fluctuations and generate power.

We can now calculate the potential difference induced by the current. Without some kind of additional interacting probe relying on a mechanism such as the spin Hall effect, it is not possible to measure separately the different conduction channels in this system because any realistic electric contact shortcuts the two channels, and we need the usual Ohm's law to relate the current to the electric field $ej = -\sigma\partial_x\Phi$. This unperturbed electric field $-\partial_x\Phi$ adds to a non-equilibrium electric field $-\partial_x V$ that may be defined from the total potential $\overline{\mu}$ as [49]:

$$e\partial_x V \equiv -\partial_x\overline{\mu} + e\partial_x\Phi = -\beta\partial_x\Delta\overline{\mu}, \tag{9.25}$$

We can thus calculate the voltage difference ΔV induced by the non-equilibrium current:

$$\boxed{e\Delta V = -\int_{-\infty}^{+\infty} \beta\partial_x\Delta\overline{\mu} = (\beta_- - \beta_L)\Delta\overline{\mu}(-l) + (\beta_R - \beta_-)\Delta\overline{\mu}(l).} \tag{9.26}$$

and the dissipated power $P \equiv eaj\Delta V$, which yields in the **thin barrier** limit (Hb):

$$P \sim -\frac{aj^2}{2\alpha}\frac{(\beta_L - \beta_R)^2}{\lambda_L - \lambda_R}. \tag{9.27}$$

The general case

Let us now briefly look into the general case where the barrier can have a thickness. In this case, the potential $\Delta\overline{\mu}$ may change sign within the barrier. Let us assume that $\Delta\overline{\mu}(-l) < 0$ and that there exists $x_0 \in]-l, l[$ such as $\Delta\overline{\mu}(x_0) = 0$, corresponding to the **negative vanishing potential** hypothesis (HV-). The continuity of the spin currents in the diode (H1) thus also imposes that $\partial_x\Delta\overline{\mu}$ be continuous in $x = x_0$. The two additional conditions $\Delta\overline{\mu}(x_0^-) = 0$ and $\Delta\overline{\mu}(x_0^+) = 0$ lead to two linear systems of three equations parametrized by x_0 that should be solved to obtain the integration constants:

$$\begin{pmatrix} e^{-l/\lambda_L} & -e^{-l/\lambda_-} & -e^{l/\lambda_-} \\ \lambda_L e^{-l/\lambda_L} & -\lambda_- e^{-l/\lambda_-} & \lambda_- e^{l/\lambda_-} \\ 0 & e^{x_0/\lambda_-} & e^{-x_0/\lambda_-} \end{pmatrix} \begin{pmatrix} A \\ B \\ C \end{pmatrix} = \frac{j}{2\alpha} \begin{pmatrix} 0 \\ \beta_L - \beta_- \\ 0 \end{pmatrix} \tag{9.28}$$

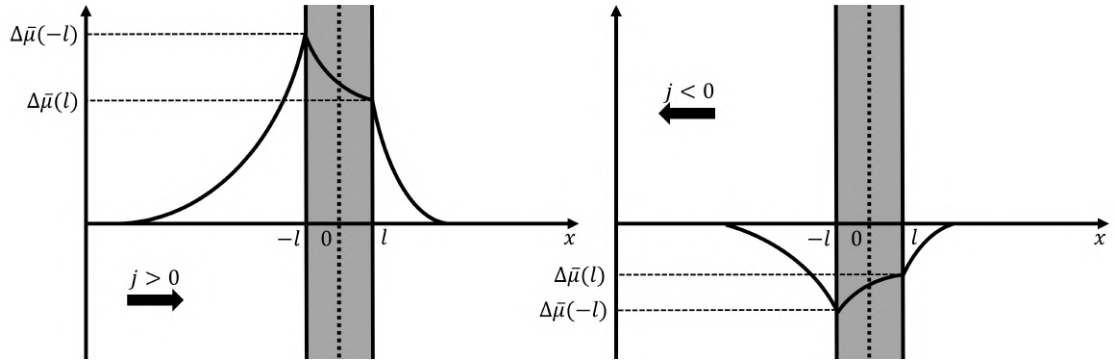

Figure 9.3: **Asymmetry of the spin potential.** Plots of the spin potential $\Delta\overline{\mu}$ with respect to x in the two cases of the positive diode (H+) where $j > 0$ (left panel) and negative diode where (H-) $j < 0$ (right panel) in the thin barrier limit (Hb). We chose $\lambda_+ < \lambda_-$ along with $|\beta_+|, |\beta_-| \ll \frac{\lambda_R\beta_L - \lambda_L\beta_R}{\lambda_L - \lambda_R} < 0$ and the same magnitude of j in both cases.

and

$$\begin{pmatrix} e^{x_0/\lambda_+} & e^{-x_0/\lambda_+} & 0 \\ -\lambda_+ e^{l/\lambda_+} & \lambda_+ e^{-l/\lambda_+} & \lambda_R e^{-l/\lambda_R} \\ e^{l/\lambda_+} & e^{-l/\lambda_+} & -e^{-l/\lambda_R} \end{pmatrix} \begin{pmatrix} D \\ E \\ F \end{pmatrix} = \frac{j}{2\alpha} \begin{pmatrix} 0 \\ \beta_R - \beta_+ \\ 0 \end{pmatrix} \tag{9.29}$$

Setting the two discriminants:

$$d_{L-} = (\lambda_L - \lambda_-)e^{-2l/\lambda_-} - (\lambda_L + \lambda_-)e^{2x_0/\lambda_-} \text{ and } d_{R+} = (\lambda_R - \lambda_+)e^{2l/\lambda_+} - (\lambda_R + \lambda_+)e^{2x_0/\lambda_+}, \tag{9.30}$$

wet get the solutions

$$\begin{cases} A = \frac{j}{2\alpha d_{L-}}(\beta_L - \beta_-)e^{l/\lambda_L}(e^{-2l/\lambda_-} - e^{2x_0/\lambda_-}) \\ B = \frac{j}{2\alpha d_{L-}}(\beta_L - \beta_-)e^{-l/\lambda_-} \\ C = -\frac{j}{2\alpha d_{L-}}(\beta_L - \beta_-)e^{-l/\lambda_-}e^{2x_0/\lambda_-} \end{cases}, \tag{9.31}$$

and

$$\begin{cases} D = -\frac{j}{2\alpha d_{R+}}(\beta_R - \beta_+)e^{l/\lambda_+} \\ E = \frac{j}{2\alpha d_{R+}}(\beta_R - \beta_+)e^{l/\lambda_+}e^{2x_0/\lambda_+} \\ F = -\frac{j}{2\alpha d_{R+}}(\beta_R - \beta_+)e^{l/\lambda_R}(e^{2l/\lambda_+} - e^{2x_0/\lambda_+}) \end{cases}. \tag{9.32}$$

Then, this linear solution needs to be complemented by a non-linear feedback that corresponds to an equation on x_0. Indeed, the solution also needs to verify the continuity equation for the spin currents (H1), leading to an extra equation:

$$\frac{B}{\lambda_-}e^{x_0/\lambda_-} - \frac{C}{\lambda_-}e^{-x_0/\lambda_-} = \frac{D}{\lambda_+}e^{x_0/\lambda_+} - \frac{E}{\lambda_+}e^{-x_0/\lambda_+}, \tag{9.33}$$

which gives after some algebra, using the above expressions for the integration constants:

$$\lambda_+\frac{\lambda_R - \lambda_+}{\beta_R - \beta_+}e^{-\frac{x_0-l}{\lambda_+}} - \lambda_+\frac{\lambda_R + \lambda_+}{\beta_R - \beta_+}e^{\frac{x_0-l}{\lambda_+}} = \lambda_-\frac{\lambda_L - \lambda_-}{\beta_L - \beta_-}e^{-\frac{x_0+l}{\lambda_-}} - \lambda_-\frac{\lambda_L + \lambda_-}{\beta_L - \beta_-}e^{\frac{x_0+l}{\lambda_-}} \tag{9.34}$$

or equivalently

$$\frac{\lambda_+}{\beta_R - \beta_+}\left[\lambda_+ \operatorname{ch}\left(\frac{x_0 - l}{\lambda_+}\right) + \lambda_R \operatorname{sh}\left(\frac{x_0 - l}{\lambda_+}\right)\right] = \frac{\lambda_-}{\beta_L - \beta_-}\left[\lambda_- \operatorname{ch}\left(\frac{x_0 + l}{\lambda_-}\right) + \lambda_L \operatorname{sh}\left(\frac{x_0 + l}{\lambda_-}\right)\right]. \tag{9.35}$$

Similarly, if we assume that $\Delta\overline{\mu}(-l) > 0$ and $\Delta\overline{\mu}$ vanishes in the diode under the **positive vanishing potential** hypothesis (HV+), we obtain a similar equation by changing λ_+ and β_+ to λ_- and β_-. The reasoning can now be studied in reverse, and we obtain that the spin-potential vanishes within the diode iff there is a solution $x_0 \in]-l, l[$ to one of these two equations.

9.1.4 Solving the equations with a stochastic current

Let us now focus on the simplest case, where $\Delta\overline{\mu}$ does not change sign in the diode ((H+) and (H-)). As we showed, a sufficiently thin barrier is guaranteeing this condition. Let us now consider that the device is subjected to a stochastic current $\mathcal{J}$ over a bandwidth J such that $\mathcal{J}$ is described by a Brownian noise $\mathcal{J} \sim \mathcal{N}(0, J)$, referenced as the **stochastic current** hypothesis (HS) in Table 9.2. Assuming that the bandwidth does not match the characteristic relaxation time of the system, no resonance should be generated from this excitation so that we can consider the system to remain in a stationary non-equilibrium state ($\partial_t n_\uparrow = \partial_t n_\downarrow = 0$) and the equations of motion remain valid. The average of the spin potential $\langle\Delta\overline{\mu}\rangle$ can now be calculated by separating the distribution with respect to the sign of $\mathcal{J}$. For writing purposes, let us define the two distributions $\Delta\overline{\mu}$ as:

$$\Delta\overline{\mu}(x < -l, j < 0) = \frac{j}{2\alpha l_-} e^{\frac{x+l}{\lambda_L}} \text{ and } \Delta\overline{\mu}(x < -l, j > 0) = \frac{j}{2\alpha l_+} e^{\frac{x+l}{\lambda_L}}, \tag{9.36}$$

and

$$\Delta\overline{\mu}(x > l, j < 0) = \frac{j}{2\alpha r_-} e^{\frac{-x+l}{\lambda_R}} \text{ and } \Delta\overline{\mu}(x > l, j > 0) = \frac{j}{2\alpha r_+} e^{\frac{-x+l}{\lambda_R}}, \tag{9.37}$$

where $l_\pm$ and $r_\pm$ are constants with the unit of a length that depend only on the geometry and the material properties. We point out that we should not need to write the spin potential within the barrier since the quantities we need to calculate only depend on the value of $\Delta\overline{\mu}$ at the interfaces, which is given by its value in the electrodes, by continuity. With these expressions, we can write the average as

$$\langle\Delta\overline{\mu}(x)\rangle = \int_{-\infty}^{0} \frac{\mathrm{d}j}{J\sqrt{2\pi}} e^{-\frac{1}{2}(\frac{j}{J})^2} \Delta\overline{\mu}(x, j < 0) + \int_{0}^{+\infty} \frac{\mathrm{d}j}{J\sqrt{2\pi}} e^{-\frac{1}{2}(\frac{j}{J})^2} \Delta\overline{\mu}(x, j > 0). \tag{9.38}$$

We can thus evaluate the average potential at the interfaces:

$$\langle\Delta\overline{\mu}(x = -l)\rangle = \frac{J}{2\alpha\sqrt{2\pi}} \left(\frac{1}{l_+} - \frac{1}{l_-}\right) \text{ and } \langle\Delta\overline{\mu}(x = l)\rangle = \frac{J}{2\alpha\sqrt{2\pi}} \left(\frac{1}{r_+} - \frac{1}{r_-}\right), \tag{9.39}$$

which leads us to the average voltage:

$$\boxed{e\langle\Delta V\rangle = \frac{J}{2\alpha\sqrt{2\pi}} \left(\frac{\beta_+ - \beta_L}{l_+} - \frac{\beta_- - \beta_L}{l_-} + \frac{\beta_R - \beta_+}{r_+} - \frac{\beta_R - \beta_-}{r_-}\right),} \tag{9.40}$$

and the average power

$$\boxed{\langle P\rangle = \sqrt{\frac{\pi}{2}} eaJ\langle\Delta V\rangle.} \tag{9.41}$$

On average, it thus looks like the device is rectifying the current fluctuations into a direct current density of magnitude $\sqrt{\frac{\pi}{2}}J$, while displaying a built-in bias voltage of $\langle \Delta V \rangle$. The sign of $\langle \Delta V \rangle$ will then tell us if the device is dissipating or producing energy. Given the passive sign convention taken, the device is active when $\langle P \rangle < 0$ and thus when $\langle \Delta V \rangle < 0$.

The strong diode case in the thin barrier limit

Let us now study a couple of limit cases to gain insights into the physics lying behind the previous calculation. We coin the **strong parallel diode limit** (HP) as the case where $\lambda_- \ll \lambda_+$ and the **strong anti-parallel diode limit** (HAP) the case where $\lambda_+ \ll \lambda_-$. These two assumptions correspond to cases where the spin diffusion is greatly enhanced for one spin carrier with respect to the other. To ensure that the sign of the spin potential remains constant within the barrier, we must still impose the thin barrier condition (Hb) $l \ll \lambda_+, \lambda_-$. In the parallel case (HP), we obtain the following expression for the potential:

$$e\langle \Delta V \rangle \sim \frac{Jl(\beta_L - \beta_R)^2}{\alpha\sqrt{2\pi}\lambda_-(\lambda_L - \lambda_R)} \Bigg\{ 1 - \frac{(\lambda_+ + \lambda_R)(\lambda_+ - \lambda_L)}{\lambda_+(\lambda_L - \lambda_R)} + \Bigg[\frac{\lambda_R}{\lambda_+} \left(\frac{\beta_L - \beta_+}{\beta_L - \beta_R} \right)^2 - \frac{\lambda_L}{\lambda_+} \left(\frac{\beta_R - \beta_+}{\beta_R - \beta_L} \right)^2 \Bigg] \Bigg\}. \quad (9.42)$$

The first term corresponds to a contribution mainly due to the difference in electrode material and spin-diffusion lengths. The second term is a correction originating from the diode material, and the third term incorporates the spin-diffusion asymmetry of the diode with respect to the electrodes. We see that the sign of $\langle \Delta V \rangle$ is mainly affected by the sign of $\lambda_L - \lambda_R$. The study of the anti-parallel case gives the same formula, replacing λ_- by λ_+ and with an opposite sign in front. This derivation thus shows that an active device may be obtained favorably in the anti-parallel diode case (HAP) if $\lambda_R > \lambda_L$ and in the parallel diode case (HP) otherwise. It also shows that a non-null potential requires $\beta_L \neq \beta_R$ such as the two electrodes must have a different asymmetry to generate an output. However, their relative difference has a bounded impact on the voltage since $0 \leqslant (\beta_L - \beta_R)^2 \leqslant 4$, and since β depends on the specific properties of the material such as structure, chemical composition and magnetization, choosing different electrodes should guarantee $\beta_R \neq \beta_L$. In particular, since β, and in particular its sign, depends on the quantization axis, β_R and β_L should strongly depend on the magnetization difference between the two electrodes, such as a favorable magnetic orientation could be sufficient for this term to contribute significantly.

The weak diode case in the thin barrier limit

We name the **weak diode** case (HW) the situation where $\lambda_+ \sim \lambda_- \equiv \lambda$, in which the spin diffusion is similar for the two spin carriers within the diode. In the thin barrier limit (Hb)

with $l \ll \lambda$, we obtain the following equivalent for the potential:

$$e\langle \Delta V \rangle \sim -\frac{Jl(\beta_+ - \beta_-)}{\alpha\sqrt{2\pi}\lambda^2}\left(\beta_+ + \beta_- + 2\frac{\lambda_L\beta_R - \lambda_R\beta_L}{\lambda_L - \lambda_R}\right) = \mathcal{O}\left(\frac{4Jl(\lambda_L + \lambda_R)}{\alpha\sqrt{2\pi}\lambda^2(\lambda_L - \lambda_R)}\right). \tag{9.43}$$

To obtain an active device, the asymmetries of the diode must then be fixed to match this asymmetry of the electrodes: the parameters β_- and β_+ have to be chosen such as to ensure that $(\beta_+ - \beta_-)\left(\beta_+ + \beta_- + 2\frac{\lambda_L\beta_R - \lambda_R\beta_L}{\lambda_L - \lambda_R}\right)$ is positive.

In this configuration, we see that the bias voltage is directly proportional to $\beta_+ - \beta_-$. Therefore, the stronger the diode asymmetry, the larger the output power will be. Physically, this reflects the increased ability of the diode to rectify the current when the magnetization of the barrier is strongly driven by the current fluctuations.

Numerical Examples

Let us take two examples in the two cases we studied before in the thin barrier limit (Hb). In the following, we take Cobalt (Co) for the left electrode and Iron (Fe) for the right electrode, so as to ensure that $\beta_L \neq \beta_R$ and $\lambda_L \neq \lambda_R$. The total conductivities of Cobalt and Iron are $e\sigma_{Co} = 1.6 \times 10^7$ S/m and $e\sigma_{Fe} = 1.0 \times 10^7$ S/m [544] and their respective polarizations in MTJs are $\beta_{Co} = \beta_L = \pm 0.35$ and $\beta_{Fe} = \beta_R = \pm 0.4$ [545] (where the sign depends on the convention of the quantization axis). We take $e^2\alpha = 10^{21}$ S/m^3 which seems to be the spin-flip order of magnitude we can expect in these materials [49, 539]. It leads to the following spin-diffusion lengths $\lambda_{Co} = \lambda_L = 120$ nm and $\lambda_{Fe} = \lambda_R = 90$ nm. In Part II, we studied MTJ designed with a barrier width of $l \approx 3$ mn (see Table 5.1) and we saw in Chapter 4 that we can expect a current noise of amplitude $I \approx 10$ nA in the device so a current density noise amplitude of $eJ \approx 4$ A/m^2 given the section of radius 20 μm of the MTJs we designed in Chapter 5, keeping in mind that taking the hole cross-section of the device greatly exceeds the effective conduction area defined by the nanotransport paths.

- We consider for example a weak diode which has similar spin-diffusion lengths for the two signs of the spin-potential (HW), inherited from the properties of the electrodes. We take $\lambda_+ = \lambda_- = 100$ nm in order to stay within the thin barrier limit (Hb). Under this approximation, evaluating the upper-bound found in Equation 9.43 gives $|\langle \Delta V \rangle| \leqslant 10^{-14}$ V which is extremely low. Looking at this result and Equation 9.43, in order to increase this voltage we need to decrease α and λ, and increase J. To obtain an appreciable result, the hypothesis of uniform spin-flip (Hα) may be too strong and a diode material with a very low spin-flip characteristic time should be chosen. Then, a diode with a very low spin-diffusion length should be beneficial but it requires to step out of the thin barrier limit (Hb) and allow the potential to vanish within the barrier. Finally, we considered that the macroscopic intensity we measured experimentally was distributed evenly across the whole section of the wire, but as we saw in Part II, the current favorably flow across hotspots in the material where the impurities are located, we should therefore distribute I over a much narrower section. Taking a radius of 1 nm for the section thus allows to gain up to 9 orders of magnitude on J, but this is still not enough to obtain a voltage that could explain the

results presented in Chapter 4, as it would lead to $\Delta V = 10^{-5}$ V, and $P = 10^{-13}$ W. In the following, we take this remark into account and choose $eJ = 10^{9}$ A/m^2.

- Let us now look at the strong diode case, which should be the preferred scenario given the spin-filtering and hysteresis abilities of the spinterface. Equation 9.42 tells us that the same order of magnitude as the weak diode case will be obtained if the three contributing terms in the brackets are of the order of unity. Given the two hypotheses of the strong diode (HP) and the thin barrier (Hb), λ_+ and λ_- are bounded from below so a large voltage may only be obtained when λ_+ is very large so that the second term dominates:

$$\langle \Delta V \rangle \sim -\frac{Jl\lambda_+(\beta_L - \beta_R)^2}{\alpha\sqrt{2\pi}\lambda_-(\lambda_L - \lambda_R)^2}. \tag{9.44}$$

  The voltage now only depends on the ratio $\frac{\lambda_+}{\lambda_-}$ which represents the rectifying power of the diode. Taking $\frac{\lambda_+}{\lambda_-} = 1 - 10\mu$m which is reasonable if the device behaves as a dynamical spin filter ($\lambda \sim 1 - 10\mu m$ in organic molecular junctions [546, 547] and semiconductor quantum wells [548] and $\lambda = 0.1 - 1$ nm in ferromagnetic metals [549]). Taking this rectification, we obtain $V = 10^{-2}$ V, which gives a power of $\langle P \rangle = -10^{-10}$ W, closer to the power observed in the experiments and the device is guaranteed to be generative. The strong diode may therefore be suited to explain the rectification. Better results may be acquired by considering extreme materials with very large spin-diffusion lengths λ, low spin-flip probabilities α and with an extended model without the uniform spin-flip hypothesis (Hα).

9.1.5 Discussion on the spin diode model rectifying current fluctuations

The above derivation showed that the spin diode can rectify a stochastic Brownian current into a direct current on average, resulting in a net power output in the cases where a negative potential bias builds up in the device. The main criticism we can address is the same as the one raised by the Brillouin paradox [534, 535, 536, 537] or the ratchet and pawl system [550, 551, 552]. It would thus seem that we may have neglected an internal compensating noise effect within the diode that would prevent the device from generating power in the absence of a temperature gradient between the diode and the source of the current noise. Although, as we have seen in Chapters 2 and 3, devices can trade conserved quantities and use them as resources to perform operations, such as the diode may rely on a spin-temperature difference between two spin reservoirs instead of thermal baths. The counter-argument to the self-rectification impossibility here would thus be that even though every part of the device is considered to be at the same temperature, the spin diode is linked to two ferromagnetic electrodes with magnetizations that can be different in strengths and orientations, which generates a thermodynamic force used by the device. Indeed, a macroscopic gradient of temperature, electronic or magnetic fields between two baths can all be used to generate work with the right system. Therefore, we expect this magnetization gradient within the device to induce an effective temperature or potential

gradient acting differently on each spin carrier, allowing the device to harvest this resource. Indeed, as we saw in the previous Chapter, the magnetism of a material can have an effect on the spin-resolved electronic filing such that it can behave as an electronic potential acting oppositely on the two spin carriers (see Section 8.2.5). A more detailed study of the spin-resolved current noise that is generated by the ferromagnets and the diode may be needed to reach a more convincing answer to this criticism. Several reports have analyzed in more depths the fluctuations analogous to the Johnson-Nyquist noise in magnetic structures [514, 553, 554, 515] but the link with the spin diode remains to be made.

This work opens the path toward the experimental study of spin-resolved current noises inside ferromagnetic tunnel junctions. One objective would then be to characterize the noise produced by the junctions in response to a spin-polarized current in the hope of finding differences in the power spectrum of those fluctuations for different amplitudes of the spin-polarized current that would be the result of a difference in the effective temperature of the two spin carriers, which we could quantify and exploit to generate energy.

We saw that the model successfully gives a close but underestimated magnitude of the power output measured in the experiments in Chapter 4, for the case of a device with a strongly rectifying diode with realistic parameters. Finely tuning the properties of the electrodes and the diode may allow it to reach the power reported in the experiments but it requires the use of a strongly non-linear material that is able to change its conductive properties depending on the constraints that are applied to it. Justifying precisely that the device studied in this work indeed presents such behaviors needs further investigation.

Although the idea of rectifying current fluctuations between two spin reservoirs with different effective electronic temperatures driven by a magnetization gradient seems promising, the difficulties associated with the treatment of stochastic phenomena leads us to try and find a more systematic model that would directly feed the magnetization gradient as a non-equilibrium resource in a phenomenological model in order to prove its power-generating ability without noises. This is the subject of the next section.

9.2 Harvesting the non-equilibrium magnetization potential at the interface

This section will challenge the hypotheses at the interface of the previous model (H1), (H2) and (H3), to see how the magnetization difference between the electrodes could be used as a thermodynamic non-equilibrium resource, so as to yield a non-vanishing solution without requiring the flow of an external direct current, so without hypotheses (HJ) nor (HS). In particular, we will discuss how a complex magnetization texture at an interface stabilized by a magnetization difference within the bulk (like a skyrmion) can modify the boundary conditions of the previous model. We will not try to justify precisely the microscopic phenomena that lead to the proposed magnitude of the added terms we consider, but we will just give qualitative explanations and references that support them.

9.2.1 Origin of a self-sustained magnetic potential at the interface

Let us first reexamine Equation 9.5 defining the free energy increment due to a process driving the system slightly away from equilibrium, in which we defined the spin-resolved magneto-electrochemical potential. Although the magnetic potential H^* is thought to contain complicated contributions coming from various sources of magnetic fields, it acts as a thermodynamic force, so the Valet-Fert theory and subsequent works [49, 538, 539, 540] consider this term to vanish at equilibrium. Indeed, since it does not seem to be a driving force in most devices because previous studies always assumed or observed passive electronics, neglecting any contribution from this term is a natural assumption when studying the response of an apparently passive electronic device to an applied current or bias voltage.

However, in the case of the spintronic engine, we would expect a contribution from this term that should not be zero everywhere in the device since the magnetization gradient, along with the change in spin diffusion properties of the materials should lead to a non-equilibrium magnetic configuration, in particular at the interfaces where the magnetic properties change abruptly. We thus expect a non-equilibrium magnetic potential at the interfaces that would be an artifact of the magnetic field inside the bulk. This magnetic potential should be self-sustained by the misalignment of the electrodes: each electrode slowly changes its internal spin structure in response to the field exerted by the other electrode.

Several identified phenomena could justify the existence of a non-zero magnetic potential at the interface:

- **Proximity effects** [555, 269, 556] are known to induce non-linear magnetic phenomena. At the microscopic level, the hybridization of a magnetic layer with localized impurities result in complex electronic interactions between the two, leading to a total magnetic field that is different from the sum of the two individual fields [19, 557, 558].

- **Surface currents** originating from the mutual influence between the paramagnetic diode material and the ferromagnetic electrodes could be the source of a non-vanishing magnetic potential at the interface. Indeed, Stokes' theorem applied to the Maxwell-Ampere relation leads to the following discontinuity relation for the magnetization: $\vec{H}_{\parallel}(x^+) - \vec{H}_{\parallel}(x^-) = \vec{j_s}$ where $\vec{H}_{\parallel}$ is the in-plane magnetization of the layer and $\vec{j_s}$ is the surface current. We thus expect the magnetization difference imposed by the electrodes to generate surface currents that will retro-actively act back on the electrons, giving rise to a force that could be described by a magnetic potential source term.

- **The spinterface**, which designates the strong hybridization of the electronic orbitals between a ferromagnetic metal and an adjacent organic layer [257, 256], is responsible for complex electronic and magnetic effects which may drive emergent active processes at the interface that result in active behaviors in response to electromagnetic asymmetries from both sides of the interface. Indeed, the spin-to-charge conversion due to the Rashba effect and the spin–momentum locking at the surface of topological insulators have been observed and identified as resulting from interfacial properties

[559]. These effects thus raise the possibility that the spinterface could host a stable amount of energy which would originate from some magnetic difference between the two baths it connects, and that it could take an active role in converting this input magnetic energy into a charge current flowing across the interface. Indeed, various studies have showed the ability of the spinterface to act as a strong spin and energy filter that is able to invert and fully spin-polarize the ≈40% spin polarization of the $3d$ ferromagnetic layer at equilibrium, which would therefore support the presence of a self-sustained localized magnetic field at the interface [264, 480, 465, 257].

- **Spin textures** like skyrmions [560], domain walls [561] and topological edge states may also induce such a thermodynamical force. When an electron moves through a smoothly varying, non-collinear magnetic structure, its spin orientation constantly changes. This adaptation induces forces that act on both the magnetic structure and the electron. These forces can be described by the electric and magnetic fields of an emergent electrodynamics [562, 467]. The topologically quantized winding number of skyrmions (a type of magnetic whirl discovered in chiral magnets) is predicted to induce exactly one quantum of emergent magnetic flux per skyrmion. As a result, a moving skyrmion is expected to induce an emergent electric field that follows Faraday's law of induction and inherits this topological quantization [563]. The ability of the device to pin and maintain a skyrmion or another type of magnetic structure quantized by a topological invariant like the Chern number could thereby result in stable non-equilibrium magnetic configuration at the interface, channeled by the nanotrasport path, translating into a magnetic potential.
- **Magnetic monopoles** are another kind of possibility closely related to magnetic textures. Although, up-to-date, no fundamental particle behaves as a magnetic monopole, quasi-particles have exhibited similar properties. They are not sources for the magnetic field but for other conjugated fields like the magnetization. These objects have been experimentally identified in spin ice systems [564, 565] or topological surface states [566] and may arise from correlations between opposite spin electrons located at both sides of the interface such as an effective attractive force of Coulomb origin mediated by the atomic structure arise between them [567]. This link between electrons akin to the mechanism of the Cooper pairs in superconductors may justify their treatment as a single magnetic monopole at a larger scale. With these magnetic monopoles, the emergence of an additional electromotive term in Faraday's equation linked to the motion of these quasi-particles [568, 569].

These considerations thus lead us to reconsider the boundary conditions set in the previous section. In particular, hypothesis (H2) stated that the surface spin scattering is only driven by the spin current. This condition should be relaxed in order to incorporate the influence of a non-zero magnetic potential at the interface. Given Equation 9.5 defining the magneto-electrochemical potential, we thus postulate an extra term in the boundary conditions $\Delta H^*(x_1)$ at an interface located in $x = x_1$, such that:

$$\overline{\mu}_\uparrow(x_1^+) - \overline{\mu}_\uparrow(x_1^-) = r_\uparrow j_\uparrow(x_1) + \mu \Delta H^*(x_1) \;\text{ and }\; \overline{\mu}_\downarrow(x_1^+) - \overline{\mu}_\downarrow(x_1^-) = r_\downarrow j_\downarrow(x_1) - \mu \Delta H^*(x_1) \tag{9.45}$$

thus yielding the discontinuity for the spin potential

$$\Delta\overline{\mu}(x_1^+) - \Delta\overline{\mu}(x_1^-) = r_\uparrow j_\uparrow(x_1) - r_\downarrow j_\downarrow(x_1) + 2\mu\Delta H^*(x_1). \tag{9.46}$$

The Equation 9.46 is therefore leading to an extra source term in the linear equations defining the integration constants of the spin potential. We propose to study the impact of this **interface magnetic potential** hypothesis (HI) on the solution of the equation on $\Delta\overline{\mu}$.

9.2.2 Solving the equations with a magnetic potential source term

Solving the equations in the case of a non-vanishing spin-potential

Let us restrict ourselves to the thin barrier limit (Hb) and consider that $\Delta\overline{\mu} < 0$ in the diode barrier (H-). Then the system 9.20 now reads with the source term (HI):

$$\begin{pmatrix} e^{-l/\lambda_L} & -e^{-l/\lambda_-} & -e^{l/\lambda_-} & 0 \\ \lambda_L e^{-l/\lambda_L} & -\lambda_- e^{-l/\lambda_-} & \lambda_- e^{l/\lambda_-} & 0 \\ 0 & -\lambda_- e^{l/\lambda_-} & \lambda_- e^{-l/\lambda_-} & \lambda_R e^{-l/\lambda_R} \\ 0 & e^{l/\lambda_-} & e^{-l/\lambda_-} & -e^{-l/\lambda_R} \end{pmatrix} \begin{pmatrix} A \\ B \\ C \\ F \end{pmatrix} = \begin{pmatrix} \mu_L \\ j(\beta_L - \beta_-)/2\alpha \\ j(\beta_R - \beta_-)/2\alpha \\ \mu_R \end{pmatrix}, \tag{9.47}$$

where we have set $2\mu\Delta H^*(-l) = \mu_L$ and $2\mu\Delta H^*(l) = \mu_R$. Neglecting the input current density $j = 0$, the inversion of the matrix thus leads to

$$\begin{cases} A = \frac{\lambda_-}{d} e^{\frac{l}{\lambda_L}} \left\{ 2\lambda_R e^{-\frac{2l}{\lambda_-}} \mu_R - \left[(\lambda_R + \lambda_-) e^{-\frac{4l}{\lambda_-}} + (\lambda_R - \lambda_-) \right] \mu_L \right\} \\ B = \frac{1}{d} e^{-\frac{l}{\lambda_-}} \left\{ \lambda_R(\lambda_- + \lambda_L)\mu_R - \lambda_L(\lambda_- + \lambda_R) e^{-\frac{2l}{\lambda_-}} \mu_L \right\} \\ C = \frac{1}{d} e^{-\frac{l}{\lambda_-}} \left\{ \lambda_R(\lambda_- - \lambda_L) e^{-\frac{2l}{\lambda_-}} \mu_R - \lambda_L(\lambda_- - \lambda_R)\mu_L \right\} \\ F = \frac{\lambda_-}{d} e^{\frac{l}{\lambda_R}} \left\{ \left[(\lambda_L - \lambda_-) e^{-\frac{4l}{\lambda_-}} + (\lambda_L + \lambda_-) \right] \mu_R - 2\lambda_L e^{-\frac{2l}{\lambda_-}} \mu_L \right\} \end{cases}. \tag{9.48}$$

In the thin barrier limit $l \ll \lambda_-, \lambda_+$ (Hb), we thus obtain the following equivalents for the spin potential at the edges of the diode material:

$$\Delta\overline{\mu}(-l^+) \sim \Delta\overline{\mu}(l^-) \sim -\frac{\lambda_L\mu_L - \lambda_R\mu_R}{\lambda_L - \lambda_R} \tag{9.49}$$

so as we indeed have a solution of constant sign $\Delta\overline{\mu} < 0$ within the barrier iff $\frac{\lambda_L\mu_L - \lambda_R\mu_R}{\lambda_L - \lambda_R} > 0$. In the opposite case (H+), since the equivalents do not depend on $\lambda_\pm$, then the same solution holds for a constant sign $\Delta\overline{\mu} > 0$.

We can now evaluate the bias voltage induced by the magnetic potential using Equation 9.26 in the thin barrier limit:

$$e\Delta V \sim -\frac{\mu_L - \mu_R}{\lambda_L - \lambda_R} \left[\lambda_R(\beta_- - \beta_L) + \lambda_L(\beta_R - \beta_-) \right]. \tag{9.50}$$

For a steady current to emerge from this bias voltage, we observe that we are faced with a difficulty, since the current density linked to this non-equilibrium voltage $ej_{ne} \equiv -e\sigma\partial_x V =$

$\sigma\beta\partial_x\Delta\overline{\mu}$ vanishes at infinity (HF), at the far edges of both ferromagnetic electrodes. This investigation shows that in the thin barrier limit, a solution of the equation with $j = 0$ is always possible since the device behaves linearly in this approximation. We shall thus consider a larger barrier ((HV+) and (HV-)) and look for conditions on the parameters that impose a solution of the equation requiring $j \neq 0$.

Solving the equations with a magnetic potential in the strong diode regime

Let us suppose in this section that $\Delta\overline{\mu}$ vanishes within the diode such that there exists $x_0 \in]-l, l[$ verifying $\Delta\overline{\mu}(x_0) = 0$. We also assume that $\Delta\overline{\mu}(-l^+) < 0$ and $\Delta\overline{\mu}(l^-) > 0$ so that we place ourselves in the **positive vanishing potential** assumption (HV+). Under this condition, the systems 9.28 and 9.29 read with the extra magnetic potential source term (HI):

$$\begin{pmatrix} e^{-l/\lambda_L} & -e^{-l/\lambda_-} & -e^{l/\lambda_-} \\ \lambda_L e^{-l/\lambda_L} & -\lambda_- e^{-l/\lambda_-} & \lambda_- e^{l/\lambda_-} \\ 0 & e^{x_0/\lambda_-} & e^{-x_0/\lambda_-} \end{pmatrix} \begin{pmatrix} A \\ B \\ C \end{pmatrix} = \begin{pmatrix} \mu_L \\ \frac{j}{2\alpha}(\beta_L - \beta_-) \\ 0 \end{pmatrix} \tag{9.51}$$

and

$$\begin{pmatrix} e^{x_0/\lambda_+} & e^{-x_0/\lambda_+} & 0 \\ -\lambda_+ e^{l/\lambda_+} & \lambda_+ e^{-l/\lambda_+} & \lambda_R e^{-l/\lambda_R} \\ e^{l/\lambda_+} & e^{-l/\lambda_+} & -e^{-l/\lambda_R} \end{pmatrix} \begin{pmatrix} D \\ E \\ F \end{pmatrix} = \begin{pmatrix} 0 \\ \frac{j}{2\alpha}(\beta_R - \beta_+) \\ \mu_R \end{pmatrix}. \tag{9.52}$$

The solution to these two systems must also verify the current continuity equation (H3) reading:

$$\frac{B}{\lambda_-}e^{x_0/\lambda_-} - \frac{C}{\lambda_-}e^{-x_0/\lambda_-} = \frac{D}{\lambda_+}e^{x_0/\lambda_+} - \frac{E}{\lambda_+}e^{-x_0/\lambda_+}, \tag{9.53}$$

We treat the source term j as a free variable and we will show that in some cases, a solution to these equations requires a non-vanishing j. We set λ to be the shorter length scale of the problem. By linearity, each constant $X \in \{A, B, C, D, E, F\}$ can now be decomposed as $X \equiv X_0 + \frac{j}{\alpha\lambda}X_1$. For $j = 0$, the systems solve into:

$$\begin{cases} A_0 = -\frac{\lambda_-}{d_{L-}} e^{\frac{l}{\lambda_L}} (e^{\frac{2x_0}{\lambda_-}} + e^{-\frac{2l}{\lambda_-}}) \mu_L \\ B_0 = -\frac{\lambda_L}{d_{L-}} e^{-\frac{l}{\lambda_-}} \mu_L \\ C_0 = \frac{\lambda_L}{d_{L-}} e^{\frac{2x_0 - l}{\lambda_-}} \mu_L \end{cases} \quad \text{and} \quad \begin{cases} D_0 = \frac{\lambda_R}{d_{R+}} e^{\frac{l}{\lambda_+}} \mu_R \\ E_0 = -\frac{\lambda_R}{d_{R+}} e^{\frac{2x_0 + l}{\lambda_+}} \mu_R \\ F_0 = \frac{\lambda_+}{d_{R+}} e^{\frac{l}{\lambda_R}} (e^{\frac{2x_0}{\lambda_+}} + e^{\frac{2l}{\lambda_+}}) \mu_R \end{cases}. \tag{9.54}$$

The continuity equation thus reads:

$$f_0(x_0) + \frac{j}{\alpha\lambda} f_1(x_0) = 0, \tag{9.55}$$

where we have set

$$f_i(x_0) \equiv \frac{B_i}{\lambda_-}e^{x_0/\lambda_-} - \frac{C_i}{\lambda_-}e^{-x_0/\lambda_-} - \frac{D_i}{\lambda_+}e^{x_0/\lambda_+} + \frac{E_i}{\lambda_+}e^{-x_0/\lambda_+}.$$

We then calculate

$$f_0(x_0) = -\frac{2\lambda_L}{d_{L-}\lambda_-} e^{\frac{x_0 - l}{\lambda_-}} \mu_L - \frac{2\lambda_R}{d_{R+}\lambda_+} e^{\frac{x_0 + l}{\lambda_+}} \mu_R. \tag{9.56}$$

For the current to be non-zero, we need this function to have a constant sign in $]-l,l[$.

If we now assume the opposite case of the **negative vanishing potential** (HV-) such as $\Delta\overline{\mu}(-l^+)>0$ and $\Delta\overline{\mu}(l^-)<0$, then we obtain a similar condition by permuting λ_+ and λ_-, which leads to the following continuity equation:

$$g_0(x_0)+\frac{j}{\alpha\lambda}g_1(x_0)=0, \tag{9.57}$$

with

$$g_0(x_0)=-\frac{2\lambda_L}{d_{L+}\lambda_+}e^{\frac{x_0-l}{\lambda_+}}\mu_L-\frac{2\lambda_R}{d_{R-}\lambda_-}e^{\frac{x_0+l}{\lambda_-}}\mu_R. \tag{9.58}$$

Let us show that neither $f_0(x_0)$ nor $g_0(x_0)$ vanish in the strong diode case (HP) or (HAP). Let us suppose that $\lambda_-\ll\lambda_+\lesssim\lambda_R\sim\lambda_L$ so that we place ourselves in the **strong parallel diode** limit (HP). We then obtain the following equivalents:

$$f_0(x_0)\sim\frac{2\mu_L}{\lambda_-}\frac{e^{\frac{x_0-l}{\lambda_-}}}{e^{\frac{2x_0}{\lambda_-}}-e^{-\frac{2l}{\lambda_-}}}\ \text{ and }\ g_0(x_0)\sim-\frac{2\mu_R}{\lambda_-}\frac{e^{\frac{x_0+l}{\lambda_-}}}{e^{\frac{2l}{\lambda_-}}-e^{\frac{2x_0}{\lambda_-}}}, \tag{9.59}$$

which show that $f_0(x_0)$ has the same sign as μ_L, and $g_0(x_0)$ has the same sign as $-\mu_R$ in the interval $]-l,l[$, therefore we must have $j\neq 0$.

Before moving towards to the study of the power generated by the device, let us check that a solution where $\Delta\overline{\mu}$ does not vanish in the diode is also prohibited under these conditions (neither (H+) or (H-) can be satisfied). We have two cases:

- Suppose first that $\Delta\overline{\mu}<0$ in the diode (H-), then, using the solution found in the previous paragraph, we get:

  $$\Delta\overline{\mu}(-l^+)\sim-\mu_L\ \text{ and }\Delta\overline{\mu}(l^-)\sim-\mu_R. \tag{9.60}$$

  Therefore, given the continuity of $\Delta\overline{\mu}$ within the diode (H1), a solution with negative sign can only exist iff both $\mu_L>0$ and $\mu_R>0$.

- Suppose now that $\Delta\overline{\mu}>0$ in the diode (H+), then we get:

  $$\Delta\overline{\mu}(-l^+)\sim e^{-\frac{2l}{\lambda_+}}\Delta\overline{\mu}(l^-)\sim\frac{\lambda_+e^{-\frac{2l}{\lambda_+}}}{(\lambda_L-\lambda_+)e^{-\frac{4l}{\lambda_+}}-(\lambda_R-\lambda_+)}[\mu_R-e^{-\frac{2l}{\lambda_+}}\mu_L]. \tag{9.61}$$

  Therefore, a solution with positive sign can only exist iff μ_R and μ_L are chosen such as this expression is positive. Given the ordering of the spin diffusion lengths $\lambda_-\ll\lambda_+\lesssim\lambda_R\sim\lambda_L$ (HP), we thus obtain that a positive solution requires $\mu_R-e^{-\frac{2l}{\lambda_+}}\mu_L<0$.

Gathering all this, in order to ensure that a solution in which the spin-potential $\Delta\overline{\mu}$ changes sign within the diode ((HV+) or (HV-)) and leads to a current, we must have:

$$\mu_L<0\ \text{ and }\ \mu_L<e^{\frac{2l}{\lambda_+}}\mu_R. \tag{9.62}$$

Let us now study the two cases where we assume $\Delta\overline{\mu}(-l^+)<0$ (HV+) and $\Delta\overline{\mu}(-l^+)>0$ (HV-).

The charge current for $\Delta\overline{\mu}(-l^+) > 0$ in the strong diode regime

With the previous analysis, we can now evaluate the current. In order to have a solution, we require that $\mu_L < e^{\frac{2l}{\lambda_+}}\mu_R$ and $\mu_L < 0$. The current j must then be a non-zero parameter that allows for a solution to the equation $g_0(x_0) + \frac{j}{\alpha\lambda_-}g_1(x_0) = 0$ to be found in $]-l, l[$. There may be a large interval for j over which this equation has a solution. Therefore, we should consider the value of j that will minimize the power, *i.e.* $|j| = \alpha\lambda_- \min_{x_0\in]-l,l[}\left|\frac{g_0(x_0)}{g_1(x_0)}\right|$. Given that we have

$$g_1(x_0) = \frac{\beta_R-\beta_-}{d_{R-}}e^{\frac{x_0+l}{\lambda_-}} + \frac{\beta_L-\beta_+}{d_{L+}}\frac{\lambda_-}{\lambda_+}e^{\frac{x_0-l}{\lambda_+}} \sim \frac{\beta_R-\beta_-}{\lambda_R}\frac{e^{\frac{x_0+l}{\lambda_-}}}{e^{\frac{2l}{\lambda_-}} - e^{\frac{2x_0}{\lambda_-}}}, \tag{9.63}$$

it follows that j is uniquely given to leading order by:

$$\boxed{j = \frac{2\alpha\mu_R\lambda_R}{\beta_R-\beta_-}.} \tag{9.64}$$

A first observation about this result is that j is not negligible because it has a non-vanishing zero-order term, so it should contribute to the values of the spin-potential at the interfaces and therefore have an impact on the voltage. Then, we observe that the sign of j is given by the sign of $\frac{\mu_R}{\beta_R-\beta_-}$ and that the current only depends on the properties of the right electrode and not the left. This is due to the two assumptions (HV-) and (HP) which together strongly suppress the electromagnetic impact of the left electrode: the diode blocks the current contribution of the left electrode which has positive spin-potential. Another remark is that we need to go to a higher order in perturbation in order to recover an equation on x_0 and find the zero value of $\Delta\overline{\mu}$ within the diode. After some algebra, we obtain:

$$\alpha\lambda_-\frac{g_0(x_0)}{g_1(x_0)} = -\frac{2\alpha\mu_R\lambda_R}{\beta_R-\beta_-} + \frac{2\alpha\lambda_-}{\lambda_+}\frac{\mathrm{sh}\left(\frac{l-x_0}{\lambda_-}\right)e^{-\frac{x_0+l}{\lambda_+}}}{\beta_R-\beta_-}\left[\mu_L - \frac{2\lambda_R}{\lambda_L}\frac{\beta_L-\beta_+}{\beta_R-\beta_-}\mu_R\right] + o\left(\frac{\lambda_-}{\lambda_+}\right) \tag{9.65}$$

The absolute minimum of this function is therefore approached for $x_0 \to l$ or $x_0 \to -l$ depending on the sign of μ_R and $\mu_L - \frac{2\lambda_R}{\lambda_L}\frac{\beta_L-\beta_+}{\beta_R-\beta_-}\mu_R$.

Let us now check that $\Delta\overline{\mu}(-l^+) > 0$ and $\Delta\overline{\mu}(l^-) < 0$ (HV-). The value of j we found is a limit that does not allow checking the sign of $\Delta\overline{\mu}$ at the edges. Let us then take $j = \frac{2\alpha\mu_R\lambda_R}{\beta_R-\beta_-} + \delta j$ with $\delta j = o\left(\frac{\lambda_-}{\lambda_+}\right)$, then we get:

$$\Delta\overline{\mu}(-l^+) \sim -\left[\mu_L - \frac{\beta_L-\beta_+}{\beta_R-\beta_-}\mu_R\right]\frac{1-e^{-2\frac{l+x_0}{\lambda_+}}}{2} \text{ and } \Delta\overline{\mu}(l^-) = -\frac{\delta j(\beta_R-\beta_-)}{2\alpha\lambda_R}. \tag{9.66}$$

Therefore, we indeed have $\Delta\overline{\mu}(-l^+) > 0$ if $\mu_L - \mu_R\frac{\beta_L-\beta_+}{\beta_R-\beta_-} > 0$ and $\Delta\overline{\mu}(l^-) < 0$ if $\delta j(\beta_R - \beta_-) > 0$. An important remark here is that the output current j resulting from the input of magnetic potential at the interface is almost killing the spin potential inside the diode at both interfaces as $x_0 \to -l$. This diode is thus converting the spin potential into a current that emerges through its feedback. A sketch of the spin-potential profile obtained in this case is presented in Figure 9.4.

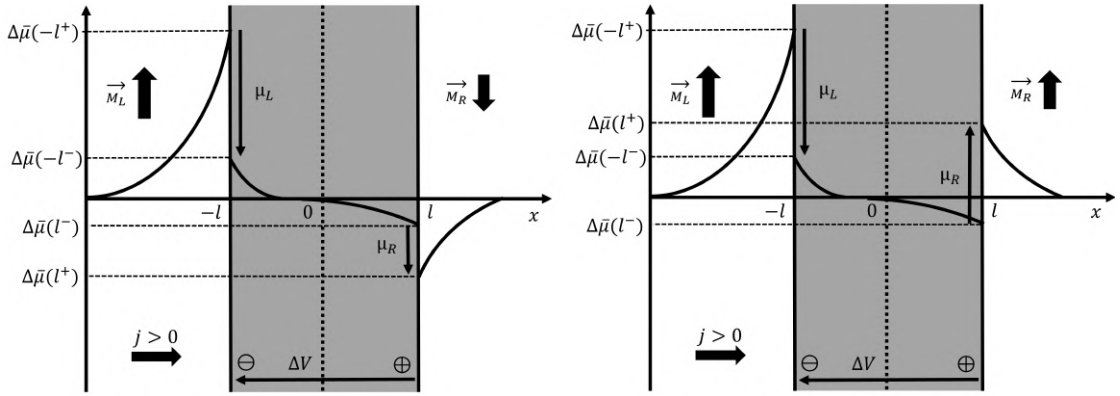

Figure 9.4: **Spin-potential profile with a magnetic potential source.** Plots of the spin potential $\Delta\overline{\mu}$ with respect to x in the AP (left) and P (right) configurations of the electrodes in the case where $\Delta\overline{\mu}$ vanishes within the diode with $\Delta\overline{\mu}((-l^-) > 0$. The situation presented corresponds to an active device which generates an output current and bias in response to the magnetic potential applied at the interfaces.

Voltage, power and working conditions

We now have all the ingredients we need to find the voltage. Evaluating the integral defining ΔV in Equation 9.26, we get:

$$e\Delta V = -\int_{-\infty}^{+\infty} \beta\partial_x\Delta\overline{\mu} = -\beta_L\Delta\overline{\mu}(-l^-) + \beta_+\Delta\overline{\mu}(-l^+) - \beta_-\Delta\overline{\mu}(l^-) + \beta_R\Delta\overline{\mu}(l^+). \quad (9.67)$$

Using the definition of the spin-potential discontinuity at the interface (Equation 9.46), it reduces to:

$$e\Delta V = (\beta_R - \beta_-)\Delta\overline{\mu}(l^-) - (\beta_L - \beta_+)\Delta\overline{\mu}(-l^+) + \beta_L\mu_L + \beta_R\mu_R \quad (9.68)$$

$$\sim -(\beta_L - \beta_+)\left[\mu_L - \frac{\beta_L - \beta_+}{\beta_R - \beta_-}\mu_R\right]\frac{1 - e^{-2\frac{l+x_0}{\lambda_+}}}{2} + \beta_L\mu_L + \beta_R\mu_R \quad (9.69)$$

$$\underset{x_0\to -l}{\longrightarrow} \beta_L\mu_L + \beta_R\mu_R. \quad (9.70)$$

As we can see, the term that depends on the spin-potential profile in the diode vanishes as $x_0 \to -l$ or $\beta_L \sim \beta_+$ or $l \ll \lambda_+$. Let us then place ourselves in one of those cases. We can finally write the power P of the device:

$$\boxed{P = jae\Delta V = \frac{2a\alpha\lambda_R\mu_R}{\beta_R - \beta_-}(\beta_R\mu_R + \beta_L\mu_L)} \quad (9.71)$$

Let us then finish by commenting on the sign and the magnitude of P. The electrodes being ferromagnetic, they are magnetically oriented and thus the spin-conduction asymmetry β may be large in the electrodes, but its precise value will depend on non-trivial parameters such as material composition and geometry. In order to gain insights into the power, assumptions have to be made on β_R and β_L. Let us physically limit study the dependence of β on the magnetism of the electrodes M_L and M_R. The left electrode was fixed

as the quantization axis (HQ) of the spin such that we assume that $\beta_L > 0$. Then, because the quantization axis may differ from the magnetic orientation of the right electrode, the sign of β_R is mainly dictated by the orientation of the right electrode with respect to the reference electrode. Also, taking into account that β_R is odd with respect to an inversion of the quantization axis, we refer to the P configuration when $\beta_R > 0$ and to the AP configuration when $\beta_R < 0$, keeping in mind that in this context, the configuration is relative to the asymmetries and not the magnetizations, although they may be closely correlated.

Since the diode material is made out of a chain of paramagnetic atoms within an insulating barrier, the magnetic orientation of this chain is imposed by the magnetization of the electrodes and the conduction is weaker than in the electrodes. Moreover, we expect the reference electrode, with the stronger magnetization, to have a stronger asymmetry than the other materials due to an increased spin-splitting. This consideration leads us to formally translate the electrode hypothesis (HM) as $\beta_-, \beta_+ \ll \beta_L$, in which case the power reduces to:

$$P \sim 2a\alpha\lambda_R\Big(\mu_R^2 + \frac{\beta_L}{\beta_R}\mu_L\mu_R\Big). \tag{9.72}$$

We observe that the first term is always positive and corresponds to some dissipation due to the current traversing the right interface, which gains some internal resistance due to spin diffusion. Then, the second term can be generative or dissipative depending on the sign of $\frac{\mu_R}{\beta_R}$. Since $\beta_L\mu_L < 0$, the device may be power-generative when $\frac{\mu_R}{\beta_R} > 0$. Let us then obtain some conditions on μ_R and μ_L for the device to produce power in the two alignment cases of the electrodes:

- In the P case, $\beta_R > 0$ so we must have $\mu_R > 0$ for energy generation. Then, the inequality $P < 0$ gives $0 < \beta_R\mu_R < -\beta_L\mu_L$.

- In the AP case, similarly, $\beta_R < 0$ such as $\mu_R < 0$ and $P < 0$ leads to the same inequality $0 < \beta_R\mu_R < -\beta_L\mu_L$.

Three remarks may be given to interpret this inequality. The quantity $\beta\mu$ can be named as the interface magnetic spin-potential and it represents some measure of the strength of the magnetic force exerted on the majority conduction spin-channel by the interface magnetic field. The above inequality thus states that a generative device may be obtained only when the magnitude of the magnetic spin-potential at the interface with the free electrode is lower than at the interface with the reference layer. A strong geometric asymmetry between the left and right sides of the barrier is thus needed for the device to work. This result thus has a strong echo on the experimental part (see Part II and References [18, 19]) and confirms the need for a electrode-diode spacer of different thickness across the junction. Different thicknesses indeed relate to different coupling parameters to atomic centers in the barrier, which in turn shape a diode characteristic. The required asymmetry could also be engineered using different spinterfaces, or even not having a spinterface on one side.

Secondly, we notice that we need β_L and μ_L to be of different sign on the left side, while we need β_R and μ_R to have the same sign on the right side. Since μ is deeply linked to a non-equilibrium magnetic field at the interface, it should be related to the magnetization of the

spinterface, and we know that the spinterface has the effect of increasing and inverting the sign of spin-polarization of a current that flows through it [257]. This should be consistent with the fact that we require $\beta_L > 0$ and $\mu_L < 0$ for the reference electrode. If the right side was completely isolated from the left side, we would then also expect a different sign on the right, but here in our microscopic device, proximity effects should be such as the strong magnetic field of the left electrode should also have an impact on the right interface so that the combined influence of the magnetism of the left and the right electrode forces μ_R to have the same sign as β_R. In other words, the magnetism of the thinner spinterface on the right side is controlled by both electrodes such that its polarization inversion property is no longer valid in this configuration where the strong opposed electrode must also be taken into account to describe the properties of the right interface.

Finally, it is important to see that for the device to be power generative, we need the current $j = \frac{2\alpha\mu_R}{\beta_R}$ to be positive regardless of the orientation of the electrode asymmetries, such that the negative pole of the device is the left electrode (see Figure 9.4). This result is in agreement with the experiments that showed that electrodes flow towards the reference electrode [18]. If we consider the left bath to be "magnetically cold" since the strong reference electrode has a higher absolute magnetization than the "magnetically hot" right bath (entropy usually shrinks with magnetization), we thus find that the current has the same direction as the "magnetic temperature gradient". A hand-waving analogy with thermoelectricity with n-type semiconductors can be made: in the left reservoir with up magnetization, the density of down-spin electrons is higher to the left than to the right, which should lead to a flow of down spins from left to right, but since the diode is rectifying this spin-current by killing the flow of down spins, an equilibration must be made through a charge current and the hot left reservoir must then lose some positive energy electrons to the left side for a balance to be reached.

Numerical Examples

The *ab-initio* calculations along with the experimental results presented in Chapter 4 suggest that the spin-splitting by the spinterface of the energy levels of the paramagnetic centers trapped inside the junction is $\Delta = 0.7$ meV [19]. Such a splitting should be the result of a permanent magnetic field inside the junction of $H = \Delta/\mu = 120$ T. Although we cannot expect this equilibrium magnetic field to account for the magnetic potential ΔH^* which is necessary to power the device in this model, its magnitude can be used to estimate the non-equilibrium magnetic field that could be trapped at the interface due to the effects envisaged in Section 9.2.1. It would thus seem reasonable that the non-equilibrium interactions resulting from the gradual alignment of the electrodes or other magnetic phenomena induce a non-equilibrium magnetic potential at the interface of the order of 0.1% of the equilibrium magnetic field. We shall thus consider $\Delta H^* = 0.1$ T, resulting in a potential $\mu = \Delta H^*/2\mu = 0.01$ meV which looks like a small potential compared to the energy scales of the system, supporting the possibility that some external phenomenon might maintain naturally such a spin-resolved bias. But we should keep in mind that, given the ability of the spinterface to display interface magnetic moments oriented in the opposite direction of those of the electrode, it might also result in a interface magnetic field $\Delta H^* \sim H$, which would lead to a spin potential of $\mu = 10$ meV. This substantial potential could explain the

large voltage observed in the experiments presented in Figure 4.6 of Chapter 4.

Let us consider several generative examples depending on the values of μ. For all these examples, we use the same parameter values as Section 9.1.4 and consider a nanotransport path of section $a = 3$ nm^2.

- Let us first suppose that the magnetism of the right electrode is weaker than that of the left electrode in the P configuration, resulting in a weak potential $\mu_R = 2.10^{-6}$ eV and a strong asymmetry. Suppose then that the spin-potential on the left is moderate such that $\mu_L = -10^{-5}$ eV. Then, the voltage is $\Delta V = -3.10^{-6}$ V, the current is $I = 3.10^{-9}$ A and the power is $P = -9.10^{-15}$ W. In this case, the current is close to the intensity measured for MgO devices but the voltage is too small to explain those results. Nonetheless, if we allow for the left electrode to display a stronger spin-potential, leading to an even greater asymmetry between the two interfaces, with $\mu_L = -10^{-2}$ eV, then the intensity remains unchanged while both the voltage and the power gain three orders of magnitude and the results for the MgO devices presented in Chapter 4 can be reproduced.

- Let us now suppose a weaker asymmetry between the interfaces and assume that both of them allow for a substantial spin potential of the order of 10^{-2} eV. With $\mu_R = 10^{-2}$ eV and $\mu_L = -2.10^{-2}$ eV. Then the voltage reads $\Delta V = -3$ mV and the current gives $I = 1.10^{-5}$ A, leading to a power of $P = -3.10^{-8}$ W. For this set of parameters, we thus recover the results obtained for molecular junctions (see Figure 4.6).

These examples show that the experimental results can be reproduced, provided that a strong non-equilibrium magnetic field of the order of 100 T be maintained at the interface, so as to generate the required voltage of the order of 10^{-3} meV. This magnetic field value is supported by Reference [465].

9.3 Discussion

In this Chapter, we considered a ferromagnetic junction in which the barrier is composed of a non-linear material whose conducting behavior depend on the spin-potential, and we extended the canonical Valet-Fert theory [49] to devices acting as spin-diodes. In the first section, we examined the ability of this diode device to rectify a stochastic charge current in order to deliver electrical power. It was indeed first suggested by Brillouin [534] that electrical diodes could rectify the Johnson-Nyquist noise coming from a resistor in order to produce work. Although its initial proposal rested on flawed assumptions, it was later experimentally [570] and theoretically [537, 536] proved that the device can indeed deliver energy, provided that a temperature gradient exists within the electrical system, although the efficiency is usually very small. These first studies on electrical ratchet effects suggest that the spintronic engine could work in a similar way.

Although, we shall not assume any temperature difference within the device, we argued in the previous Chapter that the ferromagnetic electrodes do act as both thermal reservoirs

and spin reservoirs. Intuitively, the difference in magnetism of the two electrodes due to differences in alignment or magnitude of their magnetizations should therefore induce an effective temperature difference of magnetic origin within the device that could be used as a resource by the spin ratchet material to generate work. This idea led us to study the response of the non-linear material to an uncompensated stochastic current noise that would be self-sustained by the magnetization gradient between the electrodes. Developing upon this hypothesis, we showed that the nonlinearity indeed allowed it to rectify the noise into a dc current, and build up a voltage that resulted in a generative power output in some cases dependent on the geometry of the device, its rectifying properties and the characteristics of the electrode materials. Under specific assumptions, we showed that this model was able to reproduce the voltage and the current observed in the experiments on MgO junctions, but could not explain the results obtained for molecular junctions under reasonable assumptions. Indeed, this theory based on the rectification of a current noise can only deliver a *dc* current whose amplitude is of the order of the dispersion of the input noise. Therefore, given the spectral features of the results obtained on molecular junctions featuring very low dispersion (see Figure 4.8), it seems unlikely that the magnetism within the junction results in such a strong current noise of the order of 10^{-5} A, leaving no trace in the IV.

This first section serves as a basis to initiate the systematic study of generalized thermal ratchets: just as the theory of quantum thermodynamics describes thermal reservoirs with conserved quantities in such a way that any difference in generalized charge between two reservoirs can be used as a resource to produce work, stochastic thermodynamics allows us to consider thermal reservoirs with different properties whose interactions will generate uncompensated noises that can be used by non-linear devices to produce work. The theory thus invites us to look for materials with intrinsic non-linearities and meta-stable reservoirs with additional thermodynamic invariants, different from the usual temperature, pressure and chemical potential, which can act as continuous sources of rectifiable noises. In this context, this work opens up to further investigations regarding microscopic spin and charge current noises at equilibrium within ferromagnets and more specifically within MTJs containing spinterfaces. We expect future experimental studies to reveal differences in the noise spectrum of interfacial layers adposed to ferromagnets depending on their magnetism so as to confirm the possibility of harvesting such a thermodynamic resource.

Although we cannot exclude that such a noise could be localized at the microscopic level within the junction and explain the results obtained for molecular junctions, this difficulty oriented us to look for another argument. The second section thus envisaged the possibility of a non-equilibrium interface magnetism powering the device which was until then ignored by the canonical passive spintronic theory. We showed that this interface magnetism results in an interface spin potential bias that acts as a non-equilibrium resource that the diode material can harvest to produce a dc charge current. The analytic study was able to derive the current, the power and the working conditions required for the device to act as an engine. We showed that under specific conditions regarding the diode, the electrodes and the asymmetry of the interface potentials, the power could be decomposed into two contributions: a resistive term and a generative term. Numerical applications then confirmed that it was possible to explain the results of both the oxide and molecular active junctions, provided that a strong non-equilibrium magnetic field of the order of 100 T be maintained at the interface. This condition is, for instance, naturally fulfilled by the

spinterface.

This theory is based on two main assumptions that need to be backed by further studies in order to be fully convincing. First, this model relies on a spin diode material whose conductivity varies depending on the applied spin-potential bias *i.e.* spin accumulation). Evidence of this effect may be found in junctions where transport channels formed by the excited states of a spin chain result in discrete resistance values depending on the voltage and applied magnetic field [251]. More experiments should thus be conducted in order to find materials with these properties, and confirm that our junctions can indeed behave in such a non-linear fashion. Probing the response of our devices to directed spin-polarized currents should be a first step to confirming their ability to change their conducting properties. Then, on the theory side, we believe that the study of microscopic phase transitions could lead to more insights into the designs of such non-linear materials, as a sharp structural or magnetic transformation due to a change in an order parameter of magnetic origin should lead to the change in conductivity we require for this device. Under specific thermodynamical and electromagnetic constraints, a material close to a phase transition between two states (either microscopic like the ground and excited state of a spin chain [251], or mesoscopic like the Chern number [571]) is in a thermodynamically unstable phase such as a small change in the external constraint like the spin potential can drastically change its properties.

And secondly, this model postulates a steady non-equilibrium magnetic field at the interface, that we assume constant in the model due to its macroscopic origin, just like one usually assumes a constant thermal gradient in the study of nanoscopic heat engines. While we have guided its origin within the ingredients of the spinterface, surface currents, proximity effects, magnetic textures or magnetic monopoles, the precise mechanism that justify this magnetism still needs to be thoroughly detailed. We expect that this phenomenon ultimately corresponds to boundary artifacts of the differences in magnetism between the bulk of the two ferromagnetic electrodes: the magnetization gradient between the two electrodes may be the macroscopic driver that translates into a mesoscopic magnetic non-equilibrium phenomenon located at the interface. The remaining question is now to justify how this non-equilibrium resource can be maintained in our device without an external energy input. Indeed, because this parameter is supposed constant in the model, we obtain a constant power output in the steady state, but we expect that this energy harvesting will have a back action on this potential such as it will tend to deplete it over time, just like a heat engine tends to rectify the thermal gradient applied to it. In that case, our device may therefore be considered as some kind of battery that converts the magnetic energy stored within the magnetic potential trapped at the interface until it returns to equilibrium. The question would now be to study the characteristic time of the device corresponding to the duration the device can work until the resource is depleted. Giving an estimate of the decay of the magnetic potential trapped at the interface is indeed another challenge because we expect that at least two opposing phenomena are driving the magnetism of the interface at two very different scales: we saw that the microscopic device tends to kill this interface potential and then the macroscopic magnetic misalignement of the electrodes should tend to maintain it. Although giving a precise duration is out of the scope of this manuscript, we can highlight a few elements that suggest that it could be very large: first, the non-ergodic properties of spin-glasses suggests that the time needed to reach a global equilibrium state

could be infinite, and then the hysteric property of ferromagnetic materials is known to trap them in magnetic meta-stable states from which it takes an infinite amount of time to return to equilibrium unless a strong global change in temperature or magnetic field are applied to frustrate them.

This study invites us to pursue more research into the interface magnetism between ferromagnets, spinterfaces and barriers with magnetic centers as it suggests that the nanotransport path will concentrate the infinitesimal changes of the magnetism from the bulk of the two ferromagnets due to their quasi-static alignment by structural rearrangements. We therefore suggest that magnetic vortexes or other complex magnetic structures may be at the core of the spintronic engine. Indeed, related studies have revealed the possibility of storing and harvesting energy from domain wall motion [9] or magnetic textures like skyrmions [7, 8].

parameter	description
$\vec{M}_L$, $\vec{M}_L$	magnetization of the electrodes
$2l$	length of the barrier
a	section of the wire
$N_\uparrow$, $N_\downarrow$	number of spin carriers
$n_\uparrow$, $n_\downarrow$	number density of spin carriers
N	number of electrons
$j_\uparrow$, $j_\downarrow$	spin-resolved current density
Δj	spin-current density
j	electronic current density
ν	rate of down-spin to up-spin flip
T	temperature
F	free energy
U	internal energy
S	entropy
Q	heat
W	work
V	voltage
P	power
α	characteristic spin-flip time
g	g-factor
e	elementary charge
μ_B	Bohr magneton
f	free energy density
s	entropy density

parameter	description
Φ	electro-static potential
$\vec{m}$	magnetic moment
H^*	magnetization potential
$\mu_\uparrow$, $\mu_\downarrow$	chemical potential of the spin carriers
$\overline{\mu_\uparrow}$, $\overline{\mu_\downarrow}$	magneto-electrochemical potential of the spin carriers
$\Delta\overline{\mu}$	spin-potential
$\overline{\mu}$	electron potential
$\sigma_\uparrow$, $\sigma_\downarrow$	spin-resolved conductivities
$\sigma_\uparrow^\pm$, $\sigma_\downarrow^\pm$	spin-resolved conductivities in the diode for the two signs of the spin-potential
σ	electronic conductivity
β_R, β_L	spin-based conductivity asymmetry of the electrodes
β_-, β_+	spin-based conductivity asymmetry of diode for the two signs of the spin-potential
λ_R, λ_L	spin-diffusion characteristic length of the electrodes
λ_-, λ_+	spin-diffusion characteristic length of diode for the two signs of the spin-potential
$r_\uparrow$, $r_\downarrow$	spin-resolved interface resistance
μ_R, μ_L	interface potential

Table 9.1: Table of the parameters.

code	symbolic form	name and description
(HQ)	$\vec{M}_R = M_R\vec{e}_z$, $\vec{M}_L = M_L\vec{e}_z$	**quantization axis:** the magnetization of the electrodes is along the z-axis only
(HM)	$M_R \ll M_L$ and $\beta_-, \beta_+, \beta_R \ll \beta_L$	**reference electrode:** the magnetization of the reference electrode is stronger than that of the free electrode
(HR)	$\mathrm{d}Q = T\mathrm{d}S$	**reversibility:** the device operates in a steady-state regime so that the evolution process is reversible
(HT)	T is constant	**thermal equilibrium:** the temperature is constant and uniform in the materials
(HF)	$\overline{\mu_s}(x_\infty) - \overline{\mu_s}(-x_\infty) = 0$	**global equilibrium:** no external force is applied to the device, and all potential differences between the to edges vanish
(HJ)	j is constant	**stationary current:** the device is connected to a dc current source
(HS)	$\mathcal{J} \sim \mathcal{N}(0, J)$	**stochastic current:** the device is subject to a uniform stochastic charge current noise
(HG)	V_0 is constant	**ground fixing:** an arbitrary origin of the potentials may be set somewhere in the device
(H1)	$j_s(\pm l^+) = j_s(\pm l^-)$	**spin conservation:** continuity of the spin currents across the interfaces
(H2)	$\overline{\mu_s}(\pm l^+) - \overline{\mu_s}(\pm l^-) = r_s j_s(\pm l)/e$	**interface scattering:** interface resistance due to spin scattering
(H2b)	$\overline{\mu_s}(\pm l^+) - \overline{\mu_s}(\pm l^-) = 0$	**null interface resistance:** no spin scattering across the interface
(H3)	$j(\pm l^+) - j(\pm l^-) = 0$	**charge conservation:** continuity of the charge current across the interface
(H+)	$\forall x \in]-l, l[, \Delta\overline{\mu}(x) > 0$	**positive diode:** the spin potential remains positive within the diode
(H-)	$\forall x \in]-l, l[, \Delta\overline{\mu}(x) < 0$	**negative diode:** the spin potential remains negative within the diode
(HV+)	$\Delta\overline{\mu}(-l^+) < 0, \Delta\overline{\mu}(l^-) > 0$	**positive vanishing potential:** the spin potential increases and vanishes within the diode
(HV-)	$\Delta\overline{\mu}(-l^+) > 0, \Delta\overline{\mu}(l^-) < 0$	**negative vanishing potential:** the spin potential decreases and vanishes within the diode
(Hα)	$\alpha_L = \alpha_R = \alpha_+ = \alpha_- \equiv \alpha$	**uniform spin-flip:** the spin-flip probability is identical in the material
(Hb)	$l \ll \lambda_+, \lambda_-$	**thin barrier limit:** the spin-diffusion length is higher than the barrier width
(HP)	$\lambda_- \ll \lambda_+$	**strong parallel diode limit:** the spin-diffusion length in the diode is larger for positive spin potential
(HAP)	$\lambda_+ \ll \lambda_-$	**strong anti-parallel diode limit:** the spin-diffusion length in the diode is larger for negative spin potential
(HW)	$\lambda_+ \sim \lambda_- \equiv \lambda$	**weak diode limit:** the spin-diffusion length in the diode weakly depends on the sign of the spin potential
(HI)	$\overline{\mu_s}(\pm l^+) - \overline{\mu_s}(\pm l^-) = \mu$	**interface magnetic potential:** under the null interface resistance hypothesis, the trapped magnetic field at the interface generates a spin potential source term

Table 9.2: Table of the hypotheses.

Chapter 10

The Macroscopic Model

In the previous chapter, we developed a mesoscopic model of the spintronic engine by introducing a diode material into the standard theory of non-equilibrium spin-transport across magnetic interfaces. We showed that the device could rectify stochastic charge current in order to produce power, and that it could harvest the energy of a sustained non-equilibrium magnetic field confined at the interface between the electrode and the diode material. In both the quantum model of Chapter 8 and the mesoscopic model of Chapter 9, it thus seems that the energy harvested by the device inherently originates from the difference in magnetization $\Delta\vec{M}$ of the electrodes.

Macroscopically, the misalignment of the magnetic fields produced by the ferromagnets is indeed associated with a coupling energy $E = -\int \vec{M} \cdot \vec{B} \mathrm{d}V$. Here, the integral spans both the left and the right electrode, so that the total magnetic field $\vec{B}$ contains contributions coming from both the right and left electrodes along with additional complex sources of magnetic fields confined at the interface originating from non-linear effects. At the lowest order, if we assume that in the vicinity of the ferromagnet, the magnetic field it creates is proportional to the magnetization, *i.e.* $\vec{B} = \mu\vec{M}$ where μ is some kind of permeability, using the reciprocity theorem [572], one gets the interaction energy between the left electrode taken as a fixed reference and the right electrode that is considered free:

$$E_{L/R} = -\int_R \vec{M}_R \cdot \vec{B}_L \mathrm{d}V = -\int_R \mu\vec{M}_R \cdot \vec{M}_L \mathrm{d}V. \tag{10.1}$$

We expect the proportionality parameter to vanish far away from the interface, such that the weight of this integral is concentrated near the interface, and we observe that under the constraint where $\vec{M}_R$ has a bounded magnitude, then the above functional is a potential well for $\vec{M}_R$ that is minimized when $\vec{M}_R$ and $\vec{M}_L$ are co-linear and aligned. The gradual alignment of the free layer as it rearranges its magnetic structure to align with the field that is naturally applied by the fixed layer is thus responsible for a magnetic energy relaxation. The possibility that a device, located at the interface between the two layers where this interaction energy is the highest, and which would generate electricity from the varying magnetic fields as they slowly change towards equilibrium, thus seems reasonable (see Figure 10.1).

The changing magnetic interaction energy between the two ferromagnets lead us to

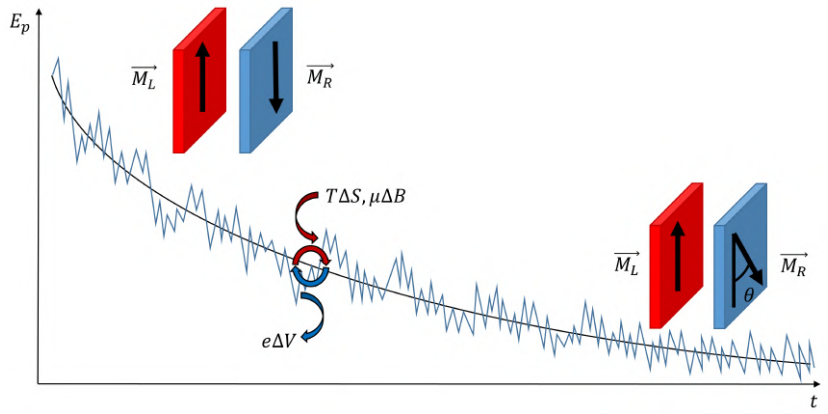

Figure 10.1: **Magnetic alignment of the electrodes fueling the engine.** Interaction energy between the two electrodes as a function of time. The electrodes are prepared in a frustrated magnetic alignment such as they progressively align towards a potential minimum. This quasi-static decrease in magnetic energy leads to a constant thermodynamical force of magnetic origin acting on the microscopic, stochastic device trapped at their interface. This nano-engine then converts heat and the magnetic exchange energy into electrical energy.

consider that the difference in magnetization between the two layers can be thought as a thermodynamic force that may drive the device, which would then convert some magnetization flux into a charge current. In other words, the magnetization of the electrode bath is acting as a magnetic potential on the electrons. The difference in magnetic potential between the two baths can therefore act as a force on the electrons that may drive a flow of charges, provided that an adapted device operate the conversion of the magnetization energy flux, as the two electrode magnetizations slowly align, into a charge flux along with an appropriate voltage so that it can extract electrical work from this magnetic potential difference (see Figure 10.1).

This Chapter plans to find a macroscopic model that can explain how this device operates at the scale of the electronic circuit, in order to complement the previous microscopic and mesoscopic approaches. The objective is then to find an equivalent circuit that can describe the system using standard electronic or spintronic components. The previous intuition invites us to look for a non-linear device that is suited to convert a magnetic potential difference into a charge current, and we wish to study the circuit with proper care such as to avoid the subtleties of self-rectification and not fall into Brillouin's paradox.

In Brillouin's first approach to the noisy diode issue [534], just like in the "ratchet-and-pawl" engine [550, 551, 552], naive considerations based on Langevin dynamics may show the possibility to extract work from self-rectifying thermal fluctuations from a system at thermal equilibrium, which is in contradiction with the second law of thermodynamics. For the ratchet, Feynmann showed that no work could be extracted from such systems [550], and for the noisy diode, a more thorough analysis developed by Sokolov showed that no self-rectification occurs within the electrical system unless a temperature difference exists between the diode and the rest of the circuit [536]. In both approaches, Feynmann and

Sokolov indeed show that the devices are passive in the absence of a non-equilibrium force such as a temperature gradient. In the following we will therefore argue that current rectification may happen in non-linear spin-diode circuits provided that a magnetic potential gradient exists between the two poles of the electronic device. In this context, we will describe the magnetic potential as the internal magnetic field of ferromagnetic electrodes whose effect is to split the energy levels of spin up and spin down electrons along the transport channel. The difference in magnetization of the ferromagnetic electrodes can thus give rise to a spin-potential bias *(i.e.* a spin accumulation) that can provide the necessary non-equilibrium resource to power the device.

In the present chapter, we consider a circuit approach to the energetics of the spintronic engine that is based on a framework of generalized electronics with two independent conducting channels that code for the two spin carriers. In the first section, we present the model and, using the formalism of stochastic electronics, we derive a master equation describing the occupation probability density of the two spin channels at one pole of the device. Then in the second section, we solve this equation and establish the working conditions under which the device can behave as an electrical generator. In the third section we discuss those results and compare them with those of the other microscopic and mesoscopic models we studied.

10.1 The spin-diode electronic model

The model under study features a couple of spin-diodes and spin-resolved resistors arranged in parallel and connected at both ends to spin-polarized electronic reservoirs. In Figure 10.2, we represent the equivalent circuit of the diode system under study with the four possible configurations of the two diodes. The reservoirs we consider can be represented by their electrochemical potential μ and their magnetic or spin potential ν which comes naturally from their permanent magnetization. The microscopic diode system schematically depicted in Figure 10.2 separates the two ferromagnetic layers such that it additionally forms a capacitor of capacitance C.

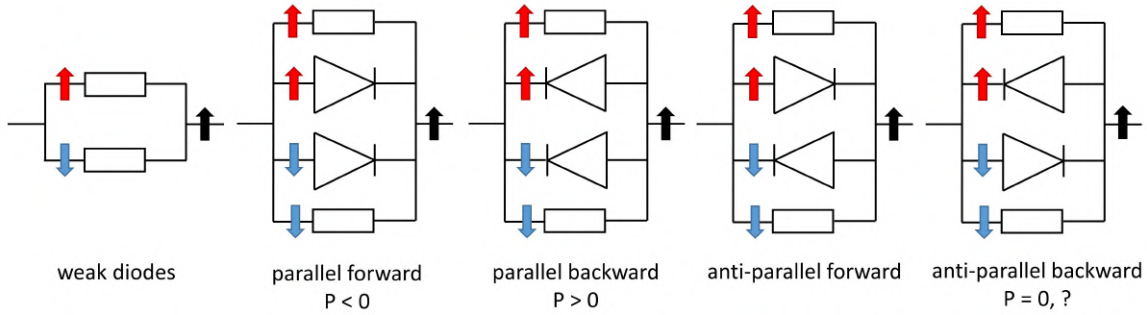

Figure 10.2: **Equivalent spin-diode circuit.** Electrical circuit of the two spin-diode model. The limit case of the weak diodes is represented along with the four possible configurations of the diodes. Up spins travel through the channels with the red arrows while down spins take the paths with the blue arrows.

10.1.1 The master equation

To establish the master equation describing the spin-diode system, we proceed in a similar way as to Sokolov's analysis[536] of Brillouin's paradox and start with a discrete state space. Contrary to his analysis, we now have two different channels for the two spin carriers. At the exit pole of the device, on the right, the electronic state may thus be represented by two numbers $q = n\xi$ representing the charge, which is the number of excess electrons in the conductor ; and $s = m\zeta$ representing the spin, or the number of discrete spins which deviate from the equilibrium state of this pole. We assume that each electron can flow through the spin-diode device through only one of the four possible channels represented in Figure 10.2 such that an electron can only pass through the resistor or the diode which corresponds to its spin. We consider all of these channels to be independent so that no spin-flip mechanism is allowed in this system: the four channels are completely uncorrelated.

The spin-diode circuit is then represented by a rate function $W_{n,n'}^{m,m'}$ that represents the probability for right pole to be in the state (n', m') knowing that the right pole was in the state (n, m). To be in physical accordance with thermodynamics, the rate should satisfy a detailed balance condition reading:

$$\boxed{W_{n,n'}^{m,m'} = W_{n',n}^{m',m} \exp\Big(\epsilon_n^m - \epsilon_{n'}^{m'}\Big),} \tag{10.2}$$

where $\epsilon_n^m - \epsilon_{n'}^{m'}$ represents the potential energy gained by an electron traveling from the left reservoir with state (n', m') to the right reservoir with state (n, m), in adimensional units of kT.

Finally, we consider that this system may be traversed by a charge and a spin current, which translates into two rates $w_\uparrow$ and $w_\downarrow$ for each spin channel.

The overall process is then modeled by the following discrete master equation describing the evolution of the probability function $p_n^m(t)$ of finding the conductor on the right side in the state (n, m) at time t:

$$\begin{aligned}\frac{\mathrm{d}p_n^m}{\mathrm{d}t} = &-w_\uparrow p_{n-1}^{m-1} - w_\downarrow p_{n-1}^{m+1} + w_\uparrow p_{n+1}^{m+1} + w_\downarrow p_{n+1}^{m-1} \\ &+ p_{n-1}^{m-1} W_{n-1,n}^{m-1,m} + p_{n-1}^{m+1} W_{n-1,n}^{m+1,m} + p_{n+1}^{m+1} W_{n+1,n}^{m+1,m} + p_{n+1}^{m-1} W_{n+1,n}^{m+1,m} \\ &- p_n^m \Big(W_{n,n-1}^{m,m-1} + W_{n,n-1}^{m,m+1} + W_{n,n+1}^{m,m+1} + W_{n,n+1}^{m,m-1} \Big).\end{aligned} \tag{10.3}$$

Introducing the functions:

$$\begin{cases} W_\uparrow(q,s) = W_\uparrow(n\xi, m\zeta) \equiv W_{n-1,n}^{m-1,m} \\ W_\downarrow(q,s) = W_\downarrow(n\xi, m\zeta) \equiv W_{n-1,n}^{m+1,m} \\ \epsilon(q,s) = \epsilon(n\xi, m\zeta) \equiv \epsilon_n^m \\ p(t,q,s) = p(t, n\xi, m\zeta) \equiv p_n^m(t) \end{cases}, \tag{10.4}$$

we show in Appendix L that the master equation reduces to a Fokker-Planck (FP) equation in the limit of $X \equiv (\xi, \zeta) \to 0$:

$$\partial_t p = \nabla\Big[W_\uparrow\big(p\nabla\epsilon + \nabla p\big)\cdot X\Big]\cdot X + \nabla\Big[W_\downarrow\big(p\nabla\epsilon + \nabla p\big)\cdot \overline{X}\Big]\cdot \overline{X} + 2w_\uparrow X\cdot\nabla p + 2w_\downarrow \overline{X}\cdot\nabla p, \tag{10.5}$$

where $\overline{X} = (\xi, -\zeta)$. Then, with the following change of variable:

$$\left\{ \begin{array}{l} q = \xi(x+y) \\ s = \zeta(x-y) \end{array} \right. \Leftrightarrow \left\{ \begin{array}{l} x = \frac{q}{2\xi} + \frac{s}{2\zeta} \\ y = \frac{q}{2\xi} - \frac{s}{2\zeta} \end{array} \right. \tag{10.6}$$

we observe that the equation simplifies into:

$$\boxed{\partial_t p = \partial_x \Big[W_\uparrow \big(p \partial_x \epsilon + \partial_x p \big) + 2 w_\uparrow p \Big] + \partial_y \Big[W_\downarrow \big(p \partial_y \epsilon + \partial_y p \big) + 2 w_\downarrow p \Big].} \tag{10.7}$$

x represents some measure of the number of up spins in the conductor while y is the number of down spins.

10.1.2 The power

The rates $W_\uparrow$ and $W_\downarrow$ are in units of frequencies and are related to the total resistance R of each channel through the capacitance formed by the electrodes by $W = 1/RC$. Since, for each spin carrier, we consider a spin diode sensitive to the number of the corresponding spins and a resistor, we consider the following rate functions:

$$\boxed{W_\uparrow(x) = G_+ + (G_\uparrow - G_+)\Theta(x) \text{ and } W_\downarrow(y) = G_- + (G_\downarrow - G_-)\Theta(y),} \tag{10.8}$$

so that $G_+ > 0$ and $G_- > 0$ are the linear parts of the conductance, and corresponding to the conductances of each channel when $x < 0$ and $y < 0$, and $G_\uparrow > 0$ and $G_\downarrow > 0$ are the conductances of the diode when $x > 0$ and $y > 0$ respectively (keep in mind that the conductances are assimilated with rates via the capacitance). Depending on the order of the conductances, we have four different situations represented in Figure 10.2: the diodes are arranged in parallel forward when $G_\uparrow > G_+$ and $G_\downarrow > G_-$, in parallel backward when $G_\uparrow < G_+$ and $G_\downarrow < G_-$, in anti-parallel forward when $G_\uparrow > G_+$ and $G_\downarrow < G_-$, and in anti-parallel backward when $G_\uparrow < G_+$ and $G_\downarrow > G_-$.

And for the energy, since the electrons go through a capacitor C, and from a reservoir of electrochemical potential μ_L and spin potential ν_L (corresponding to a magnetic potential along the quantized axis), to a reservoir of electrochemical potential μ_R and spin potential ν_R, we consider the energy:

$$\boxed{\epsilon(q,s) = \frac{E}{kT} = \frac{q^2}{2kTC} - \frac{\Delta\mu}{ekT} q - \frac{\Delta\nu}{kT} s,} \tag{10.9}$$

where $\Delta\mu \equiv \mu_R - \mu_L$ and $\Delta\nu \equiv \nu_R - \nu_L$. Using the variables x and y, we obtain:

$$\epsilon = \frac{\alpha}{2}(x+y)^2 - \mu_\uparrow x - \mu_\downarrow y \text{ with } \left\{ \begin{array}{l} \mu_\uparrow = \frac{\Delta\mu}{ekT}\xi + \frac{\Delta\nu}{kT}\zeta \\ \mu_\downarrow = \frac{\Delta\mu}{ekT}\xi - \frac{\Delta\nu}{kT}\zeta \\ \alpha = \frac{\xi^2}{kTC} \end{array} \right. . \tag{10.10}$$

In the following, we set $\Delta\mu = 0$, since we consider that there is no external bias voltage applied to the device. Without loss of generality, we also set $\Delta\nu > 0$ to favor the up spins considered as the majority spins of reference. Finally, since α is of order ξ^2, we consider

this parameter as a perturbation, $\alpha \ll \mu_\downarrow, \mu_\uparrow$. We emphasize that the potentials $\mu_\downarrow$ and $\mu_\uparrow$ correspond to the spin-resolved potential of each channel and that they are taken to be adimensional, in units of kT. With these assumptions, the energy reduces to:

$$\epsilon = -\Delta\nu s + \frac{q^2}{2C} = -\mu(x-y) + \frac{\alpha}{2}(x+y)^2 \text{ with } \mu \equiv \mu_\uparrow = -\mu_\downarrow = \frac{\Delta\nu}{kT}\zeta > 0. \quad (10.11)$$

We now have every ingredient we need to calculate the power. Going back to the discrete picture, the left reservoir receives the power in units of kT:

$$\mathcal{P} = W^{m,m+1}_{n,n+1}(\epsilon^{m+1}_{n+1} - \epsilon^m_n) - W^{m,m-1}_{n,n-1}(\epsilon^m_n - \epsilon^{m-1}_{n-1}) + W^{m,m-1}_{n,n+1}(\epsilon^{m-1}_{n+1} - \epsilon^m_n) - W^{m,m+1}_{n,n-1}(\epsilon^m_n - \epsilon^{m+1}_{n-1}). \quad (10.12)$$

Expanding to the second order, we obtain

$$\mathcal{P} = X\cdot\nabla(W_\uparrow X\cdot\nabla\epsilon) - W_\uparrow(X\cdot\nabla\epsilon)^2 + \overline{X}\cdot\nabla(W_\downarrow\overline{X}\cdot\nabla\epsilon) - W_\downarrow(\overline{X}\cdot\nabla\epsilon)^2 \quad (10.13)$$

$$= \partial_x(W_\uparrow\partial_x\epsilon) - W_\uparrow(\partial_x\epsilon)^2 + \partial_y(W_\downarrow\partial_y\epsilon) - W_\downarrow(\partial_y\epsilon)^2. \quad (10.14)$$

Integrating by parts, the average value thus reads

$$\langle\mathcal{P}\rangle = \int \mathcal{P}p\,\mathrm{d}x\mathrm{d}y = -\int W_\uparrow\partial_x\epsilon[\partial_x p + p\partial_x\epsilon]\mathrm{d}x\mathrm{d}y - \int W_\downarrow\partial_y\epsilon[\partial_y p + p\partial_y\epsilon]\mathrm{d}x\mathrm{d}y. \quad (10.15)$$

Integrating by parts again and using the master equation of p twice, noticing that some integrals of partial derivatives vanish, we get the power

$$\langle\mathcal{P}\rangle = \int \epsilon\partial_x[W_\uparrow(\partial_x p + p\partial_x\epsilon)]\mathrm{d}x\mathrm{d}y + \int \epsilon\partial_y[W_\downarrow(\partial_y p + p\partial_y\epsilon)]\mathrm{d}x\mathrm{d}y \quad (10.16)$$

$$= -\int 2w_\uparrow\epsilon\partial_x p\,\mathrm{d}x\mathrm{d}y - \int 2w_\downarrow\epsilon\partial_y p\,\mathrm{d}x\mathrm{d}y \quad (10.17)$$

$$= \int 2w_\uparrow\partial_x\epsilon\,p\mathrm{d}x\mathrm{d}y + \int 2w_\uparrow\partial_y\epsilon\,p\mathrm{d}x\mathrm{d}y. \quad (10.18)$$

Inserting the expression of the energy from Eq.10.11, the power finally reads

$$\boxed{\langle\mathcal{P}\rangle = 2\mu(w_\downarrow - w_\uparrow) + 2\alpha(w_\uparrow + w_\downarrow)\langle\mathcal{Q}\rangle \equiv \langle\mathcal{P}_0\rangle + \alpha\langle\mathcal{P}_1\rangle,} \quad (10.19)$$

where $\langle\mathcal{Q}\rangle = \int(x+y)p\,\mathrm{d}x\mathrm{d}y$ is the average adimensional charge of the right reservoir. We emphasize here that, given the sign chosen for $w_\uparrow$ and $w_\downarrow$, we employed the active sign convention that the rectifier delivers power whenever the intensity $I \propto 2w_\uparrow + 2w_\downarrow$ and the charge $\langle Q\rangle$ are positive. Therefore, to lowest order in α, the power of the device is given by the electromagnetic power of the spin-polarized current passing through the device $\langle\mathcal{P}_0\rangle$. The objective of the next part of the study will thus be to prove that the second term $\langle\mathcal{P}_1\rangle$ in this expression can be positive, which will show that the device can deliver a electrical power output, meaning a charge current and a voltage of the same sign.

10.2 Solving the equation

In this section, we will look for a solution to the FP equation Eq. 10.7 by separating the variables. We will find the conditions under which such a separable solution exists and study the corresponding operating regime of the device.

10.2.1 Integration

Let us look for a solution p to Eq. 10.7 such that $p(x,y) = f(x)g(y)$, $f, g > 0$ a.e. Since we are interested only in the first-order correction of $\langle P \rangle$, we will limit ourselves to looking for a solution of the equation in the case of $\alpha = 0$. Because of the non-linearity of the diodes, the equation takes different forms in the four quadrants of the (x,y) plane. Let us then define the four portions of the plane (see Figure 10.3):

$$\begin{cases} Q_1 \equiv \{(x,y) \in \mathbb{R}^2 \mid x > 0,\ y > 0\} \\ Q_2 \equiv \{(x,y) \in \mathbb{R}^2 \mid x > 0,\ y < 0\} \\ Q_3 \equiv \{(x,y) \in \mathbb{R}^2 \mid x < 0,\ y < 0\} \\ Q_4 \equiv \{(x,y) \in \mathbb{R}^2 \mid x < 0,\ y > 0\} \end{cases}. \tag{10.20}$$

The FP equation now reads in each quadrant:

$$\begin{cases} G_\uparrow\Big(-\mu_\uparrow\frac{f'}{f} + \frac{f''}{f}\Big) + 2w_\uparrow\frac{f'}{f} + G_\downarrow\Big(-\mu_\downarrow\frac{g'}{g} + \frac{g''}{g}\Big) + 2w_\downarrow\frac{g'}{g} = 0 & \text{for } x > 0,\ y > 0 \\ G_\uparrow\Big(-\mu_\uparrow\frac{f'}{f} + \frac{f''}{f}\Big) + 2w_\uparrow\frac{f'}{f} + G_-\Big(-\mu_\downarrow\frac{g'}{g} + \frac{g''}{g}\Big) + 2w_\downarrow\frac{g'}{g} = 0 & \text{for } x > 0,\ y < 0 \\ G_+\Big(-\mu_\uparrow\frac{f'}{f} + \frac{f''}{f}\Big) + 2w_\uparrow\frac{f'}{f} + G_-\Big(-\mu_\downarrow\frac{g'}{g} + \frac{g''}{g}\Big) + 2w_\downarrow\frac{g'}{g} = 0 & \text{for } x < 0,\ y < 0 \\ G_+\Big(-\mu_\uparrow\frac{f'}{f} + \frac{f''}{f}\Big) + 2w_\uparrow\frac{f'}{f} + G_\downarrow\Big(-\mu_\downarrow\frac{g'}{g} + \frac{g''}{g}\Big) + 2w_\downarrow\frac{g'}{g} = 0 & \text{for } x < 0,\ y > 0 \end{cases}. \tag{10.21}$$

The separation thus shows that there exists a real constant P over the whole (x,y) plane such as:

$$\begin{cases} G_\uparrow f'' + [2w_\uparrow - G_\uparrow\mu_\uparrow]f' + Pf = 0 & \text{for } x > 0 \\ G_+ f'' + [2w_\uparrow - G_+\mu_\uparrow]f' + Pf = 0 & \text{for } x < 0 \end{cases} \tag{10.22}$$

and

$$\begin{cases} G_\downarrow g'' + [2w_\downarrow - G_\downarrow\mu_\downarrow]g' - Pg = 0 & \text{for } y > 0 \\ G_- g'' + [2w_\downarrow - G_-\mu_\downarrow]g' - Pg = 0 & \text{for } y < 0 \end{cases}. \tag{10.23}$$

We can interpret P as a constant representing the power leakage from spin $\uparrow$ to spin $\downarrow$ in the device. We now have to solve these four linear equations to get the solutions on each quadrant and then use the boundary conditions to link them and construct a solution over the whole plane. We set:

$$\begin{cases} \Delta_\uparrow \equiv \left(\frac{w_\uparrow}{G_\uparrow} - \frac{\mu_\uparrow}{2}\right)^2 - \frac{P}{G_\uparrow} \\ \Delta_\downarrow = \left(\frac{w_\downarrow}{G_\downarrow} - \frac{\mu_\downarrow}{2}\right)^2 + \frac{P}{G_\uparrow} \end{cases} \text{and} \begin{cases} \Delta_+ \equiv \left(\frac{w_\uparrow}{G_+} - \frac{\mu_\uparrow}{2}\right)^2 - \frac{P}{G_+} \\ \Delta_- \equiv \left(\frac{w_\downarrow}{G_-} - \frac{\mu_\downarrow}{2}\right)^2 + \frac{P}{G_-} \end{cases}. \tag{10.24}$$

Since f and g must be positive, a physical solution exists only if

$$\Delta_\uparrow \geqslant 0,\ \Delta_\downarrow \geqslant 0 \Longrightarrow -G_\downarrow\Big(\frac{w_\downarrow}{G_\downarrow} - \frac{\mu_\downarrow}{2}\Big)^2 \leqslant P \leqslant G_\uparrow\Big(\frac{w_\uparrow}{G_\uparrow} - \frac{\mu_\uparrow}{2}\Big)^2 \tag{10.25}$$

and

$$\Delta_+ \geqslant 0,\ \Delta_- \geqslant 0 \Longrightarrow -G_-\Big(\frac{w_\downarrow}{G_-} - \frac{\mu_\downarrow}{2}\Big)^2 \leqslant P \leqslant G_+\Big(\frac{w_\uparrow}{G_+} - \frac{\mu_\uparrow}{2}\Big)^2. \tag{10.26}$$

	f	g
Q_1	$\begin{cases} x \to e^{\lambda_+^\uparrow x} & \text{if } P>0 \text{ and } \mu_\uparrow G_\uparrow < 2w_\uparrow \\ x \to e^{\lambda_-^\uparrow x} & \text{if } P<0 \text{ or } \mu_\uparrow G_\uparrow < 2w_\uparrow \end{cases}$	$\begin{cases} y \to e^{\lambda_+^\downarrow y} & \text{if } P<0 \text{ and } \mu_\downarrow G_\downarrow < 2w_\downarrow \\ y \to e^{\lambda_-^\downarrow y} & \text{if } P>0 \text{ or } \mu_\downarrow G_\downarrow < 2w_\downarrow \end{cases}$
Q_2	$\begin{cases} x \to e^{\lambda_+^\uparrow x} & \text{if } P>0 \text{ and } \mu_\uparrow G_\uparrow < 2w_\uparrow \\ x \to e^{\lambda_-^\uparrow x} & \text{if } P<0 \text{ or } \mu_\uparrow G_\uparrow < 2w_\uparrow \end{cases}$	$\begin{cases} y \to e^{\kappa_+^\downarrow y} & \text{if } P>0 \text{ or } \mu_\downarrow G_- > 2w_\downarrow \\ y \to e^{\kappa_-^\downarrow y} & \text{if } P<0 \text{ and } \mu_\downarrow G_- > 2w_\downarrow \end{cases}$
Q_3	$\begin{cases} x \to e^{\kappa_+^\uparrow x} & \text{if } P<0 \text{ or } \mu_\uparrow G_+ > 2w_\uparrow \\ x \to e^{\kappa_-^\uparrow x} & \text{if } P>0 \text{ and } \mu_\uparrow G_+ > 2w_\uparrow \end{cases}$	$\begin{cases} y \to e^{\kappa_+^\downarrow y} & \text{if } P>0 \text{ or } \mu_\downarrow G_- > 2w_\downarrow \\ y \to e^{\kappa_-^\downarrow y} & \text{if } P<0 \text{ and } \mu_\downarrow G_- > 2w_\downarrow \end{cases}$
Q_4	$\begin{cases} x \to e^{\kappa_+^\uparrow x} & \text{if } P<0 \text{ or } \mu_\uparrow G_+ > 2w_\uparrow \\ x \to e^{\kappa_-^\uparrow x} & \text{if } P>0 \text{ and } \mu_\uparrow G_+ > 2w_\uparrow \end{cases}$	$\begin{cases} y \to e^{\lambda_+^\downarrow y} & \text{if } P<0 \text{ and } \mu_\downarrow G_\downarrow < 2w_\downarrow \\ y \to e^{\lambda_-^\downarrow y} & \text{if } P>0 \text{ or } \mu_\downarrow G_\downarrow < 2w_\downarrow \end{cases}$

Table 10.1: Table of the solutions of the FP equation in the four quadrants for $P = 0$.

Let us now define the roots:

$$\begin{cases} \lambda_\pm^\uparrow \equiv -\frac{w_\uparrow}{G_\uparrow} + \frac{\mu_\uparrow}{2} \pm \sqrt{\Delta_\uparrow} \\ \lambda_\pm^\downarrow \equiv -\frac{w_\downarrow}{G_\downarrow} + \frac{\mu_\downarrow}{2} \pm \sqrt{\Delta_\downarrow} \end{cases} \text{ and } \begin{cases} \kappa_\pm^\uparrow \equiv -\frac{w_\uparrow}{G_+} + \frac{\mu_\uparrow}{2} \pm \sqrt{\Delta_+} \\ \kappa_\pm^\downarrow \equiv -\frac{w_\downarrow}{G_-} + \frac{\mu_\downarrow}{2} \pm \sqrt{\Delta_-} \end{cases} . \tag{10.27}$$

The solutions on the different part of the plane are written in Table. 10.1 and are represented in Figure 10.3 for $P = 0$. We see that there are three cases to study depending on the value of P. In the following, we will primarily focus on the solution for $P = 0$ which is the most physical, and give a few comments on the solutions with $P > 0$ or $P < 0$.

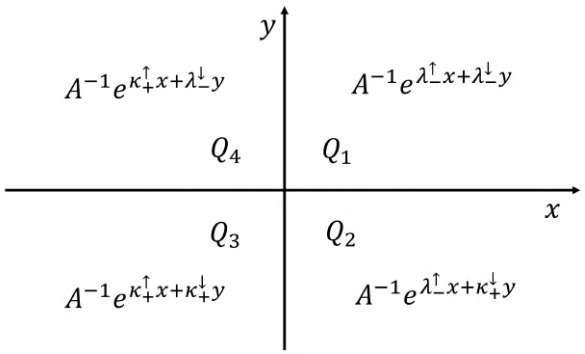

Figure 10.3: **Solution to the Fokker Planck equation.** Schematic showing the separable solution of the FP equation in the four quadrants of the plane, with $P = 0$.

10.2.2 Working conditions

Let us now study the separable solution we found depending on the value of P and evaluate the intensity and the voltage across the device in order to prove that it can behave as a generator and find the conditions under which it can show this rectifying behavior.

The case $P = 0$

Let us start by assuming that $P = 0$. The solution then requires

$$\begin{cases} \mu_\uparrow G_\uparrow < 2w_\uparrow < \mu_\uparrow G_+ \\ \mu_\downarrow G_\downarrow < 2w_\downarrow < \mu_\downarrow G_- \end{cases} \tag{10.28}$$

and since $\mu_\uparrow = -\mu_\downarrow = \mu > 0$, we already see that the solution requires $G_\uparrow < G_+$ and $G_\downarrow > G_-$, therefore, only the parallel forward configuration is possible in this case. We also immediately witness that $2w_\uparrow > 0$ and $2w_\downarrow < 0$ such as $\langle \mathcal{P}_0 \rangle = 2\mu(w_\downarrow - w_\uparrow) < 0$. Therefore, taking into account the active sign convention we adopted, the device dissipates the energy provided by the spin current flowing through it. This spin-current cannot be used to generate electrical power and will most likely be dissipated into heat. The average spin-current power is bounded by

$$-\mu^2(G_+ + G_\downarrow) < \langle \mathcal{P}_0 \rangle < -\mu^2(G_\uparrow + G_-) < 0. \tag{10.29}$$

The second law of thermodynamics tells us that at equilibrium, the device should dissipate a minimum of power. At the lowest order, the spin currents must minimize $\langle \mathcal{P}_0 \rangle$, and therefore, taking into account the previous inequality, we have:

$$2w_\uparrow = \mu G_\uparrow + \delta i_\uparrow G_\uparrow \text{ and } 2w_\downarrow = -\mu G_- - \delta i_\downarrow G_\downarrow \tag{10.30}$$

where the adimensional small variations $\delta i_\uparrow,\ \delta i_\downarrow$ are such as $\delta i_\uparrow, \delta i_\downarrow > 0$ and $\delta i_\uparrow,\ \delta i_\downarrow \ll \alpha$. These first order variations should then be optimized in order to minimize the total power $\langle P \rangle$ containing the power dissipated by the spin currents and the electrical power delivered to the capacitor and the rest of the circuit.

Let us now calculate the voltage $\langle Q \rangle$. The solution reads

$$p = A^{-1}\exp\Big(\Theta(x)\lambda_-^\uparrow x + \Theta(-x)\kappa_+^\uparrow x + \Theta(y)\lambda_-^\downarrow y + \Theta(-y)\kappa_+^\downarrow y\Big) \tag{10.31}$$

We drop the index $\lambda^\sigma \equiv \lambda_-^\sigma$ and $\kappa^\sigma \equiv \kappa_+^\sigma$ such as

$$A = \frac{1}{\lambda^\uparrow\lambda^\downarrow} - \frac{1}{\lambda^\uparrow\kappa^\downarrow} + \frac{1}{\kappa^\uparrow\kappa^\downarrow} - \frac{1}{\kappa^\uparrow\lambda^\downarrow} = \left(\frac{1}{\kappa^\uparrow} - \frac{1}{\lambda^\uparrow}\right)\left(\frac{1}{\kappa^\downarrow} - \frac{1}{\lambda^\downarrow}\right) = \frac{(\kappa^\uparrow - \lambda^\uparrow)(\kappa^\downarrow - \lambda^\downarrow)}{\kappa^\uparrow\lambda^\uparrow\kappa^\downarrow\lambda^\downarrow} \tag{10.32}$$

The average charge $\langle \mathcal{Q} \rangle$ is

$$\langle \mathcal{Q} \rangle = -\frac{A^{-1}}{\lambda^\uparrow\lambda^\downarrow}\left(\frac{1}{\lambda^\uparrow} + \frac{1}{\lambda^\downarrow}\right) + \frac{A^{-1}}{\lambda^\uparrow\kappa^\downarrow}\left(\frac{1}{\lambda^\uparrow} + \frac{1}{\kappa^\downarrow}\right) - \frac{A^{-1}}{\kappa^\uparrow\kappa^\downarrow}\left(\frac{1}{\kappa^\uparrow} + \frac{1}{\kappa^\downarrow}\right) + \frac{A^{-1}}{\kappa^\uparrow\lambda^\downarrow}\left(\frac{1}{\kappa^\uparrow} + \frac{1}{\lambda^\downarrow}\right). \tag{10.33}$$

After a bit of algebra, we get

$$\langle \mathcal{Q} \rangle = -\left(\frac{1}{\kappa^\uparrow} + \frac{1}{\lambda^\uparrow} + \frac{1}{\kappa^\downarrow} + \frac{1}{\lambda^\downarrow}\right) = \frac{1}{\frac{2w_\uparrow}{G_+} - \mu} + \frac{1}{\frac{2w_\uparrow}{G_\uparrow} - \mu} + \frac{1}{\frac{2w_\downarrow}{G_-} + \mu} + \frac{1}{\frac{2w_\downarrow}{G_\downarrow} + \mu}. \tag{10.34}$$

Rewriting this using the variations $\delta i_\uparrow$ and $\delta i_\downarrow$, we obtain:

$$\langle \mathcal{Q} \rangle = \frac{1}{\delta i_\uparrow} - \frac{1}{\delta i_\downarrow} + \frac{1}{\mu\big(1 - \frac{G_-}{G_\downarrow}\big)} - \frac{1}{\mu\big(1 - \frac{G_\uparrow}{G_+}\big)} + o(\alpha). \tag{10.35}$$

In order to obtain a finite value for $\langle \mathcal{Q} \rangle$, the leading order must vanish. Therefore, we need $\delta i_\uparrow = \delta i_\downarrow$, such as, under this condition

$$\boxed{\langle \mathcal{Q} \rangle = \frac{G_+ G_- - G_\uparrow G_\downarrow}{\mu (G_\downarrow - G_-)(G_+ - G_\uparrow)} + o(\alpha),} \tag{10.36}$$

which gives the voltage $U \equiv \xi \langle \mathcal{Q} \rangle / C$ and since the total current reads

$$\boxed{I/\xi \equiv 2w_\uparrow + 2w_\downarrow = \mu(G_\uparrow - G_-) + \delta i_\uparrow G_\uparrow - \delta i_\downarrow G_- + o(\alpha^2),} \tag{10.37}$$

we obtain the electrical power at the leading order:

$$\boxed{\langle P_1 \rangle = 2\alpha(w_\uparrow + w_\downarrow)\langle \mathcal{Q} \rangle \sim \alpha \frac{(G_\uparrow - G_-)(G_+ G_- - G_\uparrow G_\downarrow)}{(G_\downarrow - G_-)(G_+ - G_\uparrow)}.} \tag{10.38}$$

Since we already have $G_+ > G_\uparrow$ and $G_\downarrow > G_-$, we immediately find that the engine has two regimes of operation where it delivers electrical power $\langle P_1 \rangle > 0$.

- If $G_\uparrow > G_-$, and $\frac{G_+}{G_\uparrow} > \frac{G_\downarrow}{G_-}$ then the delivered intensity is positive and the voltage is negative. This situation occurs when the spin up resistor is more conductive than the spin down resistor and the relative conductance increase of the spin up diode is stronger than the spin down diode.
- If $G_\uparrow < G_-$, and $\frac{G_+}{G_\uparrow} < \frac{G_\downarrow}{G_-}$ then the delivered intensity is negative and the voltage is positive. This situation corresponds to the opposite case where the spin down path is favored over the spin down path in all components.
- Otherwise the device is passive.

One essential remark we must make here is that at this lowest order of perturbation, the power output is independent of the magnetic potential μ! As long as a magnetization difference exists between the two reservoirs, we thus expect the device to harvest the magnetic energy. The difference lies in the current being proportional to the spin bias $I \propto \mu$ and the voltage being inversely proportional to it $\langle \mathcal{Q} \rangle \propto \frac{1}{\mu}$. Of course, we expect other phenomena to take over if μ is too weak or too strong, so that the device will behave as an energy generator for as long as μ stays in the adequate range where the previous perturbation approach is valid.

These conditions show that in order to have an active device, a strong asymmetry of the two spin channels is necessary: we first need the spin channels to favor opposite directions of current flow such that the diodes are placed in the anti-parallel backward configuration, and we need one channel to be considerably more conductive than the other. Physically, this result looks coherent: since we imposed a spin-potential $\mu > 0$, up spins will be attracted to the "cold" right reservoir while down spins will be repulsed in order for the energy ϵ to be minimized. With the diodes oriented in the anti-parallel backward direction and this conduction asymmetry, the device will have a tendency to block the "hot" down spin electrons of high energy from entering the cold reservoir but to let the "cold" up spin electrons flow out of it. The engine is therefore acting against the magnetic equilibration of the electrodes, draining part of the energy that would be used to align the electrodes into a directed charge current thanks to the conduction asymmetry between the two spin channels.

The case $P \neq 0$

Assuming first that $P > 0$, the solution requires only $\mu G_\uparrow < 2w_\uparrow < \mu G_+$ such that $G_\uparrow < G_+$. The spin up diode should thus be in the backward direction but the spin down diode is free. Then, assuming that $P < 0$, the solution requires $-\mu G_\downarrow < 2w_\downarrow < -\mu G_-$ such as $G_\downarrow > G_-$. In this opposite case, the spin down diode should be in the forward direction but the spin up diode is free.

When $P \neq 0$, we are faced with a difficulty since the FP equation on each quadrant is a two-dimensional space. We thus need additional conditions in order to solve it. One could try and find a proper solution by imposing a minimization of the power $\langle P \rangle$ but the resolution is complex and out of the scope of this chapter.

Physically, when $P \neq 0$, there is a net transfer of power from one spin channel to the other. Since we assumed the independence of the channels, and still obtain some back-action, this solution should correspond to a situation that is strongly out-of-equilibrium: some process must drive a spin flip process resulting in a mixing of the two spin channels at the macroscopic scale even though they are supposed independent at the discrete level. This might explain why the solution needs extra conditions to be fully determined since it should be extended with an additional non-equilibrium assumption. We interpret this flux of energy between the two channels as a conduction loop: the electrons first travel one way into one channel, then they may flip their spin at one pole and travel back the other way in the opposite spin-channel.

The case of anti-parallel backward diodes

The previous analysis showed that, for every value of P, we must have either the up spin diode in the forward direction of the down spin diode in the backward direction such that the case of anti-parallel backward diodes is not included in this description. While it should be physically possible to implement such a device with this equivalent circuit, the assumption of the previous calculations cannot describe this configuration. This shows that no solution to the FP equation with separated variables can be suited such as a strong mixing of the two spin channels must be present for this type of device. We believe that this interdependence between the channels may result in exotic properties that could be beneficial for the energy harvesting capabilities of the device but the analytic analysis of this configuration will be strongly limited.

The limit of weak diodes

The limit of weak diodes corresponds to the case where $G_\uparrow \sim G_+$ and $G_\downarrow \sim G_-$. Assuming $P > 0$, the inequality $\mu G_\uparrow < 2w_\uparrow < \mu G_-$ such as the inequalities on P Eq. 10.25 and Eq. 10.26 give $P \leqslant G_+ \frac{\mu^2}{4}\left(1 - \frac{G_\uparrow}{G_+}\right)^2 = o(G_+ - G_\uparrow)$. Assuming $P < 0$, the same reasoning leads to the same conclusion $P = o(G_\downarrow - G_-)$. Therefore, in the case of weak diodes, the issues regarding $P \neq 0$ disappear but we expect the power output to be vanishingly small since the necessary diode effect will be small, although the previous derivation fails to give

an exact result of the power under no further assumptions.

Numerical applications

The above derivation shows us that the dissipated power strongly depends on the capacitance felt by the nanotransport channel. We can estimate this parameter in our junction by approximating the ferromagnetic electrodes as two parallel conductive plates such as the capacitance reads $C = \epsilon a/d$ where ϵ is the permittivity of the barrier, a is the area of the plates and d is the distance between the plates. From the structure presented in Chapter 5, we extract the distance $d = 2$ nm. Then, we take the relative permittivity of MgO to be $\epsilon_r = 9$ [573] such that $\epsilon = 8.10^{-11}$ F/m. Finally, we could take the area of the plates to correspond to the full section of the nanopillars designed in Chapter 5, which would give a maximum area of $a_{max} = 3.10^{-10}$ m^2 (corresponding to a radius of 10 μm) but we expect the impact of some screening effects due to the spinterface such as the nanotransport path will likely not be sensitive to such a large area. Given the sizes of the conduction hotspots revealed e.g. in Reference [574], we thus expect a much lower effective area $a_{min} = 3.10^{-14}$ m^2 (corresponding to a radius of 100 μm). This would give a microscopic capacitance C spanning the range between $C_{min} = 10^{-15}$ F and $C_{max} = 10^{-11}$ F. And we immediately see that the extracted power output will vary greatly depending the precise value.

Now, the derivation of the master equation presented in Appendix L was obtained by taking the continuum limit of a discrete master equation with respect to a charge parameter ξ and a spin parameter ζ. Typically, at the quantum level, we expect single electrons to be the main source of transport, such that the quantization of the charge is $\xi = e$ and the spin angular momentum is $\zeta = \hbar/2$. With this in mind, we can estimate the spin potential $\mu = \frac{\Delta\nu\zeta}{kT}$. Given that, at the molecular level, the magnetic field inside the junction is of the order of $B = 100$ T, the difference in magnetization of the two electrodes, leads us to consider a conservative magnetic field difference between the two ends of the nanotransport path of the order of $\Delta B \approx 10$ T, which will lead to a potential difference $\Delta\nu\zeta \approx \mu_B \Delta B \approx 0.6$ meV. Compared to the thermal energy at ambient temperature $kT = 26$ meV, it leads to $\mu = 0.02$. Keeping in mind that a strong magnetic asymmetry of the reservoirs may lead to an increased magnetic field difference of $\Delta B \approx 200$ T at the microscopic level, it is also possible that this parameter μ comes close to unity for tailored systems.

These two estimations lead us to confirm that our device lies in the perturbation regime that is necessary to use the previous derivation. At room temperature, we have $2.10^{-7} \leqslant \alpha = \frac{\xi^2}{kTC} \leqslant 2.10^{-3}$, so that we indeed have $\alpha \ll \mu$ for most of the domains considered for the parameters. Still, we point out that a potential breach of this approximation might occur when the capacitance of the nanotransport path is extremely low (which would maximize α and the power) and the spin potential is weak (which would minimize the current).

Finally, we need to evaluate the conductances of the spin channels. Given the experimental results obtained during probing, we measured that shortcut junctions presented a conductance of 10^{-2} S, while most working devices presented a total conductance of 10^{-6} S. Taking into account the conductance associated with the wires, conductances of up to 100 S could be considered for favorable channels at the level of the microscopic device.

Given these observations, these measurements can give us some intuition about what to expect from the diode system parameters G_+, G_-, $G_\downarrow$ and $G_\uparrow$. Let us then look at different examples leading to a generative current.

- Consider that the spin-up channel is more conductive than the spin-down channel: $G_+ = 10$ S, $G_\uparrow = 10^{-1}$ S, $G_\downarrow = 10^{-5}$ S, $G_- = 10^{-6}$ S. Taking the smallest value we considered for the capacitance $C = 10^{-15}$ F and the sub-optimal value for the spin bias $\mu = 0.02$, we obtain the current $I = 3.10^{-7}$ A, the voltage $U = 5$ mV and thus the power $\langle P \rangle = 1.5$ nW. We can see that with these parameters, the results of the experiments on oxide junctions (see Figure 4.4) are well approximated, both in voltage and current! We remark that if the conductance of the spin-up channel can gain two orders of magnitude, then the results for molecular junctions can also be reproduced, although such a strong conductance could be improbable even at this scale.

- Take the spin-up channel as strongly conductive and moderately rectifying such that $G_+ = 30$ S and $G_\uparrow = 1$ S, with the same spin-down channel as weakly conductive and weakly rectifying $G_\downarrow = 1.1 \times 10^{-5}$ S and $G_- = 1.10^{-5}$ S. Then with the same C and a stronger spin-potential $\mu = 0.4$, we get $I = 6.10^{-5}$ A, $U = 5$ mV and $P = 3.10^{-8}$ W, which is another way to reproduce the results obtained for molecular junctions (see Figure 4.6). We mention that in this case, the order of magnitude chosen for the conductance of the spin-down channels has little importance provided that it is lower than the order of the spin-up channels.

Similar values can be obtained by favoring down-spin over up-spin channels by symmetry, in which case the current and the voltage will be reversed.

10.3 Discussion

In this Chapter, we showed how an electronic device based on two spin-diodes oriented in the opposite direction can convert a spin-potential imbalance into a charge current and a voltage, thereby delivering a constant electrical power. Our study revealed crucial working conditions that are necessary for the device to behave as an engine. The first condition ($\alpha \ll \mu$) ensures the perturbative regime and imposes that the energy required to deposit a quantum of charge on the capacitor formed by the device be smaller than the spin-potential energy provided by the difference in magnetization between the two reservoirs. The second condition ($\langle P \rangle > 0$) ensures that the device behaves as a generator, which imposes an asymmetry between the up-spin and down-spin conduction channels ($G_\uparrow \gtrless G_-$), in congruence with an asymmetry between the rectifying power of the two diodes $\left(\frac{G_+}{G_\uparrow} \gtrless \frac{G_\downarrow}{G_-}\right)$.

The main results of this Chapter, encompassed in Equations 10.36-10.38, establish the non-equilibrium voltage, current and power stabilized by the device, as a function of the spin-potential μ applied to the device and the capacitance C and conductances G of the four spin channels (up/down and forward/backward). Strikingly, the derivation reveals that the

output power does not depend on the spin-potential μ, for as long as it satisfies the perturbative condition, since the current depends linearly on it and the voltage inversely. This counter-intuitive result suggests that the output does not depend on the input, suggesting a kind of threshold effect. The equations also reveal that both the current and the voltage are inversely dependent on the capacitance such that the power can be greatly increased for devices with extremely low capacitance, provided also that it maintains the perturbative condition. Finally, a large current requires a strong conductance with a domination of one spin channel over the other, while a large voltage requires that one of the two spin diodes be weakly rectifying in an absolute sense ($G_{\pm} \sim G_{\updownarrow}$) and compared to the other diode.

Collecting all these ingredients into one device that promises to deliver a continuous, constant and sizable output power from the spin bias is challenging but the theory does suggest that both the molecular and the oxide spintronic engines experimentally reported in Chapter 4 rely on this mechanism. It requires a strong built-in spin bias of the order of 10 meV, corresponding to a magnetic field gradient of around 100 T that is constantly maintained within the device, whose precise mechanism still needs to be elucidated in more depth even though in the previous Chapters we have provided insight into several qualitative arguments that justify its origin in the macroscopic to microscopic coupling of the electrodes with the nanotransport path, through the spinterface.

This model thus give us a way to represent the device using five intrinsic parameters : the capacitance and the four conductances of each spin-channel along with the spin-potential, which can be considered as partly intrinsic since it shall depend both on the magnetic orientation of the electrodes and on the precise magnetic features of the spinterfaces. This theory opens up a path towards further experiments which would aim at characterizing these parameters for each device. To this end, the conductances may be obtained by measuring the resistance of the device subjected to a forward or backward spin-polarized current. Being able to probe the response of the device upon injecting a pure spin current would therefore confirm whether the device indeed acts as a spin diode and can behave as a generator. Studying the response of the device to an ac voltage should give us an estimation of the capacitance. Finally, given the spin-potential that is required for the device to act as a generator, probing the micro-magnetism of a junction in the vicinity of the electrode-spinterface pair may give some insight into magnetic field at the interface, and this could be achieved through augmented scanning tunneling microscopy methods. Although finding a systematic way to inject a spin-current into the device or probing the interface of a processed sample seems technologically challenging, looking at the response of the device to an ac current is readily accessible, so future efforts should be first oriented towards this goal.

This theory also raises interesting mathematical questions. Indeed, our perturbative study based on separated variables could only yield a solution to a device in the antiparallel backward direction in the case where the "power leakage" from the up-spin diode to the down-spin diode P is null. The following question thus appears: can the other configurations of the electrodes be solved analytically and can they behave as generators under specific conditions? What is the precise physical origin of P, interpreted as a constant representing the power leakage from spin $\uparrow$ to spin $\downarrow$ in the device, and can we justify that the device will naturally converge toward a steady-state where $P = 0$? What are the so-

lutions with $P \neq 0$ and can they manifest in the steady-state in the absence of additional external forces on the device? Further mathematical investigations may thus improve our understanding of the spintronic engine, and more generally of nonlinear electronic devices featuring two non-interacting transport channels. Additionally, numerical simulations of the continuous master equation derived in this Chapter may give us more insights into transport phenomena involving both charge and spin. In the end, we emphasize that this Chapter's theory is only as a minimal toy model so as to serve as a proof of concept validating the spintronic engine as an autonomous electronic device relying on a spin-bias to produce work. Indeed, the non-linear feedback we considered for the diode is the most simple and ideal kind of rectification that we can hope to mathematically treat in a comprehensive manner, while the experiments performed in Part II showcased much richer nonlinear electrical responses, leading to chaotic phenomena which seem quite impracticable to treat numerically. Henceforth, we hope that this work will serve as a basis to study more complex non-linear responses from which we will surely discover some emergent rich behaviors akin to self-sustained steady-state oscillations.

Finally, this model raises a question which is that of the microscopic origin of the nonlinear rectification of the device. In order to satisfy microscopic reversibility and energy conservation considerations, we would indeed expect that the two spin diodes be fueled by some kind of additional power source in order to generate this non-linearity. This raises fundamental questions: what is the thermodynamic resource used by the diodes to allow for their non-linear response? What are the microscopic ingredients that justify their asymmetric behavior? And what is the exact thermodynamical behavior of the misaligned spinterfaces stabilized by the underlying magnetizations? Chapter 8 gave us some insights about these questions, which may be linked to the quantum nature of the device, and especially to the complex relationship between quantum systems with discrete energy levels, quantum measurements, special kinds of reservoirs with conserved quantities and interaction rules between all these ingredients, ultimately giving rise to an autonomous Maxwell's demon at the microscale.

Discussion et perspectives

Le travail exposé dans ce manuscrit présente deux volets, l'un expérimental, l'autre théorique.

Pour la partie expérimentale, l'objectif premier était d'abord de reproduire les résultats pionniers sur le moteur spintronique obtenus en 2019 sur les jonctions magnétiques tunnel MgO dopées Carbone, dans le but de caractériser plus finement de nouveaux dispositifs actifs et d'éclairer leur conception en vue d'une possible production industrielle. Malheureusement, cet objectif n'a pas été atteint et aucun des dispositifs MgO étudiés au cours de mon travail de thèse n'a révélé de génération d'énergie. La raison de cet échec vient vraisemblablement d'un procédé de fabrication non maîtrisé, encore trop soumis à des aléas comme le positionnement aléatoire des impuretés de Carbone dans la barrière MgO, ne permettant la formation d'un complexe aux propriétés de récolte d'énergie que dans de très rares cas où leur géométrie présente une asymétrie et des couplages aux électrodes finement choisis. Tant qu'une méthode systématique de contrôle et de piégeage de ces centres paramagnétiques ne sera pas mise au point, il est donc possible que cette voie de synthèse ne soit pas adaptée pour produire suffisamment d'échantillons. Ce travail ouvre donc la voie vers la recherche de nouveaux procédés permettant le placement précis de complexes atomiques sur des couches minces.

En revanche, même si aucun moteur n'a été rapporté, les expériences ont tout de même révélé des jonctions aux réponses électroniques et magnétiques singulières, non encore observées dans ce genre de dispositifs oxide tout-solide, mais typiques des expériences de microscopie électronique et de jonctions moléculaires. Les résultats montrent en effet des jonctions présentant des comportements memristifs, et magnétorésistifs caractérisés par des sauts de conductance réversibles à des valeurs de tension spécifiques, un signal de magnétorésistance tunnel corrélé à la conductance différentielle ainsi que différents types de bruits localisés en tension et en température. Ces résultats nous montrent ainsi que ces dispositifs disposent d'un comportement mémoire.

D'un point de vue technologique, la diversité des effets rapportés, expliquée par des phénomènes quantiques, nous montre ainsi la possibilité d'utiliser des jonctions magnétiques tunnel dopées afin de développer des dispositifs spintronique performants. Le défaut principal à ce stade reste la difficulté à répliquer un dispositif à cause d'un contrôle insuffisant sur le nano canal de transport de charge. Cet aléa mène donc à une forte proportion de dispositifs aux propriétés triviales complété d'un petit nombre de jonctions présentant des caractéristiques uniquement semblables qualitativement (largeur des pics de conductance différentes, déplacement en tension des sauts de conductance...), ce qui rend l'automatisation de la lecture ou l'écriture difficile. Par ailleurs, les expériences n'ont

révélé qu'un comportement mémoire à des températures faibles, en deçà de la température ambiante, ainsi qu'une certaine volatilité de la mémoire ce qui limite leur utilisation pratique.

Pour autant, d'un point de vue scientifique, les propriétés remarquables de ces jonctions méritent tout de même d'être étudiées en ce qu'elles se montrent capable d'être une plateforme simple d'accès à l'étude de phénomènes quantiques, magnétiques et thermodynamiques à l'oeuvre à l'échelle de quelques atomes d'intérêt dans la barrière et aux interfaces, au sein d'un dispositif microscopique. L'inconvénient étant que pour l'instant, les expériences ne permettent pas d'avoir accès à la structure fine de chaque jonction, ce qui rend difficile l'analyse des données de magnéto-transport. Pour en apprendre plus sur leur fonctionnement, il serait donc nécessaire de disposer d'autres méthodes d'analyse notamment *in operando* afin de pouvoir identifier avec plus de certitude les interactions microscopiques dominantes qui donnent lieu à ces riches comportements. Dans cette optique, un projet en partenariat avec l'Université de Stuttgart est en cours en vue de réaliser des expériences de magnéto-transport sur ces jonctions en présence de micro-ondes. Par ailleurs, un autre projet est également en préparation en partenariat avec l'Université de Lorraine et le CEA-SPEC et vise à étudier plus en détail les caractéristiques et origines des différents types de bruits dans ces jonctions. Une compréhension plus aboutie des phénomènes stochastiques à l'œuvre pourrait en effet donner un éclairage sur de nombreux sujets comme la transition entre classique et quantique, la rectification spontanée, le transfert de charge et de moment angulaire entre deux électrodes, la spintronique des interfaces...

Cette recherche nous porte donc à souhaiter la continuation de ce travail expérimental en espérant que de nouvelles initiatives soient prises pour améliorer l'architecture et les procédés de fabrication de ces potentiels moteurs spintroniques. La récompense, une énergie abondante et peu polluante, fait naturellement rêver mais le risque et les efforts qu'il faudrait vraisemblablement déployer pour y arriver sont élevés.

Pour la partie théorique, qui ne faisait pas partie du projet de thèse initial, l'enjeu était d'abord d'identifier précisément les ressources thermodynamiques utilisées par les moteurs pour produire de l'énergie ainsi que les paramètres à optimiser pour garantir une efficacité optimale et ainsi orienter la conception pratique de ces dispositifs. Derrière ce travail théorique se trouvait aussi la volonté d'établir un modèle minimal permettant d'expliquer simplement le comportement du moteur en termes de spintronique et de thermodynamique quantique en vue de fédérer ces deux communautés autour de ce projet au travers d'arguments physiques afin de dissiper les controverses que génèrent ce moteur qui semble défier les lois de la thermodynamique. Sur ce point, les trois modèles présentés dans cette thèse ont potentiellement répondu à ces attentes.

D'une part, ces trois approches complémentaires fournissent des résultats similaires et proches des expériences avec un nombre restreint de paramètres physiques. Ces différents points de vue apportent des descriptions à différentes échelles, quantique, mésoscopique et macroscopique, de telle sorte à ce que chaque communauté puisse se convaincre de la faisabilité d'un tel dispositif. Par ailleurs, la simplicité de ces trois modèles peut permettre une compréhension rapide du principe de fonctionnement du moteur sans nécessité de nombreux détails techniques. En effet, pour le moteur quantique, le cycle proposé ne comprend

que deux étapes : la mesure et la thermalisation d'un système à trois niveaux connectés à des bains, tandis que les modèles spintroniques et électroniques ne reposent que sur un dispositif présentant une non-linéarité élémentaire ainsi qu'une réponse résolue en spin.

D'autre part, ces trois modèles ont identifié une différence de *potentiel magnétique* issue d'un désalignement d'aimantation entre les deux électrodes comme la force hors équilibre permettant au moteur de fonctionner. Ce potentiel magnétique se traduit en effet par l'existence d'un potentiel chimique résolu en spin, qui s'assimile à une tension de signe opposé pour les deux valeurs de spin de l'électron, et qui peut donc être convertie par un dispositif non linéaire pour produire une tension et un courant de charge.

Ces modèles simples constituent ainsi une preuve de principe, une porte d'entrée vers une future description plus fine de ces moteurs spintroniques. Tous ouvrent sur des questions en suspens qui mériteraient d'être étudiées plus en profondeur afin d'asseoir encore mieux les propositions de description physiques présentées dans cette thèse.

D'un point de vue quantique, le défaut majeur du modèle considéré réside dans la conjonction du caractère autonome et répété de la mesure quantique, qui nécessite un apport d'énergie moyen venant de l'outil de mesure. Afin d'être pleinement satisfaisant, ce modèle doit donc être complété d'une description fine de l'interaction à l'origine de la mesure quantique. Cette boîte noire mène inévitablement à des questions fondamentales liées au problème de la mesure et de l'observateur en mécanique quantique. A ce sujet, une piste de recherche serait de modéliser la mesure à l'aide d'un qubit additionnel faiblement couplé à un seul des deux sites ainsi qu'à un troisième bain. L'intuition voudrait alors que la dynamique de ce système composite à trois sites tende vers la dynamique du système à deux sites, entretenu par la mesure périodique. La prise en compte d'un troisième site se justifie notamment par les sauts de branches observés dans les expériences et qui suggère le changement d'état d'une boîte quantique dite environnementale et dont le remplissage impacte le transport au travers d'un effet capacitif.

Une autre piste serait ensuite de complexifier le modèle présenté avec des structures plus proches de la réalité, en y intégrant par exemple la polarisation des électrodes ferromagnétiques et non simplement demi-métalliques ainsi que des propriétés d'interface plus riches au travers d'une fonction spectrale de couplage spéciale. Les possibilités d'extension de ce modèle sont nombreuses mais mènent toutes à des difficultés analytiques qui invitent à poursuivre cette étude à l'aide de méthodes numériques qu'il serait intéressant de développer afin d'explorer l'espace de paramètres de ce moteur en vue de guider leur réalisation expérimentale.

Le modèle quantique a également révélé l'impact des difficultés techniques et conceptuelles liées à la détermination du cycle limite, à l'influence des conditions initiales ainsi qu'aux effets mémoires de la thermalisation imparfaite. Ces particularités mathématiques, intrinsèquement reliées à la théorie ergodique et la théorie du chaos soulèvent des questions fondamentales quant à la définition même de l'équilibre thermodynamique et du cadre théorique mis en place pour décrire un système complexe en accord avec la seconde loi de la thermodynamique. Ainsi ce modèle bénéficierait grandement d'une description complète de la fractale représentant la région de l'espace des phases formées par les attracteurs

de cette dynamique, correspondant à l'ensemble des cycles limites accessibles en partant d'une initialisation du système à partir d'un domaine de conditions initiales. Ultimement, ce type d'étude pourrait orienter les expériences vers un procédé d'amorçage sans lequel le dispositif reste dans un état passif ainsi que nous donner des indications sur la stabilité de ces états limites moteurs piégés, qui, nécessairement, finiront par se détériorer au fur et à mesure qu'un procédé thermodynamique à une échelle supérieure finira par corriger cette instabilité par recuits successifs.

Enfin, le modèle quantique est thermodynamiquement incomplet en ce qu'il ne permet pas de déduire la puissance électrique idéale délivrée par le moteur car seul un bilan énergétique du cycle complet a été étudié, donnant une borne supérieure du travail maximal produit par la machine puisqu'on s'attend à ce qu'un flux de chaleur se dégage aussi lors de la phase de thermalisation. Afin de donner une meilleure estimation de la puissance de sortie et d'exprimer un rendement, il faudrait donc poursuivre cette étude appliquant la première loi de la thermodynamique hors équilibre (cf Equation 2.12) pour séparer le travail de la chaleur.

D'un point de vue spintronique, nous avons montré qu'un matériau présentant une réponse spintronique non-linéaire élémentaire pouvait rectifier un courant de charge stochastique pour délivrer une puissance électrique continue, et que ce même matériau était aussi capable de produire un courant et une tension électrique en réponse à l'application d'un champ magnétique hors-équilibre piégé aux interfaces, se traduisant de manière effective par la persistance d'un gradient de potentiel chimique résolu en spin. Les hypothèses de ce modèle présentent alors deux défauts qui nécessiteraient des arguments additionnels.

D'abord, il s'agirait de démontrer expérimentalement que nos dispositifs présentent bien une réponse spintronique avec une non-linéarité semblable. Ceci pourrait se faire soit à l'aide d'expériences complémentaires, soit avec des méthodes théoriques *ab-initio*. La question centrale étant de savoir d'où vient cette non-linéarité et de quel flux d'énergie se nourrit-elle pour persister.

De plus, le modèle manque encore d'une description poussée de ce que représente le potentiel magnétique d'interface hors-équilibre et de pourquoi il serait maintenu spontanément. La réponse à cette question devra nécessairement impliquer une solution aux équations de Maxwell dans ce type de matériau où deux matériaux ferromagnétiques s'échangent des charges et des spins au travers d'un nano canal de transport, de telle sorte à ce que leur dynamique macroscopique d'aimantation interne ne puisse pas être considérée comme gelée et se manifeste comme une force thermodynamique s'exerçant principalement au niveau de leur point de contact formé par la jonction. Plusieurs arguments qualitatifs supportent l'existence d'un tel champ hors-équilibre comme la forte polarisation et faible bande passante de la spinterface, les propriétés de verre de spin des électrodes à l'origine d'états métastables aux durées de vie quasi infinies, différentes anisotropies magnétiques ou des courants de surface générés par le magnétisme des électrodes mais aucune de ces pistes n'a été quantitativement suivie de telle sorte à justifier proprement la persistance de potentiel magnétique d'interface, et d'évaluer sa dynamique et sa durée de vie.

Et ensuite, plusieurs paramètres ont été négligés dans ce modèle, en particulier les résistances d'interfaces qui réduisent la tension induite par le courant spontané. Intégrer des valeurs non-nulles de résistances pourrait mener à un modèle plus réaliste et changer les conditions de fonctionnement en réduisant la puissance délivrée.

D'un point de vue macroscopique, le modèle électronique présente l'avantage de ne se préoccuper que de la réponse spintronique globale du dispositif sans s'inquiéter des phénomènes microscopiques qui sous-tendent sa phénoménologie. Des questions identiques au modèle précédent se recouvrent donc comme la justification physique de la caractéristique non linéaire du dispositif ainsi que la source du gradient de potentiel dit magnétique ou résolu en spin. Au-delà, le modèle soulève des questions d'ordre mathématiques comme la signification physique de la constante d'intégration associée à la puissance du courant de transfert de spin, et de l'existence de solutions à l'équation maîtresse dans le cas où cette constante est non nulle. Il serait alors intéressant d'étudier plus en détail les solutions à variables non séparables de cette équation, en vue d'étudier toutes les configurations du dispositif. Il se pourrait alors que d'autres paramètres conduisent à une meilleure rectification du potentiel magnétique en courant de charge.

Par ailleurs, ce modèle électronique repose uniquement sur les quatre paramètres élémentaires de conductance résolue en spin et en direction du courant, qui pourraient s'estimer expérimentalement en mesurant la réponse des dispositifs à un courant polarisé en spin. L'accès à ces valeurs pourrait alors permettre de tester la validité du modèle à partir de données déterminées physiquement et non pas extrapolées par interpolation des paramètres du modèle sur les résultats de l'expérience.

Finalement, j'espère que quelques-unes des nombreuses perspectives de recherche ouvertes par ce travail seront menées et pourront déboucher sur une technologie ou d'autres avancées dans notre compréhension fondamentale de la matière.

Conclusion

Ce travail a d'abord présenté l'état de l'art des domaines des jonctions tunnel magnétiques, de la thermodynamique quantique et des moteurs quantiques avec une insistance particulière sur les phénomènes rapportés dans les expériences sur les jonctions MgO ainsi que sur les mécanismes nécessaires à la conception d'un dispositif thermodynamique actif.

Ensuite, le volet expérimental de cette étude a permis de mettre en lumière les propriétés de jonctions magnétiques tunnel pour lesquelles le transport de charge s'effectue au travers de complexes atomiques magnétiques et d'interfaces entre un matériau ferromagnétique et d'un sélecteur de spin. Les expériences menées sur des jonctions MgO contenant des impuretés de Carbone au sein de la barrière ont démontré des réponses spintroniques riches, d'origine quantique, se traduisant par des signatures memristives et magnétorésistives singulières permettant à ces dispositifs d'être utilisés comme des composants mémoires adressables électriquement.

Puis, cette thèse a proposé trois modèles théoriques permettant d'expliquer le fonctionnement du moteur à différentes échelles. Tous ont permis d'identifier la source d'énergie exploitée par le moteur qui réside dans l'inhomogénéité du champ magnétique interne du dispositif, influencée par la dynamique d'aimantation entre les deux électrodes ferromagnétiques au travers des spinterfaces. Ce champ magnétique hors équilibre donne alors lieu à une différence de potentiel magnétique de spin qui agit comme une force thermodynamique sur les électrons. Le moteur quantique convertit cette force en une tension et un courant de charge grâce à sa réponse non-linéaire, qui se postule comme une hypothèse phénoménologique ou qui se justifie dans l'approche quantique par l'action de la mesure quantique ainsi que des règles de transport de charge au travers la structure.

Les estimations théoriques entrent en accord avec les résultats expérimentaux obtenus précédemment sur des jonctions de ce type, donnant un certain crédit à ces approches qui mériteraient ainsi d'être étudiées davantage afin d'éclaircir les différentes questions soulevées par cette étude. Les difficultés à la fois expérimentales, fondamentales et mathématiques rencontrées dessinent ainsi les limites de notre compréhension conceptuelle et pratique de la matière et nous poussent à souhaiter que ce projet continue et mène à des découvertes à l'impact disruptif !

Ce manuscrit, je l'espère, pourra ouvrir la voie à une collaboration féconde entre les domaines de la thermodynamique quantique et de la spintronique, qui nécessitent cruellement d'être combinées afin de pouvoir expliquer avec précision les mécanismes qui gouvernent les dispositifs tels que le moteur spintronique.

« If someone points out to you that your pet theory of the universe is in disagreement with Maxwell's equations – then so much the worse for Maxwell's equations. If it is found to be contradicted by observation – well, these experimentalists do bungle things sometimes. But if your theory is found to be against the second law of thermodynamics, I can give you no hope; there is nothing for it but to collapse in deepest humiliation. »

Sir Arthur Eddington

Appendices

Appendix A

Current plume of quantum interference

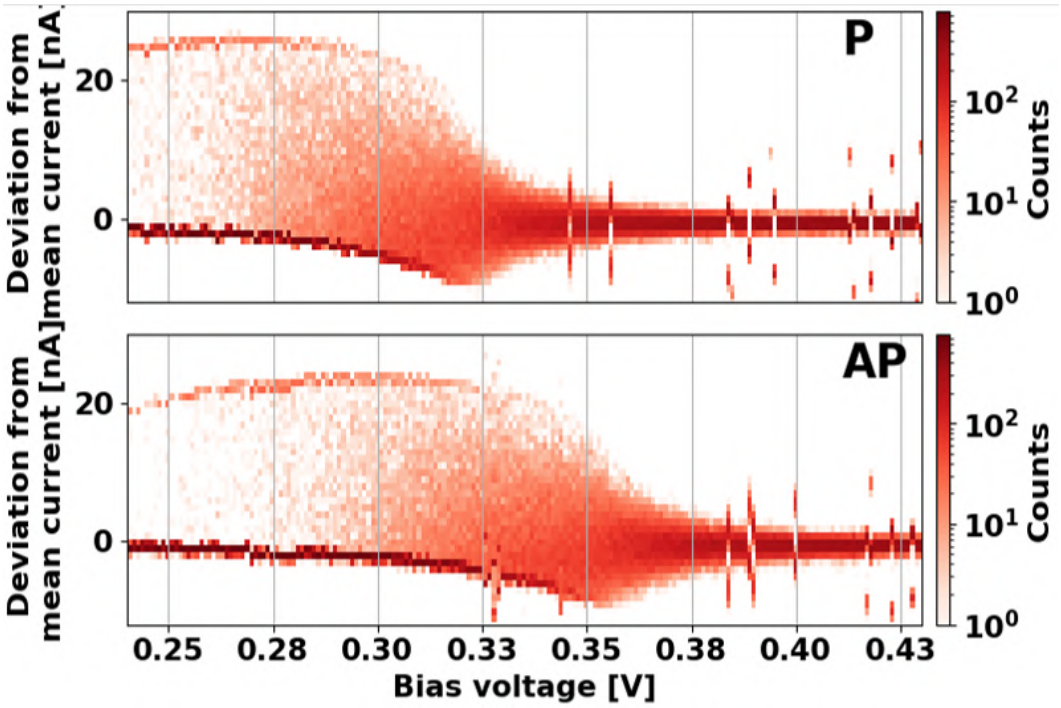

Figure A.1: **Zoom on the plume of quantum interference.** Bias dependence of the frequency of the deviation from the mean current. Data at $T = 10$ K in the MTJ's P (top) and AP (bottom) states is shown. Nanojunction C5 was used. Statistics are obtained on 800 points at each bias value.

We present in Figure A.1 a high resolution dataset of the current distribution plume reported in Figure 7.3 of the main text for the junction's P and AP states. We observe a positive 33 mV bias shift of the AP dataset due to spin accumulation. For each bias voltage we measured 800 times the junction current. The mean current is calculated and subtracted for all points inside the dataset, and

finally a histogram is computed with a bin size of 1 nA. The result of the histogram is represented in Figure A.1 by a vertical line of dots at the corresponding voltage bias, the color of a dot representing the number of counts in every bin of the histogram.

To distinguish spintronic contrast, we overlap the datasets by manually removing the shift (see Figure A.2(a)). We note that the OFF branch (lower branch) overlaps rather well. On the other hand, the ON branch (upper branch) exhibits a different deviation from mean current in the MTJ's P and AP states. We attribute this differing deviation to a slight change in the effective potential landscape due to spin-polarized hybridization between the electrodes and the localized paramagnetic barrier states.

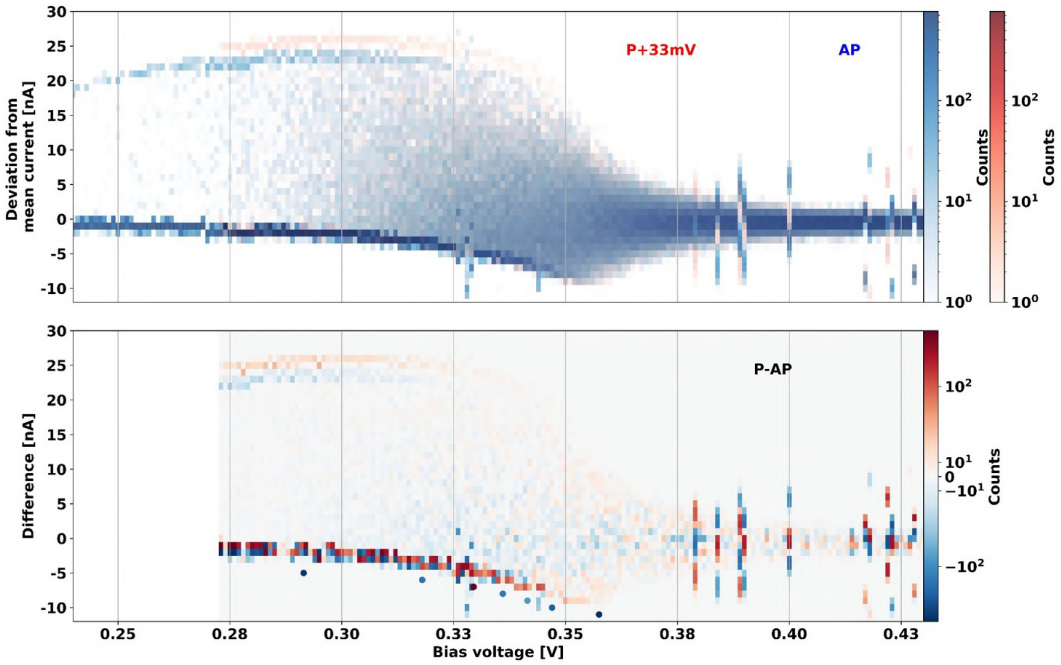

Figure A.2: **Spintronic contrast in the plume of quantum interference.** (Top) Same data as in Figure A.1, but with a +33 mV shift in the P data. (Bottom) Difference P-AP of the datasets of the top panel. The round dots below the lower branch represent an average of the lower branch difference data. They are centered around the range considered. These points are all blue-leaning: the lower branch is more strongly weighed in the MTJ's AP state.

To further examine spintronic contrast, we then consider the difference P-AP between the datasets. The results are plotted in the bottom panel of Figure A.2 We observe that the difference is very pronounced for the OFF branch. To confirm this trend, we're integrated this difference over several bias ranges. The position of the resulting round dots below the OFF branch represents the center of the range, while the color code shows the averaged result. Over the seven bias ranges considered, all averages of the OFF branch reveal that the OFF branch is more prevalent in the MTJ's AP state. We infer that the transport path responsible for the OFF branch is spin-polarized.

Appendix B

Spin accumulation at negative bias

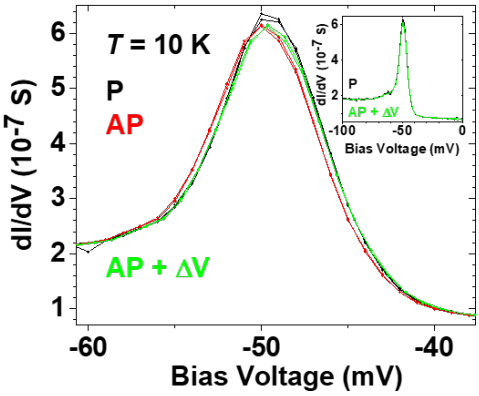

Figure B.1: **Spin accumulation on the sharpest Coulomb blockade peak found at $V < 0$.** Bias dependence of differential conductance $\mathrm{d}I/\mathrm{d}V$ at $T = 10$ K on junction G10 in the MTJ's P (black) and AP (red) states. The AP data in green was bias-shifted by +0.35 mV. This shift enables a qualitatively good overlap of the conductance peak with that seen in the P data. Inset: Overview of the conductance peak in the MTJ's P state, and the bias-shifted AP data.

In the main text, we present evidence at $V > 0$ of a shift to higher bias values of the Coulomb blockade peaks when the MTJ's magnetic state is switched from P to AP. We now consider the case of $V < 0$, and focus on the Coulomb blockade peak shown in Figure B.1. Its presence can also be switched on/off thanks to writing events E_+ and E_-, leading to different values of TMR at that bias position (see Figure 6.1(c)). The data of Figure B.1 is acquired within -100 < V (mV) < 0, *i.e.* below the writing events E_- and E_+ (see inset). An excellent overlap between the P and AP data is seen for bias value below the peak. However, as the peak onset is reached, a bias shift is clearly seen. The very close agreement in the data for the forward and reverse scans underscores that the shift is not the result of trivial charging/heating effects. To qualitatively estimate the small bias shift between the P and AP data, we manually shift the AP data. A reasonable fit is found for a bias shift of 0.35 mV.

Appendix C

Overview of the several Coulomb gaps with evolving junction state

In our datasets, we observe that heating/cooling our FeCoB/MgO/C/MgO/FeCoB junctions, and bias cycling, can alter the effective potential landscape inferred at $T = 10$ K from the current derivative. To illustrate these effects, we focus on junction G10. We plot in Figure C.1(a) select $\mathrm{d}I/\mathrm{d}V$ traces obtained after three cooldowns. We have looked for a pattern of pairs of peaks with the same energy spacing as thermal and electrical cycling were conducted. This led us to label pairs of peaks and ascribe them to the charging of a given C atom. In total we identify at least 3, and as many as 5, atoms involved in the device's electrical response. As described in the main text, these atoms can be in the main transport path. In that case, charging the atom generates a conduction peak. Alternatively, the atom in question can be tunnel coupled to a C atom that is in the transport path, and thus constitutes an 'environmental' atom. Following the deductions of Figure C.1 and accompanying

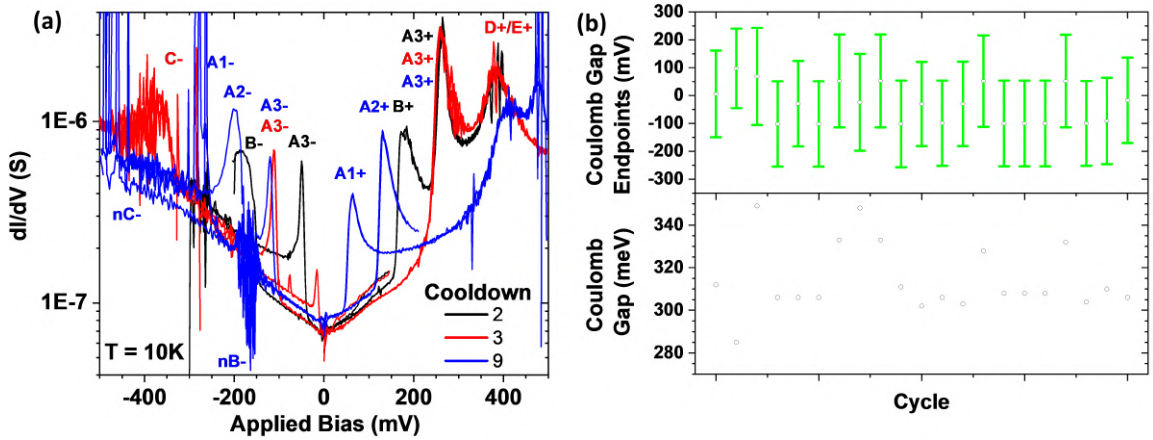

Figure C.1: **Overview of Coulomb gap energies with evolving junction state.** (a) Select $\mathrm{d}I/\mathrm{d}V$ traces for three cooldowns. (b) (top) Endpoints of the Coulomb gap for select datasets deduced from the bias spacing of pairs of conductance peaks. (bottom) The resulting Coulomb energy gap of the transport atom. Junction G10 was used. The data from four cooldowns was used.

text, we assumed that energy motion of a pair of peaks was due to changes in the environmental charge felt by the transport atom, rather than the re-attribution of 'transport' and 'environmental' roles. This logic is supported by the fairly stable energy gap between the paired peaks (see Figure C.1(b))

Using this labeling logic, we find for example, for cooldown 9, that pairs of conductance peaks can be attributed to the same carbon atom A, and that, in the course of IV cycling, three absolute energy positions of its Coulomb gap (see labels A1-, A2-, A3- and A1+, A2+ and A3+ in Figure C.1(a)) relative to the MTJ electrodes' Fermi level can be tracked as the environmental charge is varied through write events E_+ and E_-. Note how after an E_+ writing event the pair of peaks shifts to lower absolute bias. The reverse occurs for an E_- writing event. This trend in the bias shift was systematically observed, when a shift indeed occurred (see Appendix B).

We observe additional conductance peaks at higher absolute bias voltage. In the absence of a clear trend suggesting additional charging of atom A, we surmise that these peaks correspond to additional atoms (C, D...) directly in the transport path.

Comparing these cooldowns, we observe that the peak of a $\mathrm{d}I/\mathrm{d}V$ in one cooldown can spectrally correspond to noise for another cooldown. The best example is, at $V \sim -190$ mV, that of peak B- in cooldown 2 (black), and of the corresponding noise nB- in cooldown 9 (blue). We infer that atom B is present in the transport path in cooldown 2, but becomes an environmental atom in cooldown 9. This also explains the absence of peaks B- and B+ in cooldowns 3 and 9.

We also observe that, in the junction state defined by cooldowns 3 and 9, the writing event E_+ occurs just as the spectral window B+ corresponding to environmental atom B is reached with increasing positive bias around +150 mV. This illustrates the role that the charge state of the environmental atom has in the junction write process.

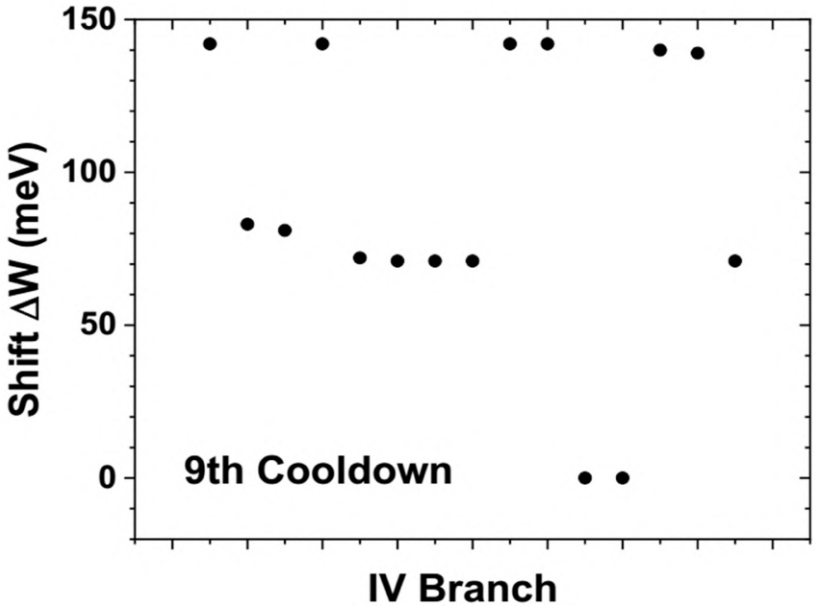

Figure C.2: **Quantization of the energy shift of the transport atom's Coulomb gap.** Absolute values are shown.

Within the junction state defined by a cooldown, writing events E_- and E_+ generate an effective bias shift that can be quantized. A $\sim$75 meV shift was observed on transport atom A during the 1357 tests of the E_- and E_+ event after cooldown 10 (see Appendix B). A shift of 111 meV was observed on atom B in a transport role, However, those junction states promoted only two pairs of peaks. We present in C.2 the energy shift Δ_W data in junction cooldown 9 arising from the presence of 3 pairs of peaks due to transport atom A. Aside from the trivial $\Delta_W = 0$ points due to write failure (see Appendix B), Δ_W takes on multiple values of 70-80 meV. Here, we make the reasonable assumption that the charge of an environmental atom can only change by 1 electron, which implies that several environmental atoms can be charged during a write event.

Appendix D

Estimation of the impurities sizes and distances

Let us approximate the impurity involved in transport as a sphere of radius r, located at a distance d from the lower electrode, with inter-electrode spacing l. In the far-field limit, the capacitance C is given in Reference [575] and reads:

$$C = \frac{4\pi\epsilon\epsilon_0 r}{1 + \left[\psi^{(0)}(\frac{d}{l}) + \psi^{(0)}(1 - \frac{d}{l}) + 2\gamma\right]\frac{r}{2l}}, \tag{D.1}$$

where $\psi^{(0)}$ is the polygamma function. Using the relation between the capacitance and the charging energy $E_C = e^2/2C = e\Delta_{CG}$, we obtain the radius of the impurity

$$r = \frac{l}{8\pi\epsilon\epsilon_0\Delta_{CG}/e + 5/3} \tag{D.2}$$

where $\frac{1}{2}\left[\psi^{(0)}(\frac{d}{l}) + \psi^{(0)}(1 - \frac{d}{l}) + 2\gamma\right] \approx -\frac{5}{3}$ with $d = 1$ nm and $l = 3$ nm as approximated from the experimental design of the stack. Taking $\epsilon = 9$ for the relative permittivity of MgO according to Reference [576], we obtain $r = 0.2$ nm. This shows that the impurities involved in the transport are of atomic sizes and should indeed correspond to single carbon atoms or dimers trapped inside the MgO lattice.

Let us now approximate both the transport and environmental quantum dots as two spheres of radius r, separated by a distance d. The capacitance C of the system is approximately given by:

$$C = \frac{2\pi\epsilon_0\epsilon r}{1 - \frac{r}{d-r}}. \tag{D.3}$$

According to the observed shift $\Delta_W = 70$ mV which shall be due to the change of charge of one environmental quantum dot by a quantum of elementary charge, we should then write:

$$e = C\Delta_W, \tag{D.4}$$

which leads to the distance between the dots:

$$d = r\left(1 + \frac{1}{1 - \frac{2\pi\epsilon\epsilon_0 r\Delta_W}{e}}\right). \tag{D.5}$$

With $r = 0.2$ nm as estimated above; we obtain the following approximation:

$$d \approx 2r, \tag{D.6}$$

such as $d = 0.4$ nm. We thus find that the distance between the transport quantum dots and the environmental charging species is of the order of the diameter of the dots, so the control dot should be a second, third or fourth neighboring site of the transport dot in the MgO lattice. This estimation confirms that we are indeed observing the interaction of a reduced number of atomic formations closely packed inside the MgO barrier which are producing single-electron effects.

Appendix E

The Quantum Master Equation

In this Appendix, we derive a quantum master equation that describes the evolution of the reduced density matrix of the QD system presented in Chapter 8.

E.1 The integro-differential master equation

Taking $\hbar = 1$, the total density matrix ρ represented in the Schrödinger picture obeys the Von-Neumann equation:

$$\frac{\mathrm{d}\rho}{\mathrm{d}t} = -\mathrm{i}[H, \rho(t)] \tag{E.1}$$

Switching to the interaction picture where any operator O reads:

$$\tilde{O}(t) = e^{\mathrm{i}(H_S+H_E)t} O e^{-\mathrm{i}(H_S+H_E)t} \,, \tag{E.2}$$

where the Von-Neumann equation now reads:

$$\frac{\mathrm{d}\tilde{\rho}}{\mathrm{d}t} = -\mathrm{i}[\tilde{H}_{SE}(t), \tilde{\rho}(t)] \,, \tag{E.3}$$

which integrates into

$$\tilde{\rho}(t) = -\mathrm{i}\int_0^t [\tilde{H}_{SE}(s), \tilde{\rho}(s)]\mathrm{d}s \,. \tag{E.4}$$

Inserting this formula back into the Von-Neumann equation leads to

$$\frac{\mathrm{d}\tilde{\rho}}{\mathrm{d}t} = -\mathrm{i}[\tilde{H}_{SE}(t),\, \tilde{\rho}(0)] - \int_0^t [\tilde{H}_{SE}(t),\, [\tilde{H}_{SE}(t'),\, \tilde{\rho}(t')]]\mathrm{d}t' \,. \tag{E.5}$$

We now invoke the Born approximation (weak coupling) which states that the system does not influence the environment, so that $\tilde{\rho}_E(t) = \tilde{\rho}_E$ and the system decomposes as a tensor product at all times, $\tilde{\rho}(t) = \tilde{\rho}_S(t) \otimes \tilde{\rho}_E$. Under this approximation, tracing out the Von-Neumann equation governing the evolution of the composite system leads to

$$\frac{\mathrm{d}\tilde{\rho}}{\mathrm{d}t} = -\mathrm{i}\mathrm{Tr}_E[\tilde{H}_{SE}(t),\, \tilde{\rho}_S(0) \otimes \tilde{\rho}_E] - \int_0^t \mathrm{Tr}_E[\tilde{H}_{SE}(t),\, [\tilde{H}_{SE}(t'),\, \tilde{\rho}_S(t') \otimes \tilde{\rho}_E]]\mathrm{d}t' \,. \tag{E.6}$$

We now write the tunnel interaction as:

$$H_{SE} = \sum_{i=1}^{4} S_i \otimes T_i \ , \tag{E.7}$$

with

$$\begin{array}{ll} S_1 \otimes T_1 = c_\uparrow^\dagger \otimes \sum_k \gamma_k c_k \equiv S_L^\dagger \otimes T_L, & S_2 \otimes T_2 = c_\uparrow \otimes \sum_k \gamma_k^* c_k^\dagger \equiv S_L \otimes T_L^\dagger, \\ S_3 \otimes T_3 = c_R^\dagger \otimes \sum_p \gamma_p c_p \equiv S_R^\dagger \otimes T_R, & S_4 \otimes T_4 = c_R \otimes \sum_p \gamma_p^* c_p^\dagger \equiv S_R \otimes T_R^\dagger \end{array} \ . \tag{E.8}$$

Then, in the interaction picture, we obtain the simple form:

$$\tilde{H}_{SE}(t) = e^{\mathrm{i}Ht} H_{SE} e^{-\mathrm{i}Ht} = \sum_{i=1}^{4} e^{\mathrm{i}H_S t} S_i e^{-\mathrm{i}H_S t} \otimes e^{\mathrm{i}H_E t} T_i e^{-\mathrm{i}H_E t} \equiv \sum_i \tilde{S}_i(t) \otimes \tilde{T}_i(t). \tag{E.9}$$

E.2 Bath operators in the interaction picture

We now need to calculate the operators T_i in the interaction picture. From the anti-commutation relations, we have, for all $l \in \mathbb{N}$:

$$c_k n_k^{l+1} = c_k c_k^\dagger c_k n_k^l = (1 - c_k^\dagger c_k) c_k n_k^l = c_k n_k^l = \ \ldots \ = c_k \ , \tag{E.10}$$

and $n_k^{l+1} c_k = 0$, therefore, expanding the exponential in series, we have:

$$c_k e^{-\mathrm{i}\epsilon_k n_k t} = \sum_{l=0}^{+\infty} \frac{(-\mathrm{i}\epsilon_k t)^l}{l!} c_k n_k^l = \sum_{l=0}^{+\infty} \frac{(-\mathrm{i}\epsilon_k t)^l}{l!} c_k = e^{-\mathrm{i}\epsilon_k t} c_k \ , \tag{E.11}$$

and

$$e^{\mathrm{i}\epsilon_k n_k t} c_k = c_k + \sum_{l=1}^{+\infty} \frac{(\mathrm{i}\epsilon_k t)^l}{l!} n_k^l c_k = c_k \ , \tag{E.12}$$

therefore

$$e^{\mathrm{i}\epsilon_k n_k t} c_k e^{-\mathrm{i}\epsilon_k n_k t} = e^{-\mathrm{i}\epsilon_k t} c_k \ , \tag{E.13}$$

and because of the commutation relation $[n_k, n_{k'}] = 0$, we obtain:

$$e^{\mathrm{i}H_E t} c_k e^{-\mathrm{i}H_E t} = e^{\mathrm{i}H_L t} c_k e^{-\mathrm{i}H_L t} = e^{\mathrm{i}\sum_{k'} \epsilon_{k'} n_{k'} t} c_k e^{-\mathrm{i}\sum_{k'} \epsilon_{k'} n_{k'} t} = e^{-\mathrm{i}\epsilon_k t} c_k \ . \tag{E.14}$$

An identical relation is obtained for $c^\dagger$ by taking the adjoint:

$$e^{\mathrm{i}H_E t} c_k^\dagger e^{-\mathrm{i}H_E t} = e^{\mathrm{i}\epsilon_k t} c_k^\dagger \ , \tag{E.15}$$

which leads to the particle number by multiplying the two previous results:

$$e^{\mathrm{i}H_E t} n_k e^{-\mathrm{i}H_E t} = n_k \ , \tag{E.16}$$

which is correct because n_k commutes with every term of H_E. The same relations can be obtained for the right lead by taking $k = p$. We now have all the elements to write the $T_i(t) \equiv e^{\mathrm{i}H_E t} T_i e^{-\mathrm{i}H_E t}$ in the interaction picture

$$\begin{array}{ll} \tilde{T}_L(t) = \sum_k \gamma_k e^{-\mathrm{i}\epsilon_k t} c_k, & \tilde{T}_R(t) = \sum_p \gamma_p e^{-\mathrm{i}\epsilon_p t} c_p \end{array} \ . \tag{E.17}$$

E.3 Averages over the bath

The average values $\langle \tilde{T}_i(t) \rangle_E = \mathrm{Tr}(\tilde{T}_i(t)\rho_E)$ in the ρ_E state can now be calculated and yield

$$\langle \tilde{T}_L(t) \rangle_E = 0 \text{ and } \langle \tilde{T}_R(t) \rangle_E = 0 \tag{E.18}$$

Indeed, we recall that the one point functions $\langle c \rangle_E$ all vanish because the number operators are hermitian and commute with H_E. Therefore, by diagonalizing in a common basis, the c and $c^\dagger$ project each eigenspace onto their perpendicular space because they change the particle number, so the trace is null.

The same argument allows us to calculate the averages $\langle \tilde{T}_i^\dagger(t)\tilde{T}_j(t') \rangle$. The only four two-point functions that do not vanish are:

$$\begin{array}{l} \langle \tilde{T}_L^\dagger(t)\tilde{T}_L(t') \rangle_E = \sum_k |\gamma_k|^2 e^{\mathrm{i}\epsilon_k(t-t')} \langle n_k \rangle_E \\ \langle \tilde{T}_L(t)\tilde{T}_L^\dagger(t') \rangle_E = \sum_k |\gamma_k|^2 e^{-\mathrm{i}\epsilon_k(t-t')} (1 - \langle n_k \rangle_E) \\ \langle \tilde{T}_R^\dagger(t)\tilde{T}_R(t') \rangle_E = \sum_p |\gamma_p|^2 e^{\mathrm{i}\epsilon_p(t-t')} \langle n_p \rangle_E \\ \langle \tilde{T}_R(t)\tilde{T}_R^\dagger(t') \rangle_E = \sum_p |\gamma_p|^2 e^{-\mathrm{i}\epsilon_p(t-t')} (1 - \langle n_p \rangle_E) \end{array} . \tag{E.19}$$

E.4 The GKSL master equation

The first term in the integro-differential equation reads:

$$\mathrm{Tr}_E[\tilde{H}_{SE}(t), \tilde{\rho}_S(0) \otimes \tilde{\rho}_E] = \sum_{i=1}^{4} [\tilde{S}_i(t), \tilde{\rho}_S(0)] \langle \tilde{T}_i(t) \rangle_E \, . \tag{E.20}$$

We can always choose a special Hamiltonian by adding a constant to it such that $\langle T_i \rangle_E = 0$. Indeed, the rescaled Hamiltonian $H = \left(H_S + \sum_i \langle T_i \rangle_E S_i\right) + H_E + H'_{SE}$, with $H'_{SE} = \sum_i S_i \otimes (T - \langle T_i \rangle_E)$ is such that $\langle T'_i \rangle_E = 0$, with $T'_i = T_i - \langle T_i \rangle_E$, while having the same dynamics. Therefore, we can discard this term in the equation.

The second term in the Von-Neumann equation reads:

$$-\int_0^t \mathrm{Tr}_E\Big([\tilde{H}_{SE}(t),\ [\tilde{H}_{SE}(t'), \tilde{\rho}_S(t) \otimes \tilde{\rho}_E]]\Big) \mathrm{d}t' \tag{E.21}$$

which expands into

$$\begin{aligned} -\int_0^t \mathrm{Tr}_E\Big(& \tilde{H}_{SE}(t)\tilde{H}_{SE}(t')\tilde{\rho}_S(t) \otimes \tilde{\rho}_E - \tilde{H}_{SE}(t')\tilde{\rho}_S(t) \otimes \tilde{\rho}_E \tilde{H}_{SE}(t) \\ & - \tilde{H}_{SE}(t)\tilde{\rho}_S(t) \otimes \tilde{\rho}_E \tilde{H}_{SE}(t') + \tilde{\rho}_S(t) \otimes \tilde{\rho}_E \tilde{H}_{SE}(t')\tilde{H}_{SE}(t) \Big) \mathrm{d}t' \, , \end{aligned} \tag{E.22}$$

reading also:

$$\int_0^t \mathrm{Tr}_E\Big([\tilde{H}_{SE}(t')\tilde{\rho}_S(t) \otimes \tilde{\rho}_E, \tilde{H}_{SE}(t)]\Big) \mathrm{d}t' + \int_0^t \mathrm{Tr}_E\Big([\tilde{H}_{SE}(t), \tilde{\rho}_S(t) \otimes \tilde{\rho}_E \tilde{H}_{SE}(t')]\Big) \mathrm{d}t' \, . \tag{E.23}$$

Invoking now the hermiticity of $\tilde{H}_{SE}$, we replace $\tilde{H}_{SE}(t)$ by $\tilde{H}_{SE}^{\dagger}(t)$ in the first term and $\tilde{H}_{SE}(t')$ by $\tilde{H}_{SE}^{\dagger}(t')$ in the second term, then we express the tunnel Hamiltonians in terms of S_i and T_i and use the cyclicity property of the trace to obtain

$$\sum_{i,j}\int_0^t \langle \tilde{T}_i^{\dagger}(t)\tilde{T}_j(t')\rangle_E [\tilde{S}_j(t')\tilde{\rho}_S(t), \tilde{S}_i^{\dagger}(t)]\mathrm{d}t' + \int_0^t \langle \tilde{T}_i^{\dagger}(t')\tilde{T}_j(t)\rangle_E [\tilde{S}_j(t), \tilde{\rho}_S(t)\tilde{S}_i^{\dagger}(t')]\mathrm{d}t' \tag{E.24}$$

Using the above expressions for the tunnel two point functions, and evolving the system operators from t' to t, only four terms remain:

$$\begin{aligned}
&\int_0^t \langle \tilde{T}_L^{\dagger}(t)\tilde{T}_L(t')\rangle_E e^{\mathrm{i}\epsilon_{\downarrow}(t'-t)}\mathrm{d}t' [\tilde{S}_L(t)\tilde{\rho}_S(t), \tilde{S}_L^{\dagger}(t)] \\
&+ \int_0^t \langle \tilde{T}_L^{\dagger}(t')\tilde{T}_L(t)\rangle_E e^{\mathrm{i}\epsilon_{\downarrow}(t-t')}\mathrm{d}t' [\tilde{S}_L(t), \tilde{\rho}_S(t)\tilde{S}_L^{\dagger}(t)] \\
&+ \int_0^t \langle \tilde{T}_R^{\dagger}(t)\tilde{T}_R(t')\rangle_E e^{\mathrm{i}\epsilon_R(t'-t)}\mathrm{d}t' [\tilde{S}_R(t)\tilde{\rho}_S(t), \tilde{S}_R^{\dagger}(t)] \\
&+ \int_0^t \langle \tilde{T}_R^{\dagger}(t')\tilde{T}_R(t)\rangle_E e^{\mathrm{i}\epsilon_R(t-t')}\mathrm{d}t' [\tilde{S}_R(t), \tilde{\rho}_S(t)\tilde{S}_R^{\dagger}(t)]
\end{aligned} . \tag{E.25}$$

With a final change of variable $s \equiv t' - t$, the integrals can now be extended to infinity such as they do not depend on t and we obtain the master equation in the interaction picture:

$$\frac{\mathrm{d}\tilde{\rho}_S}{\mathrm{d}t} = \mathcal{T}_L^{-}\mathcal{D}[\tilde{S}_L^{\dagger}(t)](\tilde{\rho}_S) + \mathcal{T}_L^{+}\mathcal{D}[\tilde{S}_L(t)](\tilde{\rho}_S) + \mathcal{T}_R^{-}\mathcal{D}[\tilde{S}_R^{\dagger}(t)](\tilde{\rho}_S) + \mathcal{T}_R^{+}\mathcal{D}[\tilde{S}_R(t)](\tilde{\rho}_S) \tag{E.26}$$

where the superoperator $\mathcal{D}$ is given by:

$$\mathcal{D}[S](\rho) = S\rho S^{\dagger} - \frac{1}{2}\{S^{\dagger}S, \rho\}\ , \tag{E.27}$$

and the coefficients are reading:

$$\boxed{\begin{array}{l}
\mathcal{T}_L^{-} = \int_0^{+\infty} \sum_k |\gamma_k|^2 e^{\mathrm{i}(\epsilon_k - \epsilon_{\downarrow})s}\langle n_k\rangle_E \,\mathrm{d}s, \\
\mathcal{T}_L^{+} = \int_0^{+\infty} \sum_k |\gamma_k|^2 e^{-\mathrm{i}(\epsilon_k - \epsilon_{\downarrow})s}(1-\langle n_k\rangle)_E \,\mathrm{d}s, \\
\mathcal{T}_R^{-} = \int_0^{+\infty} \sum_p |\gamma_p|^2 e^{\mathrm{i}(\epsilon_p - \epsilon_R)s}\langle n_p\rangle_E \,\mathrm{d}s, \\
\mathcal{T}_R^{+} = \int_0^{+\infty} \sum_p |\gamma_p|^2 e^{-\mathrm{i}(\epsilon_p - \epsilon_R)s}(1-\langle n_p\rangle)_E \mathrm{d}s
\end{array}} . \tag{E.28}$$

Going back to the Schrödinger picture, we finally get:

$$\boxed{\frac{\mathrm{d}\rho_S}{\mathrm{d}t} = -i[H_S, \rho_S] + \mathcal{T}_L^{-}\mathcal{D}[S_L^{\dagger}](\rho_S) + \mathcal{T}_L^{+}\mathcal{D}[S_L](\rho_S) + \mathcal{T}_R^{-}\mathcal{D}[S_R^{\dagger}](\rho_S) + \mathcal{T}_R^{+}\mathcal{D}[S_R](\rho_S).} \tag{E.29}$$

The constants $\mathcal{T}_L^{-}$ and $\mathcal{T}_R^{-}$ are characterize the electrons tunneling coefficients of the left and right leads, while $\mathcal{T}_L^{+}$ and $\mathcal{T}_R^{+}$ characterize the hole tunneling coefficients.

We need a final approximation to gain insights on these coefficients. Using the secular approximation, discarding the fast-oscillating terms, we get:

$$\boxed{\begin{array}{l}
\mathcal{T}_L^{-} = \sum_k |\gamma_k|^2 \langle n_k\rangle_E\ , \\
\mathcal{T}_L^{+} = \sum_k |\gamma_k|^2 (1-\langle n_k\rangle)_E, \\
\mathcal{T}_R^{-} = \sum_p |\gamma_p|^2 \langle n_p\rangle_E, \\
\mathcal{T}_R^{+} = \sum_p |\gamma_p|^2 (1-\langle n_p\rangle)_E,
\end{array}} \tag{E.30}$$

such that $\mathcal{T}^-$ and $\mathcal{T}^+$ are not independent since we should have $\mathcal{T}^+ + \mathcal{T}^- = \sum_k |\gamma_k|^2 \equiv \kappa$. This approximation thus require some detailed balance when considering perfectly thermal baths such that $\mathcal{T}^- = \kappa n_F(\mu, T)$ and $\mathcal{T}^+ = \kappa(1 - n_F(\mu, T))$, where $n_F(\mu, T) = \frac{1}{1+e^{-\mu/k_B T}}$ is the Fermi function at temperature T and electrochemical potential μ. In the following, we will discard the link between the two quantities and consider that they can be tuned relatively independently either by acting on the electron filling, the electrochemical potential, the temperature, or by invoking some non-thermal interaction between the spinterface and the QDs, which will be the topic of a future paper. We will avoid this discussion by placing ourselves mainly in the high-temperature limit such as $\mathcal{T}^- \approx \mathcal{T}^+$. Indeed, at room temperature $T = 300$ K, the thermal energy is $k_B T \approx 26$ meV which is an order of magnitude higher than the energies $\epsilon \approx 1$ meV we are considering in this system, so this approximation should hold.

E.5 Bosonic Bath

We shall now proceed as above in order to establish a Lindblad master equation accounting for this added bosonic bath. The interaction Hamiltonian now reads $H_I \equiv H_{SE} + H_{SB}$ and we decompose H_{SB} as:

$$H_{SB} = FA + FA^\dagger + F^\dagger A + F^\dagger A^\dagger, \tag{E.31}$$

where $F \equiv c_\uparrow^\dagger c_\downarrow$ is the flip operator that corresponds to the relaxation of a spin on the left dot from $\downarrow$ to $\uparrow$, and $A \equiv \sum_q \lambda_q a_q$ is the total ladder bosonic operator.

In the interaction picture, this operator becomes

$$\begin{aligned}
\tilde{H}_I(t) &= e^{i(H_E+H_B)t} H_I e^{-i(H_E+H_B)t} && \text{(E.32)}\\
&= \tilde{H}_{SE}(t) + F(t)A(t) + F(t)A^\dagger(t) + F^\dagger(t)A(t) + F^\dagger(t)A^\dagger(t) && \text{(E.33)}\\
&= \tilde{H}_{SE}(t) + \sum_q \lambda_q (e^{-it\delta} F + e^{it\delta} F^\dagger)(e^{-iqt} a_q + e^{iqt} a_q^\dagger), && \text{(E.34)}
\end{aligned}$$

where $\delta \equiv \epsilon_\downarrow - \epsilon_\uparrow$. Moving into the continuum limit, one thus gets

$$\begin{aligned}
\tilde{H}_I(t) = \tilde{H}_{SE}(t) + \int \sqrt{J(\omega)} (e^{-it(\omega+\delta)} F a(\omega) + e^{it(\delta-\omega)} F^\dagger a(\omega) + e^{-it(\delta-\omega)} F a^\dagger(\omega) \\
+ e^{it(\delta+\omega)} F^\dagger a^\dagger(\omega)) \mathrm{d}\omega, \quad \text{(E.35)}
\end{aligned}$$

where $J(\omega)$ is the density of oscillators per unit frequency, usually referred to as the spectral density of the bath. Then, employing the rotating wave approximation, we can discard the fast oscillating terms in $Fb(\omega)$ and in $F^\dagger b^\dagger(\omega)$ such as

$$\tilde{H}_I(t) = \tilde{H}_{SE}(t) + \int \sqrt{J(\omega)} (e^{it(\delta-\omega)} F^\dagger a(\omega) + e^{-it(\delta-\omega)} F a^\dagger(\omega)) \mathrm{d}\omega. \tag{E.36}$$

Using the Born-Markov approximation and the same renormalization trick as above to remove the one-particle bath terms, we can write the following equation of evolution of the reduced density matrix in the interaction picture:

$$\frac{\mathrm{d}\tilde{\rho}}{\mathrm{d}t} = -\int_0^t \mathrm{Tr}_{EB}\Big([\tilde{H}_I(t),\ [\tilde{H}_I(t'), \tilde{\rho}_S(t) \otimes \tilde{\rho}_E \otimes \tilde{\rho}_B]]\Big) \mathrm{d}t' \tag{E.37}$$

where Tr_{EB} is the partial trace over the two electrode baths and the bosonic bath.

After a bit of algebra, we separate the contributions from the electrodes and the bosonic bath and find:

$$\frac{\mathrm{d}\tilde{\rho}}{\mathrm{d}t} = \mathcal{D}_E(t)\tilde{\rho} + \int_0^t \int\int \sqrt{J(\omega)J(\omega')}\langle a^\dagger(\omega)a(\omega')\rangle e^{i(\omega t-\omega' t')}[F(t')\rho(t), F^\dagger(t)]\mathrm{d}\omega\mathrm{d}\omega'\mathrm{d}t' \\ + \int_0^t \int\int \sqrt{J(\omega)J(\omega')}\langle a(\omega)a^\dagger(\omega')\rangle e^{-i(\omega t-\omega' t')}[F^\dagger(t')\rho(t), F(t)]\mathrm{d}\omega\mathrm{d}\omega'\mathrm{d}t', \quad \text{(E.38)}$$

where the terms containing elements in $\langle a(\omega)a(\omega')\rangle$ and $\langle a^\dagger(\omega)a^\dagger(\omega')\rangle$ have been eliminated by the rotating wave approximation in energy and the superoperator $\mathcal{D}_E$ codes for the action of the electrodes and is defined as:

$$\mathcal{D}_E(t)\rho \equiv \mathcal{T}_L^-\mathcal{D}[S_L^\dagger(t)](\tilde{\rho}) + \mathcal{T}_L^+\mathcal{D}[S_L(t)](\tilde{\rho}) + \mathcal{T}_R^-\mathcal{D}[S_R^\dagger(t)](\tilde{\rho}) + \mathcal{T}_R^+\mathcal{D}[S_R(t)](\tilde{\rho}) \quad \text{(E.39)}$$

Considering that the bosonic bath is at thermal equilibrium, at temperature T, we have the following expectation values:

$$\langle a^\dagger(\omega)a(\omega')\rangle = n_B(\omega,T)\delta(\omega-\omega'), \text{ and } \langle a(\omega)a^\dagger(\omega')\rangle = (1+n_B(\omega,T))\delta(\omega-\omega'), \quad \text{(E.40)}$$

in which

$$n_B(\omega,T) = \frac{1}{e^{\omega/k_BT}-1}, \quad \text{(E.41)}$$

is the Bose-Einstein statistics. Therefore, we obtain

$$\frac{\mathrm{d}\tilde{\rho}}{\mathrm{d}t} = \mathcal{D}_E(t)\tilde{\rho} + \int_0^t \int J(\omega)n_B(\omega,T)e^{i(\omega-\delta)(t-t')}[F(t)\rho(t), F^\dagger(t)]\mathrm{d}\omega\mathrm{d}t' \\ + \int_0^t \int J(\omega)(1+n_B(\omega,T))e^{-i(\omega-\delta)(t-t')}[F^\dagger(t)\rho(t), F(t)]\mathrm{d}\omega\mathrm{d}t', \quad \text{(E.42)}$$

which, with a change of variable $s = t - t'$ leads to:

$$\frac{\mathrm{d}\tilde{\rho}}{\mathrm{d}t} = \mathcal{D}_E(t)\tilde{\rho} + \Lambda^+\mathcal{D}[F(t)](\rho) + \Lambda^-\mathcal{D}[F^\dagger(t)](\rho), \quad \text{(E.43)}$$

in which we defined

$$\boxed{\begin{array}{l}\Lambda^+ \equiv \int_0^\infty \int J(\omega)n_B(\omega,T)e^{i(\omega-\delta)s}\mathrm{d}\omega\mathrm{d}s\ , \\ \Lambda^- \equiv \int_0^\infty \int J(\omega)(1+n_B(\omega,T))e^{-i(\omega-\delta)s}\mathrm{d}\omega\mathrm{d}s.\end{array}} \quad \text{(E.44)}$$

Going back to the Schrödinger picture, we finally get the master equation as written in the main text:

$$\boxed{\begin{array}{r}\frac{\mathrm{d}\rho}{\mathrm{d}t} = -i[H_S,\rho] + \mathcal{T}_L^-\mathcal{D}[c_\uparrow^\dagger](\rho) + \mathcal{T}_L^+\mathcal{D}[c_\uparrow](\rho) + \mathcal{T}_R^-\mathcal{D}[c_R^\dagger](\rho) + \mathcal{T}_R^+\mathcal{D}[c_R](\rho) \\ +\Lambda^-\mathcal{D}[c_\downarrow^\dagger c_\uparrow](\rho) + \Lambda^+\mathcal{D}[c_\uparrow^\dagger c_\downarrow](\rho),\end{array}} \quad \text{(E.45)}$$

We alert the reader that the previous equation features coefficients Λ^+ and Λ^- that are not necessarily real numbers. Meaning that under this form, it stands as a Bloch-Redfield equation which is not completely trace-preserving. It is possible to derive a master equation in Lindblad form satisfying

these last conditions under some more approximations (see Ref. [289]), although we will leave the study of such a more complex equation to future work and consider here that the boson spectral density is strongly peaked around $\omega = \delta$, which will lead us to the following approximation:

$$\boxed{\Lambda^+ = n_B(\delta, T)D(\delta), \text{ and } \Lambda^- = (1 + n_B(\delta, T))D(\delta),} \tag{E.46}$$

where $D(\delta) = \int J(\omega)\mathrm{d}\omega$. In the end, we recover the final form of the master equation with positive coefficients. We finally point out that to address a spin splitting of $\delta \approx 10$ meV as was calculated *ab initio* in Ref. [18] and verified experimentally in Ref [19], we need a frequency of $f = 2\pi\omega \approx 10$ THz, which would be accessible to usual phonons and vibrons below and close to room temperature, such as we can hope for the lattice and molecular vibrations to be sufficient to mediate this interaction and discard the intervention of outside photons coming from natural sources.

Appendix F

Perturbative solution to the steady-state master equation

F.1 Reduction of the system

In the case where without the bosonic bath, we will now show how to find the steady-state density matrix $\rho \equiv \rho_{ss}$ such that:

$$-i[H_S, \rho] + \mathcal{T}_L^- \mathcal{D}[c_\uparrow^\dagger](\rho) + \mathcal{T}_L^+ \mathcal{D}[c_\uparrow](\rho) + \mathcal{T}_R^- \mathcal{D}[c_R^\dagger](\rho) + \mathcal{T}_R^+ \mathcal{D}[c_R](\rho) = 0. \tag{F.1}$$

This equation is a linear system of 64 equations, which seems hard to solve but can be reduced with a bit of effort, and while no usable analytical solution can be found, it is still possible to derive the approximate steady-state using perturbation theory.

Writing the steady-state master equation (F.1) in the basis reference in the main text, we notice that a set of 12 equations are independent of the 52 other and can be used to find the diagonal coefficients and four off-diagonal terms: $\rho_{14} = \langle 0 \downarrow |\rho| \downarrow 0\rangle$, $\rho_{41} = \langle \downarrow 0|\rho|0 \downarrow\rangle$, $\rho_{36} = \langle \uparrow\downarrow |\rho| 20\rangle$ and $\rho_{63} = \langle 20|\rho| \uparrow\downarrow\rangle$

$$\begin{cases}
(-\mathcal{T}_L^- - \mathcal{T}_R^-)\rho_{00} + \mathcal{T}_R^+ \rho_{11} + \mathcal{T}_L^+ \rho_{22} = 0 \\
\mathcal{T}_R^- \rho_{00} + (-\mathcal{T}_L^- - \mathcal{T}_R^+)\rho_{11} + \mathcal{T}_L^+ \rho_{33} + \mathrm{i}\gamma\rho_{14} - \mathrm{i}\gamma^*\rho_{41} = 0 \\
\mathcal{T}_L^- \rho_{00} + (-\mathcal{T}_L^+ - \mathcal{T}_R^-)\rho_{22} + \mathcal{T}_R^+ \rho_{33} = 0 \\
\mathcal{T}_L^- \rho_{11} + \mathcal{T}_R^- \rho_{22} + (-\mathcal{T}_L^+ - \mathcal{T}_R^+)\rho_{33} + \mathrm{i}\gamma\rho_{36} - \mathrm{i}\gamma^*\rho_{63} = 0 \\
(-\mathcal{T}_L^- - \mathcal{T}_R^-)\rho_{44} + \mathcal{T}_R^+ \rho_{55} + \mathcal{T}_L^+ \rho_{66} - \mathrm{i}\gamma\rho_{14} + \mathrm{i}\gamma^*\rho_{41} = 0 \\
\mathcal{T}_R^- \rho_{44} + (-\mathcal{T}_L^- - \mathcal{T}_R^+)\rho_{55} + \mathcal{T}_L^+ \rho_{77} = 0 \\
\mathcal{T}_L^- \rho_{44} + (-\mathcal{T}_L^+ - \mathcal{T}_R^-)\rho_{66} + \mathcal{T}_R^+ \rho_{77} - \mathrm{i}\gamma\rho_{36} + \mathrm{i}\gamma^*\rho_{63} = 0 \\
\mathcal{T}_L^- \rho_{55} + \mathcal{T}_R^- \rho_{66} + (-\mathcal{T}_L^+ - \mathcal{T}_R^+)\rho_{77} = 0 \\
\Big(-\mathcal{T}_L^- - \frac{\mathcal{T}_R^- + \mathcal{T}_R^+}{2} + \mathrm{i}\Delta\Big)\rho_{14} + \mathcal{T}_L^+ \rho_{36} - \mathrm{i}\gamma^*\rho_{44} + i\gamma^*\rho_{11} = 0 \\
\mathcal{T}_L^- \rho_{14} + \Big(-\mathcal{T}_L^+ - \frac{\mathcal{T}_R^- + \mathcal{T}_R^+}{2} + \mathrm{i}(\Delta + U)\Big)\rho_{36} - \mathrm{i}\gamma^*\rho_{66} + \mathrm{i}\gamma^*\rho_{33} = 0 \\
\Big(-\mathcal{T}_L^- - \frac{\mathcal{T}_R^- + \mathcal{T}_R^+}{2} - \mathrm{i}\Delta\Big)\rho_{41} + \mathcal{T}_L^+ \rho_{63} + \mathrm{i}\gamma\rho_{44} - i\gamma\rho_{11} = 0 \\
\mathcal{T}_L^- \rho_{41} + \Big(-\mathcal{T}_L^+ - \frac{\mathcal{T}_R^- + \mathcal{T}_R^+}{2} - \mathrm{i}(\Delta + U)\Big)\rho_{63} + \mathrm{i}\gamma\rho_{66} - \mathrm{i}\gamma\rho_{33} = 0
\end{cases}, \tag{F.2}$$

where we have set $\Delta = \epsilon_\downarrow - \epsilon_R$.

To study this system, we first vectorize the system and define the vector $\vec{\rho}$ such that:

$$\vec{\rho} \equiv (\rho_{00},\ \rho_{11},\ \rho_{22},\ \rho_{33},\ \rho_{44},\ \rho_{55},\ \rho_{66},\ \rho_{77}, \rho_{14},\ \rho_{41},\ \rho_{36},\ \rho_{63}) \tag{F.3}$$

$$\equiv (\rho_0,\ \rho_1,\ \rho_2,\ \rho_3,\ \rho_4,\ \rho_5,\ \rho_6,\ \rho_7,\ \rho_{14},\ \rho_{36},\ \rho_{41},\ \rho_{63}). \tag{F.4}$$

What we can now easily see by taking the complex conjugate of the system is that it yields the exact same system but with the following solution:

$$(\rho_0^*,\ \rho_1^*,\ \rho_2^*,\ \rho_3^*,\ \rho_0^*,\ \rho_1^*,\ \rho_2^*,\ \rho_3^*,\ \rho_{41}^*,\ \rho_{63}^*,\ \rho_{14}^*,\ \rho_{36}^*). \tag{F.5}$$

This checks out with the hermiticity of the density matrix, which is a good confirmation of the correctness of our calculus. Using this property, we obtain the following relations:

$$\rho_i = \rho_i^*,\ \rho_{14} = \rho_{41}^*, \text{ and } \rho_{36} = \rho_{63}^*. \tag{F.6}$$

This allows us to discard the last two equations from this system, meaning that we can discard the off-diagonal lower terms ρ_{41} and ρ_{36}, which we will get from the solved upper terms.

With this reduction, we shall now write this system in matrix format. We start by setting $\gamma \equiv re^{\mathrm{i}\phi}$. Then we choose to separate the real and imaginary parts of the rotated off-diagonal terms by setting $\rho_\downarrow \equiv \rho_\downarrow^R + \mathrm{i}\rho_\downarrow^I \equiv \mathrm{i}e^{\mathrm{i}\phi}\rho_{14}$ and $\rho_\uparrow \equiv \rho_\uparrow^R + \mathrm{i}\rho_\uparrow^I \equiv \mathrm{i}e^{\mathrm{i}\phi}\rho_{36}$. And finally, we redefine the vector $\vec{\rho}$ by deleting the last two redundant components, such that:

$$\vec{\rho} \equiv (\rho_0,\ \rho_1,\ \rho_2,\ \rho_3,\ \rho_4,\ \rho_5,\ \rho_6,\ \rho_7,\ \rho_\downarrow,\ \rho_\uparrow). \tag{F.7}$$

Starting from a system with 12 complex parameters, we have now managed to reduce it down to a system with 12 real parameters or 8 real parameters and 2 complex parameters.

This system is too complicated to be solved exactly analytically so we will use perturbation theory in order to find an approximate solution. The small parameter we should use as a perturbation shall the magnitude of the tunneling coefficient $r = |\gamma|$, which should be an order of magnitude lower than all the energy scales present in this problem.

We can now write the system in matrix format by defining $\Lambda \equiv \Lambda_0 + \mathrm{i}r\Lambda_1$ such as $\Lambda\vec{\rho} = 0$, with the block matrix

$$\Lambda_0 = \mathrm{diag}(A,\ A,\ B), \tag{F.8}$$

filled by

$$A \equiv \begin{pmatrix} -(\mathcal{T}_L^- + \mathcal{T}_R^-) & \mathcal{T}_R^+ & \mathcal{T}_L^+ & 0 \\ \mathcal{T}_R^- & -(\mathcal{T}_L^- + \mathcal{T}_R^+) & 0 & \mathcal{T}_L^+ \\ \mathcal{T}_L^- & 0 & -(\mathcal{T}_R^- + \mathcal{T}_L^+) & \mathcal{T}_R^+ \\ 0 & \mathcal{T}_L^- & \mathcal{T}_R^- & -(\mathcal{T}_L^+ + \mathcal{T}_R^+) \end{pmatrix}, \tag{F.9}$$

and

$$B = \begin{pmatrix} -\mathcal{T}_L^- - \frac{\mathcal{T}_R^- + \mathcal{T}_L^+}{2} + \mathrm{i}\Delta & \mathcal{T}_L^+ \\ \mathcal{T}_L^- & -\mathcal{T}_L^+ - \frac{\mathcal{T}_R^- + \mathcal{T}_L^+}{2} + \mathrm{i}(\Delta + U) \end{pmatrix} \tag{F.10}$$

and with the perturbation interaction matrix Λ_1 such as

$$\Lambda_1\vec{\rho} = (0,\ \rho_\downarrow^R,\ 0,\ \rho_\uparrow^R,\ -\rho_\downarrow^R,\ 0,\ -\rho_\uparrow^R,\ 0,\ \rho_4 - \rho_1,\ \rho_6 - \rho_3). \tag{F.11}$$

F.1.1 Preliminary calculus

Let us first start by diagonalizing the matrix Λ_0, meaning that we should diagonalize A and B.

The diagonalization of A is straightforward and yields the following eigenvalues

$$\begin{cases} \lambda_0 = 0 \\ \lambda_1 = -\mathcal{T}_L^- - \mathcal{T}_L^+ \\ \lambda_2 = -\mathcal{T}_R^- - \mathcal{T}_R^+ \\ \lambda_3 = -\mathcal{T}_L^- - \mathcal{T}_L^+ - \mathcal{T}_R^- - \mathcal{T}_R^+ \end{cases}, \tag{F.12}$$

with the corresponding eigenvectors

$$\begin{cases} v_0 = (\mathcal{T}_L^+\mathcal{T}_R^+,\ \mathcal{T}_L^+\mathcal{T}_R^-,\ \mathcal{T}_L^-\mathcal{T}_R^+,\ \mathcal{T}_L^-\mathcal{T}_R^-) \\ v_1 = (-\mathcal{T}_R^+,\ -\mathcal{T}_R^-,\ \mathcal{T}_R^+,\ \mathcal{T}_R^-) \\ v_2 = (-\mathcal{T}_L^+,\ \mathcal{T}_L^+,\ -\mathcal{T}_L^-,\ \mathcal{T}_L^-) \\ v_3 = (1,\ -1,\ -1,\ 1) \end{cases}. \tag{F.13}$$

As we can see, we can have non-unicity issues whenever λ_1, λ_2 or λ_3 vanishes. In the following, we will suppose that the tunneling parameters $\mathcal{T}_L^+$, $\mathcal{T}_L^-$, $\mathcal{T}_R^+$ and $\mathcal{T}_R^-$ are chosen such that λ_0 is the only null eigenvalue.

The diagonalization of B is also trivial and yields the eigenvalues

$$\begin{cases} \lambda_- = -\frac{\mathcal{T}_L^- + \mathcal{T}_L^+ + \mathcal{T}_R^- + \mathcal{T}_R^+}{2} + \mathrm{i}(\Delta + \frac{U}{2}) - \frac{1}{2}\sqrt{4\mathcal{T}_L^-\mathcal{T}_L^+ + (\mathcal{T}_L^+ - \mathcal{T}_L^- - \mathrm{i}U)^2} \\ \lambda_+ = -\frac{\mathcal{T}_L^- + \mathcal{T}_L^+ + \mathcal{T}_R^- + \mathcal{T}_R^+}{2} + \mathrm{i}(\Delta + \frac{U}{2}) + \frac{1}{2}\sqrt{4\mathcal{T}_L^-\mathcal{T}_L^+ + (\mathcal{T}_L^+ - \mathcal{T}_L^- - \mathrm{i}U)^2} \end{cases}, \tag{F.14}$$

where the square root of the complex number is chosen such that its real part is positive, and with the following eigenvectors:

$$\begin{cases} v_- = \left(\mathcal{T}_L^+ - \mathcal{T}_L^- - \mathrm{i}U - \sqrt{4\mathcal{T}_L^-\mathcal{T}_L^+ + (\mathcal{T}_L^+ - \mathcal{T}_L^- - \mathrm{i}U)^2},\ 2\mathcal{T}_L^-\right) \\ v_+ = \left(\mathcal{T}_L^+ - \mathcal{T}_L^- - \mathrm{i}U + \sqrt{4\mathcal{T}_L^-\mathcal{T}_L^+ + (\mathcal{T}_L^+ - \mathcal{T}_L^- - \mathrm{i}U)^2},\ 2\mathcal{T}_L^-\right) \end{cases}. \tag{F.15}$$

We will also need its inverse, which reads:

$$B^{-1} = \frac{1}{\det B}\begin{pmatrix} -\mathcal{T}_L^+ - \frac{\mathcal{T}_R^+ + \mathcal{T}_R^-}{2} + \mathrm{i}(\Delta + U) & -\mathcal{T}_L^+ \\ -\mathcal{T}_L^- & -\mathcal{T}_L^- - \frac{\mathcal{T}_R^+ + \mathcal{T}_R^-}{2} + \mathrm{i}\Delta \end{pmatrix} \tag{F.16}$$

where

$$\det B = \left(\mathcal{T}_L^- + \frac{\mathcal{T}_R^- + \mathcal{T}_R^+}{2} - \mathrm{i}\Delta\right)\left(\mathcal{T}_L^+ + \frac{\mathcal{T}_R^- + \mathcal{T}_R^+}{2} - \mathrm{i}(\Delta + U)\right) - \mathcal{T}_L^-\mathcal{T}_L^+ . \tag{F.17}$$

F.2 Perturbation theory: kernel approach

Let us look for a perturbed solution $\vec{\rho}$ in the kernel of Λ, meaning that we are searching $\vec{\rho}$ as an expanded form $\vec{\rho} = \vec{\rho}^{(0)} + r\vec{\rho}^{(1)} + r^2\vec{\rho}^{(2)} + o(r^2)$. Expanding the equation $\Lambda\vec{\rho} = 0$, and identifying each order leads to:

$$\Lambda_0\vec{\rho}^{(0)} = 0\Lambda_0\vec{\rho}^{(1)} = -\Lambda_1\vec{\rho}^{(0)}\Lambda_0\vec{\rho}^{(2)} = -\Lambda_1\vec{\rho}^{(1)}. \tag{F.18}$$

More generally, it is straightforward to see that we can obtain the $(i+1)$-th order from the i-th order by solving the system $\Lambda_0 \vec{\rho}^{(i+1)} = -\Lambda_1 \vec{\rho}^{(i)}$, with $\vec{\rho}^{(0)}$ in the kernel of Λ_0.

From the initial diagonalization, we immediately obtain the kernel of Λ_0, which can be written as:

$$\vec{\rho}^{(0)} = \lambda\, v_0 \otimes 0 \otimes 0 + \mu\, 0 \otimes v_0 \otimes 0 \tag{F.19}$$

where λ and μ are two real parameters.

Using the properties of the density matrix, we can eliminate one parameter. Because of the conservation of the probabilities, ρ must have a unit trace. This condition leads to:

$$\mathrm{Tr}\,\rho^{(0)} = 1 \Longrightarrow \lambda = \alpha - \mu\ , \tag{F.20}$$

where we have set $1/\alpha \equiv (\mathcal{T}_L^+ + \mathcal{T}_L^-)(\mathcal{T}_R^+ + \mathcal{T}_R^-)$. Rewriting $\mu \equiv \alpha\mu$, we thus obtain

$$\vec{\rho}^{(0)} = \alpha\Big((1-\mu)\, v_0 \otimes 0 \otimes 0 + \mu\, 0 \otimes v_0 \otimes 0\Big)\ . \tag{F.21}$$

Moreover, the positivity of the density matrix imposes $0 \leqslant \mu \leqslant 1$.

Apparently here, we now have a problem because $\rho^{(0)}$ cannot be determined uniquely because of this free λ parameter. This means that the steady-state solution to the master equation will depend on its initial condition! Fortunately, in this case, we can deduce the final state corresponding to the initial state quite easily. Indeed, we point out that $\rho^{(0)}$ taken as a density matrix should correspond to a solution of the Liouville-Von Neumann equation with $\gamma = 0$ encoded in the Hamiltonian:

$$H = \epsilon_\uparrow n_\uparrow + \epsilon_\downarrow n_\downarrow + \epsilon_R n_R + J\, n_\downarrow n_R + U\, n_\uparrow n_\downarrow + H_L + H_R + H_{SL} + H_{SR}\ . \tag{F.22}$$

Looking at this operator, it should be clear that we have the commutation relation $[H,\, n_\downarrow] = 0$. Therefore, $n_\downarrow$ is a conserved quantity during the time evolution of the whole system. This property is transferring directly to $\vec{\rho}^{(0)}$, which should therefore verify

$$\mathrm{Tr}\,\rho^{(0)} n_\downarrow = \mathrm{Tr}\,\rho(0) n_\downarrow \Leftrightarrow \mu = \langle n_\downarrow(0)\rangle\ . \tag{F.23}$$

This initial information gives us the value of μ that corresponds to the initial occupation number of the down spin energy level of the left qubit. It should be clear that the two extremal values $\mu = 0$ and $\mu = 1$ will be the most interesting.

We can now move to finding the first order $\rho^{(1)}$. We need to solve $\Lambda_0 \vec{\rho}^{(1)} = \Lambda_1 \vec{\rho}^{(0)}$. The right-hand side reads:

$$\Lambda_1 \vec{\rho}^{(0)} = (0,\ 0,\ 0,\ 0,\ 0,\ 0,\ 0,\ 0,\ \rho_4^{(0)} - \rho_1^{(0)},\ \rho_6^{(0)} - \rho_3^{(0)}) \tag{F.24}$$

$$= \Big(0,\ 0,\ 0,\ 0,\ 0,\ 0,\ 0,\ 0,\ \alpha\mathcal{T}_L^+(\mu\mathcal{T}_R^+ - (1-\mu)\mathcal{T}_R^-),\ \alpha\mathcal{T}_L^-(\mu\mathcal{T}_R^+ - (1-\mu)\mathcal{T}_R^-)\Big)\ . \tag{F.25}$$

Decomposing $\vec{\rho}^{(1)}$ as $\vec{\rho}^{(1)} = \vec{\rho}_+^{(1)} \otimes \vec{\rho}_-^{(1)} \otimes \begin{pmatrix} \rho_\downarrow^{(1)} \\ \rho_\uparrow^{(1)} \end{pmatrix}$, we immediately obtain the following three equations from the block diagonal expression of Λ_0:

$$A\vec{\rho}_+^{(1)} = 0,\ A\vec{\rho}_-^{(1)} = 0,\ \text{and}\ B\begin{pmatrix} \rho_\downarrow^{(1)} \\ \rho_\uparrow^{(1)} \end{pmatrix} = -\alpha(\mu\mathcal{T}_R^+ - (1-\mu)\mathcal{T}_R^-)\begin{pmatrix} \mathcal{T}_L^+ \\ \mathcal{T}_L^- \end{pmatrix}, \tag{F.26}$$

Let us focus first on the last system which gives a unique solution given the inversibility of B:

$$\begin{cases} \rho_{\downarrow}^{(1)} = \frac{\alpha\mathcal{T}_L^+}{\det B}(\mu\mathcal{T}_R^+ - (1-\mu)\mathcal{T}_R^-)\Big(\mathcal{T}_L^+ + \mathcal{T}_L^- + \frac{\mathcal{T}_R^- + \mathcal{T}_R^+}{2} - \mathrm{i}(\Delta + U)\Big) \\ \rho_{\uparrow}^{(1)} = \frac{\alpha\mathcal{T}_L^-}{\det B}(\mu\mathcal{T}_R^+ - (1-\mu)\mathcal{T}_R^-)\Big(\mathcal{T}_L^+ + \mathcal{T}_L^- + \frac{\mathcal{T}_R^- + \mathcal{T}_R^+}{2} - \mathrm{i}\Delta\Big) \end{cases} . \tag{F.27}$$

The general solution to the first-order equation thus leads to the unique off-diagonal terms we just found plus additional diagonal terms in the kernel of Λ_0. Having non-zero diagonal terms would give first-order corrections to the unit-trace condition of the density matrix and to the mean value of the number operators. Such solutions would therefore be less physical so we should discard them to keep the normalization of the density matrix intact.

Unfortunately, this method cannot be used to evaluate the higher orders. Indeed, we can show that the system $\Lambda_0\vec{\rho}^{(2)} = -\Lambda_1\vec{\rho}^{(1)}$ has no solution because $\Re(\rho_{\downarrow}^{(1)}) \neq \Re(\rho_{\uparrow}^{(1)})$. We shall thus limit the analysis to the first order we have just derived.

Collecting every piece together thus leads to a steady-state solution ρ^μ calculated up to first order in γ with null coefficients everywhere except:

$$\boxed{\begin{cases} \rho_{00}^\mu = \alpha(1-\mu)\mathcal{T}_L^+\mathcal{T}_R^+ \\ \rho_{11}^\mu = \alpha(1-\mu)\mathcal{T}_L^+\mathcal{T}_R^- \\ \rho_{22}^\mu = \alpha(1-\mu)\mathcal{T}_L^-\mathcal{T}_R^+ \\ \rho_{33}^\mu = \alpha(1-\mu)\mathcal{T}_L^-\mathcal{T}_R^- \\ \rho_{44}^\mu = \alpha\mu\mathcal{T}_L^+\mathcal{T}_R^+ \\ \rho_{55}^\mu = \alpha\mu\mathcal{T}_L^+\mathcal{T}_R^- \\ \rho_{66}^\mu = \alpha\mu\mathcal{T}_L^-\mathcal{T}_R^+ \\ \rho_{77}^\mu = \alpha\mu\mathcal{T}_L^-\mathcal{T}_R^- \\ \rho_{14}^\mu = -\mathrm{i}\gamma^*\frac{\alpha\mathcal{T}_L^+}{\det B}(\mu\mathcal{T}_R^+ - (1-\mu)\mathcal{T}_R^-)\Big(\mathcal{T}_L^+ + \mathcal{T}_L^- + \frac{\mathcal{T}_R^- + \mathcal{T}_R^+}{2} - \mathrm{i}(\Delta + U)\Big) \\ \rho_{36}^\mu = -\mathrm{i}\gamma^*\frac{\alpha\mathcal{T}_L^-}{\det B}(\mu\mathcal{T}_R^+ - (1-\mu)\mathcal{T}_R^-)\Big(\mathcal{T}_L^+ + \mathcal{T}_L^- + \frac{\mathcal{T}_R^- + \mathcal{T}_R^+}{2} - \mathrm{i}\Delta\Big) \\ \rho_{41}^\mu = \mathrm{i}\gamma\frac{\alpha\mathcal{T}_L^+}{\det B^*}(\mu\mathcal{T}_R^+ - (1-\mu)\mathcal{T}_R^-)\Big(\mathcal{T}_L^+ + \mathcal{T}_L^- + \frac{\mathcal{T}_R^- + \mathcal{T}_R^+}{2} + \mathrm{i}(\Delta + U)\Big) \\ \rho_{63}^\mu = \mathrm{i}\gamma\frac{\alpha\mathcal{T}_L^-}{\det B^*}(\mu\mathcal{T}_R^+ - (1-\mu)\mathcal{T}_R^-)\Big(\mathcal{T}_L^+ + \mathcal{T}_L^- + \frac{\mathcal{T}_R^- + \mathcal{T}_R^+}{2} + \mathrm{i}\Delta\Big) \end{cases}} . \tag{F.28}$$

Appendix G

Energy and Entropy for Different Measurement Protocols

G.1 On the applicability of the relation between the energy increment given by the measurement and the coherence energy

Referring to the main text, the master equation reads:

$$\frac{\mathrm{d}\rho_S}{\mathrm{d}t} = -i[H_S, \rho_S] + \mathcal{T}_L^- \mathcal{D}[c_\uparrow^\dagger](\rho_S) + \mathcal{T}_L^+ \mathcal{D}[c_\uparrow](\rho_S) + \mathcal{T}_R^- \mathcal{D}[c_R^\dagger](\rho_S) + \mathcal{T}_R^+ \mathcal{D}[c_R](\rho_S) \tag{G.1}$$

In the canonical basis we chose, we write a set of 12 equations independent of the 52 others. We can thus decompose the density matrix ρ_S taken as a vector such as $\vec{\rho}_S = \vec{\rho}_D \otimes \vec{\rho}_F$ with

$$\frac{\mathrm{d}\vec{\rho}_D}{\mathrm{d}t} = D\vec{\rho}_D \text{ and } \frac{\mathrm{d}\vec{\rho}_F}{\mathrm{d}t} = F\vec{\rho}_F, \tag{G.2}$$

where D and F are two matrices. The first equation with D is describing the evolution of the 12 coefficients we are interested in, in particular the 8 diagonal terms ; while the second equation in F dictates the evolution of the rest of the coefficients. It thus appears that when the device is initialized in a pure state, a thermal state, or any state with no coherence, then $\vec{\rho}_F(0) = 0$, which would lead to $\vec{\rho}_F(t) = e^{tF}\vec{\rho}_F(0) = 0$. This - not too restrictive - initial condition would thus imply that the 52 coefficients of ρ_S describing $\vec{\rho}_F$ remain null during the whole time-dependent evolution of the thermalizing stroke. Furthermore, the measurement is also not changing these coefficients as it is projecting the density matrix onto a diagonal state, therefore the measurement only has an effect on the coefficients described by $\vec{\rho}_D$. This thus shows that $\vec{\rho}_F = 0$ at any time, for all cycles and for all measurement protocols, provided that we start with $\vec{\rho}_F(0) = 0$.

This reduction down to the 12 coefficients reveals that the essential relation $\Delta E = -\langle C \rangle$ remains valid at any time, for all cycles, since the calculus that led to it in the main text remains the same given the shape of the density matrix.

G.2 Energy for other measurement protocols

G.2.1 Unselective measurement of the spin of the left quantum dot

Let us now study the case where the environment measures the spin of the left quantum dot at frequent times. The spin operator S reads

$$S = n_\uparrow - n_\downarrow = 1 \times n_\uparrow(1-n_\downarrow) - 1 \times n_\downarrow(1-n_\uparrow) + 0 \times (n_\uparrow n_\downarrow + (1-n_\uparrow)(1-n_\downarrow)) \,. \tag{G.3}$$

The measurement can give one of the three values 0, 1 or -1 and at time τ^+, the unselected measured state read:

$$\rho(\tau^+) = (n_\uparrow n_\downarrow + (1-n_\uparrow)(1-n_\downarrow))\rho_\uparrow(n_\uparrow n_\downarrow + (1-n_\uparrow)(1-n_\downarrow)) + n_\uparrow(1-n_\downarrow)\rho n_\uparrow(1-n_\downarrow) + n_\downarrow(1-n_\uparrow)\rho n_\downarrow(1-n_\uparrow). \tag{G.4}$$

Once again, we observe that the off-diagonal terms do not contribute to any of the projected states because they involve the tunneling of one electron between the two sites, leading to

$$\rho(\tau^+) = \sum_{i=0}^{7} \rho_{ii}|i\rangle\langle i|. \tag{G.5}$$

The calculation for the average energy increase is then straightforward and identical to the case treated in the main text, and we find the exact previous result $\langle \Delta E \rangle = -\mathrm{Tr}[C\rho]$.

G.2.2 Unselective measurement of the charge of the left quantum dot

The very same results hold when measuring the charge of the left quantum dot. In this case, the charge operator Q_L reads

$$Q_L = n_\downarrow + n_\uparrow = 0 \times (1-n_\downarrow)(1-n_\uparrow) + 1 \times (n_\uparrow(1-n_\downarrow) + n_\downarrow(1-n_\uparrow)) + 2 \times n_\downarrow n_\uparrow \,, \tag{G.6}$$

which yields the following measured state:

$$\rho(\tau^+) = (1-n_\downarrow)(1-n_\uparrow)\rho(1-n_\downarrow)(1-n_\uparrow) + (n_\uparrow(1-n_\downarrow) + n_\downarrow(1-n_\uparrow))\rho(n_\uparrow(1-n_\downarrow) + n_\downarrow(1-n_\uparrow)) + n_\downarrow n_\uparrow \rho n_\downarrow n_\uparrow. \tag{G.7}$$

And again, the off-diagonal terms do not contribute, which leads again to the previous result $\langle \Delta E \rangle = -\mathrm{Tr}[C\rho]$.

G.2.3 Unselective measurement of the total charge

As a counterexample, let us now consider an observable that acts on both quantum dots, namely the total charge $Q = n_\uparrow + n_\downarrow + n_R$, which decomposes as:

$$Q = \begin{array}{l} 0 \times (1-n_\uparrow)(1-n_\downarrow)(1-n_R) \\ +1 \times [n_\uparrow(1-n_\downarrow)(1-n_R) + (1-n_\uparrow)n_\downarrow(1-n_R) + (1-n_\uparrow)(1-n_\downarrow)n_R] \\ +2 \times [n_\uparrow n_\downarrow(1-n_R) + n_\uparrow(1-n_\downarrow)n_R + (1-n_\uparrow)n_\downarrow n_R] \\ +3 \times n_\uparrow n_\downarrow n_R \end{array} \,. \tag{G.8}$$

Just as in the previous section, we can calculate the measured state and we find the very simple result $\rho(\tau^+) = \rho$. This time, off-diagonal terms are present in the projected state, which is identical to the thermalized state! Therefore, the average energy increment ΔE vanishes! In this case, we cannot expect the measurement to energize the system on average because it does not produce the necessary separation and leaves the state unchanged.

G.2.4 Selective measurement of the occupation of the right quantum dot

Let us initialize our engine at $t_0 = 0$ in some state $\rho(0)$ such that $\mu = \langle n_\downarrow(0)\rangle$. After completing the first thermalization process, a selective partial projective measurement of the system is performed by the environment at time τ. This measurement projects the system from the steady state $\rho(\tau^-) = \rho^\mu \equiv \rho$ to a projected state $\rho^i(\tau^+)$ that depends on the measurement outcome i.

The measurement of the occupation of the right quantum dot n_R can only give one of the two values 1 or 0, which code either the presence or the absence of one electron on the right-hand QD. The two possible projected states read:

$$\begin{cases} \rho^1(\tau^+) = \frac{n_R\rho_R}{\mathrm{Tr}[n_R\rho]} \\ \rho^0(\tau^+) = \frac{(1-n_R)\rho(1-n_R)}{\mathrm{Tr}[(1-n_R)\rho]} \end{cases} . \tag{G.9}$$

The same argument holds once again: the off-diagonal terms do not contribute in the projected states because they encode the tunneling of one electron from one site to the next. Hence we calculate

$$\begin{cases} \rho^1(\tau^+) = \frac{\rho_{11}|1\rangle\langle 1|+\rho_{33}|3\rangle\langle 3|+\rho_{55}|5\rangle\langle 5|+\rho_{77}|7\rangle\langle 7|}{\rho_{11}+\rho_{33}+\rho_{55}+\rho_{77}} \\ \rho^0(\tau^+) = \frac{\rho_{00}|0\rangle\langle 0|+\rho_{22}|2\rangle\langle 2|+\rho_{44}|4\rangle\langle 4|+\rho_{66}|6\rangle\langle 6|}{\rho_{00}+\rho_{22}+\rho_{44}+\rho_{66}} \end{cases} . \tag{G.10}$$

The associated probabilities to obtain these two states are given by

$$\begin{cases} p^1(\tau^+) \equiv \mathrm{Tr}[n_R\rho] = \rho_{11} + \rho_{33} + \rho_{55} + \rho_{77} \\ p^0(\tau^+) \equiv \mathrm{Tr}[(1-n_R)\rho] = \rho_{00} + \rho_{22} + \rho_{44} + \rho_{66} \end{cases} . \tag{G.11}$$

From these quantities, we can now calculate the impact of the measurement in terms of energy and entropy. For each of the two measurement outcomes, the energy of the system respectively changes by an amount ΔE^1 and ΔE^0 such that

$$\Delta E^i = \mathrm{Tr}[H_S\rho^i(\tau^+)] - \mathrm{Tr}[H_S\rho(\tau^-)] . \tag{G.12}$$

We calculate

$$\mathrm{Tr}[H_S\rho(\tau^-)] = \sum_{i=0}^{7} H_{ii}\rho_{ii} + \gamma\rho_{14} + \gamma\rho_{36} + \gamma^*\rho_{41} + \gamma^*\rho_{63} \tag{G.13}$$

then

$$\begin{cases} \mathrm{Tr}[H_S\rho^1(\tau^+)] = \frac{H_{11}\rho_{11}+H_{33}\rho_{33}+H_{55}\rho_{55}+H_{77}\rho_{77}}{\rho_{11}+\rho_{33}+\rho_{55}+\rho_{77}} \\ \mathrm{Tr}[H_S\rho^0(\tau^+)] = \frac{H_{00}\rho_{00}+H_{22}\rho_{22}+H_{44}\rho_{44}+H_{66}\rho_{66}}{\rho_{00}+\rho_{22}+\rho_{44}+\rho_{66}} \end{cases} . \tag{G.14}$$

This allows us to derive the expected value of the energy increment $\overline{\Delta E} \equiv p^1\Delta E^1 + p^0\Delta E^0$. We emphasize the difference here between the average value of a quantum observable over all possible

quantum trajectories written between angles $\langle\cdot\rangle$ and the expectation value of a random variable coming from the measurement of the system, written with an overline $\bar{\cdot}$. We directly notice that the terms coming from the diagonal components all vanish, leaving only

$$\overline{\Delta E} = -\gamma\rho_{14} - \gamma\rho_{36} - \gamma^*\rho_{41} - \gamma^*\rho_{63} = -2\Re[\gamma(\rho_{14}+\rho_{36})] = -\mathrm{Tr}[C\rho]\,. \tag{G.15}$$

Therefore, the energy increment is identical to the case of unselective quantum measurement.

Now, for the next cycle, we need to obtain is the particle number with spin $\downarrow$ in the left quantum dot so that we can calculate the next thermalized state. Fortunately, because the two possible projected states are diagonal, we obtain directly

$$\begin{cases} \mathrm{Tr}[n_\downarrow\rho^1(\tau^+)] = \frac{\rho_{55}+\rho_{77}}{\rho_{11}+\rho_{33}+\rho_{55}+\rho_{77}} = \mu \\ \mathrm{Tr}[n_\downarrow\rho^0(\tau^+)] = \frac{\rho_{44}+\rho_{66}}{\rho_{00}+\rho_{22}+\rho_{44}+\rho_{66}} = \mu \end{cases}. \tag{G.16}$$

This means that the occupation number with spin $\downarrow$ remains unchanged after both the thermalizing and the measurement processes for both outcomes of the measurement! Therefore, the second cycle starts again with $\langle n_\downarrow(\tau^+)\rangle = \mu$, so it yields the same thermalized state just before the second measurement as in the previous cycle. This means that $\rho(2\tau^-) = \rho(\tau^-) = \rho$ and thus $\rho^i(2\tau^+) = \rho^i(\tau^+)$.

An instant recursion then allows us to explicitly obtain the state of the system at the end-point of each cycle n:

$$\begin{cases} \rho(n\tau^-) = \rho \\ \rho^1(n\tau^+) = \frac{\rho_{11}|1\rangle\langle 1|+\rho_{33}|3\rangle\langle 3|+\rho_{55}|5\rangle\langle 5|+\rho_{77}|7\rangle\langle 7|}{\rho_{11}+\rho_{33}+\rho_{55}+\rho_{77}} \\ \rho^0(n\tau^+) = \frac{\rho_{00}|0\rangle\langle 0|+\rho_{22}|2\rangle\langle 2|+\rho_{44}|4\rangle\langle 4|+\rho_{66}|6\rangle\langle 6|}{\rho_{00}+\rho_{22}+\rho_{44}+\rho_{66}} \end{cases}. \tag{G.17}$$

G.2.5 Selective measurement of the spin of the left quantum dot

Let us now study the case where the environment operates a selective measurement of the spin of the left quantum dot at frequent times. At time τ^+, the three possible projected states read:

$$\begin{cases} \rho^0(\tau^+) = \frac{n_\uparrow n_\downarrow+(1-n_\uparrow)(1-n_\downarrow)\rho n_\uparrow n_\downarrow+(1-n_\uparrow)(1-n_\downarrow)}{\mathrm{Tr}n_\uparrow n_\downarrow+(1-n_\uparrow)(1-n_\downarrow)\rho]} = \frac{\rho_{00}|0\rangle\langle 0|+\rho_{11}|1\rangle\langle 1|+\rho_{66}|6\rangle\langle 6|+\rho_{77}|7\rangle\langle 7|}{\rho_{00}+\rho_{11}+\rho_{66}+\rho_{77}} \\ \rho^1(\tau^+) = \frac{n_\uparrow(1-n_\downarrow)\rho n_\uparrow(1-n_\downarrow)}{\mathrm{Tr}[n_\uparrow(1-n_\downarrow)\rho]} = \frac{\rho_{22}|2\rangle\langle 2|+\rho_{33}|3\rangle\langle 3|}{\rho_{22}+\rho_{33}} \\ \rho^{-1}(\tau^+) = \frac{n_\downarrow(1-n_\uparrow)\rho n_\downarrow(1-n_\uparrow)}{\mathrm{Tr}[n_\downarrow(1-n_\uparrow)\rho]} = \frac{\rho_{44}|4\rangle\langle 4|+\rho_{55}|5\rangle\langle 5|}{\rho_{44}+\rho_{55}} \end{cases}, \tag{G.18}$$

with the corresponding probabilities

$$\begin{cases} p^0(\tau^+) = \mathrm{Tr}[(2n_\downarrow n_\uparrow - n_\uparrow - n_\downarrow)\rho] = \rho_{00}+\rho_{11}+\rho_{66}+\rho_{77} \\ p^1(\tau^+) = \mathrm{Tr}[n_\uparrow(1-n_\downarrow)\rho] = \rho_{22}+\rho_{33} \\ p^{-1}(\tau^+) = \mathrm{Tr}[n_\downarrow(1-n_\uparrow)\rho] = \rho_{44}+\rho_{55} \end{cases}, \tag{G.19}$$

Once again, we observe that the off-diagonal terms do not contribute to any of the projected states because they involve the tunneling of one electron between the two sites.

Therefore, we can write $\overline{\Delta E} = p^0\Delta E^0 + p^1\Delta E^1 + p^{-1}\Delta E^{-1}$ with $\Delta E^i = \mathrm{Tr}[H_S\rho^i(\tau^+)] - \mathrm{Tr}[H_S\rho]$. Given that we have

$$\begin{cases} \mathrm{Tr}[H_S\rho^0(\tau^+)] = \frac{H_{00}\rho_{00}+H_{11}\rho_{11}+H_{66}\rho_{66}+H_{77}\rho_{77}}{\rho_{00}+\rho_{11}+\rho_{66}+\rho_{77}} \\ \mathrm{Tr}[H_S\rho^1(\tau^+)] = \frac{H_{22}\rho_{22}+H_{33}\rho_{33}}{\rho_{22}+\rho_{33}} \\ \mathrm{Tr}[H_S\rho^{-1}(\tau^+)] = \frac{H_{44}\rho_{44}+H_{55}\rho_{55}}{\rho_{44}+\rho_{55}} \end{cases}, \tag{G.20}$$

we find the exact previous result $\overline{\Delta E} = -\mathrm{Tr}[C\rho]$.

Compared to the previous in the main text where the parameter μ remains unchanged for each cycle, in this case, the measurement has an impact on the spin $\downarrow$ population on the left quantum dot, which can lead to three different values for the initial condition of the next cycle:

$$\begin{cases} \mu^0(\tau^+) = \mathrm{Tr}[n_\downarrow \rho^0(\tau^+)] = \frac{\rho_{66}+\rho_{77}}{\rho_{00}+\rho_{11}+\rho_{66}+\rho_{77}} = \frac{\mu\mathcal{T}_L^-}{(1-\mu)\mathcal{T}_L^+ + \mu\mathcal{T}_L^-} \\ \mu^1(\tau^+) = \mathrm{Tr}[n_\downarrow \rho^1(\tau^+)] = 0 \\ \mu^{-1}(\tau^+) = \mathrm{Tr}[n_\downarrow \rho^{-1}(\tau^+)] = 1 \end{cases} . \tag{G.21}$$

Nonetheless, its average value $\overline{\mu} = p^0\mu^0 + p^1\mu^1 + p^{-1}\mu^{-1}$ remains unchanged:

$$\overline{\mu} = \frac{\mu\mathcal{T}_L^-}{(1-\mu)\mathcal{T}_L^+ + \mu\mathcal{T}_L^-} \times \Big[\alpha(\mathcal{T}_R^+ + \mathcal{T}_R^-)((1-\mu)\mathcal{T}_L^+ + \mu\mathcal{T}_L^-)\Big] + 1 \times \Big[\alpha\mu\mathcal{T}_L^+(\mathcal{T}_R^+ + \mathcal{T}_R^-)\Big] = \mu\,. \tag{G.22}$$

This means that the initial value at the beginning of each thermalizing stroke describes a stochastic sequence μ_n such that:

$$\mu_{n+1} = \begin{cases} \frac{\mu^n\mathcal{T}_L^-}{(1-\mu^n)\mathcal{T}_L^+ + \mu^n\mathcal{T}_L^-} & \text{with probability} \quad p^0(n\tau^+) \\ 0 & \text{with probability} \quad p^1(n\tau^+) \\ 1 & \text{with probability} \quad p^{-1}(n\tau^+) \end{cases} . \tag{G.23}$$

It is quite straightforward to see that after some time, starting from a random initial value μ^0, the sequence μ^n can only take one of the two values 0 or 1. Indeed, let us consider the first cycle, such as $\mu_{n_0} = 0$ or $\mu_{n_0} = 1$. In the first case $\mu_{n_0} = 0$, we have:

$$\mu_{n_0+1} = \begin{cases} 0 & \text{with probability} \quad p^1(n\tau^+) + p^0(n\tau^+) = 1 \\ 1 & \text{with probability} \quad p^{-1}(n\tau^+) = 0 \end{cases} . \tag{G.24}$$

Recursively, we then show that the sequence μ_n stabilizes at 0. And in the second case $\mu_{n_0} = 1$, we have:

$$\mu_{n_1+1} = \begin{cases} 0 & \text{with probability} \quad p^1(n\tau^+) = 0 \\ 1 & \text{with probability} \quad p^{-1}(n\tau^+) + p^0(n\tau^+) = 1 \end{cases} . \tag{G.25}$$

A trivial recursion hence shows the stabilization at either $\mu_n = 0$ or $\mu_n = 1$. This shows that when starting with $\mu_0 = 0$, the value of μ remains constant and is stabilized by the measurements, which guarantees that the energy increment $\overline{\Delta E}$ remains positive, i.e. that energy can potentially be extracted during each cycle.

G.2.6 Selective measurement of the charge of the left quantum dot

The very same results hold when measuring the charge of the left quantum dot. It yields the following projected states:

$$\begin{cases} \rho^0(\tau^+) = \frac{(1-n_\downarrow)(1-n_\uparrow)\rho(1-n_\downarrow)(1-n_\uparrow)}{\mathrm{Tr}[(1-n_\downarrow)(1-n_\uparrow)\rho]} = \frac{\rho_{00}|0\rangle\langle 0| + \rho_{11}|1\rangle\langle 1|}{\rho_{00}+\rho_{11}} \\ \rho^1(\tau^+) = \frac{(n_\uparrow(1-n_\downarrow)+n_\downarrow(1-n_\uparrow))\rho(n_\uparrow(1-n_\downarrow)+n_\downarrow(1-n_\uparrow))}{\mathrm{Tr}[(n_\uparrow(1-n_\downarrow)+n_\downarrow(1-n_\uparrow))\rho]} = \frac{\rho_{22}|2\rangle\langle 2| + \rho_{33}|3\rangle\langle 3| + \rho_{44}|4\rangle\langle 4| + \rho_{55}|5\rangle\langle 5|}{\rho_{22}+\rho_{33}+\rho_{44}+\rho_{55}} \\ \rho^2(\tau^+) = \frac{n_\downarrow n_\uparrow \rho n_\downarrow n_\uparrow}{\mathrm{Tr}[n_\downarrow n_\uparrow \rho]} = \frac{\rho_{66}|6\rangle\langle 6| + \rho_{77}|7\rangle\langle 7|}{\rho_{66}+\rho_{77}} \end{cases} , \tag{G.26}$$

with the associated probabilities

$$\begin{cases} p^0(\tau^+) = \mathrm{Tr}[(1-n_\downarrow)(1-n_\uparrow)\rho] = \rho_{00} + \rho_{11} \\ p^1(\tau^+) = \mathrm{Tr}[(n_\uparrow(1-n_\downarrow) + n_\downarrow(1-n_\uparrow))\rho] = \rho_{22} + \rho_{33} + \rho_{44} + \rho_{55} \\ p^2(\tau^+) = \mathrm{Tr}[n_\downarrow n_\uparrow \rho] = \rho_{66} + \rho_{77} \end{cases} . \tag{G.27}$$

Once again, the off-diagonal terms do not contribute, which leads to the following mean energies for each outcome:

$$\begin{cases} \mathrm{Tr}[H_S\rho^0(\tau^+)] = \frac{H_{00}\rho_{00}+\rho_{11}H_{11}}{\rho_{00}+\rho_{11}} \\ \mathrm{Tr}[H_S\rho^1(\tau^+)] = \frac{H_{22}\rho_{22}+\rho_{33}H_{33}+H_{44}\rho_{44}+\rho_{55}H_{55}}{\rho_{22}+\rho_{33}+\rho_{44}+\rho_{55}} \\ \mathrm{Tr}[H_S\rho^2(\tau^+)] = \frac{H_{66}\rho_{66}+\rho_{77}H_{77}}{\rho_{66}+\rho_{77}} \end{cases} , \tag{G.28}$$

This leads again to the previous result $\overline{\Delta E} = -\mathrm{Tr}[C\rho]$.

Similarly to the previous case, we find that the initial values follow a stochastic sequence μ_n such that:

$$\mu_{n+1} = \begin{cases} 0 & \text{with probability} \quad p^0(n\tau^+) \\ \frac{\mu^n \mathcal{T}_L^+}{(1-\mu^n)\mathcal{T}_L^- + \mu^n \mathcal{T}_L^+} & \text{with probability} \quad p^1(n\tau^+) \\ 1 & \text{with probability} \quad p^2(n\tau^+) \end{cases} . \tag{G.29}$$

Its average also remains constant and a recursion shows once again that after some time, the sequence stabilizes at a constant value $\mu_n = 0$ or $\mu_n = 1$ depending on which of the two is reached first.

G.2.7 Selective measurement of the total charge

Let us now consider the total charge $Q = n_\uparrow + n_\downarrow + n_R$, acting on both QD. We can calculate the four possible projected states:

$$\begin{cases} \rho^0(\tau^+) = |0\rangle\langle 0| \\ \rho^1(\tau^+) = \frac{\rho_{11}|1\rangle\langle 1| + \rho_{22}|2\rangle\langle 2| + \rho_{44}|4\rangle\langle 4| + \rho_{14}|1\rangle\langle 4| + \rho_{41}|4\rangle\langle 1|}{\rho_{11}+\rho_{22}+\rho_{44}} \\ \rho^2(\tau^+) = \frac{\rho_{33}|3\rangle\langle 3| + \rho_{55}|5\rangle\langle 5| + \rho_{66}|6\rangle\langle 6| + \rho_{36}|3\rangle\langle 6| + \rho_{63}|6\rangle\langle 3|}{\rho_{33}+\rho_{55}+\rho_{66}} \\ \rho^3(\tau^+) = |7\rangle\langle 7| \end{cases} , \tag{G.30}$$

and the probabilities:

$$\begin{cases} p^0(\tau^+) = \rho_{00} \\ p^1(\tau^+) = \rho_{11} + \rho_{22} + \rho_{44} \\ p^2(\tau^+) = \rho_{33} + \rho_{55} + \rho_{66} \\ p^3(\tau^+) = \rho_{77} \end{cases} . \tag{G.31}$$

This time, off-diagonal terms are present in the projected states! And we can now easily see that the average energy increment $\overline{\Delta E} = p^0\Delta E^0 + p^1\Delta E^1 + p^2\Delta E^2 + p^3\Delta E^3$ vanishes! In this case, we cannot expect the measurement to energize the system on average because it does not produce the necessary separation.

G.3 Entropy for the various measurement protocols

G.3.1 Second-order correction

As we have shown in Appendix F, the perturbative kernel approach solution we have derived cannot yield a second-order correction because the system is not invertible. Nonetheless, it is still possible to find such a correction using another trick. Indeed, one should remember that the density matrix is a positive hermitian matrix, but the solution we have found up to first order may not verify this positivity condition whenever $\mu = 0$ or $\mu = 1$. We shall thus try to find a second-order correction that does not change the eigenvalues of the density matrix up to second order.

Let us first remunerate the basis and set:

$$\begin{array}{c} |\tilde{0}\rangle \equiv |0\rangle = |00\rangle,\ |\tilde{1}\rangle \equiv |1\rangle = |0\downarrow\rangle,\ |\tilde{2}\rangle \equiv |4\rangle = |\downarrow 0\rangle,\ |\tilde{3}\rangle \equiv |3\rangle = |\uparrow\downarrow\rangle, \\ |\tilde{4}\rangle \equiv |6\rangle = |20\rangle,\ |\tilde{5}\rangle \equiv |5\rangle = |\downarrow\downarrow\rangle,\ |\tilde{6}\rangle \equiv |2\rangle \equiv |\uparrow 0\rangle,\ |\tilde{7}\rangle \equiv |7\rangle = |2\downarrow\rangle \end{array}, \tag{G.32}$$

such as the perturbative steady state matrix now reads in this basis

$$\rho = \begin{pmatrix} \rho_{00} & 0 & 0 & 0 & 0 & 0 & 0 & 0 \\ 0 & \rho_{11} & \rho_{14} & 0 & 0 & 0 & 0 & 0 \\ 0 & \rho_{14}^* & \rho_{44} & 0 & 0 & 0 & 0 & 0 \\ 0 & 0 & 0 & \rho_{33} & \rho_{36} & 0 & 0 & 0 \\ 0 & 0 & 0 & \rho_{36}^* & \rho_{66} & 0 & 0 & 0 \\ 0 & 0 & 0 & 0 & 0 & \rho_{55} & 0 & 0 \\ 0 & 0 & 0 & 0 & 0 & 0 & \rho_{22} & 0 \\ 0 & 0 & 0 & 0 & 0 & 0 & 0 & \rho_{77} \end{pmatrix}, \tag{G.33}$$

so that it is block-diagonal.

Let us then focus on a block $\begin{pmatrix} p_+ & ra \\ ra^* & p_- \end{pmatrix}$ with $p_+, p_- > 0$ and let us suppose without loss of generality that $p_+ > p_-$ (as we are only interested in the eigenvalues of such a matrix, one can still permute the basis vectors and rename p_+ and p_- to satisfy this condition). The eigenvalues λ_+ and λ_- then read:

$$\lambda_\pm = \frac{p_+ + p_-}{2} \pm \sqrt{\left(\frac{p_+ - p_-}{2}\right)^2 + r^2|a|^2}\,, \tag{G.34}$$

which expands into:

$$\lambda_\pm = p_\pm \pm \frac{r^2|a|^2}{p_+ - p_-} + o(r^2)\,. \tag{G.35}$$

Therefore, if we want to kill the second-order term in these eigenvalues, we may set $p_\pm \equiv p_\pm \mp \frac{r^2|a|^2}{p_+ - p_-}$.

We should now check that this correction to the diagonal indeed does not change the eigenvalues. Let us then consider the block $\begin{pmatrix} p_+ - r^2\lambda & ra \\ ra^* & p_- + r^2\lambda \end{pmatrix}$ where $\lambda \equiv \frac{|a|^2}{p_+ - p_-}$. Then the eigenvalues now read:

$$\mu_\pm = \frac{p_+ + p_-}{2} \pm \sqrt{\left(\frac{p_+ - p_-}{2}\right)^2 + r^4\lambda^2} = p_\pm + o(r^2)\,, \tag{G.36}$$

so the correction indeed does not change the eigenvalue up to the second order.

This demonstration allows us to build a second-order correction term $\rho^{(2)}$:

$$\boxed{\rho^{(2)} = \frac{|\rho_{14}|^2}{\rho_{11} - \rho_{44}}(|4\rangle\langle 4| - |1\rangle\langle 1|) + \frac{|\rho_{36}|^2}{\rho_{33} - \rho_{66}}(|6\rangle\langle 6| - |3\rangle\langle 3|)\ .} \tag{G.37}$$

G.3.2 Entropy for unselective quantum measurements

Let us study the evolution of the Von-Neumann entropy of the system at each step of the cycle. Before the measurement, for any observable separating the state we consider, the entropy of the thermalized state is given by

$$S(n\tau^-) = S(\rho) = -\mathrm{Tr}[\rho \ln \rho]\ . \tag{G.38}$$

Then, the final entropy after the measurement of the observable n_R will depend on the measurement outcome. When unselective quantum measurements breaking the coherence are performed, we have showed in the main text as well as in the previous section of this Appendix that the cycle is the same regardless of the considered observable since $\rho(n\tau^-) = \rho$ and $\rho(n\tau^+) = \sum_{i=0}^{7} \rho_{ii}|i\rangle\langle i|$. Therefore, the first term is trivial because $\rho(\tau^+)$ is diagonal and leads to

$$S(\rho(\tau^+)) = -\sum_{i=0}^{7} \rho_{ii} \ln \rho_{ii}. \tag{G.39}$$

Then the second term may be evaluated using the second order we just derived. By diagonalizing ρ, we obtain $S(\rho) = S(\rho) + o(\gamma^2)$ since the second order term has been chosen exactly so that the eigenvalues of ρ calculated at the second order remain the same as the first and zero order. In the end, we get $\Delta S = o(\gamma^2)$ and we shall not try to extend this calculation to the third order but simply consider that the measurement process is nearly isentropic, which is sufficient for the purpose of this study.

From the previous calculation, we notice that the corrections we found for ρ vanish in the entropy, only resulting in null corrections up to the third-order of this entropy. We can thus neglect the entropy change as long as we stay at low temperature and in the perturbative regime. The only statement we can make up to this point is on the sign of ΔS which should be positive because of the thermodynamic effect of unselective quantum measurements [577, 578].

This means that the measurement is reorganizing the two-QD system so that it creates localized information from a delocalized form.

G.3.3 Entropy for selective measurement of the occupation of the right quantum dot

From the previous calculation, the entropy of the thermalized state reduces to the entropy of the diagonal terms of ρ:

$$S(\rho) = -\rho_{00}\ln \rho_{00} - \rho_{11}\ln \rho_{11} - \rho_{22}\ln \rho_{22} - \rho_{33}\ln \rho_{33} + o(\gamma^2)\ . \tag{G.40}$$

Let us now study how the entropy changes after the selective measurement. The final entropy after the measurement of the observable n_R will depend on the measurement outcome. This leads to the definition of two different entropies $S^1 \equiv S(\rho^1(\tau^+))$ and $S^0 \equiv S(\rho^0(\tau^+))$, which are calculated simply because the projected states are diagonal:

$$\begin{cases} S^1 = \frac{-\rho_{11}\ln\rho_{11}-\rho_{33}\ln\rho_{33}+(\rho_{11}+\rho_{33})\ln(\rho_{11}+\rho_{33})}{\rho_{11}+\rho_{33}} \\ S^0 = \frac{-\rho_{00}\ln\rho_{00}-\rho_{22}\ln\rho_{22}+(\rho_{00}+\rho_{22})\ln(\rho_{00}+\rho_{22})}{\rho_{00}+\rho_{22}} \end{cases} . \tag{G.41}$$

This leads us to define the expected value of the entropy of the projected state $\overline{S} = p^1 S^1 + p^0 S^0$, which reads

$$\overline{S} = -\rho_{11}\ln\rho_{11}-\rho_{33}\ln\rho_{33}+(\rho_{11}+\rho_{33})\ln(\rho_{11}+\rho_{33})-\rho_{00}\ln\rho_{00}-\rho_{22}\ln\rho_{22}+(\rho_{00}+\rho_{22})\ln(\rho_{00}+\rho_{22}) . \tag{G.42}$$

So the expectancy of the entropy increase defined as $\overline{\Delta S} \equiv \overline{S} - S(\rho)$, reads

$$\overline{\Delta S} = (\rho_{00}+\rho_{22})\ln(\rho_{00}+\rho_{22}) + (\rho_{11}+\rho_{33})\ln(\rho_{11}+\rho_{33}) . \tag{G.43}$$

We witness that the sign of $\overline{\Delta S}$ is negative. This means that the reading of the measurement outcome reduces the mixture of states through the elimination of the components coding for the unmeasured states. Contrary to the case of unselective measurements, we thus find that reading the measurement outcome is reducing the entropy of the state.

This entropy difference can be minimized and we find that $\overline{\Delta S} \geqslant -\ln 2$, reaching equality whenever

$$\rho_{00}+\rho_{22} = \frac{1}{2} \text{ and } \rho_{11}+\rho_{33} = \frac{1}{2} . \tag{G.44}$$

Indeed, the measurement can yield two possible outcomes so the information extracted from the system should not exceed $\ln\ 2$ as expected.

G.3.4 Entropy for selective measurement of the charge of the left quantum dot

The derivation of the entropies of each outcome of the measurement of the charge on the left QD is again straightforward and leads to:

$$\begin{cases} S^0 = \frac{1}{\rho_{00}+\rho_{33}}[-\rho_{00}\ln\rho_{00} - \rho_{33}\ln\rho_{33} + (\rho_{00}+\rho_{33})\ln(\rho_{00}+\rho_{33})] \\ S^1 = 0 \\ S^{-1} = 0 \end{cases} . \tag{G.45}$$

This leads to the average projected entropy $\overline{\Delta S} = p^0 S^0 + p^1 S^1 + p^{-1} s^{-1}$:

$$\langle S \rangle = -\rho_{00}\ln\rho_{00} - \rho_{33}\ln\rho_{33} + (\rho_{00}+\rho_{33})\ln(\rho_{00}+\rho_{33}) , \tag{G.46}$$

and to the average entropy increase:

$$\overline{\Delta S} = \rho_{11}\ln\rho_{11} + \rho_{22}\ln\rho_{22} + (\rho_{00}+\rho_{33})\ln(\rho_{00}+\rho_{33}) < 0 . \tag{G.47}$$

This time, the minimum is different as we have $\overline{\Delta S} \geqslant -\ln 3$, with an equality when

$$\rho_{11} = \frac{1}{3},\ \rho_{22} = \frac{1}{3} \text{ and } \rho_{00}+\rho_{33} = \frac{1}{2} . \tag{G.48}$$

Again, this result is consistent with a measurement that can yield three possible values, leading to a decrease in entropy capped by $\ln 3$.

G.3.5 Entropy for selective measurement of the spin of the left quantum dot

In the case of the spin on the left QD, we have again:

$$\begin{cases} S^0 = 0 \\ S^1 = \frac{1}{\rho_{11}+\rho_{22}}[-\rho_{11}\ln\rho_{11} - \rho_{22}\ln\rho_{22} + (\rho_{11}+\rho_{22})\ln(\rho_{11}+\rho_{22})] \\ S^{-1} = 0 \end{cases} , \tag{G.49}$$

leading to

$$\overline{S} = -\rho_{11}\ln\rho_{11} - \rho_{22}\ln\rho_{22} + (\rho_{11}+\rho_{22})\ln(\rho_{11}+\rho_{22}) , \tag{G.50}$$

and

$$\overline{\Delta S} = \rho_{00}\ln\rho_{00} + \rho_{33}\ln\rho_{33} + (\rho_{11}+\rho_{22})\ln(\rho_{11}+\rho_{22}) < 0 . \tag{G.51}$$

In this case, the minimum is the same $\overline{\Delta S} \geqslant -\ln 3$, but the equality is achieved for different population

$$\rho_{00} = \frac{1}{3},\ \rho_{33} = \frac{1}{3} \text{ and } \rho_{11}+\rho_{22} = \frac{1}{2} . \tag{G.52}$$

Appendix H

Engine Operational Simulations

H.1 Numerical parameters

According to our previous experimental studies, the spin splitting Δ is estimated at $\Delta \approx 2-10$ meV from *ab-initio* analytical calculations in Ref. [18] and reveal a bias dependence as it is linked to the spintronic anisotropy. Whereas in Ref. [19], density functional theory revealed a splitting of $\Delta = 0.7$ meV. It is unclear whether the spin splitting should represent the on-site splitting $\epsilon_\downarrow - \epsilon_\uparrow$ or the two-sites splitting $\epsilon_\downarrow - \epsilon_R$. We shall thus take all ϵ in the meV range to stay in line with the previous results so we set $\epsilon_\downarrow = 8$ meV, $\epsilon_\uparrow = -3$ meV and $\epsilon_R = 1$ meV for all the simulations.

In Ref. [19], we observed experimentally a magnetic phase transition on the bulk unprocessed material of interest and found critical temperature of $T_c = 120$ K, indicating that the parameter coding for the magnetic coupling between the sites J should be of the order of $J \approx 10$ meV. In all of the simulations, we thus set $J = 8$ meV. Numerical experiments performed when changing the value of J showed that the behavior of the engine was very weakly influenced by this parameter, which is in line with the perturbative solution we derived that does not depend on J.

Therefore, the previous studies allows us to fix the energy scale of reference by setting the energies of the bare atomic quantum dots in the meV range, but it remains insufficient to give a precise value to the other parameters.

The Coulombic repulsion parameter U has been evaluated to be ranging between 10 meV and 10 eV in atomic systems from experimental and theoretical studies, so we shall study the influence of this parameter within this range ; and the tunnel coupling between the two quantum dots γ could vary between $\gamma \approx 0.01$ meV in the case where the two sites are weakly coupled to $\gamma \approx 10$ eV when the two sites are really close to each other and hybridize strongly. We shall study various possibilities for this parameter within this large range.

Finally, we set $\mathcal{T} \approx 0.01 - 0.1$ meV for most of the simulations in order for the weak-coupling approximation to hold and we studied the influence of this parameter over an extended range to show different operational regimes of the engine (see Fig.4 in the main text).

H.2 Unselective measurements

H.2.1 Measurement of right qubit

The simulations all revealed a perfect agreement between ΔE and $-\langle C \rangle$, as predicted in the main text. This concordance between the two values has been tested for all the runs we did involving unselective measurements, which confirms the validity of our analysis.

In Fig. H.1(a) and (b), we show additional information corresponding to Fig.3 in the main text. This plot shows the evolution of μ during the operation of a large number of cycles. It confirms the observation of a transitory regime lasting for about 10^5 cycles during which $\mu = 1/2 + \mathrm{d}\mu$, $\mathrm{d}\mu > 0$, is steadily decreasing while ΔE is presenting a steep decrease then an erratic behavior around 0, before reaching a stationary regime after 4.10^5 cycles. A peculiar point we should raise regarding this experiment is that, we do observe a convergence towards $\mu = \mu_c = 1/2$ for these parameters, as predicted by the perturbation model, with a singular difference though, revealing that $\Delta E > 0$ while $\mu > \mu_c$, which should be prohibited in the first order solution. This shows that the perturbation solution we developed can be relevant for predicting the operational steady-state for the engine, but it fails to render the right behavior of the system in the neighborhood of this point.

The two experiments feature a singular difference: in Fig. H.1(a), μ is stable in the limit cycle, saturating at $\mathrm{d}\mu = 2.86 \times 10^{-8}$ meV while in Fig. H.1(b), μ is decreasing linearly very slowly, saturating at $\mathrm{d}\mu = 3.46 \times 10^{-8}$ meV but with a decrease of the order of $\Delta\mu \approx 10^{-17}$ per cycle. Though this slow decrease in μ is not influencing the energy increment ΔE which stays constant. At this point we do not know the origin of such an infinitesimal drift in μ, it could be physical but it could also originate from numerical floating point approximations. If this linear decrease persist, we expect a measurable effect on μ after cycle number $\mathrm{d}\mu/\Delta\mu \approx 10^9$ cycles corresponding to a time $t = 10^9\tau \approx 1$ ms. It shows that another phase transition could occur after this time or we could reach a stable steady-state just as we found in Fig. H.1(a). We leave this point to future studies and consider that the system stays trapped around the non-equilibrium state we find after 10^6 cycles.

H.2.2 Power-dissipating regime

As we saw in the main text and above, the initial state ρ_0 is a critical parameter which is strongly influencing the limit cycle the system will reach after a while.

To illustrate this claim, we show in Fig.H.2 a simulation run of the engine with the same parameters than in Fig.3 in the main text, but with the initial condition $\rho_0 = |\uparrow\downarrow\rangle\langle\uparrow\downarrow|$. In Fig.H.2(b), we notice the same three phases pointed in the main text: the first cycles are characterised by a rapid decrease of the energy increment towards 0, then a stochastic phase around 0 is observed, and finally after about 10^5 cycles, the system gets trapped in a limit non-equilibrium state with two possible energy increment $\Delta E = -3.4$ meV and $\Delta E = -2.3$ peV, leading to an average $\mathbb{E}[\Delta E] = -2.9$ peV. This negative value thus show that the limit cycle is dissipative in this case. In Fig.H.2(b), we observe that μ is increasing from 0 to almost 0.5 during the first 10^5 cycles, following an exponential line shape very similar to the previous experiments presented in Fig.H.1. But the limit cycle is such

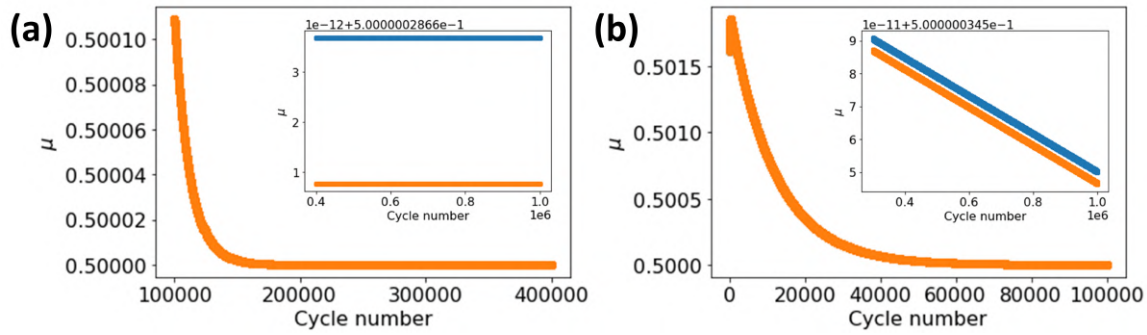

Figure H.1: **Simulation results of μ.** The corrected perturbative results (orange) derived from Appendix F and the numerically calculated solution at 4 ps (blue) are shown. The transitional regime of the first 10^5 cycles are shown in the main figures and the insets show the non-equilibrium steady-state after 4.10^5 cycles. The parameters used are $\epsilon_\downarrow = 8,\ \epsilon_\uparrow = -3,\ \epsilon_R = 1,\ J = 8,\ U = 1000,\ \gamma = 0.1,\ \mathcal{T}_L^+ = \mathcal{T}_L^- = 0.1,\ \mathcal{T}_R^- = \mathcal{T}_R^+ = 0.01$. For (a) $\rho_0 = |\downarrow\downarrow\rangle\langle\downarrow\downarrow|$ and for (b) $\rho_0 = \frac{1}{2}|\uparrow\downarrow\rangle\langle\uparrow\downarrow| + \frac{1}{2}|\downarrow\downarrow\rangle\langle\downarrow\downarrow|$.

as $\mathrm{d}\mu < 0$ for this run, which leads to this dissipative phase. We finally observe that the limit cycle feature an infinitesimal linear decrease of μ just as in Fig.H.1(b). And without giving more details, we notice that this behavior emerges when we can get two possible values of the energy increment ΔE for the limit cycle. It could be that this drift of μ is ultimately leading to a closure of the energy gap between the two limit values of ΔE.

This study shows that a particular priming is necessary for the engine to work, meaning that the initial state of the system must be carefully tailored in order to reach an active limit cycle which will persist after a long time. We argue that this crucial fine tuning originates from the non-ergodicity of the cycle we are studying. Indeed, systems without this property cannot thermalize such that their trajectory is limited to some bounded region of the phase space ; in which case the system stays trapped in the local potential well of a metastable state endowed with singular properties that differ from the global equilibrium thermal state. It thus appears that the frequent quantum measurements performed on the system is limiting the ability of the system to visit the whole phase space, thus trapping it in an active state for what seems to be eternity, until a small perturbation outside the scope of the present study eventually allows it to gain enough energy to move to another phase space domain.

H.2.3 Measurement of left qubit

As we saw in Appendix G, the behavior of the engine might be different depending on the observable we choose for the measurement. We showed previously that changing the observable does not change the energy increment one can hope to harvest, and in fact, in the case of the unselective measurements, we argue that this choice will not change the time evolution of the engine in any way. Indeed, based on previous calculations, it is straightforward to see that the projective channel $\rho \to \sum_k \Pi_k \rho \Pi_k$ is exactly the same channel if we decide to measure n_R, Q or S, as they all have the same effect of deleting the off-diagonal terms in ρ, while keeping its diagonal unchanged. This

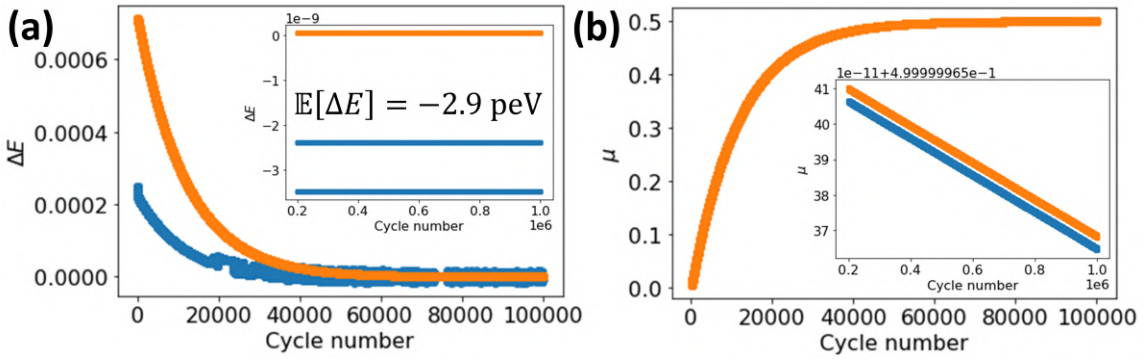

Figure H.2: **Simulation results of a dissipative device.** ΔE in (a) and μ in (b). The corrected perturbative results (orange) derivated from Appendix F and the numerically calculated solution at 4 ps (blue) are shown. The transitional regime of the first 10^5 cycles are shown in the main figures and the insets show the non-equilibrium steady-state after 4.10^5 cycles. The parameters used are $\epsilon_\downarrow = 8,\ \epsilon_\uparrow = -3,\ \epsilon_R = 1,\ J = 8,\ U = 1000,\ \gamma = 0.1,\ \mathcal{T}_L^+ = \mathcal{T}_L^- = 0.1,\ \mathcal{T}_R^- = \mathcal{T}_R^+ = 0.01$. The initial state was set to $\rho_0 = |\downarrow\downarrow\rangle\langle\downarrow\downarrow|$ and lead to a dissipative steady-state contrary to the cases presented in the main text.

argument shows that the engine is completely independent from the choice of the measurement basis, provided that it separates the two QDs, thereby killing the coherence terms between them. Data not shown in which we compared several engine runs with the same parameters but different measurement protocols allowed us to verify this statement as all those simulations led to the same evolution of the density matrix.

However, we should emphasize that each observable will lead a different behavior when studying selective measurement protocols because of the non-linear probability rescaling that is applied in this case. Hence, the evolution of the linear system is independent on the local measurement basis chosen to measure the system, the situation becomes less trivial when the measurement result relative to a specific local basis is read as this result starts to condition an erratic evolution of the system. Further details is given below regarding the choice of observable for selective measurements.

H.3 Selective measurement

H.3.1 Measurement of the right qubit

In comparison, we show in Fig. H.3 and Fig. H.4 the results of numerical simulations obtained for the same set of parameters used in Fig.3 in the main text, but for selective measurements. Compared to the unselective case, when starting with the sate $\rho_0 = |\uparrow\downarrow\rangle\langle\uparrow\downarrow|$ we first notice a striking difference, which is the appearance of a negative branch in the line shapes of ΔE and $-\langle C\rangle$. This new possible state emerges from the two measurement possibilities of n_R. One result will energize the system, the other will lower its energy, while on average keeping the energy increment positive. Such alternation is not present in the corresponding unselective measurement because it projects linearly the system onto one mixed state, so the behavior is more continuous and remains positive.

Nevertheless, we emphasize that we should not need to provide any form of work during the thermalization process when the measurement decreases the energy of the system because the quantum dots will just equilibrate themselves with the baths without the need for an external energy input: heat alone will suffice to reset the state.

We also showed in Fig.3 in the main text that unselective measurements can result in discontinuous alternating behavior. This stochastic process is not due to the randomness of a measurement result but to a sensitivity on the initial conditions. We can compare this experiment to its equivalent for selective measurements, presented in Fig. H.4. Compared to the unselective case where $\mu = 1/2 + \mathrm{d}\mu$ is alternating fast, within a clear uptrend, in the selective case, μ looks like a random walk around $\mu = 1/2$. It leads in the unselective case to a stable and sharp bimodal distribution for ΔE and $\langle C \rangle$ which contrasts with the plots for the selective case: $\langle C \rangle$ is also bimodal but its distribution is not positive and its dispersion is larger around the modes. This negative feature comes from the two measurement outcomes leading to energy-dissipating projections, and the dispersion comes from a stronger sensitivity to the initial conditions, induced by the non-linear projective measurement. With the selection of the measurement, ΔE now has four modes (two modes are superposed but distinct around zero in Fig. H.4(a))! Two of them originate from the two measurement outcomes and, each of them splits into two because of the sensitivity to the initial conditions, mainly represented by the value of μ.

It is important to point out that the quality $\Delta E = -\langle C \rangle$ is no longer valid here. Indeed, because of the random motion of ΔE induced by the selection mechanism, this equality is only valid for the statistical average over the measurement outcomes $\overline{\Delta E} = -\langle C \rangle$. With the property of ergodicity, this average could in principle be identical to the temporal average $\mathbb{E}[\Delta E]$ over many cycles. Nonetheless, this equality is not achieved here for both runs. For the data displayed in Fig. H.3 we obtain $\mathbb{E}[\Delta E] = 129$ neV while $\mathbb{E}[-\langle C \rangle] = 1.5$ neV and for Fig. H.4 we have $\mathbb{E}[\Delta E] = -1.8$ neV while $\mathbb{E}[-\langle C \rangle] = -0.5$ peV. It could be that we did not reach a sufficient number of cycles to reach a closer equality. Indeed, the multimodal quasi-symmetric distribution of ΔE has a standard deviation of the order of a few meV, while its average is at least three orders of magnitude lower, which means that we need a sample of at least $N = 10^6$ and ideally $N = 10^9$ cycles to estimate $-\langle C \rangle$ with ΔE.

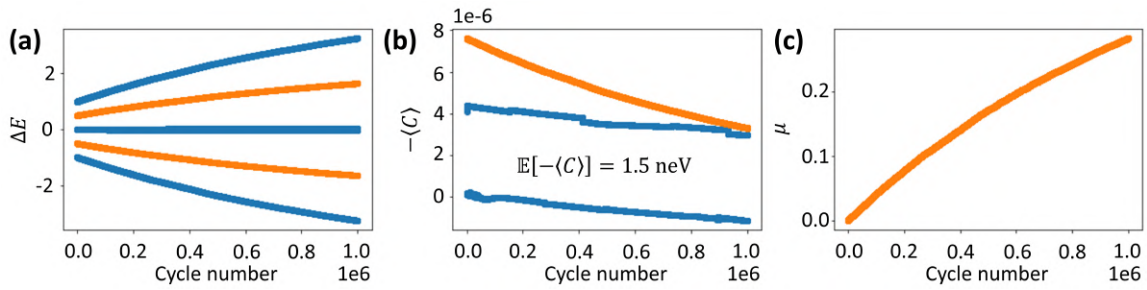

Figure H.3: **Simulation results of an active device for selective measurements.** Simulation results of ΔE in (a) and $-\langle T \rangle$ in (b) and μ in (c) for 10^6 cycles when measuring n_R. The parameters used are $\epsilon_\downarrow = 8,\ \epsilon_\uparrow = -3,\ \epsilon_R = 1,\ J = 8,\ U = 1000,\ \gamma = 0.01,\ \mathcal{T}_L^+ = \mathcal{T}_L^- = 0.1,\ \mathcal{T}_R^+ = \mathcal{T}_R^- = 0.01$ and with the initial condition $\rho_0 = |\downarrow\downarrow\rangle\langle\downarrow\downarrow|$.

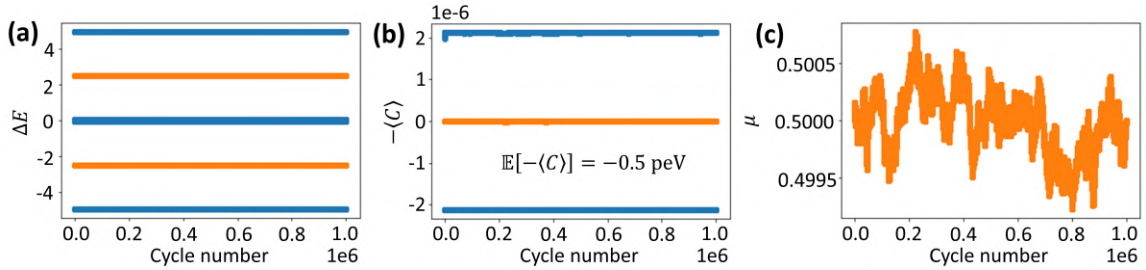

Figure H.4: **Simulation results of a passive device for selective measurements.** Simulation results of ΔE in (a) and $-\langle T \rangle$ in (b) and μ in (c) for 10^6 cycles when measuring n_R. The parameters used are $\epsilon_\downarrow = 8,\ \epsilon_\uparrow = -3,\ \epsilon_R = 1,\ J = 8,\ U = 1000,\ \gamma = 0.01,\ \mathcal{T}_L^+ = \mathcal{T}_L^- = 0.1,\ \mathcal{T}_R^+ = \mathcal{T}_R^- = 0.01$ and with the initial condition $\rho_0 = \frac{1}{2}|\uparrow\downarrow\rangle\langle\uparrow\downarrow| + \frac{1}{2}|\downarrow\downarrow\rangle\langle\downarrow\downarrow|$.

These experiments show that reading the measurement result can be detrimental to the engine's performance as it generates power-dissipating cycles, which are counter-balanced by energizing cycles of larger amplitudes, thus resulting in a device with stronger power fluctuations. The non-linear random walk issued by the selection of the measurement is in this case mostly undesirable because of the stochastic chaotic behavior it entails: indeed, the projection onto a specific eigenstate drastically changes the initial conditions of the next cycle, which can place it in a unfavorable domain ($\mu > \mu_c$), where the system will be trapped in a power-dissipating phase. Indeed, we calculated the temporal averages over the cycles and found for the unselective case run presented in Fig.3(b) in the main text $\mathbb{E}[\Delta E] = 2.9$ peV, which compare with the value found for the selective case $\mathbb{E}[\Delta E] = -0.5$ peV. We thus notice that the device is on average passive for the selective case but active in the unselective case! Hence, it looks like selecting the measurement forces the system to stay in a out-of-equilibrium behavior, stabilizing its quantum behavior via a Zeno effect which keep the initial conditions in memory for a longer time, such as it can behave only statistically when studied for a larger time-scale; while unselective measurements allow for a faster convergence towards a cyclic steady-state which is closer to a statistical thermal state in which the history of the system becomes less significant. It would thus seem like unselective measurements are restricting the trajectory of the system, pinning it in a favorable or unfavorable region of phase space depending on the initial condition, while selective measurements does allow the system to statistically jump between more domains which would then make it more sensible to strong fluctuations that could be detrimental to the power output.

Although we have seen that selective measurement may be detrimental to the engine efficiency due to the quantum-trajectory like behavior, they allow stabilization for a larger duration. Finally, we shall keep in mind that selective measurement may very well be more adapted to other kinds of Maxwell demons which could better use this stroboscopic and negentropic quantum feature to their advantage, eventually through a feedback that could counter the larger fluctuations induced by selection.

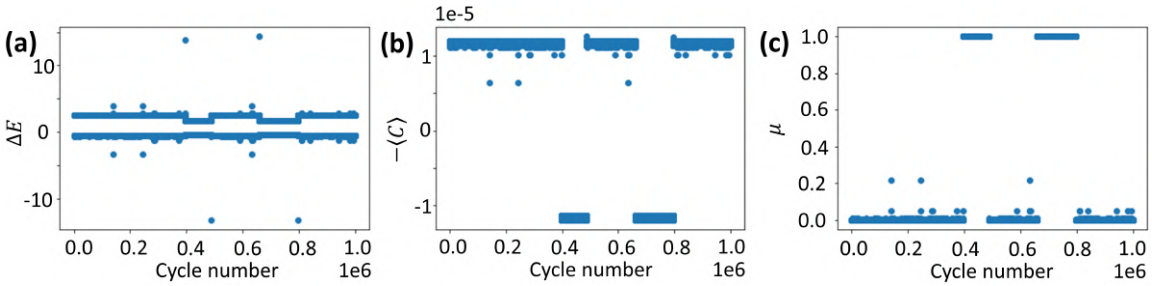

Figure H.5: **Simulation results when measuring the charge on the left quantum dot.** Simulation results of ΔE in (a) and $-\langle C\rangle$ in (b) and μ in (c) for 10^6 cycles when measuring the charge Q of the left QD. The parameters used are $\epsilon_\downarrow = 8,\ \epsilon_\uparrow = -3,\ \epsilon_R = 1,\ J = 8,\ U = 1,\ \gamma = 0.01,\ \mathcal{T}_L^+ = 5,\ \mathcal{T}_R^+ = \mathcal{T}_L^- = \mathcal{T}_R^- = 1$ and with the initial condition $\rho_0 = |\uparrow\downarrow\rangle\langle\uparrow\downarrow|$.

H.3.2 Measurement of the left qubit

As detailed in Appendix G, measuring the charge or the spin of the left qubit leads to a qualitatively very different behavior for the engine with selective measurements. Indeed, the measurement of n_R leaves the initial parameter $\mu = \langle n_\downarrow\rangle$ unchanged up to the first order, therefore the system is slowly drifting from the initial condition μ_0 because the components that encode the population $n_\downarrow$ in the density matrix are progressively mixing due to higher order terms ; contrary to a measurement on the left quantum dot which is stabilizing the population μ, forcing it to remain close to 0 or 1.

In Fig. H.5, we show a test run of 10^6 cycles of the engine when we measure the spin of the left qubit. We observe in Fig. H.5(c) a stabilization of μ close to 0 or 1, and that the system indeed stays longer in the state 0 than in the state 1, which should ensure that the measurement is energizing the system on average.

The data of Fig. H.5(a) and (b) confirms this point by yielding a positive value for the temporal averages $\mathbb{E}[\Delta E] \approx 18\ \mu$eV and $\mathbb{E}[-\langle C\rangle] \approx 8.7$ neV. Once again, we notice a discrepancy between the two values: averaging over time steps is not equivalent to averaging over the measurement outcomes. The reason we may get different results for these two averages is that the information of the initial state can persist over time and is somewhat transferred from cycle to cycle due to the incomplete thermalization. It thus remains unclear at this point whether it is possible to harvest quantum fluctuation energy with this system after a long time, as the temporal average $\mathbb{E}[\Delta E]$ remains close to 0, and with a fluctuating sign depending on the parameters and initial conditions. Indeed, numerical experiments (not shown) that are identical to the present ones revealed the strong dependence of its sign on the parameters chosen. A more detailed analysis of the relation between the initial density of state, the temporal average and the measurement average is beyond the scope of the current paper and will be the subject of a separate study. Here, we shall only state that ergodicity will be of use in order to study the temporal transfer of information, and will ultimately link the temporal and measurement averages to some measure of $\langle C\rangle$ over the space of initial density matrices. This followup study should provide a definitive answer to the question of harvesting quantum fluctuations with this system after a long time, and may lead to profound connections between thermodynamics, quantum measurement and ergodicity.

H.3.3 Proof of energy generation

At the end of each cycle, while the first-order solution showed that after some time, the system would get stuck in one of the two values $\mu_n = 0$ or $\mu_n = 1$, the numerical experiment in Fig.H.5 showed that there is still a small probability to jump back to $\mu_{n+1} = 1 - \mu_n$. This means that the charge of the left quantum dot - driven by the occupation of the down spin energy level - may change during the operation of a cycle.

As shown in the main text, the system may behave as an engine during the cycle n whenever $\mu_n < 0$. Therefore, we can hope to extract energy continuously from this system when the expectation value $\overline{\mu}_n$ is negative. This should be the case if the probability $p \equiv \mathbb{P}(\mu_{n+1} = 1|\mu_n = 0)$ to jump from $\mu_n = 0$ to $\mu_{n+1} = 1$ is lower than the symmetric probability $q \equiv \mathbb{P}(\mu_{n+1} = 0|\mu_n = 1)$ to jump from $\mu_n = 1$ to $\mu_{n+1} = 0$; in which case it would guarantee a longer lifetime in the state $\mu = 0$ than in the state $\mu = 1$. Intuitively, one could hope to achieve such asymmetry whenever U is sufficiently small. Indeed, a small U would allow for excessive charging on the left site, hence it would favor a state with a charge of 0 or 2 which would then relax into the thermalized state with a charge of 1, eventually releasing more power if measuring 2 is more probable than measuring 1.

To prove this physical intuition, we begin with the second order correction we have derived in section G.3.1, which allows us to refine the sequence μ_n. We have:

$$\mu_{n+1} = \begin{cases} 0 & \text{if} \quad \mu_n = 0 \quad \text{with probability} \quad 1-p \\ 1 & \text{if} \quad \mu_n = 0 \quad \text{with probability} \quad p \\ 0 & \text{if} \quad \mu_n = 1 \quad \text{with probability} \quad q \\ 1 & \text{if} \quad \mu_n = 1 \quad \text{with probability} \quad 1-q \end{cases}, \tag{H.1}$$

where

$$\begin{cases} p = \rho^0_{66} + \rho^0_{77} = \frac{|\rho^0_{63}|^2}{\rho^0_{33} - \rho^0_{66}} = \frac{|\gamma|^2\alpha^2}{|\det B|^2}\mathcal{T}^-_L\mathcal{T}^-_R[(s+r)^2 + (\Delta+U)^2] \\ q = \rho^1_{00} + \rho^1_{11} = \frac{|\rho^1_{14}|^2}{\rho^1_{44} - \rho^1_{11}} = \frac{|\gamma|^2\alpha^2}{|\det B|^2}\mathcal{T}^+_L\mathcal{T}^+_R[(s+r)^2 + \Delta^2] \end{cases}. \tag{H.2}$$

Using the total probability formula, we can then write:

$$\begin{cases} \mathbb{P}(\mu_{n+1} = 0) = (1-p)\mathbb{P}(\mu_n = 0) + q\mathbb{P}(\mu_n = 1) \\ \mathbb{P}(\mu_{n+1} = 1) = p\mathbb{P}(\mu_n = 0) + (1-q)\mathbb{P}(\mu_n = 1) \end{cases}, \tag{H.3}$$

which reads in matrix format $\mathbb{P}(\mu_{n+1}) = M\mathbb{P}(\mu_n)$ with $M = \begin{pmatrix} 1-p & q \\ p & 1-q \end{pmatrix}$. This matrix M thus describes the transition of a Markov chain, and in order to study the behaviour or μ_n at long times, we shall study the stationary distribution. The diagonalization of M is straightforward and yields:

$$M = \frac{1}{p(p+q)} \begin{pmatrix} q & -p \\ p & p \end{pmatrix} \begin{pmatrix} 1 & 0 \\ 0 & 1-p-q \end{pmatrix} \begin{pmatrix} p & p \\ -p & q \end{pmatrix}, \tag{H.4}$$

which shows that after some time:

$$M^n \underset{n\to+\infty}{\longrightarrow} \frac{1}{p+q} \begin{pmatrix} q & q \\ p & p \end{pmatrix}. \tag{H.5}$$

Therefore,

$$\overline{\mu_n} = \mathbb{P}(\mu_n = 1) \underset{n\to+\infty}{\longrightarrow} \overline{\mu_\infty} \equiv \frac{1}{1+\frac{q}{p}} = \frac{1}{1+\frac{\mathcal{T}_L^+\mathcal{T}_R^+}{\mathcal{T}_L^-\mathcal{T}_R^-}\frac{(s+r)^2+\Delta^2}{(s+r)^2+(\Delta+U)^2}}, \tag{H.6}$$

when starting with $P(\mu_0 = 0) = 1$ and $P(\mu_0 = 1) = 0$. This leads to the condition:

$$\overline{\mu_\infty} < \mu^c \Leftrightarrow p < \frac{\mathcal{T}_R^-}{\mathcal{T}_R^+} q \Leftrightarrow 1 \leqslant \frac{(s+r)^2+(\Delta+U)^2}{(s+r)^2+\Delta^2} < \frac{\mathcal{T}_L^+}{\mathcal{T}_R^-}. \tag{H.7}$$

This result partially confirms our intuition by showing two points. First, our conjecture was almost correct, meaning that $p < q$ may not be sufficient to allow for energy generation, but we shall instead require $p < \frac{\mathcal{T}_R^-}{\mathcal{T}_R^+} q$ to guarantee it. This shows that a higher $\frac{\mathcal{T}_R^-}{\mathcal{T}_R^+}$ ratio would increase the value of μ^c and increase the range of parameters that allow for energy generation.

Second, U must indeed be small enough in order to fulfill the condition H.7. This inequality additionally shows another critical point, which is the condition $\mathcal{T}_L^- < \mathcal{T}_L^+$. In physical terms, it means that the injection of electrons on the left side must be stronger than the injection of holes, and the opposite should be true on the right side to maximize μ_c. Intuitively, this should favor a flux of electrons going from left to right, so that it would create a current going above the built-in potential ladder imposed by the placement of the energy levels. This describes exactly the behavior of an active device.

Appendix I

Sampling experiments

I.1 Comparison between the perturbative and the numerical solutions

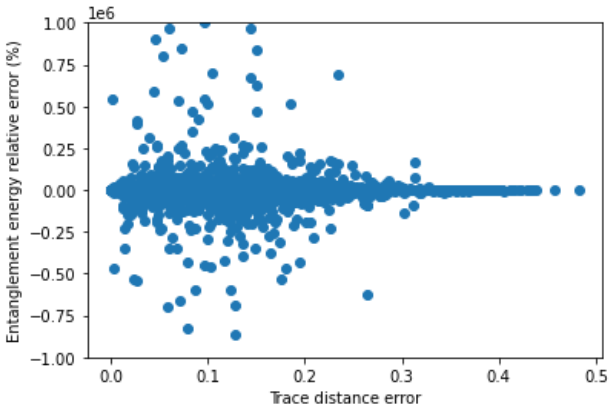

Figure I.1: **Sampling experiment comparing the perturbative to the numerical solutions.** Distribution of the trace distance error and the coherence energy error between the perturbative and the numerical solution.

Our perturbative solution holds only shortly after each thermalization stroke, yet we expect the exact final state to be reached only after many cycles, and partial thermalization can occur. To evaluate the robustness of this approximation, we now perform simulations using QuTip. We calculated the density matrix at time $t = 1$ meV$^{-1} \approx 4$ ps, and ΔE, starting from different pure states and with different parameters taken randomly within a range that is compatible with the perturbative assumption. More precisely, we calculated the perturbative and the numerical solution for a set of 10^6 corpus of parameters taken uniformly within a physically reasonable range that preserves the relative positions of the energy levels. For this experiment, we have chosen a uniform sampling of the parameters such as $\epsilon_\uparrow \in [\![-100, 99]\!]$, $\epsilon_\downarrow \in [\![\epsilon_\uparrow + 1, 100]\!]$, $\epsilon_R \in [\![\epsilon_\uparrow, \epsilon_\downarrow]\!]$, $J \in [\![1, 100]\!]$, $U \in [\![1, 1000]\!]$, $10^4\gamma \in [\![10, 1000]\!]$, $\mathcal{T}_L^+$, $\mathcal{T}_L^-$, $\mathcal{T}_R^-$, $\mathcal{T}_R^+ \in [\![1, 100]\!]$ and ρ_0 a random 8×8 density matrix.

Results of this experiment are presented in Fig I.1 and show a sample of 10^6 trials, the trace distance between the perturbative solution ρ and the calculated solution σ defined by $T(\rho, \sigma) = \frac{1}{2}\mathrm{Tr}\sqrt{(\rho-\sigma)(\rho-\sigma)^\dagger}$ is lower than 0.5 and the corresponding error on ΔE can reach up to 10^8.

The statistics show that 98% of the runs lead to an error on ΔE higher than 1%. This shows that the derived perturbative solution is clearly unable to describe the coherence energy created through partial thermalization.

Although this first experiment clearly shows the limits of the perturbative approach to accurately describe the state at the end of the thermalization step, it may still be usable to give qualitative interpretations of the operation of the engine and orient the search for optimal parameters. In the main text, we also display one special case where the perturbative solution remains pretty close to the numerical solution at the level of a single cycle.

I.2 Comparison between the partially thermalized and the steady-state solutions

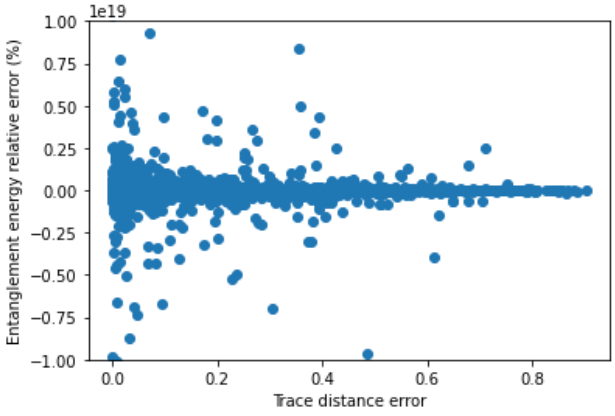

Figure I.2: **Sampling experiment comparing the partially thermalized state to the steady-state solutions.** Distribution of the trace distance error and the coherence energy error between the perturbative and the numerical solution.

Ideally, we would want to achieve full thermalization during the thermalizing stroke, meaning that the system would reach the steady-state of the master equation, independent from time. Getting close to full thermalization would indeed completely wipe out the memory of the initial condition, hence making the cycle more reliable and easier to study. We therefore wanted to test this assertion by comparing the partially thermalized solution after $\tau = 4$ ps with the numerically calculated steady-state solution for a large sample of the set of parameters, using the same method as above.

Using the same ranges of parameters used in the previous experiments, we therefore calculated the trace distance error and the coherence energy error between the two numerically calculated states for a sample size of 10^6. The results presented in Fig I.2 once again show a large discrepancy between the two solutions, with a trace distance error reaching up to 0.9 and a coherence energy error of up to 10^{21}. This experiment thus shows that the cycle time of 4 ps is largely insufficient to fully thermalize the system with the baths. Nonetheless, this partial thermalization may not be critical to the efficiency of the engine. In fact, it may even be beneficial! Indeed, as we will show, the coherence energy that is obtained after a duration of 4 ps is much larger and smoother than the energy that can be achieved with full thermalization. This means that the energy provided by the quantum measurement to the system may be greater by up to 20 orders of magnitude in the case of partial thermalization than when the steady-state is reached. This can be seen by witnessing the scale of the vertical axis in Fig I.2. And even though a larger magnitude of the coherence energy can be detrimental to the power output, in the end, due to increasing fluctuations,

it seems that partial thermalization would still be valuable to enhance the power of the device given the very low magnitude of $|\langle C \rangle|$ and the sign variability obtained for the steady-state.

Appendix J

On the maximization of the coherence energy

J.1 Regime where $\gamma \gg U \sim \epsilon \sim \mathcal{T}$

Gaining insights into the influence of the parameters on the device is necessary to guide a potential optimization for a physical implementation. To this end, we performed several numerical experiments in which we plotted $-\langle T \rangle$ as a function of different pairs of parameters, while keeping the other fixed, for different regimes.

In the regime where $\gamma \gg U \sim \epsilon \sim \mathcal{T}$, the data is represented in Fig J.1. Figures (a), (b) and (c) show the dependence of $\Delta = \epsilon_\downarrow - \epsilon_\uparrow$, γ and U with respect to $\mathcal{T}_L^+ = \mathcal{T}_L^-$. We notice that, in this regime, maximizing Δ is beneficial to the coherence energy, but γ and U present a sweet spot around $\gamma \approx 1 - 10$ and $U \approx 10^3 - 10^4$. Intuitively, maximizing Δ could indeed lead to a higher energizing of the system as this difference in energy between the two levels is strongly linked to a built-in potential ladder in the device. We also notice that when $\mathcal{T}_L$ is too strong, then the coherence energy decreases. The sweet spot for γ and U may be explained by arguing that tunnelling may be impaired when these two parameters become either too strong or too weak.

Then, Figures (d), (e) and (f) display the same dependence of Δ, γ and U but with respect to $\mathcal{T}_R^+ = \mathcal{T}_R^-$. The same tendencies can be observed: $-\langle C \rangle$ is maximal when Δ is maximal, and when $\gamma \approx 10$ and $U \approx 10^3$. The interesting feature in this case is the appearance of a chaotic phase at high $\mathcal{T}_R$. Here, the coherence energy almost vanishes and its sign is subject to strong fluctuations that depend on small variations of the parameters. This chaotic phase can also be observed in panel (g). We therefore ascribe its origin to an interaction with the right electrode that overcomes the tunneling interaction between the two QDs, thereby killing the coherence energy between the two sites. We understand the influence of $\mathcal{T}_L$ to be less significant than the influence of $\mathcal{T}_R$ because the left electrode is not directly linked by a tunnel interaction to the two spin energy levels of interest. Indeed, in our hypothesis, only the $\uparrow$ level is connected to the lead while tunneling between the dots couple the $\downarrow$ level of the left site with the right site.

This first experiment thus leads us to the following regimes in which we can hope to maximize

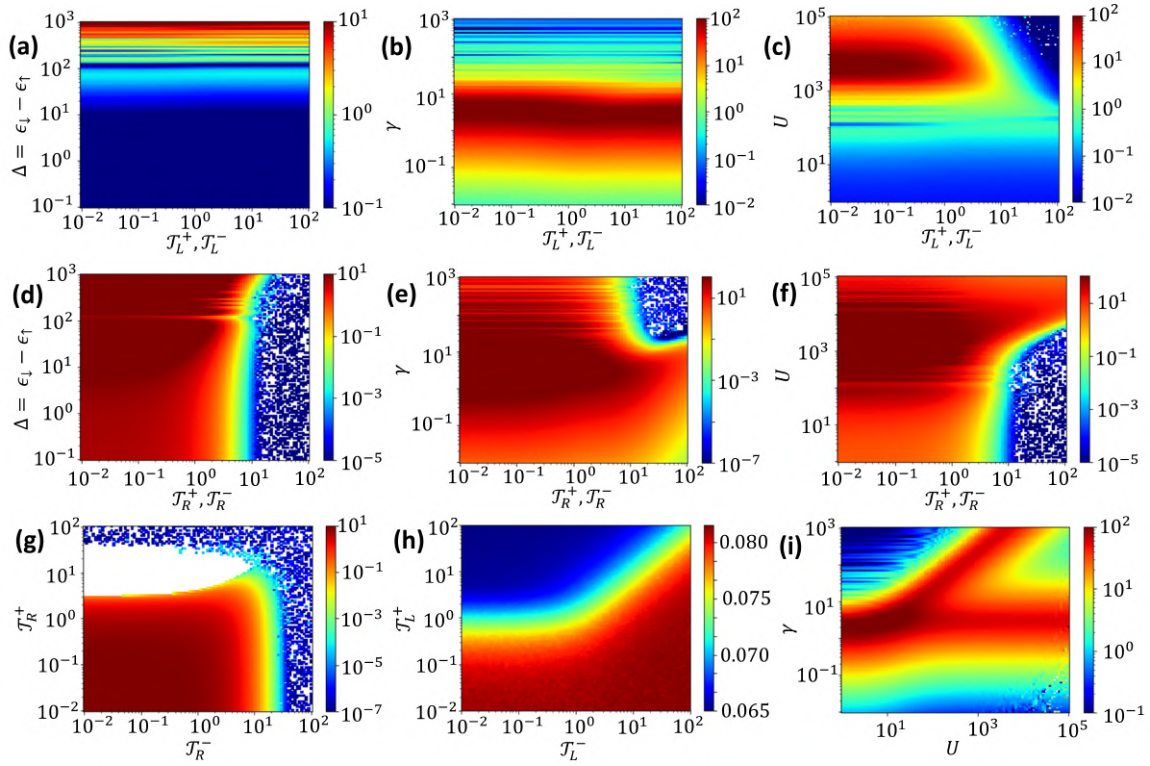

Figure J.1: **Color plots of the coherence energy for a strong hopping parameter.** Color plots of the coherence energy $-\langle C \rangle$ calculated after 4 ps as a function of various pairs of parameters. For all figures, the fixed parameters are set to $\epsilon_\downarrow = 8,\ \epsilon_\uparrow = -3,\ \epsilon_R = 1,\ J = 8,\ U = 10,\ \gamma = 1000,\ \mathcal{T}_L^+ = 1,\ \mathcal{T}_L^- = 1,\ \mathcal{T}_R^+ = 5,\ \mathcal{T}_R^- = 5$

$-\langle C \rangle$: $\mathcal{T} \ll \epsilon$, then $\gamma \sim \epsilon$ or $\gamma \sim U \gg \epsilon$. Let us study these two regimes corresponding to the two branches we can identify in Fig J.1(i).

J.2 Regime where $\gamma \gg U \sim \epsilon \gg \mathcal{T}$.

We therefore repeated the previous simulation with different parameters corresponding first to the branch where $\gamma \gg U \sim \epsilon$. The results presented in Fig J.2 are ordered in the same manner as in Fig J.1 such that we will just comment on the differences. Contrary to the previous case, we witness this time that there is a sweet spot for Δ for both the $\mathcal{T}_L$ and the $\mathcal{T}_R$ dependence and we should have $\Delta \sim U$ to maximize $-\langle C \rangle$. This can be explained by arguing that in this case U is very large, so increasing Δ even more should kill the eventual flow of electrons because they are not be able to overcome both the potential barrier imposed by the placement of the energy levels and the repulsive Coulombic energy. Fig J.2(a), (b) and (c) also shows that there is also a sweet spot for $\mathcal{T}_L$ such as $\mathcal{T}_L \sim \epsilon$. This can be explained through the fact that a stronger coupling to the left is now needed to overcome the on-site Coulomb interaction, but this is not the case for $\mathcal{T}_R$ which could be minimized, and this should be due to the stronger link between the interdot-coupling and the right electrode which is sufficient to overcome this repulsion even in the weak coupling regime.

In Fig J.2(g), we also notice the presence of the both the dissipative and the chaotic phases

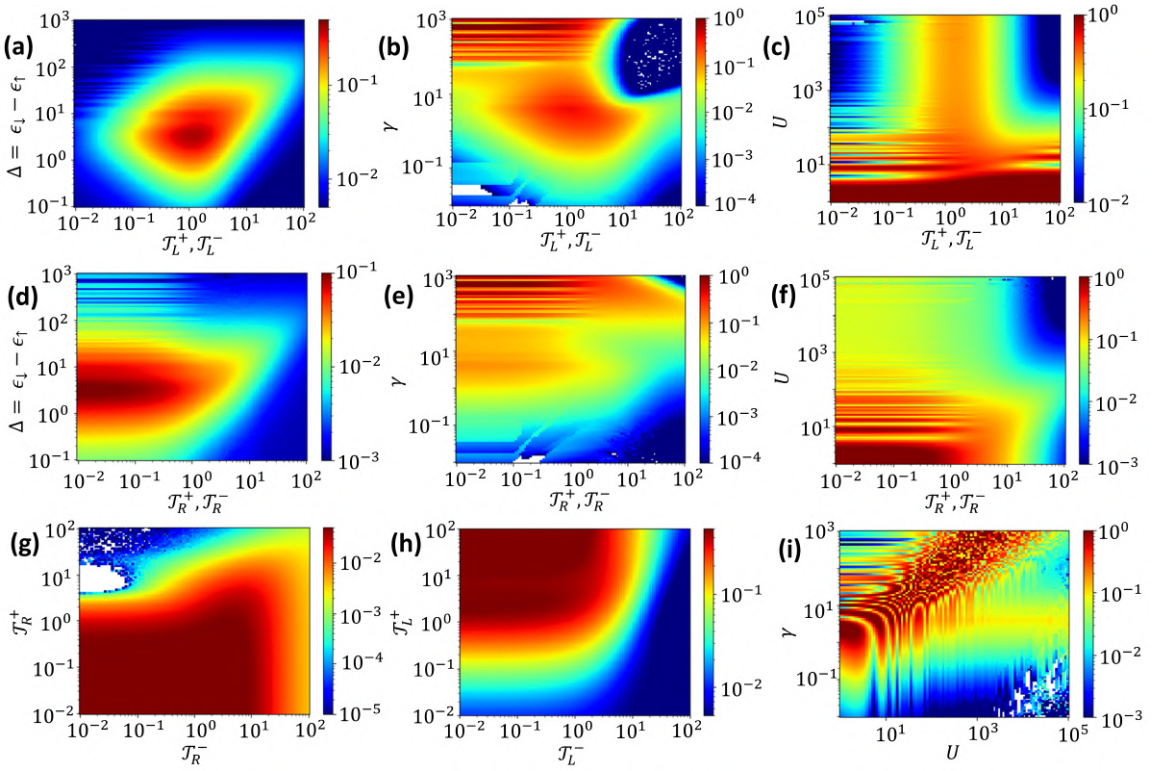

Figure J.2: **Color plots of the coherence energy for a weak coupling.** Color plots of the coherence energy $-\langle C \rangle$ calculated after 4 ps as a function of various pairs of parameters. For all figures, the fixed parameters are set to $\epsilon_\downarrow = 8$, $\epsilon_\uparrow = -3$, $\epsilon_R = 1$, $J = 8$, $U = 3000$, $\gamma = 2$, $\mathcal{T}_L^+ = 0.1$, $\mathcal{T}_L^- = 0.1$, $\mathcal{T}_R^+ = 0.1$, $\mathcal{T}_R^- = 0.1$

depending on the parameter $\mathcal{T}_R$, but the parameter extent of these phases has been considerably reduced as $\mathcal{T}_R$ appears to become less relevant given the magnitude of U. Finally, Fig J.2(i) once again features these two distinct branches $\gamma \sim U$ and $\gamma \sim 1$ with the particularities that the branch $\gamma \sim U$ now leads to a clearly superior coherence energy and that strong vertical and horizontal fluctuations can now be observed. It seem that as $-\langle C \rangle$ becomes stronger, the fluctuations with respect to the different parameters also become stronger.

J.3 Regime where $\gamma \sim U \gg \epsilon \gg \mathcal{T}$.

In this last simulation, we study the regime of the higher branch in the γ-U plane where $\gamma \sim U$. The first striking feature we notice is the presence of strong fluctuations around zones with a higher coherence energy in all plots, which can reach up to $-\langle C \rangle \sim 10^3$. We interpret this as evidence that we are scanning quite close to the global maximum of $-\langle C \rangle$ in this range of parameters.

The following observations follow from Fig J.3.(a)-(f): the dependence with respect to Δ is unclear and $-\langle C \rangle$ can be maximized as long as $\Delta \gtrsim \epsilon$; both $\mathcal{T}_R$ and $\mathcal{T}_L$ should not be too large and we witness the emergence of a chaotic phase for $\mathcal{T} \gtrsim \epsilon$, this time also for $\mathcal{T}_L$. This phase transition may now be observed for $\mathcal{T}_L$ in this range as this parameter now becomes more relevant in the considered

scale; and finally, we confirm that the maximum is indeed approached when $\gamma \sim U \sim 10^3\epsilon$.

Fig J.3(h) presents a particularly notable difference that, in this case, we should maximize $\mathcal{T}_L^-$ over $\mathcal{T}_L^+$, which could mean that a current going in the reverse direction in the vicinity of the left electrode is favored. A satisfying qualitative explanation for this current inversion remains to be found.

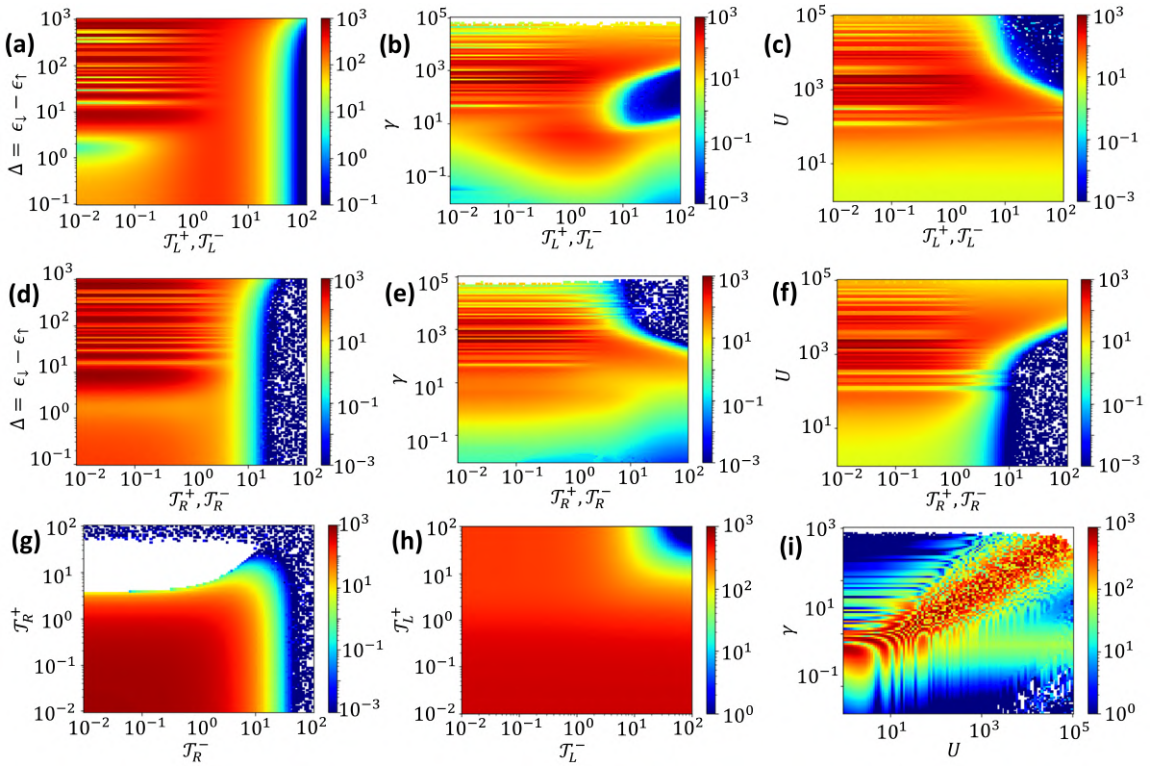

Figure J.3: **Color plots of the coherence energy for strong Coulomb repulsion.** Color plots of the coherence energy $-\langle C \rangle$ calculated after 4 ps as a function of various pairs of parameters. For all figures, the fixed parameters are set to $\epsilon_\downarrow = 8$, $\epsilon_\uparrow = -3$, $\epsilon_R = 1$, $J = 8$, $U = 1000$, $\gamma = 1000$, $\mathcal{T}_L^+ = 0.1$, $\mathcal{T}_L^- = 0.1$, $\mathcal{T}_R^+ = 0.1$, $\mathcal{T}_R^- = 0.1$

Appendix K

Bosonic Catalysis.

K.1 Engine powered by a non-thermal bosonic bath

Referring to Appendix E, we have showed that the bosonic coupling coefficients coding for the interaction between the bosonic bath and the system read

$$\Lambda^+ = n_B(\delta, T)D(\delta), \text{ and } \Lambda^- = (1 + n_B(\delta, T))D(\delta), \tag{K.1}$$

which implies that $\Lambda^- > \Lambda^+$ for a perfectly thermal bath. Nonetheless, it is possible to obtain asymmetric coefficients through squeezing [358, 354, 356, 511], broken symmetries [524], non-Hermitian skin effect [525, 526] or non-linear processes [527]. Such a bath could then present a special filling and correlations so that one could obtain an effective negative temperature [311, 579] that would lead to $\Lambda^+ > \Lambda^-$, in which case this bath could provide the necessary non-equilibrium resources to feed the engine and boost its power beyond what it can extract from vacuum fluctuations. To complement the datasets in the main text, we present thus present in Fig.K.1 the complete color plots that analyze the dependence of $-\langle C\rangle$ with respect to different pairs of parameters. The data shows that in order to maximize energy generation, there are sweet spots for the parameters which need to be chosen such as $\gamma \approx \epsilon$ or $\gamma \approx 10^3\epsilon$, $\mathcal{T} \lesssim 0.1\epsilon$, $U \approx 10^3\epsilon$.

K.2 Engine powered by chemical potential bias or a spin bias

At thermal and chemical equilibrium, the coupling coefficients to the two leads read

$$\mathcal{T}_L^+ = \kappa(1 - n_F) = \kappa\left(1 - \frac{1}{1 + e^{\beta_L(\mu_L + m_L)}}\right) \text{ and } \mathcal{T}_L^- = \kappa n_F = \frac{\kappa}{1 + e^{\beta_L\beta(\mu_L + m_L)}} \tag{K.2}$$

with $\beta = 1/k_BT$.

Therefore, if a chemical potential $\mu_L > 0$ is applied to the left electrode, or a spin bias $m_L > 0$, it follows that the Fermi-Dirac distribution is now favoring electrons instead of holes, and leads to

$\mathcal{T}_L^+ > \mathcal{T}_L^-$, such as the parameters place the system in the energy-generating quadrant we see in Fig.K.1. This resource is now sufficient to extract estimable work, even when the bosonic bath is not endowed with a non-thermal feature, in which case it only acts as a catalyst that favors the tunneling of electrons between the two leads but it does not behave as a heat sink only able to dissipate waste energy.

In Fig.K.2, we present the steady-state solution in the case of a system powered by a potential bias such as $\mathcal{T}_L^+ = 2\mathcal{T}_L^-$ which codes for $\mu_L = -k_B T \ln 2 \approx -30$ meV at room temperature.

K.3 Engine powered by thermal gradient

Now, if the two electrodes equilibrate at the same chemical potential $\mu \neq 0$ such as the left electrode is hotter than the right one, we can also expect to obtain a power generating device since we can obtain $\mathcal{T}_R^+ \ll \mathcal{T}_R^-$ while keeping $\mathcal{T}_L^+ \gtrsim \mathcal{T}_R^-$ such as the parameters will still place the system in the power-generating quadrant in Fig.K.1.

In Fig.K.3, we present the steady-state solution in the case of a system powered by a temperature difference such as $\mathcal{T}_L^- = \mathcal{T}_L^+$ while $\mathcal{T}_R^- = 10\mathcal{T}_R^+$ which codes for an infinite temperature on the left side and a temperature of $k_B T_R = \mu \ln 9$ on the right side.

K.4 Power-dissipating regime

When all reservoirs are at thermal and chemical equilibrium, the steady-state of the engine is dissipative in accordance with the second law of thermodynamics.

In Fig.K.4, we show that when $\mathcal{T}_L^- \leq \mathcal{T}_L^+, \mathcal{T}_R^- \leq \mathcal{T}_R^+$ and $\Lambda^+ \leq \Lambda^-$, the engine remains passive, meaning that $\Delta E = -\langle C \rangle < 0$.

K.5 Discussion

It is important to note that the color plots presented in Fig. K.1-K.4 display the inter-dot coupling energy $-\langle C \rangle$ in the steady-state $\overline{\rho}$, so after full thermalization of the system, and not the state after a duration $\tau = 4$ ps that was calculated for the previous case with measurements only and no direct tunneling. The appreciable positive value of $-\langle C \rangle$ in this case thus reveals that this non-equilibrium steady-state is sufficient to obtain a continuous power output of the device, even without the help of the frequent measurements. Nonetheless, it would only lead to a power output much lower than with the help of the measurement which has the effect of accelerating the tunneling process by forcing the system to release the internal energy it gathers during the thermalization stroke. The non-thermal behavior of the cycle is therefore greatly increasing the ability of the device to harvest energy from the baths.

In this section, we have argued that a non-thermal feature of the baths was necessary in order

to obtain a power-generating cycle, which seems to be in slight disagreement with the previous case where we have showed that quantum measurements alone were sufficient to harvest energy through the vacuum, without any non-thermal assumption about the baths. The conflict can be resolved when we notice again that Fig. K.1-K.4 considered the general steady-state of the master equation, and not the state after some time $\tau \ll \tau_{th}$ where τ_{th} is the thermalization time. It would thus be possible to extract energy in a situation where the baths are in a passive configuration by harvesting the resource of the measurement thanks to a partial thermalization of the system that would favor a system in a higher energy than its projection at a time τ. Although this is possible, simulations not shown have revealed that without an additional resource from the baths, the power output was similar than in the case with measurements alone through the vacuum, such that it cannot explain the results of the experiments. In addition, the bosonic bath is leading to a much faster thermalization of the system, which thus requires a higher and more stable frequency of measurements that could be harder to observe in this material.

We have shown that a slight deviation of the coupling coefficients to the baths $\mathcal{T}$ and Λ from the thermal and chemical equilibrium situation can be sufficient for this system to act as a powerful generator. Since these coefficients ultimately depend on the populations of the energy levels of the baths and their correlation function, the issue comes down to finding the resources that allow the baths to stay out of strict thermal equilibrium. Building upon the work on generalized thermodynamics [361, 362], it would seem that this non-thermal filling could originate from a conserved quantity such as the magnetization of the ferromagnetic electrodes, rather than from a thermal of electrochemical potential bias. Future studies will explore this lead in order to find the minimal autonomous resources that can power this device.

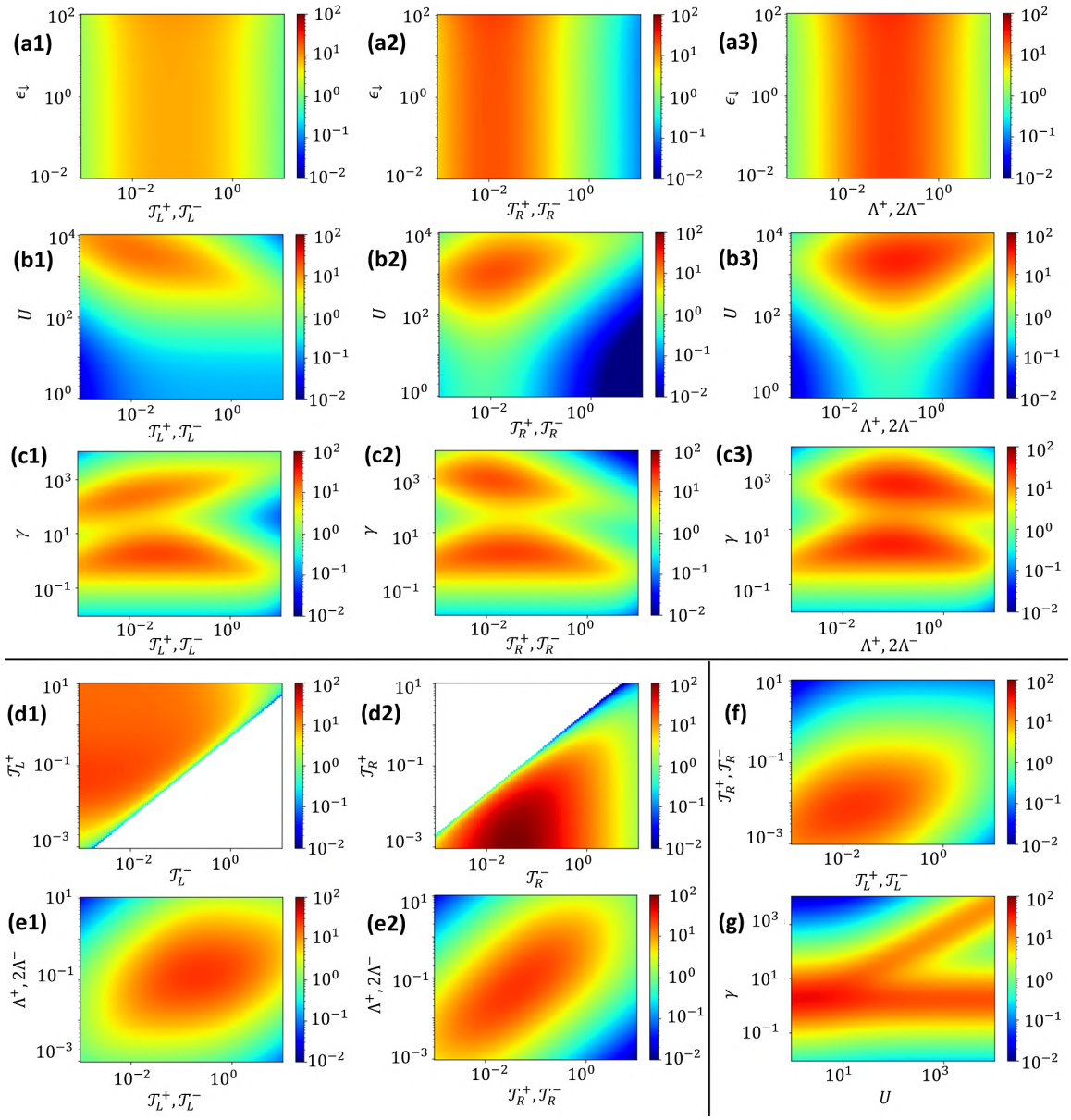

Figure K.1: **Color plots of the coherence energy with a bosonic pump.** Color plots of the coherence energy $-\langle C \rangle$ calculated for the steady-state $\overline{\rho}$ as a function of various pairs of parameters. For all figures, the fixed parameters are set to $\epsilon_\downarrow = 8$, $\epsilon_\uparrow = -3$, $\epsilon_R = 1$, $J = 8$, $U = 1000$, $\gamma = 1000$, $\mathcal{T}_L^- = 0.1$, $\mathcal{T}_L^+ = 0.1$, $\mathcal{T}_R^- = 0.1$, $\mathcal{T}_R^+ = 0.1$, $\Lambda^+ = 0.02$, $\Lambda^- = 0.01$.

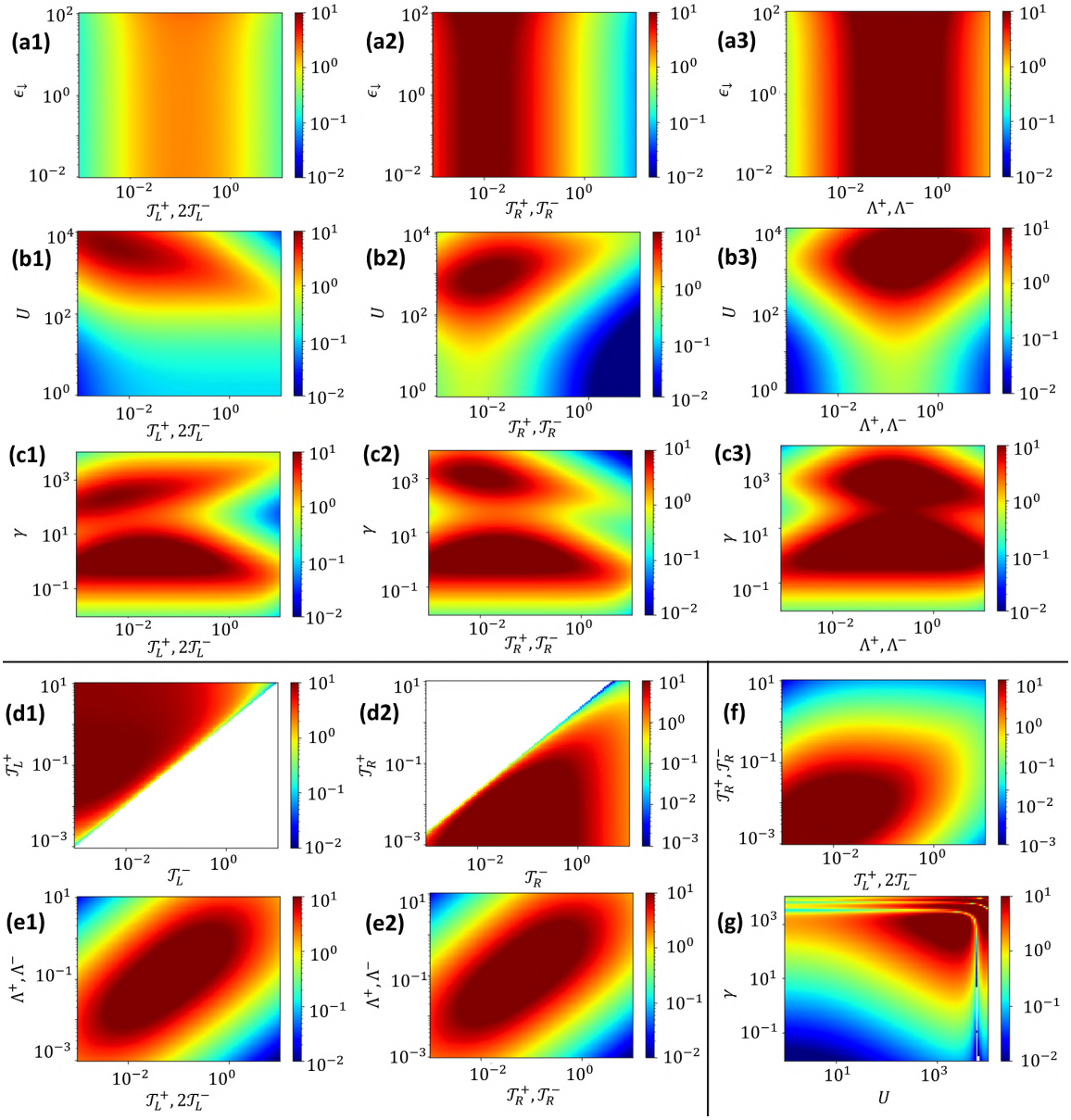

Figure K.2: **Color plots of the coherence energy with a chemical or spin bias.** Color plots of the coherence energy $-\langle C \rangle$ calculated for the steady-state $\overline{\rho}$ as a function of various pairs of parameters. For all figures, the fixed parameters are set to $\epsilon_\downarrow = 8,\ \epsilon_\uparrow = -3,\ \epsilon_R = 1,\ J = 8,\ U = 1000,\ \gamma = 1000,\ \mathcal{T}_L^- = 0.1,\ \mathcal{T}_L^+ = 0.2,\ \mathcal{T}_R^- = 0.1,\ \mathcal{T}_R^+ = 0.1,\ \Lambda^+ = 0.01,\ \Lambda^- = 0.0101$.

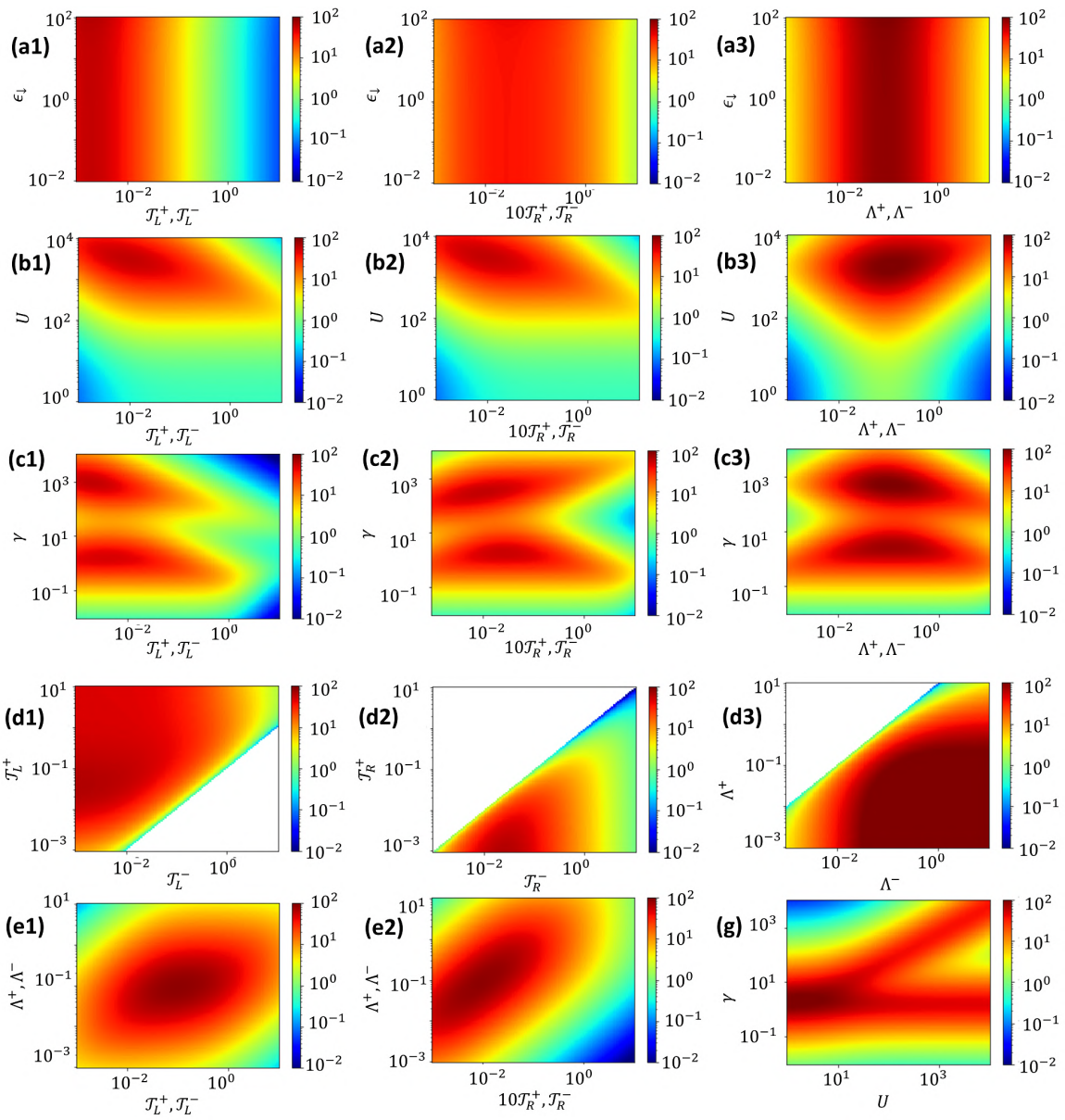

Figure K.3: **Color plots of the coherence energy with a thermal gradient.** Color plots of the coherence energy $-\langle C \rangle$ calculated for the steady-state $\overline{\rho}$ as a function of various pairs of parameters. For all figures, the fixed parameters are set to $\epsilon_\downarrow = 8,\ \epsilon_\uparrow = -3,\ \epsilon_R = 1,\ J = 8,\ U = 1000,\ \gamma = 1000,\ \mathcal{T}_L^- = 0.1,\ \mathcal{T}_L^+ = 0.1,\ \mathcal{T}_R^- = 0.1,\ \mathcal{T}_R^+ = 0.01,\ \Lambda^+ = 0.01,\ \Lambda^- = 0.0101$.

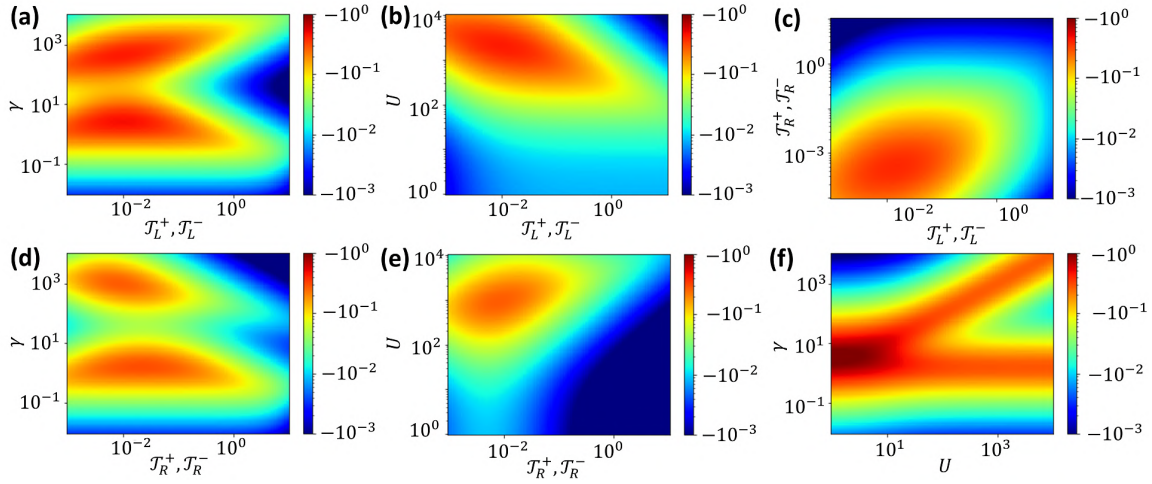

Figure K.4: **Color plots of the coherence energy for a passive device.** Color plots of the coherence energy $-\langle C \rangle$ calculated for the steady-state $\overline{\rho}$ as a function of various pairs of parameters. For all figures, the fixed parameters are set to $\epsilon_\downarrow = 8$, $\epsilon_\uparrow = -3$, $\epsilon_R = 1$, $J = 8$, $U = 1000$, $\gamma = 1000$, $\mathcal{T}_L^- = 0.1$, $\mathcal{T}_L^+ = 0.1$, $\mathcal{T}_R^- = 0.01$, $\mathcal{T}_R^+ = 0.01$, $\Lambda^+ = 0.01$, $\Lambda^- = 0.0101$.

Appendix L

Derivation of the Fokker-Planck equation

The objective is to derive a continuous formulation of the rate equation Eq. 10.3 presented in chapter 10:

$$\begin{aligned}\frac{\mathrm{d}p_n^m}{\mathrm{d}t} = &-w_\uparrow p_{n-1}^{m-1} - w_\downarrow p_{n-1}^{m+1} + w_\uparrow p_{n+1}^{m+1} + w_\downarrow p_{n+1}^{m-1} \\ &+ p_{n-1}^{m-1} W_{n-1,n}^{m-1,m} + p_{n-1}^{m+1} W_{n-1,n}^{m+1,m} + p_{n+1}^{m+1} W_{n+1,n}^{m+1,m} + p_{n+1}^{m-1} W_{n+1,n}^{m+1,m} \\ &- p_n^m \Big(W_{n,n-1}^{m,m-1} + W_{n,n-1}^{m,m+1} + W_{n,n+1}^{m,m+1} + W_{n,n+1}^{m,m-1} \Big). \end{aligned} \tag{L.1}$$

We set $q = n\xi$, $s = m\zeta$ and we define $X \equiv (\xi, \zeta)$, $\overline{X} \equiv (\xi, -\zeta)$. Expanding all terms up to the second order in X, we have

$$p_{n-1}^{m-1} W_{n-1,n}^{m-1,m} = p(q-\xi, s-\zeta) W_\uparrow(q,s) = pW_\uparrow - W_\uparrow \nabla p \cdot X + \frac{W_\uparrow}{2} X \cdot H_p X + o(X^2),$$

$$p_{n-1}^{m+1} W_{n-1,n}^{m+1,m} = p(q-\xi, s+\zeta) W_\downarrow(q,s) = pW_\downarrow - W_\uparrow \nabla p \cdot \overline{X} + \frac{W_\uparrow}{2} \overline{X} \cdot H_p \overline{X} + o(X^2),$$

$$\begin{aligned} p_{n+1}^{m+1} W_{n+1,n}^{m+1,m} &= p(q+\xi, s+\zeta) W_\uparrow(q+\xi, s+\zeta) \exp\Big(\epsilon(q+\xi, s+\zeta) - \epsilon(q,s)\Big) \\ &= pW_\uparrow + \Big(W_\uparrow \nabla p \cdot X + p \nabla W_\uparrow \cdot X + pW_\uparrow \nabla \epsilon \cdot X \Big) + \Big(\frac{pW_\uparrow}{2} X \cdot H_\epsilon X \\ &\quad + \frac{pW_\uparrow}{2} (\nabla \epsilon \cdot X)^2 + \frac{p}{2} X \cdot H_{W_\uparrow} X + \frac{W_\uparrow}{2} X \cdot H_p X + W_\uparrow (\nabla p \cdot X)(\nabla \epsilon \cdot X) \\ &\quad + p(\nabla W_\uparrow \cdot X)(\nabla \epsilon \cdot X) + (\nabla p \cdot X)(\nabla W_\uparrow \cdot X) \Big) + o(X^2), \end{aligned}$$

$$
\begin{aligned}
p_{n+1}^{m-1} W_{n+1,n}^{m-1,m} &= p(q+\xi, s-\zeta) W_{\downarrow}(q+\xi, s-\zeta) \exp\Big(\epsilon(q+\xi, s-\zeta) - \epsilon(q,s)\Big) \\
&= pW_{\downarrow} + \Big(W_{\downarrow}\nabla p \cdot \overline{X} + p\nabla W_{\downarrow} \cdot \overline{X} + pW_{\downarrow}\nabla\epsilon \cdot \overline{X}\Big) + \Big(\frac{pW_{\downarrow}}{2}\overline{X} \cdot H_{\epsilon}\overline{X} + \\
&\quad \frac{pW_{\downarrow}}{2}(\nabla\epsilon \cdot \overline{X})^2 + \frac{p}{2}\overline{X} \cdot H_{W_{\downarrow}}\overline{X} + \frac{W_{\uparrow}}{2}\overline{X} \cdot H_p\overline{X} + W_{\downarrow}(\nabla p \cdot \overline{X})(\nabla\epsilon \cdot \overline{X}) \\
&\quad + p(\nabla W_{\downarrow} \cdot \overline{X})(\nabla\epsilon \cdot \overline{X}) + (\nabla p \cdot \overline{X})(\nabla W_{\downarrow} \cdot \overline{X})\Big) + o(X^2),
\end{aligned}
$$

$$
\begin{aligned}
-p_n^m W_{n,n-1}^{m,m-1} &= -p(q,s) W_{\uparrow}(q,s) \exp\Big(\epsilon(q,s) - \epsilon(q-\xi, s-\zeta)\Big) \\
&= -pW_{\uparrow} - pW_{\uparrow}\nabla\epsilon \cdot X + \frac{pW_{\uparrow}}{2} X \cdot H_{\epsilon} X - \frac{pW_{\uparrow}}{2}(\nabla\epsilon \cdot X)^2 + o(X^2),
\end{aligned}
$$

$$
\begin{aligned}
-p_n^m W_{n,n-1}^{m,m+1} &= -p(q,s) W_{\uparrow}(q,s) \exp\Big(\epsilon(q,s) - \epsilon(q-\xi, s+\zeta)\Big) \\
&= -pW_{\downarrow} - pW_{\downarrow}\nabla\epsilon \cdot \overline{X} + \frac{pW_{\downarrow}}{2}\overline{X} \cdot H_{\epsilon}\overline{X} - \frac{pW_{\downarrow}}{2}(\nabla\epsilon \cdot \overline{X})^2 + o(X^2),
\end{aligned}
$$

$$
-p_n^m W_{n,n+1}^{m,m+1} = -p(q,s) W_{\uparrow}(q+\xi, s+\zeta) = -pW_{\uparrow} - p\nabla W_{\uparrow} \cdot X - \frac{p}{2} X \cdot H_{W_{\uparrow}} X + o(X^2),
$$

$$
-p_n^m W_{n,n+1}^{m,m-1} = -p(q,s) W_{\downarrow}(q+\xi, s-\zeta) = -pW_{\downarrow} - p\nabla W_{\downarrow} \cdot X - \frac{p}{2}\overline{X} \cdot H_{W_{\downarrow}}\overline{X} + o(X^2),
$$

$$
w_{\uparrow}\Big(p_{n+1}^{m+1} - p_{n-1}^{m-1}\Big) = w_{\uparrow}\Big(p(q+\xi, s+\zeta) - p(q-\xi, s-\zeta)\Big) = 2w_{\uparrow} X \cdot \nabla p + o(X^2),
$$

$$
w_{\downarrow}\Big(p_{n+1}^{m-1} - p_{n-1}^{m+1}\Big) = w_{\uparrow}\Big(p(q+\xi, s-\zeta) - p(q-\xi, s+\zeta)\Big) = 2w_{\downarrow}\overline{X} \cdot \nabla p + o(X^2).
$$

Gathering all this, we thus obtain:

$$
\begin{aligned}
\partial_t p = p(\nabla W_{\uparrow}\cdot X)(\nabla\epsilon\cdot X) + W_{\uparrow}(\nabla\epsilon\cdot X)(\nabla p\cdot X) + (\nabla W_{\uparrow}\cdot X)(\nabla p\cdot X) + pW_{\uparrow} X\cdot H_{\epsilon} X + W_{\uparrow} X\cdot H_p X \\
+ p(\nabla W_{\downarrow}\cdot\overline{X})(\nabla\epsilon\cdot\overline{X}) + W_{\downarrow}(\nabla\epsilon\cdot\overline{X})(\nabla p\cdot\overline{X}) + (\nabla W_{\downarrow}\cdot\overline{X})(\nabla p\cdot\overline{X}) + pW_{\downarrow}\overline{X}\cdot H_{\epsilon}\overline{X} + W_{\downarrow}\overline{X}\cdot H_p\overline{X} \\
+ 2w_{\uparrow} X\cdot\nabla p + 2w_{\downarrow}\overline{X}\cdot\nabla p + o(X^2). \quad \text{(L.2)}
\end{aligned}
$$

And finally, using the properties of the gradient operator, we end up with the equation:

$$
\partial_t p = \nabla\Big[W_{\uparrow}\big(p\nabla\epsilon + \nabla p\big)\cdot X\Big]\cdot X + \nabla\Big[W_{\downarrow}\big(p\nabla\epsilon + \nabla p\big)\cdot\overline{X}\Big]\cdot\overline{X} + 2w_{\uparrow} X\cdot\nabla p + 2w_{\downarrow}\overline{X}\cdot\nabla p \quad \text{(L.3)}
$$

Bibliographie

[1] Guangsai Yang et al. “The role of spin in thermoelectricity”. In: *Nature Reviews Physics* 5.8 (July 2023), pp. 466–482. ISSN: 2522-5820. DOI: 10.1038/s42254-023-00604-0. URL: http://dx.doi.org/10.1038/s42254-023-00604-0.

[2] Inseon Oh et al. “A scalable molecule-based magnetic thin film for spin-thermoelectric energy conversion”. In: *Nature Communications* 12.1 (Feb. 2021). ISSN: 2041-1723. DOI: 10.1038/s41467-021-21058-x. URL: http://dx.doi.org/10.1038/s41467-021-21058-x.

[3] Sa Tu et al. “Record thermopower found in an IrMn-based spintronic stack”. In: *Nature Communications* 11.1 (Apr. 2020). ISSN: 2041-1723. DOI: 10.1038/s41467-020-15797-6. URL: http://dx.doi.org/10.1038/s41467-020-15797-6.

[4] Jorge Puebla et al. “Spintronic devices for energy-efficient data storage and energy harvesting”. In: *Communications Materials* 1.1 (May 2020). ISSN: 2662-4443. DOI: 10.1038/s43246-020-0022-5. URL: http://dx.doi.org/10.1038/s43246-020-0022-5.

[5] Raghav Sharma et al. “Electrically connected spin-torque oscillators array for 2.4 GHz WiFi band transmission and energy harvesting”. In: *Nature Communications* 12.1 (May 2021). ISSN: 2041-1723. DOI: 10.1038/s41467-021-23181-1. URL: http://dx.doi.org/10.1038/s41467-021-23181-1.

[6] Like Zhang et al. “Ultrahigh detection sensitivity exceeding 105 V/W in spin-torque diode”. In: *Applied Physics Letters* 113.10 (Sept. 2018). ISSN: 1077-3118. DOI: 10.1063/1.5047547. URL: http://dx.doi.org/10.1063/1.5047547.

[7] Dalton Jones et al. “Energy storage in magnetic textures driven by vorticity flow”. In: *Physical Review B* 102.14 (Oct. 2020). 2023-12-13, p. 140411. ISSN: 2469-9950, 2469-9969. DOI: 10.1103/PhysRevB.102.140411. URL: https://link.aps.org/doi/10.1103/PhysRevB.102.140411.

[8] Junji Fujimoto et al. “Spin–charge conversion and current vortex in spin–orbit coupled systems”. In: *APL Materials* 9.6 (June 2021). 2023-11-22, p. 060904. ISSN: 2166-532X. DOI: 10.1063/5.0049882. URL: https://pubs.aip.org/apm/article/9/6/060904/1061729/Spin-charge-conversion-and-current-vortex-in-spin.

[9] Gerrit E. W. Bauer et al. “Nanoscale magnetic heat pumps and engines”. In: *Physical Review B* 81.2 (Jan. 2010). 2023-12-14, p. 024427. ISSN: 1098-0121, 1550-235X. DOI: 10.1103/PhysRevB.81.024427. URL: https://link.aps.org/doi/10.1103/PhysRevB.81.024427.

[10] Sourav Bhattacharjee and Amit Dutta. “Quantum thermal machines and batteries”. en. In: *The European Physical Journal B* 94.12 (Dec. 2021). Number: 12. ISSN: 1434-6028, 1434-6036. DOI: 10.1140/epjb/s10051-021-00235-3. URL: https://link.springer.com/10.1140/epjb/s10051-021-00235-3.

[11] Asli Tuncer and Özgür E Müstecaplioğlu. “Quantum Thermodynamics and Quantum Coherence Engines”. In: *Turkish Journal of Physics* 44.5 (Oct. 2020). ISSN: 1303-6122. DOI: 10.3906/fiz-2009-12. URL: http://dx.doi.org/10.3906/fiz-2009-12.

[12] Yun-Hao Shi et al. “Quantum coherence in a quantum heat engine”. In: *Journal of Physics A-Mathematical and Theoretical* 53.8 (Feb. 2020). ISSN: 1751-8113. DOI: 10.1088/1751-8121/ab6a6b.

[13] G. Francica et al. “Quantum Coherence and Ergotropy”. en. In: *Physical Review Letters* 125.18 (Oct. 2020). Number: 18. ISSN: 0031-9007, 1079-7114. DOI: 10.1103/PhysRevLett.125.180603. URL: https://link.aps.org/doi/10.1103/PhysRevLett.125.180603.

[14] Cyril Elouard and Andrew N. Jordan. “Efficient Quantum Measurement Engines”. en. In: *Physical Review Letters* 120.26 (June 2018). Number: 26. ISSN: 0031-9007, 1079-7114. DOI: 10.1103/PhysRevLett.120.260601. URL: https://link.aps.org/doi/10.1103/PhysRevLett.120.260601.

[15] Cyril Elouard et al. “Extracting Work from Quantum Measurement in Maxwell’s Demon Engines”. en. In: *Physical Review Letters* 118.26 (June 2017). Number: 26. ISSN: 0031-9007, 1079-7114. DOI: 10.1103/PhysRevLett.118.260603. URL: http://link.aps.org/doi/10.1103/PhysRevLett.118.260603.

[16] Maron F. Anka, Thiago R. de Oliveira, and Daniel Jonathan. “Measurement-based quantum heat engine in a multilevel system”. In: *Physical Review E* 104.5 (Nov. 2021). Number: 5. ISSN: 2470-0045, 2470-0053. DOI: 10.1103/PhysRevE.104.054128. URL: https://link.aps.org/doi/10.1103/PhysRevE.104.054128.

[17] Alexia Auffèves. “Quantum Technologies Need a Quantum Energy Initiative”. en. In: *PRX Quantum* 3.2 (June 2022). Number: 2. ISSN: 2691-3399. DOI: 10.1103/PRXQuantum.3.020101. URL: https://link.aps.org/doi/10.1103/PRXQuantum.3.020101.

[18] K. Katcko et al. “Spin-driven electrical power generation at room temperature”. In: *Communications Physics* 2.1 (Dec. 2019). 2021-04-09. ISSN: 2399-3650. DOI: 10.1038/s42005-019-0207-8. URL: http://www.nature.com/articles/s42005-019-0207-8.

[19] Bhavishya Chowrira et al. “Quantum Advantage in a Molecular Spintronic Engine that Harvests Thermal Fluctuation Energy”. en. In: *Advanced Materials* 34.49 (Dec. 2022). Number: 49, p. 2206688. ISSN: 0935-9648, 1521-4095. DOI: 10.1002/adma.202206688. URL: https://onlinelibrary.wiley.com/doi/10.1002/adma.202206688.

[20] M. N. Baibich et al. “Giant Magnetoresistance of (001)Fe/(001)Cr Magnetic Superlattices”. In: *Physical Review Letters* 61.21 (Nov. 1988), pp. 2472–2475. ISSN: 0031-9007. DOI: 10.1103/physrevlett.61.2472. URL: http://dx.doi.org/10.1103/PhysRevLett.61.2472.

[21] G. Binasch et al. “Enhanced magnetoresistance in layered magnetic structures with antiferromagnetic interlayer exchange”. In: *Physical Review B* 39.7 (Mar. 1989), pp. 4828–4830. ISSN: 0163-1829. DOI: 10.1103/physrevb.39.4828. URL: http://dx.doi.org/10.1103/PhysRevB.39.4828.

[22] Albert Fert. “Origin, Development, and Future of Spintronics (Nobel Lecture)”. In: *Angewandte Chemie International Edition* 47.32 (July 2008), pp. 5956–5967. ISSN: 1521-3773. DOI: 10.1002/anie.200801093. URL: http://dx.doi.org/10.1002/anie.200801093.

[23] Evgeny Y Tsymbal, Oleg N Mryasov, and Patrick R LeClair. “Spin-dependent tunnelling in magnetic tunnel junctions”. In: *Journal of Physics: Condensed Matter* 15.4 (Jan. 2003), R109–R142. ISSN: 0953-8984. DOI: 10.1088/0953-8984/15/4/201. URL: http://dx.doi.org/10.1088/0953-8984/15/4/201.

[24] J. M. MacLaren, X.-G. Zhang, and W. H. Butler. “Validity of the Julliere model of spin-dependent tunneling”. In: *Physical Review B* 56.18 (Nov. 1997), pp. 11827–11832. ISSN: 1095-3795. DOI: 10.1103/physrevb.56.11827. URL: http://dx.doi.org/10.1103/PhysRevB.56.11827.

[25] Yu Ji, Jie Liu, and Chunsheng Yang. “Novel modeling and dynamic simulation of magnetic tunnel junctions for spintronic sensor development”. en. In: *Journal of Physics D: Applied Physics* 50.2 (Jan. 2017). Number: 2, p. 025005. ISSN: 0022-3727, 1361-6463. DOI: 10.1088/1361-6463/50/2/025005. URL: https://iopscience.iop.org/article/10.1088/1361-6463/50/2/025005.

[26] J. C. Slonczewski. “Conductance and exchange coupling of two ferromagnets separated by a tunneling barrier”. In: *Physical Review B* 39.10 (Apr. 1989), pp. 6995–7002. ISSN: 0163-1829. DOI: 10.1103/physrevb.39.6995. URL: http://dx.doi.org/10.1103/PhysRevB.39.6995.

[27] Yunong Qi, D. Y. Xing, and Jinming Dong. “Relation between Julliere and Slonczewski models of tunneling magnetoresistance”. In: *Physical Review B* 58.5 (Aug. 1998), pp. 2783–2787. ISSN: 1095-3795. DOI: 10.1103/physrevb.58.2783. URL: http://dx.doi.org/10.1103/PhysRevB.58.2783.

[28] J. S. Moodera et al. “Large Magnetoresistance at Room Temperature in Ferromagnetic Thin Film Tunnel Junctions”. In: *Physical Review Letters* 74.16 (Apr. 1995), pp. 3273–3276. ISSN: 1079-7114. DOI: 10.1103/physrevlett.74.3273. URL: http://dx.doi.org/10.1103/PhysRevLett.74.3273.

[29] T. Miyazaki and N. Tezuka. “Giant magnetic tunneling effect in Fe/Al2O3/Fe junction”. In: *Journal of Magnetism and Magnetic Materials* 139.3 (Jan. 1995), pp. L231–L234. ISSN: 0304-8853. DOI: 10.1016/0304-8853(95)90001-2. URL: http://dx.doi.org/10.1016/0304-8853(95)90001-2.

[30] W. H. Butler et al. “Spin-dependent tunneling conductance of Fe | MgO | Fe sandwiches”. en. In: *Physical Review B* 63.5 (Jan. 2001). Number: 5. ISSN: 0163-1829, 1095-3795. DOI: 10.1103/PhysRevB.63.054416. URL: https://link.aps.org/doi/10.1103/PhysRevB.63.054416.

[31] J. Mathon and A. Umerski. “Theory of tunneling magnetoresistance of an epitaxial Fe/MgO/Fe(001) junction”. In: *Physical Review B* 63.22 (May 2001). ISSN: 1095-3795. DOI: 10.1103/physrevb.63.220403. URL: http://dx.doi.org/10.1103/PhysRevB.63.220403.

[32] S. Ikeda et al. “Tunnel magnetoresistance of 604% at 300K by suppression of Ta diffusion in CoFeB/MgO/CoFeB pseudo-spin-valves annealed at high temperature”. en. In: *Applied Physics Letters* 93.8 (Aug. 2008). Number: 8, p. 082508. ISSN: 0003-6951, 1077-3118. DOI: 10.1063/1.2976435. URL: http://aip.scitation.org/doi/10.1063/1.2976435.

[33] Sai Li et al. “Experimental demonstration of skyrmionic magnetic tunnel junction at room temperature”. In: *Science Bulletin* 67.7 (Apr. 2022), pp. 691–699. ISSN: 2095-9273. DOI: 10.1016/j.scib.2022.01.016. URL: http://dx.doi.org/10.1016/j.scib.2022.01.016.

[34] Jian-Gang (Jimmy) Zhu and Chando Park. “Magnetic tunnel junctions”. In: *Materials Today* 9.11 (Nov. 2006), pp. 36–45. ISSN: 1369-7021. DOI: 10.1016/s1369-7021(06)71693-5. URL: http://dx.doi.org/10.1016/S1369-7021(06)71693-5.

[35] Oliver Schebaum et al. “Tunnel magnetoresistance in alumina, magnesia and composite tunnel barrier magnetic tunnel junctions”. In: *Journal of Magnetism and Magnetic Materials* 323.11 (June 2011), pp. 1525–1528. ISSN: 0304-8853. DOI: 10.1016/j.jmmm.2011.01.011. URL: http://dx.doi.org/10.1016/j.jmmm.2011.01.011.

[36] Bradley Parks et al. “Superparamagnetic perpendicular magnetic tunnel junctions for true random number generators”. In: *AIP Advances* 8.5 (Dec. 2017). ISSN: 2158-3226. DOI: 10.1063/1.5006422. URL: http://dx.doi.org/10.1063/1.5006422.

[37] Nilson Maciel et al. “Magnetic Tunnel Junction Applications”. In: *Sensors* 20.1 (Dec. 2019), p. 121. ISSN: 1424-8220. DOI: 10.3390/s20010121. URL: http://dx.doi.org/10.3390/s20010121.

[38] S.Z. Peng et al. *Magnetic Tunnel Junctions for Spintronics: Principles and Applications*. Dec. 2014. DOI: 10.1002/047134608x.w8231. URL: http://dx.doi.org/10.1002/047134608X.W8231.

[39] Viola Krizakova et al. “Tailoring the Switching Efficiency of Magnetic Tunnel Junctions by the Fieldlike Spin-Orbit Torque”. In: *Physical Review Applied* 18.4 (Oct. 2022). ISSN: 2331-7019. DOI: 10.1103/physrevapplied.18.044070. URL: http://dx.doi.org/10.1103/PhysRevApplied.18.044070.

[40] Viola Krizakova et al. “Spin-orbit torque switching of magnetic tunnel junctions for memory applications”. In: *Journal of Magnetism and Magnetic Materials* 562 (Nov. 2022), p. 169692. ISSN: 0304-8853. DOI: 10.1016/j.jmmm.2022.169692. URL: http://dx.doi.org/10.1016/j.jmmm.2022.169692.

[41] Eva Grimaldi et al. “Single-shot dynamics of spin–orbit torque and spin transfer torque switching in three-terminal magnetic tunnel junctions”. In: *Nature Nanotechnology* 15.2 (Jan. 2020), pp. 111–117. ISSN: 1748-3395. DOI: 10.1038/s41565-019-0607-7. URL: http://dx.doi.org/10.1038/s41565-019-0607-7.

[42] Murat Cubukcu et al. “Ultra-Fast Perpendicular Spin–Orbit Torque MRAM”. In: *IEEE Transactions on Magnetics* 54.4 (Apr. 2018), pp. 1–4. ISSN: 1941-0069. DOI: 10.1109/tmag.2017.2772185. URL: http://dx.doi.org/10.1109/TMAG.2017.2772185.

[43] A. Mizrahi et al. *Controlling the phase locking of unstable magnetic bits for ultra-low power computation*. 2016. arXiv: 1605.06932 [cond-mat.mtrl-sci].

[44] K. Watanabe et al. “Shape anisotropy revisited in single-digit nanometer magnetic tunnel junctions”. In: *Nature Communications* 9.1 (Feb. 2018). ISSN: 2041-1723. DOI: 10.1038/s41467-018-03003-7. URL: http://dx.doi.org/10.1038/s41467-018-03003-7.

[45] Kwang-Seok Kim, B.K. Cho, and T.W. Kim. “Switching and reliability issues of magnetic tunnel junctions for high-density memory device”. In: *Current Applied Physics* 6 (Aug. 2006), e86–e91. ISSN: 1567-1739. DOI: 10.1016/j.cap.2006.01.018. URL: http://dx.doi.org/10.1016/j.cap.2006.01.018.

[46] Andrés Conca Parra et al. “Microstructure Design for Fast Lifetime Measurements of Magnetic Tunneling Junctions”. In: *Sensors* 19.3 (Jan. 2019), p. 583. ISSN: 1424-8220. DOI: 10.3390/s19030583. URL: http://dx.doi.org/10.3390/s19030583.

[47] C.M. Choi et al. “Reliability of magnetic tunnel junctions with a spinel MgAl2O4 film”. In: *Electronics Letters* 53.2 (Jan. 2017), pp. 119–121. ISSN: 1350-911X. DOI: 10.1049/el.2016.3007. URL: http://dx.doi.org/10.1049/el.2016.3007.

[48] Lishu Zhang et al. “Recent progress and challenges in magnetic tunnel junctions with 2D materials for spintronic applications”. In: *Applied Physics Reviews* 8.2 (Apr. 2021). ISSN: 1931-9401. DOI: 10.1063/5.0032538. URL: http://dx.doi.org/10.1063/5.0032538.

[49] T. Valet and A. Fert. “Theory of the perpendicular magnetoresistance in magnetic multilayers”. In: *Physical Review B* 48.10 (Sept. 1993). 2023-11-27, pp. 7099–7113. ISSN: 0163-1829, 1095-3795. DOI: 10.1103/PhysRevB.48.7099. URL: https://link.aps.org/doi/10.1103/PhysRevB.48.7099.

[50] A. Barthélémy et al. “Magnetoresistance and spin electronics”. In: *Journal of Magnetism and Magnetic Materials* 242–245 (Apr. 2002), pp. 68–76. ISSN: 0304-8853. DOI: 10.1016/s0304-8853(01)01193-3. URL: http://dx.doi.org/10.1016/S0304-8853(01)01193-3.

[51] Byung Chan Lee. “Spin Current in Magnetic Tunnel Junctions”. In: *Journal of the Korean Physical Society* 58.4 (Apr. 2011), pp. 855–858. ISSN: 0374-4884. DOI: 10.3938/jkps.58.855. URL: http://dx.doi.org/10.3938/jkps.58.855.

[52] L. Sheng, D. Y. Xing, and D. N. Sheng. “Theory of the zero-bias anomaly in magnetic tunnel junctions: Inelastic tunneling via impurities”. In: *Physical Review B* 70.9 (Sept. 2004). ISSN: 1550-235X. DOI: 10.1103/physrevb.70.094416. URL: http://dx.doi.org/10.1103/PhysRevB.70.094416.

[53] J. C. Slonczewski. “Currents, torques, and polarization factors in magnetic tunnel junctions”. In: *Physical Review B* 71.2 (Jan. 2005). ISSN: 1550-235X. DOI: 10.1103/physrevb.71.024411. URL: http://dx.doi.org/10.1103/PhysRevB.71.024411.

[54] M Bowen et al. “Half-metallicity proven using fully spin-polarized tunnelling”. In: *Journal of Physics: Condensed Matter* 17.41 (Sept. 2005), pp. L407–L409. ISSN: 1361-648X. DOI: 10.1088/0953-8984/17/41/l02. URL: http://dx.doi.org/10.1088/0953-8984/17/41/L02.

[55] Y. Miura. “First-Principles Studies on Spin-Dependent Transport of Magnetic Junctions with Half-Metallic Heusler Compounds”. In: *Journal of the Magnetics Society of Japan* 47.4 (July 2023), pp. 90–102. ISSN: 1882-2932. DOI: 10.3379/msjmag.2307r005. URL: http://dx.doi.org/10.3379/msjmag.2307R005.

[56] Julian P. Velev et al. “Magnetic Tunnel Junctions with Ferroelectric Barriers: Prediction of Four Resistance States from First Principles”. In: *Nano Letters* 9.1 (Jan. 2009), pp. 427–432. ISSN: 1530-6992. DOI: 10.1021/nl803318d. URL: http://dx.doi.org/10.1021/nl803318d.

[57] Derek Waldron, Lei Liu, and Hong Guo. “Ab initio simulation of magnetic tunnel junctions”. In: *Nanotechnology* 18.42 (Sept. 2007), p. 424026. ISSN: 1361-6528. DOI: 10.1088/0957-4484/18/42/424026. URL: http://dx.doi.org/10.1088/0957-4484/18/42/424026.

[58] H. Itoh and J. Inoue. “Theory of Tunnel Magnetoresistance”. In: *Journal of the Magnetics Society of Japan* 30.1 (2006), pp. 1–37. ISSN: 1880-4004. DOI: 10.3379/jmsjmag.30.1. URL: http://dx.doi.org/10.3379/JMSJMAG.30.1.

[59] Atsufumi Hirohata et al. “Review on spintronics: Principles and device applications”. In: *Journal of Magnetism and Magnetic Materials* 509 (2020), p. 166711.

[60] Jonathan Z. Sun. “Spin-transfer torque switched magnetic tunnel junction for memory technologies”. In: *Journal of Magnetism and Magnetic Materials* 559 (Oct. 2022), p. 169479. ISSN: 0304-8853. DOI: 10.1016/j.jmmm.2022.169479. URL: http://dx.doi.org/10.1016/j.jmmm.2022.169479.

[61] Zhongrui Wang et al. “Resistive switching materials for information processing”. In: *Nature Reviews Materials* 5.3 (Jan. 2020), pp. 173–195. ISSN: 2058-8437. DOI: 10.1038/s41578-019-0159-3. URL: http://dx.doi.org/10.1038/s41578-019-0159-3.

[62] Akihito Sawa. “Resistive switching in transition metal oxides”. en. In: *Materials Today* 11.6 (June 2008). Number: 6, pp. 28–36. ISSN: 13697021. DOI: 10.1016/S1369-7021(08)70119-6. URL: https://linkinghub.elsevier.com/retrieve/pii/S1369702108701196.

[63] Sense Jan van der Molen and Peter Liljeroth. “Charge transport through molecular switches”. en. In: *Journal of Physics: Condensed Matter* 22.13 (Apr. 2010). Number: 13, p. 133001. ISSN: 0953-8984, 1361-648X. DOI: 10.1088/0953-8984/22/13/133001. URL: https://iopscience.iop.org/article/10.1088/0953-8984/22/13/133001.

[64] Emanuel Lörtscher et al. “Reversible and Controllable Switching of a Single-Molecule Junction”. In: 2.8-9 (Aug. 2006), pp. 973–977. DOI: 10.1002/smll.200600101. URL: https://doi.org/10.1002/smll.200600101.

[65] Eike Linn et al. “Complementary resistive switches for passive nanocrossbar memories”. en. In: *Nature Materials* 9.5 (May 2010). Number: 5, pp. 403–406. ISSN: 1476-1122, 1476-4660. DOI: 10.1038/nmat2748. URL: https://www.nature.com/articles/nmat2748.

[66] Yingmei Han et al. “Electric-field-driven dual-functional molecular switches in tunnel junctions”. en. In: *Nature Materials* 19.8 (Aug. 2020). Number: 8, pp. 843–848. ISSN: 1476-1122, 1476-4660. DOI: 10.1038/s41563-020-0697-5. URL: http://www.nature.com/articles/s41563-020-0697-5.

[67] Y. B. Nian et al. “Evidence for an Oxygen Diffusion Model for the Electric Pulse Induced Resistance Change Effect in Transition-Metal Oxides”. en. In: *Physical Review Letters* 98.14 (Apr. 2007). Number: 14. ISSN: 0031-9007, 1079-7114. DOI: 10.1103/PhysRevLett.98.146403. URL: https://link.aps.org/doi/10.1103/PhysRevLett.98.146403.

[68] D. Halley et al. “Electrical switching in Fe/Cr/MgO/Fe magnetic tunnel junctions”. en. In: *Applied Physics Letters* 92.21 (May 2008). Number: 21, p. 212115. ISSN: 0003-6951, 1077-3118. DOI: 10.1063/1.2938696. URL: http://aip.scitation.org/doi/10.1063/1.2938696.

[69] Inrok Hwang et al. “Resistive switching transition induced by a voltage pulse in a Pt/NiO/Pt structure”. en. In: *Applied Physics Letters* 97.5 (Aug. 2010). Number: 5, p. 052106. ISSN: 0003-6951, 1077-3118. DOI: 10.1063/1.3477953. URL: http://aip.scitation.org/doi/10.1063/1.3477953.

[70] Eric Bertin et al. “Random barrier double-well model for resistive switching in tunnel barriers”. en. In: *Journal of Applied Physics* 109.8 (Apr. 2011). Number: 8, p. 083712. ISSN: 0021-8979, 1089-7550. DOI: 10.1063/1.3561497. URL: http://aip.scitation.org/doi/10.1063/1.3561497.

[71] Sungho Kim et al. “Physical electro-thermal model of resistive switching in bi-layered resistance-change memory”. en. In: *Scientific Reports* 3.1 (Apr. 2013). Number: 1. ISSN: 2045-2322. DOI: 10.1038/srep01680. URL: https://www.nature.com/articles/srep01680.

[72] J. M. Aguiar-Hualde and M. Alouani. “Taming the resistive switching in Fe/MgO/V/Fe magnetic tunnel junctions: An ab initio study”. In: *Journal of Magnetism and Magnetic Materials* 372 (2014), pp. 167–172. ISSN: 0304-8853. DOI: 10.1016/j.jmmm.2014.07.063. URL: https://doi.org/10.1016/j.jmmm.2014.07.063.

[73] M. Menghini et al. “Resistive switching on MgO-based metal-insulator-metal structures grown by molecular beam epitaxy: Resistive switching on MgO-based metal-insulator-metal structures grown by molecular beam epitaxy”. en. In: *physica status solidi (c)* 12.1-2 (Jan. 2015). Number: 1-2, pp. 246–249. ISSN: 18626351. DOI: 10.1002/pssc.201400192. URL: https://onlinelibrary.wiley.com/doi/10.1002/pssc.201400192.

[74] Florian Schwarz et al. “Field-induced conductance switching by charge-state alternation in organometallic single-molecule junctions”. en. In: *Nature Nanotechnology* 11.2 (Feb. 2016). Number: 2, pp. 170–176. ISSN: 1748-3387, 1748-3395. DOI: 10.1038/nnano.2015.255. URL: http://www.nature.com/articles/nnano.2015.255.

[75] M. Bowen et al. “Bias-crafted magnetic tunnel junctions with bistable spin-dependent states”. en. In: *Applied Physics Letters* 89.10 (Sept. 2006). Number: 10, p. 103517. ISSN: 0003-6951, 1077-3118. DOI: 10.1063/1.2345592. URL: http://aip.scitation.org/doi/10.1063/1.2345592.

[76] Biao Jin, Gang Su, and Qing-Rong Zheng. “Quasiparticle charge imbalance, first-order phase transition and quantum criticality in ferromagnet/superconductor/ ferromagnet double-tunnel junctions”. en. In: *Journal of Applied Physics* 96.10 (Nov. 2004). Number: 10, pp. 5654–5657. ISSN: 0021-8979, 1089-7550. DOI: 10.1063/1.1804247. URL: http://aip.scitation.org/doi/10.1063/1.1804247.

[77] Wei-Gang Wang et al. “Electric-field-assisted switching in magnetic tunnel junctions”. en. In: *Nature Materials* 11.1 (Jan. 2012). Number: 1, pp. 64–68. ISSN: 1476-1122, 1476-4660. DOI: 10.1038/nmat3171. URL: http://www.nature.com/articles/nmat3171.

[78] Stefan Wagner et al. “Switching of a coupled spin pair in a single-molecule junction”. en. In: *Nature Nanotechnology* 8.8 (Aug. 2013). Number: 8, pp. 575–579. ISSN: 1748-3387, 1748-3395. DOI: 10.1038/nnano.2013.133. URL: http://www.nature.com/articles/nnano.2013.133.

[79] V.I. Kozub, Y.M. Galperin, and V.M. Vinokur. “Coulomb blockade-tuned indirect exchange in ferromagnetic nanostructures”. In: *Journal of Magnetism and Magnetic Materials* 465 (Nov. 2018). 2021-11-30, pp. 304–308. ISSN: 03048853. DOI: 10.1016/j.jmmm.2018.06.022. URL: https://linkinghub.elsevier.com/retrieve/pii/S0304885318305250.

[80] H. Kohlstedt et al. “Theoretical current-voltage characteristics of ferroelectric tunnel junctions”. en. In: *Physical Review B* 72.12 (Sept. 2005). Number: 12. ISSN: 1098-0121, 1550-235X. DOI: 10.1103/PhysRevB.72.125341. URL: https://link.aps.org/doi/10.1103/PhysRevB.72.125341.

[81] Toshio Miyamachi et al. “Robust spin crossover and memristance across a single molecule”. en. In: *Nature Communications* 3.1 (Jan. 2012). Number: 1, p. 938. ISSN: 2041-1723. DOI: 10.1038/ncomms1940. URL: http://www.nature.com/articles/ncomms1940.

[82] Jesús Martínez-Blanco et al. “Gating a single-molecule transistor with individual atoms”. en. In: *Nature Physics* 11.8 (Aug. 2015). Number: 8, pp. 640–644. ISSN: 1745-2473, 1745-2481. DOI: 10.1038/nphys3385. URL: http://www.nature.com/articles/nphys3385.

[83] Pham Nam Hai and Masaaki Tanaka. “Memristive magnetic tunnel junctions with MnAs nanoparticles”. en. In: *Applied Physics Letters* 107.12 (Sept. 2015). Number: 12, p. 122404. ISSN: 0003-6951, 1077-3118. DOI: 10.1063/1.4931141. URL: http://aip.scitation.org/doi/10.1063/1.4931141.

[84] Bandana Das et al. “Memristive, memcapacitive and meminductive behavior of single and co-doped cadmium selenide nanocomposites under different doping environment”. en. In: *Journal of Materials Science: Materials in Electronics* 29.1 (Jan. 2018). Number: 1, pp. 546–557. ISSN: 0957-4522, 1573-482X. DOI: 10.1007/s10854-017-7946-7. URL: http://link.springer.com/10.1007/s10854-017-7946-7.

[85] Hirendra Das, Qiang Xu, and Pranayee Datta. “Effect of ZnS and PbS shell on membehavior of CdS quantum dots”. en. In: *Journal of Materials Science: Materials in Electronics* (Feb. 2021). 2023-02-09. ISSN: 0957-4522, 1573-482X. DOI: 10.1007/s10854-021-05415-6. URL: http://link.springer.com/10.1007/s10854-021-05415-6.

[86] S. W. Wu et al. “Conductance Hysteresis and Switching in a Single-Molecule Junction”. en. In: *The Journal of Physical Chemistry C* 112.14 (Apr. 2008). Number: 14, pp. 5241–5244. ISSN: 1932-7447, 1932-7455. DOI: 10.1021/jp7114548. URL: https://pubs.acs.org/doi/10.1021/jp7114548.

[87] Michael Galperin, Mark A. Ratner, and Abraham Nitzan. “Hysteresis, Switching, and Negative Differential Resistance in Molecular Junctions: A Polaron Model”. en. In: *Nano Letters* 5.1 (Jan. 2005). Number: 1, pp. 125–130. ISSN: 1530-6984, 1530-6992. DOI: 10.1021/nl048216c. URL: https://pubs.acs.org/doi/10.1021/nl048216c.

[88] D. Mozyrsky, M. B. Hastings, and I. Martin. “Intermittent polaron dynamics: Born-Oppenheimer approximation out of equilibrium”. en. In: *Physical Review B* 73.3 (Jan. 2006). Number: 3. ISSN: 1098-0121, 1550-235X. DOI: 10.1103/PhysRevB.73.035104. URL: https://link.aps.org/doi/10.1103/PhysRevB.73.035104.

[89] J. Inoue et al. “Temperature dependence of tunnel conductance in ferromagnetic double barrier junctions”. en. In: *Surface Science* 438.1-3 (Sept. 1999). Number: 1-3, pp. 336–340. ISSN: 00396028. DOI: 10.1016/S0039-6028(99)00599-3. URL: https://linkinghub.elsevier.com/retrieve/pii/S0039602899005993.

[90] V. Hung Nguyen, V. Lien Nguyen, and T. Anh Pham. “Current and shot noise in double barrier resonant tunneling structures in a longitudinal magnetic field”. en. In: *Physical Review B* 76.23 (Dec. 2007). Number: 23. ISSN: 1098-0121, 1550-235X. DOI: 10.1103/PhysRevB.76.235326. URL: https://link.aps.org/doi/10.1103/PhysRevB.76.235326.

[91] G. Feng, Sebastiaan van Dijken, and J. M. D. Coey. “MgO-based double barrier magnetic tunnel junctions with thin free layers”. en. In: *Journal of Applied Physics* 105.7 (Apr. 2009). Number: 7, p. 07C926. ISSN: 0021-8979, 1089-7550. DOI: 10.1063/1.3072474. URL: http://aip.scitation.org/doi/10.1063/1.3072474.

[92] Bingshan Tao et al. “Coherent Resonant Tunneling through Double Metallic Quantum Well States”. en. In: *Nano Letters* 19.5 (May 2019). Number: 5, pp. 3019–3026. ISSN: 1530-6984, 1530-6992. DOI: 10.1021/acs.nanolett.9b00205. URL: https://pubs.acs.org/doi/10.1021/acs.nanolett.9b00205.

[93] Amina Belkadi, Ayendra Weerakkody, and Garret Moddel. “Demonstration of resonant tunneling effects in metal-double-insulator-metal (MI2M) diodes”. In: *Nature Communications* 12.1 (May 2021). ISSN: 2041-1723. DOI: 10.1038/s41467-021-23182-0. URL: http://dx.doi.org/10.1038/s41467-021-23182-0.

[94] Yizi Xu, D. Ephron, and M. R. Beasley. “Directed inelastic hopping of electrons through metal-insulator-metal tunnel junctions”. en. In: *Physical Review B* 52.4 (July 1995). Number: 4, pp. 2843–2859. ISSN: 0163-1829, 1095-3795. DOI: 10.1103/PhysRevB.52.2843. URL: https://link.aps.org/doi/10.1103/PhysRevB.52.2843.

[95] Do Bang, T. Nozaki, and Y. Suzuki. “Strong quantum interference effect in fully epitaxial Cr/Fe/MgO/Fe magnetic tunnel junctions with ultrathin-Fe electrodes at room temperature”. en. In: *Journal of Applied Physics* 109.7 (Apr. 2011). Number: 7, p. 07C719. ISSN: 0021-8979, 1089-7550. DOI: 10.1063/1.3556780. URL: http://aip.scitation.org/doi/10.1063/1.3556780.

[96] Ayaz Arif Khan et al. “Elastic and inelastic conductance in Co-Fe-B/MgO/Co-Fe-B magnetic tunnel junctions”. en. In: *Physical Review B* 82.6 (Aug. 2010). Number: 6. ISSN: 1098-0121, 1550-235X. DOI: 10.1103/PhysRevB.82.064416. URL: https://link.aps.org/doi/10.1103/PhysRevB.82.064416.

[97] X. W. Tu, G. Mikaelian, and W. Ho. “Controlling Single-Molecule Negative Differential Resistance in a Double-Barrier Tunnel Junction”. en. In: *Physical Review Letters* 100.12 (Mar. 2008). Number: 12. ISSN: 0031-9007, 1079-7114. DOI: 10.1103/PhysRevLett.100.126807. URL: https://link.aps.org/doi/10.1103/PhysRevLett.100.126807.

[98] Richard A. Kiehl et al. “Charge storage model for hysteretic negative-differential resistance in metal-molecule-metal junctions”. en. In: *Applied Physics Letters* 88.17 (Apr. 2006). Number: 17, p. 172102. ISSN: 0003-6951, 1077-3118. DOI: 10.1063/1.2195696. URL: http://aip.scitation.org/doi/10.1063/1.2195696.

[99] William C. Brown. “Microwave to DC converter”. 1969. URL: https://worldwide.espacenet.com/patent/search?q=pn%3DUS3434678A.

[100] Asha Sharma et al. “A carbon nanotube optical rectenna”. In: *Nature Nanotechnology* 10.12 (Sept. 2015), pp. 1027–1032. ISSN: 1748-3395. DOI: 10.1038/nnano.2015.220. URL: http://dx.doi.org/10.1038/nnano.2015.220.

[101] Melad M. Olaimat, Vahid Nayyeri, and Omar M. Ramahi. “Simulation and optimization of rectenna systems”. In: *Scientific Reports* 13.1 (Oct. 2023). ISSN: 2045-2322. DOI: 10.1038/s41598-023-44401-2. URL: http://dx.doi.org/10.1038/s41598-023-44401-2.

[102] Zixu Zhu et al. “Graphene geometric diodes for terahertz rectennas”. In: *Journal of Physics D: Applied Physics* 46.18 (Apr. 2013), p. 185101. ISSN: 1361-6463. DOI: 10.1088/0022-3727/46/18/185101. URL: http://dx.doi.org/10.1088/0022-3727/46/18/185101.

[103] Dhaneesh Kumar et al. “Manifestation of Strongly Correlated Electrons in a 2D Kagome Metal–Organic Framework”. In: *Advanced Functional Materials* 31.48 (Sept. 2021). ISSN: 1616-3028. DOI: 10.1002/adfm.202106474. URL: http://dx.doi.org/10.1002/adfm.202106474.

[104] Anand Manaparambil et al. “Nonequilibrium spintronic transport through Kondo impurities”. en. In: *Physical Review B* 106.12 (Sept. 2022). Number: 12. ISSN: 2469-9950, 2469-9969. DOI: 10.1103/PhysRevB.106.125413. URL: https://link.aps.org/doi/10.1103/PhysRevB.106.125413.

[105] P. W. Anderson. “Localized Magnetic States in Metals”. In: *Physical Review* 124.1 (Oct. 1961), pp. 41–53. ISSN: 0031-899X. DOI: 10.1103/physrev.124.41. URL: http://dx.doi.org/10.1103/PhysRev.124.41.

[106] J. Kondo. “Resistance Minimum in Dilute Magnetic Alloys”. In: *Progress of Theoretical Physics* 32.1 (July 1964), pp. 37–49. ISSN: 1347-4081. DOI: 10.1143/ptp.32.37. URL: http://dx.doi.org/10.1143/PTP.32.37.

[107] U. Fano. “Effects of Configuration Interaction on Intensities and Phase Shifts”. en. In: *Physical Review* 124.6 (Dec. 1961). Number: 6, pp. 1866–1878. ISSN: 0031-899X. DOI: 10.1103/PhysRev.124.1866. URL: https://link.aps.org/doi/10.1103/PhysRev.124.1866.

[108] H. O. Frota. “Shape of the Kondo resonance”. en. In: *Physical Review B* 45.3 (Jan. 1992). Number: 3, pp. 1096–1099. ISSN: 0163-1829, 1095-3795. DOI: 10.1103/PhysRevB.45.1096. URL: https://link.aps.org/doi/10.1103/PhysRevB.45.1096.

[109] K. Nagaoka et al. “Temperature Dependence of a Single Kondo Impurity”. en. In: *Physical Review Letters* 88.7 (Feb. 2002). Number: 7. ISSN: 0031-9007, 1079-7114. DOI: 10.1103/PhysRevLett.88.077205. URL: https://link.aps.org/doi/10.1103/PhysRevLett.88.077205.

[110] Sebastian Frank and David Jacob. “Orbital signatures of Fano-Kondo line shapes in STM adatom spectroscopy”. en. In: *Physical Review B* 92.23 (Dec. 2015). Number: 23. ISSN: 1098-0121, 1550-235X. DOI: 10.1103/PhysRevB.92.235127. URL: https://link.aps.org/doi/10.1103/PhysRevB.92.235127.

[111] Laëtitia Farinacci et al. “Interfering Tunneling Paths through Magnetic Molecules on Superconductors: Asymmetries of Kondo and Yu-Shiba-Rusinov Resonances”. en. In: *Physical Review Letters* 125.25 (Dec. 2020). Number: 25. ISSN: 0031-9007, 1079-7114. DOI: 10.1103/PhysRevLett.125.256805. URL: https://link.aps.org/doi/10.1103/PhysRevLett.125.256805.

[112] I. Fernández-Torrente, K. J. Franke, and J. I. Pascual. “Vibrational Kondo Effect in Pure Organic Charge-Transfer Assemblies”. en. In: *Physical Review Letters* 101.21 (Nov. 2008). Number: 21. ISSN: 0031-9007, 1079-7114. DOI: https://doi.org/10.1103/PhysRevLett.101.217203. URL: https://link.aps.org/doi/10.1103/PhysRevLett.101.217203.

[113] Ying-Shuang Fu, Qi-Kun Xue, and Roland Wiesendanger. “Spin-Resolved Splitting of Kondo Resonances in the Presence of RKKY-Type Coupling”. en. In: *Physical Review Letters* 108.8 (Feb. 2012). Number: 8. ISSN: 0031-9007, 1079-7114. DOI: 10.1103/PhysRevLett.108.087203. URL: https://link.aps.org/doi/10.1103/PhysRevLett.108.087203.

[114] F. Schwarz et al. “Nonequilibrium Steady-State Transport in Quantum Impurity Models: A Thermofield and Quantum Quench Approach Using Matrix Product States”. en. In: *Physical Review Letters* 121.13 (Sept. 2018). Number: 13. ISSN: 0031-9007, 1079-7114. DOI: 10.1103/PhysRevLett.121.137702. URL: https://link.aps.org/doi/10.1103/PhysRevLett.121.137702.

[115] D. Rakhmilevitch et al. “Electron-Vibration Interaction in the Presence of a Switchable Kondo Resonance Realized in a Molecular Junction”. en. In: *Physical Review Letters* 113.23 (Dec. 2014). Number: 23. ISSN: 0031-9007, 1079-7114. DOI: 10.1103/PhysRevLett.113.236603. URL: https://link.aps.org/doi/10.1103/PhysRevLett.113.236603.

[116] F. Pistolesi, Ya. M. Blanter, and Ivar Martin. “Self-consistent theory of molecular switching”. en. In: *Physical Review B* 78.8 (Aug. 2008). Number: 8. ISSN: 1098-0121, 1550-235X. DOI: 10.1103/PhysRevB.78.085127. URL: https://link.aps.org/doi/10.1103/PhysRevB.78.085127.

[117] Eli Y. Wilner et al. “Nonequilibrium quantum systems with electron-phonon interactions: Transient dynamics and approach to steady state”. en. In: *Physical Review B* 89.20 (May 2014). Number: 20. ISSN: 1098-0121, 1550-235X. DOI: 10.1103/PhysRevB.89.205129. URL: https://link.aps.org/doi/10.1103/PhysRevB.89.205129.

[118] Rok Žitko. “Kondo resonance lineshape of magnetic adatoms on decoupling layers”. en. In: *Physical Review B* 84.19 (Nov. 2011). Number: 19. ISSN: 1098-0121, 1550-235X. DOI: 10.1103/PhysRevB.84.195116. URL: https://link.aps.org/doi/10.1103/PhysRevB.84.195116.

[119] D.-J. Choi et al. “Kondo Resonance of a Co Atom Exchange Coupled to a Ferromagnetic Tip”. en. In: *Nano Letters* 16.10 (Oct. 2016). Number: 10, pp. 6298–6302. ISSN: 1530-6984, 1530-6992. DOI: 10.1021/acs.nanolett.6b02617. URL: https://pubs.acs.org/doi/10.1021/acs.nanolett.6b02617.

[120] G. D. Scott and T.-C. Hu. “Gate-controlled Kondo effect in a single-molecule transistor with elliptical ferromagnetic leads”. en. In: *Physical Review B* 96.14 (Oct. 2017). Number: 14. ISSN: 2469-9950, 2469-9969. DOI: 10.1103/PhysRevB.96.144416. URL: https://link.aps.org/doi/10.1103/PhysRevB.96.144416.

[121] T. Yamamoto, T. Kato, and M. Matsuo. “Spin current at a magnetic junction as a probe of the Kondo state”. en. In: *Physical Review B* 104.12 (Sept. 2021). Number: 12. ISSN: 2469-9950, 2469-9969. DOI: 10.1103/PhysRevB.104.L121401. URL: https://link.aps.org/doi/10.1103/PhysRevB.104.L121401.

[122] N. Sergueev et al. “Spin-polarized transport through a quantum dot: Anderson model with on-site Coulomb repulsion”. en. In: *Physical Review B* 65.16 (Apr. 2002). Number: 16, p. 165303. ISSN: 0163-1829, 1095-3795. DOI: 10.1103/PhysRevB.65.165303. URL: https://link.aps.org/doi/10.1103/PhysRevB.65.165303.

[123] D. Goldhaber-Gordon et al. “From the Kondo Regime to the Mixed-Valence Regime in a Single-Electron Transistor”. en. In: *Physical Review Letters* 81.23 (Dec. 1998). Number: 23, pp. 5225–5228. ISSN: 0031-9007, 1079-7114. DOI: http://doi.org/10.1103/PhysRevLett.81.5225. URL: https://link.aps.org/doi/10.1103/PhysRevLett.81.5225.

[124] Henning Prüser et al. “Long-range Kondo signature of a single magnetic impurity”. en. In: *Nature Physics* 7.3 (Mar. 2011). Number: 3, pp. 203–206. ISSN: 1745-2473, 1745-2481. DOI: 10.1038/nphys1876. URL: http://www.nature.com/articles/nphys1876.

[125] Q. Dubout et al. “Controlling the Spin of Co Atoms on Pt(111) by Hydrogen Adsorption”. en. In: *Physical Review Letters* 114.10 (Mar. 2015). Number: 10. ISSN: 0031-9007, 1079-7114. DOI: 10.1103/PhysRevLett.114.106807. URL: https://link.aps.org/doi/10.1103/PhysRevLett.114.106807.

[126] Manuel Gruber, Alexander Weismann, and Richard Berndt. “The Kondo resonance line shape in scanning tunnelling spectroscopy: instrumental aspects”. en. In: *Journal of Physics: Condensed Matter* 30.42 (Oct. 2018). Number: 42, p. 424001. ISSN: 0953-

8984, 1361-648X. DOI: 10.1088/1361-648X/aadfa3. URL: https://iopscience.iop.org/article/10.1088/1361-648X/aadfa3.

[127] Annika Kurzmann et al. "Kondo effect and spin–orbit coupling in graphene quantum dots". In: *Nature Communications* 12.1 (Oct. 2021). ISSN: 2041-1723. DOI: 10.1038/s41467-021-26149-3. URL: http://dx.doi.org/10.1038/s41467-021-26149-3.

[128] R. Delagrange et al. "Emission noise and high frequency cut-off of the Kondo effect in a quantum dot". en. In: *Physical Review B* 97.4 (Jan. 2018). Number: 4. ISSN: 2469-9950, 2469-9969. DOI: 10.1103/PhysRevB.97.041412. URL: https://link.aps.org/doi/10.1103/PhysRevB.97.041412.

[129] S. Zhang et al. "Quenching of Magnetoresistance by Hot Electrons in Magnetic Tunnel Junctions". en. In: *Physical Review Letters* 79.19 (Nov. 1997). Number: 19, pp. 3744–3747. ISSN: 0031-9007, 1079-7114. DOI: 10.1103/PhysRevLett.79.3744. URL: https://link.aps.org/doi/10.1103/PhysRevLett.79.3744.

[130] Jagadeesh S. Moodera and George Mathon. "Spin polarized tunneling in ferromagnetic junctions". en. In: *Journal of Magnetism and Magnetic Materials* 200.1-3 (Oct. 1999). Number: 1-3, pp. 248–273. ISSN: 03048853. DOI: 10.1016/S0304-8853(99)00515-6. URL: https://linkinghub.elsevier.com/retrieve/pii/S0304885399005156.

[131] Hyunsoo Yang, See-Hun Yang, and Stuart S. P. Parkin. "Crossover from Kondo-Assisted Suppression to Co-Tunneling Enhancement of Tunneling Magnetoresistance via Ferromagnetic Nanodots in MgO Tunnel Barriers". en. In: *Nano Letters* 8.1 (Jan. 2008). Number: 1, pp. 340–344. ISSN: 1530-6984, 1530-6992. DOI: 10.1021/nl072930n. URL: https://pubs.acs.org/doi/10.1021/nl072930n.

[132] Volker Drewello et al. "Inelastic electron tunneling spectra of MgO-based magnetic tunnel junctions with different electrode designs". en. In: *Physical Review B* 79.17 (May 2009). Number: 17. ISSN: 1098-0121, 1550-235X. DOI: 10.1103/PhysRevB.79.174417. URL: https://link.aps.org/doi/10.1103/PhysRevB.79.174417.

[133] Braj Bhusan Singh and Sujeet Chaudhary. "Inelastic tunneling conductance and magnetoresistance investigations in dual ion-beam sputtered CoFeB(110)/MgO/CoFeB (110) magnetic tunnel junctions". en. In: *Journal of Applied Physics* 115.15 (Apr. 2014). Number: 15, p. 153903. ISSN: 0021-8979, 1089-7550. DOI: 10.1063/1.4871679. URL: http://aip.scitation.org/doi/10.1063/1.4871679.

[134] Patrycja Tulewicz et al. "Large Voltage-Tunable Spin Valve Based on a Double Quantum Dot". en. In: *Physical Review Applied* 16.1 (July 2021). Number: 1. ISSN: 2331-7019. DOI: 10.1103/PhysRevApplied.16.014029. URL: https://link.aps.org/doi/10.1103/PhysRevApplied.16.014029.

[135] Juba Bouaziz, Filipe Souza Mendes Guimarães, and Samir Lounis. "A new view on the origin of zero-bias anomalies of Co atoms atop noble metal surfaces". In: *Nature Communications* 11.1 (Nov. 2020). ISSN: 2041-1723. DOI: 10.1038/s41467-020-19746-1. URL: http://dx.doi.org/10.1038/s41467-020-19746-1.

[136] Sangjun Jeon, Sungmin Kim, and Young Kuk. "Zero-bias anomaly and role of electronic correlations in a disordered metal film". In: *New Journal of Physics* 22.8 (Aug. 2020), p. 083045. ISSN: 1367-2630. DOI: 10.1088/1367-2630/aba3e7. URL: http://dx.doi.org/10.1088/1367-2630/aba3e7.

[137] Y. Ren et al. "Zero-bias anomaly of quantum point contacts in the low-conductance limit". In: *Physical Review B* 82.4 (July 2010). ISSN: 1550-235X. DOI: 10.1103/physrevb.82.045313. URL: http://dx.doi.org/10.1103/PhysRevB.82.045313.

[138] K. A. Matveev and L. I. Glazman. "Coulomb blockade of activated conduction". en. In: *Physical Review B* 54.15 (Oct. 1996). Number: 15, pp. 10339–10341. ISSN: 0163-1829, 1095-3795. DOI: 10.1103/PhysRevB.54.10339. URL: https://link.aps.org/doi/10.1103/PhysRevB.54.10339.

[139] Parvathy Harikumar and S. Mathi Jaya. "Non-Equilibrium Green's Function Modeling of the Transport Characteristics of Magnetic Tunnel Junctions Containing Anderson Impurities". en. In: *SPIN* 10.01 (Mar. 2020). Number: 01. ISSN: 2010-3247, 2010-3255. DOI: 10.1142/S201032472050006X. URL: https://www.worldscientific.com/doi/10.1142/S201032472050006X.

[140] Ireneusz Weymann et al. "Tunnel magnetoresistance of quantum dots coupled to ferromagnetic leads in the sequential and cotunneling regimes". en. In: *Physical Review B* 72.11 (Sept. 2005). Number: 11. ISSN: 1098-0121, 1550-235X. DOI: 10.1103/PhysRevB.72.115334. URL: https://link.aps.org/doi/10.1103/PhysRevB.72.115334.

[141] I Weymann and J Barnaś. "Transport through two-level quantum dots weakly coupled to ferromagnetic leads". en. In: *Journal of Physics: Condensed Matter* 19.9 (Mar. 2007). Number: 9, p. 096208. ISSN: 0953-8984, 1361-648X. DOI: 10.1088/0953-8984/19/9/096208. URL: https://iopscience.iop.org/article/10.1088/0953-8984/19/9/096208.

[142] A U Sharafutdinov and I S Burmistrov. "Cotunneling current through a two-level quantum dot coupled to magnetic leads: the role of exchange interaction". en. In: *Journal of Physics: Condensed Matter* 24.15 (Apr. 2012). Number: 15, p. 155301. ISSN: 0953-8984, 1361-648X. DOI: 10.1088/0953-8984/24/15/155301. URL: https://iopscience.iop.org/article/10.1088/0953-8984/24/15/155301.

[143] Lei Zhang et al. “Bi-stable electronic states of cobalt phthalocyanine molecules on two-dimensional vanadium diselenide”. In: *Applied Materials Today* 18 (Mar. 2020). 2023-01-20, p. 100535. ISSN: 23529407. DOI: 10.1016/j.apmt.2019.100535. URL: https://www.sciencedirect.com/science/article/abs/pii/S2352940719306171.

[144] Anna Płomińska and Ireneusz Weymann. “Magnetoresistive properties of a double magnetic molecule spin valve in different geometrical arrangements”. en. In: *Journal of Magnetism and Magnetic Materials* 480 (June 2019). 2022-10-21, pp. 11–21. ISSN: 03048853. DOI: 10.1016/j.jmmm.2019.02.041. URL: https://linkinghub.elsevier.com/retrieve/pii/S0304885318335662.

[145] Y. Lu et al. “Spin-Polarized Inelastic Tunneling through Insulating Barriers”. en. In: *Physical Review Letters* 102.17 (Apr. 2009). Number: 17, p. 176801. ISSN: 0031-9007, 1079-7114. DOI: 10.1103/PhysRevLett.102.176801. URL: https://link.aps.org/doi/10.1103/PhysRevLett.102.176801.

[146] K. Wrześniewski and I. Weymann. “Dark states in spin-polarized transport through triple quantum dot molecules”. en. In: *Physical Review B* 97.7 (Feb. 2018). Number: 7. ISSN: 2469-9950, 2469-9969. DOI: 10.1103/PhysRevB.97.075425. URL: https://link.aps.org/doi/10.1103/PhysRevB.97.075425.

[147] Arne Brataas et al. “Spin Accumulation in a Quantum Cluster Resolved in Tunnel Junctions”. en. In: *Japanese Journal of Applied Physics* 40.Part 1, No. 4A (Apr. 2001). Number: Part 1, No. 4A, pp. 2329–2335. ISSN: 0021-4922, 1347-4065. DOI: 10.1143/JJAP.40.2329. URL: https://iopscience.iop.org/article/10.1143/JJAP.40.2329.

[148] K. Hamaya et al. “Oscillatory changes in the tunneling magnetoresistance effect in semiconductor quantum-dot spin valves”. en. In: *Physical Review B* 77.8 (Feb. 2008). Number: 8. ISSN: 1098-0121, 1550-235X. DOI: 10.1103/PhysRevB.77.081302. URL: https://link.aps.org/doi/10.1103/PhysRevB.77.081302.

[149] Yanchao Zhang and Zhenzhen Xie. “Inverse currents in Coulomb-coupled quantum dots”. en. In: *Physical Review E* 104.6 (Dec. 2021). Number: 6. ISSN: 2470-0045, 2470-0053. DOI: 10.1103/PhysRevE.104.064142. URL: https://link.aps.org/doi/10.1103/PhysRevE.104.064142.

[150] Hongkun Park et al. “Nanomechanical oscillations in a single-C60 transistor”. en. In: *Nature* 407.6800 (Sept. 2000). Number: 6800, pp. 57–60. ISSN: 0028-0836, 1476-4687. DOI: 10.1038/35024031. URL: http://www.nature.com/articles/35024031.

[151] W. Wulfhekel et al. “Large spin effects in Coulomb blockade of Fe / MgO / Fe tunnel junctions”. en. In: *Physical Review B* 72.21 (Dec. 2005). Number: 21. ISSN: 1098-0121, 1550-235X. DOI: 10.1103/PhysRevB.72.212407. URL: https://link.aps.org/doi/10.1103/PhysRevB.72.212407.

[152] Y Nogi et al. “Preparation and magnetotransport properties of MgO-barrier-based magnetic double tunnel junctions including nonmagnetic nanoparticles”. en. In: *Journal of Physics D: Applied Physics* 40.5 (Mar. 2007). Number: 5, pp. 1242–1246. ISSN: 0022-3727, 1361-6463. DOI: 10.1088/0022-3727/40/5/S06. URL: https://iopscience.iop.org/article/10.1088/0022-3727/40/5/S06.

[153] Tetsunori Koda et al. “Spin Accumulation in Cr Nanoparticles in Single Electron Tunneling Regime”. en. In: *IEEE Transactions on Magnetics* 46.6 (June 2010). Number: 6, pp. 2060–2062. ISSN: 0018-9464. DOI: 10.1109/TMAG.2010.2044870. URL: http://ieeexplore.ieee.org/document/5467577/.

[154] T.V. Pham et al. “Spin-dependent tunneling in magnetic tunnel junctions with Fe nanoparticles embedded in an MgO matrix”. en. In: *Solid State Communications* 183 (Apr. 2014). 2023-02-09, pp. 18–21. ISSN: 00381098. DOI: 10.1016/j.ssc.2013.12.023. URL: https://linkinghub.elsevier.com/retrieve/pii/S0038109813006108.

[155] Frederick S Thomas et al. “Highly symmetric and tunable tunnel couplings in InAs/InP nanowire heterostructure quantum dots”. In: *Nanotechnology* 31.13 (Jan. 2020), p. 135003. ISSN: 1361-6528. DOI: 10.1088/1361-6528/ab5ce6. URL: http://dx.doi.org/10.1088/1361-6528/ab5ce6.

[156] Lanlan Sun et al. “Single-molecule electronics: from chemical design to functional devices”. en. In: *Chem. Soc. Rev.* 43.21 (2014). Number: 21, pp. 7378–7411. ISSN: 0306-0012, 1460-4744. DOI: 10.1039/C4CS00143E. URL: http://xlink.rsc.org/?DOI=C4CS00143E.

[157] Michael Galperin, Mark A Ratner, and Abraham Nitzan. “Molecular transport junctions: vibrational effects”. en. In: *Journal of Physics: Condensed Matter* 19.10 (Mar. 2007). Number: 10, p. 103201. ISSN: 0953-8984, 1361-648X. DOI: 10.1088/0953-8984/19/10/103201. URL: https://iopscience.iop.org/article/10.1088/0953-8984/19/10/103201.

[158] Jens Koch, Felix von Oppen, and A. V. Andreev. “Theory of the Franck-Condon blockade regime”. en. In: *Physical Review B* 74.20 (Nov. 2006). Number: 20. ISSN: 1098-0121, 1550-235X. DOI: 10.1103/PhysRevB.74.205438. URL: https://link.aps.org/doi/10.1103/PhysRevB.74.205438.

[159] Ahmed Kenawy, Janine Splettstoesser, and Maciej Misiorny. “Tunnel magnetoresistance of magnetic molecules with spin-vibron coupling”. en. In: *AIP Advances* 7.5 (May 2017). Number: 5, p. 055708. ISSN: 2158-3226. DOI: 10.1063/1.4974285. URL: http://aip.scitation.org/doi/10.1063/1.4974285.

[160] C. Schinabeck et al. “Current noise in single-molecule junctions induced by electronic-vibrational coupling”. en. In: *Physical Review B* 90.7 (Aug. 2014). Number: 7. ISSN: 1098-0121, 1550-235X. DOI: 10.1103/PhysRevB.90.075409. URL: https://link.aps.org/doi/10.1103/PhysRevB.90.075409.

[161] Alexander McCaskey et al. “Electron-vibron coupling effects on electron transport via a single-molecule magnet”. en. In: *Physical Review B* 91.12 (Mar. 2015). Number: 12. ISSN: 1098-0121, 1550-235X. DOI: 10.1103/PhysRevB.91.125419. URL: https://link.aps.org/doi/10.1103/PhysRevB.91.125419.

[162] R. Avriller, B. Murr, and F. Pistolesi. “Bistability and displacement fluctuations in a quantum nanomechanical oscillator”. en. In: *Physical Review B* 97.15 (Apr. 2018). Number: 15. ISSN: 2469-9950, 2469-9969. DOI: 10.1103/PhysRevB.97.155414. URL: https://link.aps.org/doi/10.1103/PhysRevB.97.155414.

[163] Amir Eskandari-asl. “Influence of a thermal bath on the transport properties of an open molecular junction”. en. In: *Journal of Physics and Chemistry of Solids* 122 (Nov. 2018). 2022-11-16, pp. 198–202. ISSN: 00223697. DOI: 10.1016/j.jpcs.2018.06.019. URL: https://linkinghub.elsevier.com/retrieve/pii/S0022369718305407.

[164] Natalya A Zimbovskaya. “Charge and heat current rectification by a double-dot system within the Coulomb blockade regime”. en. In: *Journal of Physics: Condensed Matter* 32.32 (July 2020). Number: 32, p. 325302. ISSN: 0953-8984, 1361-648X. DOI: 10.1088/1361-648X/ab83e9. URL: https://iopscience.iop.org/article/10.1088/1361-648X/ab83e9.

[165] Dexian Sun et al. “Origins of asymmetric charge transport properties of weakly coupled molecular junctions”. en. In: *Physical Review B* 99.12 (Mar. 2019). Number: 12. ISSN: 2469-9950, 2469-9969. DOI: 10.1103/PhysRevB.99.125423. URL: https://link.aps.org/doi/10.1103/PhysRevB.99.125423.

[166] Patrick Haughian et al. “Lifting the Franck-Condon blockade in driven quantum dots”. en. In: *Physical Review B* 94.20 (Nov. 2016). Number: 20. ISSN: 2469-9950, 2469-9969. DOI: 10.1103/PhysRevB.94.205412. URL: https://link.aps.org/doi/10.1103/PhysRevB.94.205412.

[167] Dmitry A. Ryndyk, Pino D’Amico, and Klaus Richter. “Single-spin polaron memory effect in quantum dots and single molecules”. en. In: *Physical Review B* 81.11 (Mar. 2010). Number: 11. ISSN: 1098-0121, 1550-235X. DOI: 10.1103/PhysRevB.81.115333. URL: https://link.aps.org/doi/10.1103/PhysRevB.81.115333.

[168] M. Bagheri Tagani and H. Rahimpour Soleimani. “Inelastic transport through double quantum dot systems”. en. In: *Physica B: Condensed Matter* 406.21 (Nov. 2011). Number: 21, pp. 4056–4059. ISSN: 09214526. DOI: 10.1016/j.physb.2011.07.047. URL: https://linkinghub.elsevier.com/retrieve/pii/S0921452611007241.

[169] R. Härtle and M. Thoss. “Resonant electron transport in single-molecule junctions: Vibrational excitation, rectification, negative differential resistance, and local cooling”. en. In: *Physical Review B* 83.11 (Mar. 2011). Number: 11. ISSN: 1098-0121, 1550-235X. DOI: 10.1103/PhysRevB.83.115414. URL: https://link.aps.org/doi/10.1103/PhysRevB.83.115414.

[170] Klaus Ferdinand Albrecht et al. “Bistability signatures in nonequilibrium charge transport through molecular quantum dots”. en. In: *Physical Review B* 86.8 (Aug. 2012). Number: 8. ISSN: 1098-0121, 1550-235X. DOI: 10.1103/PhysRevB.86.081412. URL: https://link.aps.org/doi/10.1103/PhysRevB.86.081412.

[171] A. Donarini, A. Yar, and M. Grifoni. “Vibration induced memory effects and switching in ac-driven molecular nanojunctions”. en. In: *The European Physical Journal B* 85.9 (Sept. 2012). Number: 9. ISSN: 1434-6028, 1434-6036. DOI: 10.1140/epjb/e2012-30407-5. URL: http://link.springer.com/10.1140/epjb/e2012-30407-5.

[172] Chit Siong Lau et al. “Redox-Dependent Franck–Condon Blockade and Avalanche Transport in a Graphene–Fullerene Single-Molecule Transistor”. en. In: *Nano Letters* 16.1 (Jan. 2016). Number: 1, pp. 170–176. ISSN: 1530-6984, 1530-6992. DOI: 10.1021/acs.nanolett.5b03434. URL: https://pubs.acs.org/doi/10.1021/acs.nanolett.5b03434.

[173] Daniel Secker et al. “Resonant Vibrations, Peak Broadening, and Noise in Single Molecule Contacts: The Nature of the First Conductance Peak”. en. In: *Physical Review Letters* 106.13 (Mar. 2011). Number: 13. ISSN: 0031-9007, 1079-7114. DOI: 10.1103/PhysRevLett.106.136807. URL: https://link.aps.org/doi/10.1103/PhysRevLett.106.136807.

[174] S. W. Wu et al. “Control of Relative Tunneling Rates in Single Molecule Bipolar Electron Transport”. en. In: *Physical Review Letters* 93.23 (Dec. 2004). Number: 23. ISSN: 0031-9007, 1079-7114. DOI: 10.1103/PhysRevLett.93.236802. URL: https://link.aps.org/doi/10.1103/PhysRevLett.93.236802.

[175] Chuancheng Jia et al. “Covalently bonded single-molecule junctions with stable and reversible photoswitched conductivity”. en. In: *Science* 352.6292 (June 2016). Number: 6292, pp. 1443–1445. ISSN: 0036-8075, 1095-9203. DOI: 10.1126/science.aaf6298. URL: https://www.science.org/doi/10.1126/science.aaf6298.

[176] Jens Koch and Felix von Oppen. “Franck-Condon Blockade and Giant Fano Factors in Transport through Single Molecules”. en. In: *Physical Review Letters* 94.20 (May 2005). Number: 20. ISSN: 0031-9007, 1079-7114. DOI: 10.1103/PhysRevLett.94.206804. URL: https://doi.org/10.1103/PhysRevLett.94.206804.

[177] N. Néel, J. Kröger, and R. Berndt. "Two-Level Conductance Fluctuations of a Single-Molecule Junction". en. In: *Nano Letters* 11.9 (Sept. 2011). Number: 9, pp. 3593–3596. ISSN: 1530-6984, 1530-6992. DOI: 10.1021/nl201327c. URL: https://pubs.acs.org/doi/10.1021/nl201327c.

[178] J. Gaudioso, L. J. Lauhon, and W. Ho. "Vibrationally Mediated Negative Differential Resistance in a Single Molecule". en. In: *Physical Review Letters* 85.9 (Aug. 2000). Number: 9, pp. 1918–1921. ISSN: 0031-9007, 1079-7114. DOI: https://doi.org/10.1103/PhysRevLett.85.1918. URL: https://link.aps.org/doi/10.1103/PhysRevLett.85.1918.

[179] Agostino Migliore and Abraham Nitzan. "Irreversibility and Hysteresis in Redox Molecular Conduction Junctions". en. In: *Journal of the American Chemical Society* 135.25 (June 2013). Number: 25, pp. 9420–9432. ISSN: 0002-7863, 1520-5126. DOI: 10.1021/ja401336u. URL: https://pubs.acs.org/doi/10.1021/ja401336u.

[180] James O. Thomas et al. "Understanding resonant charge transport through weakly coupled single-molecule junctions". en. In: *Nature Communications* 10.1 (Dec. 2019). Number: 1. ISSN: 2041-1723. DOI: 10.1038/s41467-019-12625-4. URL: http://www.nature.com/articles/s41467-019-12625-4.

[181] Jiwoong Park et al. "Coulomb blockade and the Kondo effect in single-atom transistors". en. In: *Nature* 417.6890 (June 2002). Number: 6890, pp. 722–725. ISSN: 0028-0836, 1476-4687. DOI: 10.1038/nature00791. URL: http://www.nature.com/articles/nature00791.

[182] Stefan Ballmann et al. "Experimental Evidence for Quantum Interference and Vibrationally Induced Decoherence in Single-Molecule Junctions". en. In: *Physical Review Letters* 109.5 (July 2012). Number: 5, p. 056801. ISSN: 0031-9007, 1079-7114. DOI: 10.1103/PhysRevLett.109.056801. URL: https://link.aps.org/doi/10.1103/PhysRevLett.109.056801.

[183] Kun Wang. "DNA-Based Single-Molecule Electronics: From Concept to Function". en. In: *Journal of Functional Biomaterials* 9.1 (Jan. 2018). Number: 1, p. 8. ISSN: 2079-4983. DOI: 10.3390/jfb9010008. URL: http://www.mdpi.com/2079-4983/9/1/8.

[184] Enrique Burzurí et al. "Franck–Condon Blockade in a Single-Molecule Transistor". en. In: *Nano Letters* 14.6 (June 2014). Number: 6, pp. 3191–3196. ISSN: 1530-6984, 1530-6992. DOI: 10.1021/nl500524w. URL: https://pubs.acs.org/doi/10.1021/nl500524w.

[185] Jonas Schuff et al. "Identifying Pauli spin blockade using deep learning". In: *Quantum* 7 (Aug. 2023), p. 1077. ISSN: 2521-327X. DOI: 10.22331/q-2023-08-08-1077. URL: http://dx.doi.org/10.22331/q-2023-08-08-1077.

[186] N. S. Lai et al. “Pauli Spin Blockade in a Highly Tunable Silicon Double Quantum Dot”. In: *Scientific Reports* 1.1 (Oct. 2011). ISSN: 2045-2322. DOI: 10.1038/srep00110. URL: http://dx.doi.org/10.1038/srep00110.

[187] T. Saygun et al. “Voltage-Induced Switching Dynamics of a Coupled Spin Pair in a Molecular Junction”. en. In: *Nano Letters* 16.4 (Apr. 2016). Number: 4, pp. 2824–2829. ISSN: 1530-6984, 1530-6992. DOI: 10.1021/acs.nanolett.6b00628. URL: https://pubs.acs.org/doi/10.1021/acs.nanolett.6b00628.

[188] Chuyao Tong et al. “Pauli Blockade of Tunable Two-Electron Spin and Valley States in Graphene Quantum Dots”. In: *Physical Review Letters* 128.6 (Feb. 2022). ISSN: 1079-7114. DOI: 10.1103/physrevlett.128.067702. URL: http://dx.doi.org/10.1103/PhysRevLett.128.067702.

[189] F. Qassemi, W. A. Coish, and F. K. Wilhelm. “Stationary and Transient Leakage Current in the Pauli Spin Blockade”. en. In: *Physical Review Letters* 102.17 (Apr. 2009). Number: 17. ISSN: 0031-9007, 1079-7114. DOI: 10.1103/PhysRevLett.102.176806. URL: https://link.aps.org/doi/10.1103/PhysRevLett.102.176806.

[190] Sinan Bugu et al. “Preparing Multipartite Entangled Spin Qubits via Pauli Spin Blockade”. en. In: *Scientific Reports* 10.1 (Dec. 2020). Number: 1, p. 3481. ISSN: 2045-2322. DOI: 10.1038/s41598-020-60299-6. URL: http://www.nature.com/articles/s41598-020-60299-6.

[191] J. Fransson and M. Råsander. “Pauli spin blockade in weakly coupled double quantum dots”. en. In: *Physical Review B* 73.20 (May 2006). Number: 20. ISSN: 1098-0121, 1550-235X. DOI: 10.1103/PhysRevB.73.205333. URL: https://link.aps.org/doi/10.1103/PhysRevB.73.205333.

[192] J. Danon and Yu. V. Nazarov. “Pauli spin blockade in the presence of strong spin-orbit coupling”. en. In: *Physical Review B* 80.4 (July 2009). Number: 4. ISSN: 1098-0121, 1550-235X. DOI: 10.1103/PhysRevB.80.041301. URL: https://link.aps.org/doi/10.1103/PhysRevB.80.041301.

[193] Anna Płomińska and Ireneusz Weymann. “Pauli spin blockade in double molecular magnets”. en. In: *Physical Review B* 94.3 (July 2016). Number: 3. ISSN: 2469-9950, 2469-9969. DOI: 10.1103/PhysRevB.94.035422. URL: https://link.aps.org/doi/10.1103/PhysRevB.94.035422.

[194] Maciej Misiorny and Józef Barnaś. “Spin polarized transport through a single-molecule magnet: Current-induced magnetic switching”. en. In: *Physical Review B* 76.5 (Aug. 2007). Number: 5. ISSN: 1098-0121, 1550-235X. DOI: 10.1103/PhysRevB.76.054448. URL: https://link.aps.org/doi/10.1103/PhysRevB.76.054448.

[195] J. de Bruijckere et al. “Ground-State Spin Blockade in a Single-Molecule Junction”. en. In: *Physical Review Letters* 122.19 (May 2019). Number: 19. ISSN: 0031-9007, 1079-7114. DOI: 10.1103/PhysRevLett.122.197701. URL: https://link.aps.org/doi/10.1103/PhysRevLett.122.197701.

[196] Justin K. Perron, M. D. Stewart, and Neil M. Zimmerman. “A new regime of Pauli-spin blockade”. In: *Journal of Applied Physics* 119.13 (Apr. 2016). ISSN: 1089-7550. DOI: 10.1063/1.4945393. URL: http://dx.doi.org/10.1063/1.4945393.

[197] Yun-Pil Shim. “Pauli spin blockade in a resonant triple quantum dot molecule”. In: *Journal of Applied Physics* 132.6 (Aug. 2022). ISSN: 1089-7550. DOI: 10.1063/5.0098716. URL: http://dx.doi.org/10.1063/5.0098716.

[198] P. Paufler. “Magnetic and Other Properties of Oxides and Related Compounds”. In: *Crystal Research and Technology* 18.12 (Jan. 1983), pp. 1546–1546. ISSN: 1521-4079. DOI: 10.1002/crat.2170181220. URL: http://dx.doi.org/10.1002/crat.2170181220.

[199] Andrew Gibson, Roger Haydock, and John P. LaFemina. “Stability of vacancy defects in MgO: The role of charge neutrality”. In: *Physical Review B* 50.4 (July 1994), pp. 2582–2592. ISSN: 1095-3795. DOI: 10.1103/physrevb.50.2582. URL: http://dx.doi.org/10.1103/PhysRevB.50.2582.

[200] R. C. Whited and W. C. Walker. “Exciton Spectra of CaO and MgO”. In: *Physical Review Letters* 22.26 (June 1969), pp. 1428–1430. ISSN: 0031-9007. DOI: 10.1103/physrevlett.22.1428. URL: http://dx.doi.org/10.1103/PhysRevLett.22.1428.

[201] G. H. Rosenblatt et al. “Luminescence of F and F+ centers in magnesium oxide”. In: *Physical Review B* 39.14 (May 1989), pp. 10309–10318. ISSN: 0163-1829. DOI: 10.1103/physrevb.39.10309. URL: http://dx.doi.org/10.1103/PhysRevB.39.10309.

[202] Philipp Haas, Fabien Tran, and Peter Blaha. “Calculation of the lattice constant of solids with semilocal functionals”. In: *Physical Review B* 79.8 (Feb. 2009). ISSN: 1550-235X. DOI: 10.1103/physrevb.79.085104. URL: http://dx.doi.org/10.1103/PhysRevB.79.085104.

[203] F. Bonell et al. “Consequences of interfacial Fe-O bonding and disorder in epitaxial Fe/MgO/Fe(001) magnetic tunnel junctions”. In: *Physical Review B* 79.22 (June 2009). ISSN: 1550-235X. DOI: 10.1103/physrevb.79.224405. URL: http://dx.doi.org/10.1103/PhysRevB.79.224405.

[204] H. L. Meyerheim et al. “Geometrical and Compositional Structure at Metal-Oxide Interfaces: MgO on Fe(001)”. In: *Physical Review Letters* 87.7 (July 2001). ISSN: 1079-7114. DOI: 10.1103/physrevlett.87.076102. URL: http://dx.doi.org/10.1103/PhysRevLett.87.076102.

[205] S Yuasa and D D Djayaprawira. “Giant tunnel magnetoresistance in magnetic tunnel junctions with a crystalline MgO(001) barrier”. In: *Journal of Physics D: Applied Physics* 40.21 (Oct. 2007), R337–R354. ISSN: 1361-6463. DOI: 10.1088/0022-3727/40/21/r01. URL: http://dx.doi.org/10.1088/0022-3727/40/21/r01.

[206] Shinji Yuasa et al. “Giant room-temperature magnetoresistance in single-crystal Fe/MgO/Fe magnetic tunnel junctions”. en. In: *Nature Materials* 3.12 (Dec. 2004). Number: 12, pp. 868–871. ISSN: 1476-1122, 1476-4660. DOI: 10.1038/nmat1257. URL: http://www.nature.com/articles/nmat1257.

[207] M. Bowen et al. “Large magnetoresistance in Fe/MgO/FeCo(001) epitaxial tunnel junctions on GaAs(001)”. In: *Applied Physics Letters* 79.11 (Sept. 2001), pp. 1655–1657. ISSN: 1077-3118. DOI: 10.1063/1.1404125. URL: http://dx.doi.org/10.1063/1.1404125.

[208] Stuart S. P. Parkin et al. “Giant tunnelling magnetoresistance at room temperature with MgO (100) tunnel barriers”. en. In: *Nature Materials* 3.12 (Dec. 2004). Number: 12, pp. 862–867. ISSN: 1476-1122, 1476-4660. DOI: 10.1038/nmat1256. URL: http://www.nature.com/articles/nmat1256.

[209] F Schleicher et al. “Consolidated picture of tunnelling spintronics across oxygen vacancy states in MgO”. en. In: *Journal of Physics D: Applied Physics* 52.30 (July 2019). Number: 30, p. 305302. ISSN: 0022-3727, 1361-6463. DOI: 10.1088/1361-6463/ab1f4d. URL: https://iopscience.iop.org/article/10.1088/1361-6463/ab1f4d.

[210] Andy Paul Chen et al. “Effects of B and C doping on tunneling magnetoresistance in CoFe/MgO magnetic tunnel junctions”. en. In: *Physical Review B* 98.4 (July 2018). Number: 4. ISSN: 2469-9950, 2469-9969. DOI: 10.1103/PhysRevB.98.045129. URL: https://link.aps.org/doi/10.1103/PhysRevB.98.045129.

[211] Beata Taudul, M. Bowen, and M. Alouani. “Impact of single and double oxygen vacancies on electronic transport in Fe/MgO/Fe magnetic tunnel junctions”. en. In: *Journal of Applied Physics* 128.14 (Oct. 2020). Number: 14, p. 143902. ISSN: 0021-8979, 1089-7550. DOI: 10.1063/5.0019718. URL: http://aip.scitation.org/doi/10.1063/5.0019718.

[212] H. L. Meyerheim et al. “Surface x-ray diffraction analysis of the MgO/Fe(001) interface: Evidence for an FeO layer”. In: *Physical Review B* 65.14 (Apr. 2002). ISSN: 1095-3795. DOI: 10.1103/physrevb.65.144433. URL: http://dx.doi.org/10.1103/PhysRevB.65.144433.

[213] X.-G. Zhang, W. H. Butler, and Amrit Bandyopadhyay. “Effects of the iron-oxide layer in Fe-FeO-MgO-Fe tunneling junctions”. In: *Physical Review B* 68.9 (Sept. 2003). ISSN: 1095-3795. DOI: 10.1103/physrevb.68.092402. URL: http://dx.doi.org/10.1103/PhysRevB.68.092402.

[214] J. Mathon and A. Umerski. “Theory of resonant tunneling in an epitaxial Fe/Au/MgO/Au/Fe(001) junction”. In: *Physical Review B* 71.22 (June 2005). ISSN: 1550-235X. DOI: 10.1103/physrevb.71.220402. URL: http://dx.doi.org/10.1103/PhysRevB.71.220402.

[215] Yan Wang et al. “First-principles study of Fe/MgO based magnetic tunnel junctions with Mg interlayers”. In: *Physical Review B* 82.5 (Aug. 2010). ISSN: 1550-235X. DOI: 10.1103/physrevb.82.054405. URL: http://dx.doi.org/10.1103/PhysRevB.82.054405.

[216] H. X. Yang et al. “First-principles investigation of the very large perpendicular magnetic anisotropy at Fe/MgO and Co/MgO interfaces”. In: *Physical Review B* 84.5 (Aug. 2011). ISSN: 1550-235X. DOI: 10.1103/physrevb.84.054401. URL: http://dx.doi.org/10.1103/PhysRevB.84.054401.

[217] J. W. Koo et al. “Large perpendicular magnetic anisotropy at Fe/MgO interface”. In: *Applied Physics Letters* 103.19 (Nov. 2013). ISSN: 1077-3118. DOI: 10.1063/1.4828658. URL: http://dx.doi.org/10.1063/1.4828658.

[218] S. H. Liang et al. “Large and robust electrical spin injection into GaAs at zero magnetic field using an ultrathin CoFeB/MgO injector”. In: *Physical Review B* 90.8 (Aug. 2014). ISSN: 1550-235X. DOI: 10.1103/physrevb.90.085310. URL: http://dx.doi.org/10.1103/PhysRevB.90.085310.

[219] J. G. Park et al. “Challenging issues for terra-bit-level perpendicular STT-MRAM”. In: *2014 IEEE International Electron Devices Meeting*. IEEE, Dec. 2014. DOI: 10.1109/iedm.2014.7047081. URL: http://dx.doi.org/10.1109/IEDM.2014.7047081.

[220] S. X. Huang, T. Y. Chen, and C. L. Chien. “Spin polarization of amorphous CoFeB determined by point-contact Andreev reflection”. In: *Applied Physics Letters* 92.24 (June 2008), p. 242509. ISSN: 1077-3118. DOI: 10.1063/1.2949740. URL: http://dx.doi.org/10.1063/1.2949740.

[221] J. Hayakawa et al. “Effect of high annealing temperature on giant tunnel magnetoresistance ratio of CoFeB/MgO/CoFeB magnetic tunnel junctions”. en. In: *Applied Physics Letters* 89.23 (Dec. 2006). Number: 23, p. 232510. ISSN: 0003-6951, 1077-3118. DOI: 10.1063/1.2402904. URL: http://aip.scitation.org/doi/10.1063/1.2402904.

[222] Y. S. Choi et al. “Transmission electron microscopy study on the polycrystalline CoFeB/MgO/CoFeB based magnetic tunnel junction showing a high tunneling magnetoresistance, predicted in single crystal magnetic tunnel junction”. en. In: *Journal of Applied Physics* 101.1 (Jan. 2007). Number: 1, p. 013907. ISSN: 0021-8979, 1089-7550. DOI: 10.1063/1.2407270. URL: http://aip.scitation.org/doi/10.1063/1.2407270.

[223] G. X. Miao et al. “Disturbance of Tunneling Coherence by Oxygen Vacancy in Epitaxial Fe/MgO/Fe Magnetic Tunnel Junctions”. In: *Physical Review Letters* 100.24 (June 2008). ISSN: 1079-7114. DOI: 10.1103/physrevlett.100.246803. URL: http://dx.doi.org/10.1103/PhysRevLett.100.246803.

[224] D. J. Kim et al. “Control of defect-mediated tunneling barrier heights in ultrathin MgO films”. In: *Applied Physics Letters* 97.26 (Dec. 2010). ISSN: 1077-3118. DOI: 10.1063/1.3531652. URL: http://dx.doi.org/10.1063/1.3531652.

[225] F. Schleicher et al. “Localized states in advanced dielectrics from the vantage of spin- and symmetry-polarized tunnelling across MgO”. In: *Nature Communications* 5.1 (Aug. 2014). ISSN: 2041-1723. DOI: 10.1038/ncomms5547. URL: http://dx.doi.org/10.1038/ncomms5547.

[226] F Schleicher et al. “Consolidated picture of tunnelling spintronics across oxygen vacancy states in MgO”. In: *Journal of Physics D: Applied Physics* 52.30 (May 2019), p. 305302. ISSN: 1361-6463. DOI: 10.1088/1361-6463/ab1f4d. URL: http://dx.doi.org/10.1088/1361-6463/ab1f4d.

[227] Beata Taudul et al. “Tunneling Spintronics across MgO Driven by Double Oxygen Vacancies”. In: *Advanced Electronic Materials* 3.7 (May 2017). ISSN: 2199-160X. DOI: 10.1002/aelm.201600390. URL: http://dx.doi.org/10.1002/aelm.201600390.

[228] Zhongchang Wang et al. “Atomic-Scale Structure and Local Chemistry of CoFeB–MgO Magnetic Tunnel Junctions”. In: *Nano Letters* 16.3 (Feb. 2016), pp. 1530–1536. ISSN: 1530-6992. DOI: 10.1021/acs.nanolett.5b03627. URL: http://dx.doi.org/10.1021/acs.nanolett.5b03627.

[229] Jonathan J. Bean and Keith P. McKenna. “Stability of point defects near MgO grain boundaries in FeCoB/MgO/FeCoB magnetic tunnel junctions”. en. In: *Physical Review Materials* 2.12 (Dec. 2018). Number: 12. ISSN: 2475-9953. DOI: 10.1103/PhysRevMaterials.2.125002. URL: https://link.aps.org/doi/10.1103/PhysRevMaterials.2.125002.

[230] Arieh Aviram and Mark A. Ratner. “Molecular rectifiers”. In: *Chemical Physics Letters* 29.2 (Nov. 1974), pp. 277–283. ISSN: 0009-2614. DOI: 10.1016/0009-2614(74)85031-1. URL: http://dx.doi.org/10.1016/0009-2614(74)85031-1.

[231] V. Dediu et al. “Room temperature spin polarized injection in organic semiconductor”. In: *Solid State Communications* 122.3–4 (Apr. 2002), pp. 181–184. ISSN: 0038-1098. DOI: 10.1016/s0038-1098(02)00090-x. URL: http://dx.doi.org/10.1016/S0038-1098(02)00090-X.

[232] Z. H. Xiong et al. “Giant magnetoresistance in organic spin-valves”. In: *Nature* 427.6977 (Feb. 2004), pp. 821–824. ISSN: 1476-4687. DOI: 10.1038/nature02325. URL: http://dx.doi.org/10.1038/nature02325.

[233] T L Francis et al. “Large magnetoresistance at room temperature in semiconducting polymer sandwich devices”. In: *New Journal of Physics* 6 (Dec. 2004), pp. 185–185. ISSN: 1367-2630. DOI: 10.1088/1367-2630/6/1/185. URL: http://dx.doi.org/10.1088/1367-2630/6/1/185.

[234] Ö. Mermer et al. “Large magnetoresistance in nonmagnetic conjugated semiconductor thin film devices”. In: *Physical Review B* 72.20 (Nov. 2005). ISSN: 1550-235X. DOI: 10.1103/physrevb.72.205202. URL: http://dx.doi.org/10.1103/PhysRevB.72.205202.

[235] Lin Huang et al. “High tunneling magnetoresistance induced by symmetry and quantum interference in magnetic molecular junctions”. en. In: *Journal of Materials Chemistry C* 9.18 (2021). Number: 18, pp. 5876–5884. ISSN: 2050-7526, 2050-7534. DOI: 10.1039/D1TC00688F. URL: http://xlink.rsc.org/?DOI=D1TC00688F.

[236] Martin Pope, Charles E. Swenberg, and Martin Pope. *Electronic processes in organic crystals and polymers*. 2nd ed. Monographs on the physics and chemistry of materials #56. New York: Oxford University Press, 1999. ISBN: 9780195129632.

[237] Edgar A. Silinsh. *Organic Molecular Crystals: Their Electronic States*. Ed. by Manuel Cardona, Peter Fulde, and Hans-Joachim Queisser. Vol. 16. Springer Series in Solid-State Sciences. 2024-05-05. Berlin, Heidelberg: Springer Berlin Heidelberg, 1980. ISBN: 9783642814662 9783642814648. DOI: 10.1007/978-3-642-81464-8. URL: https://link.springer.com/10.1007/978-3-642-81464-8.

[238] V. I. Krinichnyi, S. D. Chemerisov, and Ya. S. Lebedev. “EPR and charge-transport studies of polyaniline”. In: *Physical Review B* 55.24 (June 1997), pp. 16233–16244. ISSN: 1095-3795. DOI: 10.1103/physrevb.55.16233. URL: http://dx.doi.org/10.1103/PhysRevB.55.16233.

[239] S. Pramanik et al. “Observation of extremely long spin relaxation times in an organic nanowire spin valve”. In: *Nature Nanotechnology* 2.4 (Mar. 2007), pp. 216–219. ISSN: 1748-3395. DOI: 10.1038/nnano.2007.64. URL: http://dx.doi.org/10.1038/nnano.2007.64.

[240] Xikang Zhao, Saadia T. Chaudhry, and Jianguo Mei. “Heterocyclic Building Blocks for Organic Semiconductors”. In: *Heterocyclic Chemistry in the 21st Century - A Tribute to Alan Katritzky*. Elsevier, 2017, pp. 133–171. ISBN: 9780128111741. DOI: 10.1016/bs.aihch.2016.04.009. URL: http://dx.doi.org/10.1016/bs.aihch.2016.04.009.

[241] Greg Szulczewski, Stefano Sanvito, and Michael Coey. “A spin of their own”. In: *Nature Materials* 8.9 (Sept. 2009), pp. 693–695. ISSN: 1476-4660. DOI: 10.1038/nmat2518. URL: http://dx.doi.org/10.1038/nmat2518.

[242] Dali Sun, Eitan Ehrenfreund, and Z. Valy Vardeny. "The first decade of organic spintronics research". In: *Chem. Commun.* 50.15 (2014), pp. 1781–1793. ISSN: 1364-548X. DOI: 10.1039/c3cc47126h. URL: http://dx.doi.org/10.1039/C3CC47126H.

[243] Sriharsha V. Aradhya and Latha Venkataraman. "Single-molecule junctions beyond electronic transport". en. In: *Nature Nanotechnology* 8.6 (June 2013). Number: 6, pp. 399–410. ISSN: 1748-3387, 1748-3395. DOI: 10.1038/nnano.2013.91. URL: http://www.nature.com/articles/nnano.2013.91.

[244] Michael G. Walter, Alexander B. Rudine, and Carl C. Wamser. "Porphyrins and phthalocyanines in solar photovoltaic cells". In: *Journal of Porphyrins and Phthalocyanines* 14.09 (2010), pp. 759–792. ISSN: 1099-1409. DOI: http://dx.doi.org/10.1142/S1088424610002689. URL: http://dx.doi.org/10.1142/S1088424610002689.

[245] Akitaka Hoshino, Yoshiko Takenaka, and Hideki Miyaji. "Redetermination of the crystal structure of alpha-copper phthalocyanine grown on KCl". In: *Acta Crystallographica Section B Structural Science* 59.3 (May 2003), pp. 393–403. ISSN: 0108-7681. DOI: 10.1107/s010876810300942x. URL: http://dx.doi.org/10.1107/S010876810300942X.

[246] Michele Serri et al. "High-temperature antiferromagnetism in molecular semiconductor thin films and nanostructures". en. In: *Nature Communications* 5.1 (May 2014). Number: 1, p. 3079. ISSN: 2041-1723. DOI: 10.1038/ncomms4079. URL: http://www.nature.com/articles/ncomms4079.

[247] Meng-Sheng Liao and Steve Scheiner. "Electronic structure and bonding in metal phthalocyanines, Metal=Fe, Co, Ni, Cu, Zn, Mg". In: *The Journal of Chemical Physics* 114.22 (June 2001), pp. 9780–9791. ISSN: 1089-7690. DOI: 10.1063/1.1367374. URL: http://dx.doi.org/10.1063/1.1367374.

[248] Xi Chen et al. "Probing Superexchange Interaction in Molecular Magnets by Spin-Flip Spectroscopy and Microscopy". In: *Physical Review Letters* 101.19 (Nov. 2008). ISSN: 1079-7114. DOI: 10.1103/physrevlett.101.197208. URL: http://dx.doi.org/10.1103/PhysRevLett.101.197208.

[249] Michele Serri et al. "High-temperature antiferromagnetism in molecular semiconductor thin films and nanostructures". In: *Nature Communications* 5.1 (Jan. 2014). ISSN: 2041-1723. DOI: 10.1038/ncomms4079. URL: http://dx.doi.org/10.1038/ncomms4079.

[250] C. Barraud et al. "Phthalocyanine based molecular spintronic devices". en. In: *Dalton Transactions* 45.42 (2016). Number: 42, pp. 16694–16699. ISSN: 1477-9226, 1477-9234. DOI: 10.1039/C6DT02467J. URL: http://xlink.rsc.org/?DOI=C6DT02467J.

[251] Kostantine Katcko et al. “Encoding Information on the Excited State of a Molecular Spin Chain”. en. In: *Advanced Functional Materials* 31.15 (Apr. 2021). Number: 15, p. 2009467. ISSN: 1616-301X, 1616-3028. DOI: 10.1002/adfm.202009467. URL: https://onlinelibrary.wiley.com/doi/10.1002/adfm.202009467.

[252] H Vázquez et al. “Dipole formation at metal/PTCDA interfaces: Role of the Charge Neutrality Level”. In: *Europhysics Letters (EPL)* 65.6 (Mar. 2004), pp. 802–808. ISSN: 1286-4854. DOI: 10.1209/epl/i2003-10131-2. URL: http://dx.doi.org/10.1209/epl/i2003-10131-2.

[253] Mickael L. Perrin et al. “Large tunable image-charge effects in single-molecule junctions”. In: *Nature Nanotechnology* 8.4 (Mar. 2013), pp. 282–287. ISSN: 1748-3395. DOI: 10.1038/nnano.2013.26. URL: http://dx.doi.org/10.1038/nnano.2013.26.

[254] Clément Barraud et al. “Unravelling the role of the interface for spin injection into organic semiconductors”. In: *Nature Physics* 6.8 (June 2010), pp. 615–620. ISSN: 1745-2481. DOI: 10.1038/nphys1688. URL: http://dx.doi.org/10.1038/nphys1688.

[255] Stefano Sanvito. “Seeing the spin through”. In: *Nature* 467.7316 (Oct. 2010), pp. 664–665. ISSN: 1476-4687. DOI: 10.1038/467664a. URL: http://dx.doi.org/10.1038/467664a.

[256] Sophie Delprat et al. “Molecular spintronics: the role of spin-dependent hybridization”. In: *Journal of Physics D: Applied Physics* 51.47 (Nov. 2018). 2024-03-20, p. 473001. ISSN: 0022-3727, 1361-6463. DOI: 10.1088/1361-6463/aad9dc. URL: https://iopscience.iop.org/article/10.1088/1361-6463/aad9dc.

[257] Fatima Djeghloul et al. “High Spin Polarization at Ferromagnetic Metal–Organic Interfaces: A Generic Property”. In: *The Journal of Physical Chemistry Letters* 7.13 (July 2016). 2024-03-20, pp. 2310–2315. ISSN: 1948-7185, 1948-7185. DOI: 10.1021/acs.jpclett.6b01112. URL: https://pubs.acs.org/doi/10.1021/acs.jpclett.6b01112.

[258] C. Iacovita et al. “Visualizing the Spin of Individual Cobalt-Phthalocyanine Molecules”. In: *Physical Review Letters* 101.11 (Sept. 2008). ISSN: 1079-7114. DOI: 10.1103/physrevlett.101.116602. URL: http://dx.doi.org/10.1103/PhysRevLett.101.116602.

[259] Stefan Schmaus et al. “Giant magnetoresistance through a single molecule”. In: *Nature Nanotechnology* 6.3 (Feb. 2011), pp. 185–189. ISSN: 1748-3395. DOI: 10.1038/nnano.2011.11. URL: http://dx.doi.org/10.1038/nnano.2011.11.

[260] Stefan Lach et al. “Metal–Organic Hybrid Interface States of A Ferromagnet/Organic Semiconductor Hybrid Junction as Basis For Engineering Spin Injection in Organic Spintronics”. In: *Advanced Functional Materials* 22.5 (Dec. 2011), pp. 989–997. ISSN: 1616-3028. DOI: 10.1002/adfm.201102297. URL: http://dx.doi.org/10.1002/adfm.201102297.

[261] L. Schulz et al. “Erratum: Engineering spin propagation across a hybrid organic/ inorganic interface using a polar layer”. In: *Nature Materials* 10.3 (Feb. 2011), pp. 252–252. ISSN: 1476-4660. DOI: 10.1038/nmat2962. URL: http://dx.doi.org/10.1038/nmat2962.

[262] Karthik V. Raman et al. “Interface-engineered templates for molecular spin memory devices”. In: *Nature* 493.7433 (Jan. 2013), pp. 509–513. ISSN: 1476-4687. DOI: 10.1038/nature11719. URL: http://dx.doi.org/10.1038/nature11719.

[263] Kenji Yoshida et al. “Gate-Tunable Large Negative Tunnel Magnetoresistance in Ni–C60–Ni Single Molecule Transistors”. In: *Nano Letters* 13.2 (Jan. 2013), pp. 481–485. ISSN: 1530-6992. DOI: 10.1021/nl303871x. URL: http://dx.doi.org/10.1021/nl303871x.

[264] F. Djeghloul et al. “Direct observation of a highly spin-polarized organic spinterface at room temperature”. In: *Scientific Reports* 3.1 (Feb. 2013). 2024-03-20, p. 1272. ISSN: 2045-2322. DOI: 10.1038/srep01272. URL: https://www.nature.com/articles/srep01272.

[265] K. Bairagi et al. “Tuning the Magnetic Anisotropy at a Molecule-Metal Interface”. In: *Physical Review Letters* 114.24 (June 2015). ISSN: 1079-7114. DOI: 10.1103/physrevlett.114.247203. URL: http://dx.doi.org/10.1103/PhysRevLett.114.247203.

[266] Fatma Al Ma’Mari et al. “Beating the Stoner criterion using molecular interfaces”. In: *Nature* 524.7563 (Aug. 2015), pp. 69–73. ISSN: 1476-4687. DOI: 10.1038/nature14621. URL: http://dx.doi.org/10.1038/nature14621.

[267] W. H. Meiklejohn and C. P. Bean. “New Magnetic Anisotropy”. In: *Physical Review* 105.3 (Feb. 1957), pp. 904–913. ISSN: 0031-899X. DOI: 10.1103/physrev.105.904. URL: http://dx.doi.org/10.1103/PhysRev.105.904.

[268] J Nogués and Ivan K Schuller. “Exchange bias”. In: *Journal of Magnetism and Magnetic Materials* 192.2 (Feb. 1999), pp. 203–232. ISSN: 0304-8853. DOI: 10.1016/s0304-8853(98)00266-2. URL: http://dx.doi.org/10.1016/S0304-8853(98)00266-2.

[269] P.K. Manna and S.M. Yusuf. “Two interface effects: Exchange bias and magnetic proximity”. In: *Physics Reports* 535.2 (Feb. 2014). 2024-04-19, pp. 61–99. ISSN: 03701573. DOI: 10.1016/j.physrep.2013.10.002. URL: https://linkinghub.elsevier.com/retrieve/pii/S0370157313003773.

[270] Masakiyo Tsunoda et al. “Magnetic anisotropy and rotational hysteresis loss in exchange coupled Ni–Fe/Mn–Ir films”. In: *Journal of Applied Physics* 87.9 (May 2000), pp. 4375–4388. ISSN: 1089-7550. DOI: 10.1063/1.373081. URL: http://dx.doi.org/10.1063/1.373081.

[271] Miguel Kiwi. “Exchange bias theory”. In: *Journal of Magnetism and Magnetic Materials* 234.3 (Sept. 2001), pp. 584–595. ISSN: 0304-8853. DOI: 10.1016/s0304-8853(01)00421-8. URL: http://dx.doi.org/10.1016/S0304-8853(01)00421-8.

[272] Manuel Gruber et al. “Exchange bias and room-temperature magnetic order in molecular layers”. In: *Nature Materials* 14.10 (July 2015), pp. 981–984. ISSN: 1476-4660. DOI: 10.1038/nmat4361. URL: http://dx.doi.org/10.1038/nmat4361.

[273] Clément Barraud et al. “Unidirectional Spin-Dependent Molecule-Ferromagnet Hybridized States Anisotropy in Cobalt Phthalocyanine Based Magnetic Tunnel Junctions”. In: *Physical Review Letters* 114.20 (May 2015). ISSN: 1079-7114. DOI: 10.1103/physrevlett.114.206603. URL: http://dx.doi.org/10.1103/PhysRevLett.114.206603.

[274] C. Barraud et al. “Phthalocyanine based molecular spintronic devices”. In: *Dalton Transactions* 45.42 (2016), pp. 16694–16699. ISSN: 1477-9234. DOI: http://dx.doi.org/10.1039/C6DT02467J. URL: http://dx.doi.org/10.1039/C6DT02467J.

[275] Junhyeon Jo et al. “Molecular Tunability of Magnetic Exchange Bias and Asymmetrical Magnetotransport in Metalloporphyrin/Co Hybrid Bilayers”. In: *ACS Nano* 13.1 (Dec. 2018), pp. 894–903. ISSN: 1936-086X. DOI: 10.1021/acsnano.8b08689. URL: http://dx.doi.org/10.1021/acsnano.8b08689.

[276] Junhyeon Jo et al. “Emergence of Multispinterface and Antiferromagnetic Molecular Exchange Bias via Molecular Stacking on a Ferromagnetic Film”. In: *Advanced Functional Materials* 30.11 (Jan. 2020). ISSN: 1616-3028. DOI: 10.1002/adfm.201908499. URL: http://dx.doi.org/10.1002/adfm.201908499.

[277] Quentin Arnoux et al. “Controlling the magnetic exchange coupling in hybrid heterojunctions via spacer layers of pi-conjugated molecules”. In: *Physical Review B* 99.14 (Apr. 2019). ISSN: 2469-9969. DOI: 10.1103/physrevb.99.144405. URL: http://dx.doi.org/10.1103/PhysRevB.99.144405.

[278] Victoria E. Campbell et al. “Engineering the magnetic coupling and anisotropy at the molecule–magnetic surface interface in molecular spintronic devices”. In: *Nature Communications* 7.1 (Dec. 2016). ISSN: 2041-1723. DOI: 10.1038/ncomms13646. URL: http://dx.doi.org/10.1038/ncomms13646.

[279] Patrick P. Potts. *Quantum Thermodynamics*. 2024. DOI: 10.48550/ARXIV.2406.19206. URL: https://arxiv.org/abs/2406.19206.

[280] Md. Manirul Ali, Wei-Ming Huang, and Wei-Min Zhang. "Quantum thermodynamics of single particle systems". In: *Scientific Reports* 10.1 (Aug. 2020). ISSN: 2045-2322. DOI: 10.1038/s41598-020-70450-y. URL: http://dx.doi.org/10.1038/s41598-020-70450-y.

[281] Heinz-Peter Breuer and Francesco Petruccione. *The theory of open quantum systems*. eng. Repr. Oxford: Clarendon Press, 2010. ISBN: 9780199213900.

[282] John von Neumann. *Mathematical Foundations of Quantum Mechanics: New Edition*. Ed. by Nicholas A. Wheeler. Princeton University Press, Apr. 2018. ISBN: 9781400889921. DOI: 10.1515/9781400889921. URL: http://dx.doi.org/10.1515/9781400889921.

[283] Ruth E. Kastner. *A Physical Basis for the Second Law of Thermodynamics: Quantum Nonunitarity*. en. preprint. 2023-04-24. PHYSICAL SCIENCES, Jan. 2017. DOI: 10.20944/preprints201701.0108.v1. URL: https://www.preprints.org/manuscript/201701.0108/v1.

[284] Francesco Campaioli, Jared H. Cole, and Harini Hapuarachchi. "Quantum Master Equations: Tips and Tricks for Quantum Optics, Quantum Computing, and Beyond". In: *PRX Quantum* 5.2 (June 2024). ISSN: 2691-3399. DOI: 10.1103/prxquantum.5.020202. URL: http://dx.doi.org/10.1103/PRXQuantum.5.020202.

[285] Sadao Nakajima. "On Quantum Theory of Transport Phenomena: Steady Diffusion". In: *Progress of Theoretical Physics* 20.6 (Dec. 1958), pp. 948–959. ISSN: 0033-068X. DOI: 10.1143/ptp.20.948. URL: http://dx.doi.org/10.1143/PTP.20.948.

[286] Robert Zwanzig. "Ensemble Method in the Theory of Irreversibility". In: *The Journal of Chemical Physics* 33.5 (Nov. 1960), pp. 1338–1341. ISSN: 1089-7690. DOI: 10.1063/1.1731409. URL: http://dx.doi.org/10.1063/1.1731409.

[287] Ronnie Kosloff. "Quantum Thermodynamics: A Dynamical Viewpoint". In: *Entropy* 15.12 (May 2013), pp. 2100–2128. ISSN: 1099-4300. DOI: 10.3390/e15062100. URL: http://dx.doi.org/10.3390/e15062100.

[288] Juzar Thingna, Jian-Sheng Wang, and Peter Hänggi. "Generalized Gibbs state with modified Redfield solution: Exact agreement up to second order". In: *The Journal of Chemical Physics* 136.19 (May 2012). ISSN: 1089-7690. DOI: 10.1063/1.4718706. URL: http://dx.doi.org/10.1063/1.4718706.

[289] Gavin McCauley et al. "Accurate Lindblad-form master equation for weakly damped quantum systems across all regimes". en. In: *npj Quantum Information* 6.1 (Aug. 2020). Number: 1, p. 74. ISSN: 2056-6387. DOI: 10.1038/s41534-020-00299-6. URL: https://www.nature.com/articles/s41534-020-00299-6.

[290] Yi-Neng Zhou. "Generalized Lindblad master equation for measurement-induced phase transition". en. In: *SciPost Physics Core* 6.1 (Mar. 2023). Number: 1. ISSN: 2666-9366. DOI: 10.21468/SciPostPhysCore.6.1.023. URL: https://scipost.org/10.21468/SciPostPhysCore.6.1.023.

[291] S. Wenderoth, H.-P. Breuer, and M. Thoss. "Quantifying the influence of the initial state on the dynamics of an open quantum system". en. In: *Physical Review A* 107.2 (Feb. 2023). Number: 2. ISSN: 2469-9926, 2469-9934. DOI: 10.1103/PhysRevA.107.022211. URL: https://link.aps.org/doi/10.1103/PhysRevA.107.022211.

[292] Davide Nigro. "On the uniqueness of the steady-state solution of the Lindblad Gorini Kossakowski Sudarshan equation". en. In: *Journal of Statistical Mechanics: Theory and Experiment* 2019.4 (Apr. 2019). Number: 4, p. 043202. ISSN: 1742-5468. DOI: 10.1088/1742-5468/ab0c1c. URL: https://iopscience.iop.org/article/10.1088/1742-5468/ab0c1c.

[293] Bernd Michael Fernengel and Barbara Drossel. "Explicit expressions for stationary states of the Lindblad equation for a finite state space". en. In: *Journal of Physics A: Mathematical and Theoretical* 56.38 (Sept. 2023). Number: 38, p. 385205. ISSN: 1751-8113, 1751-8121. DOI: 10.1088/1751-8121/acee35. URL: https://iopscience.iop.org/article/10.1088/1751-8121/acee35.

[294] Guy Cohen and Michael Galperin. "Green's function methods for single molecule junctions". In: *The Journal of Chemical Physics* 152.9 (Mar. 2020), p. 090901. ISSN: 1089-7690. DOI: 10.1063/1.5145210. URL: http://dx.doi.org/10.1063/1.5145210.

[295] Vincent F. Kershaw and Daniel S. Kosov. "Nonequilibrium Green's function theory for nonadiabatic effects in quantum electron transport". In: *The Journal of Chemical Physics* 147.22 (Dec. 2017). ISSN: 1089-7690. DOI: 10.1063/1.5007071. URL: http://dx.doi.org/10.1063/1.5007071.

[296] Michael Iv, Saar Rahav, and Uri Peskin. "Emergence of Boltzmann Subspaces in Open Quantum Systems Far from Equilibrium". en. In: *Physical Review Letters* 132.11 (Mar. 2024). Number: 11, p. 110401. ISSN: 0031-9007, 1079-7114. DOI: 10.1103/PhysRevLett.132.110401. URL: https://link.aps.org/doi/10.1103/PhysRevLett.132.110401.

[297] John Goold et al. "The role of quantum information in thermodynamics—a topical review". en. In: *Journal of Physics A: Mathematical and Theoretical* 49.14 (Apr. 2016). 2024-05-15, p. 143001. ISSN: 1751-8113, 1751-8121. DOI: 10.1088/1751-8113/49/14/143001. URL: https://iopscience.iop.org/article/10.1088/1751-8113/49/14/143001.

[298] Manabendra Nath Bera et al. “Thermodynamics as a Consequence of Information Conservation”. en. In: *Quantum* 3 (Feb. 2019). arXiv:1707.01750 [quant-ph], p. 121. ISSN: 2521-327X. DOI: 10.22331/q-2019-02-14-121. URL: http://arxiv.org/abs/1707.01750.

[299] Dominik Šafránek, J. M. Deutsch, and Anthony Aguirre. “Quantum coarse-grained entropy and thermalization in closed systems”. en. In: *Physical Review A* 99.1 (Jan. 2019). Number: 1 arXiv:1803.00665 [cond-mat, physics:quant-ph], p. 012103. ISSN: 2469-9926, 2469-9934. DOI: 10.1103/PhysRevA.99.012103. URL: http://arxiv.org/abs/1803.00665.

[300] Mary Beth Ruskai. “Inequalities for quantum entropy: A review with conditions for equality”. In: *Journal of Mathematical Physics* 43.9 (Sept. 2002), pp. 4358–4375. ISSN: 1089-7658. DOI: 10.1063/1.1497701. URL: http://dx.doi.org/10.1063/1.1497701.

[301] DÉNES PETZ. “Monotonicity of quantum relative entropy revisited”. In: *Reviews in Mathematical Physics* 01 (Mar. 2003), pp. 79–91. ISSN: 1793-6659. DOI: 10.1142/s0129055x03001576. URL: https://worldscientific.com/doi/10.1142/S0129055X03001576.

[302] A. E Allahverdyan, R Balian, and Th. M Nieuwenhuizen. “Maximal work extraction from finite quantum systems”. In: *Europhysics Letters (EPL)* 67.4 (Aug. 2004). Number: 4, pp. 565–571. ISSN: 0295-5075, 1286-4854. DOI: 10.1209/epl/i2004-10101-2. URL: https://iopscience.iop.org/article/10.1209/epl/i2004-10101-2.

[303] Gianluca Francica et al. “Daemonic ergotropy: enhanced work extraction from quantum correlations”. en. In: *npj Quantum Information* 3.1 (Dec. 2017). Number: 1. ISSN: 2056-6387. DOI: 10.1038/s41534-017-0012-8. URL: http://www.nature.com/articles/s41534-017-0012-8.

[304] Bariş Çakmak. “Ergotropy from coherences in an open quantum system”. en. In: *Physical Review E* 102.4 (Oct. 2020). Number: 4. ISSN: 2470-0045, 2470-0053. DOI: 10.1103/PhysRevE.102.042111. URL: https://link.aps.org/doi/10.1103/PhysRevE.102.042111.

[305] Jia-shun Yan and Jun Jing. “Charging by Quantum Measurement”. In: *Physical Review Applied* 19.6 (June 2023). ISSN: 2331-7019. DOI: 10.1103/physrevapplied.19.064069. URL: http://dx.doi.org/10.1103/PhysRevApplied.19.064069.

[306] Jukka P. Pekola. “Quantum thermodynamics at low temperatures”. In: *Europhysics News* 52.3 (2021), pp. 15–17. ISSN: 1432-1092. DOI: 10.1051/epn/2021302. URL: http://dx.doi.org/10.1051/epn/2021302.

[307] Patryk Lipka-Bartosik, Martí Perarnau-Llobet, and Nicolas Brunner. "Operational Definition of the Temperature of a Quantum State". In: *Physical Review Letters* 130.4 (Jan. 2023). ISSN: 1079-7114. DOI: 10.1103/physrevlett.130.040401. URL: http://dx.doi.org/10.1103/PhysRevLett.130.040401.

[308] Charles A. Stafford. "Local temperature of an interacting quantum system far from equilibrium". en. In: *Physical Review B* 93.24 (June 2016). Number: 24. ISSN: 2469-9950, 2469-9969. DOI: 10.1103/PhysRevB.93.245403. URL: https://link.aps.org/doi/10.1103/PhysRevB.93.245403.

[309] Charles A. Stafford and Abhay Shastry. "Local entropy of a nonequilibrium fermion system". en. In: *The Journal of Chemical Physics* 146.9 (Mar. 2017). Number: 9, p. 092324. ISSN: 0021-9606, 1089-7690. DOI: 10.1063/1.4975810. URL: http://aip.scitation.org/doi/10.1063/1.4975810.

[310] Mohit Lal Bera et al. "Steady-state quantum thermodynamics with synthetic negative temperatures". In: *Physical Review Research* 6.1 (Mar. 2024). ISSN: 2643-1564. DOI: 10.1103/physrevresearch.6.013318. URL: http://dx.doi.org/10.1103/PhysRevResearch.6.013318.

[311] S. Braun et al. "Negative Absolute Temperature for Motional Degrees of Freedom". en. In: *Science* 339.6115 (Jan. 2013). Number: 6115, pp. 52–55. ISSN: 0036-8075, 1095-9203. DOI: 10.1126/science.1227831. URL: https://www.science.org/doi/10.1126/science.1227831.

[312] Roie Dann and Ronnie Kosloff. "Unification of the first law of quantum thermodynamics". In: *New Journal of Physics* 25.4 (Apr. 2023), p. 043019. ISSN: 1367-2630. DOI: 10.1088/1367-2630/acc967. URL: http://dx.doi.org/10.1088/1367-2630/acc967.

[313] Krzysztof Ptaszyński and Massimiliano Esposito. "Thermodynamics of Quantum Information Flows". en. In: *Physical Review Letters* 122.15 (Apr. 2019). Number: 15, p. 150603. ISSN: 0031-9007, 1079-7114. DOI: 10.1103/PhysRevLett.122.150603. URL: https://link.aps.org/doi/10.1103/PhysRevLett.122.150603.

[314] Parth Kumar and Charles A. Stafford. *On the First Law of Thermodynamics in Time-Dependent Open Quantum Systems*. 2022. DOI: 10.48550/ARXIV.2208.06544. URL: https://arxiv.org/abs/2208.06544.

[315] Curt A. Moyer. "Timelines and Quantum Time Operators". en. In: *Foundations of Physics* 45.4 (Apr. 2015). Number: 4, pp. 382–403. ISSN: 0015-9018, 1572-9516. DOI: 10.1007/s10701-015-9870-0. URL: http://link.springer.com/10.1007/s10701-015-9870-0.

[316] Joan A. Vaccaro. "Quantum asymmetry between time and space". en. In: *Proceedings of the Royal Society A: Mathematical, Physical and Engineering Sciences* 472.2185 (Jan. 2016). 2023-11-07, p. 20150670. ISSN: 1364-5021, 1471-2946. DOI: 10.1098/rspa.2015.0670. URL: http://arxiv.org/abs/1502.04012.

[317] T. Goto, K. Yamaguchi, and N. Sudo. "On the Time Operator in Quantum Mechanics: Three Typical Examples". In: *Progress of Theoretical Physics* 66.5 (Nov. 1981), pp. 1525–1538. ISSN: 1347-4081. DOI: 10.1143/ptp.66.1525. URL: http://dx.doi.org/10.1143/PTP.66.1525.

[318] Kurt Jacobs. "Quantum measurement and the first law of thermodynamics: The energy cost of measurement is the work value of the acquired information". en. In: *Physical Review E* 86.4 (Oct. 2012). Number: 4, p. 040106. ISSN: 1539-3755, 1550-2376. DOI: 10.1103/PhysRevE.86.040106. URL: https://link.aps.org/doi/10.1103/PhysRevE.86.040106.

[319] Spencer Rogers and Andrew N. Jordan. "Postselection and quantum energetics". In: *Physical Review A* 106.5 (Nov. 2022). ISSN: 2469-9926. DOI: 10.1103/PhysRevA.106.052214.

[320] Camille L. Latune and Cyril Elouard. *Thermodynamically reversible quantum measurements and related work costs*. en. Issue: arXiv:2402.16037 arXiv:2402.16037 [quant-ph]. Feb. 2024. URL: http://arxiv.org/abs/2402.16037.

[321] Kaixun Tu and Qing Wang. *Causality and a possible interpretation of quantum mechanics*. en. Issue: arXiv:2402.05450 arXiv:2402.05450 [quant-ph]. Feb. 2024. URL: http://arxiv.org/abs/2402.05450.

[322] Edgar Shaghoulian. *Quantum gravity and the measurement problem in quantum mechanics*. 2023. DOI: 10.48550/ARXIV.2305.10635. URL: https://arxiv.org/abs/2305.10635.

[323] Peter Talkner and Peter Hänggi. "Aspects of quantum work". en. In: *Physical Review E* 93.2 (Feb. 2016). Number: 2. ISSN: 2470-0045, 2470-0053. DOI: 10.1103/PhysRevE.93.022131. URL: https://link.aps.org/doi/10.1103/PhysRevE.93.022131.

[324] S. Alipour et al. "Correlations in quantum thermodynamics: Heat, work, and entropy production". In: *Scientific Reports* 6.1 (Oct. 2016). ISSN: 2045-2322. DOI: 10.1038/srep35568. URL: http://dx.doi.org/10.1038/srep35568.

[325] Philipp Strasberg and Andreas Winter. "First and Second Law of Quantum Thermodynamics: A Consistent Derivation Based on a Microscopic Definition of Entropy". In: *PRX Quantum* 2.3 (Aug. 2021). ISSN: 2691-3399. DOI: 10.1103/prxquantum.2.030202. URL: http://dx.doi.org/10.1103/PRXQuantum.2.030202.

[326] Wellington L. Ribeiro, Gabriel T. Landi, and Fernando L. Semião. "Quantum thermodynamics and work fluctuations with applications to magnetic resonance". In: *American Journal of Physics* 84.12 (Dec. 2016), pp. 948–957. ISSN: 1943-2909. DOI: 10.1119/1.4964111. URL: http://dx.doi.org/10.1119/1.4964111.

[327] Fernando Brandão et al. “The second laws of quantum thermodynamics”. In: *Proceedings of the National Academy of Sciences* 112.11 (Feb. 2015), pp. 3275–3279. ISSN: 1091-6490. DOI: 10.1073/pnas.1411728112. URL: http://dx.doi.org/10.1073/pnas.1411728112.

[328] Herbert Spohn. “Entropy production for quantum dynamical semigroups”. en. In: *Journal of Mathematical Physics* 19.5 (May 1978). Number: 5, pp. 1227–1230. ISSN: 0022-2488, 1089-7658. DOI: 10.1063/1.523789. URL: http://aip.scitation.org/doi/10.1063/1.523789.

[329] Adam M. Kaufman et al. “Quantum thermalization through entanglement in an isolated many-body system”. en. In: *Science* 353.6301 (Aug. 2016). Number: 6301, pp. 794–800. ISSN: 0036-8075, 1095-9203. DOI: 10.1126/science.aaf6725. URL: https://www.science.org/doi/10.1126/science.aaf6725.

[330] I. Prigogine and Cl. George. “The second law as a selection principle: The microscopic theory of dissipative processes in quantum systems”. en. In: *Proceedings of the National Academy of Sciences* 80.14 (July 1983). Number: 14, pp. 4590–4594. ISSN: 0027-8424, 1091-6490. DOI: 10.1073/pnas.80.14.4590. URL: https://pnas.org/doi/full/10.1073/pnas.80.14.4590.

[331] Göran Lindblad. “Entropy, information and quantum measurements”. en. In: *Communications in Mathematical Physics* 33.4 (Dec. 1973). Number: 4, pp. 305–322. ISSN: 0010-3616, 1432-0916. DOI: 10.1007/BF01646743. URL: http://link.springer.com/10.1007/BF01646743.

[332] Masashi Ban. “State reduction, information and entropy in quantum measurement processes”. en. In: *Journal of Physics A: Mathematical and General* 32.9 (Mar. 1999). Number: 9, pp. 1643–1665. ISSN: 0305-4470, 1361-6447. DOI: 10.1088/0305-4470/32/9/012. URL: https://iopscience.iop.org/article/10.1088/0305-4470/32/9/012.

[333] Shunlong Luo. “Information conservation and entropy change in quantum measurements”. en. In: *Physical Review A* 82.5 (Nov. 2010). Number: 5, p. 052103. ISSN: 1050-2947, 1094-1622. DOI: 10.1103/PhysRevA.82.052103. URL: https://link.aps.org/doi/10.1103/PhysRevA.82.052103.

[334] Noam Erez. “Thermodynamics of projective quantum measurements”. In: *Physica Scripta* T151 (Nov. 2012). 2023-04-17, p. 014028. ISSN: 0031-8949, 1402-4896. DOI: 10.1088/0031-8949/2012/T151/014028. URL: https://doi.org/10.1088/0031-8949/2012/T151/014028.

[335] Stuart Kauffman. “Is There a Fourth Law for Non-Ergodic Systems That Do Work to Construct Their Expanding Phase Space?” en. In: *Entropy* 24.10 (Sept. 2022). Number: 10, p. 1383. ISSN: 1099-4300. DOI: 10.3390/e24101383. URL: https://www.mdpi.com/1099-4300/24/10/1383.

[336] Milivoje M. Kostic. "The Second Law and Entropy Misconceptions Demystified". In: *Entropy* 22.6 (June 2020), p. 648. ISSN: 1099-4300. DOI: 10.3390/e22060648. URL: http://dx.doi.org/10.3390/e22060648.

[337] G. Parisi. "Infinite Number of Order Parameters for Spin-Glasses". In: *Physical Review Letters* 43.23 (Dec. 1979), pp. 1754–1756. ISSN: 0031-9007. DOI: 10.1103/physrevlett.43.1754. URL: http://dx.doi.org/10.1103/PhysRevLett.43.1754.

[338] Massimo Bernaschi et al. "Strong ergodicity breaking in aging of mean-field spin glasses". In: *Proceedings of the National Academy of Sciences* 117.30 (July 2020), pp. 17522–17527. ISSN: 1091-6490. DOI: 10.1073/pnas.1910936117. URL: http://dx.doi.org/10.1073/pnas.1910936117.

[339] Koun Shirai. "A thermodynamic description of the glass state and the glass transition". In: *Journal of Physics Communications* 4.8 (Aug. 2020), p. 085015. ISSN: 2399-6528. DOI: 10.1088/2399-6528/abae16. URL: http://dx.doi.org/10.1088/2399-6528/abae16.

[340] Michael Saccone et al. "Real-space observation of ergodicity transitions in artificial spin ice". In: *Nature Communications* 14.1 (Sept. 2023). ISSN: 2041-1723. DOI: 10.1038/s41467-023-41235-4. URL: http://dx.doi.org/10.1038/s41467-023-41235-4.

[341] John C. Mauro and Morten M. Smedskjaer. "Statistical mechanics of glass". In: *Journal of Non-Crystalline Solids* 396–397 (Aug. 2014), pp. 41–53. ISSN: 0022-3093. DOI: 10.1016/j.jnoncrysol.2014.04.009. URL: http://dx.doi.org/10.1016/j.jnoncrysol.2014.04.009.

[342] Jean-Luc Garden and Hervé Guillou. *Thermodynamics of Glasses*. Feb. 2021. DOI: 10.1002/9781118801017.ch3.2. URL: http://dx.doi.org/10.1002/9781118801017.ch3.2.

[343] Kaonan Micadei et al. "Reversing the direction of heat flow using quantum correlations". en. In: *Nature Communications* 10.1 (June 2019). Number: 1. ISSN: 2041-1723. DOI: 10.1038/s41467-019-10333-7. URL: https://www.nature.com/articles/s41467-019-10333-7.

[344] Germano D'Abramo. "The peculiar status of the second law of thermodynamics and the quest for its violation". en. In: *Studies in History and Philosophy of Science Part B: Studies in History and Philosophy of Modern Physics* 43.4 (Nov. 2012). Number: 4, pp. 226–235. ISSN: 13552198. DOI: 10.1016/j.shpsb.2012.05.004. URL: https://linkinghub.elsevier.com/retrieve/pii/S1355219812000421.

[345] Philippe Guillemant, Cherifa Abid, and Marc Medale. *Characterizing the transition from classical to quantum as an irreversible loss of physical information*. 2013. DOI: 10.48550/ARXIV.1311.5349. URL: https://arxiv.org/abs/1311.5349.

[346] Philippe Guillemant, Marc Medale, and Cherifa Abid. “A discrete classical space–time could require 6 extra-dimensions”. en. In: *Annals of Physics* 388 (Jan. 2018). 2023-03-16, pp. 428–442. ISSN: 00034916. DOI: 10.1016/j.aop.2017.11.023. URL: https://linkinghub.elsevier.com/retrieve/pii/S000349161730338X.

[347] Julian De Vuyst et al. *Gravitational entropy is observer-dependent*. 2024. arXiv: 2405.00114 [hep-th].

[348] E. T. Jaynes. “Gibbs vs Boltzmann Entropies”. In: *American Journal of Physics* 33.5 (May 1965), pp. 391–398. ISSN: 1943-2909. DOI: 10.1119/1.1971557. URL: http://dx.doi.org/10.1119/1.1971557.

[349] Christopher W Wächtler et al. “Stochastic thermodynamics of self-oscillations: the electron shuttle”. In: *New Journal of Physics* 21.7 (July 2019), p. 073009. ISSN: 1367-2630. DOI: 10.1088/1367-2630/ab2727. URL: http://dx.doi.org/10.1088/1367-2630/ab2727.

[350] Stephen Wolfram. *The second law: resolving the mystery of the second law of thermodynamics*. Champaign, IL: Wolfram Media, Inc, 2023. ISBN: 9781579550837.

[351] M. O. Scully. “Extracting Work from a Single Heat Bath via Vanishing Quantum Coherence”. en. In: *Science* 299.5608 (Feb. 2003). Number: 5608, pp. 862–864. ISSN: 00368075, 10959203. DOI: 10.1126/science.1078955. URL: https://www.sciencemag.org/lookup/doi/10.1126/science.1078955.

[352] Deniz Türkpençe and Özgür E. Müstecaplioğlu. “Quantum fuel with multilevel atomic coherence for ultrahigh specific work in a photonic Carnot engine”. In: *Physical Review E* 93.1 (Jan. 2016). ISSN: 2470-0053. DOI: 10.1103/physreve.93.012145. URL: http://dx.doi.org/10.1103/PhysRevE.93.012145.

[353] Federico Amato et al. “Heating and cooling processes via phaseonium-driven dynamics of cascade systems”. In: *Physical Review A* 109.4 (Apr. 2024). ISSN: 2469-9934. DOI: 10.1103/physreva.109.043705. URL: http://dx.doi.org/10.1103/PhysRevA.109.043705.

[354] Gonzalo Manzano et al. “Entropy production and thermodynamic power of the squeezed thermal reservoir”. en. In: *Physical Review E* 93.5 (May 2016). Number: 5. ISSN: 2470-0045, 2470-0053. DOI: 10.1103/PhysRevE.93.052120. URL: https://link.aps.org/doi/10.1103/PhysRevE.93.052120.

[355] Gonzalo Manzano. “Squeezed thermal reservoir as a generalized equilibrium reservoir”. en. In: *Physical Review E* 98.4 (Oct. 2018). Number: 4, p. 042123. ISSN: 2470-0045, 2470-0053. DOI: 10.1103/PhysRevE.98.042123. URL: https://link.aps.org/doi/10.1103/PhysRevE.98.042123.

[356] Jan Klaers et al. “Squeezed Thermal Reservoirs as a Resource for a Nanomechanical Engine beyond the Carnot Limit”. en. In: *Physical Review X* 7.3 (Sept. 2017). Number: 3. ISSN: 2160-3308. DOI: 10.1103/PhysRevX.7.031044. URL: https://link.aps.org/doi/10.1103/PhysRevX.7.031044.

[357] Federico Centrone, Luca Mancino, and Mauro Paternostro. “Charging batteries with quantum squeezing”. In: *Physical Review A* 108.5 (Nov. 2023). ISSN: 2469-9934. DOI: 10.1103/physreva.108.052213. URL: http://dx.doi.org/10.1103/PhysRevA.108.052213.

[358] Wolfgang Niedenzu et al. “Quantum engine efficiency bound beyond the second law of thermodynamics”. en. In: *Nature Communications* 9.1 (Dec. 2018). Number: 1. ISSN: 2041-1723. DOI: 10.1038/s41467-017-01991-6. URL: http://www.nature.com/articles/s41467-017-01991-6.

[359] Sameer Sonar et al. “Squeezing Enhances Quantum Synchronization”. en. In: *Physical Review Letters* 120.16 (Apr. 2018). Number: 16. ISSN: 0031-9007, 1079-7114. DOI: 10.1103/PhysRevLett.120.163601. URL: https://link.aps.org/doi/10.1103/PhysRevLett.120.163601.

[360] Sareh Shahidani. “Thermodynamic forces and flows between a thermal bath and a squeezed thermal bath: Application to optomechanical systems”. In: *Physical Review A* 105.6 (June 2022). ISSN: 2469-9934. DOI: 10.1103/physreva.105.063516. URL: http://dx.doi.org/10.1103/PhysRevA.105.063516.

[361] Joan A. Vaccaro and Stephen M. Barnett. “Information erasure without an energy cost”. en. In: *Proceedings of the Royal Society A: Mathematical, Physical and Engineering Sciences* 467.2130 (June 2011). Number: 2130, pp. 1770–1778. ISSN: 1364-5021, 1471-2946. DOI: 10.1098/rspa.2010.0577. URL: https://doi.org/10.1098/rspa.2010.0577.

[362] Yelena Guryanova et al. “Thermodynamics of quantum systems with multiple conserved quantities”. en. In: *Nature Communications* 7.1 (July 2016). Number: 1. ISSN: 2041-1723. DOI: 10.1038/ncomms12049. URL: https://www.nature.com/articles/ncomms12049.

[363] Edward Bormashenko. “Entropy, Information, and Symmetry; Ordered Is Symmetrical, II: System of Spins in the Magnetic Field”. en. In: *Entropy* 22.2 (Feb. 2020). Number: 2, p. 235. ISSN: 1099-4300. DOI: 10.3390/e22020235. URL: https://www.mdpi.com/1099-4300/22/2/235.

[364] Shayan Majidy. *Noncommuting charges' effect on the thermalization of local observables*. 2024. arXiv: 2403.13046 [quant-ph].

[365] Nicole Yunger Halpern, Michael E. Beverland, and Amir Kalev. "Noncommuting conserved charges in quantum many-body thermalization". en. In: *Physical Review E* 101.4 (Apr. 2020). Number: 4, p. 042117. ISSN: 2470-0045, 2470-0053. DOI: 10.1103/PhysRevE.101.042117. URL: https://link.aps.org/doi/10.1103/PhysRevE.101.042117.

[366] Gonzalo Manzano, Juan M.R. Parrondo, and Gabriel T. Landi. "Non-Abelian Quantum Transport and Thermosqueezing Effects". en. In: *PRX Quantum* 3.1 (Jan. 2022). Number: 1, p. 010304. ISSN: 2691-3399. DOI: 10.1103/PRXQuantum.3.010304. URL: https://link.aps.org/doi/10.1103/PRXQuantum.3.010304.

[367] Shayan Majidy et al. "Noncommuting conserved charges in quantum thermodynamics and beyond". en. In: *Nature Reviews Physics* (Oct. 2023). arXiv:2306.00054 [cond-mat, physics:hep-lat, physics:hep-th, physics:nucl-th, physics:quant-ph]. ISSN: 2522-5820. DOI: 10.1038/s42254-023-00641-9. URL: http://arxiv.org/abs/2306.00054.

[368] Nicole Yunger Halpern et al. "Microcanonical and resource-theoretic derivations of the thermal state of a quantum system with noncommuting charges". en. In: *Nature Communications* 7.1 (July 2016). Number: 1 arXiv:1512.01189 [cond-mat, physics:quant-ph], p. 12051. ISSN: 2041-1723. DOI: 10.1038/ncomms12051. URL: http://arxiv.org/abs/1512.01189.

[369] Florian Kranzl et al. "Experimental Observation of Thermalization with Noncommuting Charges". In: *PRX Quantum* 4.2 (Apr. 2023). ISSN: 2691-3399. DOI: 10.1103/prxquantum.4.020318. URL: http://dx.doi.org/10.1103/PRXQuantum.4.020318.

[370] Mohamed Amine Zoui et al. "A Review on Thermoelectric Generators: Progress and Applications". In: *Energies* 13.14 (July 2020), p. 3606. ISSN: 1996-1073. DOI: 10.3390/en13143606. URL: http://dx.doi.org/10.3390/en13143606.

[371] Cristina Artini et al. "Roadmap on thermoelectricity". In: *Nanotechnology* 34.29 (May 2023), p. 292001. ISSN: 1361-6528. DOI: 10.1088/1361-6528/acca88. URL: http://dx.doi.org/10.1088/1361-6528/acca88.

[372] Byeongmoon Lee et al. "High-performance compliant thermoelectric generators with magnetically self-assembled soft heat conductors for self-powered wearable electronics". In: *Nature Communications* 11.1 (Nov. 2020). ISSN: 2041-1723. DOI: 10.1038/s41467-020-19756-z. URL: http://dx.doi.org/10.1038/s41467-020-19756-z.

[373] T.E. Humphrey and H. Linke. "Quantum, cyclic, and particle-exchange heat engines". In: *Physica E: Low-dimensional Systems and Nanostructures* 29.1–2 (Oct. 2005), pp. 390–398. ISSN: 1386-9477. DOI: 10.1016/j.physe.2005.05.038. URL: http://dx.doi.org/10.1016/j.physe.2005.05.038.

[374] Pratibha Singh and S. K. Shukla. “Advances in polyaniline-based nanocomposites”. In: *Journal of Materials Science* 55.4 (Oct. 2019), pp. 1331–1365. ISSN: 1573-4803. DOI: 10.1007/s10853-019-04141-z. URL: http://dx.doi.org/10.1007/s10853-019-04141-z.

[375] T. J. Seebeck. “Ueber die magnetische Polarisation der Metalle und Erze durch Temperaturdifferenz”. In: *Annalen der Physik* 82.3 (Jan. 1826), pp. 253–286. ISSN: 1521-3889. DOI: 10.1002/andp.18260820302. URL: http://dx.doi.org/10.1002/andp.18260820302.

[376] Sachin Verma and Ajay Singh. “Non-equilibrium thermoelectric transport across normal metal– quantum dot– superconductor hybrid system within the Coulomb blockade regime”. en. In: *Journal of Physics: Condensed Matter* 34.15 (Apr. 2022). Number: 15, p. 155601. ISSN: 0953-8984, 1361-648X. DOI: 10.1088/1361-648X/ac4ced. URL: https://iopscience.iop.org/article/10.1088/1361-648X/ac4ced.

[377] Björn Sothmann et al. “Rectification of thermal fluctuations in a chaotic cavity heat engine”. en. In: *Physical Review B* 85.20 (May 2012). Number: 20 arXiv:1201.2796 [cond-mat], p. 205301. ISSN: 1098-0121, 1550-235X. DOI: 10.1103/PhysRevB.85.205301. URL: http://arxiv.org/abs/1201.2796.

[378] Martin Josefsson et al. “A quantum-dot heat engine operating close to the thermodynamic efficiency limits”. en. In: *Nature Nanotechnology* 13.10 (Oct. 2018). Number: 10, pp. 920–924. ISSN: 1748-3387, 1748-3395. DOI: 10.1038/s41565-018-0200-5. URL: http://www.nature.com/articles/s41565-018-0200-5.

[379] Sara Kheradsoud et al. “Power, Efficiency and Fluctuations in a Quantum Point Contact as Steady-State Thermoelectric Heat Engine”. en. In: *Entropy* 21.8 (Aug. 2019). Number: 8, p. 777. ISSN: 1099-4300. DOI: 10.3390/e21080777. URL: https://www.mdpi.com/1099-4300/21/8/777.

[380] Seungil Baek et al. “Nanoscale homojunction thermoelectric generator built in defect-engineered MoS2”. In: *Physical Review B* 107.19 (May 2023). ISSN: 2469-9969. DOI: 10.1103/physrevb.107.195411. URL: http://dx.doi.org/10.1103/PhysRevB.107.195411.

[381] Tianye Wei et al. “A graphene-nanoribbon-based thermoelectric generator”. In: *Carbon* 210 (June 2023), p. 118053. ISSN: 0008-6223. DOI: 10.1016/j.carbon.2023.118053. URL: http://dx.doi.org/10.1016/j.carbon.2023.118053.

[382] K. Uchida et al. “Observation of the spin Seebeck effect”. In: *Nature* 455.7214 (Oct. 2008), pp. 778–781. ISSN: 1476-4687. DOI: 10.1038/nature07321. URL: http://dx.doi.org/10.1038/nature07321.

[383] Gene Siegel et al. “Robust longitudinal spin-Seebeck effect in Bi-YIG thin films”. In: *Scientific Reports* 4.1 (Mar. 2014). ISSN: 2045-2322. DOI: 10.1038/srep04429. URL: http://dx.doi.org/10.1038/srep04429.

[384] Stephen R. Boona, Sarah J. Watzman, and Joseph P. Heremans. “Research Update: Utilizing magnetization dynamics in solid-state thermal energy conversion”. In: *APL Materials* 4.10 (July 2016). ISSN: 2166-532X. DOI: 10.1063/1.4955027. URL: http://dx.doi.org/10.1063/1.4955027.

[385] A.R. Mackintosh and L. Sill. “The thermoelectric power in chromium and vanadium”. In: *Journal of Physics and Chemistry of Solids* 24.4 (Apr. 1963), pp. 501–506. ISSN: 0022-3697. DOI: 10.1016/0022-3697(63)90145-8. URL: http://dx.doi.org/10.1016/0022-3697(63)90145-8.

[386] Jannis Maiwald and Philipp Gegenwart. “Interplay of 4f and 3d moments in EuFe2As2 iron pnictides”. In: *physica status solidi (b)* 254.1 (July 2016). ISSN: 1521-3951. DOI: 10.1002/pssb.201600150. URL: http://dx.doi.org/10.1002/pssb.201600150.

[387] Guillermo Lopez-Polin et al. “High-Power-Density Energy-Harvesting Devices Based on the Anomalous Nernst Effect of Co/Pt Magnetic Multilayers”. In: *ACS Applied Energy Materials* 5.9 (Sept. 2022), pp. 11835–11843. ISSN: 2574-0962. DOI: 10.1021/acsaem.2c02422. URL: http://dx.doi.org/10.1021/acsaem.2c02422.

[388] Minghang Li et al. “Large Anomalous Nernst Effects at Room Temperature in Fe3Pt Thin Films”. In: *Advanced Materials* 35.32 (July 2023). ISSN: 1521-4095. DOI: 10.1002/adma.202301339. URL: http://dx.doi.org/10.1002/adma.202301339.

[389] Satya N. Guin et al. “Anomalous Nernst effect beyond the magnetization scaling relation in the ferromagnetic Heusler compound Co2MnGa”. In: *NPG Asia Materials* 11.1 (Apr. 2019). ISSN: 1884-4057. DOI: 10.1038/s41427-019-0116-z. URL: http://dx.doi.org/10.1038/s41427-019-0116-z.

[390] Taishi Chen et al. “Large anomalous Nernst effect and nodal plane in an iron-based kagome ferromagnet”. In: *Science Advances* 8.2 (Jan. 2022). ISSN: 2375-2548. DOI: 10.1126/sciadv.abk1480. URL: http://dx.doi.org/10.1126/sciadv.abk1480.

[391] Yusen Yang et al. “Anomalous enhancement of the Nernst effect at the crossover between a Fermi liquid and a strange metal”. In: *Nature Physics* 19.3 (Jan. 2023), pp. 379–385. ISSN: 1745-2481. DOI: 10.1038/s41567-022-01904-5. URL: http://dx.doi.org/10.1038/s41567-022-01904-5.

[392] Andrew Rex. “Maxwell’s Demon—A Historical Review”. In: *Entropy* 19.6 (May 2017), p. 240. ISSN: 1099-4300. DOI: 10.3390/e19060240. URL: http://dx.doi.org/10.3390/e19060240.

[393] Sai Vinjanampathy and Janet Anders. "Quantum Thermodynamics". en. In: *Contemporary Physics* 57.4 (Oct. 2016). arXiv:1508.06099 [quant-ph], pp. 545–579. ISSN: 0010-7514, 1366-5812. DOI: 10.1080/00107514.2016.1201896. URL: http://arxiv.org/abs/1508.06099.

[394] Orly Shenker and Meir Hemmo. "Maxwell's Demon in Quantum Mechanics". In: *Entropy* 22.3 (Feb. 2020), p. 269. ISSN: 1099-4300. DOI: 10.3390/e22030269. URL: http://dx.doi.org/10.3390/e22030269.

[395] Léo Touzo et al. "Optimal work extraction and the minimum description length principle". In: *Journal of Statistical Mechanics: Theory and Experiment* 2020.9 (Sept. 2020), p. 093403. ISSN: 1742-5468. DOI: 10.1088/1742-5468/abacb3. URL: http://dx.doi.org/10.1088/1742-5468/abacb3.

[396] M. B. Plenio and V. Vitelli. "The physics of forgetting: Landauer's erasure principle and information theory". In: *Contemporary Physics* 42.1 (Jan. 2001), pp. 25–60. ISSN: 1366-5812. DOI: 10.1080/00107510010018916. URL: http://dx.doi.org/10.1080/00107510010018916.

[397] A. Mert Bozkurt, Bariş Pekerten, and İnanç Adagideli. "Work extraction and Landauer's principle in a quantum spin Hall device". en. In: *Physical Review B* 97.24 (June 2018). Number: 24. ISSN: 2469-9950, 2469-9969. DOI: 10.1103/PhysRevB.97.245414. URL: https://link.aps.org/doi/10.1103/PhysRevB.97.245414.

[398] Mario A. Ciampini et al. *Experimental nonequilibrium memory erasure beyond Landauer's bound*. 2021. DOI: 10.48550/ARXIV.2107.04429. URL: https://arxiv.org/abs/2107.04429.

[399] Jackson S. S. T. Wright et al. "Quantum heat engine operating between thermal and spin reservoirs". en. In: *Physical Review A* 97.5 (May 2018). Number: 5. ISSN: 2469-9926, 2469-9934. DOI: 10.1103/PhysRevA.97.052104. URL: https://link.aps.org/doi/10.1103/PhysRevA.97.052104.

[400] T. Croucher and J. A. Vaccaro. "Thermodynamics of memory erasure via a spin reservoir". en. In: *Physical Review E* 103.4 (Apr. 2021). Number: 4. ISSN: 2470-0045, 2470-0053. DOI: 10.1103/PhysRevE.103.042140. URL: https://link.aps.org/doi/10.1103/PhysRevE.103.042140.

[401] Jan Klaers. "Landauer's Erasure Principle in a Squeezed Thermal Memory". en. In: *Physical Review Letters* 122.4 (Jan. 2019). Number: 4, p. 040602. ISSN: 0031-9007, 1079-7114. DOI: 10.1103/PhysRevLett.122.040602. URL: https://link.aps.org/doi/10.1103/PhysRevLett.122.040602.

[402] Kensaku Chida et al. "Power generator driven by Maxwell's demon". en. In: *Nature Communications* 8.1 (Aug. 2017). Number: 1. ISSN: 2041-1723. DOI: 10.1038/ncomms15301. URL: http://www.nature.com/articles/ncomms15301.

[403] Kensaku Chida et al. “Thermal-noise suppression in nano-scale Si field-effect transistors by feedback control based on single-electron detection”. en. In: *Applied Physics Letters* 107.7 (Aug. 2015). Number: 7, p. 073110. ISSN: 0003-6951, 1077-3118. DOI: 10.1063/1.4928656. URL: http://aip.scitation.org/doi/10.1063/1.4928656.

[404] J. V. Koski et al. “On-Chip Maxwell’s Demon as an Information-Powered Refrigerator”. en. In: *Physical Review Letters* 115.26 (Dec. 2015). Number: 26. ISSN: 0031-9007, 1079-7114. DOI: 10.1103/PhysRevLett.115.260602. URL: https://link.aps.org/doi/10.1103/PhysRevLett.115.260602.

[405] Justin P. Bergfield et al. “Probing Maxwell’s Demon with a Nanoscale Thermometer”. en. In: *ACS Nano* 7.5 (May 2013). Number: 5, pp. 4429–4440. ISSN: 1936-0851, 1936-086X. DOI: 10.1021/nn401027u. URL: https://pubs.acs.org/doi/10.1021/nn401027u.

[406] Krzysztof Ptaszynski. “Autonomous quantum Maxwell’s demon based on two exchange-coupled quantum dots”. en. In: *Physical Review E* 97.1 (Jan. 2018). Number: 1. ISSN: 2470-0045, 2470-0053. DOI: 10.1103/PhysRevE.97.012116. URL: https://link.aps.org/doi/10.1103/PhysRevE.97.012116.

[407] Stella Seah, Stefan Nimmrichter, and Valerio Scarani. “Maxwell’s Lesser Demon: A Quantum Engine Driven by Pointer Measurements”. en. In: *Physical Review Letters* 124.10 (Mar. 2020). Number: 10. ISSN: 0031-9007, 1079-7114. DOI: 10.1103/PhysRevLett.124.100603. URL: https://link.aps.org/doi/10.1103/PhysRevLett.124.100603.

[408] Krzysztof Ptaszyński and Massimiliano Esposito. “Entropy Production in Open Systems: The Predominant Role of Intraenvironment Correlations”. en. In: *Physical Review Letters* 123.20 (Nov. 2019). 2024-07-19, p. 200603. ISSN: 0031-9007, 1079-7114. DOI: 10.1103/PhysRevLett.123.200603. URL: https://link.aps.org/doi/10.1103/PhysRevLett.123.200603.

[409] Baldo-Luis Najera-Santos et al. “Autonomous Maxwell’s demon in a cavity QED system”. en. In: *Physical Review Research* 2.3 (July 2020). Number: 3. ISSN: 2643-1564. DOI: 10.1103/PhysRevResearch.2.032025. URL: https://link.aps.org/doi/10.1103/PhysRevResearch.2.032025.

[410] Tong Fu et al. “Finite-time quantum measurement cooling beyond the Carnot limit”. In: *Journal of Applied Physics* 134.2 (July 2023). ISSN: 1089-7550. DOI: 10.1063/5.0154341. URL: http://dx.doi.org/10.1063/5.0154341.

[411] Michele Campisi, Jukka Pekola, and Rosario Fazio. “Feedback-controlled heat transport in quantum devices: theory and solid-state experimental proposal”. en. In: *New Journal of Physics* 19.5 (May 2017). Number: 5, p. 053027. ISSN: 1367-2630. DOI: 10.1088/1367-2630/aa6acb. URL: https://iopscience.iop.org/article/10.1088/1367-2630/aa6acb.

[412] Francisco J. Peña et al. “Otto Engine: Classical and Quantum Approach”. In: *Entropy* 22.7 (July 2020), p. 755. ISSN: 1099-4300. DOI: 10.3390/e22070755. URL: http://dx.doi.org/10.3390/e22070755.

[413] Giulia Piccitto, Michele Campisi, and Davide Rossini. “The Ising critical quantum Otto engine”. In: *New Journal of Physics* 24.10 (Oct. 2022). ISSN: 1367-2630. DOI: 10.1088/1367-2630/ac963b.

[414] Suman Chand and Asoka Biswas. “Measurement-induced operation of two-ion quantum heat machines”. en. In: *Physical Review E* 95.3 (Mar. 2017). Number: 3, p. 032111. ISSN: 2470-0045, 2470-0053. DOI: 10.1103/PhysRevE.95.032111. URL: https://link.aps.org/doi/10.1103/PhysRevE.95.032111.

[415] Krzysztof Ptaszyński. “Non-Markovian thermal operations boosting the performance of quantum heat engines”. en. In: *Physical Review E* 106.1 (July 2022). Number: 1. ISSN: 2470-0045, 2470-0053. DOI: 10.1103/PhysRevE.106.014114. URL: https://link.aps.org/doi/10.1103/PhysRevE.106.014114.

[416] Jifei Zhao and Youyang Xu. “Influence of an indefinite causal order on an Otto heat engine”. en. In: *Communications in Theoretical Physics* 74.2 (Feb. 2022). Number: 2, p. 025601. ISSN: 0253-6102, 1572-9494. DOI: 10.1088/1572-9494/ac490d. URL: https://iopscience.iop.org/article/10.1088/1572-9494/ac490d.

[417] Edoardo Maria Centamori, Michele Campisi, and Vittorio Giovannetti. *Spin-chain based quantum thermal machines*. 2023. DOI: 10.48550/ARXIV.2303.15574. URL: https://arxiv.org/abs/2303.15574.

[418] Nicolás F. Del Grosso et al. “Quantum Otto cycle in a superconducting cavity in the nonadiabatic regime”. In: *Physical Review A* 105.2 (Feb. 2022). ISSN: 2469-9934. DOI: 10.1103/physreva.105.022202. URL: http://dx.doi.org/10.1103/PhysRevA.105.022202.

[419] J.-W. Zhang et al. “Dynamical control of quantum heat engines using exceptional points”. en. In: *Nature Communications* 13.1 (Oct. 2022). Number: 1. ISSN: 2041-1723. DOI: 10.1038/s41467-022-33667-1. URL: https://www.nature.com/articles/s41467-022-33667-1.

[420] Shishir Khandelwal, Nicolas Brunner, and Géraldine Haack. “Signatures of Liouvillian Exceptional Points in a Quantum Thermal Machine”. en. In: *PRX Quantum* 2.4 (Dec. 2021). Number: 4. ISSN: 2691-3399. DOI: 10.1103/PRXQuantum.2.040346. URL: https://link.aps.org/doi/10.1103/PRXQuantum.2.040346.

[421] Rogério J. De Assis et al. “Efficiency of a Quantum Otto Heat Engine Operating under a Reservoir at Effective Negative Temperatures”. en. In: *Physical Review Letters* 122.24 (June 2019). Number: 24, p. 240602. ISSN: 0031-9007, 1079-7114. DOI: 10.1103/PhysRevLett.122.240602. URL: https://link.aps.org/doi/10.1103/PhysRevLett.122.240602.

[422] Sajjad Hashemi Abasabadi, Sayyed Yahya Mirafzali, and Hamid Reza Baghshahi. "Quantum Otto heat engine with Pöschl–Teller potential in contact with coherent thermal bath". In: *Scientific Reports* 13.1 (June 2023). ISSN: 2045-2322. DOI: 10.1038/s41598-023-37681-1. URL: http://dx.doi.org/10.1038/s41598-023-37681-1.

[423] Nathan M Myers et al. "Boosting engine performance with Bose–Einstein condensation". en. In: *New Journal of Physics* 24.2 (Feb. 2022). Number: 2, p. 025001. ISSN: 1367-2630. DOI: 10.1088/1367-2630/ac47cc. URL: https://iopscience.iop.org/article/10.1088/1367-2630/ac47cc.

[424] Jing Li, E. Ya Sherman, and Andreas Ruschhaupt. "Quantum heat engine based on a spin-orbit- and Zeeman-coupled Bose-Einstein condensate". en. In: *Physical Review A* 106.3 (Sept. 2022). Number: 3. ISSN: 2469-9926, 2469-9934. DOI: 10.1103/PhysRevA.106.L030201. URL: https://link.aps.org/doi/10.1103/PhysRevA.106.L030201.

[425] C L Latune, I Sinayskiy, and F Petruccione. "Collective heat capacity for quantum thermometry and quantum engine enhancements". In: *New Journal of Physics* 22.8 (Aug. 2020). Number: 8, p. 083049. ISSN: 1367-2630. DOI: 10.1088/1367-2630/aba463. URL: https://iopscience.iop.org/article/10.1088/1367-2630/aba463.

[426] Camille L. Latune, Graeme Pleasance, and Francesco Petruccione. "Cyclic Quantum Engines Enhanced by Strong Bath Coupling". en. In: *Physical Review Applied* 20.2 (Aug. 2023). Number: 2. ISSN: 2331-7019. DOI: 10.1103/PhysRevApplied.20.024038. URL: https://journals.aps.org/prapplied/abstract/10.1103/PhysRevApplied.20.024038.

[427] Suman Chand, Shubhrangshu Dasgupta, and Asoka Biswas. "Finite-time performance of a single-ion quantum Otto engine". en. In: *Physical Review E* 103.3 (Mar. 2021). Number: 3, p. 032144. ISSN: 2470-0045, 2470-0053. DOI: 10.1103/PhysRevE.103.032144. URL: https://link.aps.org/doi/10.1103/PhysRevE.103.032144.

[428] Suman Chand and Asoka Biswas. "Critical-point behavior of a measurement-based quantum heat engine". en. In: *Physical Review E* 98.5 (Nov. 2018). Number: 5, p. 052147. ISSN: 2470-0045, 2470-0053. DOI: 10.1103/PhysRevE.98.052147. URL: https://link.aps.org/doi/10.1103/PhysRevE.98.052147.

[429] Shimshon Kallush, Roie Dann, and Ronnie Kosloff. "Controlling the uncontrollable: Quantum control of open-system dynamics". In: *Science Advances* 8.44 (Nov. 2022). ISSN: 2375-2548. DOI: 10.1126/sciadv.add0828. URL: http://dx.doi.org/10.1126/sciadv.add0828.

[430] Christiane P. Koch et al. “Quantum optimal control in quantum technologies. Strategic report on current status, visions and goals for research in Europe”. In: *EPJ Quantum Technology* 9.1 (July 2022). ISSN: 2196-0763. DOI: 10.1140/epjqt/s40507-022-00138-x. URL: http://dx.doi.org/10.1140/epjqt/s40507-022-00138-x.

[431] Jens Nettersheim et al. “Power of a Quasispin Quantum Otto Engine at Negative Effective Spin Temperature”. en. In: *PRX Quantum* 3.4 (Dec. 2022). Number: 4. ISSN: 2691-3399. DOI: 10.1103/PRXQuantum.3.040334. URL: https://link.aps.org/doi/10.1103/PRXQuantum.3.040334.

[432] John P. S. Peterson et al. “Experimental Characterization of a Spin Quantum Heat Engine”. en. In: *Physical Review Letters* 123.24 (Dec. 2019). Number: 24. ISSN: 0031-9007, 1079-7114. DOI: 10.1103/PhysRevLett.123.240601. URL: https://link.aps.org/doi/10.1103/PhysRevLett.123.240601.

[433] Otavio A. D. Molitor and Gabriel T. Landi. “Stroboscopic two-stroke quantum heat engines”. en. In: *Physical Review A* 102.4 (Oct. 2020). Number: 4. ISSN: 2469-9926, 2469-9934. DOI: 10.1103/PhysRevA.102.042217. URL: https://link.aps.org/doi/10.1103/PhysRevA.102.042217.

[434] James Klatzow et al. “Experimental Demonstration of Quantum Effects in the Operation of Microscopic Heat Engines”. en. In: *Physical Review Letters* 122.11 (Mar. 2019). Number: 11. ISSN: 0031-9007, 1079-7114. DOI: 10.1103/PhysRevLett.122.110601. URL: https://link.aps.org/doi/10.1103/PhysRevLett.122.110601.

[435] B. Ahmadi et al. “Nonreciprocal Quantum Batteries”. In: *Physical Review Letters* 132.21 (May 2024). ISSN: 1079-7114. DOI: 10.1103/physrevlett.132.210402. URL: http://dx.doi.org/10.1103/PhysRevLett.132.210402.

[436] James Q. Quach et al. “Superabsorption in an organic microcavity: Toward a quantum battery”. In: *Science Advances* 8.2 (Jan. 2022). ISSN: 2375-2548. DOI: 10.1126/sciadv.abk3160. URL: http://dx.doi.org/10.1126/sciadv.abk3160.

[437] Francesco Tacchino et al. “Charging a quantum battery via nonequilibrium heat current”. en. In: *Physical Review E* 102.6 (Dec. 2020). Number: 6. ISSN: 2470-0045, 2470-0053. DOI: 10.1103/PhysRevE.102.062133. URL: https://link.aps.org/doi/10.1103/PhysRevE.102.062133.

[438] Mark T. Mitchison, John Goold, and Javier Prior. “Charging a quantum battery with linear feedback control”. en. In: *Quantum* 5 (July 2021). 2022-03-04, p. 500. ISSN: 2521-327X. DOI: 10.22331/q-2021-07-13-500. URL: https://quantum-journal.org/papers/q-2021-07-13-500/.

[439] Stefan Aimet and Hyukjoon Kwon. “Engineering a heat engine purely driven by quantum coherence”. In: *Phys. Rev. A* 107 (1 Jan. 2023), p. 012221. DOI: 10.1103/PhysRevA.107.012221. URL: https://link.aps.org/doi/10.1103/PhysRevA.107.012221.

[440] Fang Zhao, Fu-Quan Dou, and Qing Zhao. “Quantum battery of interacting spins with environmental noise”. en. In: *Physical Review A* 103.3 (Mar. 2021). Number: 3. ISSN: 2469-9926, 2469-9934. DOI: 10.1103/PhysRevA.103.033715. URL: https://link.aps.org/doi/10.1103/PhysRevA.103.033715.

[441] Tiago F. F. Santos and Marcelo F. Santos. “Efficiency of optically pumping a quantum battery and a two-stroke heat engine”. In: *Phys. Rev. A* 106 (5 Nov. 2022), p. 052203. DOI: 10.1103/PhysRevA.106.052203. URL: https://link.aps.org/doi/10.1103/PhysRevA.106.052203.

[442] Juliette Monsel et al. “The Energetic Cost of Work Extraction”. en. In: *Physical Review Letters* 124.13 (Mar. 2020). Number: 13. ISSN: 0031-9007, 1079-7114. DOI: 10.1103/PhysRevLett.124.130601. URL: https://link.aps.org/doi/10.1103/PhysRevLett.124.130601.

[443] Noah Van Horne et al. “Single-atom energy-conversion device with a quantum load”. en. In: *npj Quantum Information* 6.1 (Dec. 2020). Number: 1. ISSN: 2056-6387. DOI: 10.1038/s41534-020-0264-6. URL: http://www.nature.com/articles/s41534-020-0264-6.

[444] Karen V. Hovhannisyan, Felipe Barra, and Alberto Imparato. “Charging assisted by thermalization”. en. In: *Physical Review Research* 2.3 (Sept. 2020). Number: 3. ISSN: 2643-1564. DOI: 10.1103/PhysRevResearch.2.033413. URL: https://link.aps.org/doi/10.1103/PhysRevResearch.2.033413.

[445] Gaoyan Zhu et al. “Charging Quantum Batteries via Indefinite Causal Order: Theory and Experiment”. en. In: *Physical Review Letters* 131.24 (Dec. 2023). Number: 24, p. 240401. ISSN: 0031-9007, 1079-7114. DOI: 10.1103/PhysRevLett.131.240401. URL: https://link.aps.org/doi/10.1103/PhysRevLett.131.240401.

[446] Juliette Monsel et al. “Geometric energy transport and refrigeration with driven quantum dots”. en. In: *Physical Review B* 106.3 (July 2022). Number: 3, p. 035405. ISSN: 2469-9950, 2469-9969. DOI: 10.1103/PhysRevB.106.035405. URL: https://link.aps.org/doi/10.1103/PhysRevB.106.035405.

[447] Junjie Liu, Kenneth A. Jung, and Dvira Segal. “Periodically Driven Quantum Thermal Machines from Warming up to Limit Cycle”. en. In: *Physical Review Letters* 127.20 (Nov. 2021). Number: 20. ISSN: 0031-9007, 1079-7114. DOI: https://doi.org/10.1103/PhysRevLett.127.200602. URL: https://link.aps.org/doi/10.1103/PhysRevLett.127.200602.

[448] Matteo Carrega et al. “Engineering Dynamical Couplings for Quantum Thermodynamic Tasks”. en. In: *PRX Quantum* 3.1 (Feb. 2022). Number: 1. ISSN: 2691-3399. DOI: 10.1103/PRXQuantum.3.010323. URL: https://link.aps.org/doi/10.1103/PRXQuantum.3.010323.

[449] Yong Lu et al. “Steady-State Heat Transport and Work With a Single Artificial Atom Coupled to a Waveguide: Emission Without External Driving”. en. In: *PRX Quantum* 3.2 (Apr. 2022). Number: 2. ISSN: 2691-3399. DOI: 10.1103/PRXQuantum.3.020305. URL: https://link.aps.org/doi/10.1103/PRXQuantum.3.020305.

[450] J. Stevens et al. “Energetics of a Single Qubit Gate”. en. In: *Physical Review Letters* 129.11 (Sept. 2022). Number: 11, p. 110601. ISSN: 0031-9007, 1079-7114. DOI: 10.1103/PhysRevLett.129.110601. URL: https://link.aps.org/doi/10.1103/PhysRevLett.129.110601.

[451] B. Misra and E. C. G. Sudarshan. “The Zeno’s paradox in quantum theory”. In: *Journal of Mathematical Physics* 18.4 (Apr. 1977), pp. 756–763. ISSN: 1089-7658. DOI: 10.1063/1.523304. URL: http://dx.doi.org/10.1063/1.523304.

[452] Victor Mukherjee, Abraham G. Kofman, and Gershon Kurizki. “Anti-Zeno quantum advantage in fast-driven heat machines”. In: *Communications Physics* 3.1 (Jan. 2020). ISSN: 2399-3650. DOI: 10.1038/s42005-019-0272-z. URL: http://dx.doi.org/10.1038/s42005-019-0272-z.

[453] Noam Erez et al. “Thermodynamic control by frequent quantum measurements”. en. In: *Nature* 452.7188 (Apr. 2008). Number: 7188, pp. 724–727. ISSN: 0028-0836, 1476-4687. DOI: 10.1038/nature06873. URL: http://www.nature.com/articles/nature06873.

[454] Stefano Gherardini et al. “Stabilizing open quantum batteries by sequential measurements”. en. In: *Physical Review Research* 2.1 (Jan. 2020). Number: 1. ISSN: 2643-1564. DOI: 10.1103/PhysRevResearch.2.013095. URL: https://link.aps.org/doi/10.1103/PhysRevResearch.2.013095.

[455] Zhiyuan Lin et al. “Suppressing coherence effects in quantum-measurement-based engines”. en. In: *Physical Review A* 104.6 (Dec. 2021). Number: 6. ISSN: 2469-9926, 2469-9934. DOI: 10.1103/PhysRevA.104.062210. URL: https://link.aps.org/doi/10.1103/PhysRevA.104.062210.

[456] Léa Bresque et al. “Two-Qubit Engine Fueled by Entanglement and Local Measurements”. en. In: *Physical Review Letters* 126.12 (Mar. 2021). Number: 12. ISSN: 0031-9007, 1079-7114. DOI: 10.1103/PhysRevLett.126.120605. URL: https://link.aps.org/doi/10.1103/PhysRevLett.126.120605.

[457] M Hamed Mohammady and Janet Anders. “A quantum Szilard engine without heat from a thermal reservoir”. en. In: *New Journal of Physics* 19.11 (Nov. 2017). Number: 11, p. 113026. ISSN: 1367-2630. DOI: 10.1088/1367-2630/aa8ba1. URL: https://iopscience.iop.org/article/10.1088/1367-2630/aa8ba1.

[458] Wentao Ji et al. “Spin Quantum Heat Engine Quantified by Quantum Steering”. en. In: *Physical Review Letters* 128.9 (Mar. 2022). Number: 9. ISSN: 0031-9007, 1079-7114. DOI: 10.1103/PhysRevLett.128.090602. URL: https://link.aps.org/doi/10.1103/PhysRevLett.128.090602.

[459] Juyeon Yi, Peter Talkner, and Yong Woon Kim. “Single-temperature quantum engine without feedback control”. en. In: *Physical Review E* 96.2 (Aug. 2017). Number: 2. ISSN: 2470-0045, 2470-0053. DOI: 10.1103/PhysRevE.96.022108. URL: http://link.aps.org/doi/10.1103/PhysRevE.96.022108.

[460] Cyril Elouard et al. “An Interaction-Free Quantum Measurement-Driven Engine”. en. In: *Foundations of Physics* 50.11 (Nov. 2020). Number: 11, pp. 1294–1314. ISSN: 0015-9018, 1572-9516. DOI: 10.1007/s10701-020-00381-1. URL: https://link.springer.com/10.1007/s10701-020-00381-1.

[461] Étienne Jussiau et al. “Many-body quantum vacuum fluctuation engines”. In: *Phys. Rev. Res.* 5 (3 Aug. 2023), p. 033122. DOI: http://dx.doi.org/10.1103/PhysRevResearch.5.033122. URL: https://link.aps.org/doi/10.1103/PhysRevResearch.5.033122.

[462] João Ferreira et al. “Transport and Nonreciprocity in Monitored Quantum Devices: An Exact Study”. en. In: *Physical Review Letters* 132.13 (Mar. 2024). Number: 13, p. 136301. ISSN: 0031-9007, 1079-7114. DOI: 10.1103/PhysRevLett.132.136301. URL: https://link.aps.org/doi/10.1103/PhysRevLett.132.136301.

[463] Lorenzo Buffoni et al. “Quantum Measurement Cooling”. en. In: *Physical Review Letters* 122.7 (Feb. 2019). Number: 7. ISSN: 0031-9007, 1079-7114. DOI: 10.1103/PhysRevLett.122.070603. URL: https://link.aps.org/doi/10.1103/PhysRevLett.122.070603.

[464] Franklin L. S. Rodrigues and Eric Lutz. “Nonequilibrium thermodynamics of quantum coherence beyond linear response”. In: *Communications Physics* 7.1 (Feb. 2024). ISSN: 2399-3650. DOI: 10.1038/s42005-024-01548-2. URL: http://dx.doi.org/10.1038/s42005-024-01548-2.

[465] S. Javaid et al. “Impact on Interface Spin Polarization of Molecular Bonding to Metallic Surfaces”. In: *Physical Review Letters* 105.7 (Aug. 2010). 2024-03-20, p. 077201. ISSN: 0031-9007, 1079-7114. DOI: 10.1103/PhysRevLett.105.077201. URL: https://link.aps.org/doi/10.1103/PhysRevLett.105.077201.

[466] Guo-Xing Miao et al. “Spin regulation in composite spin-filter barrier devices”. In: *Nature Communications* 5.1 (May 2014). 2021-04-09. ISSN: 2041-1723. DOI: 10.1038/ncomms4682. URL: http://www.nature.com/articles/ncomms4682.

[467] Pham Nam Hai et al. “Electromotive force and huge magnetoresistance in magnetic tunnel junctions”. In: *Nature* 458.7237 (Mar. 2009). 2021-04-09, pp. 489–492. ISSN: 0028-0836, 1476-4687. DOI: 10.1038/nature07879. URL: http://www.nature.com/articles/nature07879.

[468] Maciej Misiorny and Ireneusz Weymann. “Transverse anisotropy effects on spin-resolved transport through large-spin molecules”. en. In: *Physical Review B* 90.23 (Dec. 2014). Number: 23. ISSN: 1098-0121, 1550-235X. DOI: 10.1103/PhysRevB.90.235409. URL: https://link.aps.org/doi/10.1103/PhysRevB.90.235409.

[469] Jonas Fransson, Jie Ren, and Jian-Xin Zhu. “Electrical and Thermal Control of Magnetic Exchange Interactions”. en. In: *Physical Review Letters* 113.25 (Dec. 2014). Number: 25. ISSN: 0031-9007, 1079-7114. DOI: 10.1103/PhysRevLett.113.257201. URL: https://link.aps.org/doi/10.1103/PhysRevLett.113.257201.

[470] D. C. Ralph. “The electromotive force of MnAs nanoparticles”. In: *Nature* 474.7350 (June 2011), E6–E6. ISSN: 1476-4687. DOI: 10.1038/nature10142. URL: http://dx.doi.org/10.1038/nature10142.

[471] S. E. Barnes and S. Maekawa. “Generalization of Faraday’s Law to Include Nonconservative Spin Forces”. In: *Physical Review Letters* 98.24 (June 2007). ISSN: 1079-7114. DOI: 10.1103/physrevlett.98.246601. URL: http://dx.doi.org/10.1103/PhysRevLett.98.246601.

[472] Holger Thierschmann et al. “Three-terminal energy harvester with coupled quantum dots”. In: *Nature Nanotechnology* 10.10 (Aug. 2015), pp. 854–858. ISSN: 1748-3395. DOI: 10.1038/nnano.2015.176. URL: http://dx.doi.org/10.1038/nnano.2015.176.

[473] Philipp Strasberg et al. “Quantum and Information Thermodynamics: A Unifying Framework Based on Repeated Interactions”. In: *Physical Review X* 7.2 (Apr. 2017). DOI: 10.1103/physrevx.7.021003. URL: https://doi.org/10.1103/physrevx.7.021003.

[474] B. Yurke et al. “Observation of 4.2-K equilibrium-noise squeezing via a Josephson-parametric amplifier”. en. In: *Physical Review Letters* 60.9 (Feb. 1988). Number: 9, pp. 764–767. ISSN: 0031-9007. DOI: 10.1103/PhysRevLett.60.764. URL: https://link.aps.org/doi/10.1103/PhysRevLett.60.764.

[475] Onur Hosten et al. “Measurement noise 100 times lower than the quantum-projection limit using entangled atoms”. In: *Nature* 529.7587 (Jan. 2016). 2021-04-12, pp. 505–508. ISSN: 0028-0836, 1476-4687. DOI: 10.1038/nature16176. URL: http://www.nature.com/articles/nature16176.

[476] Rafael Sánchez, Janine Splettstoesser, and Robert S. Whitney. "Nonequilibrium System as a Demon". en. In: *Physical Review Letters* 123.21 (Nov. 2019). Number: 21. ISSN: 0031-9007, 1079-7114. DOI: 10.1103/PhysRevLett.123.216801. URL: https://link.aps.org/doi/10.1103/PhysRevLett.123.216801.

[477] Michele Campisi and Rosario Fazio. "The power of a critical heat engine". en. In: *Nature Communications* 7.1 (Sept. 2016). Number: 1. ISSN: 2041-1723. DOI: 10.1038/ncomms11895. URL: http://www.nature.com/articles/ncomms11895.

[478] Vasco Cavina, Andrea Mari, and Vittorio Giovannetti. "Slow Dynamics and Thermodynamics of Open Quantum Systems". en. In: *Proceedings* 12.1 (July 2019). Number: 1, p. 19. ISSN: 2504-3900. DOI: 10.3390/proceedings2019012019. URL: https://www.mdpi.com/2504-3900/12/1/19.

[479] K. Bader, M. Winkler, and J. van Slageren. "Tuning of molecular qubits: very long coherence and spin–lattice relaxation times". In: *Chemical Communications* 52.18 (2016), pp. 3623–3626. ISSN: 1364-548X. DOI: 10.1039/c6cc00300a. URL: http://dx.doi.org/10.1039/C6CC00300A.

[480] Michał Studniarek et al. "Probing a Device's Active Atoms". In: *Advanced Materials* 29.19 (Mar. 2017). ISSN: 1521-4095. DOI: 10.1002/adma.201606578. URL: http://dx.doi.org/10.1002/adma.201606578.

[481] J. D. Vasquez Jaramillo and J. Fransson. "Charge Transport and Entropy Production Rate in Magnetically Active Molecular Dimer". en. In: *arXiv:1702.05389 [cond-mat]* (Jan. 2018). arXiv: 1702.05389. DOI: 10.1021/acs.jpcc.7b10350. URL: http://arxiv.org/abs/1702.05389.

[482] J. Bernos et al. "Impact of electron-electron interactions induced by disorder at interfaces on spin-dependent tunneling in Co-Fe-B/MgO/Co-Fe-B magnetic tunnel junctions". In: *Physical Review B* 82.6 (Aug. 2010). ISSN: 1550-235X. DOI: 10.1103/physrevb.82.060405. URL: http://dx.doi.org/10.1103/PhysRevB.82.060405.

[483] Shinji Yuasa et al. "Characterization of growth and crystallization processes in CoFeB/MgO/ CoFeB magnetic tunnel junction structure by reflective high-energy electron diffraction". In: *Applied Physics Letters* 87.24 (Dec. 2005). ISSN: 1077-3118. DOI: 10.1063/1.2140612. URL: http://dx.doi.org/10.1063/1.2140612.

[484] M. Mizuguchi et al. "In situ scanning tunneling microscopy observations of polycrystalline MgO(001) tunneling barriers grown on amorphous CoFeB electrode". In: *Applied Physics Letters* 91.1 (July 2007). ISSN: 1077-3118. DOI: 10.1063/1.2754372. URL: http://dx.doi.org/10.1063/1.2754372.

[485] Y. S. Choi et al. “Transmission electron microscopy study on the polycrystalline CoFeB/MgO/CoFeB based magnetic tunnel junction showing a high tunneling magnetoresistance, predicted in single crystal magnetic tunnel junction”. In: *Journal of Applied Physics* 101.1 (Jan. 2007). ISSN: 1089-7550. DOI: 10.1063/1.2407270. URL: http://dx.doi.org/10.1063/1.2407270.

[486] W. E. Gifford. “The Gifford-McMahon Cycle”. In: *Advances in Cryogenic Engineering*. Springer US, 1966, pp. 152–159. ISBN: 9781475705225. DOI: 10.1007/978-1-4757-0522-5_16. URL: http://dx.doi.org/10.1007/978-1-4757-0522-5_16.

[487] Ufuk Halisdemir. “Probing the impact of structural defects on spin dependent tunneling using photons”. 2016STRAE018. PhD thesis. 2016. URL: http://www.theses.fr/2016STRAE018/document.

[488] A. F. G. Wyatt. “Anomalous Densities of States in Normal Tantalum and Niobium”. en. In: *Physical Review Letters* 13.13 (Sept. 1964). Number: 13, pp. 401–404. ISSN: 0031-9007. DOI: 10.1103/PhysRevLett.13.401. URL: https://link.aps.org/doi/10.1103/PhysRevLett.13.401.

[489] Joel A. Appelbaum and L. Y. L. Shen. “Zero-Bias-Conductance-Peak Anomaly of Ta-I -Al Tunnel Junctions at 0.3 K and 90 kG”. en. In: *Physical Review B* 5.2 (Jan. 1972). Number: 2, pp. 544–553. ISSN: 0556-2805. DOI: 10.1103/PhysRevB.5.544. URL: https://link.aps.org/doi/10.1103/PhysRevB.5.544.

[490] Dmitry A. Ryndyk. “Electron-Electron Interaction and Coulomb Blockade”. en. In: *Theory of Quantum Transport at Nanoscale*. Vol. 184. Book Authors: _:n251. Cham: Springer International Publishing, 2016, pp. 123–147. ISBN: 978-3-319-24086-2 978-3-319-24088-6. DOI: 10.1007/978-3-319-24088-6_5. URL: http://link.springer.com/10.1007/978-3-319-24088-6_5.

[491] A. J. Keller et al. “Cotunneling Drag Effect in Coulomb-Coupled Quantum Dots”. In: *Physical Review Letters* 117.6 (Aug. 2016). 2021-06-01. ISSN: 0031-9007, 1079-7114. DOI: 10.1103/PhysRevLett.117.066602. URL: https://link.aps.org/doi/10.1103/PhysRevLett.117.066602.

[492] Enrique Burzuri et al. “Franck–Condon Blockade in a Single-Molecule Transistor”. In: 14.6 (May 2014), pp. 3191–3196. DOI: 10.1021/nl500524w. URL: https://doi.org/10.1021/nl500524w.

[493] Marc Ganzhorn et al. “Strong spin–phonon coupling between a single-molecule magnet and a carbon nanotube nanoelectromechanical system”. In: 8.3 (Feb. 2013), pp. 165–169. DOI: 10.1038/nnano.2012.258. URL: https://doi.org/10.1038/nnano.2012.258.

[494] J. J. Parks et al. “Mechanical Control of Spin States in Spin-1 Molecules and the Underscreened Kondo Effect”. In: 328.5984 (June 2010), pp. 1370–1373. DOI: 10.1126/science.1186874. URL: https://doi.org/10.1126/science.1186874.

[495] Sense Jan van der Molen and Peter Liljeroth. “Charge transport through molecular switches”. In: 22.13 (Mar. 2010), p. 133001. DOI: 10.1088/0953-8984/22/13/133001. URL: https://doi.org/10.1088/0953-8984/22/13/133001.

[496] Yu-Jia Zeng et al. “Significantly enhanced thermoelectric performance of molecular junctions by the twist angle dependent phonon interference effect”. In: 8.23 (2020), pp. 11884–11891. DOI: 10.1039/d0ta02423f. URL: https://doi.org/10.1039/d0ta02423f.

[497] Julia E. Greenwald et al. “Highly nonlinear transport across single-molecule junctions via destructive quantum interference”. In: 16.3 (Dec. 2020), pp. 313–317. DOI: 10.1038/s41565-020-00807-x. URL: https://doi.org/10.1038/s41565-020-00807-x.

[498] Andrew D. Kent and Daniel C. Worledge. “A new spin on magnetic memories”. In: *Nature Nanotechnology* 10.3 (Mar. 2015), pp. 187–191. DOI: 10.1038/nnano.2015.24. URL: https://doi.org/10.1038/nnano.2015.24.

[499] Jacob Torrejon et al. “Neuromorphic computing with nanoscale spintronic oscillators”. In: *Nature* 547.7664 (July 2017). 2023-01-03, pp. 428–431. ISSN: 0028-0836, 1476-4687. DOI: 10.1038/nature23011. URL: http://www.nature.com/articles/nature23011.

[500] Like Zhang et al. “Ultrahigh detection sensitivity exceeding 10^5 V/W in spin-torque diode”. In: *Applied Physics Letters* 113.10 (Sept. 2018). 2023-01-03, p. 102401. ISSN: 0003-6951, 1077-3118. DOI: 10.1063/1.5047547. URL: http://aip.scitation.org/doi/10.1063/1.5047547.

[501] Thomas Leoni et al. “Controlling the Charge State of a Single Redox Molecular Switch”. In: *Physical Review Letters* 106.21 (May 2011). 2023-01-20. ISSN: 0031-9007, 1079-7114. DOI: 10.1103/PhysRevLett.106.216103. URL: https://link.aps.org/doi/10.1103/PhysRevLett.106.216103.

[502] Lukas Gerhard et al. “An electrically actuated molecular toggle switch”. In: *Nature Communications* 8.1 (Mar. 2017). 2023-01-20, p. 14672. ISSN: 2041-1723. DOI: 10.1038/ncomms14672. URL: https://www.nature.com/articles/ncomms14672.

[503] Michael Galperin, Mark A Ratner, and Abraham Nitzan. “Molecular transport junctions: vibrational effects”. en. In: *Journal of Physics: Condensed Matter* 19.10 (Mar. 2007). Number: 10, p. 103201. ISSN: 0953-8984, 1361-648X. DOI: 10.1088/0953-8984/19/10/103201. URL: https://iopscience.iop.org/article/10.1088/0953-8984/19/10/103201.

[504] M. Wierzbicki and R. Swirkowicz. “Influence of interference effects on thermoelectric properties of double quantum dots”. en. In: *Physical Review B* 84.7 (Aug. 2011). Number: 7. ISSN: 1098-0121, 1550-235X. DOI: 10.1103/PhysRevB.84.075410. URL: https://link.aps.org/doi/10.1103/PhysRevB.84.075410.

[505] Jagadeesh S. Moodera, Guo-Xing Miao, and Tiffany S. Santos. “Frontiers in spin-polarized tunneling”. In: *Physics Today* 63.4 (Apr. 2010). 2023-01-03, pp. 46–51. ISSN: 0031-9228, 1945-0699. DOI: 10.1063/1.3397043. URL: http://doi.org/10.1063/1.3397043.

[506] David M.-T. Kuo, Shiue-Yuan Shiau, and Yia-chung Chang. “Theory of spin blockade, charge ratchet effect, and thermoelectrical behavior in serially coupled quantum dot system”. en. In: *Physical Review B* 84.24 (Dec. 2011). Number: 24. ISSN: 1098-0121, 1550-235X. DOI: 10.1103/PhysRevB.84.245303. URL: https://link.aps.org/doi/10.1103/PhysRevB.84.245303.

[507] Maciej Misiorny, Ireneusz Weymann, and Józef Barnaś. “Spin effects in transport through single-molecule magnets in the sequential and cotunneling regimes”. en. In: *Physical Review B* 79.22 (June 2009). Number: 22, p. 224420. ISSN: 1098-0121, 1550-235X. DOI: 10.1103/PhysRevB.79.224420. URL: https://link.aps.org/doi/10.1103/PhysRevB.79.224420.

[508] Sai Vinjanampathy and Janet Anders. “Quantum thermodynamics”. In: *CONTEMPORARY PHYSICS* 57.4 (Dec. 2016), pp. 545–579. ISSN: 0010-7514. DOI: 10.1080/00107514.2016.1201896.

[509] Brecht Donvil. “Thermodynamics of a periodically driven qubit”. en. In: *Journal of Statistical Mechanics: Theory and Experiment* 2018.4 (Apr. 2018). Number: 4, p. 043104. ISSN: 1742-5468. DOI: 10.1088/1742-5468/aab857. URL: https://iopscience.iop.org/article/10.1088/1742-5468/aab857.

[510] Johannes Roßnagel et al. “Nanoscale Heat Engine Beyond the Carnot Limit”. In: *Physical review letters* 112 (Jan. 2014), p. 030602. DOI: 10.1103/PhysRevLett.112.030602.

[511] Yang Xiao et al. *Thermodynamics and Fluctuations in Quantum Heat Engines under Reservoir Squeezing*. 2022. DOI: 10.48550/ARXIV.2209.05885. URL: https://arxiv.org/abs/2209.05885.

[512] M. Bowen et al. “Observation of Fowler–Nordheim hole tunneling across an electron tunnel junction due to total symmetry filtering”. en. In: *Physical Review B* 73.14 (Apr. 2006). Number: 14. ISSN: 1098-0121, 1550-235X. DOI: 10.1103/PhysRevB.73.140408. URL: https://link.aps.org/doi/10.1103/PhysRevB.73.140408.

[513] Samuel Larocque et al. “Shot Noise of a Temperature-Biased Tunnel Junction”. In: *Physical Review Letters* 125.10 (Sept. 2020). 2023-01-06. ISSN: 0031-9007, 1079-7114. DOI: 10.1103/PhysRevLett.125.106801. URL: https://link.aps.org/doi/10.1103/PhysRevLett.125.106801.

[514] Juan Pedro Cascales et al. “Shot Noise in Epitaxial Double-Barrier Magnetic Tunnel Junctions”. In: *IEEE Transactions on Magnetics* 49.7 (July 2013). 2024-02-22, pp. 4347–4350. ISSN: 0018-9464, 1941-0069. DOI: 10.1109/TMAG.2013.2243410. URL: http://ieeexplore.ieee.org/document/6559229/.

[515] Hui-Qiang Guo et al. “Low frequency noise in asymmetric double barrier magnetic tunnel junctions with a top thin MgO layer”. In: *Chinese Physics B* 24.7 (July 2015). 2024-02-22, p. 078504. ISSN: 1674-1056. DOI: 10.1088/1674-1056/24/7/078504. URL: https://iopscience.iop.org/article/10.1088/1674-1056/24/7/078504.

[516] Christian Ertler and Jaroslav Fabian. “Self-sustained Magnetoelectric Oscillations in Magnetic Resonant Tunneling Structures”. In: *Physical Review Letters* 101.7 (Aug. 2008). 2023-11-07, p. 077202. ISSN: 0031-9007, 1079-7114. DOI: https://doi.org/10.1103/PhysRevLett.101.077202. URL: https://link.aps.org/doi/10.1103/PhysRevLett.101.077202.

[517] Peiji Zhao, Dwight L. Woolard, and H. L. Cui. “Multisubband theory for the origination of intrinsic oscillations within double-barrier quantum well systems”. In: *Physical Review B* 67.8 (Feb. 2003). 2023-11-07, p. 085312. ISSN: 0163-1829, 1095-3795. DOI: 10.1103/PhysRevB.67.085312. URL: https://link.aps.org/doi/10.1103/PhysRevB.67.085312.

[518] Rui Bo et al. “Controllable spin diode based on a semiconductor quantum dot”. In: *Japanese Journal of Applied Physics* 61.6 (June 2022). 2023-11-02, p. 060910. ISSN: 0021-4922, 1347-4065. DOI: 10.35848/1347-4065/ac701e. URL: https://iopscience.iop.org/article/10.35848/1347-4065/ac701e.

[519] Giovanni Jona-Lasinio, Carlo Presilla, and Federico Capasso. “Chaotic quantum phenomena without classical counterpart”. In: *Physical Review Letters* 68.15 (Apr. 1992). 2023-11-07, pp. 2269–2272. ISSN: 0031-9007. DOI: 10.1103/PhysRevLett.68.2269. URL: https://link.aps.org/doi/10.1103/PhysRevLett.68.2269.

[520] J. Galan and E. Freire. “Chaos in a mean field model of coupled quantum wells; bifurcations of periodic orbits in a symmetric hamiltonian system”. In: *Reports on Mathematical Physics* 44.1-2 (Aug. 1999). 2023-11-07, pp. 87–94. ISSN: 00344877. DOI: 10.1016/S0034-4877(99)80148-7. URL: https://linkinghub.elsevier.com/retrieve/pii/S0034487799801487.

[521] Gonzalo Manzano, Francesco Plastina, and Roberta Zambrini. “Optimal Work Extraction and Thermodynamics of Quantum Measurements and Correlations”. en. In: *Physical Review Letters* 121.12 (Sept. 2018). Number: 12. ISSN: 0031-9007, 1079-7114. DOI: 10.1103/PhysRevLett.121.120602. URL: https://link.aps.org/doi/10.1103/PhysRevLett.121.120602.

[522] Sahand Hormoz. “Quantum collapse and the second law of thermodynamics”. en. In: *Physical Review E* 87.2 (Feb. 2013). Number: 2, p. 022129. ISSN: 1539-3755, 1550-2376. DOI: 10.1103/PhysRevE.87.022129. URL: https://link.aps.org/doi/10.1103/PhysRevE.87.022129.

[523] Seth Lloyd. “Use of mutual information to decrease entropy: Implications for the second law of thermodynamics”. en. In: *Physical Review A* 39.10 (May 1989). Number: 10, pp. 5378–5386. ISSN: 0556-2791. DOI: 10.1103/PhysRevA.39.5378. URL: https://link.aps.org/doi/10.1103/PhysRevA.39.5378.

[524] Yariv Yanay and Aashish A. Clerk. “Reservoir engineering of bosonic lattices using chiral symmetry and localized dissipation”. en. In: *Physical Review A* 98.4 (Oct. 2018). Number: 4, p. 043615. ISSN: 2469-9926, 2469-9934. DOI: 10.1103/PhysRevA.98.043615. URL: https://link.aps.org/doi/10.1103/PhysRevA.98.043615.

[525] Xin Li et al. *Reciprocal Reservoir Induced Non-Hermitian Skin Effect*. 2023. DOI: 10.48550/ARXIV.2307.15792. URL: https://arxiv.org/abs/2307.15792.

[526] Xiujuan Zhang et al. “A review on non-Hermitian skin effect”. en. In: *Advances in Physics: X* 7.1 (Dec. 2022). Number: 1, p. 2109431. ISSN: 2374-6149. DOI: 10.1080/23746149.2022.2109431. URL: https://www.tandfonline.com/doi/full/10.1080/23746149.2022.2109431.

[527] Georg Wolschin. “Nonlinear diffusion of fermions and bosons”. en. In: *Europhysics Letters* 140.4 (Nov. 2022). Number: 4, p. 40002. ISSN: 0295-5075, 1286-4854. DOI: 10.1209/0295-5075/aca17a. URL: https://iopscience.iop.org/article/10.1209/0295-5075/aca17a.

[528] Pham Nam Hai et al. “Electromotive Force and Huge Magnetoresistance in Magnetic Tunnel Junctions”. In: *Nature* 458.7237 (Mar. 2009). 2017-12-19, pp. 489–492. ISSN: 1476-4687. DOI: 10.1038/nature07879.

[529] M Bowen. “Atom-level electronic physicists are needed to develop practical engines with a quantum advantage”. In: *Npj Quantum Inf.* 9.1 (Mar. 2023).

[530] Michael Harder, Yongsheng Gui, and Can-Ming Hu. “Electrical detection of magnetization dynamics via spin rectification effects”. In: *Physics Reports* 661 (Nov. 2016). 2023-07-26, pp. 1–59. ISSN: 03701573. DOI: 10.1016/j.physrep.2016.10.002. URL: https://linkinghub.elsevier.com/retrieve/pii/S0370157316303167.

[531] Koichi Maezawa. *Resonant Tunneling Diodes*. Apr. 2005. DOI: 10.1002/0471654507.eme380. URL: http://dx.doi.org/10.1002/0471654507.eme380.

[532] B. K. Ridley. "Negative Differential Resistance: A Brief History and Review". In: *NATO ASI Series*. Springer US, 1993, pp. 1–21. ISBN: 9781461528227. DOI: 10.1007/978-1-4615-2822-7_1. URL: http://dx.doi.org/10.1007/978-1-4615-2822-7_1.

[533] D.J. Paul. "Nanoelectronics". In: *Encyclopedia of Physical Science and Technology*. Elsevier, 2003, pp. 285–301. DOI: 10.1016/b0-12-227410-5/00469-5. URL: http://dx.doi.org/10.1016/B0-12-227410-5/00469-5.

[534] L. Brillouin. "Can the Rectifier Become a Thermodynamical Demon?" In: *Physical Review* 78.5 (June 1950). 2024-03-20, pp. 627–628. ISSN: 0031-899X. DOI: 10.1103/PhysRev.78.627.2. URL: https://link.aps.org/doi/10.1103/PhysRev.78.627.2.

[535] Alois Marek. "A note to recent theories of brownian motion in non-linear systems". In: *Physica* 25.7–12 (Jan. 1959), pp. 1358–1367. ISSN: 0031-8914. DOI: 10.1016/0031-8914(59)90056-4. URL: http://dx.doi.org/10.1016/0031-8914(59)90056-4.

[536] I. M Sokolov. "On the energetics of a nonlinear system rectifying thermal fluctuations". In: *Europhysics Letters (EPL)* 44.3 (Nov. 1998). 2023-10-10, pp. 278–283. ISSN: 0295-5075, 1286-4854. DOI: 10.1209/epl/i1998-00470-4. URL: https://iopscience.iop.org/article/10.1209/epl/i1998-00470-4.

[537] I. M. Sokolov. "Reversible fluctuation rectifier". In: *Physical Review E* 60.4 (Oct. 1999). 2024-04-26, pp. 4946–4949. ISSN: 1063-651X, 1095-3787. DOI: 10.1103/PhysRevE.60.4946. URL: https://link.aps.org/doi/10.1103/PhysRevE.60.4946.

[538] M. R. Sears and W. M. Saslow. "Spin Accumulation at Ferromagnet/Non-magnetic Material Interfaces". In: *Physical Review B* 85.1 (Jan. 2012). arXiv:1108.4969 [cond-mat], p. 014404. ISSN: 1098-0121, 1550-235X. DOI: 10.1103/PhysRevB.85.014404. URL: http://arxiv.org/abs/1108.4969.

[539] Wayne M. Saslow. "Spin pumping of current in non-uniform conducting magnets". en. In: *Physical Review B* 76.18 (Nov. 2007). 2023-12-04, p. 184434. ISSN: 1098-0121, 1550-235X. DOI: 10.1103/PhysRevB.76.184434. URL: https://link.aps.org/doi/10.1103/PhysRevB.76.184434.

[540] Mark Johnson and R. H. Silsbee. "Thermodynamic analysis of interfacial transport and of the thermomagnetoelectric system". en. In: *Physical Review B* 35.10 (Apr. 1987). 2023-12-04, pp. 4959–4972. ISSN: 0163-1829. DOI: 10.1103/PhysRevB.35.4959. URL: https://link.aps.org/doi/10.1103/PhysRevB.35.4959.

[541] Lars Onsager. "Reciprocal Relations in Irreversible Processes. I." In: *Physical Review* 37.4 (Feb. 1931), pp. 405–426. ISSN: 0031-899X. DOI: 10.1103/physrev.37.405. URL: http://dx.doi.org/10.1103/physrev.37.405.

[542] J.-E. Wegrowe et al. "Magnetization reversal driven by spin-injection : a mesoscopic spin-transfer effect". In: *Physical Review B* 77.17 (May 2008). arXiv:0801.1019 [cond-mat], p. 174408. ISSN: 1098-0121, 1550-235X. DOI: 10.1103/PhysRevB.77.174408. URL: http://arxiv.org/abs/0801.1019.

[543] Jean-Eric Wegrowe and Henri-Jean Drouhin. "Spin-Currents and Spin-Pumping Forces for Spintronics". In: *Entropy* 13.2 (Jan. 2011). 2021-04-12, pp. 316–331. ISSN: 1099-4300. DOI: 10.3390/e13020316. URL: http://www.mdpi.com/1099-4300/13/2/316.

[544] Raymond A Serway. *Principles of physics*. 2nd ed. Florence, KY: Brooks/Cole, Aug. 1997.

[545] Jun-ichiro Inoue. "GMR, TMR and BMR". In: *Nanomagnetism and Spintronics*. Elsevier, 2009, pp. 15–92. DOI: 10.1016/b978-0-444-53114-8.00002-9. URL: http://dx.doi.org/10.1016/B978-0-444-53114-8.00002-9.

[546] Shu-Jen Wang et al. "Long spin diffusion lengths in doped conjugated polymers due to enhanced exchange coupling". In: *Nature Electronics* 2.3 (Mar. 2019), pp. 98–107. ISSN: 2520-1131. DOI: 10.1038/s41928-019-0222-5. URL: http://dx.doi.org/10.1038/s41928-019-0222-5.

[547] Xurong Shi et al. "Enhancement of spin diffusion length in tunneling junctions by benzene ring insertion into the saturated alkyl sulfonic acid". In: *Applied Physics Express* 15.7 (June 2022), p. 073001. ISSN: 1882-0786. DOI: 10.35848/1882-0786/ac7120. URL: http://dx.doi.org/10.35848/1882-0786/ac7120.

[548] G. Wang et al. "Gate control of the electron spin-diffusion length in semiconductor quantum wells". In: *Nature Communications* 4.1 (Sept. 2013). ISSN: 2041-1723. DOI: 10.1038/ncomms3372. URL: http://dx.doi.org/10.1038/ncomms3372.

[549] G. Zahnd et al. "Spin diffusion length and polarization of ferromagnetic metals measured by the spin-absorption technique in lateral spin valves". In: *Physical Review B* 98.17 (Nov. 2018). ISSN: 2469-9969. DOI: 10.1103/physrevb.98.174414. URL: http://dx.doi.org/10.1103/PhysRevB.98.174414.

[550] Richard P Feynman. *The Feynman lectures on physics*. Upper Saddle River, NJ: Pearson, Jan. 1963.

[551] Marcelo O. Magnasco and Gustavo Stolovitzky. "Feynman's Ratchet and Pawl". In: *Journal of Statistical Physics* 93.3/4 (Nov. 1998). 2024-03-20, pp. 615–632. ISSN: 0022-4715. DOI: 10.1023/B:JOSS.0000033245.43421.14. URL: http://link.springer.com/10.1023/B:JOSS.0000033245.43421.14.

[552] Juan M. R. Parrondo and Pep Español. “Criticism of Feynman’s analysis of the ratchet as an engine”. In: *American Journal of Physics* 64.9 (Sept. 1996). 2024-03-20, pp. 1125–1130. ISSN: 0002-9505, 1943-2909. DOI: 10.1119/1.18393. URL: https://pubs.aip.org/ajp/article/64/9/1125/1054886/Criticism-of-Feynman-s-analysis-of-the-ratchet-as.

[553] Moritz Frey and Hermann Grabert. “Current Noise in Tunnel Junctions”. In: *Fortschritte der Physik* 65.6-8 (June 2017). arXiv:1607.03803 [cond-mat], p. 1600055. ISSN: 0015-8208, 1521-3978. DOI: 10.1002/prop.201600055. URL: http://arxiv.org/abs/1607.03803.

[554] H.B. Sun and G.J. Milburn. “Quantum theory for current noise in resonant tunnelling devices”. In: *Superlattices and Microstructures* 23.3-4 (Mar. 1998). 2024-02-22, pp. 883–891. ISSN: 07496036. DOI: 10.1006/spmi.1997.0549. URL: https://linkinghub.elsevier.com/retrieve/pii/S0749603697905498.

[555] Igor Žutić et al. “Proximitized materials”. In: *Materials Today* 22 (Jan. 2019). 2023-12-04, pp. 85–107. ISSN: 13697021. DOI: 10.1016/j.mattod.2018.05.003. URL: https://www.sciencedirect.com/science/article/pii/S1369702118301111.

[556] Oldřich Coufal. “One Hundred and Fifty Years of Skin Effect”. In: *Applied Sciences* 13.22 (Nov. 2023). 2024-04-19, p. 12416. ISSN: 2076-3417. DOI: https://doi.org/10.3390/app132212416. URL: https://www.mdpi.com/2076-3417/13/22/12416.

[557] M. Ye. Zhuravlev, E. Y. Tsymbal, and A. V. Vedyayev. “Impurity-Assisted Interlayer Exchange Coupling across a Tunnel Barrier”. en. In: *Physical Review Letters* 94.2 (Jan. 2005). 2024-03-20, p. 026806. ISSN: 0031-9007, 1079-7114. DOI: 10.1103/PhysRevLett.94.026806. URL: https://link.aps.org/doi/10.1103/PhysRevLett.94.026806.

[558] Andreas J. Heinrich et al. “Quantum-coherent nanoscience”. In: *Nature Nanotechnology* 16.12 (Nov. 2021), pp. 1318–1329. ISSN: 1748-3395. DOI: 10.1038/s41565-021-00994-1. URL: http://dx.doi.org/10.1038/s41565-021-00994-1.

[559] Mirko Cinchetti, V. Alek Dediu, and Luis E. Hueso. “Activating the molecular spinterface”. In: *Nature Materials* 16.5 (Apr. 2017), pp. 507–515. ISSN: 1476-4660. DOI: 10.1038/nmat4902. URL: http://dx.doi.org/10.1038/nmat4902.

[560] Alexei N. Bogdanov and Christos Panagopoulos. “Physical foundations and basic properties of magnetic skyrmions”. In: *Nature Reviews Physics* 2.9 (July 2020), pp. 492–498. ISSN: 2522-5820. DOI: 10.1038/s42254-020-0203-7. URL: http://dx.doi.org/10.1038/s42254-020-0203-7.

[561] Shengyuan A. Yang et al. “Universal Electromotive Force Induced by Domain Wall Motion”. In: *Physical Review Letters* 102.6 (Feb. 2009). ISSN: 1079-7114. DOI: 10.1103/physrevlett.102.067201. URL: http://dx.doi.org/10.1103/PhysRevLett.102.067201.

[562] G E Volovik. “Linear momentum in ferromagnets”. In: *Journal of Physics C: Solid State Physics* 20.7 (Mar. 1987), pp. L83–L87. ISSN: 0022-3719. DOI: 10.1088/0022-3719/20/7/003. URL: http://dx.doi.org/10.1088/0022-3719/20/7/003.

[563] T. Schulz et al. “Emergent electrodynamics of skyrmions in a chiral magnet”. In: *Nature Physics* 8.4 (Feb. 2012), pp. 301–304. ISSN: 1745-2481. DOI: 10.1038/nphys2231. URL: http://dx.doi.org/10.1038/nphys2231.

[564] C. Castelnovo, R. Moessner, and S. L. Sondhi. “Magnetic monopoles in spin ice”. In: *Nature* 451.7174 (Jan. 2008), pp. 42–45. ISSN: 1476-4687. DOI: 10.1038/nature06433. URL: http://dx.doi.org/10.1038/nature06433.

[565] M. W. Ray et al. “Observation of Dirac monopoles in a synthetic magnetic field”. In: *Nature* 505.7485 (Jan. 2014), pp. 657–660. ISSN: 1476-4687. DOI: 10.1038/nature12954. URL: http://dx.doi.org/10.1038/nature12954.

[566] Xiao-Liang Qi et al. “Inducing a Magnetic Monopole with Topological Surface States”. In: *Science* 323.5918 (Feb. 2009), pp. 1184–1187. ISSN: 1095-9203. DOI: 10.1126/science.1167747. URL: http://dx.doi.org/10.1126/science.1167747.

[567] M. C. Diamantini, C. A. Trugenberger, and V. M. Vinokur. “Quantum magnetic monopole condensate”. In: *Communications Physics* 4.1 (Feb. 2021). ISSN: 2399-3650. DOI: 10.1038/s42005-021-00531-5. URL: http://dx.doi.org/10.1038/s42005-021-00531-5.

[568] F. Moulin. *Magnetic monopoles and Lorentz force*. 2002. DOI: 10.48550/ARXIV.MATH-PH/0203043. URL: https://arxiv.org/abs/math-ph/0203043.

[569] S. R. Giblin et al. “Creation and measurement of long-lived magnetic monopole currents in spin ice”. In: *Nature Physics* 7.3 (Feb. 2011), pp. 252–258. ISSN: 1745-2481. DOI: 10.1038/nphys1896. URL: http://dx.doi.org/10.1038/nphys1896.

[570] J. B. Gunn and J. L. Staples. “Spontaneous Reverse Current due to the Brillouin EMF in a diode”. In: *Applied Physics Letters* 14.2 (Jan. 1969). 2024-04-26, pp. 54–56. ISSN: 0003-6951, 1077-3118. DOI: 10.1063/1.1652709. URL: https://pubs.aip.org/apl/article/14/2/54/41611/SPONTANEOUS-REVERSE-CURRENT-DUE-TO-THE-BRILLOUIN.

[571] Elis Roberts, Jan Behrends, and Benjamin Béri. *Quantum tunneling in the presence of a topology-changing fermionic bath*. 2021. DOI: 10.48550/ARXIV.2112.14280. URL: https://arxiv.org/abs/2112.14280.

[572] Jean G. Van Bladel. *Electromagnetic Fields*. Wiley, Sept. 2006. ISBN: 9780470124581. DOI: 10.1002/047012458x. URL: http://dx.doi.org/10.1002/047012458X.

[573] "CRC Handbook of Chemistry and Physics, 86th Edition Edited by David R. Lide (National Institute of Standards and Technology). CRC Press (an imprint of Taylor and Francis Group): Boca Raton, FL. 2005. 2544 pp. $125.96. ISBN 0-8493-0486-5." In: *Journal of the American Chemical Society* 128.16 (Apr. 2006). Publisher: American Chemical Society, pp. 5585–5585. ISSN: 0002-7863. DOI: 10.1021/ja0598681. URL: https://doi.org/10.1021/ja0598681.

[574] D. J. Kim et al. "Control of defect-mediated tunneling barrier heights in ultrathin MgO films". en. In: *Applied Physics Letters* 97.26 (Dec. 2010). Number: 26, p. 263502. ISSN: 0003-6951, 1077-3118. DOI: 10.1063/1.3531652. URL: http://aip.scitation.org/doi/10.1063/1.3531652.

[575] Aaron M. Drews, Mikolaj Kowalik, and Kyle J. M. Bishop. "Charge and force on a conductive sphere between two parallel electrodes: A Stokesian dynamics approach". In: *Journal of Applied Physics* 116.7 (Aug. 2014). 2023-02-13, p. 074903. ISSN: 0021-8979, 1089-7550. DOI: 10.1063/1.4893308. URL: http://aip.scitation.org/doi/10.1063/1.4893308.

[576] David R Lide et al. *CRC Handbook of Chemistry and Physics*. CRC Press, June 2016. ISBN: 9781315380476. DOI: 10.1201/9781315380476. URL: http://dx.doi.org/10.1201/9781315380476.

[577] Michael A. Nielsen, Isaac Chuang, and Lov K. Grover. "Quantum Computation and Quantum Information". In: *American Journal of Physics* 70.5 (May 2002), pp. 558–559. ISSN: 0002-9505. DOI: 10.1119/1.1463744. eprint: https://pubs.aip.org/aapt/ajp/article-pdf/70/5/558/7529938/558_2_online.pdf. URL: https://doi.org/10.1119/1.1463744.

[578] P. Kammerlander and J. Anders. "Coherence and measurement in quantum thermodynamics". In: *Scientific Reports* 6.1 (Feb. 2016). DOI: 10.1038/srep22174. URL: https://doi.org/10.1038/srep22174.

[579] Guillaume Gauthier et al. "Giant vortex clusters in a two-dimensional quantum fluid". en. In: *Science* 364.6447 (June 2019). Number: 6447, pp. 1264–1267. ISSN: 0036-8075, 1095-9203. DOI: 10.1126/science.aat5718. URL: https://www.science.org/doi/10.1126/science.aat5718.

Mathieu LAMBLIN

Quantum Spintronic Energy Harvesters

Résumé

Les moteurs quantiques promettent de réaliser des sources d'énergie abondantes, denses et respectueuses de l'environnement.

Cette thèse montre expérimentalement que des jonctions ferromagnétiques tunnel contenant des impuretés magnétiques peuvent servir pour le stockage de l'information et la récolte d'énergie.

Ce travail propose ensuite trois modèles théoriques permettant d'expliquer l'origine de la génération d'énergie observée : un modèle quantique microscopique basé sur une chaîne de spin connectée à deux réservoirs électroniques polarisés, un modèle phénoménologique mésoscopique qui repose sur un matériau non-linéaire rectifiant les fluctuations magnétiques à l'interface entre deux électrodes ferromagnétiques et un électronique macroscopique qui étudie la caractéristique de deux diodes de spin en parallèle.

Les conclusions similaires de ces trois approches montrent donc la possibilité de récolter l'énergie magnétique entre deux réservoirs au moyen d'une interface microscopique.

Mots clés : Spintronique, Thermodynamique Quantique, Jonctions Magnétiques Tunnel, Démon de Maxwell, Boites Quantiques, Fluctuations Quantiques, Mesure Quantique, Intrication, Cohérence Quantique, Électronique Stochastique, Blocage de Coulomb, Magnétorésistance, Memristance.

Résumé en anglais

Quantum engines have attracted extensive research as they give us a glimpse of abundant, dense, and environmentally friendly power sources.

This thesis experimentally studies ferromagnetic tunnel junctions containing magnetic impurities which can be used for information storage and energy harvesting.

Then, this work proposes three theoretical models that explain the observed energy generation: a microscopic quantum model in which a spin chain is connected to two spin-polarized electronic reservoirs, a phenomenological mesoscopic model based on a non-linear material rectifying the magnetic fluctuations at the interface between two misaligned ferromagnetic electrodes, and an electronic macroscopic model which studies the characteristic of two parallel spin diodes.

The concomitant conclusions of those three approaches thus show the possibility of harvesting the magnetic energy between two reservoirs through a microscopic interface.

Keywords: Spintronics, Quantum Thermodynamics, Magnetic Tunnel Junctions, Maxwell's Demon, Quantum Dots, Quantum Fluctuations, Quantum Measurement, Quantum Entanglement, Quantum Coherence, Stochastic Electronics, Coulomb Blockade, Magnetoresistance, Memristance.